

# AGARD

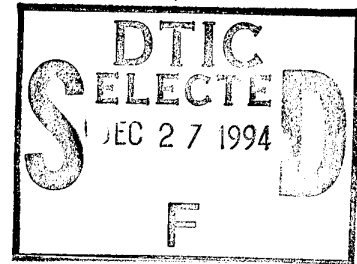
ADVISORY GROUP FOR AEROSPACE RESEARCH & DEVELOPMENT

7 RUE ANCELLE, 92200 NEUILLY-SUR-SEINE, FRANCE

AGARD REPORT 803

## Optimum Design Methods for Aerodynamics

(Les Méthodes de Conception Optimale  
pour l'Aérodynamique)



*The material assembled in this report was prepared under the combined sponsorship of the AGARD Fluid Dynamics Panel, the Consultant and Exchange Program of AGARD, and the von Karman Institute (VKI) for Fluid Dynamics. It was presented at an AGARD-FDP-VKI Special Course at the VKI, Rhode-Saint-Genèse, Belgium, 25-29 April 1994.*

19941221 067



**NORTH ATLANTIC TREATY ORGANIZATION**

This document has been approved  
for public release and sale; its  
distribution is unlimited.

Published November 1994

Distribution and Availability on Back Cover



# The Mission of AGARD

According to its Charter, the mission of AGARD is to bring together the leading personalities of the NATO nations in the fields of science and technology relating to aerospace for the following purposes:

- Recommending effective ways for the member nations to use their research and development capabilities for the common benefit of the NATO community;
- Providing scientific and technical advice and assistance to the Military Committee in the field of aerospace research and development (with particular regard to its military application);
- Continuously stimulating advances in the aerospace sciences relevant to strengthening the common defence posture;
- Improving the co-operation among member nations in aerospace research and development;
- Exchange of scientific and technical information;
- Providing assistance to member nations for the purpose of increasing their scientific and technical potential;
- Rendering scientific and technical assistance, as requested, to other NATO bodies and to member nations in connection with research and development problems in the aerospace field.

The highest authority within AGARD is the National Delegates Board consisting of officially appointed senior representatives from each member nation. The mission of AGARD is carried out through the Panels which are composed of experts appointed by the National Delegates, the Consultant and Exchange Programme and the Aerospace Applications Studies Programme. The results of AGARD work are reported to the member nations and the NATO Authorities through the AGARD series of publications of which this is one.

Participation in AGARD activities is by invitation only and is normally limited to citizens of the NATO nations.

The content of this publication has been reproduced directly from material supplied by AGARD or the authors.

Published November 1994

Copyright © AGARD 1994  
All Rights Reserved

ISBN 92-836-1007-5



Printed by Canada Communication Group  
45 Sacré-Cœur Blvd., Hull (Québec), Canada K1A 0S7

# Recent Publications of the Fluid Dynamics Panel

## AGARDOGRAPHS (AG)

**Scale Effects on Aircraft and Weapon Aerodynamics**  
AGARD AG-323, July 1994

**Design and Testing of High-Performance Parachutes**  
AGARD AG-319, November 1991

**Experimental Techniques in the Field of Low Density Aerodynamics**  
AGARD AG-318 (E), April 1991

**Techniques Expérimentales Liées à l'Aérodynamique à Basse Densité**  
AGARD AG-318 (FR), April 1990

**A Survey of Measurements and Measuring Techniques in Rapidly Distorted Compressible Turbulent Boundary Layers**  
AGARD AG-315, May 1989

## REPORTS (R)

**Missile Aerodynamics**  
AGARD R-804, Special Course Notes, June 1994

**Progress in Transition Modelling**  
AGARD R-793, Special Course Notes, April 1994

**Shock-Wave/Boundary-Layer Interactions in Supersonic and Hypersonic Flows**  
AGARD R-792, Special Course Notes, August 1993

**Unstructured Grid Methods for Advection Dominated Flows**  
AGARD R-787, Special Course Notes, May 1992

**Skin Friction Drag Reduction**  
AGARD R-786, Special Course Notes, March 1992

## ADVISORY REPORTS (AR)

**Quality Assessment for Wind Tunnel Testing**  
AGARD AR-304, Report of WG15, July 1994

**Air Intakes of High Speed Vehicles**  
AGARD AR-270, Report of WG13, September 1991

**Appraisal of the Suitability of Turbulence Models in Flow Calculations**  
AGARD AR-291, Technical Status Review, July 1991

**Rotary-Balance Testing for Aircraft Dynamics**  
AGARD AR-265, Report of WG11, December 1990

**Calculation of 3D Separated Turbulent Flows in Boundary Layer Limit**  
AGARD AR-255, Report of WG10, May 1990

## CONFERENCE PROCEEDINGS (CP)

**Wall Interference, Support Interference and Flow Field Measurements**  
AGARD CP-535, July 1994

**Computational and Experimental Assessment of Jets in Cross Flow**  
AGARD CP-534, November 1993

**High-Lift System Aerodynamics**  
AGARD CP-515, September 1993

**Theoretical and Experimental Methods in Hypersonic Flows**  
AGARD CP-514, April 1993

**Aerodynamic Engine/Airframe Integration for High Performance Aircraft and Missiles**  
AGARD CP-498, September 1992

**Effects of Adverse Weather on Aerodynamics**  
AGARD CP-496, December 1991

**Manoeuvring Aerodynamics**  
AGARD CP-497, November 1991

**Vortex Flow Aerodynamics**  
AGARD CP-494, July 1991

**Missile Aerodynamics**  
AGARD CP-493, October 1990

**Aerodynamics of Combat Aircraft Controls and of Ground Effects**  
AGARD CP-465, April 1990

**Computational Methods for Aerodynamic Design (Inverse) and Optimization**  
AGARD CP-463, March 1990

**Applications of Mesh Generation to Complex 3-D Configurations**  
AGARD CP-464, March 1990

**Fluid Dynamics of Three-Dimensional Turbulent Shear Flows and Transition**  
AGARD CP-438, April 1989

**Validation of Computational Fluid Dynamics**  
AGARD CP-437, December 1988

**Aerodynamic Data Accuracy and Quality: Requirements and Capabilities in Wind Tunnel Testing**  
AGARD CP-429, July 1988

**Aerodynamics of Hypersonic Lifting Vehicles**  
AGARD CP-428, November 1987

**Aerodynamic and Related Hydrodynamic Studies Using Water Facilities**  
AGARD CP-413, June 1987

**Applications of Computational Fluid Dynamics in Aeronautics**  
AGARD CP-412, November 1986

**Store Airframe Aerodynamics**  
AGARD CP-389, August 1986

**Unsteady Aerodynamics — Fundamentals and Applications to Aircraft Dynamics**  
AGARD CP-386, November 1985

**Aerodynamics and Acoustics of Propellers**  
AGARD CP-366, February 1985

**Improvement of Aerodynamic Performance through Boundary Layer Control and High Lift Systems**  
AGARD CP-365, August 1984

**Wind Tunnels and Testing Techniques**  
AGARD CP-348, February 1984

**Aerodynamics of Vortical Type Flows in Three Dimensions**  
AGARD CP-342, July 1983

**Missile Aerodynamics**  
AGARD CP-336, February 1983

**Prediction of Aerodynamic Loads on Rotorcraft**  
AGARD CP-334, September 1982

**Wall Interference in Wind Tunnels**  
AGARD CP-335, September 1982

# Preface

This volume is a compilation of the edited proceedings of the "Optimum Design Methods for Aerodynamics" course held at the von Karman Institute for Fluid Dynamics in Rhode Saint Genèse Belgium, 25-29 April 1994. The material assembled in this Report was prepared and presented under the combined sponsorship of the AGARD Fluid Dynamics Panel, and the von Karman Institute for Fluid Dynamics.

Techniques for designing modern aerospace systems which either maximize a beneficial aerodynamic performance feature, or minimize a less desirable characteristic while recognizing other design constraints, have moved from the research lab to the design room in recent years. This has become possible because of the integration of efficient aerodynamic and geometric codes with optimization methods to form efficient, and powerful, design and analysis computer tools. The objective of this course was to distribute and share fundamental information on the development and use of these tools.

# Préface

Ce volume est un recueil des textes présentés lors du Cours sur «Les méthodes de calcul optimisées pour l'aérodynamique» organisé par l'Institut Von Karman de dynamique des fluides à Rhode Saint Genèse en Belgique du 25 au 29 avril 1994.

Les cours contenus dans ce rapport ont été élaborés et présentés sous l'égide conjointe du Panel AGARD de la dynamique des fluides et l'Institut Von Karman de dynamique des fluides.

Des techniques de conception de systèmes aérospatiaux modernes soit qui maximisent une caractéristique de performance aérodynamique, soit qui minimisent une caractéristique moins avantageuse, tout en tenant compte des autres contraintes de conception, sont passées du laboratoire de recherche au bureau d'étude en l'espace de quelques années. Ceci est devenu possible grâce à l'association de codes géométriques et aérodynamiques performants à des méthodes d'optimisation, ce qui a permis de réaliser des outils informatiques d'analyse et de conception puissants et efficaces.

Ce cours a eu pour objectif de diffuser et de commenter les informations de base concernant le développement et la mise en œuvre de ces outils.

# Special Course Staff

## SPECIAL COURSE DIRECTOR

Professor J. Periaux  
Dassault Aviation — DGT/DEA  
78 Quai Marcel Dassault  
92214 St. Cloud Cedex  
France

## LECTURERS

Professor O. Pironneau  
University Paris VI  
Labo Analyse Numérique  
Tour 55-65-Place Jussieu 4  
75252 Paris Cedex 05  
France

Dr. A. Van der Velden  
Deutsche Aerospace Airbus  
EF 14 Aerodynamic Design  
Huenefeldstrasse 1-5  
28199 Bremen  
Germany

Prof P. Chaviaropoulos  
Nat. Techn. Univ. of Athens  
LTT-Section Fluid  
Dept. Mech.Eng  
P.O. Box 64069  
15710 Athens  
Greece

Professor Th. Labrujere  
Theor. Aerodyn. Fluid Dynamics Div.  
NLR  
Anthony Fokkerweg 2  
1059 CM Amsterdam  
Netherlands

Professor A. Jameson  
Princeton University  
Aerospace Eng.  
MAE Dept. — D309 E  
Princeton NJ 08544-5213  
United States

Dr. M.D. Salas  
NASA Langley Research Center  
Fluid Mechanics Division  
Mail Code 159  
Hampton Virginia 23681-0001  
United States

## SPECIAL COURSE COORDINATOR

Professor G. Degrez  
Von Karman Institute for Fluid Dynamics  
Chaussee de Waterloo, 72  
1640 Rhode-Saint-Genèse  
Belgium

## PANEL EXECUTIVE

Mr. J.K. Molloy

**Mail from Europe:**  
AGARD/OTAN  
Attn: FDP Executive  
7, rue Ancelle  
92200 Neuilly-sur-Seine  
France

**Mail from US and Canada:**  
AGARD/NATO  
Attn: FDP Executive  
Unit 21551  
APO AE 09777

# Contents

	Page
<b>Recent Publications of the Fluid Dynamics Panel</b>	iii
<b>Preface/Préface</b>	v
<b>Special Course Staff</b>	vi
	<b>Reference</b>
<b>Single-Pass Method for the Solution of Inverse Potential and Rotational Problems. Part I: 2-D and Quasi 3-D Theory and Application</b> by P. Chaviaropoulos, V. Dedoussis and K.D. Papailiou	1
<b>Single-Pass Method for the Solution of Inverse Potential and Rotational Problems. Part II: Fully 3-D Potential Theory and Applications</b> by P. Chaviaropoulos, V. Dedoussis and K.D. Papailiou	2
<b>Optimum Aerodynamic Design via Boundary Control</b> by A. Jameson	3
<b>Residual-Correction Type and Related Computational Methods for Aerodynamic Design — Part I: Airfoil and Wing Design</b> by Th. Labrujère	4
<b>Residual-Correction Type and Related Computational Methods for Aerodynamic Design — Part II: Multi-Point Airfoil Design</b> by Th. Labrujère	5
<b>Optimal Shape Design for Aerodynamics</b> by O. Pironneau	6
<b>Airfoil Optimization by the One-Shot Method</b> by G. Kuruvila, Shlomo Ta'asan and M.D. Salas	7
<b>Tools for Applied Engineering Optimization</b> by A. Van der Velden	8
<b>The Global Aircraft Shape</b> by A. Van der Velden	9
<b>Aerodynamic Shape Optimization</b> by A. Van der Velden	10
<b>Review of the Europt Project Aero-0026</b> by B. Mantel, J. Periaux and B. Stoufflet	11

**SINGLE-PASS METHOD FOR THE SOLUTION OF INVERSE  
POTENTIAL AND ROTATIONAL PROBLEMS.  
PART I: 2-D AND QUASI 3-D THEORY AND APPLICATION**

P. Chaviaropoulos, V. Dedoussis<sup>1</sup> and K.D. Papailiou

National Technical University of Athens

Lab. of Thermal Turbomachines

P.O. Box 64069, 157 10 Athens, Greece.

### SUMMARY

A methodology for the solution of the 2-D and 3-D inverse inviscid subsonic flow problem is introduced. The proposed methodology handles the 2-D and axisymmetric rotational and the 3-D potential target pressure problem in a single-pass manner. The method is based on a potential function/stream function formulation where the physical space is mapped onto a natural one using the potential and stream function(s) as body-fitted coordinates. A novel procedure based on differential geometry and generalized tensor analysis arguments is employed to formulate the method in a modular way. The governing equations for the inverse problem are derived through the metrics compatibility condition on the natural space. Geometry is determined by integrating generalized Frenet equations along the natural coordinate lines. Rotationality, when present, is due to incoming (stagnation) thermodynamic quantities and/or pre-swirl gradients. The Clebsch formulation is, then, adopted to decompose the velocity field into a potential and a rotational part. To validate the method inverse calculation results are compared to results of direct "reproduction" calculations. The design procedure of some optimized shapes is also presented. Part I of this lecture focuses on 2-D and axisymmetric inverse potential or rotational flow problems, while the fully 3-D inverse potential problem is considered in Part II.

### LIST OF SYMBOLS

$\alpha, b, c, d, e, f$  velocity Eq.(31) coefficients  
 $c_p, c_y$  specific heats  
 $\vec{g}_i, \vec{g}^j$  covariant and contravariant base vectors of natural  $(\phi, \psi)$  coordinate system  
 $g^{ij}$  conjugate metrics tensor of natural  $(\phi, \psi)$  coordinate system  
 $G_{ij}$  metrics tensor of computational  $(\xi, \eta)$  coordinate system  
 $h$  enthalpy  
 $\vec{L}$  position vector  
 $K$  Riemann curvature of the (S) surface  
 $M$  Mach number  
 $\vec{N}$  unit base vector in the peripheral direction

$s$  entropy  
 $T$  temperature  
 $\vec{V}$  velocity vector  
 $(x, y)$  (physical) Cartesian coordinate system  
 $\alpha$  drift function  
 $\alpha_h, \alpha_s, \alpha_v$  Clebsch decomposition coefficients associated with enthalpy, entropy and swirl gradients  
 $\beta$  angle between  $\nabla_s \phi, \nabla_s \psi$   
 $\gamma$  specific heats ratio  
 $\Gamma_{ij}^l$  Christoffel symbol of second kind  
 $\lambda$  entropy gradient coefficient  
 $\mu$  swirl gradient coefficient  
 $\nu$  total enthalpy gradient coefficient  
 $(\xi, \eta)$  computational coordinate system  
 $\rho$  density  
 $\tilde{\rho}(=r\rho)$  modified density  
 $(\phi, \psi)$  potential function, stream function  
 $\vec{\Omega}$  natural coordinate system  
 $\vec{\omega}$  vorticity vector

### Subscripts

$i, j, l, q (=1, 2)$  covariant tensor indices  
 $o$  known position indicator  
 $ref$  reference quantity  
 $t$  total quantity  
 $s$  (s) surface component  
 $N$  N-wise component  
 $\xi, \eta, \phi, \psi$  partial derivatives with respect to  $\xi, \eta, \phi$  or  $\psi$  respectively

### Superscripts

$i, j, l, q (=1, 2)$  contravariant tensor indices

### 1. INTRODUCTION

The operation of aircrafts, propulsion and energy conversion systems and process industry equipment relies heavily on the performance of their aerodynamic components, such as air intakes, nozzles, wings, cascades, etc. The development of reliable automated methods which will reduce the human expertise interference in the design loop and will increase

<sup>1</sup> Also in Dept. of Industrial Management, University of Piraeus, 185 34 Piraeus, Greece.

the quality and duration of the products is one of the CFD challenges for the next decade. Although the optimum design concept is so old as the theory of aerodynamics itself, the maturation of analysis methods and the continuously increasing computer power have placed it back in stage. A comprehensive review of the evolution of optimal shape design methods has been presented by Dulikravich (Ref.1) and more recently by Labrujere and Sloof (Ref.2).

In designing aerodynamic components engineers aim to minimize or prevent losses associated with wall boundary layer separation and/or the occurrence of a shock. It is known that boundary layer behavior, as well as the occurrence of a shock, is controlled by the characteristics of the pressure distribution along the walls of the flow field. The need, therefore, of having accurate and efficient inverse design methods that provide the designer with a shape that corresponds to a prescribed wall pressure or velocity (for inviscid flow models) distribution is evident.

First attempts to develop such target pressure methods are traced back in mid-forties when inverse potential methods based on conformal mapping and potential theory have been applied to the design of airfoils. In the fifties, Stanitz (Ref.3) developed his inverse potential method for compressible flows. Applying a body-fitted coordinate transformation, Stanitz derived the inverse potential flow equations on a "natural" computational plane employing the potential function and the stream function as independent variables. The two-dimensional (2-D) inverse problem can then be solved if "target" velocity (or pressure) distributions are imposed over the complete boundaries of the domain. Stanitz's method being more flexible than the conformal mapping ones has been extended to axisymmetric flows (Ref.4) as well as to turbomachinery flows including the planar and the axisymmetric rotating or non-rotating cascades (Refs 5-7). The 2-D potential target pressure problem has been recently reconsidered by Barron (Ref.8), who provided an alternative formulation using the Von-Mises transformation by Volpe (Ref.9) who developed iterative profile closure conditions for compressible flows and by the present authors (Ref.10) who reformulated the airfoil design problem using differential geometry principles.

The computational cost of all the above-mentioned "target pressure" -inverse- methods is equivalent to that of analysis -direct- methods. For reasons which will be explained below we will refer to these methods as "single-pass" methods. The "single-pass" methods are very efficient in terms of the computational cost and provide a physical insight to the design problem. Conceptually, however, they are restricted to 2-D potential flows only. Some extensions to rotational flows using the Clebsch transformation are reported by Borges (Ref.11) and by the present authors (Refs 12,13). Stanitz (Ref.14) extended his original 2-D potential method to three dimensional (3-D) flows. A disadvantage of the

"single-pass" methods is related to their inability to incorporate flow or geometrical side-constraints. Thus, the designers expertise remains crucial for determining the "appropriate" target pressure distribution.

In the effort to circumvent the drawbacks of "single-pass" methods, optimization methods appeared in the design field as an alternative. These methods solve a general minimization problem, the cost function of which expresses desired flow properties along with flow or geometrical constraints. This cost function is computed using a standard direct solver and the designer may decide upon the complexity level of the state equations to be solved. The solution of the optimization problem (the "target pressure" problem being one variant) is obtained as a sequence of direct problem solutions. Although the formulation of the design problem seems to be straightforward, these methods are still time consuming (some hundreds of direct problems are sometimes solved in the optimization process, plus the regriding overhead) while in complicated 3-D flows the grid deformation and adaption problem may become crucial for the convergence of the algorithm. Convergence may be accelerated using suitable parametrization techniques (Ref.15) or hierarchical optimization techniques (Ref.16). An alternative approach springs from the reformulation of the general optimization problem using optimal control theory (Ref.17). Then the descend direction may be obtained from the solution of an "adjoint" state equation which is usually similar to the state equation itself. This technique reduces the computational cost a lot, provided that the adjoint equation exists.

Although optimization methods appear to be a remedy for the design problem this is not completely true. There are difficulties in specifying the appropriate cost function for a precise problem. If, for example, the shock drag minimization problem is to be solved for a transonic airfoil, a hanging shock solution may be obtained if no curvature constraints are imposed on the profile. Optimization of lift versus drag at a specific incidence may cause, as a second example, severe off-design problems. It seems that the formulation of the optimization problem using global flow measures (such as lift and drag) in an automated procedure is a very risky policy. It seems much better to control the flow behaviour at the local level and that explains why the "target pressure" conditions are widely used as optimality conditions by the optimisation methods as well. Even in this case, however, the results may be misleading. If, for instance the prescribed inviscid target pressure distribution is not consistent in terms of profile closure, the minimization algorithm will provide a solution which may be far from the desired one in physical terms (the transition point location may be altered or flow separation may be produced because of local deceleration of the flow). Additionally, optimization methods provide no information on the existence and the uniqueness of the solution of a flow (design) problem. They

lack, therefore, the physical insight of "single-pass" methods.

The purpose of Part I of the lecture is to present a unified methodology for the solution of the inverse target pressure problem in a "single-pass" manner. The proposed methodology tackles inviscid rotational subsonic flows which develop on arbitrary prescribed surfaces in a quasi-3D manner and can be applied to the design of 2-D or axisymmetric internal (ducts, nozzles, cascades) and 2-D external (airfoils) flow configurations.

The method is based on the potential function - streamfunction formulation and in that respect presents some similarities with the one developed by Stanitz (Ref.3) for irrotational flows. Clebsch formulation is employed to decompose the velocity vector into a "potential" and a rotational part, the latter expressed as the product of a (scalar) drift function with the stream function gradient. Exploiting the fact that in inviscid flows, solid boundaries are streamlines, a body-fitted coordinate transformation is carried out which maps the physical space (on which the geometry of the boundaries is sought) onto the potential function-streamfunction  $(\phi, \psi)$  space. The potential function and the streamfunction are the independent non-orthogonal curvilinear coordinates.

An interesting novelty of the method is that the main second-order nonlinear elliptic partial differential equation (PDE) for the velocity magnitude is derived using differential geometry arguments rather than manipulating the basic flow equations themselves. This equation results directly from the metrics compatibility condition which is expressed in terms of flow quantities on the natural  $(\phi, \psi)$  space. This equation, in conjunction with a transport equation for the drift function of the Clebsch decomposition, provide the solution of the flow field.

The calculation procedure involves two main steps. In the first step the discretized governing equations are solved for the flow quantities using a fast iterative incomplete factorization scheme. Having calculated the flow field, the corresponding geometry is determined, by straightforward integration of Frenet equations along potential lines and/or streamlines. For 2-D flows the flow and geometry calculations are completely decoupled. In axisymmetric flows, however, the radial coordinate  $R$  appears in the expressions of the metrics implying that the flow field and the geometry solutions are coupled.

To validate the method several "reproduction" calculations, including 2-D and axisymmetric nozzles and ducts, 2-D airfoils, 2-D and quasi 3-D axisymmetric non-rotating cascades, have been carried out. The favorable comparisons between inverse results and those of direct, analysis, codes indicate the reliability of the method. Results concerning the design of optimized blades for horizontal axis wind turbines

are also presented.

## 2. ASSUMPTIONS AND BASIC EQUATIONS

The design method proposed in this lecture concerns steady, subsonic, inviscid and adiabatic flows of a perfect gas. Rotationality, when present, is due to incoming (stagnation) thermodynamic quantities and or pre-swirl (in axisymmetric flows) gradients. In order to present a unified theory for 2-D and quasi 3-D flows we consider the conservation laws which govern the flow field developing on an arbitrary shaped stream surface (S) with varying streamtube thickness  $\Delta n$ . This surface may represent the plane of a 2-D flow, or the meridional plane of an axisymmetric flow, or the  $(S_1)$  -blade to blade- surface of a peripheral cascade.

Under the above assumptions, the (unified) conservation laws read.

### Continuity equation

$$\nabla_S \cdot (\tilde{\rho} \vec{v}_S) = 0 \quad (1)$$

### Momentum equation

(S) surface component

$$\vec{v}_S \times \vec{\Omega}_N = \nabla_S h_t - T \nabla_S S - \frac{V_N}{R} \nabla_S (RV_N) \quad (2)$$

normal (to S-surface) component

$$\vec{v}_S \cdot \nabla_S (RV_N) = 0 \quad (3)$$

### Energy equation

$$\vec{v}_S \cdot \nabla_S h_t = 0 \quad (4)$$

Subscript S denotes properties on the (S) surface and subscript N properties along the normal to the (S) surface direction.  $\nabla_S$  stands for the surface gradient operator. The defining relation for the N-wise vorticity component  $\vec{\Omega}_N$  is:

$$\vec{\Omega}_N = \nabla_S \times \vec{v}_S \quad (5)$$

When an axisymmetric flow is considered  $R$  is a genuine variable representing the radial distance from the axis of symmetry. The definition of the modified density  $\tilde{\rho}$  and the normal velocity component  $V_N$  for the three different cases which are considered here is given in Table 1.

(S) surface	$\bar{\rho}$	$V_N$
2-D plane flow	$\rho$	0
axisymmetric flow	$\rho R$	Peripheral Vel. $V_u$
blade to blade flow	$\rho \Delta n$	0

Table 1

Rearranging Eq. (2) and taking into account Eqs (3) and (4), we get the entropy conservation law

$$\vec{v} \cdot \nabla_S S = 0 \quad (6)$$

The above system of equations is supplemented by the following density equation:

$$\left( \frac{\rho}{\rho_{ref}} \right)^{\gamma-1} = \frac{h}{h_{ref}} e^{-\left( \frac{s-s_{ref}}{c_v} \right)} \quad (7)$$

where subscript ref denotes reference conditions and  $\gamma$  is the ratio of specific heats  $c_p/c_v$ .

The perfect gas assumption implies that enthalpy changes are proportional to those of temperature, i.e.  $dh = c_p dT$ . The stagnation enthalpy  $h_t$  is defined as

$$h_t = h + \frac{1}{2} (V_s^2 + V_N^2) \quad (8)$$

### 3. THE INVERSE TARGET VELOCITY PROBLEM

For a given geometry, the solution of Eqs (1) to (8) supplemented by an appropriate set of boundary conditions, provides the complete inviscid flow field. This solution is called a *direct* solution of the flow problem. When the inverse problem is considered, we are looking for the geometry which exhibits on it (i.e. on the boundary of the flow domain) certain prescribed flow qualities. Evidently, the steady Eqs (1) to (8) have to be satisfied by the inverse solver.

In the present work, the inverse target velocity problem which is tackled, may be defined as follows:

*"For a given shape of the (S) surface, inflow conditions  $h_{t,s}, V_N, |V_S|$  as well as prescribed magnitude of the velocity  $V_S$  along the lateral boundaries -solid walls- (in terms of their arc length), determine: (i) the flow field which satisfies the inviscid conservation laws and (ii) the corresponding geometry".*

As it will be demonstrated below this inverse target velocity problem is a well-posed one.

## 4. POTENTIAL-TYPE/STREAM FUNCTION FORMULATION

The purpose of this section is to introduce the potential function and the stream function which will serve as "natural coordinates" in the formulation of the present inverse design method.

### 4.1 Stream Function

A stream function on the (S) surface is introduced through the following relation

$$\bar{\rho} \vec{v}_S = \nabla_S \psi \times \vec{N} \quad (9)$$

where  $\vec{N}$  is the unit vector normal to the (S) surface. The stream function is defined in such a way so that the continuity Eq.(1) is satisfied identically. Note that the definition of the stream function for the general case is analogous to the usual two-dimensional one with the exception that the density is replaced by the modified density term  $\bar{\rho}$ .

### 4.2 Clebsch Formulation

Clebsch formulation (Ref.18) is used to decompose the surface velocity field into an irrotational and a rotational part is usually expressed as a linear combination of  $\nabla_S h_t$ ,  $\nabla_S s$  and  $\nabla_S (RV_N)$  which are responsible for the rotational character of the flow [see Eq.(2)]. Since the above gradients are normal to the velocity vector  $\vec{V}_S$  and lie on (S) they are parallel to one another. Taking advantage of this property one may express the rotational part of the velocity using one gradient, only, and a single coefficient (e.g. Ref.12). In order to treat all kinds of rotational flow in a unified way, a variant of the Clebsch formulation based on the stream function was adopted.

The Clebsch decomposition of  $\vec{V}_S$  used here reads:

$$\vec{V}_S = \nabla_S \phi + \alpha \nabla_S \psi \quad (10)$$

where  $\phi$  is the potential function on the (S) surface and  $\alpha$  is a generalized drift function. It is emphasized that in potential flows  $\alpha$  vanishes yielding the standard expression for the velocity vector  $\vec{V}_S = \nabla_S \phi$ . Eq.(9) indicates that  $\nabla_S \psi$ , being normal to  $\vec{V}_S$ , is parallel to  $\nabla_S h_t$ ,  $\nabla_S s$  and  $\nabla_S (RV_N)$ . Introducing the coefficients  $\lambda, \mu, \nu$  we may write:

$$\nabla_S h_t = \lambda \nabla_S \psi, \quad \nabla_S s = \mu \nabla_S \psi, \quad \nabla_S (RV_N) = \nu \nabla_S \psi \quad (11)$$

Applying the surface curl operator on Eq.(10) and taking

into account Eq.(11) it is seen that

$$\nabla_S \lambda \times \nabla_S \psi = \nabla_S \mu \times \nabla_S \psi = \nabla_S v \times \nabla_S \psi = 0 \quad (12)$$

As it has been stated above  $\nabla_S \lambda$ ,  $\nabla_S \mu$  and  $\nabla_S v$  being parallel to  $\nabla_S \psi$  are normal to the surface velocity vector ( $\vec{V}_S$ ). We can write, therefore, that:

$$\vec{V}_S \cdot \nabla_S \lambda = \vec{V}_S \cdot \nabla_S \mu = \vec{V}_S \cdot \nabla_S v = 0 \quad (13)$$

Transport equations (13) simply state that  $\lambda$ ,  $\mu$  and  $v$  are conserved along, i.e. remain constant on, the surface streamlines. Consequently, we may write that  $\lambda = \lambda(\psi)$ ,  $\mu = \mu(\psi)$  and  $v = v(\psi)$ . Eqs (3), (4) and (6) also indicate that  $h_t = h_t(\psi)$ ,  $s = s(\psi)$  and  $RV_N = RV_N(\psi)$ .

Applying the surface curl operator on Eq. (10) yields the following expression for the N-wise vorticity component

$$\vec{\Omega}_N = \nabla_S \alpha \times \nabla_S \psi \quad (14)$$

Introducing Eq.(14) and relations (11) to the momentum Eq.(2), we get after some manipulations that

$$\begin{aligned} \vec{V}_S \times (\nabla_S \alpha \times \nabla_S \psi) &= -\nabla_S \psi (\vec{V}_S \cdot \nabla_S \alpha) = \\ &= \left( \lambda - \mu T - v \frac{V_N}{R} \right) \nabla_S \psi \end{aligned} \quad (15)$$

Noting that  $\nabla_S \psi$  never vanishes (with the exception of stagnation points), Eq.(15) yields the following transport equation for the generalized drift function  $\alpha$

$$\vec{V}_S \cdot \nabla_S \alpha = -\lambda + \mu T + v \frac{V_N}{R} \quad (16)$$

## 5. NATURAL $(\varphi, \psi)$ CURVILINEAR COORDINATE SYSTEM

The potential function and the stream function, i.e. the natural coordinates, on the meridional plane, are considered to be the independent variables. The defining Eqs (9) and (10) provide the contravariant base of the  $(\varphi, \psi)$  coordinate system. Associating coordinate indices 1 and 2 with the  $\varphi$  and  $\psi$  coordinates respectively, the contravariant base reads:

$$\vec{g}^1 = \nabla_S \varphi = \vec{V}_S - \alpha \nabla_S \psi \quad (17)$$

$$\vec{g}^2 = \nabla_S \psi = \vec{N} \times \vec{\rho} \vec{V}_S \quad (18)$$

The dot product  $\nabla_S \varphi \cdot \nabla_S \psi$  is definitely nonzero since  $\nabla_S \psi$  is normal to  $\vec{V}_S$ . This indicates that, unlike irrotational flow, in the present rotational one the  $(\varphi, \psi)$  coordinate system is nonorthogonal.

The conjugate (contravariant) metrics of the  $(\varphi, \psi)$  system, which actually define the body-fitted physical space to the natural  $(\varphi, \psi)$  space transformation, are evaluated via the defining relations and Eqs (17), (18) as following:

$$g^{11} \equiv \vec{g}^1 \cdot \vec{g}^1 = V_S^2 + \alpha^2 |\nabla_S \psi|^2 = V_S^2 [1 + (\alpha \vec{\rho})^2] = \frac{V_S^2}{\sin^2 \beta} \quad (19)$$

$$g^{22} \equiv \vec{g}^2 \cdot \vec{g}^2 = (\vec{\rho} V_S)^2 \quad (20)$$

$$g^{12} = g^{21} \equiv \vec{g}^1 \cdot \vec{g}^2 = -\alpha \vec{\rho} V_S |\nabla_S \psi| = -\alpha \vec{\rho}^2 V_S^2 = \frac{\vec{\rho} V_S^2}{\tan \beta} \quad (21)$$

where  $\beta$  is the angle formed between  $\nabla_S \varphi$  and  $\nabla_S \psi$  on the (S) surface. The following expression for the (coordinate) angle  $\beta$  results from Eqs (19) and (21)

$$\tan \beta = -\frac{1}{\alpha \vec{\rho}} \quad (22)$$

The covariant metrics  $g_{ij}$  ( $i, j=1, 2$ ) may be expressed in terms of the contravariant ones following standard tensor relations (Ref.19):

$$g^{m1} g_{1n} = \delta_n^m \quad (23)$$

In terms of flow quantities the covariant metrics of the  $(\varphi, \psi)$  coordinate system are:

$$g_{11} = \frac{1}{V_S^2}, \quad g_{22} = \frac{1}{(\vec{\rho} V_S \sin \beta)^2}, \quad (24)$$

$$g_{12} = g_{21} = -\frac{1}{\vec{\rho} V_S^2 \tan \beta}$$

and the Jacobian of the coordinate transformation yields

$$J = \det^{1/2} (g_{ij}) = \frac{1}{(\vec{\rho} V_S^2)^2} \quad (25)$$

## 6. GOVERNING EQUATIONS

The objective of this section is to present and discuss the derivation of the equations that are actually solved by the present method for determining the flowfield and the geometry. Differential geometry and generalized tensor analysis arguments are employed in order to derive the governing equations. The present procedure, which treats the inverse problem as a geometrical rather than a flow one, proved to be quite modular and efficient in several inverse design applications both in two (Refs 10,12,13) and three dimensions (Refs 20,21,22).

### 6.1 Velocity equation

An equation for the magnitude of the surface velocity component  $V_S$  is obtained from the metrics compatibility condition, which has to be satisfied by any parametrization of (S), including the  $(\phi, \psi)$  natural coordinates one. In two-dimensional spaces the curvature tensor has one independent component  $R_{1212}$  (Ref.19) which is equal to the Riemannian curvature  $K$  of the (S) surface considered

$$\frac{1}{J^2} R_{1212} = K \quad (26)$$

$K$  is an intrinsic property of the surface and, in general, is non-zero. Surfaces with zero Riemannian curvature are i) the plane surface, i.e. 2-D or meridional flow case, ii) the cylinder and iii) the cone.

For any  $(x^1, x^2)$  parametrization of the (S) surface the  $R_{1212}$  term is expressed as:

$$R_{1212} = \frac{\partial}{\partial x^1} [22, 1] - \frac{\partial}{\partial x^2} [21, 1] + \Gamma_{21}^1 [12, 1] - \Gamma_{22}^2 [11, 1] \quad (27)$$

and

$$[mn, l] = \frac{1}{2} \left( \frac{\partial g_{ml}}{\partial x^n} + \frac{\partial g_{ml}}{\partial x^m} - \frac{\partial g_{mn}}{\partial x^l} \right) \quad (28)$$

$$\Gamma_{mn}^q = g^{q1} [mn, 1] \quad (29)$$

with  $m, n, l, q = 1, 2$ . Eqs (28) and (29) define the Christoffel symbols of the first and second kind, respectively.

When the  $(x^1, x^2)$  parametrization of (S) is an orthogonal one, the expressions of the Christoffel symbols are simplified considerably and Eq.(27) yields

$$K = -\frac{1}{J} \left[ \frac{\partial}{\partial x^1} \left( \frac{1}{\sqrt{g_{11}}} \frac{\partial \sqrt{g_{22}}}{\partial x^1} \right) + \frac{\partial}{\partial x^2} \left( \frac{1}{\sqrt{g_{22}}} \frac{\partial \sqrt{g_{11}}}{\partial x^2} \right) \right] \quad (30)$$

Considering that the coordinate system describing the two-dimensional space, i.e. the (S) surface, is the  $(\phi, \psi)$  one and noting that its metrics are expressed as functions of the flow quantities via Eqs (19),(20),(21) and (24), the curvature compatibility condition (26) provides a PDE for the velocity magnitude  $V_S$  in terms of the modified density  $\tilde{\rho}$  and the local coordinate angle  $\beta$ . Associating coordinate indices 1 and 2 with the  $\phi$  and  $\psi$  coordinates, respectively, one gets, after substitutions, the following equation:

$$a(\ln V_S)_{\phi\phi} + b(\ln V_S)_{\phi\psi} + c(\ln V_S)_{\psi\psi} + d(\ln V_S)_{\phi} + e(\ln V_S)_{\psi} = f + K/V_S^2 \quad (31)$$

where

$$a(\tilde{\rho}, \beta) = \frac{1}{\sin^2 \beta}$$

$$b(\tilde{\rho}, \beta) = \frac{2\tilde{\rho}}{\tan \beta}$$

$$c(\tilde{\rho}, \beta) = \tilde{\rho}^2$$

$$d(\tilde{\rho}, \beta) = -\frac{1}{\sin^2 \beta} \left[ (\ln \tilde{\rho})_{\phi} + \tilde{\rho} \beta_{\psi} + \frac{2}{\tan \beta} \beta_{\phi} \right]$$

$$e(\tilde{\rho}, \beta) = \tilde{\rho}^2 (\ln \tilde{\rho})_{\psi} - \frac{\tilde{\rho}}{\sin^2 \beta} \beta_{\phi}$$

$$f(\tilde{\rho}, \beta) = -\frac{1}{\sin^2 \beta} (\ln \tilde{\rho})_{\phi\phi} - \frac{\tilde{\rho}}{\tan \beta} (\ln \tilde{\rho})_{\phi\psi} + \frac{(\ln \tilde{\rho})_{\phi}}{\sin^2 \beta} \left[ (\ln \tilde{\rho})_{\phi} + \tilde{\rho} \beta_{\psi} + \frac{3}{\tan \beta} \beta_{\phi} \right] - \frac{1}{\sin^2 \beta \tan \beta} \beta_{\phi\phi} - \frac{\tilde{\rho}}{\sin^2 \beta} \beta_{\phi\psi} + \frac{2\tilde{\rho}}{\sin^2 \beta \tan \beta} \beta_{\phi} \beta_{\psi} + \frac{2 \cos^2 \beta + 1}{\sin^4 \beta} (\beta_{\phi})^2$$

and subscripts  $\phi$  and  $\psi$  indicate corresponding partial derivatives. The nonlinear second order PDE, Eq. (31), is the main governing equation of the flowfield and represents the velocity equation sought. For irrotational flows, where  $\beta = 90^\circ$  (potential lines are normal to streamlines) Eq. (31) simplifies to

$$(\ln V_S)_{\phi\phi} + (\ln \tilde{\rho})_{\phi\phi} + \tilde{\rho}^2 (\ln V_S)_{\psi\psi} - (\ln \tilde{\rho})_{\phi} (\ln V_S)_{\psi} - (\ln \tilde{\rho})_{\psi}^2 + \tilde{\rho}^2 (\ln \tilde{\rho})_{\psi} (\ln V_S)_{\psi} = K/V_S^2 \quad (32)$$

For the 2-D case Eq.(32) is the same with that given by Stanitz (Ref.3). Equation (32) can be, also, written in the form (Ref.10):

$$\left[ \frac{1}{\tilde{\rho}} (1 - M^2) (\ln V_S)_{\phi} \right]_{\phi} + [\tilde{\rho} (\ln V_S)_{\psi}]_{\psi} = K/(\tilde{\rho} V_S^2) \quad (33)$$

where  $M$  is the local Mach number. Noting that the  $\phi$ -direction coincides with the flow direction, the nature, elliptic or hyperbolic, of the velocity equation depends on the value of the local Mach number. In that sense, Eq. (33) is mathematically similar to the full-potential equation.

It is emphasized that, in the present method, the velocity PDE, Eq.(31) is derived in a novel way by considering differential geometry arguments only and not by manipulating the basic flow equations themselves (in Ref.12

it has been shown explicitly that the two ways of deriving the velocity equation are equivalent). In that respect the present methodology is quite modular in formulating inverse problems. One has just to select an appropriate natural coordinates system and express the metrics in terms of flow quantities. The governing equations result, thenafter, using a standard procedure.

The coefficients of Eq.(31) are functions of  $\bar{\rho}$  and  $\beta$ . The modified density function  $\bar{\rho}$ , defined in Table 1, is a function of the thermodynamic density  $\rho$  which is governed by Eq.(7). With the exception of the 2-D flow case  $\rho$  is also a function of the (unknown)-design-geometry sought. This implies that, in general, the flow and geometry solution procedures cannot be separated and carried out in an independent manner. To close the problem one has to provide an equation for the coordinate angle  $\beta$ . The latter is related to the drift function  $\alpha$  through Eq. (22).

### 6.2 Transport Equation for the Drift Function

The drift function is calculated from the transport Eq.(16). On the  $(\phi, \psi)$  coordinate system this equation reads:

$$V_s^2 \alpha_\phi = -\lambda + \mu T + v \frac{V_N}{R} \quad (34)$$

Eq. (34) is an ODE along the streamlines of the flow field. For a given velocity and total enthalpy field the temperature  $T$  which appears in the RHS of Eq. (34) is computed from Eq. (8). The normal velocity term which is present in axisymmetric flows only, is computed from the  $(RV_N)$  distribution. It is noted that the drift function is coupled to the geometry because of this term.

The total enthalpy as well as the entropy and the swirl  $(RV_N)$  are prescribed at the inlet of the flow field as  $h_t = h_t(\psi)$ ,  $s = s(\psi)$  and  $RV_N = RV_N(\psi)$ , implicitly setting the level of the rotational character of the flow considered. Taking into account that  $h_t, s$  and  $RV_N$  are conserved along the streamlines, i.e. on  $\Psi = \text{const.}$  lines [refer to Eqs (3,5,6)], it is concluded that  $h_t, s$  and  $RV_N$  are known, i.e. are set up *a priori*, on the entire flow domain. The distributions  $\lambda = \lambda(\psi), \mu = \mu(\psi)$  and  $v = v(\psi)$  are determined at the inlet via the defining Eqs (11). Since  $\lambda, \mu$  and  $v$  are conserved along the streamlines, Eqs (13), their distribution throughout the flowfield is, also, known *a priori*.

### 6.3 Geometry Equations

The calculation of the geometry is based on the generalized Frenet equations. Let  $(\vec{g}_1, \vec{g}_2)$  be the covariant base for the  $(\phi, \psi)$  parametrization of the (S) surface. Then, by definition,

$$\vec{g}_1 = \frac{\partial \vec{r}}{\partial \phi}, \quad \vec{g}_2 = \frac{\partial \vec{r}}{\partial \psi} \quad (35)$$

where  $\vec{r}$  is the position vector, the components of which

represent the geometry sought. The variation of the covariant base along the coordinate line directions is expressed in terms of the Christoffel symbols as

$$\frac{\partial}{\partial \phi} \begin{pmatrix} \vec{g}_1 \\ \vec{g}_2 \end{pmatrix} = \begin{pmatrix} \Gamma_{11}^1 & \Gamma_{11}^2 \\ \Gamma_{21}^1 & \Gamma_{21}^2 \end{pmatrix} \begin{pmatrix} \vec{g}_1 \\ \vec{g}_2 \end{pmatrix} \quad (36)$$

$$\frac{\partial}{\partial \psi} \begin{pmatrix} \vec{g}_1 \\ \vec{g}_2 \end{pmatrix} = \begin{pmatrix} \Gamma_{12}^1 & \Gamma_{12}^2 \\ \Gamma_{22}^1 & \Gamma_{22}^2 \end{pmatrix} \begin{pmatrix} \vec{g}_1 \\ \vec{g}_2 \end{pmatrix} \quad (37)$$

Since, on the  $(\phi, \psi)$  parametrization, Christoffel symbols are expressions of flow field quantities the corresponding coefficient matrices of Eqs (36) and (37) are considered to be known.

The expressions of  $\Gamma_{2j}^i$  ( $i, j=1,2$ ) are given below for completeness

$$\begin{aligned} \Gamma_{21}^1 &= -\frac{1}{V_s \sin \beta} (V_s)_\psi + \frac{\bar{\rho} V_s^2}{2 \tan \beta} \left[ \frac{1}{(\bar{\rho} V_s \sin \beta)^2} \right]_\phi \\ \Gamma_{21}^2 &= -\frac{\bar{\rho}}{V_s \tan \beta} (V_s)_\psi + \frac{(\bar{\rho} V_s)^2}{2} \left[ \frac{1}{(\bar{\rho} V_s \sin \beta)^2} \right]_\phi \\ \Gamma_{22}^1 &= -\left( \frac{V_s}{\sin \beta} \right)^2 \left\{ \left( \frac{1}{\bar{\rho} V_s^2 \tan \beta} \right)_\psi + \frac{1}{2} \left[ \frac{1}{(\bar{\rho} V_s \sin \beta)^2} \right]_\phi \right\} + \\ &+ \frac{1}{2} \frac{\bar{\rho} V_s^2}{\tan \beta} \left[ \frac{1}{(\bar{\rho} V_s \sin \beta)^2} \right]_\psi \\ \Gamma_{22}^2 &= -\frac{\bar{\rho} V_s^2}{\tan \beta} \left\{ \left( \frac{1}{\bar{\rho} V_s^2 \tan \beta} \right)_\psi + \frac{1}{2} \left[ \frac{1}{(\bar{\rho} V_s \sin \beta)^2} \right]_\phi \right\} + \\ &+ \frac{1}{2} (\bar{\rho} V_s)^2 \left[ \frac{1}{(\bar{\rho} V_s \sin \beta)^2} \right]_\psi \end{aligned} \quad (38)$$

The integration of Eq.(36) along a  $\psi = \text{const.}$  line or of Eq.(37) along a  $\phi = \text{const.}$  line provides the covariant base. The Cartesian components of the geometry are determined, thenafter, by straightforward integrations of Eq.(35).

### 7. $(\phi, \psi)$ DOMAIN OF INTEGRATION AND BOUNDARY CONDITIONS

The inverse problem has a unique solution on the  $(\phi, \psi)$  plane provided that appropriate boundary conditions are specified for the velocity, the drift function and the geometry equations, Eqs (31), (34), (35-37) respectively.

The drift function  $\alpha$  is governed by the ODE (34), for which initial boundary conditions are required along the inlet section.  $\alpha$ , which controls the size of  $\tan \beta$ , i.e. the local

skewness of the  $(\phi, \psi)$  coordinate system, is specified as an arbitrary constant along the inlet section without affecting the final flowfield solution.  $h_{t,s}$  and  $RV_N$  distributions are also prescribed along the inlet section, implicitly specifying the thermodynamic density.

Initial conditions are also required for the integration of the geometry Eqs (35-37). The position vector  $\vec{r}_0$  and the direction of  $(\vec{g}_1)_0$  are fixed at a pre-selected location.  $\vec{r}_0$  serves as an initial condition for Eq.(35). The direction of  $(\vec{g}_1)_0$  is sufficient for specifying  $\vec{g}_1$  since its magnitude is known  $|\vec{g}_1| = \sqrt{g_{11}} = (1/V_S)$  [see Eq.(24)]. The same holds for the magnitude of  $\vec{g}_2$  while its direction is related to the  $\vec{g}_1$  direction through the coordinate angle  $\beta$ .  $(\vec{g}_1, \vec{g}_2)_0$  form the initial boundary conditions for Eq. (36) or (37).

The velocity equation, being of elliptic type, requires boundary conditions all around the integration domain. In practice the designer prescribes the  $V_S$  velocity magnitude as a function of the solid walls arc lengths, i.e.  $V_S = V_S(L)$ . In both irrotational and rotational flows the potential  $\phi$  is related to the arc length  $L$  on the solid walls (streamlines) via the relation  $d\phi = \vec{V}_S \cdot d\vec{L}$ . Obviously, the prescribed  $V_S = V_S(L)$  distribution corresponds to an easily obtainable  $V_S = V_S(\phi)$  distribution, where  $\phi$  is determined to within an arbitrary constant.

The  $V_S$  velocity magnitude is also prescribed along the inlet and outlet sections. On these sections the stream function definition yields  $d\psi = \rho \vec{V}_S \cdot d\vec{L}$  and, consequently,  $V_S = V_S(\psi)$ . Usually a zero  $\psi$  value is assigned to one of the solid walls. A  $(\phi, \psi)$  domain of integration is, thus, constructed, for which velocity boundary conditions of Dirichlet type are prescribed on the complete boundary while thermodynamic and geometrical boundary conditions are fixed on the inlet section.

The shape of the  $(\phi, \psi)$  domain depends on the nature of the problem considered. For internal flows, for example, the  $(\phi, \psi)$  domain is trapezoidal, bounded by the  $\psi=0$  and  $\psi = \psi_{max}$  parallel lines ( $\psi_{max}$  is related to the total mass-flux). For external flow computations the far field boundary and, consequently, its image on the  $(\phi, \psi)$  plane may be arbitrarily shaped. The  $(\phi, \psi)$  domain which corresponds to an isolated airfoil design problem is shown in figure 1. One may notice the double image of the trailing edge (TE) point (one for the suction side and another for the pressure side), which is due to the circulation. The boundary conditions of the normalized velocity  $V = V_S/V_\infty$  are also shown in the figure.

**8. NUMERICAL METHOD**

The governing equations are discretized and integrated numerically using finite difference schemes. The standard procedures for direct methods involving grid generation, body-fitted coordinate transformation, discretization and

iterative solvers apply to the inverse problem solution, as well.

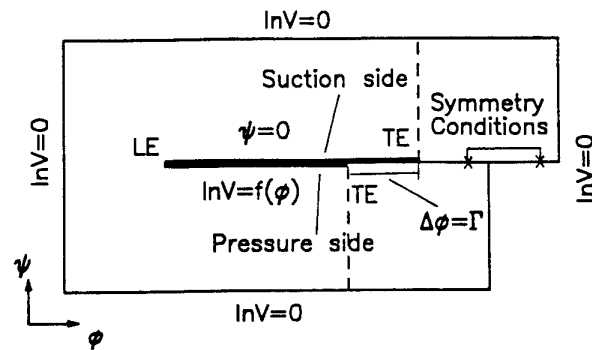


Fig.1  $(\phi, \psi)$  plane and velocity boundary conditions.

The defined  $(\phi, \psi)$  domain of integration may have irregular shape. An auxiliary numerical transformation is employed which maps the irregular  $(\phi, \psi)$  domain to a rectangular one with square unit cells in a computational  $(\xi, \eta)$  plane. In most cases an H-type grid on the  $(\phi, \psi)$  plane with the  $\eta = const.$  lines corresponding to  $\psi = const.$  lines results from this transformation. This kind of computational grid is very convenient for the treatment of the transport equations. However, in certain cases, like the design of an airfoil with rounded leading edge, a C-type coordinate transformation improves the quality of the results in the sensitive region near the leading edge (see Ref.10).

**8.1 Coordinate transformation**

Considering the  $(\phi, \psi)$  to  $(\xi, \eta)$  coordinate transformation all the governing, flow and geometry, equations are expressed on the  $(\xi, \eta)$  plane employing the following operator transformations

$$\begin{aligned}
 L_\psi ( ) &= \frac{1}{G^2} [ \Psi_\eta^2 ( )_{\xi\xi} - 2\Psi_\xi \Psi_\eta ( )_{\xi\eta} + \Psi_\xi^2 ( )_{\eta\eta} ] \\
 L_\phi ( ) &= \frac{1}{G^2} [ \Phi_\eta^2 ( )_{\xi\xi} - 2\Phi_\xi \Phi_\eta ( )_{\xi\eta} + \Phi_\xi^2 ( )_{\eta\eta} ] \\
 G &= \Phi_\xi \Psi_\eta - \Phi_\eta \Psi_\xi \\
 ( )_{\phi\phi} &= L_\psi ( ) - L_\psi ( \psi ) ( )_\psi - L_\psi ( \phi ) ( )_\phi \\
 ( )_{\psi\psi} &= L_\phi ( ) - L_\phi ( \psi ) ( )_\psi - L_\phi ( \phi ) ( )_\phi \\
 ( )_\phi &= \frac{1}{G} [ \Psi_\eta ( )_\xi - \Psi_\xi ( )_\eta ] \\
 ( )_\psi &= \frac{1}{G} [ \Phi_\xi ( )_\eta - \Phi_\eta ( )_\xi ]
 \end{aligned}
 \tag{39}$$

**8.2 Numerical Integration of the Velocity Equation**

The velocity equation is linearized by assuming that the  $\rho$  and  $\beta$  distributions are known from the previous iteration level. Discretizing partial derivatives employing central

second-order accurate differencing (in subsonic flows) a system of algebraic equations with 9-diagonal banded nonsymmetric characteristic matrix is obtained. This is solved using the Modified Strongly Implicit Procedure (MSIP, Ref.23) which employs an incomplete L-U decomposition of the 9-diagonal matrix. For 2-D potential problems where the velocity equation is decoupled from the geometry and the  $\beta$ -terms vanish, the convergence properties of the velocity solver are enhanced using the linear restarting GMRES (Ref.24) method combined with the incomplete L-U preconditioner of the MSIP method.

### 8.3 Numerical Integration of the Drift Equation

Once the velocity field is determined, at each iteration level, the transport equation for the drift function is integrated using a second-order accurate Runge-Kutta scheme. The newly calculated  $\alpha$  distribution provides a better estimate for  $\beta$  via Eq.(22). A better estimate for  $\rho$  is calculated from Eq.(7).

### 8.4 Integration of the Geometry Equations

The geometry calculation is performed by integrating Eqs (35-37). Computational experience showed that inaccuracies associated with the error accumulation of the geometry calculation are minimized if one determines a reference-central streamline first and then, starting from it, determines the wall(s) by integrating along  $\xi = \text{const.}$  lines. In order to enhance the accuracy of the geometry computation a staggering discretization technique is followed where the flow quantities are computed at the grid nodes, while the Christoffel symbols and the covariant base  $(\bar{g}_1, \bar{g}_2)$  are computed at mid-cells and mid-nodes respectively. The system of Eqs. (36) or (37) is solved using a second order accurate Runge-Kutta scheme. Similar schemes are employed for the integration of Eq.(35).

### 8.5 Artificial Density

An artificial density scheme is used in the solution of the velocity equation when the local Mach number exceeds the critical value. Taking advantage of the resemblance of the velocity equation to the full-potential equation, the artificial density scheme which is employed, is identical to that proposed by Holst (Ref.25) for the solution of the direct transonic flow problem. In more detail, the thermodynamic density is upwinded in the supersonic region according to the following scheme:

$$\bar{\rho} = \rho - \mu \delta_s \rho \quad \mu = \max \{ 0, [1 - (M_c / M)^2] \} \quad (40)$$

where  $\delta_s(\ )$  is the ( $\phi$ -wise) streamwise upwind derivative operator and  $M_c$  is the cut-off Mach number. It should be noted that this artificial density scheme, in conjunction with the proposed flow field solver, can handle low transonic cases only. Special care with respect to the preconditioner of the velocity equation should be taken, if strong shock waves

are present in the flow field.

## 9. RESULTS AND DISCUSSION

The inverse design method proposed in this work has been validated for irrotational and rotational flows in several "reproduction" calculations. The term "reproduction" is used in the sense that, for a given geometry, a direct -analysis- code provides the boundary velocity distributions which are then used by the inverse method to reproduce the original shape. Such reproduction cases are presented for 2-D and axisymmetric internal and external flows. The application of the inverse method to the design of a family of laminar airfoils with optimized suction side velocity distribution is also discussed. An automated procedure for achieving closed airfoil profiles is presented.

### 9.2 2-D Internal Flows

In this particular case the reproduction procedure has been reversed. The inverse solver provides a geometry compatible with a prescribed "target velocity" and the direct solver is called upon to reproduce the prescribed boundary velocity (pressure) distribution. The direct method used for the comparisons employs the Clebsch formulation discussed in the previous sections and carries out the calculation in terms of  $\phi, \alpha$  and  $s$ , while  $h_t$  is considered to be constant throughout the flow field.

In all of the rotational test cases the entropy distribution is set *a priori* not in an entirely arbitrary manner. Entropy level of different streamlines at the inlet section is computed according to the relation:

$$s_{\psi} = - \frac{V_s}{T} V_{s_{\psi}} \quad (41)$$

This relation is derived by assuming that the vorticity which corresponds to the velocity gradient at the inlet is compatible with the one which corresponds to the entropy gradient. In addition, it is necessary to assume that the inlet section is straight and that the flow is evolving very slowly in the vicinity of the inlet, i.e. that streamlines there are almost parallel. *A posteriori* observations of the rotational cases results, see Figs. 4-7 and 11-13, satisfy these conditions to a great extent. Actually, it can be shown that specifying both the velocity and entropy gradients along the inlet section is equivalent to specifying the streamwise gradient of the velocity. The solution, geometry, therefore near the inlet adjusts itself, so that the streamwise velocity gradient is the same as the implicitly imposed one.

Results for the symmetric convergent-divergent nozzle are presented in Figs 2-5. Calculations were carried out with a (51x21) grid with  $\Delta\psi = 1, \Delta\phi_{\text{lower wall}} = 1$  and  $M_{\text{ref}} = 0.15$ . Imposed -target- wall velocity distribution for both the irrotational and rotational cases is shown in Fig. 2. The non-

constant part of this distribution is described by a sinusoidal function with linearly increasing amplitude. For the irrotational case uniform inlet and outlet velocity distributions are specified. In the rotational case symmetric parabolic velocity profiles with peak values 1.4 and 2.5 in the inlet and outlet sections, respectively, are assumed.

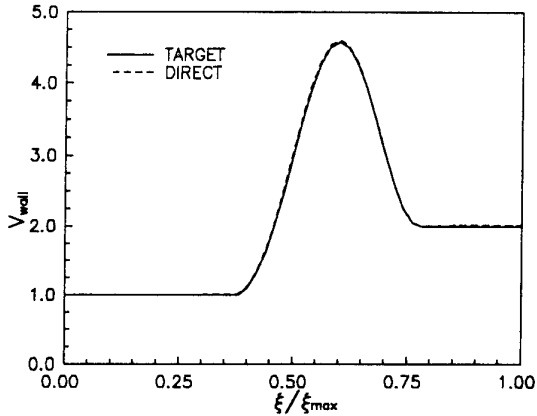


Fig.2 Target and direct calculation wall velocity distribution for rotational nozzle case.

Wall velocity distribution for the rotational case calculated with the direct method is also included in Fig.2. This distribution agrees very well with the target distribution. Small discrepancies observed in the divergent part of the nozzle may very well be due to the fact that the integration of the drift transport equation in the direct method is carried out with a first-order accurate scheme. Calculated flow field distributions of the Mach number, which achieves values as high as 0.72, and the potential function are shown in Figs 3-5. Inverse and direct solver results, denoted by solid and dashed lines, respectively, are entirely symmetric. Their agreement is very good, indicating the reliability of the present method.

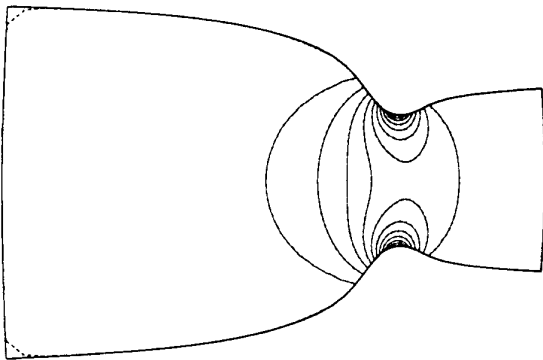


Fig.3 Mach contours of inverse (—) and direct (----) methods for irrotational nozzle case ( $M_{min}=0.15, \Delta M=0.05$ ).

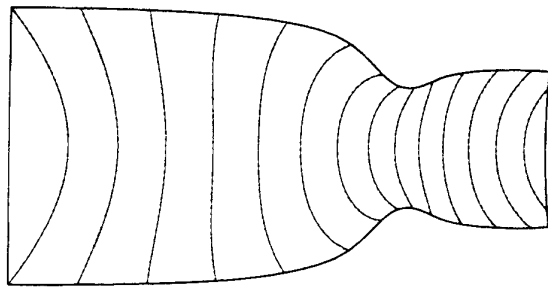


Fig.4 Potential lines of inverse (—) and direct (----) methods for rotational nozzle case ( $\phi_{min}=0, \Delta\phi=4$ ).

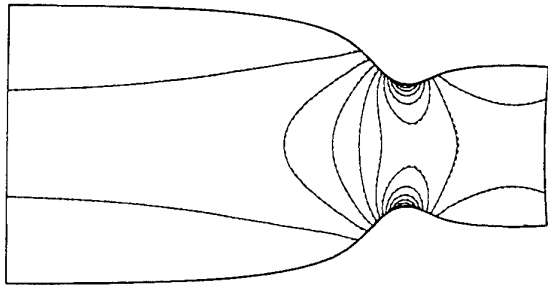


Fig.5 Mach contours of inverse (—) and direct (----) methods for rotational nozzle case ( $M_{min}=0.15, \Delta M=0.05$ ).

For the elbow channel case calculations were performed with a (65x17) grid with  $\Delta\psi=0.5, \Delta\phi_{lower\ wall}=1$ . Target wall velocity distributions on the upper and lower channel walls for both the irrotational and rotational cases are shown in Fig.6. Their characteristic is that the flow on both walls of the channel never decelerates.

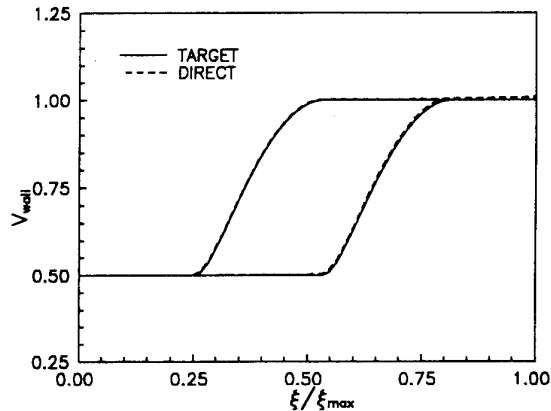


Fig.6 Target and direct calculation wall velocity distributions for rotational elbow channel case.

In the irrotational case uniform velocity distributions are imposed at the inlet and outlet sections, the Mach number at the outlet being  $M_{ref}=0.7993$ . This test case corresponds to the well-documented elbow case of Stanitz (Ref.3). The Mach number contours calculated with the inverse and direct methods, presented in Fig.7 are almost identical.

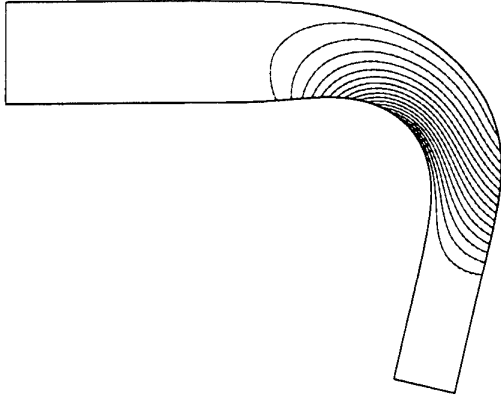


Fig.7 Mach contours of inverse (—) and direct (-----) methods for irrotational elbow channel case ( $M_{min}=0.4$ ,  $\Delta M=0.025$ ).

In the rotational elbow case symmetric parabolic velocity profiles with peak values of 0.58 and 1.1 are imposed with  $M_{ref}=0.6$ . Wall velocity distributions calculated with the direct method are compared to the target ones in Fig.6. They exhibit very satisfactory agreement. Results for the potential function, the Mach number and the drift function are presented in Figs 8-10, respectively. Inverse method results agree quite well with those of the direct method (compare solid and dashed line contours, respectively). Small discrepancies observed near the outlet of the channel are possibly due to inaccuracies involved with the integration of the thermal drift equation in the direct method.

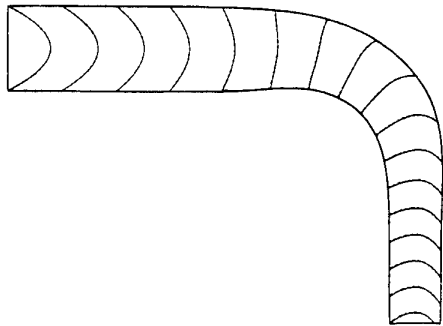


Fig.8 Potential lines of inverse (—) and direct (-----) method for rotational elbow channel case ( $\phi_{min}=0, \Delta\phi=4$ ).

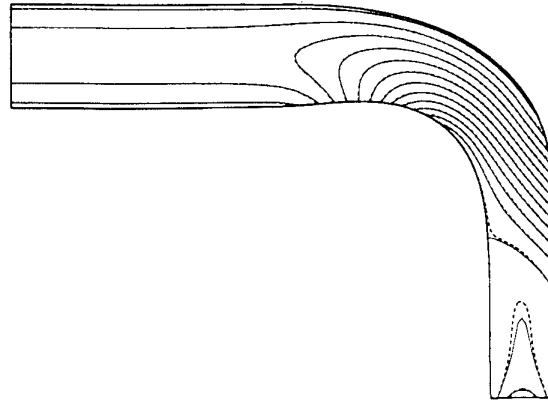


Fig.9 Mach contours of inverse (—) and direct (-----) methods for rotational elbow channel case ( $M_{min}=0.3$ ,  $\Delta M=0.025$ ).

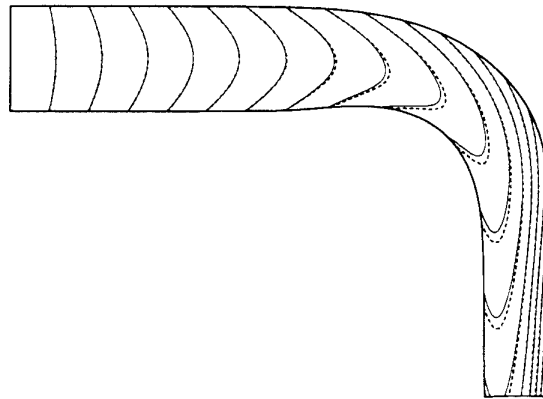


Fig.10 Thermal drift function contours of inverse (—) and direct (-----) methods for rotational elbow channel case ( $\alpha_{min} = -80$ ,  $\Delta\alpha = 10$ ).

## 9.2 Axisymmetric Flows - Meridional Plane Calculations

Reproduction results for two "real-life" geometries, corresponding to the (nonbladed) annular duct of a two-stage axial compressor (Ref.26) and the duct of a radial compressor (Ref.27) are presented here. In both cases duct-flow computations were performed for subsonic irrotational and rotational flow conditions. The rotationality of the flow is due to a linear inlet meridional velocity profile, which in conjunction with the assumed uniform temperature and pressure profiles produces a compatible nonuniform total

(stagnation) enthalpy distribution. The inlet velocity variation was of the order of 30% and 10% for the axial and radial cases respectively. For flow uniformity reasons, both geometries have been extended upstream and downstream. A  $126 \times 30$  grid was used for both direct and inverse computations in the axial compressor duct, while a  $70 \times 20$  grid was used for the radial compressor case. All inverse computations are initialized with a rectangular geometry, which is a severe test for the robustness of the numerical scheme, especially for the radial compressor case.

Contrary to the 2-D case the flow field and the geometry are strongly coupled in the inverse axisymmetric formulation. Convergence of the inverse solver is established within  $10^{-7}$  tolerance for the r.m.s. value of the velocity equation residual. Computational experiments showed that underrelaxing the velocity solution and the geometry (R-coordinate) was necessary to both achieve and accelerate convergence. Typically 170 iterations are required for convergence using a 0.4 relaxation factor for the velocity field and a 0.1 factor for the radial coordinate field. The computational cost for the rotational case with the  $126 \times 30$  grid is about 225 CPU seconds in one processor of an Alliant FX-80 machine. The direct code employed for these computation is a reduced duct-flow version of a  $(\psi, \omega)$  meridional code (Ref.28).

Direct and inverse calculation results for the Mach number field along with the original (dashed lines) and reproduced (solid lines) geometries for the axial compressor duct with irrotational and rotational flow conditions are presented in Figs 11 and 12 respectively. The agreement of the direct and inverse results is very good, although different grids and numerical schemes [ $(\psi, \omega)$  formulation for the direct method and Clebsch formulation for the inverse one] have been employed.

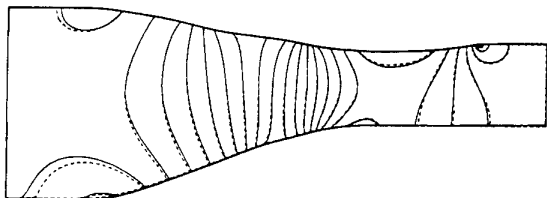


Fig. 11 Mach contours of inverse (—) and direct (---) methods for irrotational axial compressor duct ( $M_{\min}=0.135$ ,  $\Delta M=0.015$ ).

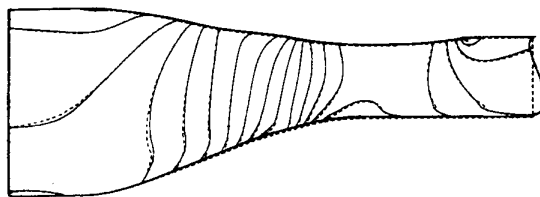


Fig. 12 Mach contours of inverse (—) and direct (---) methods for rotational axial compressor duct ( $M_{\min}=0.105$ ,  $\Delta M=0.015$ ).

In the rotational case, part of the incoming rotationality is introduced via a linear inlet swirl distribution (associated with a constant peripheral velocity distribution). The distorted outflow section observed in Fig.12 is due to the irregular  $(\varphi, \psi)$  domain of integration. As it can be seen from Fig.13, where the original and reproduced duct walls are compared in more detail, the outflow section distortion has almost no effect on the quality of the reproduction of the lateral solid boundaries. This is expected, since in the near-outflow region, streamwise gradients of all flow quantities are almost negligible.

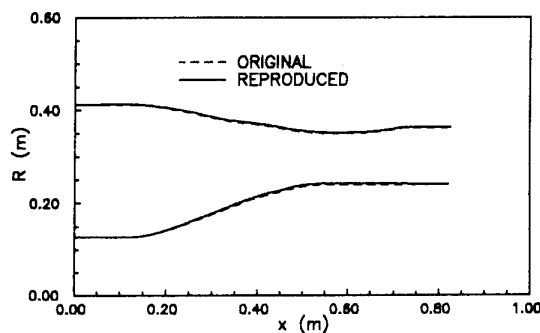


Fig. 13 Inner and outer wall geometries of axial compressor duct with rotational flow.

Reproduction results for the radial compressor duct in terms of the Mach number field with irrotational and rotational flow conditions are presented in Figs 14 and 15. The agreement between inverse (solid lines) and direct (dashed lines) methods results is very good despite the facts that the mean curvature of the duct is quite high and that the grid employed is not fine enough (in the streamwise sense) so to describe accurately the strong curvature changes observed along the inner wall.

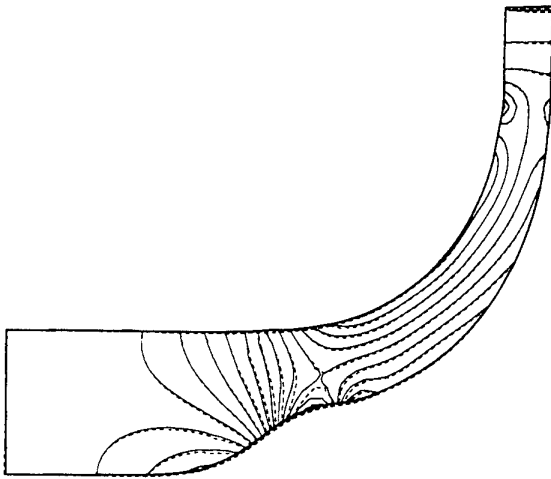


Fig. 14 Mach contours of inverse (—) and direct (---) methods for irrotational radial compressor duct ( $M_{\min}=0.15$ ,  $\Delta M=0.015$ ).

Detailed comparison of the original and reproduced wall geometries for the radial compressor duct with rotational flow conditions is shown in Fig. 16. The corresponding H-type  $(\xi, \eta)$  grid produced is included in Fig. 17. It is seen very clearly that in the inner flow region grid lines,  $\xi=\text{const.}$  and  $\eta=\text{const.}$  lines are nonorthogonal, corresponding to  $\phi=\text{const.}$  and  $\psi=\text{const.}$  lines, respectively.

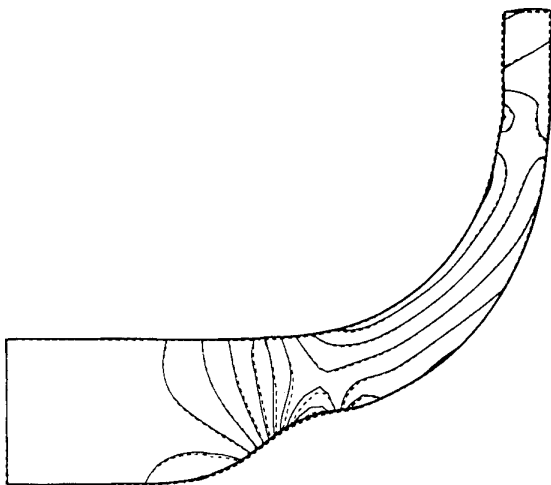


Fig. 15 Mach contours of inverse (—) and direct (---) methods for rotational axial compressor duct ( $M_{\min}=0.12$ ,  $\Delta M=0.015$ ).

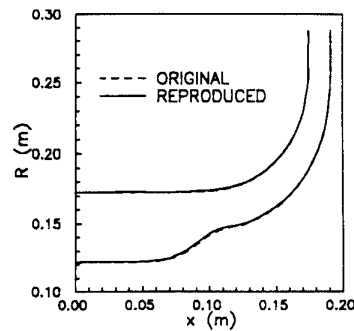


Fig. 16 Inner and outer wall geometries of radial compressor duct with rotational flow.

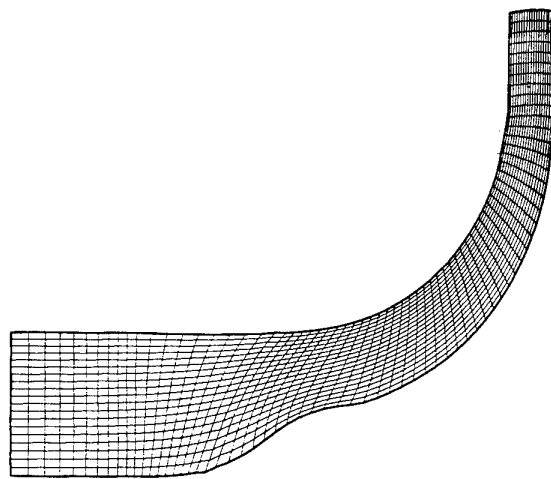


Fig. 17 Calculated grid of radial compressor duct with rotational flow.

### 9.3 Plane and Axisymmetric Cascade Flows

Several stationary cascade test cases were used in order to validate the accuracy and capabilities of the present inverse method. The cases considered were selected in such a way so to cover a wide range of geometric configurations and the complete Mach number range of application of the method. Complete outline of the test cases utilized for the validation of the method are reported in (Ref.29). Indicative "reproduction" results included here.

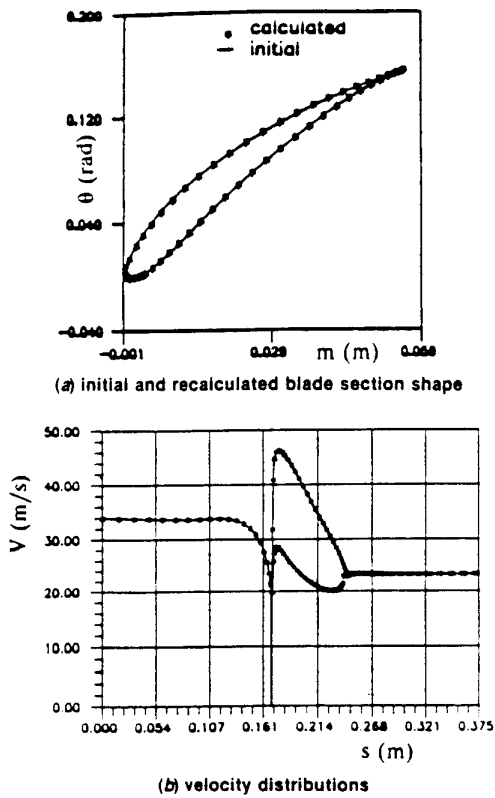


Fig.18 The Gostelow cascade test case.

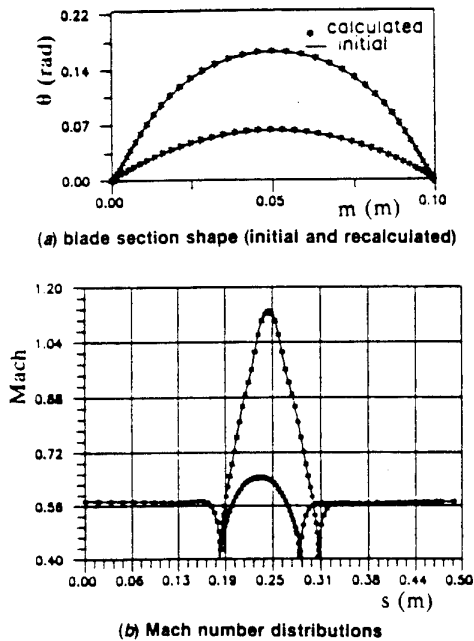


Fig.19 The Hobson cascade test case.

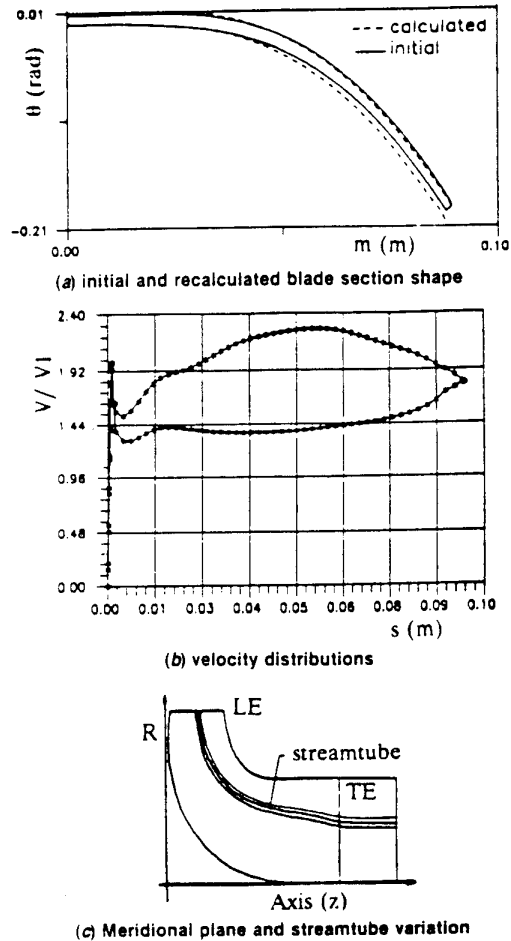


Fig.20 Radial inflow turbine test case.

The Gostelow (Ref.30) exact case (incompressible flow, compressor plane cascade) is considered in Fig.18. The initial and reproduced blade section shape is shown in Fig.18a in terms of its meridional and peripheral angle ( $m, \theta$ ) coordinates. The corresponding normalized target velocity distribution is shown in Fig.18b in terms of the profile arc length  $s$ .

Results for the Hobson (Ref.31) exact case (high Mach number, high turning, low pitch to chord ratio plane cascade) are shown in Fig.19. The meridional and peripheral angle coordinates of the initial and reproduced blade section shape are shown in Fig.19a, while the corresponding Mach number distribution is presented in Fig.19b.

A radial inflow turbine case (Ref...), with strong variation of the radial coordinate  $R$  and variation of the streamtube thickness  $\Delta n$  is considered in Fig.20. The initial and

reproduced blade shapes are shown in Fig.20a and the corresponding normalized velocity distribution in Fig. 20b. The streamtube thickness and radial distance variation of the considered case on the meridional plane is presented in Fig.20c.

Typically, the number of grid points utilized for the calculations presented above is (80x15) and the computer time needed for the complete solution was 20 CPU, seconds in a single processor of an ALLIANT FX-80 computer. H-type grids on the  $(\phi, \psi)$  plane have been used in all cases. The flow model employed was the irrotational one.

#### 9.4 Isolated Airfoils

For airfoil calculations C-type grids were used on the  $(\phi, \psi)$  plane. The adopted flow model is the irrotational one. The preconditioned GMRES solver was employed for all the test cases presented in this section. The validation of the inverse method developed was based on two "reproduction" test cases: an incompressible and a low transonic one.

The NACA 63215 profile was reproduced for incompressible flow conditions and zero incidence. A 159x17 C-type computational grid was used for both the direct and the inverse computations. Convergence history of the inverse method is presented in Fig.21 as the maximum residual of the velocity equation versus the GMRES(4) iterations. The

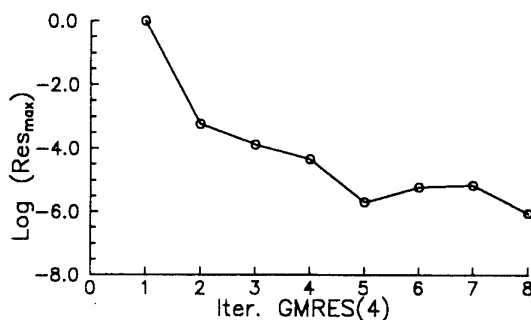


Fig.21 Convergence history of the velocity equation.

cost of each GMRES(4) iteration consists of four preconditioned residual computations and one approximate matrix factorization. The original and the reproduced profile shapes as well as the corresponding wall velocity distributions are shown in Fig.22. The accuracy of the reproduction procedure is evident.

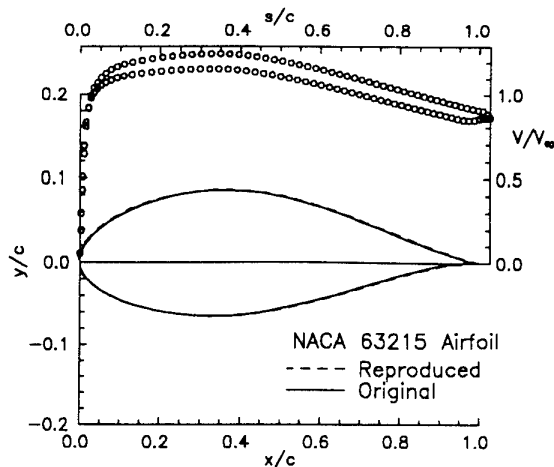


Fig.22 Wall velocity distribution and calculated geometry for the NACA 63215 airfoil.

The Korn profile was reproduced for low transonic (shock-free) flow conditions ( $M_\infty = .75$ ) and zero incidence. A 165x21 C-type computational grid was used for both direct and inverse computations. The original and reproduced profile shapes and the corresponding boundary velocity distributions are presented in Fig. 23.

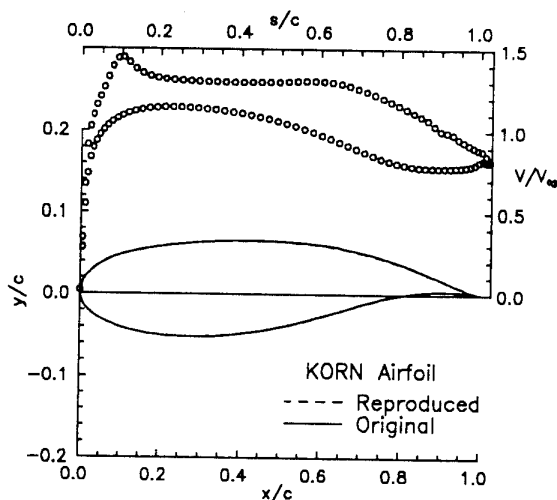


Fig.23 Wall velocity distributions and calculated geometry for the Korn airfoil.

Having validated the proposed inverse method, it was then used for designing new airfoils (see Refs 32, 33). In this framework the inverse inviscid method is coupled to an inverse integral viscous method. For prescribed values of the

lift coefficient ( $C_L$ ) and Reynolds number, the latter method can provide an optimized suction side velocity distribution in terms of minimum contribution to the airfoil's drag coefficient ( $C_D$ ).

The design procedure was applied to two different kinds of design.

- a) A tip blade section design for a Horizontal Axis Wind Turbine with  $Re=10^6$  and 0.2% level of external turbulence suitable for wind tunnel testing, which took place at the Southampton University facilities. The corresponding optimized suction and pressure side velocity distributions are shown in Fig. 24a. The resulting profile shape, which is 18% thick, is shown in Fig. 24b. The above airfoil was

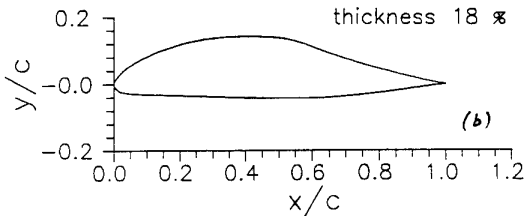
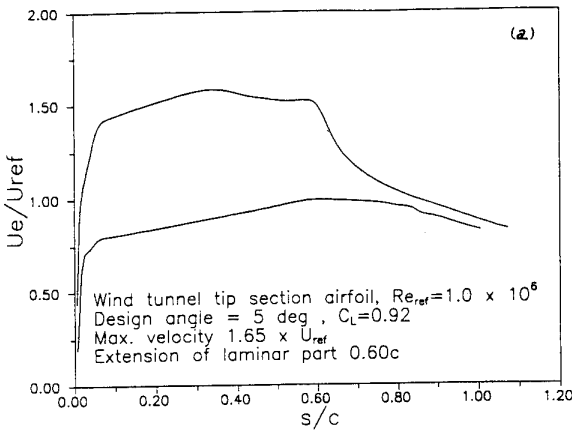


Fig.24 Wind-tunnel profile a) optimized velocity distributions b) profile shape.

manufactured at Southampton University (see Ref. 34) and tested at the design Reynolds number and turbulence level. The calculated and measured characteristic  $C_L$  and  $C_D$  distributions versus the incidence angle are shown in Fig. 25.

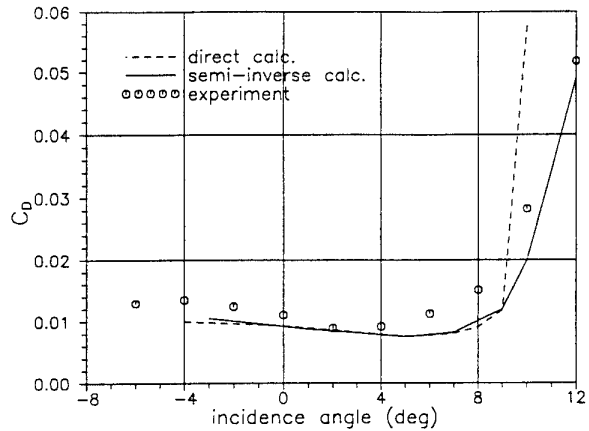
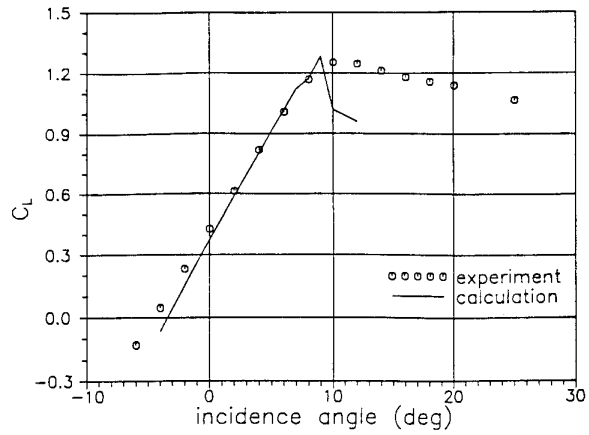


Fig.25  $C_L$ ,  $C_D$  curves for the wind-tunnel profile.

- b) Three blade sections (hub, mid, tip) according to RISO's specifications for optimum wind turbine operation (Ref. 34). These designs were aimed at improving the performance of an existing Danwin Wind Turbine. The  $Re$  numbers were  $1.8 \times 10^6$  for the hub and  $2.35 \times 10^6$  for the mid and tip sections. The turbulence level was at  $T_U=2\%$ , a value which was considered to be realistic for wind turbine operating conditions, (quite a few doubts exist as to the real atmospheric turbulence levels affecting the onset of transition in an unpredictable manner). The design requirements were:
  - i) the maximum lift of each profile given as 1.79, 1.38 and 1.16 for the hub, mid and tip sections
  - ii) the desired range of linear operation of the three airfoils
  - iii) the flatness of the drag characteristics in the linear region while maintaining the minimum drag value as low as possible

iv) flat post-stall behaviour of the  $C_L$  curve. The optimized (designed) profile shapes are shown in Fig. 26.

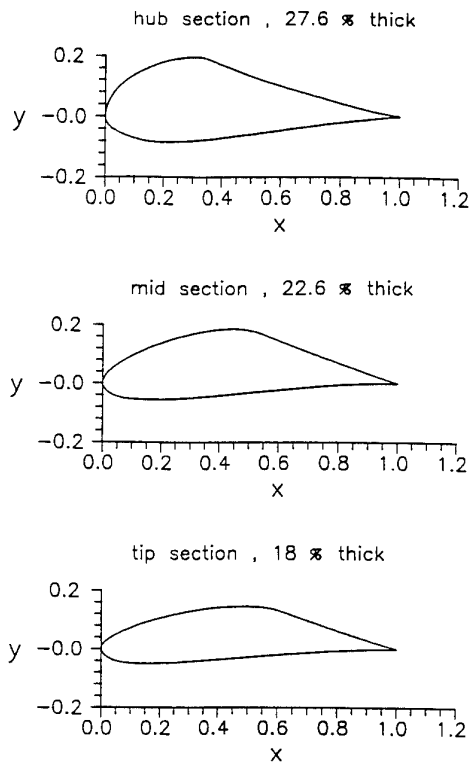


Fig. 26 Hub, mid and tip profile shapes.

It is well known that for a fixed suction side velocity distribution, the pressure side one cannot be prescribed arbitrarily. In order the calculated profile shape to be closed, this velocity distribution should satisfy certain constraints. In the present work, in order to achieve closed profile geometries, a general procedure, similar to that of Volpe and Melnik (Ref. 35) has been developed which updates the wall velocity distributions iteratively. The procedure can be applied over the complete Mach number regime. It uses two control parameters, the ratio of the arc length of the suction side to the pressure one ( $S_s$ ) and a velocity multiplier ( $\sigma$ ). The procedure starts by assuming an initial pressure side velocity distribution, which is "nearly" compatible with the prescribed  $C_L$  value. Then assuming that  $R_x^n$  and  $R_y^n$  are the (normalized by the chord length) x- and y-wise distances respectively, of the suction and pressure side trailing edge points, at the  $n^{\text{th}}$  iteration level, the following iterative Newton scheme can be established:

In general Jacobian  $(\partial R / \partial Q)^n$  is computed numerically. It has been shown, however, that if the velocity logarithm and the flow angle gradients are linearly related, which is nearly

$$0 = R^{n+1} - R^n + \left( \frac{\partial R}{\partial Q} \right)^n \Delta Q ; \quad \Delta Q = Q^{n+1} - Q^n \quad (42)$$

where

$$\underline{R} = \begin{pmatrix} R_x \\ R_y \end{pmatrix} \quad \underline{Q} = \begin{pmatrix} S_s \\ \sigma \end{pmatrix}$$

true for subsonic flows, this Jacobian can be evaluated analytically, see Ref. 10.

The resulting iterative scheme reads:

$$S_s^{n+1} = S_s^n - R_x^n \quad V^{n+1} = \sigma^n V^n = e^{R_y^n} V^n \quad (43)$$

In practice, this procedure proved to be quite fast, resulting to closed profiles, to within 5 to 10 iterations, with tolerance of the order of  $10^{-5}$  of the chord. A typical convergence history of the iterative profile closure scheme for a design test case is shown in Fig. 27.

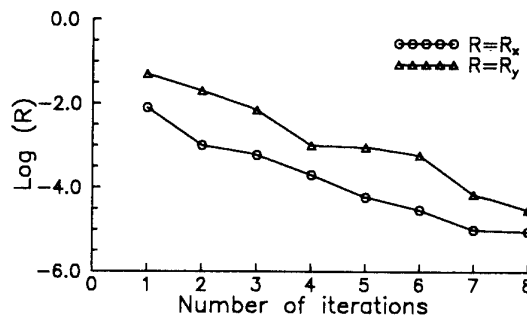


Fig. 27 Convergence history of the profile closure iterative scheme.

## 10. CONCLUSIONS

The development on an inverse method which could be applied to compressible, potential or rotational, 2-D, axisymmetric and quasi 3-D flow configurations has been described. The method is based on the potential function/stream function formulation. The Clebsh formulation has been adopted to decompose the velocity vector into a potential and a rotational part, which is related to the stream function gradient via a drift function governed by a transport equation. The method is formulated in a mathematically formal, as well as in a modular and universal way in terms of a modified density, employing differential geometry and generalized tensor analysis arguments. The main, velocity magnitude, governing equation is derived through the

metrics compatibility condition on the natural coordinates spaces. Computational results presented concern reproduction test cases and optimized laminar airfoils for wind turbines.

#### ACKNOWLEDGEMENTS

Part of this work was financed by the DG XII of the European Economic Community in the context of the BRITE-EURAM AERO-0026-C(TT) and JOUR-0079-C(SMA) projects.

#### REFERENCES

1. Dulikravich, G.S., "Aerodynamic Shape Design", AGARD Report 780; Special Course on Inverse Methods for Airfoil Design for Aeronautical and Turbomachinery Applications, May 1990.
2. Labrujere, T.E. and Slooff, J.W., "Computational Methods for the Aerodynamic Design of Aircraft Components", Annual Review of Fluid Mechanics, 25, 1993, pp 183-214.
3. Stanitz, J.D., "Design of Two-Dimensional Channels with Prescribed Velocity Distributions Along the Channel Walls", NACA Report 1115, 1953.
4. Nelson, C.D. and Yang, T., "Design of Branched and Unbranched Axially Symmetrical Duct with Specified Pressure Distribution", AIAA J., 15, 9, 1977, pp 1272-1277.
5. Schmidt, E., "Computation of Supercritical Compressor and Turbine Cascades with a Design Method for Transonic Flows", American Society of Mechanical Engineers, Journal of Engineering for Power, 102, 1980, pp 68-74.
6. Hawthorne, W.R., Wang, C., Tan, C.S. and McCune, J.E., "Theory of Blade Design for Large Deflections: Part I - Two-Dimensional Cascade", ASME Journal of Engineering for Gas Turbines and Power, 106, 2, 1984, pp 346-353.
7. Bonataki, E., Chaviaropoulos, P. and Papailiou, K.D., "An Inverse Inviscid Method for the Design of Quasi-Three Dimensional Rotating Turbomachinery Cascades", Proceedings of the 3rd International Conference on Inverse Design Concepts and Optimization in Engineering Sciences, ICIDES-III (University Park, PA), edited by G.S. Dulikravich, Sept. 1991, pp 189-200.
8. Barron, R.M., "A Non-iterative Technique for Design of Aerofoils in Incompressible Potential Flow", Commun. Appl. Numer. Methods, 6, pp 557-564.
9. Volpe, G. "Geometric and Surface Pressure Restrictions in Airfoil Design. Special Course on Inverse Methods for Airfoil Design for Aeronautical and Turbomachinery Applications", AGARD Report 780.
10. Chaviaropoulos, P., Dedoussis, V. and Papailiou, K.D., "Compressible Flow Airfoil Design Using Natural Coordinates", Computer Methods in Appl. Mechanics and Eng., Vol. 110, pp.131-142, 1993.
11. Borges, J.E., "A Proposed Through-flow Inverse Method for the Design of Mixed-flow Pumps", Proceedings, 3<sup>rd</sup> International Conference on Inverse Design Concepts and Optimization in Engineering Sciences (ICIDES-III), pp 177-188.
12. Dedoussis, V., Chaviaropoulos, P. and Papailiou, K.D., "Rotational Compressible Inverse Design Method for Two-Dimensional, Internal Flow Configurations", AIAA Journal, 31, 3, 1993, pp 551-558.
13. Koumandakis, M., Dedoussis, V., Chaviaropoulos, P. and Papailiou, K.D., "Design of Axisymmetric Channels with Rotational Flow", AIAA Journal of Propulsion & Power (to appear) also as AIAA Paper 93-3117, 1994.
14. Stanitz, J.D., "A Review of Certain Inverse Methods for the Design of Ducts with 2- or 3-Dimensional Flow", Applied Mechanics Review, 41, 6, 1988, pp 217-238.
15. Greff, E., Forbrich, D. and Schwarten, H., "Application of Direct Inverse Analogy (DIVA) and Viscous Design Optimization Techniques", Proceedings ICIDES-III, 1991, pp 307-324.
16. Beux, F. and Dervieux, A., "A Hierarchical Approach for Shape Optimization", INRIA contr., BRITE EURAM proj. 1082, 12-month Rep., Part 2, 1991.
17. Cabuk, H., Sung, C.-H. and Modi, V., "Adjoint Operator Approach to Shape Design for Internal Incompressible Flows", Proceedings, 3<sup>rd</sup> International Conference on Inverse Design Concepts and Optimization in Engineering Sciences (ICIDES-III), 1991, pp 391-404.
18. Lamb, H., "Hydrodynamics", 6th ed., Dover, New York, 1945, p 248.
19. Synge, J.L. and Schild, A., "Tensor Calculus", New York, Dover, 1978.
20. Dedoussis, V., Chaviaropoulos, P. and Papailiou, K.D., "A 3-D Inverse Methodology Applied to the Design of Axisymmetric Ducts", ASME Paper 92-GT-290, 1992.
21. Chaviaropoulos, P., Dedoussis, V. and Papailiou, K.D., "On the 3-D Inverse Potential Target Pressure Problem. Part I - Theoretical Aspects and Method Formulation", 1993, submitted for publication to J. Fluid Mech.
22. Dedoussis, V., Chaviaropoulos, P. and Papailiou, K.D., "On the Fully 3-D Inverse Potential Target Pressure Problem. Part II - Numerical Aspects and Application to Duct Design", 1993, submitted for

- publication to J. Fluid Mech.
23. Zedan, M. and Schneider, G.E., "A Three-Dimensional Modified Strongly Implicit Procedure for Heat Conduction", AIAA Journal, 21, 1983, pp. 295-303.
  24. Saad, Y. and Schultz, M.M., "GMRES: A Generalized Minimal Residual Algorithm for Solving Nonsymmetric Linear Systems", Res. Rep. YALEU/DCS/RR-254, 1983.
  25. Holst, T.L., "Numerical Computation of Transonic Flow Governed by the Full-Potential Equation", Comput. Fluid Dynamics VKI LS 1983-04.
  26. Rugger, R.S. and Benser, W.A., "Performance of a Highly Loaded Two-Stage Axial-Flow Fan", NASA TMX 3076, 1974.
  27. Bois, G. and Vouillarmet, A., "Analyse de l' Ecoulement Delivre par le Router d' un Compresseur Centrifuge", AIAAF, 21eme Colloque d' Aerodynamique Applique, Ecully, France, 1984.
  28. Kioussis, P., Chaviaropoulos, P., and Papailiou, K.D., "Meridional Flow Calculation Using Advanced CFD Techniques", ASME Paper 92-GT-325, 1992.
  29. Bonataki, E., "Inviscid Subsonic Inverse Method for the Design of Blade Sections along Arbitrary Axisymmetric Stream Surfaces with Varying Stream Tube Width", Ph.D. thesis, 1991, NTUA, Greece.
  30. Gostelow, J.P., "Potential Flow Through Cascades- A Comparison Between Exact and Approximate Solutions", A.R.C., CP No. 807, 1963.
  31. Jones, D.J., "Test Cases for Inviscid Flow Field Methods, Rereference Test Cases and Contributors", AGARD AR-211, 1985.
  32. Chaviaropoulos, P., Bouras, B., Leoutsakos, G. and Papailiou, K.D., "Design of Optimized Profiles for Stall Regulated HAWTs. Part I: Design Concepts and Method Formulation", Journal of Wind Engineering to appear.
  33. Leoutsakos, G., Bouras, B., Chaviaropoulos, P. and Papailiou, K.D., "Design of Optimized Profiles for Stall Regulated HAWTs. Part II: Airfoil Design Method Validation and Assessment", Journal of Wind Engineering to appear.
  34. Hoadley, D., Wellicome, J.F., Madsen, H.A., Bouras, B., Chaviaropoulos, P., Leoutsakos, G. and Papailiou K.D., "Aerofoil Section Design and Assessment", Final Report on Contract JOUR 0079-C(SMA), CEC DG XII, April 1993.
  35. Volpe, G. and Melnik, R.E., "Method for Designing Closed Airfoils for Arbitrary Supercritical Speed Distributions", J. of Aircraft, 23, 1986, pp. 775-782.

**SINGLE-PASS METHOD FOR THE SOLUTION OF INVERSE  
POTENTIAL AND ROTATIONAL PROBLEMS  
PART II: FULLY 3-D POTENTIAL THEORY AND APPLICATIONS**

P. Chaviaropoulos, V. Dedoussis<sup>1</sup> and K.D. Papailiou

National Technical University of Athens

Lab. of Thermal Turbomachines

P.O. Box 64069, 157 10 Athens, Greece.

### SUMMARY

A potential function/stream function formulation is introduced for the solution of the fully 3-D inverse potential "target pressure" problem. Potential function and two stream vectors are used as the independent natural coordinates, whilst the velocity magnitude, as well as, the aspect ratio and the cross-section angle of the elementary streamtubes are assumed to be the dependent ones. A novel procedure based on differential geometry is employed to formulate the method. The governing differential equations are derived by requiring the curvature tensor of the flat 3-D physical Euclidian space, expressed in terms of the curvilinear natural coordinates, to be zero. The resulting equations are discussed and investigated with particular emphasis to the existence and uniqueness of their solution. It is shown that the general 3-D inverse potential problem with target pressure boundary conditions only, is ill-posed accepting multiple solutions. This multiplicity is alleviated by considering elementary streamtubes with orthogonal cross-sections. The assumption of orthogonal stream surfaces reduces the number of dependent variables by one, simplifying the governing equations to an elliptic PDE for the velocity magnitude and to a second order ODE for the streamtube aspect ratio. The solution of these two equations provides the flow field. Geometry is determined independently by integrating Frenet equations along the natural coordinate lines, after the flow field has been calculated. The numerical implementation as well as validation test cases for the proposed inverse methodology are presented in the last part of the lecture.

### LIST OF SYMBOLS

$\vec{e}_n, \vec{e}^{mn}$	covariant and contravariant base vectors of $(\phi, \psi, \eta)$ coordinate system
$g^{mn}$	conjugate metrics tensor of $(\phi, \psi, \eta)$ coordinate system
$g_{mn}$	metrics tensor of $(\phi, \psi, \eta)$ coordinate system
$L_1, L_2, L_3, L_4$	submatrices of Jacobian matrix $\partial R / \partial X$
$[mn, l]$	Christoffel symbol of first kind
M	Mach number
P	Preconditioning matrix
$P_1, P_2, P_3, P_4$	submatrices of preconditioning matrix [P]
$\vec{r}$	position vector
$R_{rm}$	Ricci curvature tensor
R	vector of residuals of V-,t-equations

s	streamline arc length
t	aspect ratio of cross-section of elementary streamtube
$\vec{V}$	velocity vector
(x,y,z)	physical space Cartesian coordinate system
X	vector (of logarithms) of dependent variables V,t
$\gamma$	specific heats ratio
$\Gamma_{mn}^l$	Christoffel symbol of second kind
$\Delta\tau$	pseudo-time step
$\theta$	angle between base vectors $\vec{e}_2, \vec{e}_3$
$\rho$	density
$(\phi, \psi, \eta)$	potential function, stream functions natural curvilinear coordinate system

### Subscripts

m,n,l,p,r(=1,2,3)	covariant tensor indices
o	known position indicator
$\infty$	reference quantity
$\phi, \psi, \eta$	partial derivatives with respect to $\phi, \psi$ or $\eta$

### Superscripts

m,n,l,p,r(=1,2,3)	contravariant tensor indices
-------------------	------------------------------

## 1. INTRODUCTION

The need of developing optimum design tools in the context of applied aero-thermodynamics has been discussed in Part I of this lecture (Ref.1). A brief overview of the currently available design methods has been also attempted there. Making the distinction between "single-pass" and optimization methods their relative merits and drawbacks have been presented. In the framework of the "single-pass" methods the present authors have developed an inverse target pressure solver which can handle 2-D and axisymmetric potential or rotational flow problems. The extension of this methodology in three dimensions is the subject of this lecture.

Let us first address the question of existence and uniqueness of solution of the inverse "target pressure" problem using the simplest flow model, that is, the incompressible potential flow. In 2-D this problem is equivalent to the solution of a Laplace equation for the velocity logarithm on the transformed plane with Dirichlet type boundary conditions

<sup>1</sup> Also in Dept. of Industrial Management, University of Piraeus, 185 34 Piraeus, Greece.

(Ref.2). In this case the inverse target pressure problem is linear and accepts a unique admissible solution in simply connected regions. However, this is not true for multi-connected regions, the isolated airfoil case for example, where additional constraints should be satisfied by the target pressure distribution in order to ensure the closure of the airfoil profile. A set of integral constraints has been developed by Lighthill (Ref.3), but no explicit set of such constraints is available for compressible flows. It is well known, on the other hand, that even if these constraints are satisfied the closed profile may be non-admissible (e.g. reentering airfoils). In 3-D the question has not been answered even for the simplest case of incompressible potential flows in simply connected geometries. Stanitz's work (Refs 4,5) indicates that contrary to the 2-D case the 3-D problem is nonlinear. He also reported convergence difficulties in several test cases he tried. To the authors opinion this is due to the non-uniqueness of the solution.

As mentioned above, the purpose of this work is to present a "single-pass" inverse potential method for the solution of the general 3-D target pressure problem. Similar to the approach proposed by Stanitz (Ref.4), a potential function  $\phi$  and two stream functions  $\psi$  and  $\eta$  are introduced as the "natural" coordinates. A body-fitted coordinate transformation is employed to map the physical  $(x,y,z)$  space on which the boundaries of the flow field are unknown onto the natural  $(\phi,\psi,\eta)$  space. Computational boundaries on the latter space are fixed simply because, in inviscid flows, lateral boundaries are stream surfaces, i.e.  $\psi = \text{const.}$  or  $\eta = \text{const.}$  surfaces, while inflow and outflow boundaries can be considered to be potential ones. Thus assuming that the velocity distribution (prescribed pressure) is given on the lateral, as well as on the inflow and outflow boundaries of the flow field, one is faced with solving a boundary value problem on the  $(\phi,\psi,\eta)$  space.

The novelty of the present method is that the inverse target pressure problem is treated as a geometrical problem rather than a fluid dynamics one. A mathematically formal way, employing differential geometry and generalized tensor analysis arguments has been adopted in order to formulate the problem and derive a novel set of governing equations. Actually, the metrics of the  $(\phi,\psi,\eta)$  natural space, which are expressed in terms of flow quantities, should satisfy the zero curvature condition of the 3-D Euclidean (flat) space. A closed set of three PDEs is, thus, derived in terms of the velocity magnitude  $V$  and the aspect ratio  $t$  and the skew angle  $\theta$  of the elementary streamtube cross-section. Both the formulation of the method and the resulting equations are quite different from those proposed by Stanitz (Ref.4), although the same set of dependent and independent variables has been used.

It is seen that the 3-D inverse problem with velocity (pressure) only boundary conditions is an ill-posed problem accepting multiple solutions. This is due to the insufficient number of available boundary conditions. The extra boundary conditions required to remove the multiplicity may be introduced in several ways. One way, for example, is to prescribe desirable  $\theta$ -values along the lateral boundaries

(stream surfaces). An alternative way of removing the multiplicity is to decrease the degrees of freedom of the problem and seek for a particular solution in the resulting reduced space of geometries. In this work the latter approach has been adopted, thus, avoiding the introduction of extra information which is not always available. In this context, it has been shown that the problem accepts as a particular solution elementary streamtubes with orthogonal cross-sections. This way, the number of dependent variables is reduced by one and the governing equations simplify to an elliptic-type PDE for the velocity magnitude and to a second order ODE for the streamtube aspect ratio. The solution of these two equations provides the flow field in a single-pass manner without requiring any feedback from the geometry. In a subsequent step, geometry is determined independently by integrating Frenet equations along the natural coordinate lines. The decoupling of flow and geometry equations is obviously attractive from the computational point of view. However, the present method being a single-pass one, cannot inherently incorporate sophisticated flow or geometrical constraints. Some control on the geometry is effected *a priori* via the flow-field boundary conditions, e.g. Dirichlet velocity conditions on the boundary of the natural coordinate space are related to the arc length of the boundary streamlines.

The governing flow equations are discretized on the  $(\phi,\psi,\eta)$  space using centered finite differencing. A staggered  $V$ - $t$  computational stencil is employed in order to enhance the accuracy of the discretization in the near boundary regions. The resulting discrete system of equations is linearized to form a Newton iteration step. The explicit Jacobian inversion in the Newton step is avoided by employing a fast iterative linear system solver, based on the preconditioned restarting GMRES(m) algorithm (Ref.6). An incomplete L-U preconditioner, resulting from the MSIP approximate factorization scheme (Ref.7), premultiplies the velocity block of the Jacobian matrix, while tridiagonal preconditioning is applied to the  $t$ -block of the Jacobian matrix.

As it has been already stated, the geometry is calculated by integrating Frenet equations along the  $(\phi,\psi,\eta)$  coordinate lines after the flow field has been determined. Frenet equations form coupled systems of ODEs expressing the variation of the covariant base  $(\vec{g}_1, \vec{g}_2, \vec{g}_3)$  and the position vector  $\vec{r}$  along the natural coordinates lines. In order to enhance the accuracy of the discretization, a staggered computational stencil is also employed. A Crank-Nicolson type, second order accurate, space marching scheme is used for the numerical integration of the discrete equations.

In the last part of this lecture, the proposed method is validated for several "reproduction" test cases including axisymmetric and fully 3-D flows.

## 2. PROBLEM STATEMENT AND BASIC EQUATIONS

The inverse target pressure problem can be stated as:

"Given a prescribed target velocity (pressure) distribution on the entire (lateral, inflow and outflow) boundary of a 3-D flow field determine the corresponding boundary shape".

In the present work it has been assumed that the flow is three-dimensional, steady, compressible, inviscid and irrotational. It has been also assumed that the fluid is a perfect gas.

Under the above assumptions the flow equations simplify to

#### Continuity equation

$$\nabla \cdot (\rho \vec{v}) = 0 \quad (1)$$

#### Irrotationality condition

$$\nabla \times \vec{v} = 0 \quad (2)$$

Density equation (energy conservation for isentropic changes)

$$\rho = \left[ 1 + \frac{\gamma-1}{2} M_{ref}^2 (1 - V^2) \right]^{1/(\gamma-1)} \quad (3)$$

In the above equations the velocity  $V$  is normalized with a reference value  $V_{ref}$  and the density  $\rho$  with the corresponding  $\rho_{ref}$  value.  $M_{ref}$  is the Mach number at the reference point.  $\gamma$  is the ratio of specific heats  $c_p/c_v$ .

The irrotationality condition of the velocity field expressed by Eq.(2) is satisfied identically, by requiring the velocity vector to be the gradient of a scalar function, i.e. potential function. The potential function  $\phi$  is defined by the relation:

$$\vec{v} = \nabla \phi \quad (4)$$

The continuity Eq.(1) can be identically satisfied by introducing two stream functions  $\psi, \eta$  (Ref.8) defined by the relation

$$\rho \vec{v} = \nabla \psi \times \nabla \eta \quad (5)$$

Eq.(5) indicates that the velocity vector is tangent to both  $\psi = \text{const.}$  and  $\eta = \text{const.}$  surfaces, which are appropriately termed as stream surfaces. Obviously, intersections of stream surfaces, which belong to a different family, are streamlines. Schematically potential and stream surfaces are shown in Fig.1.

The potential function  $\phi$  and the two stream functions  $\psi, \eta$  are considered to be the independent variables. The physical  $(x, y, z)$  space on which the boundaries of the flow field sought are unknown, is mapped onto the natural  $(\phi, \psi, \eta)$  space via a body-fitted coordinate transformation.

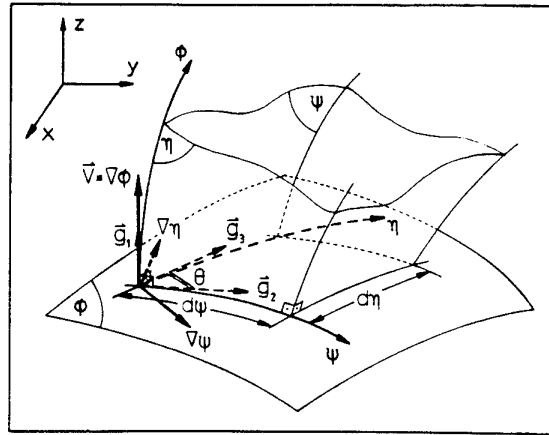


Fig.1 Natural  $(\phi, \psi, \eta)$  coordinate system and elementary streamtubes

### 3. THE CONCEPT

Differential geometry and generalized tensor analysis arguments are employed in order to derive the governing equations. For the sake of completeness an overview of differential geometry principles has been included in Annex A. The line of thought is as follows:

Consider a representation of the 3-D  $(x, y, z)$  Euclidean space in terms of the natural curvilinear coordinates  $(\phi, \psi, \eta)$ . Euclidean space being a flat one has zero curvature. Referring to the Ricci curvature tensor the zero curvature condition reads:

$$R_{xm} = 0 \quad \text{with } x, m = 1, 2, 3 \quad (6)$$

From the definition of the Ricci tensor and the Christoffel symbols  $\Gamma_{ij}^k$ , see Eqs (A8)-(A10), it is observed that the zero curvature condition is expressed in terms of the elements of the metrics tensor and their first and second order partial derivatives. In that sense, the flat space condition provides six metrics compatibility conditions which have to be satisfied for any parametrization of the physical space, including the  $(\phi, \psi, \eta)$  one. In the present formulation the  $(\phi, \psi, \eta)$  natural coordinates have been adopted having the advantage that the corresponding metrics tensor is expressed in terms of flow quantities only. The governing equations of the inverse flow problem in the  $(\phi, \psi, \eta)$  space, therefore, are provided via the satisfaction of the zero curvature conditions.

It is emphasized, however, that the six metrics compatibility conditions (6) are not independent, since in Riemannian geometry the Ricci tensor elements satisfy the following Bianchi identities (Ref.9).

$$g^{im} R_{xm, k} - g^{im} R_{rk, m} - g^{ij} R_{ik, j} = 0 \quad (7)$$

with  $i, j, k, r, m = 1, 2, 3$

Bianchi identities provide three ( $k = 1, 2, 3$ ) equations interrelating the covariant derivatives  $(R_{ij, k})$  of the curvature tensor elements, thus, reducing the overall number of independent metrics compatibility conditions to three only. According to

According to the discussion in Malvern (Ref.10), satisfaction of either the diagonal zero curvature conditions, Eqs (6), or the off-diagonal ones only, is not sufficient for the flatness of the physical 3-D space. For a simply connected region, this is established if either one of the set of the three conditions is satisfied in the interior of the field and the other one on the boundaries. Evidently, this combination results to a boundary value problem.

#### 4. METHOD FORMULATION

The contravariant base of the natural curvilinear  $(\phi, \psi, \eta)$  coordinate system is:

$$\begin{aligned}\bar{g}^1 &= \nabla\phi \\ \bar{g}^2 &= \nabla\psi \\ \bar{g}^3 &= \nabla\eta\end{aligned}\quad (8)$$

where indices 1,2,3 are associated with the  $\phi, \psi, \eta$  coordinates respectively.

The metrics and the conjugate (contravariant) metrics of the  $(\phi, \psi, \eta)$  system are evaluated, using Eqs (4) and (5) and standard tensor relations. In terms of flow quantities the metrics and conjugate metrics of the  $(\phi, \psi, \eta)$  coordinate system are:

$$\begin{aligned}g_{11} &= \frac{1}{V^2} & g^{11} &= V^2 \\ g_{22} &= \frac{1}{\rho V t \sin\theta} & g^{22} &= \frac{\rho V t}{\sin\theta} \\ g_{23} &= g_{32} = \frac{1}{\rho V t \tan\theta} & g^{23} &= g^{32} = \frac{-\rho V}{\tan\theta} \\ g_{33} &= \frac{t}{\rho V \sin\theta} & g^{33} &= \frac{\rho V}{t \sin\theta} \\ g_{12} &= g_{21} = g_{13} = g_{31} = 0 & g^{12} &= g^{21} = g^{13} = g^{31} = 0\end{aligned}\quad (9)$$

where  $\theta$  is the angle between  $\bar{g}_2$  and  $\bar{g}_3$  (or the angle at which a  $\psi = \text{const.}$  surface intersects a  $\eta = \text{const.}$  stream surface on a potential,  $\phi = \text{const.}$ , surface, see Fig.1) and  $t$  is a variable defined as:

$$t^2 = \frac{g_{33}}{g_{22}}\quad (10)$$

Variable  $t$  represents the aspect ratio of the cross-section ( $\phi = \text{const.}$  section) of the elementary streamtube defined by the stream surfaces  $\psi, \psi + d\psi = \text{const.}$  and  $\eta, \eta + d\eta = \text{const.}$ , with  $d\psi = d\eta$ .

The off-diagonal elements of the metrics and conjugate metrics tensor,  $g_{ij}$  and  $g^{ij}$  (with  $i=1$  and  $j=2,3$ ) respectively, are zero since via the defining relations (4) and (5) both  $\nabla\psi$  and  $\nabla\eta$  are normal to  $\nabla\phi$ , i.e.  $\nabla\phi \cdot \nabla\psi = \nabla\phi \cdot \nabla\eta = 0$  (note that in general  $\nabla\psi \cdot \nabla\eta = g^{23} \neq 0$ ).

The elementary distance  $ds$  expressed in terms of the natural coordinates is:

$$ds^2 = g_{11} d\phi^2 + g_{22} d\psi^2 + g_{33} d\eta^2 + 2g_{23} d\psi d\eta\quad (11)$$

Introducing Eqs (9) in the defining relations of the Christoffel symbols [see Eqs (A8) and (A9)], expressions of the latter in terms of the dependent variables  $-V, \rho, t, \theta$  are derived. For example:

$$\begin{aligned}\Gamma_{11}^1 &= -(\ln V)_\phi \\ \Gamma_{11}^2 &= \frac{\rho}{V t \sin\theta} (\ln V)_\psi - \frac{\rho}{V t \tan\theta} (\ln V)_\eta \\ \Gamma_{11}^3 &= \frac{-\rho}{V t \tan\theta} (\ln V)_\psi + \frac{\rho t}{V \sin\theta} (\ln V)_\eta\end{aligned}\quad (12)$$

where indices  $\phi, \psi$  and  $\eta$  denote partial derivatives.

The governing PDEs for  $V, t$  and  $\theta$  are derived by the following combinations of the zero conditions for the elements of the Ricci tensor:

$$-R_{11}/g_{11} = 0\quad (13)$$

$$-R_{22}/g_{22} + R_{33}/g_{33} = 0\quad (14)$$

$$R_{22}/g_{22} + R_{33}/g_{33} - 2R_{23}/g_{23} - R_{11}/g_{11} = 0\quad (15)$$

Eqs (13)-(15) supplemented by Eq.(3), constitute a closed set of PDEs for the quantities  $V, \rho, t, \theta$ . Satisfying three only compatibility conditions is in accordance with the number of independent variables considered ( $V, t, \theta$ ) as well as with the overall number of independent conditions. Strictly, Eqs (13)-(15) constitute necessary but not sufficient conditions for the flatness of the 3-D space considered.

As it will be demonstrated in the following sections, this particular linear combination of the individual Ricci tensor elements, leads to a tractable set of governing equations, which can be solved for the flow quantities in a self-contained, "single-pass", manner requiring no geometry feed-back. The geometry is determined in a subsequent step by transforming the flow solution on the natural space, to the physical, Cartesian, one.

#### 5. GOVERNING EQUATIONS OF THE FLOW FIELD

For the sake of simplicity, the developed form of the governing Eqs (13) to (15) is given for the incompressible case only. Respectively, these equations read:

Velocity (V) equation

$$\begin{aligned}
& (\ln V)_{\phi\phi} + \frac{1}{2}(1 + \cot^2\theta) \{ (\ln V)_{\phi} \\
& + (\ln \sin\theta)_{\phi} \}^2 - (\ln t)_{\phi}^2 \\
& - \frac{1}{2} \cot^2\theta \{ (\ln V)_{\phi} + (\ln \tan\theta)_{\phi} \}^2 \\
& + \frac{\rho t}{V \sin\theta} \{ (\ln V)_{\psi\psi} - (\ln V)_{\psi} [ (\ln V)_{\psi} \\
& + (\ln \sin\theta)_{\psi} - (\ln t)_{\psi} ] \} \\
& + \frac{\rho}{t V \sin\theta} \{ (\ln V)_{\eta\eta} \\
& - (\ln V)_{\eta} [ (\ln V)_{\eta} + (\ln \sin\theta)_{\eta} \\
& + (\ln t)_{\eta} ] \} - \frac{\rho \cot\theta}{V} \{ - (\ln V)_{\psi\eta} \\
& + (\ln V)_{\psi} [ (\ln V)_{\eta} + (\ln \tan\theta)_{\eta} ] \\
& + (\ln V)_{\eta} [ (\ln V)_{\psi} + (\ln \tan\theta)_{\psi} ] \} = 0
\end{aligned} \tag{16}$$

where  $\cot\theta = (\tan\theta)^{-1}$ .

Aspect ratio (t) equation

$$\begin{aligned}
& (\ln t)_{\phi\phi} - 2(\ln t)_{\phi} (\ln \sin\theta)_{\phi} \\
& + \frac{\rho \sin\theta}{V} \{ t (\ln V)_{\psi\psi} - \frac{1}{t} (\ln V)_{\eta\eta} \} \\
& + \frac{1}{\cos\theta} \{ (\ln V)_{\eta} (\ln \sin\theta)_{\psi} \\
& - (\ln V)_{\psi} (\ln \sin\theta)_{\eta} \} = 0
\end{aligned} \tag{17}$$

Skew angle ( $\theta$ ) equation

$$\begin{aligned}
& (\ln \sin\theta)_{\phi\phi} + \cot^2\theta \{ (\ln t)_{\phi}^2 + (\ln \cos\theta)_{\phi}^2 \\
& - \frac{\rho \sin\theta}{V} \{ t (\ln V)_{\psi\psi} + \frac{1}{t} (\ln V)_{\eta\eta} \} \} \\
& + \frac{\rho}{V} \cot\theta \{ 2 (\ln V)_{\psi\eta} + (\ln V)_{\psi} (\ln t)_{\eta} \\
& - (\ln V)_{\eta} (\ln t)_{\psi} \} = 0
\end{aligned} \tag{18}$$

Eqs (16) to (18) form a closed system of PDEs for the dependent variables  $V$ ,  $t$  and  $\theta$ , representing therefore the governing equations for the general 3-D inverse potential (incompressible) problem. The above system of equations forms a boundary value problem for the three dependent variables. According to the definition of the "target pressure" inverse problem, complete boundary conditions are only available for the velocity magnitude, while there are no boundary conditions for  $t$  and  $\theta$  along the lateral boundaries.

Following the discussion presented in the previous section it was investigated whether the two compatibility conditions which have not been taken into account could provide this extra information for  $t$  and  $\theta$ . The development of these conditions revealed that it is not possible to obtain a set of equations which contains information intrinsic to the lateral boundary only. This is mainly due to the presence of second

order mixed derivatives, e.g.  $(\ln V)_{\phi\psi}$  in the  $R_{12}=0$  condition, along with first order ones with respect to all three coordinate directions. These cannot be eliminated using the available information. It could be argued, therefore, that the 3-D inverse potential "target pressure" problem, as addressed above, is ill-posed, accepting multiple solutions.

The multiplicity of the solution could be removed by providing extra information for either  $t$  or  $\theta$  along the lateral boundaries (stream surfaces). An alternative way of removing the multiplicity of the solution without introducing extra *a priori* unknown information, is by reducing the degrees of freedom of the problem. In this work the latter strategy has been adopted. Actually, the dependency of the solution on  $\theta$  may be removed by observing that  $\theta$ -equation (18) is satisfied identically for constant  $\theta=90^\circ$ . This implies that a flow with elementary streamtubes with rectangular cross-sections represents a particular solution of the inverse potential target pressure problem. Assuming that  $\theta = \text{const.} = 90^\circ$ ,  $\theta$ -equation becomes redundant, while  $V$ - and  $t$ -equations, (16) and (17) respectively, are simplified considerably and a unique solution may be obtained with the available velocity boundary conditions. A similar analysis is valid for compressible flows as well.

Hereafter, therefore, we deal with the following well-posed version of the general 3-D inverse target pressure problem:

*"Given a prescribed target velocity (pressure) on the entire boundary of a 3-D flow field made up of orthogonal elementary streamtubes, determine the corresponding boundary shape".*

With the assumption of orthogonal streamtubes the resulting governing equations for compressible flow are:

Velocity (V) equation

$$\begin{aligned}
& (\ln V)_{\phi\phi} + (\ln p)_{\phi\phi} + \frac{\rho t}{V} (\ln V)_{\psi\psi} \\
& + \frac{\rho}{t V} (\ln V)_{\eta\eta} + \frac{1}{2} \{ (\ln V)_{\phi}^2 - (\ln t)_{\phi}^2 \\
& - (\ln p)_{\phi}^2 \} - \frac{\rho t}{V} (\ln V)_{\psi} [ (\ln V)_{\psi} - (\ln t)_{\psi} ] \\
& - \frac{\rho}{t V} (\ln V)_{\eta} [ (\ln V)_{\eta} + (\ln t)_{\eta} ] = 0
\end{aligned} \tag{19}$$

Aspect ratio (t) equation

$$\begin{aligned}
& (\ln t)_{\phi\phi} - (\ln p)_{\phi} (\ln t)_{\phi} + \frac{\rho t}{V} [ (\ln V)_{\psi\psi} \\
& + (\ln V)_{\psi} (\ln p)_{\psi} ] - \frac{\rho}{t V} [ (\ln V)_{\eta\eta} \\
& + (\ln V)_{\eta} (\ln p)_{\eta} ] = 0
\end{aligned} \tag{20}$$

**5.1 Discussion on the Flow Equations**

Appropriate boundary conditions for the solution of the flow equations are discussed in this section. The analysis is

restricted to the compressible form of the governing equations which have been derived with the assumption of orthogonal streamtubes cross-section.

Assuming a given  $t$ -field, then Eq.(19) represents an elliptic-type quasi-linear PDE for  $(\ln V)$ . In accordance with the standard "full potential" equations the mathematical, elliptic or hyperbolic, character of the velocity equation (19), in the streamwise sense, is controlled by the size of the local Mach number; i.e. subsonic or supersonic flow conditions respectively. Considering Eq.(3), it can be shown that

$$(\ln \rho)_\phi = -M^2 (\ln V)_\phi \quad (21)$$

where  $M$  is the local Mach number. Introducing Eq.(21) to (19) and rearranging the second order partial derivative terms, it is straightforward to show that the resulting equation is elliptic in the streamwise ( $\phi$ ) direction when  $M < 1$ , and hyperbolic when  $M > 1$ . Evidently, for subsonic flows, velocity boundary conditions should be specified all round the integration domain.

In the context of the present work, where internal configurations are considered, velocity is specified (Dirichlet type conditions) on the limiting lateral stream surfaces (walls), either as  $V = V(\phi, \psi)|_{\eta = \text{const}}$  or  $V = V(\phi, \eta)|_{\psi = \text{const}}$  and on the inlet and outlet sections, which are assumed to be potential surfaces, as  $V = V(\psi, \eta)|_{\phi = \text{const}}$ . On the solid walls potential  $\phi$  is related to streamline arc length  $s$  via the relation  $d\phi = V ds$ . It is obvious, therefore, that  $V = V(\phi, \psi)|_{\eta = \text{const}}$ , for instance, could be considered as  $V = V(s, \psi)|_{\eta = \text{const}}$ . The distribution  $V = V(s)$  is usually specified rather than  $V = V(\phi)$ .

The aspect ratio Eq.(20) may be considered as a second order ODE along the streamlines (i.e. in the  $\phi$ -wise direction). In that respect, Eq.(20) forms a boundary value problem requiring boundary conditions for  $t$  on the inflow and outflow boundaries only. Dirichlet type boundary conditions are imposed on the inlet section, the actual value depending on the  $\psi$ - $\eta$  discretization (e.g.  $t=1$  for  $\Delta\psi = \Delta\eta$ ). Assuming that the flow on the outlet section is "non-evolving", i.e. fully developed, a zero Neumann boundary condition is specified there.

It is emphasized that the closed set of Eqs (19) and (20) which govern the flow field without requiring any geometry feedback, form a strongly non-linear problem for  $V$  and  $t$ , even for the simplest, the potential incompressible, 3-D case.

## 5.2 Reduced Forms of the Flow Equations

In order to check the validity of the new governing equations proposed for the general 3-D inverse problem, some simple cases have been examined.

### 5.2.1 2-D Compressible Case

The 2-D form of the compressible flow equations is derived by considering that the flow derivatives vanish along one of the  $\psi$ - or  $\eta$ -directions and that the corresponding metric is constant, say equal to one. Obviously, the assumption of orthogonal streamtubes is valid also for the 2-D case.

Assuming that  $g_{33} = 1$  and  $\theta = 90^\circ$ , then  $t$  is implicitly defined via the metrics expressions (9) as

$$t = \rho V \quad (22)$$

With  $t$  given by Eq.(22) and taking into account that  $\eta$ -wise derivatives vanish, Eqs (19) and (20), governing the  $V$ - and  $t$ -field respectively, become identical with one another reducing to

$$\begin{aligned} & (\ln V)_{\phi\phi} + (\ln \rho)_{\phi\phi} + \rho^2 (\ln V)_{\psi\psi} \\ & - (\ln \rho)_\phi (\ln V)_\phi - (\ln \rho)_\phi^2 \\ & + \rho^2 (\ln \rho)_\psi (\ln V)_\psi = 0 \end{aligned} \quad (23)$$

Eq.(23) is the well known equation of Stanitz (Ref.2) for 2-D potential compressible flows (see also Part I of the lecture, Ref.1).

### 5.2.2 Axisymmetric Compressible Case

Another case where the assumption of orthogonal streamtubes is self evident is the axisymmetric flow with zero peripheral velocity component. Associating  $\eta = \text{const.}$  surfaces with meridional planes and, thus, neglecting the  $\eta$ -wise derivatives, Eqs (19) and (20) are reduced to

$$\begin{aligned} & (\ln V)_{\phi\phi} + (\ln \rho)_{\phi\phi} + \frac{\rho t}{V} (\ln V)_{\psi\psi} \\ & + \frac{1}{2} [ (\ln V)_\phi^2 - (\ln t)_\phi^2 - (\ln \rho)_\phi^2 ] \\ & - \frac{\rho t}{V} (\ln V)_\psi [ (\ln V)_\psi - (\ln t)_\psi ] = 0 \end{aligned} \quad (24)$$

$$\begin{aligned} & (\ln t)_{\phi\phi} - (\ln \rho)_\phi (\ln t)_\phi + \frac{\rho t}{V} [ (\ln V)_{\psi\psi} \\ & + (\ln V)_\psi (\ln \rho)_\psi ] = 0 \end{aligned} \quad (25)$$

Treating the axisymmetric case as a particular 3-D one, we get the advantage of solving  $V$ - and  $t$ -equations simultaneously. This way, the need of iterating between the flow field and geometry solutions, required by other axisymmetric approaches which are extensions of standard 2-D inverse methods and have the local radial distance  $R$  as a principal variable (e.g. Refs 1, 11), is alleviated. The flow field and geometry calculation procedures, therefore, remain entirely independent. Effectively,  $t$ -equation plays the role of a  $R$ -equation. Note that it can be shown that  $t$  is proportional to  $R^2$ .

## 6. GEOMETRY CALCULATION

Ultimately, the objective of an inverse method is to calculate the geometry which complies with the prescribed flow qualities -properties-. In the previous sections it has been shown that the flow Eqs (19) and (20) governing the 3-D inverse potential target pressure problem form a closed set of PDEs on the natural coordinates space, requiring no information, feedback, from the physical geometry itself. The purpose of this section is to demonstrate how the target

geometry is obtained, once the flow field has been determined.

According to the analysis presented in Annex A the Cartesian coordinates of the geometry position vector  $\vec{r}$  can be evaluated in two steps by integrating Eqs (A7) and (A1) along any one of the natural coordinates lines. If, for example, a  $\psi = \text{const.}, \eta = \text{const.}$  streamline is considered, Eq.(A7) provides the following system of ODEs

$$\frac{d}{d\phi} \begin{bmatrix} \vec{g}_1 \\ \vec{g}_2 \\ \vec{g}_3 \end{bmatrix} = [A_\phi] \begin{bmatrix} \vec{g}_1 \\ \vec{g}_2 \\ \vec{g}_3 \end{bmatrix}; [A_\phi] = \begin{bmatrix} \Gamma_{11}^1 & \Gamma_{11}^2 & \Gamma_{11}^3 \\ \Gamma_{21}^1 & \Gamma_{21}^2 & \Gamma_{21}^3 \\ \Gamma_{31}^1 & \Gamma_{31}^2 & \Gamma_{31}^3 \end{bmatrix} \quad (26)$$

where the matrix  $[A_\phi]$  elements, being a sub-set of the (twenty seven) Christoffel symbols, are analytical expressions of the (known) flow quantities and their partial derivatives on the natural space.

Eqs (26), which represent a generalized form of the Frenet equations, may be integrated to provide the covariant vector base if appropriate initial conditions are prescribed for  $(\vec{g}_1, \vec{g}_2, \vec{g}_3)$ . The Cartesian coordinates of the geometry can be evaluated then, by integrating the covariant base along any one of the natural coordinates. Starting, therefore, from a known position  $\vec{r}_0$ , then

$$\vec{r} = \vec{r}_0 + \int_{\phi_0}^{\phi} \vec{g}_1 d\phi \quad (27)$$

It should be noted that the evaluation of the  $[A_\phi]$  matrix elements involves inner flow information even when the integration of the system of Eqs (26) is performed along the flow field boundaries. This is the reason why the solution of the flow field equations precedes the geometry calculation.

## 7. NUMERICAL INTEGRATION OF FLOW EQUATIONS

The objective of this section is to discuss in detail the discretization, the linearization and the iterative solver employed for the numerical integration of the system of flow Eqs (19) and (20).

### 7.1 Discretization

$(\ln V)$  and  $(\ln t)$  are considered to be the dependent computational variables. First and second order partial derivatives are discretized using second order accurate central differencing on a uniform  $(\phi, \psi, \eta)$  grid. Derivatives of  $(\ln \rho)$  are directly related to the  $(\ln V)$  derivatives through Eq.(3).

On the cross-flow plane the discretization of the equations has been effected on a staggered grid.  $t$ -nodes are off-set with respect to the  $V$ - and  $\rho$ -nodes, which are considered to be the actual grid nodes, by half a cell distance, both in the  $\psi$ - and  $\eta$ -directions. Namely, if  $I, J$  and  $K$  indices are associated to the grid nodes in the  $\phi$ -,  $\psi$ -,  $\eta$ -directions respectively, then  $V$  and  $\rho$  are stored at  $(I, J, K)$  locations, whilst  $t$  is stored at  $(I, J + 1/2, K + 1/2)$  locations, see Fig.2.

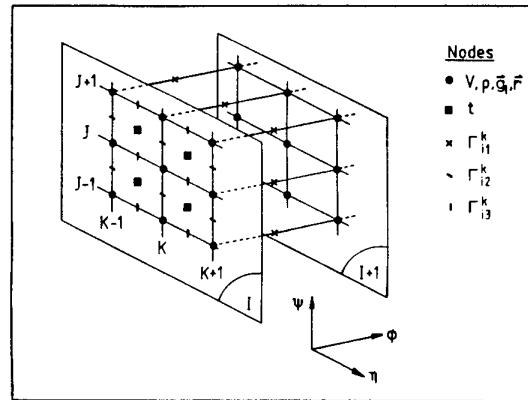


Fig.2 Staggered computational stencil for the flow field and geometry calculations

The advantage of this staggering practice is twofold. From the numerical point of view, the first order cross-flow derivatives of  $(\ln V)$  and  $(\ln t)$  are tightly coupled. At mid-cell locations,  $(\ln V)$  and  $(\ln t)$  cross-flow derivatives are approximated assuming linear variation within the cells. For example

$$\begin{aligned} [(\ln V)_\psi]_{I, J+\frac{1}{2}, K+\frac{1}{2}} &= \frac{1}{2\Delta\psi} [(\ln V)_{I, J+1, K+1} \\ &- (\ln V)_{I, J, K+1} + (\ln V)_{I, J+1, K} - (\ln V)_{I, J, K}] \end{aligned} \quad (28)$$

This implies that there is no need of one-sided differencing on the boundary cells for the discretization of  $(\ln V)_\psi$  and  $(\ln V)_\eta$  contained in  $t$ -equation (20). The required mid-cells values,  $V_{I, J+1/2, K+1/2}$  for the  $t$ -equation and  $t_{I, J, K}$  for the  $V$ -equation (19) are approximated assuming linear variation of  $(\ln V)$  and  $(\ln t)$  in the corresponding cell. The definition of  $t$  as the elementary streamtube aspect ratio, on the other hand, requires  $t$  to be stored at the centroid of the streamtube cross-section. In that respect, the adopted staggering practice is also physically sound.

The central differencing practice for  $V$ -equation limits the present approach to subsonic flows only, where the equation is elliptic. In the case of transonic flow, upwind differencing in the streamwise,  $\phi$ -wise, direction should be used.

### 7.2 Linearization

The  $V$ - and  $t$ -equations are highly nonlinear and have different mathematical character. It has been decided, therefore, to solve them in a coupled iterative mode. A Newton procedure, where nonlinear terms are expanded in the iteration space using Taylor series is employed to linearize the discrete system of equations. This linearization procedure results to the following iteration:

$$0 = R^{n+1} = R^n + \left[ \frac{\partial R}{\partial X} \right]^n \Delta X \quad (29)$$

$$X^{n+1} = X^n + \Delta X \quad ; \quad X = \begin{bmatrix} \ln V \\ \ln t \end{bmatrix} \quad (30)$$

where superscript (n) denotes the iteration level and R is the residual vector of the V- and t-system of equations.

In writing the linearization relation (29), the dependence of the governing equation on  $\rho$  is not shown explicitly. This is because  $\rho$  is frozen during the (V,t) iteration (a practice which is very common in subsonic flow computations). The density field is updated after (V,t)<sup>n+1</sup> have been determined, using the algebraic Eq.(3).

### 7.3 Solution Algorithm

The solution of the discrete block system of Eq.(29) is carried out using an iterative technique based on a preconditioned gradient method. Preconditioning is essential since matrix  $(\partial R/\partial X)$  is stiff. The most obvious choice for the preconditioning matrix [P] is

$$[P] \sim \left[ \frac{\partial R}{\partial X} \right]^{-1} \quad (31)$$

Indicating the dependence of  $(\partial R/\partial X)$  on the unknowns V and t this Jacobian matrix can be expressed in terms of corresponding submatrices as:

$$\left[ \frac{\partial R}{\partial X} \right] = \begin{bmatrix} L_1 & L_2 \\ L_3 & L_4 \end{bmatrix} \quad (32)$$

Neglecting the effect of submatrix [L<sub>2</sub>], a preconditioning matrix may be obtained in the form:

$$[P] = \begin{bmatrix} P_1 & 0 \\ P_3 & P_4 \end{bmatrix} \quad (33)$$

where

$$\begin{aligned} [P_1] &\sim [L_1]^{-1} \\ [P_4] &\sim [L_4]^{-1} \\ [P_3] &\sim [L_4]^{-1} [L_3] [L_1]^{-1} \sim [P_4] [L_3] [P_1] \end{aligned} \quad (34)$$

In its discrete form [P<sub>1</sub>] is derived by an incomplete L-U decomposition of [L<sub>1</sub>] using the MSIP technique (Ref.7). [P<sub>4</sub>] is approximated by

$$[P_4] = \left\{ \frac{[I]}{\Delta \tau} + [L_4] \right\}^{-1} \quad (35)$$

Operator [P<sub>4</sub>] is related to the inversion of a tridiagonal matrix since [L<sub>4</sub>], which expresses the dependence of t-equation on (ln t), is an one-dimensional three-point discrete operator. The pseudo-time term ( $[I]/\Delta \tau$ ) serves as a relaxation parameter, while its positive sign contributes to the diagonal dominance of the tridiagonal matrix. Appropriate values of  $\Delta \tau$  have been determined via computational experimentation.

The preconditioned form of the Newton step, i.e. Eq.(29) premultiplied by the [P] matrix, is solved with the linear, restarting GMRES (m) algorithm (Ref.6).

## 8. NUMERICAL INTEGRATION OF GEOMETRY EQUATIONS

The calculation of the geometry which exhibits the prescribed flow properties is the actual objective of an inverse method. In that sense the numerical schemes which are used for the integration of the geometry equations should be very accurate. Compared to the inner-flow region the calculation of the lateral boundaries is more demanding, because the required flow information is not completely available there. This effect is more pronounced on the edges (intersections of the limiting stream surfaces of different family) where the  $\psi$ - and  $\eta$ -wise surface derivatives are discontinuous. To circumvent this difficulty stagger grid techniques have been employed. Details of the discretization and integration procedure of the geometry equations are discussed in this section.

### 8.1 Discretization

The covariant base  $(\vec{g}_1, \vec{g}_2, \vec{g}_3)$  is computed on the actual grid nodes (I,J,K) which are V- and  $\rho$ -nodes. Depending on the direction of the integration of Eq.(26), the corresponding Christoffel symbols appearing in its RHS are stored at different locations. Noting that the Christoffel symbols are expressed in terms of the first order derivatives of the flow quantities (V,t, $\rho$ ), the staggering to be adopted should be such, so that the discrete form of these derivatives use inner-grid information avoiding, as much as possible, variables extrapolation. Thus, the  $\Gamma_{ij}^k$  Christoffel symbols, which are associated with the streamwise ( $\phi$ -wise) direction of the covariant base integration, are calculated at  $(I+1/2, J, K)$  locations. Accordingly, the  $\Gamma_{i2}^k$  and  $\Gamma_{i3}^k$  symbols, associated with the  $\psi$ - and  $\eta$ -wise integrations respectively, are calculated at  $(I, J+1/2, K)$  and  $(I, J, K+1/2)$  locations respectively (see Fig.2). It is noted that the assumptions adopted for the variation of the flow variables in the grid cells are also used in the actual evaluation of the  $\Gamma_{ij}^k$  symbols.

### 8.2 Solution Algorithm

The numerical integration of the geometry Eqs (26) and (27) is performed in two steps. First, the covariant base  $\vec{g}_i$  is determined applying an implicit second order accurate Crank-Nikolson scheme along the natural coordinates. Along the streamwise coordinate, for instance, the discrete form of Eq.(26) reads:

$$\begin{aligned} \frac{[G]_{I+1, J, K} - [G]_{I, J, K}}{\Delta \phi} &= \\ &= [A_\phi]_{I+1/2, J, K} \frac{1}{2} \{ [G]_{I+1, J, K} + [G]_{I, J, K} \} \end{aligned} \quad (36)$$

or, dropping the cross-plane indices

$$[G]_{I+1} - [G]_I = \frac{1}{2} \Delta \phi [A_\phi]_{I+1/2} \{ [G]_{I+1} + [G]_I \} \quad (37)$$

where

$$[G] = \begin{bmatrix} \vec{g}_1 \\ \vec{g}_2 \\ \vec{g}_3 \end{bmatrix} = \begin{bmatrix} g_{1x} & g_{1y} & g_{1z} \\ g_{2x} & g_{2y} & g_{2z} \\ g_{3x} & g_{3y} & g_{3z} \end{bmatrix} \quad (38)$$

with x,y,z indices indicating the corresponding Cartesian components. Quantities appearing in Eqs (36) and (37) are compatible with the discretization strategy presented in the previous paragraph. Assuming that  $[G]_I$  is known,  $[G]_{I+1}$  is provided through

$$[G]_{I+1} = \left\{ [I] - \frac{\Delta\phi}{2} [A_\phi]_{I+1/2} \right\}^{-1} \left\{ [I] + \frac{\Delta\phi}{2} [A_\phi]_{I+1/2} \right\} [G]_I \quad (39)$$

with  $[I]$  being the 3x3 identity matrix. Equations similar to Eq.(39) hold for the  $\psi$ - and  $\eta$ -wise integrations.

To determine the covariant base distribution on the complete grid, Eq.(39) is first applied for the center-line. The integration of Eq.(39) starts from the inlet section on which the orientation of the orthogonal covariant base is arbitrarily specified, its size being controlled by the corresponding metrics which in turn are expressions of the V and t boundary distributions. On each cross-flow plane, i.e. potential ( $\phi = \text{const.}$ ) surface,  $[G]$  is determined via a combination of  $\psi$ - and  $\eta$ -wise integrations. Starting from the calculated covariant base on the central grid node (center-line distribution), two  $\psi$ -wise integrations (in the positive and negative sense) are carried out in order to determine the  $[G]$  distribution along the central  $\eta$ -family grid line. This latter distribution provides the initial conditions for the  $\eta$ -wise integrations which are carried out along all  $\psi$ -family grid lines. Obviously, the order of  $\psi$ - and  $\eta$ -wise integrations performed for the calculation of the  $[G]$  distribution on the cross-flow plane may be interchanged. An averaging practice has been adopted in this work. In duct flow applications the above directional integration scheme was found to be the most effective in terms of minimal error accumulation.

Having calculated the  $[G]$  field, the geometry is determined by straightforward second order accurate numerical integrations of Eqs (27) along the  $(\phi, \psi, \eta)$  grid following a similar directional integration strategy. On the cross-flow plane ( $\phi = \text{const.}$  surfaces) for instance, the  $\psi$ - and  $\eta$ -wise integrations read respectively:

$$\vec{r}_{I, \psi+1, K} = \vec{r}_{I, \psi, K} + \Delta\psi \frac{1}{2} (\vec{g}_{2, \psi+1, K} + \vec{g}_{2, \psi, K}) \quad (40)$$

$$\vec{r}_{I, \psi, K+1} = \vec{r}_{I, \psi, K} + \Delta\eta \frac{1}{2} (\vec{g}_{3, I, \psi, K+1} + \vec{g}_{3, I, \psi, K}) \quad (41)$$

In accordance with the scheme used for the covariant base calculation, the sought geometry at  $(I, J, K)$  locations, i.e. the position vector  $\vec{r}_{I, J, K}$ , is finally obtained with straightforward averaging.

The magnitude of the covariant base vectors is directly related to the metrics (note that  $\vec{g}_i \cdot \vec{g}_i = (\vec{g}_i)^2 = g_{ii}$ ; repeated indices are not summed here). The metrics, on the other hand, are expressed in terms of the flow quantities V, t and  $\phi$ . It is evident that the covariant base vectors, calculated via the numerical integration of the geometry Eqs (26) and (27) should be compatible with (the already known) corresponding metrics. Stanitz (Ref.5) found it necessary to incorporate a magnitude correction within the geometry calculation procedure, so to ensure the compatibility between the geometry and the flow field (a direction correction for the base vectors was also incorporated). The velocity equation, that Stanitz (Refs 4, 5) is using, has coefficients which are explicit functions of geometric parameters. It seems, that corrections are necessary so to minimize possible adverse (nonlinear) feedback of geometry errors, within the overall calculation procedure. In our method and for the design test cases attempted it was not necessary to cater for any geometry correction technique. Perhaps, this is due to the principal characteristic of the proposed 3-D inverse method that the flow and geometry calculation procedures are decoupled, i.e. they are entirely independent.

## 9. RESULTS AND DISCUSSION

The inverse design methodology proposed here has been applied to determine the geometry of several axisymmetric and one 3-D duct. In axisymmetric flows the reduced form of flow Eqs (24), (25) is used. Since these equations consist a special form of the 3-D set, i.e. Eqs (19), (20), the experience gained from the numerical integration of the reduced set of PDEs is directly transferable to the fully 3-D one. In order to establish the accuracy of the method, inverse calculation results are compared to direct 'reproduction' results. Note that the term 'reproduction' is used in the following sense: "The boundary velocity distributions calculated by a direct -analysis- method, which is applied to the geometry produced by an inverse method, should ideally be the same, reproduce, the velocity boundary conditions -target distributions- of the inverse calculation".

### 9.1 Axisymmetric Duct Test Cases

Results for an accelerating duct, with 0.2 inlet Mach number, are presented in Figs 3-5. Imposed -target- wall velocity distribution is shown in Fig.3. The non-constant part of this distribution is a half cycle sinusoidal function.

The grid (i.e. potential lines and streamlines) 'generated' by the inverse method and calculated Mach number contours are presented in Figs 4 and 5 respectively. The wall velocity distribution calculated with a direct method (Ref.13) is also included in Fig.3. This agrees very well with the target distribution, indicating the accuracy of the proposed methodology.

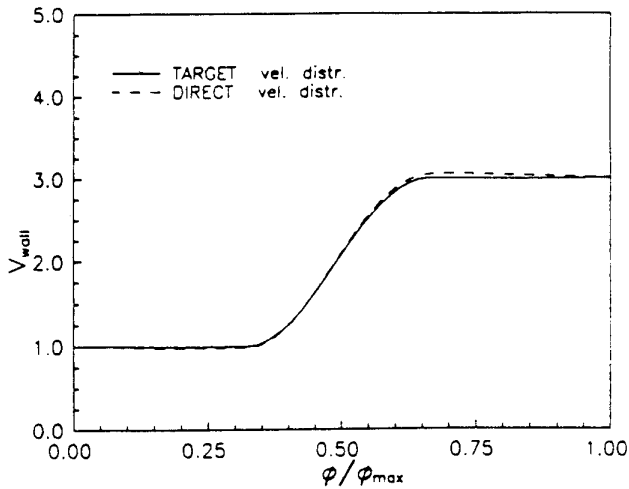


Fig.3 Target and direct calculation wall velocity distributions for the accelerating duct case

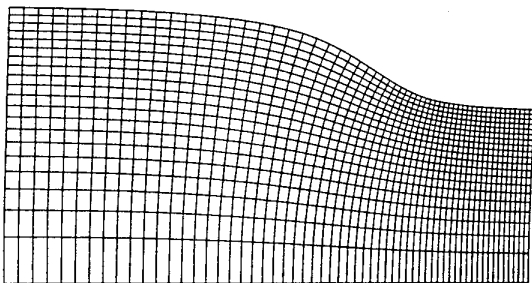


Fig.4 Calculated grid for the accelerating duct case

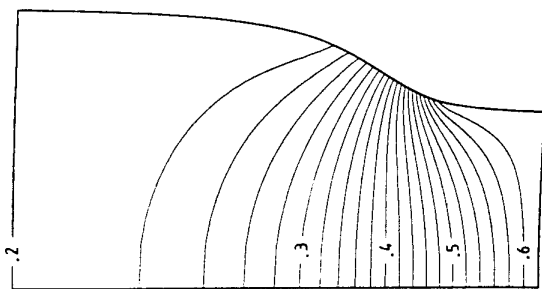


Fig.5 Inverse calculation Mach contours for the accelerating duct case

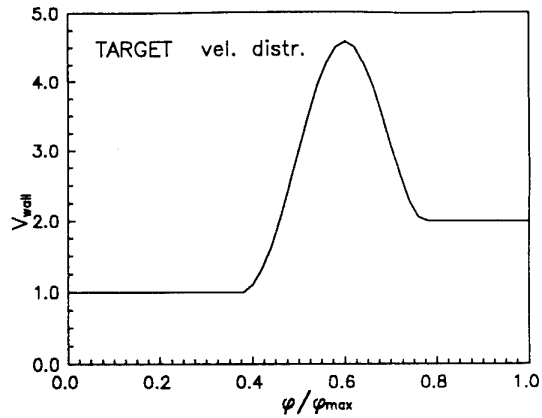


Fig.6 Target velocity distribution for the convergent-divergent nozzle case

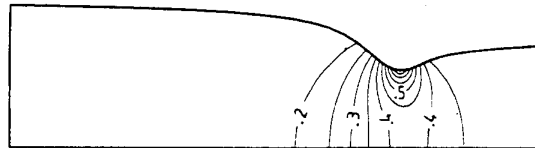


Fig.7 Inverse calculation Mach contours for the axisymmetric convergent-divergence nozzle case

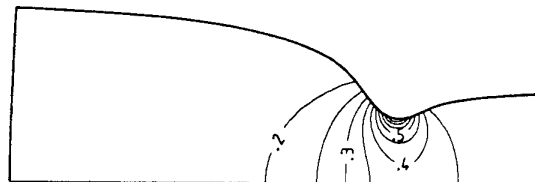


Fig.8 Inverse calculation Mach contours for the 2-D convergent-divergent nozzle case

Calculations for designing a convergent-divergent axisymmetric nozzle, with 0.15 inlet Mach number, have been also carried out. The target wall velocity distribution is shown in Fig.6. The non-constant part of the distribution is described by a full cycle sinusoidal function with linearly increasing amplitude. Mach contour results are presented in Fig.7. It is interesting to compare this axisymmetric nozzle with the one shown in Fig.8, which is a 2-D nozzle, with almost the same aspect ratio, designed with the same target velocity distribution (Ref.12).

**9.2 3-D Double Turning Duct Test Case**

This case concerns the reproduction of a 3-D subsonic, double turning converging duct. The geometry of the duct, which is shown in Fig.9a, has been defined analytically (Workshop on Selected Inverse and Optimum Design Problems, organized by Brite Euram Project 1082 partners,

June 1992). Inlet Mach number is set to 0.2, leading to a high subsonic exit Mach number of the order of 0.75.

A full-potential 3-D solver (Ref.14) is employed to obtain the flow field and the velocity distribution on the lateral walls of the duct. The wall (as well as the inlet and outlet) velocity distributions calculated by the direct solver are used as input by the 3-D inverse method in order to reproduce the geometry of the duct. The 3-D inverse solver, however, requires the velocity distributions along the boundary (limiting) streamlines which, in general, do not coincide with the boundary grid lines of the direct solver. A special purpose post-processor has been developed "translating" the flow field calculated by the direct code to a form which can be comprehended by the inverse method. The numerical errors accumulated in the interpolation procedures, carried out by the post-processor, affect to some extent, the accuracy of the "reproduction". To minimize the numerical errors involved, a relatively fine (30x15x15) computational grid was used in the direct computation.

A 43x15x15 uniform grid was generated on the  $(\phi, \psi, \eta)$  space. The computational cost associated with the inverse problem solution is of the order of 650 CPU secs in one processor of

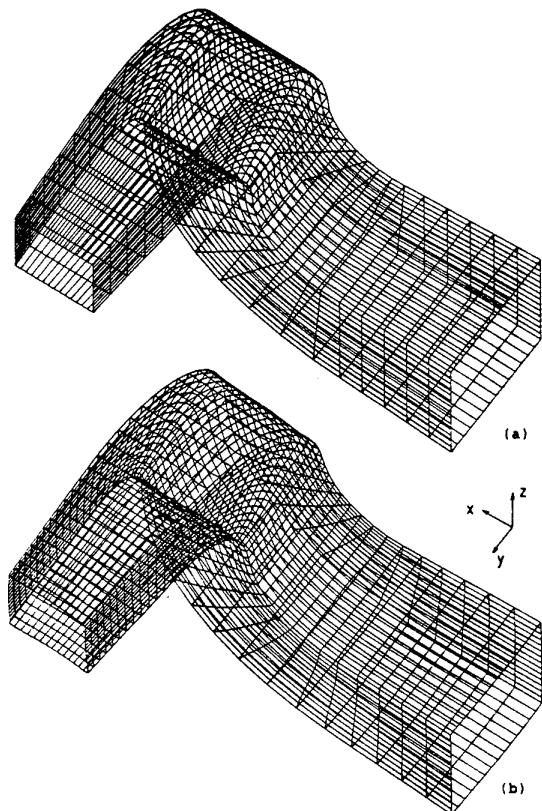


Fig.9 Perspective views of (a) the original and (b) the reproduced 3-D double turning duct

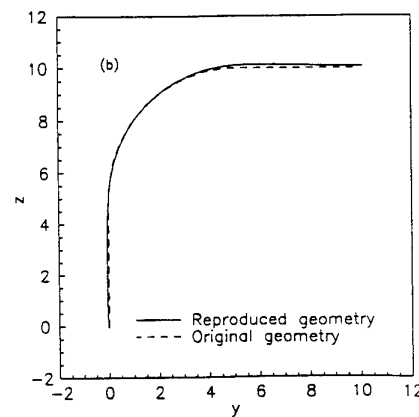
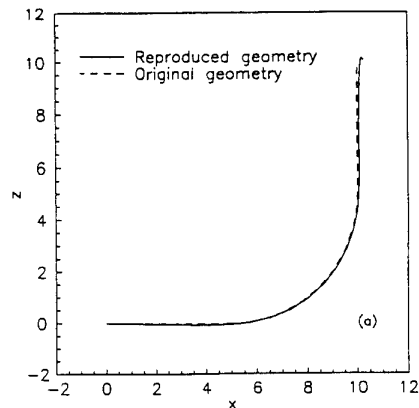


Fig.10 Projections of the center-line of the original and the reproduced duct on (a) the  $(x,z)$  and (b) on the  $(z,y)$  plane

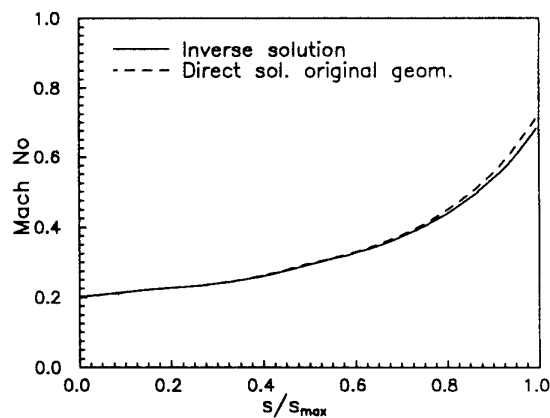


Fig.11 Mach number distributions along the center-line of the double turning duct

an Alliant FX 80 computer. A representative view of the original and reproduced duct geometries is presented in Figs 9a and 9b respectively, while geometries of the corresponding center-lines on the  $(x,z)$  and  $(y,z)$  planes are compared in Figs 10a and 10b. It should be noted that the center-line

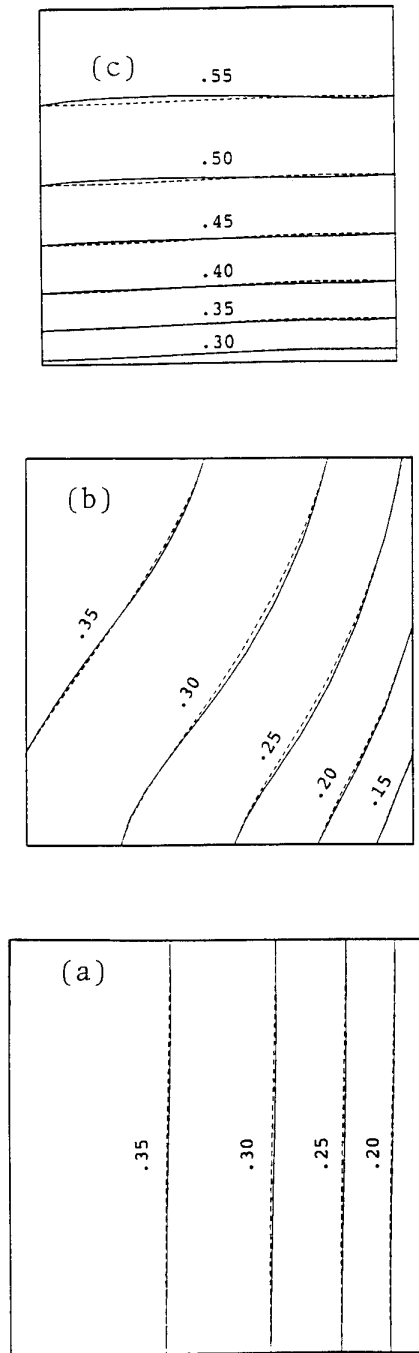


Fig.12 Mach number contours of inverse (—) and direct (---) method on sections normal to the center-line of the duct at (a)  $s=1/3s_{\max}$  (b)  $s=1/2s_{\max}$  and (c)  $s=2/3s_{\max}$

of the reproduced geometry is not a direct output of the inverse method. Its geometry is determined by averaging the calculated Cartesian coordinates of the four streamline vertices. This practice is acceptable since the duct under discussion has square cross section. The satisfactory compari-

sons of both the center-line and the lateral wall geometries indicate the accuracy of the proposed 3-D inverse method. Inevitably, some discrepancies are introduced by the interpolations and the different discretization schemes which are used in the direct and inverse solvers. Small discrepancies of the geometry near the vertices of the duct are due to the singular behaviour of the edge-streamlines.

Mach number distributions calculated with the inverse and direct solvers along the center-line of the duct are compared in Fig.11. As the flow proceeds downstream, the Mach number is increasing, which is expected since the duct is converging. The agreement between direct and inverse calculation distributions is very good. It is believed that the small discrepancies observed near the exit region are partly due to the error accumulation of the geometry integrations and partly due to the inappropriate "non-evolving" zero Neumann boundary condition for  $t$  (actually the direct calculation indicates that the flow is "evolving" near the exit). Inverse and direct solver Mach number contours (solid and dashed lines respectively) on three cross sections normal to the center-line at the locations  $s=1/3, 1/2, 2/3 s_{\max}$ ,  $s$  being the center-line arc length, are presented in Fig.12. In spite of the fact that a 3-D interpolation procedure was used to produce these contours the reproduction is quite accurate.

## 10. CONCLUSIONS

An inverse potential methodology is introduced for the solution of the fully 3-D target pressure problem. The method is based on a body-fitted coordinate transformation which maps the physical space onto a natural one. Potential function and two stream functions are used as the natural coordinates (independent variables), whilst the velocity magnitude, as well as, the aspect ratio and the skew angle of the elementary streamtube cross-section are considered to be the dependent ones.

A novel set of governing equations for the inverse 3-D problem is proposed which is derived using differential geometry and generalized tensor analysis arguments. The general 3-D inverse problem is treated as a geometrical one which has to satisfy the zero-curvature metrics compatibility conditions of the 3-D Euclidean, flat, space. It is shown that in the general case the 3-D inverse "target pressure" problem is ill-posed, accepting multiple solutions.

A particular solution of the 3-D inverse problem is shown to be the one with elementary streamtubes with orthogonal cross-section, i.e. orthogonal stream surfaces are assumed. The governing equations and their boundary conditions are presented and discussed for this case. Reduced forms of these equations for the 2-D and axisymmetric flows are also examined. It is shown that resulting system of governing equations can be solved with velocity only boundary conditions because of the special form of the aspect ratio equation. On the natural coordinates space the flow field is determined in a self-contained manner without requiring any feedback from the actual geometry. The geometry is determined after the flow solution has been calculated, by integrating the generalized Frenet equations along the

natural coordinates lines.

The inverse method is validated in several "reproduction" test cases. The very good agreement between direct and inverse solver results indicate the reliability of the proposed method.

#### ACKNOWLEDGEMENT

This work was financed by the DG XII of the European Economic Community in the context of the BRITE-EURAM AERO-0026-C(TT) "Optimum Design in Aerodynamics" Project.

#### REFERENCES

1. Chaviaropoulos, P., Dedoussis, V. and Papailiou, K.D., "Single-pass Method for the Solution of Inverse Potential and Rotational Problems. Part I: 2-D and Quasi 3-D Theory and Applications", AGARD FDP/VKI Special Course on OPTIMUM DESIGN METHODS FOR AERODYNAMICS, Von Karman Institute, April 1994.
2. Stanitz, J.D., "Design of Two-Dimensional Channels with Prescribed Velocity Distributions Along the Channel Walls", NACA Report 1115, 1953.
3. Lighthill, M.J., "A New Method of Two-Dimensional Aerodynamic Design", ARC R&M 2112, 1945.
4. Stanitz, J.D., "General Design Method for Three-Dimensional Potential Flow Fields. I-Theory", NASA CR 3288, 1980.
5. Stanitz, J.D., "General Design Method for Three-Dimensional Potential Flow Fields. II-Computer Program DIN3D1 for Simple Unbranched Ducts", NASA CR 3926, 1985.
6. Saad, Y. and Schultz, M.M., "GMRES: A Generalized Minimal Residual Algorithm for Solving Nonsymmetric Linear Systems", Department of Computer Science, Yale University Rep. YALEU/DCS/RR-254, 1983.
7. Zedan, M. and Schneider, G.E., "A Three-Dimensional Modified Strongly Implicit Procedure for Heat Conduction", AIAA J., 21, 2, February 1983, pp 295-303.
8. Yih, C.S., "Stream functions in three-dimensional flows", *Houille Blanche* 12, 1957, pp 445-450.
9. Synge, J.L. and Schild, A., "Tensor Calculus", New York, Dover, 1978.
10. Malvern, L.E., "Introduction to the Mechanics of a Continuous Medium", New Jersey, Prentice-Hall, 1969.
11. Nelson, C.D. and Yang, T., "Design of Branched and Unbranched Axially Symmetrical Ducts with Specified Pressure Distribution", AIAA J., 15, 9, September 1977, pp 1272-1277.
12. Dedoussis, V., Chaviaropoulos, P. and Papailiou, K.D., "Rotational Compressible Inverse Design Method for Two-Dimensional, Internal Flow Configurations", AIAA J., 31, 3, March 1993, pp 551-558.
13. Kioussis, P., Chaviaropoulos, P. and Papailiou, K.D., "Meridional Flow Calculation Using Advanced CFD Techniques", ASME Paper 92-GT-325, 1992.
14. Chaviaropoulos, P., Giannakoglou, K. and Papailiou, K.D., "Novel Scalar-Vector Potential Formulation for Three-Dimensional Inviscid, Rotational Flow Problems", AIAA J., 26, 10, October 1988, pp 1734-1739.

## ANNEX A

## DIFFERENTIAL GEOMETRY OVERVIEW

In this Annex key elements of differential geometry are presented. More details may be found in any differential geometry or tensor calculus book (e.g. Ref.9).

Let  $x^i$  ( $i=1,2,3$ ) be the Cartesian coordinates and  $u^j$  ( $j=1,2,3$ ) a body-fitted parametrization of the flow field considered. Let  $\bar{g}_i$  and  $\bar{g}^j$  represent the covariant and contravariant orthonormal vector bases defined as:

$$\bar{g}_i = \frac{\partial \bar{r}}{\partial u^i} \quad \bar{g}^j = \nabla u^j \quad ; \quad \bar{g}_i \cdot \bar{g}^j = \delta_i^j \quad (A1)$$

where

$$\bar{r} = (x^1, x^2, x^3) \quad ; \quad \nabla = \left( \frac{\partial}{\partial x^1}, \frac{\partial}{\partial x^2}, \frac{\partial}{\partial x^3} \right) \quad (A2)$$

are the position vector and the gradient operator respectively.  $\delta_i^j$  is the Kronecker delta.

The covariant and contravariant metrics tensors are defined respectively as:

$$g_{ij} = \bar{g}_i \cdot \bar{g}_j \quad g^{ij} = \bar{g}^i \cdot \bar{g}^j \quad (A3)$$

The contravariant metrics (or conjugate metrics)  $g^{ij}$  represent the cofactors of the covariant metrics satisfying the following identity:

$$g^{ij} g_{jk} = \delta_k^i \quad (A4)$$

where repeated indices denote summation (Einstein convention).

The Jacobian J of the coordinate transformation may be expressed in terms of the covariant (or contravariant) metrics as

$$J^2 = \det(g_{ij}) = \det^{-1}(g^{ij}) \quad (A5)$$

and the metric (infinitesimal distance) is expressed on the transformed domain as:

$$ds^2 = g_{ij} du^i du^j \quad (A6)$$

The partial derivatives of the covariant (and contravariant) bases with respect to the curvilinear coordinates are expressed in terms of the Christoffel symbols of the second kind  $\Gamma_{ij}^k$  as:

$$\frac{\partial \bar{g}_i}{\partial u^j} = \Gamma_{ij}^k \bar{g}_k \quad (A7)$$

The Christoffel symbols of the first and second kind,  $[ij,k]$  and  $\Gamma_{ij}^k$  respectively, are defined in terms of partial derivatives of the metrics tensor as:

$$[ij,k] = \frac{1}{2} \left( \frac{\partial g_{ik}}{\partial u^j} + \frac{\partial g_{jk}}{\partial u^i} - \frac{\partial g_{ij}}{\partial u^k} \right) \quad (A8)$$

$$\Gamma_{ij}^k = g^{km} [ij,m] \quad (A9)$$

The space curvature tensor is expressed in terms of the Christoffel symbols and their derivatives. It has six independent entries that form the symmetric Ricci curvature tensor  $R_{r\eta}$  defined as

$$R_{rm} = \frac{\partial \Gamma_{rn}^n}{\partial u^m} - \frac{\partial \Gamma_{rm}^n}{\partial u^n} + \Gamma_{rn}^p \Gamma_{pm}^n - \Gamma_{rm}^p \Gamma_{pn}^n \quad (A10)$$

The Euclidean space being a flat space has zero curvature. Referring to the Ricci curvature tensor the zero curvature condition reads

$$R_{rm} = 0 \quad \text{with } r, m = 1, 2, 3 \quad (A11)$$

# Optimum Aerodynamic Design via Boundary Control\*

*Antony Jameson*

Department of Mechanical and Aerospace Engineering  
Princeton University  
Princeton, New Jersey, 08544 U.S.A.

## ABSTRACT

These lectures describe the implementation of optimization techniques based on control theory for airfoil and wing design. In previous studies [10, 11] it was shown that control theory could be used to devise an effective optimization procedure for two-dimensional profiles in which the shape is determined by a conformal transformation from a unit circle, and the control is the mapping function. Recently the method has been implemented in an alternative formulation which does not depend on conformal mapping, so that it can more easily be extended to treat general configurations [16]. The method has also been extended to treat the Euler equations, and results are presented for both two and three dimensional cases, including the optimization of a swept wing.

## 1 FORMULATION OF THE DESIGN PROBLEM AS A CONTROL PROBLEM

Ultimately, the designer seeks to optimize the geometric shape of a configuration taking into account the trade-offs between aerodynamic performance, structure weight, and the requirement for internal volume to contain fuel and payload. The subtlety and complexity of fluid flow is such that it is unlikely that repeated trials in an interactive analysis and design procedure can lead to a truly optimum design. Progress toward automatic design has been restricted by the extreme computing costs that might be incurred from brute force numerical optimization. However, useful design methods have been devised for various simplified cases, such as two-dimensional airfoils in viscous flows [17] and wings in inviscid flows. The computational costs for these methods result directly from the vast number of flow solutions that are required to obtain a converged design.

Alternatively, it has been recognized that the designer generally has an idea of the kind of pressure distribution that will lead to the desired performance. Thus, it is useful to consider the inverse problem of calculating the shape that will lead to a given pressure distribution. The

method is advantageous, since only one flow solution is required to obtain the desired design. Unfortunately, a physically realizable shape may not necessarily exist, unless the pressure distribution satisfies certain constraints. Thus the problem must be very carefully formulated.

The problem of designing a two-dimensional profile to attain a desired pressure distribution was first studied by Lighthill, who solved it for the case of incompressible flow with a conformal mapping of the profile to a unit circle [13]. The speed over the profile is

$$q = \frac{1}{h} |\nabla \phi|,$$

where  $\phi$  is the potential which is known for incompressible flow and  $h$  is the modulus of the mapping function. The surface value of  $h$  can be obtained by setting  $q = q_d$ , where  $q_d$  is the desired speed, and since the mapping function is analytic, it is uniquely determined by the value of  $h$  on the boundary. A solution exists for a given speed  $q_\infty$  at infinity only if

$$\frac{1}{2\pi} \oint q d\theta = q_\infty,$$

and there are additional constraints on  $q$  if the profile is required to be closed.

The difficulty that the objective may be unattainable can be circumvented by regarding the design problem as a control problem in which the control is the shape of the boundary. A variety of alternative formulations of the design problem can then be treated systematically within the framework of the mathematical theory for control of systems governed by partial differential equations [14]. This approach to optimal aerodynamic design was introduced by Jameson [10, 11], who examined the design problem for compressible flow with shock waves, and devised adjoint equations to determine the gradient for both potential flow and also flows governed by the Euler equations. More recently Ta'asan, Kuruwila, and Salas, implemented a one shot approach in which the constraint represented by the flow equations is only required to be satisfied by the final converged solution [20]. Pironneau has also studied the use of control theory for optimum shape design of systems governed by elliptic equations [15].

\*Lectures for the Von Karman Institute, Brussels, April, 1994.

Suppose that the control is defined by a function  $\mathcal{F}(\xi)$  of some independent variable  $\xi$  or in the discrete case a vector with components  $\mathcal{F}_i$ . Also suppose that the desired objective is measured by a cost function  $I$ . This may, for example, measure the deviation from a desired surface pressure distribution, but it can also represent other measures of performance such as lift and drag. Thus the design problem is recast into a numerical optimization procedure. This has the advantage that if the objective, say, of a target pressure distribution, is unattainable, it is still possible to find a minimum of the cost function. Now a variation  $\delta\mathcal{F}$  in the control produces a variation  $\delta I$  in the cost. Following control theory,  $\delta I$  can be expressed to first order as an inner product

$$\delta I = (\mathcal{G}, \delta\mathcal{F}),$$

where the gradient  $\mathcal{G}$  is independent of the particular variation  $\delta\mathcal{F}$ , and can be determined by solving an adjoint equation. For a discrete system of equations

$$(\mathcal{G}, \delta\mathcal{F}) \equiv \sum \mathcal{G}_i \delta\mathcal{F}_i$$

and for an infinitely dimensional system

$$(\mathcal{G}, \delta\mathcal{F}) \equiv \int \mathcal{G}(\xi) \delta\mathcal{F} d\xi.$$

In either case, if one makes a shape change

$$\delta\mathcal{F} = -\lambda\mathcal{G}, \quad (1)$$

where  $\lambda$  is sufficiently small and positive, then

$$\delta I = -\lambda(\mathcal{G}, \mathcal{G}) < 0$$

assuring a reduction in  $I$ .

For flow about an airfoil or wing, the aerodynamic properties which define the cost function are functions of the flow-field variables ( $w$ ) and the physical location of the boundary, which may be represented by the function  $\mathcal{F}$ , say. Then

$$I = I(w, \mathcal{F}),$$

and a change in  $\mathcal{F}$  results in a change

$$\delta I = \frac{\partial I^T}{\partial w} \delta w + \frac{\partial I^T}{\partial \mathcal{F}} \delta \mathcal{F}, \quad (2)$$

in the cost function. As pointed out by Baysal and Ele-shaky [2] each term in (2), except for  $\delta w$ , can be easily obtained.  $\frac{\partial I}{\partial w}$  and  $\frac{\partial I}{\partial \mathcal{F}}$  can be obtained directly without a flowfield evaluation since they are partial derivatives.  $\delta\mathcal{F}$  can be determined by either working out the exact analytical values from a mapping, or by successive grid generation for each design variable, so long as this cost is significantly less than the cost of the flow solution. Brute force methods evaluate the gradient by making a small change in each design variable separately, and then recalculate both the grid and flow-field variables. This

requires a number of additional flow calculations equal to the number of design variables. Using control theory, the governing equations of the flowfield are introduced as a constraint in such a way that the final expression for the gradient does not require reevaluation of the flowfield. In order to achieve this  $\delta w$  must be eliminated from (2). The governing equation  $R$  expresses the dependence of  $w$  and  $\mathcal{F}$  within the flowfield domain  $D$ ,

$$R(w, \mathcal{F}) = 0,$$

Thus  $\delta w$  is determined from the equation

$$\delta R = \left[ \frac{\partial R}{\partial w} \right] \delta w + \left[ \frac{\partial R}{\partial \mathcal{F}} \right] \delta \mathcal{F} = 0. \quad (3)$$

Next, introducing a Lagrange Multiplier  $\psi$ , we have

$$\begin{aligned} \delta I &= \frac{\partial I^T}{\partial w} \delta w + \frac{\partial I^T}{\partial \mathcal{F}} \delta \mathcal{F} - \psi^T \left( \left[ \frac{\partial R}{\partial w} \right] \delta w + \left[ \frac{\partial R}{\partial \mathcal{F}} \right] \delta \mathcal{F} \right) \\ &= \left\{ \frac{\partial I^T}{\partial w} - \psi^T \left[ \frac{\partial R}{\partial w} \right] \right\} \delta w + \left\{ \frac{\partial I^T}{\partial \mathcal{F}} - \psi^T \left[ \frac{\partial R}{\partial \mathcal{F}} \right] \right\} \delta \mathcal{F} \end{aligned}$$

Choosing  $\psi$  to satisfy the adjoint equation

$$\left[ \frac{\partial R}{\partial w} \right]^T \psi = \frac{\partial I}{\partial w} \quad (4)$$

the first term is eliminated, and we find that

$$\delta I = \mathcal{G} \delta \mathcal{F} \quad (5)$$

where

$$\mathcal{G} = \frac{\partial I^T}{\partial \mathcal{F}} - \psi^T \left[ \frac{\partial R}{\partial \mathcal{F}} \right].$$

The advantage is that (5) is independent of  $\delta w$ , with the result that the gradient of  $I$  with respect to an arbitrary number of design variables can be determined without the need for additional flow-field evaluations. The main cost is in solving the adjoint equation (4). In general, the adjoint problem is about as complex as a flow solution. If the number of design variables is large, the cost differential between one adjoint solution and the large number of flowfield evaluations required to determine the gradient by brute force becomes compelling. Instead of introducing a Lagrange multiplier,  $\psi$ , one can solve (3) for  $\delta w$  as

$$\delta w = - \left[ \frac{\partial R}{\partial w} \right]^{-1} \left[ \frac{\partial R}{\partial \mathcal{F}} \right] \delta \mathcal{F},$$

and insert the result in (2). This is the implicit gradient approach, which is essentially equivalent to the control theory approach, as has been pointed out by Shubin and Frank [18, 19]. In any event there is an advantage in determining the gradient  $\mathcal{G}$  by the solution of the adjoint equation.

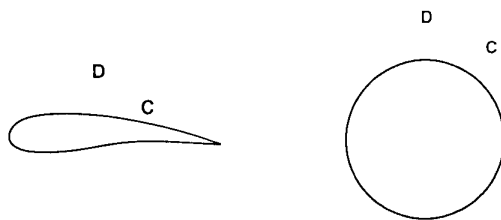
After making such a modification, the gradient can be recalculated and the process repeated to follow a path of steepest descent (1) until a minimum is reached. In order

to avoid violating constraints, such as a minimum acceptable wing thickness, the gradient may be projected into the allowable subspace within which the constraints are satisfied. In this way one can devise procedures which must necessarily converge at least to a local minimum, and which can be accelerated by the use of more sophisticated descent methods such as conjugate gradient or quasi-Newton algorithms. There is the possibility of more than one local minimum, but in any case the method will lead to an improvement over the original design. Furthermore, unlike the traditional inverse algorithms, any measure of performance can be used as the cost function.

The next section presents the formulation for the case of airfoils in transonic flow. The governing equation is taken to be the transonic potential flow equation, and the profile is generated by conformal mapping from a unit circle. Thus the control is taken to be the modulus of the mapping function on the boundary. This leads to a generalization of Lighthill's method both to compressible flow, and to design for more general criteria. Numerical results are presented in Section 3. The mathematical development resembles, in certain respects, the method of calculating transonic potential flow developed by Brisseau, Pironneau, Glowinski, Periaux, Perrier and Poirier, who reformulated the solution of the flow equations as a least squares problem in control theory [3].

## 2 AIRFOIL DESIGN FOR POTENTIAL FLOW USING CONFORMAL MAPPING

Consider the case of two-dimensional compressible inviscid flow. In the absence of shock waves, an initially irrotational flow will remain irrotational, and we can assume that the velocity vector  $\mathbf{q}$  is the gradient of a potential  $\phi$ . In the presence of weak shock waves this remains a fairly good approximation.



1a:  $z$ -Plane.

1b:  $\sigma$ -Plane.

Figure 1: Conformal Mapping.

Let  $p$ ,  $\rho$ ,  $c$ , and  $M$  be the pressure, density, speed-of-sound, and Mach number  $q/c$ . Then the potential flow equation is

$$\nabla \cdot (\rho \nabla \phi) = 0, \quad (6)$$

where the density is given by

$$\rho = \left\{ 1 + \frac{\gamma - 1}{2} M_\infty^2 (1 - q^2) \right\}^{\frac{1}{\gamma - 1}}, \quad (7)$$

while

$$p = \frac{\rho^\gamma}{\gamma M_\infty^2}, \quad c^2 = \frac{\gamma p}{\rho}. \quad (8)$$

Here  $M_\infty$  is the Mach number in the free stream, and the units have been chosen so that  $p$  and  $q$  have a value of unity in the far field.

Suppose that the domain  $D$  exterior to the profile  $C$  in the  $z$ -plane is conformally mapped on to the domain exterior to a unit circle in the  $\sigma$ -plane as sketched in Figure 1. Let  $R$  and  $\theta$  be polar coordinates in the  $\sigma$ -plane, and let  $r$  be the inverted radial coordinate  $\frac{1}{R}$ . Also let  $h$  be the modulus of the derivative of the mapping function

$$h = \left| \frac{dz}{d\sigma} \right|. \quad (9)$$

Now the potential flow equation becomes

$$\frac{\partial}{\partial \theta} (\rho \phi_\theta) + r \frac{\partial}{\partial r} (r \rho \phi_r) = 0 \quad \text{in } D, \quad (10)$$

where the density is given by equation (7), and the circumferential and radial velocity components are

$$u = \frac{r \phi_\theta}{h}, \quad v = \frac{r^2 \phi_r}{h}, \quad (11)$$

while

$$q^2 = u^2 + v^2. \quad (12)$$

The condition of flow tangency leads to the Neumann boundary condition

$$v = \frac{1}{h} \frac{\partial \phi}{\partial r} = 0 \quad \text{on } C. \quad (13)$$

In the far field, the potential is given by an asymptotic estimate, leading to a Dirichlet boundary condition at  $r = 0$  [6].

Suppose that it is desired to achieve a specified velocity distribution  $q_d$  on  $C$ . Introduce the cost function

$$I = \frac{1}{2} \int_C (q - q_d)^2 d\theta,$$

The design problem is now treated as a control problem where the control function is the mapping modulus  $h$ , which is to be chosen to minimize  $I$  subject to the constraints defined by the flow equations (6–13).

A modification  $\delta h$  to the mapping modulus will result in variations  $\delta \phi$ ,  $\delta u$ ,  $\delta v$ , and  $\delta \rho$  to the potential, velocity components, and density. The resulting variation in the cost will be

$$\delta I = \int_C (q - q_d) \delta q d\theta, \quad (14)$$

where, on  $C$ ,  $q = u$ . Also,

$$\delta u = r \frac{\delta \phi_\theta}{h} - u \frac{\delta h}{h}, \quad \delta v = r^2 \frac{\delta \phi_r}{h} - v \frac{\delta h}{h},$$

while according to equation (7)

$$\frac{\partial \rho}{\partial u} = -\frac{\rho u}{c^2}, \quad \frac{\partial \rho}{\partial v} = -\frac{\rho v}{c^2}.$$

It follows that  $\delta \phi$  satisfies

$$L\delta\phi = -\frac{\partial}{\partial\theta} \left( \rho M^2 \phi_\theta \frac{\delta h}{h} \right) - r \frac{\partial}{\partial r} \left( \rho M^2 r \phi_r \frac{\delta h}{h} \right)$$

where

$$L \equiv \frac{\partial}{\partial\theta} \left\{ \rho \left( 1 - \frac{u^2}{c^2} \right) \frac{\partial}{\partial\theta} - \frac{\rho uv}{c^2} r \frac{\partial}{\partial r} \right\} + r \frac{\partial}{\partial r} \left\{ \rho \left( 1 - \frac{v^2}{c^2} \right) r \frac{\partial}{\partial r} - \frac{\rho uv}{c^2} \frac{\partial}{\partial\theta} \right\}. \quad (15)$$

Then, if  $\psi$  is any periodic differentiable function which vanishes in the far field,

$$\int_D \frac{\psi}{r^2} L \delta\phi \, dS = \int_D \rho M^2 \nabla\phi \cdot \nabla\psi \frac{\delta h}{h} \, dS, \quad (16)$$

where  $dS$  is the area element  $r \, dr \, d\theta$ , and the right hand side has been integrated by parts.

Now we can augment equation (14) by subtracting the constraint (16). The auxiliary function  $\psi$  then plays the role of a Lagrange multiplier. Thus,

$$\delta I = \int_C (q - q_d) q \frac{\delta h}{h} \, d\theta - \int_C \delta\phi \frac{\partial}{\partial\theta} \left( \frac{q - q_d}{h} \right) \, d\theta - \int_D \frac{\psi}{r^2} L \delta\psi \, dS + \int_D \rho M^2 \nabla\phi \cdot \nabla\psi \frac{\delta h}{h} \, dS.$$

Now suppose that  $\psi$  satisfies the adjoint equation

$$L\psi = 0 \quad \text{in } D \quad (17)$$

with the boundary condition

$$\frac{\partial\psi}{\partial r} = \frac{1}{\rho} \frac{\partial}{\partial\theta} \left( \frac{q - q_d}{h} \right) \quad \text{on } C. \quad (18)$$

Then, integrating by parts,

$$\int_D \frac{\psi}{r^2} L \delta\phi \, dS = - \int_C \rho \psi_r \delta\phi \, d\theta,$$

and

$$\delta I = - \int_C (q - q_d) q \frac{\delta h}{h} \, d\theta + \int_D \rho M^2 \nabla\phi \cdot \nabla\psi \frac{\delta h}{h} \, dS. \quad (19)$$

Here the first term represents the direct effect of the change in the metric, while the area integral represents a correction for the effect of compressibility. When the

second term is deleted the method reduces to a variation of Lighthill's method [13].

Equation (19) can be further simplified to represent  $\delta I$  purely as a boundary integral because the mapping function is fully determined by the value of its modulus on the boundary. Set

$$\log \frac{dz}{d\sigma} = \mathcal{F} + i\beta,$$

where

$$\mathcal{F} = \log \left| \frac{dz}{d\sigma} \right| = \log h,$$

and

$$\delta\mathcal{F} = \frac{\delta h}{h}.$$

Then  $\mathcal{F}$  satisfies Laplace's equation

$$\Delta\mathcal{F} = 0 \quad \text{in } D,$$

and if there is no stretching in the far field,  $\mathcal{F} \rightarrow 0$ . Also  $\delta\mathcal{F}$  satisfies the same conditions. Introduce another auxiliary function  $P$  which satisfies

$$\Delta P = \rho M^2 \nabla\psi \cdot \nabla\psi \quad \text{in } D, \quad (20)$$

and

$$P = 0 \quad \text{on } C.$$

Then, the area integral in equation (19) is

$$\int_D \Delta P \delta\mathcal{F} \, dS = \int_C \delta\mathcal{F} \frac{\partial P}{\partial r} \, d\theta - \int_D P \Delta \delta\mathcal{F} \, dS,$$

and finally

$$\delta I = \int_C \mathcal{G} \delta\mathcal{F} \, d\theta,$$

where  $\mathcal{F}_c$  is the boundary value of  $\mathcal{F}$ , and

$$\mathcal{G} = \frac{\partial P}{\partial r} - (q - q_d) q. \quad (21)$$

This suggests setting

$$\delta\mathcal{F}_c = -\lambda\mathcal{G}$$

so that if  $\lambda$  is a sufficiently small positive quantity

$$\delta I = - \int_C \lambda \mathcal{G}^2 \, d\theta < 0.$$

Arbitrary variations in  $\mathcal{F}$  cannot, however, be admitted. The condition that  $\mathcal{F} \rightarrow 0$  in the far field, and also the requirement that the profile should be closed, imply constraints which must be satisfied by  $\mathcal{F}$  on the boundary  $C$ . Suppose that  $\log \left( \frac{dz}{d\sigma} \right)$  is expanded as a power series

$$\log \left( \frac{dz}{d\sigma} \right) = \sum_{n=0}^{\infty} \frac{c_n}{\sigma^n}, \quad (22)$$

where only negative powers are retained, because otherwise  $\left(\frac{dz}{d\sigma}\right)$  would become unbounded for large  $\sigma$ . The condition that  $\mathcal{F} \rightarrow 0$  as  $\sigma \rightarrow \infty$  implies

$$c_0 = 0.$$

Also, the change in  $z$  on integration around a circuit is

$$\Delta z = \int \frac{dz}{d\sigma} d\sigma = 2\pi i c_1,$$

so the profile will be closed only if

$$c_1 = 0.$$

In order to satisfy these constraints, we can project  $\mathcal{G}$  onto the admissible subspace for  $\mathcal{F}_c$  by setting

$$c_0 = c_1 = 0. \quad (23)$$

Then the projected gradient  $\tilde{\mathcal{G}}$  is orthogonal to  $\mathcal{G} - \tilde{\mathcal{G}}$ , and if we take

$$\delta\mathcal{F}_c = -\lambda\tilde{\mathcal{G}},$$

it follows that to first order

$$\begin{aligned} \delta I &= - \int_C \lambda \mathcal{G} \tilde{\mathcal{G}} d\theta = - \int_C \lambda (\tilde{\mathcal{G}} + \mathcal{G} - \tilde{\mathcal{G}}) \mathcal{G} d\theta \\ &= - \int_C \lambda \tilde{\mathcal{G}}^2 d\theta < 0. \end{aligned}$$

If the flow is subsonic, this procedure should converge toward the desired speed distribution since the solution will remain smooth, and no unbounded derivatives will appear. If, however, the flow is transonic, one must allow for the appearance of shock waves in the trial solutions, even if  $q_d$  is smooth. Then  $q - q_d$  is not differentiable. This difficulty can be circumvented by a more sophisticated choice of the cost function. Consider the choice

$$I = \frac{1}{2} \int_C \left( \lambda_1 \mathcal{Z}^2 + \lambda_2 \left( \frac{d\mathcal{Z}}{d\theta} \right)^2 \right) d\theta, \quad (24)$$

where  $\lambda_1$  and  $\lambda_2$  are parameters, and the periodic function  $\mathcal{Z}(\theta)$  satisfies the equation

$$\lambda_1 \mathcal{Z} - \lambda_2 \frac{d^2 \mathcal{Z}}{d\theta^2} = q - q_d. \quad (25)$$

Then,

$$\begin{aligned} \delta I &= \int_C \left( \lambda_1 \mathcal{Z} \delta \mathcal{Z} + \lambda_2 \frac{d\mathcal{Z}}{d\theta} \frac{d}{d\theta} \delta \mathcal{Z} \right) d\theta \\ &= \int_C \mathcal{Z} \left( \lambda_1 \delta \mathcal{Z} - \lambda_2 \frac{d^2}{d\theta^2} \delta \mathcal{Z} \right) d\theta = \int_C \mathcal{Z} \delta q d\theta. \end{aligned}$$

Thus,  $\mathcal{Z}$  replaces  $q - q_d$  in the previous formulas, and if one modifies the boundary condition (18) to

$$\frac{\partial \psi}{\partial r} = \frac{1}{\rho} \frac{\partial}{\partial \theta} \left( \frac{\mathcal{Z}}{h} \right) \quad \text{on } C, \quad (26)$$

the formula for the gradient becomes

$$\mathcal{G} = \frac{\partial P}{\partial r} - \mathcal{Z} q \quad (27)$$

instead of equation (21). Smoothing can also be introduced directly in the descent procedure by choosing  $\delta\mathcal{F}_c$  to satisfy

$$\delta\mathcal{F}_c - \frac{\partial}{\partial \theta} \beta \frac{\partial}{\partial \theta} \delta\mathcal{F}_c = -\lambda\mathcal{G}, \quad (28)$$

where  $\beta$  is a smoothing parameter. Then to first order

$$\begin{aligned} \int \mathcal{G} \delta\mathcal{F} &= -\frac{1}{\lambda} \int \left( \delta\mathcal{F}_c^2 - \delta\mathcal{F}_c \frac{\partial}{\partial \theta} \beta \frac{\partial}{\partial \theta} \delta\mathcal{F}_c \right) d\theta \\ &= -\frac{1}{\lambda} \int \left( \delta\mathcal{F}_c^2 + \beta \left( \frac{\partial}{\partial \theta} \delta\mathcal{F}_c \right)^2 \right) d\theta < 0. \end{aligned}$$

The smoothed correction should now be projected onto the admissible subspace.

The final design procedure is thus as follows. Choose an initial profile and corresponding mapping function  $\mathcal{F}$ . Then:

1. Solve the flow equations (6-13) for  $\phi, u, v, q, \rho$ .
2. Solve the ordinary differential equation (25) for  $\mathcal{Z}$ .
3. Solve the adjoint equation (15 and 17) or  $\psi$  subject to the boundary condition (26).
4. Solve the auxiliary Poisson equation (20) for  $P$ .
5. Evaluate  $\mathcal{G}$  by equation (27)
6. Correct the boundary mapping function  $\mathcal{F}_c$  by  $\delta\mathcal{F}_c$  calculated from equation (28), projected onto the admissible subspace defined by (23).
7. Return to step 1.

### 3 NUMERICAL TESTS OF OPTIMAL AIRFOIL DESIGN FOR POTENTIAL FLOW USING CONFORMAL MAPPING

The practical realization of the design procedure depends on the availability of sufficiently fast and accurate numerical procedures for the implementation of the essential steps, in particular the solution of both the flow and the adjoint equations. If the numerical procedures are not accurate enough, the resulting errors in the gradient may impair or prevent the convergence of the descent procedure. If the procedures are too slow, the cumulative computing time may become excessive. In this case, it was possible to build the design procedure around the author's computer program FLO36, which solves the transonic potential flow equation in conservation form in a domain mapped to the unit disk. The solution is obtained by a very rapid multigrid alternating direction method. The original

scheme is described in Reference [7]. The program has been much improved since it was originally developed, and well converged solutions of transonic flows on a mesh with 128 cells in the circumferential direction and 32 cells in the radial direction are typically obtained in 5-20 multi-grid cycles. The scheme uses artificial dissipative terms to introduce upwind biasing which simulates the rotated difference scheme [6], while preserving the conservation form. The alternating direction method is a generalization of conventional alternating direction methods, in which the scalar parameters are replaced by upwind difference operators to produce a scheme which remains stable when the type changes from elliptic to hyperbolic as the flow becomes locally supersonic [7]. The conformal mapping is generated by a power series of the form of equation (22) with an additional term

$$\left(1 - \frac{\epsilon}{\phi}\right) \log \left(1 - \frac{1}{\sigma}\right)$$

to allow for a wedge angle  $\epsilon$  at the trailing edge. The coefficients are determined by an iterative process with the aid of fast Fourier transforms [6].

The adjoint equation has a form very similar to the flow equation. While it is linear in its dependent variable, it also changes type from elliptic in subsonic zones of the flow to hyperbolic in supersonic zones of the flow. Thus, it was possible to adapt exactly the same algorithm to solve both the adjoint and the flow equations, but with reverse biasing of the difference operators in the downwind direction in the adjoint equation, corresponding to the reversed direction of the zone of dependence. The Poisson equation (20) is solved by the Buneman algorithm.

An alternative procedure would be to derive the exact adjoint equation corresponding to the discrete equations which approximate the potential flow equation. This would produce the exact derivative of the discrete cost function with respect to the discrete control, at the expense of very complicated formulas and a costly inversion procedure. The discrete adjoint equation would then be a particular discretization of the differential adjoint equation corresponding precisely to the discretization used for the flow equation. The efficiency of the present approach, which uses separate discretizations of the flow and adjoint equations, depends on the fact that in the limit of zero mesh width the discrete adjoint solution converges to the true adjoint solution. This allows the use of a rather simple discretization of the adjoint equation modeled after the discretization of the flow equation. Numerical experiments confirm that in practice separate discretizations of the flow and adjoint equations yields good convergence to an optimum solution.

As an example of the application of the method, Figure 3 presents a calculation in which an airfoil was redesigned to improve its transonic performance by reducing the pressure drag induced by the appearance of a shock wave. The drag coefficient was therefore included in the

cost function so that equation (24) is replaced by

$$I = \frac{1}{2} \int_C \left( \lambda_1 Z^2 + \lambda_2 \left( \frac{dZ}{d\theta} \right)^2 \right) d\theta + \lambda_3 C_d,$$

where  $\lambda_3$  is a parameter which may be varied to alter the trade-off between drag reduction and deviation from the desired pressure distribution. Representing the drag as

$$D = \int_C (p - p_\infty) \frac{dy}{d\theta} d\theta,$$

the procedure of Section 2 may be used to determine the gradient by solving the adjoint equation with a modified boundary condition. A penalty on the desired pressure distribution is still needed to avoid a situation in which the optimum shape is a flat plate with no lift and no drag.

It was also desired to preserve the subsonic characteristics of the airfoil. Therefore two design points were specified, Mach 0.20 and Mach 0.720, and in each case the lift coefficient was forced to be 0.6. The composite cost function was taken to be the sum of the values of the cost function at the two design points. The transonic drag coefficient was reduced from 0.0191 to 0.0001 in 8 design cycles. In order to achieve this reduction the airfoil had to be modified so that its subsonic pressure distribution became more peaky at the leading edge. This is consistent with the results of experimental research on transonic airfoils, in which it has generally been found necessary to have a peaky subsonic pressure distribution in order to delay the onset of the transonic drag rise. It is also important to control the adverse pressure gradient on the rear upper surface, which can lead to premature separation of the viscous boundary layer. It can be seen that there is no steepening of this gradient due to the redesign.

#### 4 DESIGN FOR POTENTIAL FLOW USING A FINITE VOLUME DISCRETIZATION SCHEME

While the use of conformal mapping, as it has been presented in sections 2 and 3, leads to an effective design method for two dimensional profiles, it is not easy to treat more complex configurations because of the difficulty in devising appropriate numerical mapping methods. Moreover, conformal mapping is limited to two dimensional transformations. In this section an alternative formulation using a general coordinate transformation is adopted. This is intended to be a precursor to the three dimensional problem.

Consider the case of two-dimensional compressible inviscid flow. A general transformation from cartesian coordinates  $x$  and  $y$  to the coordinates  $\xi$  and  $\eta$  can be represented by the transformation

$$K = \begin{bmatrix} \frac{\partial x}{\partial \xi} & \frac{\partial x}{\partial \eta} \\ \frac{\partial y}{\partial \xi} & \frac{\partial y}{\partial \eta} \end{bmatrix}.$$

The potential flow equation can be written in divergence form as

$$\frac{\partial}{\partial x}(\rho u) + \frac{\partial}{\partial y}(\rho v) = 0 \quad \text{in } D, \quad (29)$$

where  $u$  and  $v$  represent the Cartesian velocity components. The coordinate transformations may be defined

$$\begin{aligned} \begin{Bmatrix} u \\ v \end{Bmatrix} &= \begin{Bmatrix} \phi_x \\ \phi_y \end{Bmatrix} = \begin{bmatrix} \frac{\partial \xi}{\partial x} & \frac{\partial \eta}{\partial x} \\ \frac{\partial \xi}{\partial y} & \frac{\partial \eta}{\partial y} \end{bmatrix} \begin{Bmatrix} \phi_\xi \\ \phi_\eta \end{Bmatrix} \\ &= K^{T-1} \begin{Bmatrix} \phi_\xi \\ \phi_\eta \end{Bmatrix}. \end{aligned} \quad (30)$$

Also

$$\begin{Bmatrix} \phi_\xi \\ \phi_\eta \end{Bmatrix} = \begin{bmatrix} \frac{\partial x}{\partial \xi} & \frac{\partial y}{\partial \xi} \\ \frac{\partial x}{\partial \eta} & \frac{\partial y}{\partial \eta} \end{bmatrix} \begin{Bmatrix} \phi_x \\ \phi_y \end{Bmatrix} = K^T \begin{Bmatrix} \phi_x \\ \phi_y \end{Bmatrix},$$

Then

$$\frac{\partial}{\partial \xi}(\rho J U) + \frac{\partial}{\partial \eta}(\rho J V) = 0 \quad \text{in } D. \quad (31)$$

where  $J$  is the Jacobian

$$J = \det(K) = \frac{\partial x}{\partial \xi} \frac{\partial y}{\partial \eta} - \frac{\partial x}{\partial \eta} \frac{\partial y}{\partial \xi}.$$

Here,  $U$  and  $V$  represent the contravariant velocities

$$\begin{aligned} \begin{Bmatrix} U \\ V \end{Bmatrix} &= \frac{1}{J} \begin{bmatrix} \frac{\partial y}{\partial \eta} & -\frac{\partial x}{\partial \eta} \\ -\frac{\partial y}{\partial \xi} & \frac{\partial x}{\partial \xi} \end{bmatrix} \begin{Bmatrix} u \\ v \end{Bmatrix} \\ &= K^{-1} \begin{Bmatrix} u \\ v \end{Bmatrix} = K^{-1} K^{T-1} \begin{Bmatrix} \phi_\xi \\ \phi_\eta \end{Bmatrix} \end{aligned}$$

Thus,

$$U = A_{11}\phi_\xi + A_{12}\phi_\eta \quad (32)$$

$$V = A_{12}\phi_\xi + A_{22}\phi_\eta. \quad (33)$$

where

$$A = (K^T K)^{-1} = \begin{bmatrix} A_{11} & A_{12} \\ A_{12} & A_{22} \end{bmatrix}$$

Consider first the case in which the cost function is defined such as to achieve a target speed distribution:

$$\begin{aligned} I &= \frac{1}{2} \int_C (q - q_d)^2 ds \\ &= \frac{1}{2} \int_C (q - q_d)^2 \left( \frac{ds}{d\xi} \right) d\xi, \end{aligned} \quad (34)$$

where  $q_d$  is the desired speed distribution and  $C$  is the airfoil surface.

The design problem is now treated as a control problem where the control function is the airfoil shape, which is to be chosen to minimize  $I$  subject to the constraints

defined by the flow equations (29–33). The first variation of the cost function is

$$\begin{aligned} \delta I &= \int_C (q - q_d) \delta q \left( \frac{ds}{d\xi} \right) d\xi \\ &+ \frac{1}{2} \int_C (q - q_d)^2 \delta \left( \frac{ds}{d\xi} \right) d\xi \\ &= \int_C (q - q_d) \frac{\partial(\delta\phi)}{\partial \xi} d\xi \\ &+ \frac{1}{2} \int_C (q - q_d)^2 \delta \left( \frac{ds}{d\xi} \right) d\xi \\ &+ \int_C (q - q_d) \frac{\partial\phi}{\partial \xi} \delta \left( \frac{d\xi}{ds} \right) \frac{ds}{d\xi} d\xi, \end{aligned} \quad (35)$$

since on the wall

$$q_w = \frac{\partial\phi}{\partial s} = \frac{\partial\phi}{\partial \xi} \frac{\partial \xi}{\partial s}.$$

In general we need to find how a modification to the airfoil geometry causes a variation  $\delta\phi$ , as well a variation in the grid parameters  $\delta A_{11}$ ,  $\delta A_{12}$ ,  $\delta A_{22}$ , and  $\delta J$ . The variations in  $U$ ,  $V$  and  $\rho$  are

$$\delta U = \delta(A_{11})\phi_\xi + A_{11}\delta\phi_\xi + \delta(A_{12})\phi_\eta + A_{12}\delta\phi_\eta$$

$$\delta V = \delta(A_{12})\phi_\xi + A_{12}\delta\phi_\xi + \delta(A_{22})\phi_\eta + A_{22}\delta\phi_\eta$$

$$\begin{aligned} \delta\rho &= -\frac{\rho}{c^2} \left[ U \frac{\partial}{\partial \xi} + V \frac{\partial}{\partial \eta} \right] \delta\phi \\ &- \frac{\rho}{2c^2} [\delta A_{11}\phi_\xi^2 + 2\delta A_{12}\phi_\eta\phi_\xi + \delta A_{22}\phi_\eta^2]. \end{aligned}$$

It follows that  $\delta\phi$  satisfies

$$\begin{aligned} L\delta\phi &= -\frac{\partial}{\partial \xi} Q(\delta J, \delta A_{11}, \delta A_{12}, \delta A_{22}) \\ &- \frac{\partial}{\partial \eta} P(\delta J, \delta A_{11}, \delta A_{12}, \delta A_{22}), \end{aligned} \quad (36)$$

where

$$\begin{aligned} L \equiv & \frac{\partial}{\partial \xi} \left[ \rho J \left( A_{11} - \frac{U^2}{c^2} \right) \frac{\partial}{\partial \xi} \right] \\ & + \rho J \left( A_{12} - \frac{UV}{c^2} \right) \frac{\partial}{\partial \eta} \\ & + \frac{\partial}{\partial \eta} \left[ \rho J \left( A_{12} - \frac{UV}{c^2} \right) \frac{\partial}{\partial \xi} \right] \\ & + \rho J \left( A_{22} - \frac{V^2}{c^2} \right) \frac{\partial}{\partial \eta} \end{aligned} \quad (37)$$

and

$$\begin{aligned} Q(\delta J, \delta A_{11}, \delta A_{12}, \delta A_{22}) &= \rho U \delta J \\ &+ \rho J \phi_\xi \left( 1 - \frac{U\phi_\xi}{2c^2} \right) \delta A_{11} \\ &+ \rho J \phi_\eta \left( 1 - \frac{U\phi_\xi}{c^2} \right) \delta A_{12} \\ &+ \rho J \phi_\eta \left( -\frac{U\phi_\eta}{2c^2} \right) \delta A_{22} \\ P(\delta J, \delta A_{11}, \delta A_{12}, \delta A_{22}) &= \rho V \delta J \end{aligned}$$

$$\begin{aligned}
& +\rho J\phi_\eta \left(1 - \frac{V\phi_\eta}{2c^2}\right) \delta A_{22} \\
& +\rho J\phi_\xi \left(1 - \frac{V\phi_\eta}{c^2}\right) \delta A_{12} \\
& +\rho J\phi_\xi \left(-\frac{V\phi_\xi}{2c^2}\right) \delta A_{11}.
\end{aligned}$$

If  $\psi$  is any periodic function vanishing in the far field, equation (36) can be multiplied by  $\psi$  and integrated over the domain. After integrating the right hand side by parts we arrive at

$$\begin{aligned}
\int_D \psi L\delta\phi d\xi d\eta &= \int_D \frac{\partial\psi}{\partial\xi} Q + \frac{\partial\psi}{\partial\eta} P d\xi d\eta \\
&+ \int_C \{\psi\rho J [\delta A_{12}\phi_\xi + \delta A_{22}\phi_\eta]\} d\xi. \quad (38)
\end{aligned}$$

Now subtracting (38) from (35),

$$\begin{aligned}
\delta I &= - \int_C \frac{\partial(q - q_d)}{\partial\xi} \delta\phi d\xi \\
&+ \int_C \frac{1}{2} (q - q_d)^2 \delta \left(\frac{ds}{d\xi}\right) d\xi \\
&+ \int_C (q - q_d) \frac{\partial\phi}{\partial\xi} \delta \left(\frac{d\xi}{ds}\right) \frac{ds}{d\xi} d\xi \\
&- \int_D \psi L\delta\phi d\xi d\eta \\
&+ \int_D \frac{\delta\psi}{\delta\xi} Q + \frac{\delta\psi}{\delta\eta} P d\xi d\eta \\
&+ \int_C \{\psi\rho J [\delta A_{12}\phi_\xi + \delta A_{22}\phi_\eta]\} d\xi.
\end{aligned}$$

Then setting up the adjoint system we have

$$L\psi = 0 \quad \text{in } D, \quad (39)$$

with the boundary condition

$$\rho J (A_{12}\psi_\xi + A_{22}\psi_\eta) = -\frac{\partial}{\partial\xi} (q - q_d). \quad (40)$$

After applying the second form of Green's theorem to (39) we get

$$\begin{aligned}
\int_D \psi L\delta\phi dS &= \int_C \{\psi\rho J [\delta A_{12}\phi_\xi + \delta A_{22}\phi_\eta]\} d\xi \\
&+ \int_C \{\delta\phi\rho J [\delta A_{12}\psi_\xi + \delta A_{22}\psi_\eta]\} d\xi.
\end{aligned}$$

Finally the variation can be defined as

$$\begin{aligned}
\delta I &= \frac{1}{2} \int_C (q - q_d)^2 \delta \left(\frac{ds}{d\xi}\right) d\xi \\
&+ \int_C (q - q_d) \frac{\partial\phi}{\partial\xi} \delta \left(\frac{d\xi}{ds}\right) \frac{ds}{d\xi} d\xi \\
&+ \int_D \frac{\partial\psi}{\partial\xi} Q + \frac{\partial\psi}{\partial\eta} P d\xi d\eta. \quad (41)
\end{aligned}$$

No general analytic grid transformation is generally available for the finite volume formulation. Furthermore, the variation with respect to the grid quantities is now spread into  $\delta A_{11}$ ,  $\delta A_{12}$ ,  $\delta A_{22}$ , and  $\delta J$  instead of just the modulus of the transformation as was the case for conformal mapping. Therefore, to construct  $\delta I$ , an independent basis space of perturbation functions  $b_i$ ,  $i = 1, 2, \dots, n$  ( $n$  = number of design variables) is chosen that allows for the needed freedom of the design space. Thus, the shape  $\mathcal{F}$  now becomes  $\mathcal{F}(b_i)$ , where the functions  $b_i$  now represent the control. The variations  $\delta A_{11}$ ,  $\delta A_{12}$ ,  $\delta A_{22}$ , and  $\delta J$  are obtained by a direct finite difference procedure with respect to each design variable  $b_i$ . Once  $\delta I$  is obtained, any optimization procedure can be employed to minimize the cost with respect to the given basis  $b_i$ .

If the flow is subsonic, this procedure should converge toward the desired speed distribution since the solution will remain smooth, and no unbounded derivatives will appear. If, however, the flow is transonic, one must allow for the appearance of shock waves in the trial solutions, even if  $q_d$  is smooth. In such instances  $q - q_d$  is not differentiable. As in section 2, the cost function is redefined as

$$I = \frac{1}{2} \int_C \left( \lambda_1 \mathcal{Z}^2 + \lambda_2 \left(\frac{d\mathcal{Z}}{d\xi}\right)^2 \right) d\xi,$$

where  $\lambda_1$  and  $\lambda_2$  are parameters, and the periodic function  $\mathcal{Z}(\xi)$  satisfies the equation

$$\lambda_1 \mathcal{Z} - \lambda_2 \frac{d^2 \mathcal{Z}}{d\xi^2} = q - q_d. \quad (42)$$

Then,

$$\begin{aligned}
\delta I &= \int_C \left( \lambda_1 \mathcal{Z} \delta \mathcal{Z} + \lambda_2 \frac{d\mathcal{Z}}{d\xi} \frac{d}{d\xi} \delta \mathcal{Z} \right) d\xi \\
&= \int_C \mathcal{Z} \left( \lambda_1 \delta \mathcal{Z} - \lambda_2 \frac{d^2}{d\xi^2} \delta \mathcal{Z} \right) d\xi = \int_C \mathcal{Z} \delta q d\xi.
\end{aligned}$$

Thus,  $\mathcal{Z}$  replaces  $q - q_d$  in the previous formula and one modifies the boundary condition (40) to

$$\rho J (A_{12}\psi_\xi + A_{22}\psi_\eta) = -\frac{\partial}{\partial\xi} (\mathcal{Z}) \quad \text{on } C. \quad (43)$$

For the case where the cost function is drag, (34) is replaced by,

$$I = \int_C p \frac{\partial y}{\partial \xi} d\xi. \quad (44)$$

The first variation of the cost function is now,

$$\begin{aligned}
\delta I &= \int_C \delta p \frac{\partial y}{\partial \xi} d\xi + \int_C p \delta \left(\frac{\partial y}{\partial \xi}\right) d\xi \\
&= \int_C \frac{\partial \left(\rho q \frac{\partial y}{\partial s}\right)}{\partial \xi} \delta \phi d\xi - \int_C \rho q \frac{\partial \phi}{\partial \xi} \frac{\partial y}{\partial \xi} \delta \left(\frac{\partial \xi}{\partial s}\right) d\xi \\
&+ \int_C p \delta \left(\frac{\partial y}{\partial \xi}\right) d\xi. \quad (45)
\end{aligned}$$

Thus, (41) becomes

$$\begin{aligned} \delta I = & - \int_C \rho q \frac{\partial \phi}{\partial \xi} \frac{\partial y}{\partial \xi} \delta \left( \frac{\partial \xi}{\partial s} \right) d\xi \\ & + \int_C p \delta \left( \frac{\partial y}{\partial \xi} \right) d\xi \\ & + \int_D \frac{\partial \psi}{\partial \xi} Q + \frac{\partial \psi}{\partial \eta} P d\xi d\eta, \end{aligned} \quad (46)$$

where the boundary condition on  $\psi$ , (40) or (42), is replaced with

$$\rho J (A_{12} \psi_\xi + A_{22} \psi_\eta) = - \frac{\partial}{\partial \xi} \left( \rho q \frac{\partial y}{\partial s} \right) \quad (47)$$

or

$$\lambda_1 Z - \lambda_2 \frac{d^2 Z}{d\xi^2} = \rho q \frac{\partial y}{\partial s}. \quad (48)$$

The entire procedure can be summarized for the cost function based on target speed distribution as follows:

1. Solve the flow equations (29–33) for  $\phi$ ,  $u$ ,  $v$ ,  $q$ ,  $\rho$ ,  $U$ , and  $V$ .
2. Smooth the cost function if necessary by (42).
3. Solve the adjoint equation (37 and 39) for  $\psi$  subject to the boundary condition (40) or (43).
4. For each  $i$  independently perturb the design variables,  $b_i$ , and calculate the necessary metric variations ( $\delta A_{11}$ ,  $\delta A_{12}$ ,  $\delta A_{22}$ ,  $\delta J$ , and  $\delta \left( \frac{dy}{ds} \right)$ ) by recalculating the perturbed grid with automatic grid generation.
5. Directly evaluate  $\delta I$  by equation (41).
6. Project  $\delta I$  into a feasible direction subject to any constraints to obtain  $\delta \tilde{I}$ .
7. Feed  $\delta \tilde{I}$  as the gradient with respect to  $b_i$  to a quasi-Newton optimization procedure.
8. Calculate the search direction with a quasi-Newton algorithm and perform a line search.
9. Return to 1 if the process has not converged.

In practice the method resembles that used by Hicks *et al.* [17] with the control theory replacing the brute force, finite difference based, gradient calculation. The current formulation has an advantage by requiring computational work proportional to  $2 + m$  flow solver evaluations ( $m$  being the number of calculations required per line search) per design cycle as opposed to  $1 + m + n$ . Thus, unlike conventional design optimization programs, the current method's computational cost does not hinge upon the number of design variables provided the grid regeneration is fast and automatic. The method also has the advantage of being quite general, allowing arbitrary choices for both the design variables and the optimization technique.

## 5 NUMERICAL IMPLEMENTATION OF THE GENERALIZED POTENTIAL FLOW DESIGN METHOD

The practical implementation of the generalized potential flow design method, as with the conformal potential method, relies heavily upon fast accurate solvers for both the state ( $\phi$ ) and co-state ( $\psi$ ) fields. Further, to improve the speed and realizability of the methods, a robust choice of the optimization algorithm must be made. Finally, appropriate design variables must be chosen which allow sufficient freedom in realizable designs. In this work, the author's FLO42 full potential computer program and the QNMDIF (by Gill, Murray and Wright [4]) quasi-Newton optimization algorithm are employed.

In FLO42 the flow solution is obtained by a rapid multigrid alternating direction method [7]. The scheme uses artificial dissipative terms to introduce upwind biasing which simulates the rotated difference scheme [6] while preserving the conservation form. The alternating direction method is a generalization of conventional alternating direction methods in which the scalar parameters are replaced by upwind difference operators to produce a scheme which remains stable as the equations change type from elliptic to hyperbolic in accordance with the flow becoming locally supersonic [7].

QNMDIF is an unconstrained quasi-Newton optimization algorithm that calculates updates to a Cholesky factored Hessian matrix by the BFGS (Broyden-Fletcher-Goldfarb-Shanno) rank-two procedure. Hence, information about the curvature of the design space feeds in through the successive gradient calculations.

Since the primary computational costs arise from not only the flow solution algorithm but also the adjoint solution algorithm, both need to be computationally efficient. The adjoint equation has a form very similar to the flow equation. While it is linear in its dependent variable, it also changes type from elliptic (in subsonic zones of the flow) to hyperbolic (in supersonic zones of the flow). Thus, it was possible to adapt exactly the same algorithm to solve both the adjoint and the flow equations, but with reverse biasing of the difference operators in the downwind direction for the adjoint equation, corresponding to its reversed direction of the zone of dependence. A multigrid method is used to accelerate the convergence of a generalized alternating direction scheme in a manner similar to the flow solver.

Design variables are chosen with the following form, suggested by Hicks and Henne [5]:

$$\begin{aligned} b(x) &= \sin \left( \pi x \frac{\log_{10}(5)}{\log_{10}(4)} \right)^{t_2} \\ b(x) &= x^{t_1} (1-x) e^{-t_2 x}, \end{aligned}$$

where  $t_1$  and  $t_2$  control the center and thickness of the perturbation and  $x$  is the normalized chord length. When distributed over the entire chord on both upper and lower surfaces these analytic perturbation functions admit a large

possible design space. They have the advantage of being space based functions, as opposed to frequency based functions, and thus they allow for local control of the design. They can be chosen such that symmetry, thickness, or volume can be explicitly constrained. Further, particular choices of these variables will concentrate the design effort in regions where refinement is needed, while leaving the rest of the airfoil section virtually undisturbed. The disadvantage of these functions is that they do not form a complete basis space, nor are they orthogonal. Thus, they do not guarantee that a solution, for example, of the inverse problem for a realizable target pressure distribution will necessarily be attained. Here they are employed due to their ease of use and ability to produce a wide variation of shapes with a limited number of design variables.

The generalized potential flow design algorithm based on the finite volume scheme has been applied to a variety of test cases, which are described in the following paragraphs. These include both non-lifting cases, where a symmetric target pressure distribution is specified and the optimization is started from an arbitrary symmetric initial guess, and lifting cases where the target pressure distribution is specified, and finally cases which verify the capability of the method to find profiles with minimum drag.

The first non-lifting example shown in Figure 4, illustrates that for subsonic flow,  $M_\infty = 0.2$  and  $\alpha = 0^\circ$ , a given airfoil shape, in this case a NACA 64012, can be recovered by starting from an arbitrary shape and specifying the target pressure distribution. A close look at the final solution shows that a small discrepancy is evident at the trailing edge. This may be associated with the lack of completeness of our basis space. In the next example, see Figure 5, the design takes place at  $M_\infty = 0.8$ ,  $\alpha = 0^\circ$ , where the initial NACA 0012 airfoil is driven towards the subsonic pressure distribution of the NACA 64021. In this case the target pressure distribution exceeds  $C_p^*$  for  $M_\infty = 0.8$ . Therefore, the pressure distribution represents shock free transonic flow. Since, in general, such a pressure distribution may not be realizable, the program approaches the target with the nearest feasible pressure distribution. An examination of Figure 5 demonstrates that a very weak shock in the designed pressure distribution replaces the smooth transition to subsonic flow seen in the target distribution. In the final example non-lifting case of Figure 6, an arbitrary pressure distribution which does contain a shock wave and is realizable, is used as the target. Here the computer program was able to obtain the corresponding airfoil geometry along with the correct shock wave location with a high degree of accuracy, as can be seen both in the pressure distribution and in the airfoils.

The second group of test cases address the problem of attaining a desired pressure distribution for lifting airfoils. The most convenient method of obtaining such solutions with the present design method is to determine the lift coefficient associated with the target pressure distribution,

and match this lift with the initial airfoil. The design progresses with the flow solver and the adjoint system being driven by constant circulation instead of fixed angle of attack. The first example using this technique, shown in Figure 7, drives the NACA 0012 airfoil toward the target pressure distribution for the NACA 64A410 airfoil at  $M_\infty = 0.735$ ,  $\alpha = 0^\circ$ , and  $C_l = 0.75$ . This case requires a shift in the shock location and a significant change in the profile shape such that the target pressure distribution is obtained. The final solution almost exactly recovers the pressure distribution and the airfoil shape. In the next example, Figure 8, the NACA 0012 airfoil is again used as the starting condition to obtain the pressure distribution of the GAW72 airfoil operating at  $M_\infty = 0.7$ ,  $\alpha = -2^\circ$ , and  $C_l = 0.57$ . This case is difficult since the target airfoil has a cusped trailing edge while the initial airfoil has a finite trailing edge. As was seen in some of the non-lifting cases, there are small discrepancies evident near the trailing edge that may be due to the incomplete basis of the chosen design variables. The difference in the profiles between the final design and actual GAW72 is partly due to the fact that the GAW72 coordinates place the trailing edge at a non-zero  $y$  ordinate while the NACA 0012 places the trailing edge at  $y = 0$ . Also, the redesigned airfoil is subject to an arbitrary rotation since the angle of attack is free during optimization. The last test case in which the design program is run in inverse mode involves driving the NACA 0012 airfoil at  $M_\infty = 0.75$  to obtain the target pressure distribution of the RAE airfoil at the same Mach number,  $\alpha = 1.0^\circ$ , and  $C_l = 0.80$ . Due to the steep favorable pressure gradient at the leading edge upper surface and the strong shock exhibited (see Figure 9) by the RAE airfoil at these conditions this case represents quite a difficult test for the program. The method recovers the target pressure distribution almost exactly. A comparison of the profiles reveals that the the designed airfoil has no observable differences when overlaid with the original airfoil.

The last group of results introduces drag as the cost function. Again the design process is carried out in the fixed lift mode. In Figure 10, the first drag minimization example, a NACA 0012 is again used as a starting airfoil. The design takes place at  $M_\infty = 0.75$  and  $C_l = 0.50$  where a strong shock causes considerable wave drag in the initial airfoil. To make the problem interesting, the optimization is carried out such that symmetry of the design is preserved. The final design is a symmetric airfoil with an increased maximum thickness that operates at the same lift coefficient, but has a reduction in drag from  $C_d = 0.0127$  to  $C_d = 0.0016$ . In the final test case (see Figure 9) the camber distribution is optimized instead of thickness distribution. The design starts from a NACA 64A410 airfoil operating at  $M_\infty = 0.75$ , and  $C_l = 0.60$  which displays 42 counts of drag according to the potential flow calculation. By allowing only changes to the camber distribution, a final airfoil is produced which maintains  $C_l = 0.60$  but does so with only 4 counts of drag.

## 6 DESIGN OF AIRFOILS USING THE EULER EQUATIONS

This section extends the application of control theory for aerodynamic shape optimization to the Euler equations for two dimensional flow. Consider the case of compressible flow over an airfoil. In the absence of separation and other strong viscous effects, the flow is well approximated by the Euler equations. In contrast to the previous implementations which relied on the isentropic potential equation, here strong inviscid shocks are modeled correctly with entropy production. Consider the flow in a domain  $D$ . The profile defines the inner boundary  $C$ , while the outer boundary  $B$  is assumed to be distant from the profile. Let  $p, \rho, u, v, E$  and  $H$  denote the pressure, density, Cartesian velocity components, total energy and total enthalpy. For a perfect gas

$$p = (\gamma - 1) \rho \left\{ E - \frac{1}{2} (u^2 + v^2) \right\}, \quad (49)$$

and

$$\rho H = \rho E + p, \quad (50)$$

where  $\gamma$  is the ratio of the specific heats. The Euler equations may then be written as

$$\frac{\partial w}{\partial t} + \frac{\partial f}{\partial x} + \frac{\partial g}{\partial y} = 0 \quad \text{in } D, \quad (51)$$

where  $x$  and  $y$  are Cartesian coordinates,  $t$  is the time coordinate and

$$w = \begin{Bmatrix} \rho \\ \rho u \\ \rho v \\ \rho E \end{Bmatrix}, \quad f = \begin{Bmatrix} \rho u \\ \rho u^2 + p \\ \rho uv \\ \rho u H \end{Bmatrix}, \quad g = \begin{Bmatrix} \rho v \\ \rho v^2 + p \\ \rho v H \end{Bmatrix}. \quad (52)$$

Consider a coordinate transformations to computational coordinates  $\xi, \eta$  with the transformation matrix

$$K = \begin{bmatrix} \frac{\partial x}{\partial \xi} & \frac{\partial x}{\partial \eta} \\ \frac{\partial y}{\partial \xi} & \frac{\partial y}{\partial \eta} \end{bmatrix},$$

and the Jacobian

$$J = \frac{\partial x}{\partial \xi} \frac{\partial y}{\partial \eta} - \frac{\partial x}{\partial \eta} \frac{\partial y}{\partial \xi}.$$

Introduce contravariant velocity components

$$\begin{Bmatrix} U \\ V \end{Bmatrix} = K^{-1} \begin{Bmatrix} u \\ v \end{Bmatrix} = \frac{1}{J} \begin{bmatrix} \frac{\partial y}{\partial \eta} & -\frac{\partial x}{\partial \eta} \\ -\frac{\partial y}{\partial \xi} & \frac{\partial x}{\partial \xi} \end{bmatrix} \begin{Bmatrix} u \\ v \end{Bmatrix}.$$

The Euler equations can be written as

$$\frac{\partial W}{\partial t} + \frac{\partial F}{\partial \xi} + \frac{\partial G}{\partial \eta} = 0 \quad \text{in } D, \quad (53)$$

with

$$W = J \begin{Bmatrix} \rho \\ \rho u \\ \rho v \\ \rho E \end{Bmatrix}, \quad F = J \begin{Bmatrix} \rho U \\ \rho U u + \frac{\partial \xi}{\partial x} p \\ \rho U v + \frac{\partial \xi}{\partial y} p \\ \rho U H \end{Bmatrix}, \quad G = J \begin{Bmatrix} \rho V \\ \rho V u + \frac{\partial \eta}{\partial x} p \\ \rho V v + \frac{\partial \eta}{\partial y} p \\ \rho V H \end{Bmatrix}. \quad (54)$$

Assume now that the computational coordinate system conforms to the airfoil section in such a way that the surface  $C$  is represented by  $\eta = 0$ . Then the flow is determined as the steady state solution of the equation (54) subject to the flow tangency condition

$$V = 0 \quad \text{on } C, \quad (55)$$

At the far field boundary  $B$ , conditions are specified for incoming waves, while outgoing waves are determined by the solution.

Consider the case of the inverse problem where the cost function may be defined as

$$I = \frac{1}{2} \int_C (p - p_d)^2 ds = \frac{1}{2} \int_C (p - p_d)^2 \left( \frac{ds}{d\xi} \right) d\xi,$$

where  $p_d$  is the desired pressure. The design problem is now treated as a control problem where the control function is the airfoil shape, which is to be chosen to minimize  $I$  subject to the constraints defined by the flow equations (53–55). A variation in the shape will cause a variation  $\delta p$  in the pressure in addition to a variation in the geometry and consequently the variation in the cost function becomes

$$\delta I = \int_C (p - p_d) \delta p \left( \frac{ds}{d\xi} \right) d\xi + \frac{1}{2} \int_C (p - p_d)^2 \delta \left( \frac{ds}{d\xi} \right) d\xi. \quad (56)$$

Since  $p$  depends on  $w$  through the equation of state (51–52), the variation  $\delta p$  can be determined from the variation  $\delta w$ . Define the Jacobian matrices

$$A_1 = \frac{\partial f}{\partial w}, \quad A_2 = \frac{\partial g}{\partial w}, \quad C_i = \sum_j J K_{ij}^{-1} A_j. \quad (57)$$

Then the equation for  $\delta w$  in the steady state becomes

$$\frac{\partial}{\partial \xi} (\delta F) + \frac{\partial}{\partial \eta} (\delta G) = 0, \quad (58)$$

where

$$\begin{aligned}\delta F &= C_1 \delta w + \delta \left( J \frac{\partial \xi}{\partial x} \right) f + \delta \left( J \frac{\partial \xi}{\partial y} \right) g \\ \delta G &= C_2 \delta w + \delta \left( J \frac{\partial \eta}{\partial x} \right) f + \delta \left( J \frac{\partial \eta}{\partial y} \right) g.\end{aligned}$$

Now, multiplying by a vector co-state variable  $\psi$  and integrating over the domain

$$\int_D \psi^T \left( \frac{\partial \delta F}{\partial \xi} + \frac{\partial \delta G}{\partial \eta} \right) d\xi d\eta = 0,$$

and if  $\psi$  is differentiable this may be integrated by parts to give

$$\begin{aligned}\int_D \left( \frac{\partial \psi^T}{\partial \xi} \delta F + \frac{\partial \psi^T}{\partial \eta} \delta G \right) d\xi d\eta &= \\ \int_B (n_1 \psi^T \delta F + n_2 \psi^T \delta G) d\xi &+ \\ + \int_C (n_1 \psi^T \delta F + n_2 \psi^T \delta G) d\xi,\end{aligned}$$

where  $n_i$  are the components of a unit vector normal to the boundary. No boundary integrals appear in the  $\eta$  direction because the mesh is assumed to be of  $O$ -type, with the result that the solution is periodic in the  $\xi$  coordinate thereby canceling the  $\eta$  boundary integrals. Thus the variation in the cost function may now be written

$$\begin{aligned}\delta I &= \int_C (p - p_d) \delta p \left( \frac{ds}{d\xi} \right) d\xi \\ &+ \frac{1}{2} \int_C (p - p_d)^2 \delta \left( \frac{ds}{d\xi} \right) d\xi \\ &+ \int_D \left( \frac{\partial \psi^T}{\partial \xi} \delta F + \frac{\partial \psi^T}{\partial \eta} \delta G \right) d\xi d\eta \\ &- \int_B (n_1 \psi^T \delta F + n_2 \psi^T \delta G) d\xi \\ &- \int_C (n_1 \psi^T \delta F + n_2 \psi^T \delta G) d\xi.\end{aligned}$$

On the profile  $n_1 = 0$  and  $n_2 = -1$ . It follows from equation (55) that

$$\delta G = J \begin{Bmatrix} 0 \\ \frac{\partial \eta}{\partial x} \delta p \\ \frac{\partial \eta}{\partial y} \delta p \\ 0 \end{Bmatrix} + p \begin{Bmatrix} 0 \\ \delta \left( J \frac{\partial \eta}{\partial x} \right) \\ \delta \left( J \frac{\partial \eta}{\partial y} \right) \\ 0 \end{Bmatrix}. \quad (59)$$

Suppose now that  $\psi$  is the steady state solution of the adjoint equation

$$\frac{\partial \psi}{\partial t} - C_1^T \frac{\partial \psi}{\partial \xi} - C_2^T \frac{\partial \psi}{\partial \eta} = 0 \quad \text{in } D. \quad (60)$$

At the outer boundary incoming characteristics for  $\psi$  correspond to outgoing characteristics for  $\delta w$ . Consequently, one can choose boundary conditions for  $\psi$  such that

$$n_i \psi^T C_i \delta w = 0.$$

Then if the coordinate transformation is such that  $\delta (JK^{-1})$  is negligible in the far field, the only remaining boundary term is

$$\int_C \psi^T \delta G d\xi.$$

Thus by letting  $\psi$  satisfy the boundary condition,

$$J \left( \psi_2 \frac{\partial \eta}{\partial x} + \psi_3 \frac{\partial \eta}{\partial y} \right) = -(p - p_d) \frac{ds}{d\xi} \quad \text{on } C, \quad (61)$$

we find finally that

$$\begin{aligned}\delta I &= \frac{1}{2} \int_C (p - p_d)^2 \delta \left( \frac{ds}{d\xi} \right) d\xi \\ &+ \int_D \frac{\partial \psi^T}{\partial \xi} \left( \delta \left( J \frac{\partial \xi}{\partial x} \right) f + \delta \left( J \frac{\partial \xi}{\partial y} \right) g \right) d\xi d\eta \\ &+ \int_D \frac{\partial \psi^T}{\partial \eta} \left( \delta \left( J \frac{\partial \eta}{\partial x} \right) f + \delta \left( J \frac{\partial \eta}{\partial y} \right) g \right) d\xi d\eta \\ &+ \int_C \left\{ \psi_2 \delta \left( J \frac{\partial \eta}{\partial x} \right) + \psi_3 \delta \left( J \frac{\partial \eta}{\partial y} \right) \right\} p d\xi.\end{aligned} \quad (62)$$

If the flow is subsonic, this procedure should converge toward the desired pressure distribution since the solution will remain smooth, and no unbounded derivatives will appear. If, however, the flow is transonic, one must allow for the appearance of shock waves in the trial solutions, even if  $p_d$  is smooth. In such instances  $p - p_d$  is not differentiable. As in the case of potential flow, this difficulty can be circumvented by a more sophisticated choice of the cost function. Consider the choice

$$I = \frac{1}{2} \int_C \left( \lambda_1 Z^2 + \lambda_2 \left( \frac{dZ}{d\xi} \right)^2 \right) \frac{ds}{d\xi} d\xi,$$

where  $\lambda_1$  and  $\lambda_2$  are parameters, and the periodic function  $Z(\xi)$  satisfies the equation

$$\lambda_1 Z - \lambda_2 \frac{d^2 Z}{d\xi^2} = p - p_d. \quad (63)$$

Then,

$$\begin{aligned}\delta I &= \int_C \left( \lambda_1 Z \delta Z + \lambda_2 \frac{dZ}{d\xi} \frac{d}{d\xi} \delta Z \right) \frac{ds}{d\xi} d\xi \\ &= \int_C Z \left( \lambda_1 \delta Z - \lambda_2 \frac{d^2}{d\xi^2} \delta Z \right) \frac{ds}{d\xi} d\xi \\ &= \int_C Z \delta q \frac{ds}{d\xi} d\xi.\end{aligned}$$

Thus,  $Z$  replaces  $p - p_d$  with a corresponding modification to the boundary condition for the adjoint equations.

A convenient way to treat an airfoil is to use a conformal mapping of the profile in the  $z$  plane to a near circle in the  $\sigma$  plane, followed by shearing of the radial coordinate to make the system boundary conforming. Polar coordinates are introduced in the mapped plane  $\sigma$ . When mapped back to the physical plane this gives a smooth,

nearly orthogonal grid. This procedure is intermediate between the use of a full conformal mapping as in section 2 and an arbitrary numerically generated grid as in section 4. We can now specialize our generalized design procedure to treat this grid system. Define the first conformal mapping from  $z$  to  $\sigma$  by letting the derivative of the mapping function be

$$\frac{dz}{d\sigma} = he^{i\beta}.$$

Now using polar coordinates  $r$ , and  $\theta$  in the  $\sigma$  plane, the first transformation matrix is

$$K_1 = \begin{bmatrix} x_\theta & x_r \\ y_\theta & y_r \end{bmatrix} = h \begin{bmatrix} rs & c \\ -cs & s \end{bmatrix},$$

and we can define contravariant velocities

$$\begin{Bmatrix} U \\ V \end{Bmatrix} = \begin{bmatrix} s & -c \\ c & s \end{bmatrix} \begin{Bmatrix} u \\ v \end{Bmatrix},$$

where

$$s = \sin(\beta - \theta), \quad c = \cos(\beta - \theta).$$

The Euler equations can now be represented in the  $\sigma$  plane as

$$\frac{\partial(rh^2W)}{\partial t} + \frac{\partial(hF)}{\partial\theta} + \frac{\partial(rhG)}{\partial r} = 0 \quad \text{in } D, \quad (64)$$

where

$$W = \begin{Bmatrix} \rho \\ \rho u \\ \rho v \\ \rho E \end{Bmatrix}, \quad F = \begin{Bmatrix} \rho U \\ \rho U u + sp \\ \rho U v - cp \\ \rho U H \end{Bmatrix}, \quad G = \begin{Bmatrix} \rho V \\ \rho V u + cp \\ \rho V v + sp \\ \rho V H \end{Bmatrix}. \quad (65)$$

Now let the final computational coordinates be defined by a radial shearing transformation

$$\theta = \xi, \quad r = \eta + S(\xi)$$

and the transformation matrix

$$K_2 = \begin{bmatrix} \frac{\partial\theta}{\partial\xi} & \frac{\partial\theta}{\partial\eta} \\ \frac{\partial r}{\partial\xi} & \frac{\partial r}{\partial\eta} \end{bmatrix} = \begin{bmatrix} 1 & 0 \\ \frac{\partial S}{\partial\xi} & 1 \end{bmatrix}, \quad \det(K_2) = 1.$$

Now we can identify the complete transformation matrix as

$$K = K_1 K_2 = h \begin{bmatrix} rs + S_\xi c & c \\ -rc + S_\xi s & s \end{bmatrix},$$

while the fluxes are

$$\begin{aligned} hF &= h(sf - cg) \\ &= y_\eta f - x_\eta g \end{aligned}$$

and

$$\begin{aligned} h[(\eta + S)G - S_\xi F] &= h[(\eta + S)c - S_\xi s] f \\ &\quad + h[(\eta + S)s + S_\xi c] g \\ &= x_\xi g - y_\xi f. \end{aligned}$$

Thus the Euler equations assume the form

$$\begin{aligned} \frac{\partial}{\partial t} ((\eta + S)h^2W) \\ + \frac{\partial}{\partial\xi} (hF) + \frac{\partial}{\partial\eta} (h(\eta + S)G - hS_\xi F) = 0, \end{aligned}$$

while the surface tangency condition on the velocity becomes

$$x_\xi v - y_\xi u = h[(\eta + S)V - S_\xi U] = 0.$$

Now we take  $S(\xi)$  as the control. It is also convenient to represent the inverse problem by the cost function

$$I = \frac{1}{2} \int_C (p - p_d)^2 d\theta = I = \frac{1}{2} \int_C (p - p_d)^2 d\xi.$$

This eliminates terms in  $\delta\left(\frac{ds}{d\xi}\right)$  from the gradient. The variations in the fluxes become

$$\begin{aligned} \delta(hF) &= C_1 \delta w \\ \delta[h(\eta + S)G - hS_\xi F] &= C_2 \delta w + h\delta SG - h\delta S_\xi F \end{aligned}$$

where  $C_1$  and  $C_2$  are the Jacobian matrices defined in equation (57). Choosing  $\psi$  to satisfy the adjoint equation (60) with the boundary condition

$$x_\xi \psi_3 - y_\xi \psi_2 = h[(\eta + S)s + S_\xi c] \psi_\eta = p - p_d$$

the variation in the cost reduces to

$$\begin{aligned} \delta I &= \int_C (p - p_d) \delta p d\xi \\ &\quad + \int_D \psi^T \left( \frac{\partial}{\partial\xi} \delta F + \frac{\partial}{\partial\eta} \delta G \right) d\xi d\eta \\ &= \int_C \psi^T (\delta S h \bar{G} - \delta S_\xi h \bar{F}) d\xi \\ &\quad + \int_D \psi^T \frac{\partial}{\partial\xi} (\delta S h G + \delta S_\xi h F) d\xi d\eta, \end{aligned}$$

where  $F$  and  $G$  are the fluxes defined in equation (65), and  $\bar{F}$  and  $\bar{G}$  are  $F$  and  $G$  with the pressure terms deleted. Define

$$\begin{aligned} P &= \psi^T h \bar{F} + \int \psi^T \frac{\partial}{\partial\eta} (hF) d\eta \\ Q &= \psi^T h \bar{G} + \int \psi^T \frac{\partial}{\partial\eta} (hG) d\eta. \end{aligned}$$

Then

$$\begin{aligned}\delta I &= \int_C (Q\delta S - P\delta S_\xi) d\xi \\ &= \int_C \mathcal{G}\delta S d\xi,\end{aligned}$$

where the gradient is

$$\mathcal{G} = Q + \frac{\partial P}{\partial \xi}. \quad (66)$$

The entire procedure can be summarized as follows.

1. Solve the flow equations (51–55) for  $\rho$ ,  $u$ ,  $v$ ,  $p$ ,  $E$ ,  $H$ ,  $U$ , and  $V$ .
2. Smooth the cost function if necessary by (63).
3. Solve the adjoint equations (60) for  $\psi$  subject to the boundary condition (61).
4. Calculate  $P$  and  $Q$  from the variation in the control  $S(\xi)$ .
5. Evaluate  $\mathcal{G}$  by equation (66)
6. Project  $\mathcal{G}$  into a feasible direction subject to any constraints to obtain  $\tilde{\mathcal{G}}$ .
7. Correct the mapping in the direction of steepest decent

$$\delta S(\xi) = -\lambda \tilde{\mathcal{G}}.$$

or by using  $\tilde{\mathcal{G}}$  as the gradient in a quasi-Newton or conjugate gradient search method.

8. Return to 1.

## 7 IMPLEMENTATION OF THE EULER BASED DESIGN METHOD

The practical implementation of design method relies heavily upon fast accurate solvers for both the state ( $w$ ) and co-state ( $\psi$ ) fields. Further, to improve the speed and realizability of the method, a robust choice of the optimization algorithm must be made. In this work, the author's FLO82 full computer program has been used to solve the Euler equations. This program uses a multi stage time stepping scheme with multi grid acceleration to obtain very rapid steady state solutions, typically in 25 steps [8, 9]. The adjoint equations are solved by a similar method, in which the flux calculations for the Euler equations are replaced by the corresponding formulas for the adjoint equation.

In the initial tests a simple gradient procedure has been used as the optimization process. To preserve the smoothness of the profile the gradient is smoothed at each step in a similar manner to that used in the method of

section 2. Thus the change in the shape function  $S(\xi)$  is defined by solving

$$\delta S - \frac{\partial}{\partial \xi} \beta \frac{\partial}{\partial \xi} \delta S = -\lambda \mathcal{G},$$

where  $\beta$  is a smoothing parameter. Then, to first order, the variation in the cost is

$$\begin{aligned}\delta I &= \int \mathcal{G}\delta S d\xi \\ &= -\int \frac{1}{\lambda} \left[ \delta S - \delta S \frac{\partial}{\partial \xi} \beta \frac{\partial}{\partial \xi} \delta S \right] d\xi \\ &= -\int \frac{1}{\lambda} \left[ \delta S^2 + \beta \left( \frac{\partial}{\partial \xi} \delta S \right)^2 \right] d\xi \\ &< 0.\end{aligned}$$

The option to minimize the pressure drag coefficient

$$I = C_d = \frac{1}{\frac{1}{2}\rho_\infty q_\infty^2 \bar{c}} \int_C p \frac{\partial y}{\partial \xi} d\xi,$$

where  $\bar{c}$  is the chord length, has also been included. To prevent the procedure from trying to reduce drag by reducing the profile to a non-lifting flat plate a target pressure distribution is retained in the cost function, which becomes

$$I = \frac{1}{2}\Omega_1 \int_C (p - p_d)^2 d\xi + \Omega_2 C_d$$

where  $\Omega_1$  and  $\Omega_2$  are weighting parameters. Also the calculations are performed at a fixed lift coefficient corresponding to that of the target pressure distribution, while the angle of attack is allowed to vary as needed. Three test cases are presented for the design algorithm. The first two address the problem of attaining a desired pressure distribution. The first example using this technique, shown in Figure 12, drives the Korn airfoil toward the target pressure distribution for the NACA 64A410 airfoil at  $M_\infty = 0.75$ ,  $\alpha = 0^\circ$ , and  $C_l = 0.7$ . This case requires a shift in the shock location and a significant change in the profile shape such that the target pressure distribution is obtained. The final solution almost exactly recovers the pressure distribution and the airfoil shape. In the next example, Figure 13, the Korn airfoil operating at  $M_\infty = 0.78$  is used as the starting condition to obtain the pressure distribution of the same airfoil operating at  $M_\infty = 0.75$ ,  $\alpha = 0^\circ$ , and  $C_l = 0.64$ . This case is difficult since the target pressure distribution may not be realizable from a physical profile. Note that while the achieved pressure distribution is very close to the target pressure distribution, the drag of 77 counts is much larger than the zero drag experienced by the Korn airfoil at its design point. The third test case introduces drag as the cost function. Again the design process is carried out in the fixed lift mode. In Figure 14, a NACA 64A410 is again used as a starting airfoil. The design takes place at

$M_\infty = 0.75$  and  $C_l = 0.68$  where a strong shock causes considerable wave drag in the initial airfoil. To preserve a reasonable lifting airfoil shape the cost function is constructed as a blend of preserving the original pressure distribution and reducing the drag. The final design has a reduction in drag from  $C_d = 0.0144$  to  $C_d = 0.0018$ .

### 8 THREE DIMENSIONAL DESIGN USING THE EULER EQUATIONS

In order to illustrate further the application of control theory to aerodynamic design problems, sections 8 and 9 treat the case of three-dimensional wing design, again using the inviscid Euler equations as the mathematical model for compressible flow. In this case it proves convenient to denote the Cartesian coordinates and velocity components by  $x_1, x_2, x_3$  and  $u_1, u_2, u_3$ , and to use the convention that summation over  $i = 1$  to 3 is implied by a repeated index  $i$ . The three-dimensional Euler equations may be written as

$$\frac{\partial w}{\partial t} + \frac{\partial f_i}{\partial x_i} = 0 \quad \text{in } D, \quad (67)$$

where

$$w = \begin{Bmatrix} \rho \\ \rho u_1 \\ \rho u_2 \\ \rho u_3 \\ \rho E \end{Bmatrix}, \quad f_i = \begin{Bmatrix} \rho u_i \\ \rho u_i u_1 + p \delta_{i1} \\ \rho u_i u_2 + p \delta_{i2} \\ \rho u_i u_3 + p \delta_{i3} \\ \rho u_i H \end{Bmatrix} \quad (68)$$

and  $\delta_{ij}$  is the Kronecker delta function. Also,

$$p = (\gamma - 1) \rho \left\{ E - \frac{1}{2} (u_i^2) \right\}, \quad (69)$$

and

$$\rho H = \rho E + p \quad (70)$$

where  $\gamma$  is the ratio of the specific heats. Consider a transformation to coordinates  $\xi_1, \xi_2, \xi_3$  where

$$K_{ij} = \left[ \frac{\partial x_i}{\partial \xi_j} \right], \quad J = \det(K), \quad K_{ij}^{-1} = \left[ \frac{\partial \xi_i}{\partial x_j} \right].$$

Introduce contravariant velocity components as

$$\begin{Bmatrix} U_1 \\ U_2 \\ U_3 \end{Bmatrix} = K^{-1} \begin{Bmatrix} u_1 \\ u_2 \\ u_3 \end{Bmatrix}$$

The Euler equations can now be written as

$$\frac{\partial W}{\partial t} + \frac{\partial F_i}{\partial \xi_i} = 0 \quad \text{in } D, \quad (71)$$

with

$$W = J \begin{Bmatrix} \rho \\ \rho u_1 \\ \rho u_2 \\ \rho u_3 \\ \rho E \end{Bmatrix}, \quad F_i = J \begin{Bmatrix} \rho U_i \\ \rho U_i u_1 + \frac{\partial \xi_i}{\partial x_1} p \\ \rho U_i u_2 + \frac{\partial \xi_i}{\partial x_2} p \\ \rho U_i u_3 + \frac{\partial \xi_i}{\partial x_3} p \\ \rho U_i H \end{Bmatrix}. \quad (72)$$

Assume now that the new computational coordinate system conforms to the wing in such a way that the wing surface  $B_W$  is represented by  $\xi_2 = 0$ . Then the flow is determined as the steady state solution of equation (71) subject to the flow tangency condition

$$U_2 = 0 \quad \text{on } B_W. \quad (73)$$

At the far field boundary  $B_F$ , conditions are specified for incoming waves, as in the two-dimensional case, while outgoing waves are determined by the solution.

Suppose now that it is desired to control the surface pressure by varying the wing shape. It is convenient to retain a fixed computational domain. Variations in the shape then result in corresponding variations in the mapping derivatives defined by  $H$ . Introduce the cost function

$$I = \frac{1}{2} \iint_{B_W} (p - p_d)^2 d\xi_1 d\xi_3,$$

where  $p_d$  is the desired pressure. The design problem is now treated as a control problem where the control function is the wing shape, which is to be chosen to minimize  $I$  subject to the constraints defined by the flow equations (71-72). A variation in the shape will cause a variation  $\delta p$  in the pressure and consequently the a variation in the cost function

$$\delta I = \iint_{B_W} (p - p_d) \delta p \, d\xi_1 d\xi_3. \quad (74)$$

Since  $p$  depends on  $w$  through the equation of state (69-70), the variation  $\delta p$  can be determined from the variation  $\delta w$ . Define the Jacobian matrices

$$A_i = \frac{\partial f_i}{\partial w}, \quad C_i = JK_{ij}^{-1} A_j. \quad (75)$$

Then the equation for  $\delta w$  in the steady state becomes

$$\frac{\partial}{\partial \xi_i} (\delta F_i) = 0, \quad (76)$$

where

$$\delta F_i = C_i \delta w + \delta \left( J \frac{\partial \xi_i}{\partial x_j} \right) f_j.$$

Now, multiplying by a vector co-state variable  $\psi$  and integrating over the domain

$$\int_{D_j} \psi^T \left( \frac{\partial \delta F_i}{\partial \xi_i} \right) d\xi_j = 0,$$

and if  $\psi$  is differentiable this may be integrated by parts to give

$$\int_{D_j} \left( \frac{\partial \psi^T}{\partial \xi_i} \delta F_i \right) d\xi_j = \int_B (n_i \psi^T \delta F_i) d\xi_B,$$

where  $n_i$  are components of a unit vector normal to the boundary. Thus the variation in the cost function may

now be written

$$\begin{aligned} \delta I = & \iint_{B_W} (p - p_d) \delta p \, d\xi_1 d\xi_3 \\ & - \int_{D_j} \left( \frac{\partial \psi^T}{\partial \xi_i} \delta F_i \right) d\xi_j \\ & + \int_B (n_i \psi^T \delta F_i) d\xi_B. \end{aligned} \quad (77)$$

On the wing surface  $B_W$ ,  $n_1 = n_3 = 0$  and it follows from equation (73) that

$$\delta F_2 = J \begin{Bmatrix} 0 \\ \frac{\partial \xi_2}{\partial x_1} \delta p \\ \frac{\partial \xi_2}{\partial x_2} \delta p \\ \frac{\partial \xi_2}{\partial x_3} \delta p \\ 0 \end{Bmatrix} + p \begin{Bmatrix} 0 \\ \delta \left( J \frac{\partial \xi_2}{\partial x_1} \right) \\ \delta \left( J \frac{\partial \xi_2}{\partial x_2} \right) \\ \delta \left( J \frac{\partial \xi_2}{\partial x_3} \right) \\ 0 \end{Bmatrix}. \quad (78)$$

Suppose now that  $\psi$  is the steady state solution of the adjoint equation

$$\frac{\partial \psi}{\partial t} - C_i^T \frac{\partial \psi}{\partial \xi_i} = 0 \quad \text{in } D. \quad (79)$$

At the outer boundary incoming characteristics for  $\psi$  correspond to outgoing characteristics for  $\delta w$ . Consequently, as in the two-dimensional case, one can choose boundary conditions for  $\psi$  such that

$$n_i \psi^T C_i \delta w = 0.$$

Then if the coordinate transformation is such that  $\delta (JK^{-1})$  is negligible in the far field, the only remaining boundary term is

$$- \iint_{B_W} \psi^T \delta F_2 \, d\xi_1 d\xi_3.$$

Thus by letting  $\psi$  satisfy the boundary condition,

$$J \left( \psi_2 \frac{\partial \xi_2}{\partial x_1} + \psi_3 \frac{\partial \xi_2}{\partial x_2} + \psi_4 \frac{\partial \xi_2}{\partial x_3} \right) = (p - p_d) \quad \text{on } B_W, \quad (80)$$

we find finally that

$$\begin{aligned} \delta I = & \int_D \frac{\partial \psi^T}{\partial \xi_i} \delta \left( J \frac{\partial \xi_i}{\partial x_j} \right) f_j \, d\xi_D \\ & - \iint_{B_W} \left\{ \psi_2 \frac{\partial \xi_2}{\partial x_1} + \psi_3 \frac{\partial \xi_2}{\partial x_2} + \psi_4 \frac{\partial \xi_2}{\partial x_3} \right\} p \, d\xi_1 d\xi_3. \end{aligned} \quad (81)$$

A convenient way to treat a wing is to introduce sheared parabolic coordinates as shown in figure 2 through the transformation

$$\begin{aligned} x &= x_0(\zeta) + \frac{1}{2} a(\zeta) \left\{ \xi^2 - (\eta + S(\xi, \zeta))^2 \right\} \\ y &= y_0(\zeta) + a(\zeta) \xi (\eta + S(\xi, \zeta)) \\ z &= \zeta. \end{aligned}$$

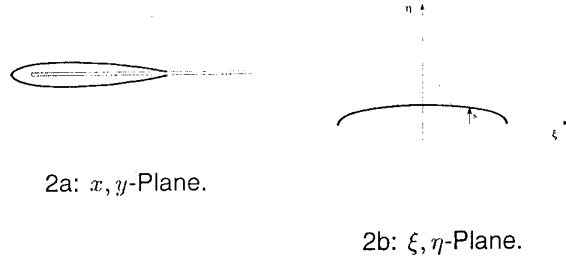


Figure 2: Sheared Parabolic Mapping.

Here  $x = x_1$ ,  $y = x_2$ ,  $z = x_3$  are the Cartesian coordinates, and  $\xi$  and  $\eta + S$  correspond to parabolic coordinates generated by the mapping

$$x + iy = x_0 + iy_0 + \frac{1}{2} a(\zeta) \{ \xi + i(\eta + S) \}^2$$

at a fixed span station  $\zeta$ .  $x_0(\zeta)$  and  $y_0(\zeta)$  are the coordinates of a singular line which is swept to lie just inside the leading edge of a swept wing, while  $a(\zeta)$  is a scale factor to allow for spanwise chord variations. The surface  $\eta = 0$  is a shallow bump corresponding to the wing surface, with a height  $S(\xi, \zeta)$  determined by the equation

$$\xi + iS = \sqrt{2(x_{B_W} + iy_{B_W})},$$

where  $x_{B_W}(z)$  and  $y_{B_W}(z)$  are coordinates of points lying on the wing surface. We now treat  $S(\xi, \zeta)$  as the control.

In this case the transformation matrix  $\frac{\partial x_i}{\partial \xi_j}$  becomes

$$\begin{aligned} K &= \begin{bmatrix} a(\xi - (\eta + S)S_\xi) & -a(\eta + S) & A - a(\eta + S)S_\zeta \\ a(\eta + S + \xi S_\xi) & a\xi & B + a\xi S_\zeta \\ 0 & 0 & 1 \end{bmatrix} \\ &= \begin{bmatrix} x_\xi & x_\eta & A + x_\eta S_\zeta \\ y_\xi & y_\eta & B + y_\eta S_\zeta \\ 0 & 0 & 1 \end{bmatrix}, \end{aligned}$$

where

$$A = a_\zeta \frac{x - x_0}{a} + x_{0\zeta}, \quad B = a_\zeta \frac{y - y_0}{a} + y_{0\zeta}.$$

Now,

$$J = x_\xi y_\eta - x_\eta y_\xi = \xi^2 + (\eta + S)^2$$

and

$$JK^{-1} = \begin{bmatrix} y_\eta & -x_\eta & x_\eta B - y_\eta A \\ -y_\xi & x_\xi & y_\xi A - x_\xi B - JS_\zeta \\ 0 & 0 & J \end{bmatrix}.$$

Then under a modification  $\delta S$

$$\begin{aligned} \delta x_\xi &= -a(\delta S S_\xi + (\eta + S)\delta S_\xi) \\ \delta x_\eta &= -a\delta S \\ \delta y_\xi &= a(\delta S + \xi \delta S_\xi) \\ \delta y_\eta &= 0. \end{aligned}$$

Thus

$$\delta J = 2a^2 (\eta + S) \delta S$$

and

$$\delta (JK^{-1}) = \begin{bmatrix} 0 & a\delta S & -aB\delta S \\ -\delta y_\xi & \delta x_\xi & \mathcal{D} \\ 0 & 0 & \delta J \end{bmatrix}.$$

where

$$\mathcal{D} = \delta y_\xi A - \delta x_\xi B - a_c \frac{J}{a} \delta S - \delta J S_\zeta - J \delta S_z.$$

Inserting these formulas in equation (81) we find that the volume integral in  $\delta I$  is

$$\begin{aligned} & \iiint \frac{\partial \psi^T}{\partial \xi} \delta S f_2 d\xi d\eta d\zeta \\ & - \iiint \frac{\partial \psi^T}{\partial \eta} \{-\delta y_\xi f_1 + \delta x_\xi f_2 + \mathcal{D} f_3\} d\xi d\eta d\zeta \\ & + \iiint \frac{\partial \psi^T}{\partial \zeta} \delta J f_3 d\xi d\eta d\zeta, \end{aligned}$$

where  $S$  and  $\delta S$  are independent of  $\eta$ . Therefore, integrating over  $\eta$ , the variation in the cost function can be reduced to a surface integral of the form

$$\delta I = \iint_{B_w} (P(\xi, \zeta) \delta S - Q(\xi, \zeta) \delta S_\xi - R(\xi, \zeta) \delta S_\zeta) d\xi d\zeta$$

Here

$$\begin{aligned} P &= a(\psi_2 + S_\xi \psi_3 + C\psi_4) p \\ & - \int \frac{\partial \psi^T}{\partial \xi} \{\xi f_1 + (\eta + S) f_2 + (\xi A + (\eta + S) B) f_3\} d\eta \\ & - \int \frac{\partial \psi^T}{\partial \eta} (f_1 + S_\xi f_2 + C f_3) d\eta \\ & - \int \frac{\partial \psi^T}{\partial \zeta} J d\eta \end{aligned}$$

$$\begin{aligned} Q &= a(\xi \psi_2 + (\eta + S) \psi_3) p \\ & + \int \frac{\partial \psi^T}{\partial \eta} \{\xi f_1 + (\eta + S) f_2 + (\xi A + (\eta + S) B) f_3\} d\eta \end{aligned}$$

$$\begin{aligned} R &= J\psi_4 p \\ & + \int \frac{\partial f_3}{\partial \eta} J\psi_4 d\eta, \end{aligned}$$

where

$$C = 2a(\eta + S) S_\zeta - A - B S_\xi + \frac{J}{a}.$$

Also the shape change will be confined to a boundary region of the  $\xi - \zeta$  plane, so we can integrate by parts to obtain

$$\delta I = \iint_{B_w} \left( P + \frac{\partial Q}{\partial \xi} + \frac{\partial R}{\partial \zeta} \right) \delta S d\xi d\zeta.$$

Thus to reduce  $I$  we can choose

$$\delta S = -\lambda \left( P + \frac{\partial Q}{\partial \xi} + \frac{\partial R}{\partial \zeta} \right),$$

where  $\lambda$  is sufficiently small and non-negative.

In order to impose a thickness constraint we can define a baseline surface  $S_0(\xi, \zeta)$  below which  $S(\xi, \zeta)$  is not allowed to fall. Now if we take  $\lambda = \lambda(\xi, \zeta)$  as a non-negative function such that

$$S(\xi, \zeta) + \delta S(\xi, \zeta) \geq S_0(\xi, \zeta).$$

Then the constraint is satisfied, while

$$\delta I = - \iint_{B_w} \lambda \left( P + \frac{\partial Q}{\partial \xi} + \frac{\partial R}{\partial \zeta} \right)^2 d\xi d\zeta \leq 0.$$

## 9 IMPLEMENTATION OF THE THREE DIMENSIONAL METHOD FOR WING DESIGN

Since three dimensional calculations are much more expensive than two dimensional calculations, it is extremely important for the practical implementation of the method to use fast solution algorithms for the flow and the adjoint equations. In this case the author's FLO87 computer program has been used as the basis of the design method. FLO87 solves the three dimensional Euler equations with a cell-centered finite volume scheme, and uses residual averaging and multigrid acceleration to obtain very rapid steady state solutions, usually in 25 to 50 multigrid cycles [8, 9]. Upwind biasing is used to produce nonoscillatory solutions, and assure the clean capture of shock waves. This is introduced through the addition of carefully controlled numerical diffusion terms, with a magnitude of order  $\Delta x^3$  in smooth parts of the flow. The program corresponds closely to FLO82, which was used to implement the design method for the two dimensional Euler equations. The adjoint equations are treated in the same way as the flow equations. The fluxes are first estimated by central differences, and then modified by downwind biasing through numerical diffusive terms which are supplied by the same subroutines that were used for the flow equations.

The method has been tested for the optimization of a swept wing. The planform was fixed while the wing sections were free to be changed arbitrarily by the design method. The wing has a unit-semi-span, with 36 degrees leading edge sweep. It has a compound trapezoidal planform, with straight taper from a root chord of 0.38 to a chord of 0.26 at the 30 percent span station, and straight taper from there to a chord of 0.12 at the tip, with an aspect ratio of 8.7. The initial wing sections were based on the Korn airfoil, which was designed for shock free flow at Mach 0.75 with a lift coefficient of 0.63, and has a thickness to chord ratio of 11.5 percent [1]. The thickness to chord ratio was increased by a factor of 1.2 at the root and decreased by a ratio of 0.8 at the tip, with a linear variation across the span. The inboard sections were rotated upwards to give 3.5 degrees twist across the span.

The two dimensional pressure distribution of the Korn airfoil at its design point was introduced as a target pressure distribution uniformly across the span. This target is

presumably not realizable, but serves to favor the establishment of relatively benign pressure distribution. The total inviscid drag coefficient, due to the combination of vortex and shock wave drag, was also included in the cost function. Calculations were performed with the lift coefficient forced to approach a fixed value by adjusting the angle of attack every fifth iteration of the flow solution. It was found that the computational costs can be reduced by using only 15 multigrid cycles in each flow solution, and in each adjoint solution. Although this is not enough for full convergence, it proves sufficient to provide a shape modification which leads to an improvement. Figures 15, 16, and 17 show the result of a calculation at Mach number of 0.82, with the lift coefficient forced to approach a value of 0.5. This calculation was performed on a mesh with 192 intervals in the  $\xi$  direction wrapping around the wing, 32 intervals in the normal  $\eta$  direction and 48 intervals in the spanwise  $\zeta$  direction, giving a total of 294912 cells. The wing was specified by 33 sections, each with 128 points, giving a total of 4224 design variables. The plots show the initial wing geometry and pressure distribution, and the modified geometry and pressure distribution after 8 design cycles. The total inviscid drag was reduced from 0.0185 to 0.0118. The initial design exhibits a very strong shock wave in the inboard region. It can be seen that this is completely eliminated, leaving a very weak shock wave in the outboard region. The drag reduction is mainly accomplished in the first four design cycles but the pressure distribution continues to be adjusted to become more like the Korn pressure distribution.

To verify the solution, the final geometry, after 8 design cycles, was analyzed with another method using the computer program FLO67. This program uses a cell-vertex formulation, and has recently been modified to incorporate a local extremum diminishing algorithm with a very low level of numerical diffusion [12]. When run to full convergence it was found that the redesigned wing has a drag coefficient of 0.0107 at Mach 0.82 at a lift coefficient of 0.5, with a corresponding lift to drag ratio of 47. The result is illustrated in Figure 18. A calculation at Mach 0.500 shows a drag coefficient of 0.0100 for a lift coefficient of 0.5. Since in this case the flow is entirely subsonic, this provides an estimate of the vortex drag for this planform and lift distribution. Thus the design method has reduced the shock wave drag coefficient to about 0.0007. For a representative transport aircraft the parasite drag coefficient of the wing due to skin friction is about 0.0050. Also the fuselage drag coefficient is about 0.0050, the nacelle drag coefficient is about 0.0015, the empennage drag coefficient is about 0.0006. This would give a total drag coefficient  $C_D = 0.0243$  for a lift coefficient of 0.5, corresponding to a lift to drag ratio  $L/D = 20.5$ . This would be a substantial improvement over the values obtained by currently flying transport aircraft.

As a further test the redesign was also performed at a higher Mach number of 0.85. The initial geometry

and pressure distributions, and the result of the redesign after 10 design cycles are displayed in Figures 19, 20 and 21. In this case the total inviscid drag was reduced from 0.0261 to 0.0132. Again this result has been checked with FLO67, and when the flow calculation is fully converged, it is found that the total inviscid drag coefficient is 0.0118 at a lift coefficient of 0.5, indicating a shock wave drag coefficient of 0.0018. Allowing for the other sources of drag for the complete aircraft, it is likely that the best operating point for maximum lift to drag ratio would be at a somewhat higher lift coefficient.

## 10 CONCLUSION

In the period since this approach to optimal shape design was first proposed by the author [10], the method has been verified by numerical implementation for both potential flow and flows modeled by the Euler equations. It has been demonstrated that it can be successfully used with a finite volume formulation to perform calculations with arbitrary numerically generated grids [16]. The first results which have been obtained for swept wings with the three dimensional Euler equations suggest that the method has now matured to the point where it can be a very useful tool for the design of new airplanes. Even in the case of three dimensional flows, the computational requirements are so moderate that the calculations can be performed with workstations such as the IBM RISC 6000 series. A design cycle on a  $192 \times 32 \times 48$  mesh takes about  $1\frac{1}{2}$  hours on an IBM model 530 workstation, allowing overnight completion of a design calculation for a swept wing.

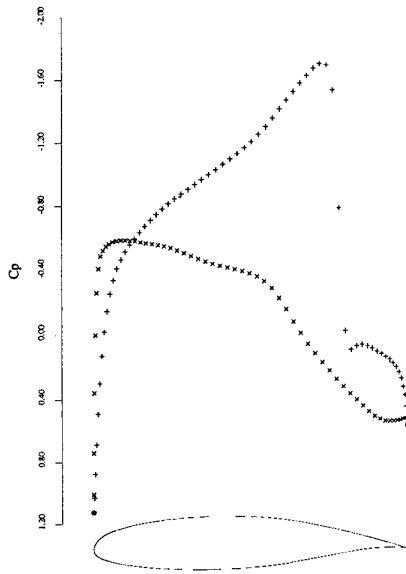
## 11 ACKNOWLEDGMENTS

The author is grateful to James Reuther not only for his assistance in assembling the text with  $\text{\LaTeX}$ , but also for supplying results from our joint work on the use of control theory to optimize flows calculated on arbitrary grids with discretization by the finite volume method [16]. This research has benefited greatly from the generous support of the AFOSR under grant number AFOSR-91-0391, ARPA under grant number N00014-92-J-1976, USRA through RIACS, and IBM. The warm hospitality of the Aeronautics and Astronautics Department of Stanford University, and NASA Ames Research Center, provided a very favorable environment for the pursuit of this research while the author was on leave from Princeton University.

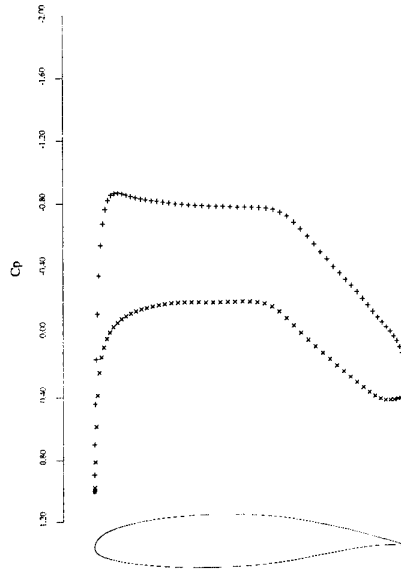
## References

- [1] F. Bauer, P. Garabedian, D. Korn, and A. Jameson. *Supercritical Wing Sections II*. Springer Verlag, New York, 1975.
- [2] O. Baysal and M. E. Elleshaky. Aerodynamic design optimization using sensitivity analysis and computational fluid dynamics. *AIAA paper 91-0471*, 29th

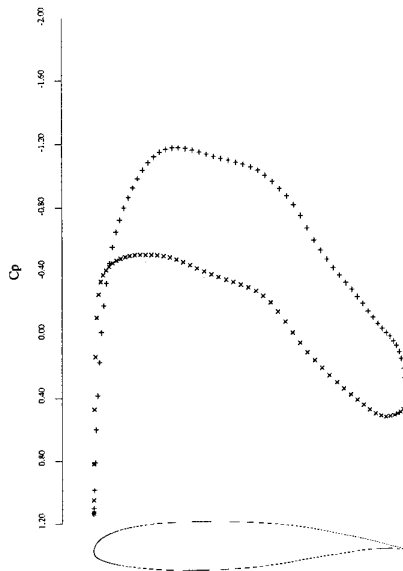
- Aerospace Sciences Meeting, Reno, Nevada, January 1991.
- [3] M.O. Bristeau, O. Pironneau, R. Glowinski, J. Periaux, P. Perrier, and G. Poirier. On the numerical solution of nonlinear problems in fluid dynamics by least squares and finite element methods (II). application to transonic flow simulations. In J. St. Doltsinis, editor, *Proceedings of the 3rd International Conference on Finite Element Methods in Nonlinear Mechanics, FENOMECH 84, Stuttgart, 1984*, pages 363–394, North Holland, 1985.
- [4] P.E. Gill, W. Murray, and M.H. Wright. *Practical Optimization*. Academic Press, 1981.
- [5] R. M. Hicks and P. A. Henne. Wing design by numerical optimization. *Journal of Aircraft*, 15:407–412, 1978.
- [6] A. Jameson. Iterative solution of transonic flows over airfoils and wings, including flows at Mach 1. *Communications on Pure and Applied Mathematics*, 27:283–309, 1974.
- [7] A. Jameson. Acceleration of transonic potential flow calculations on arbitrary meshes by the multiple grid method. *AIAA paper 79-1458*, Fourth AIAA Computational Fluid Dynamics Conference, Williamsburg, Virginia, July 1979.
- [8] A. Jameson. Solution of the Euler equations by a multigrid method. *Applied Mathematics and Computations*, 13:327–356, 1983.
- [9] A. Jameson. Multigrid algorithms for compressible flow calculations. In W. Hackbusch and U. Trottenberg, editors, *Lecture Notes in Mathematics, Vol. 1228*, pages 166–201. Proceedings of the 2nd European Conference on Multigrid Methods, Cologne, 1985, Springer-Verlag, 1986.
- [10] A. Jameson. Aerodynamic design via control theory. *Journal of Scientific Computing*, 3:233–260, 1988.
- [11] A. Jameson. Automatic design of transonic airfoils to reduce the shock induced pressure drag. In *Proceedings of the 31st Israel Annual Conference on Aviation and Aeronautics, Tel Aviv*, pages 5–17, February 1990.
- [12] A. Jameson. Artificial diffusion, upwind biasing, limiters and their effect on accuracy and multigrid convergence in transonic and hypersonic flows. *AIAA paper 93-3359*, AIAA 11th Computational Fluid Dynamics Conference, Orlando, Florida, July 1993.
- [13] M.J. Lighthill. A new method of two-dimensional aerodynamic design. *R & M 1111*, Aeronautical Research Council, 1945.
- [14] J.L. Lions. *Optimal Control of Systems Governed by Partial Differential Equations*. Springer-Verlag, New York, 1971. Translated by S.K. Mitter.
- [15] O. Pironneau. *Optimal Shape Design for Elliptic Systems*. Springer-Verlag, New York, 1984.
- [16] J. Reuther and A. Jameson. Control theory based airfoil design for potential flow and a finite volume discretization. *AIAA paper 91-499*, 32th Aerospace Sciences Meeting and Exhibit, Reno, Nevada, January 1994.
- [17] J. Reuther, C.P. van Dam, and R. Hicks. Subsonic and transonic low-Reynolds-number airfoils with reduced pitching moments. *Journal of Aircraft*, 29:297–298, 1992.
- [18] G. R. Shubin. Obtaining cheap optimization gradients from computational aerodynamics codes. *Internal paper AMS-TR-164*, Boeing Computer Services, June 1991.
- [19] G. R. Shubin and P. D. Frank. A comparison of the implicit gradient approach and the variational approach to aerodynamic design optimization. *internal paper AMS-TR-164*, Boeing Computer Services, April 1991.
- [20] S. Ta'asan, G. Kuruwila, and M. D. Salas. Aerodynamic design and optimization in one shot. *AIAA paper 91-005*, 30th Aerospace Sciences Meeting and Exhibit, Reno, Nevada, January 1992.



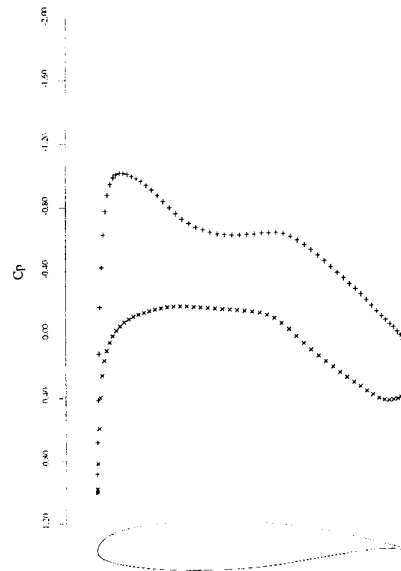
3a:  $C_p$  after Zero Design Cycles.  
Design Mach 0.72,  $C_l = 0.5982$ ,  $C_d = 0.0191$ .



3b:  $C_p$  after Zero Design Cycles.  
Design Mach 0.2,  $C_l = 0.5998$ ,  $C_d = -0.0001$ .



3c:  $C_p$  after Eight Design Cycles.  
Design Mach 0.72,  $C_l = 0.5999$ ,  $C_d = 0.0001$ .



3d:  $C_p$  after Eight Design Cycles.  
Design Mach 0.2,  $C_l = 0.5998$ ,  $C_d = -0.0001$ .

Figure 3: Optimization of an Airfoil at Two Design Points.

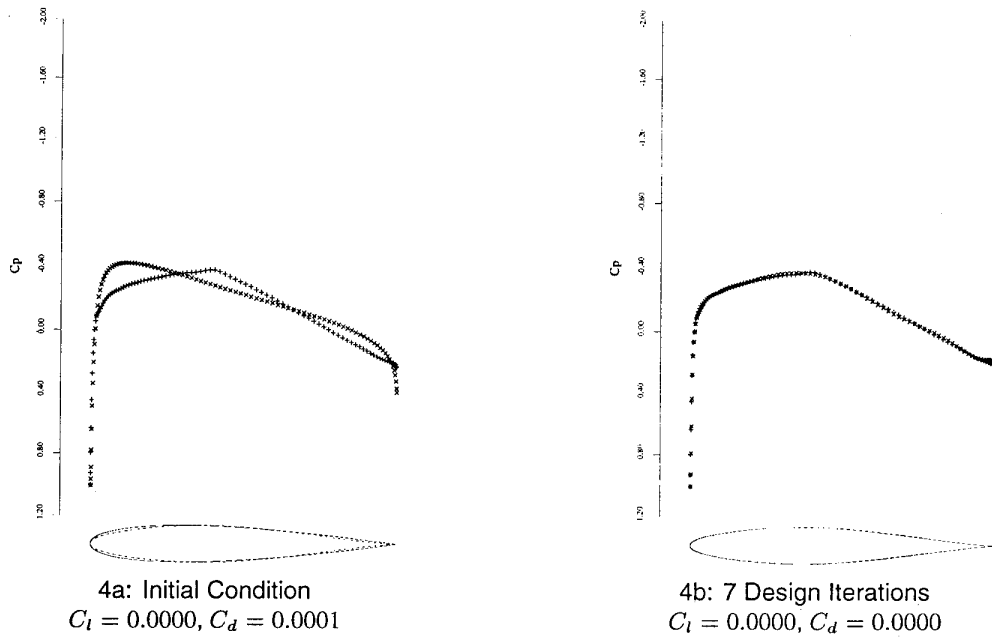


Figure 4: Subsonic Non-Lifting Design Case,  $M = 0.2, \alpha = 0^\circ$ .

—, × Initial Airfoil: NACA 0012.  
 ---, + Target  $C_p$ : NACA 64012,  $M = 0.2$ .  
 Inverse Design

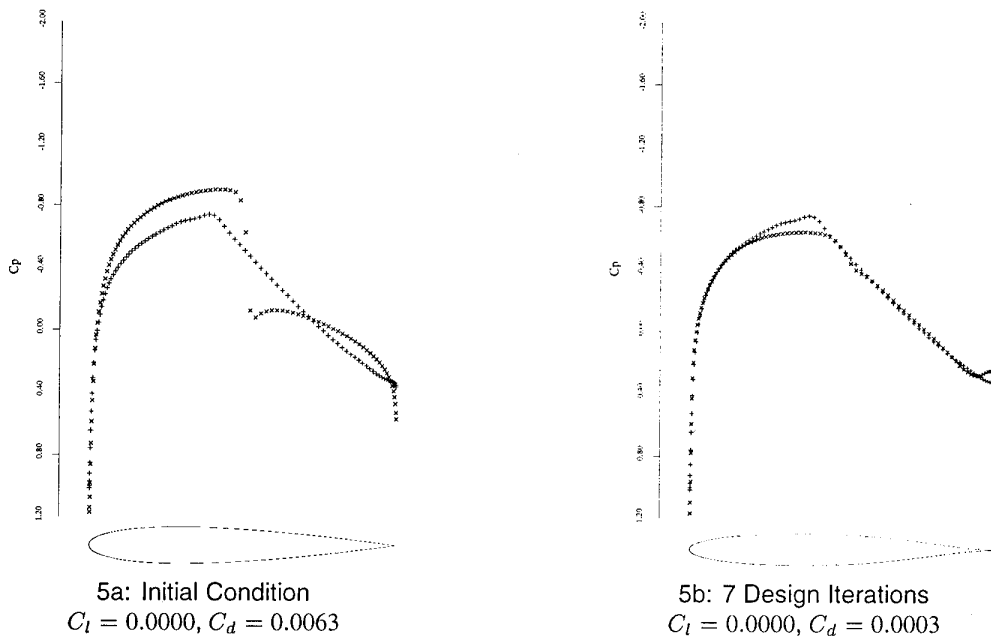


Figure 5: Transonic Non-Lifting Design Case,  $M = 0.8, \alpha = 0^\circ$ .

—, × Initial Airfoil: NACA 0012.  
 ---, + Target  $C_p$ : NACA 64021,  $M = 0.2$ .  
 Inverse Design

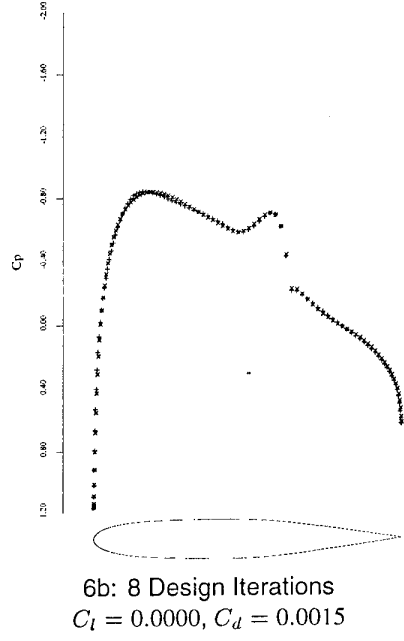
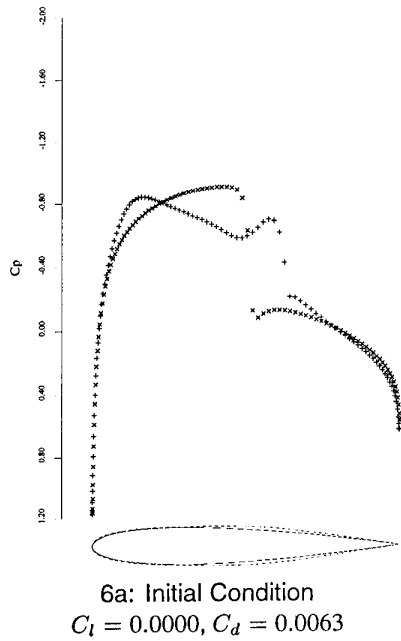


Figure 6: Transonic Non-Lifting Design Case,  $M = 0.8, \alpha = 0^\circ$ .  
 —, x Initial Airfoil: NACA 0012.  
 ---, + Target  $C_p$ : NACA 64X,  $M = 0.8$ .  
 Inverse Design

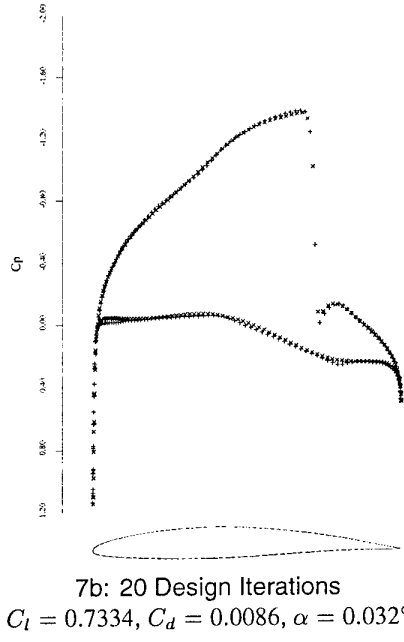
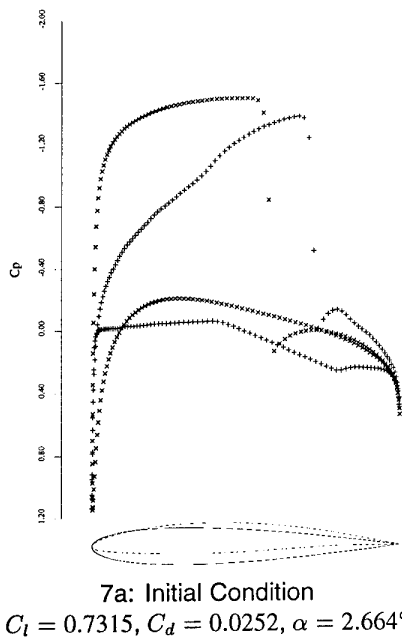
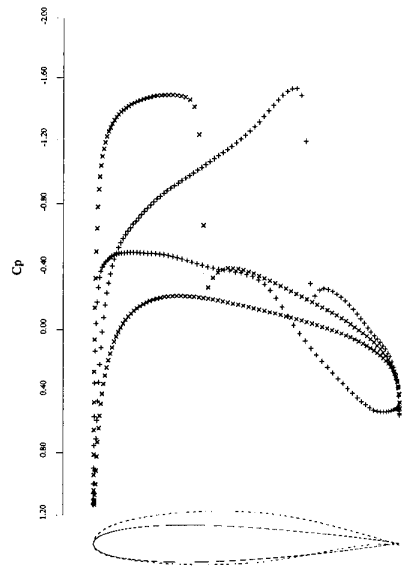
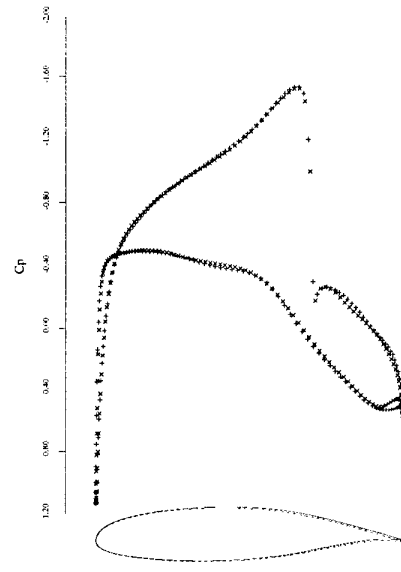


Figure 7: Transonic Lifting Design Case,  $M = 0.735$  Fixed Lift.  
 —, x Initial Airfoil: NACA 0012.  
 ---, + Target  $C_p$ : NACA 64A410,  $M = 0.735, C_l = 0.73$ .  
 Inverse Design



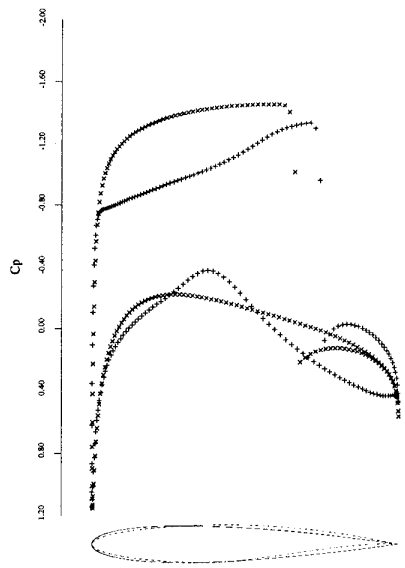
8a: Initial Condition  
 $C_l = 0.5492, C_d = 0.0047, \alpha = 2.709^\circ$



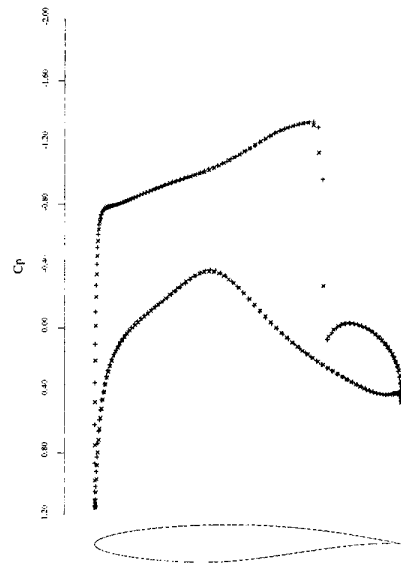
8b: 30 Design Iterations  
 $C_l = 0.5496, C_d = 0.0045, \alpha = -1.508^\circ$

Figure 8: Transonic Lifting Design Case,  $M = 0.70$ , Fixed Lift.

—, x Initial Airfoil: NACA 0012.  
 ---, + Target  $C_p$ : GAW72,  $M = 0.70$ .  
 Inverse Design



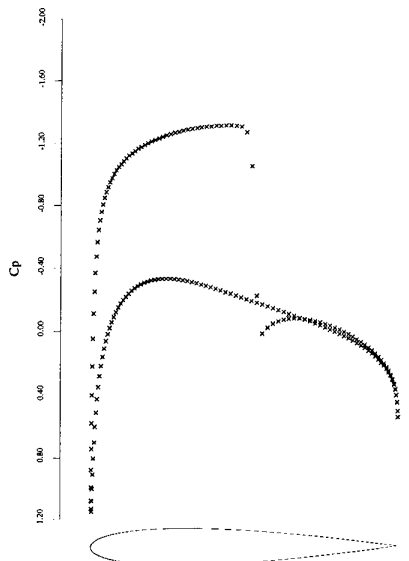
9a: Initial Condition  
 $C_l = 0.7946, C_d = 0.0358, \alpha = 2.364^\circ$



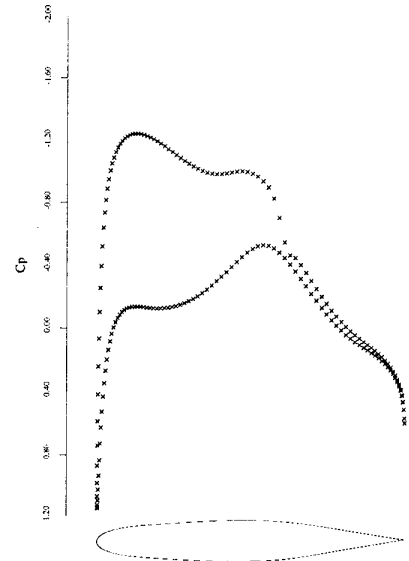
9b: 27 Design Iterations  
 $C_l = 0.7971, C_d = 0.0108, \alpha = 1.053^\circ$

Figure 9: Transonic Lifting Design Case,  $M = 0.75$  Fixed Lift.

—, x Initial Airfoil: NACA 0012.  
 ---, + Target  $C_p$ : RAE,  $M = 0.75$ .  
 Inverse Design

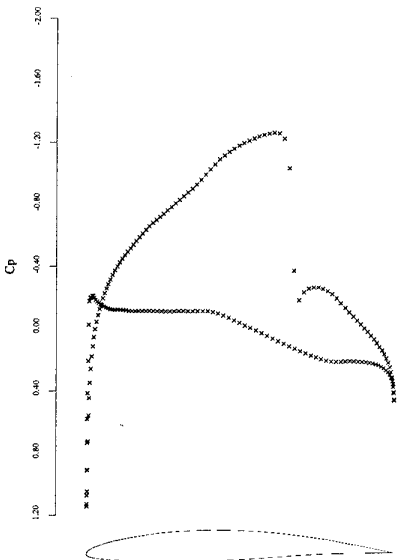


10a: Initial Condition  
 $C_l = 0.5037, C_d = 0.0127, \alpha = 1.856^\circ$

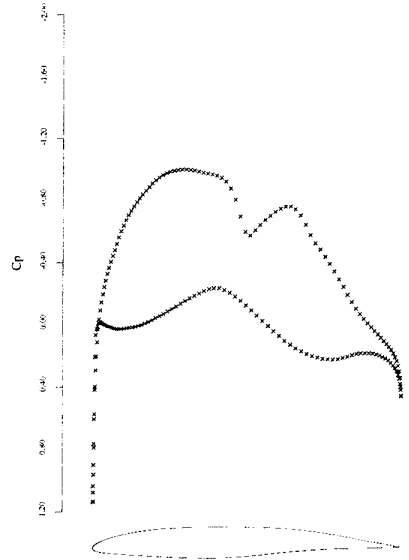


10b: 2 Design Iterations  
 $C_l = 0.5042, C_d = 0.0016, \alpha = 1.990^\circ$

Figure 10: Transonic Lifting Design Case,  $M = 0.75$ , Fixed Lift.  
 —, x Initial Airfoil: NACA 0012.  
 Symetric Drag Minimization.

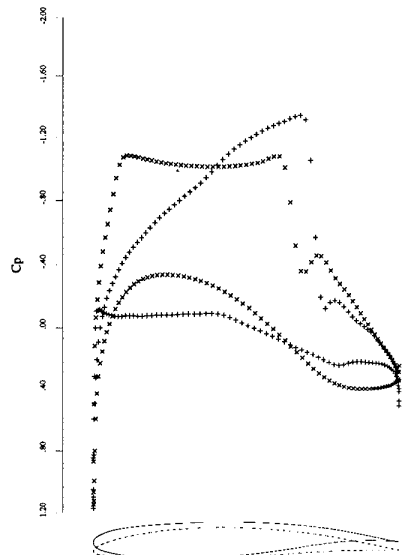


11a: Initial Condition  
 $C_l = 0.5964, C_d = 0.0042, \alpha = -0.464^\circ$

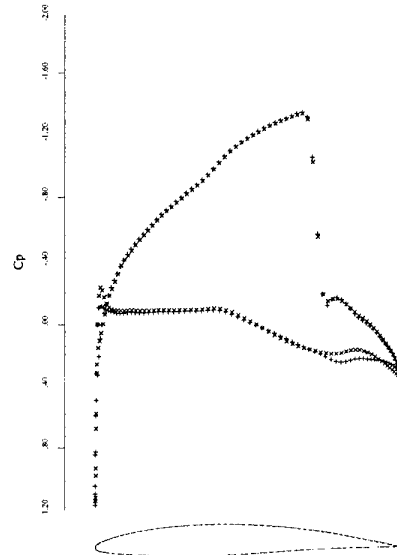


11b: 2 Design Iterations  
 $C_l = 0.5966, C_d = 0.0004, \alpha = 0.175^\circ$

Figure 11: Transonic Lifting Design Case,  $M = 0.735$  Fixed Lift.  
 —, x Initial Airfoil: NACA 64A410.  
 Camber Only Drag Minimization.



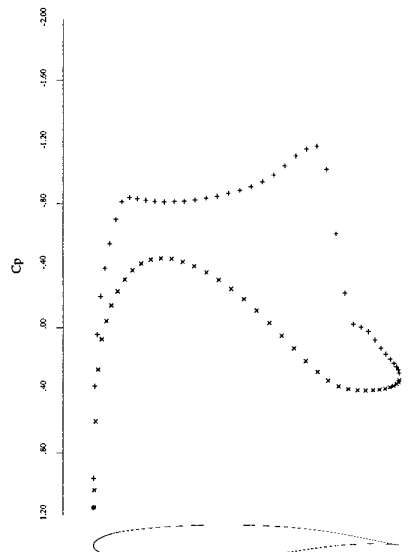
12a: Initial Condition  
 $C_l = 0.7019, C_d = 0.0015, \alpha = 0.266^\circ$



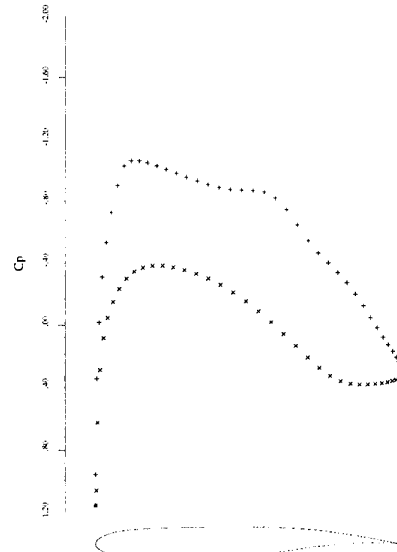
12b: 40 Design Iterations  
 $C_l = 0.6612, C_d = 0.0136, \alpha = -0.037^\circ$

Figure 12: Lifting Design Case,  $M = 0.75$ , Fixed Lift Mode.

—, x Initial Airfoil: Korn.  
 ---, + Target  $C_p$ : NACA 64012,  $M = 0.75$ .  
 Inverse Design



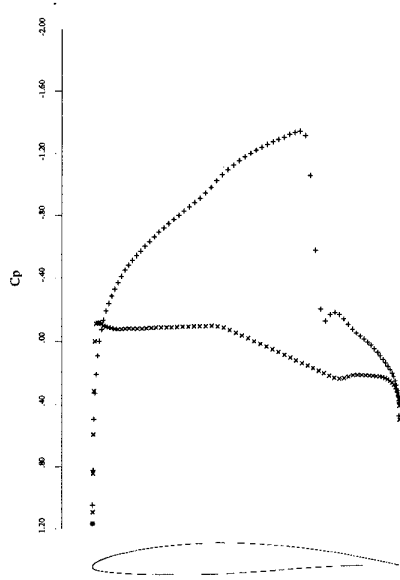
13a: Initial Condition  
 $C_l = 0.6432, C_d = 0.0155, \alpha = -0.229^\circ$



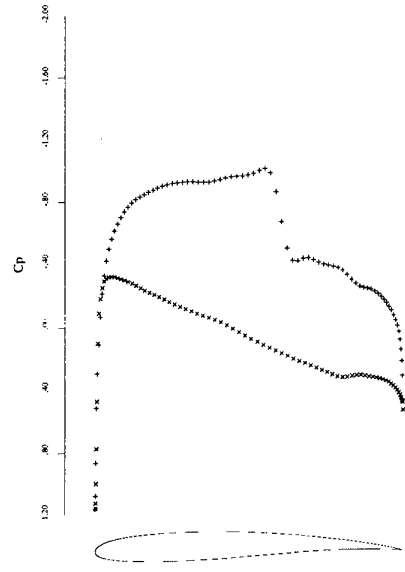
13b: 20 Design Iterations  
 $C_l = 0.6297, C_d = 0.0077, \alpha = 0.033^\circ$

Figure 13: Lifting Design Case,  $M = 0.78$  Fixed Lift Mode

Initial Airfoil: Korn.  
 Target  $C_p$ : Korn,  $M = 0.75$ .  
 Inverse Design

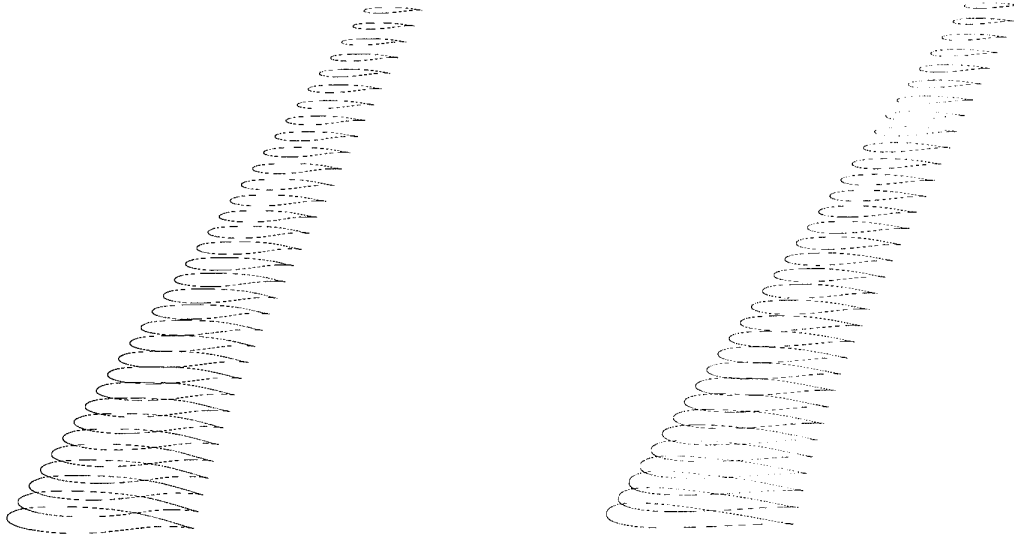


14a: Initial Condition  
 $C_l = 0.6778, C_d = 0.0144, \alpha = -0.096^\circ$



14b: 25 Design Iterations  
 $C_l = 0.6855, C_d = 0.0010, \alpha = -0.722^\circ$

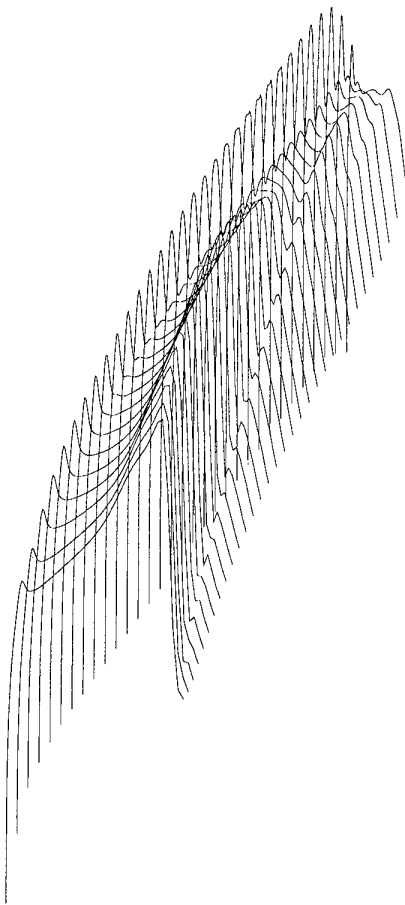
Figure 14: Lifting Design Case,  $M = 0.75$ , Fixed Lift Mode.  
 Initial Airfoil: NACA 64A410.  
 Drag Reduction



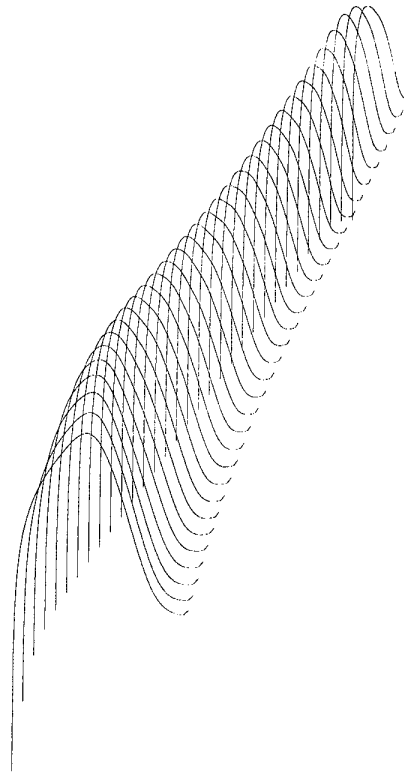
15a: Initial Wing  
 $C_l = 0.5001, C_d = 0.0185, \alpha = -0.958^\circ$

15b: 8 Design Iterations  
 $C_l = 0.4929, C_d = 0.0118, \alpha = 0.172^\circ$

Figure 15: Lifting Design Case,  $M = 0.82$ , Fixed Lift Mode.  
Drag Reduction

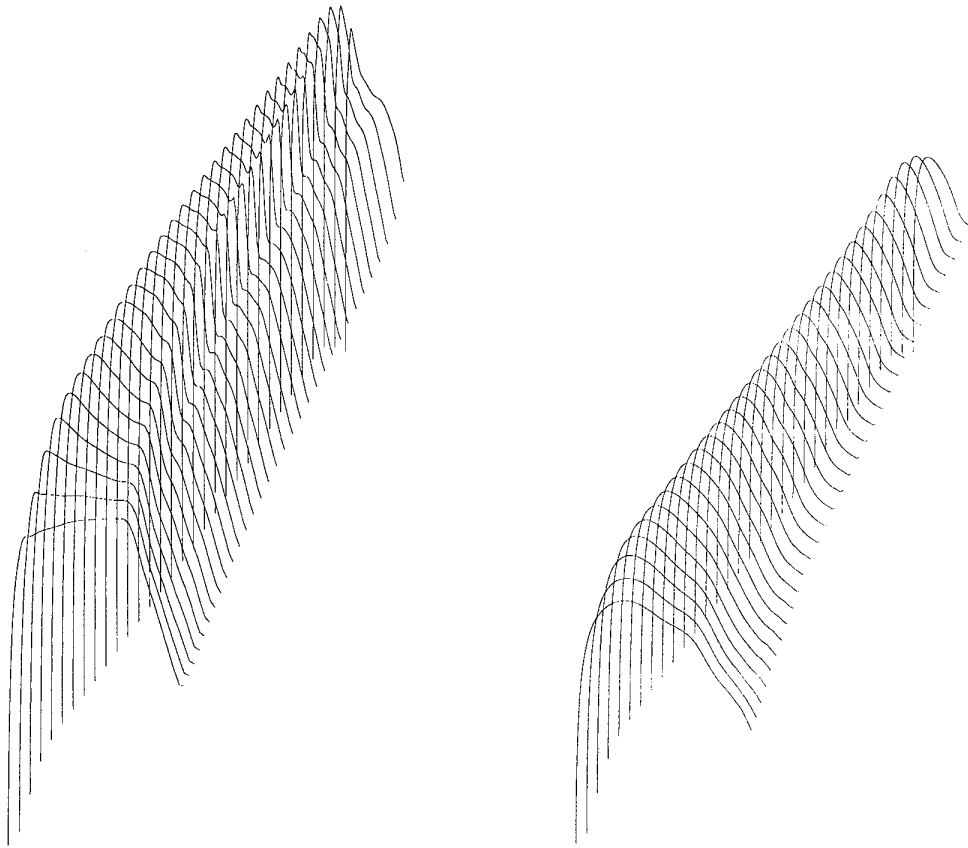


UPPER SURFACE PRESSURE



LOWER SURFACE PRESSURE

Figure 16: Lifting Design Case,  $M = 0.82$ , Fixed Lift Mode.  
Initial Wing: Modified Korn.  
 $C_L = 0.5001$ ,  $C_D = 0.0185$ ,  $\alpha = -0.958^\circ$   
Drag Reduction



UPPER SURFACE PRESSURE

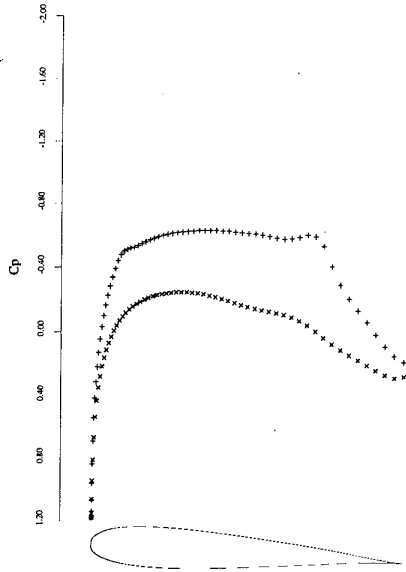
LOWER SURFACE PRESSURE

Figure 17: Lifting Design Case,  $M = 0.82$ , Fixed Lift Mode.

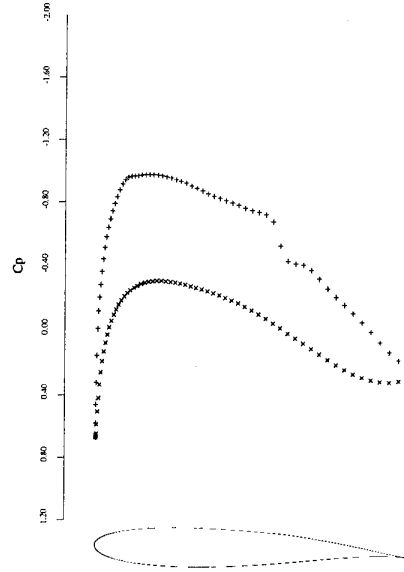
Design after 8 cycles

$C_L = 0.4929$ ,  $C_D = 0.0118$ ,  $\alpha = 0.172^\circ$

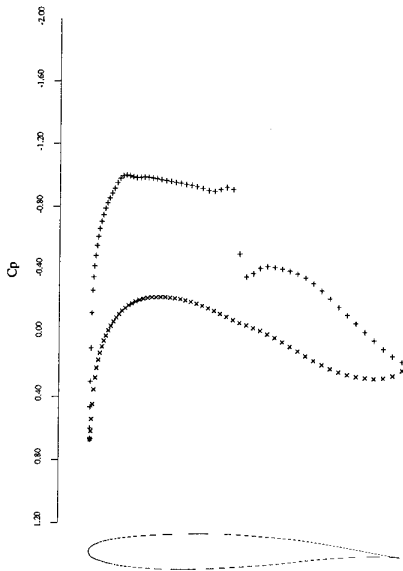
Drag Reduction



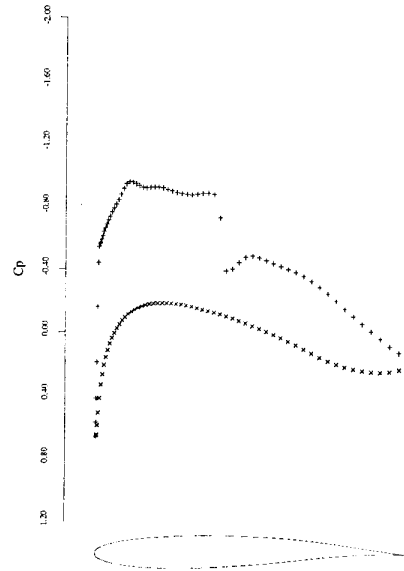
18a: span station  $z = 0.00$



18b: span station  $z = 0.25$

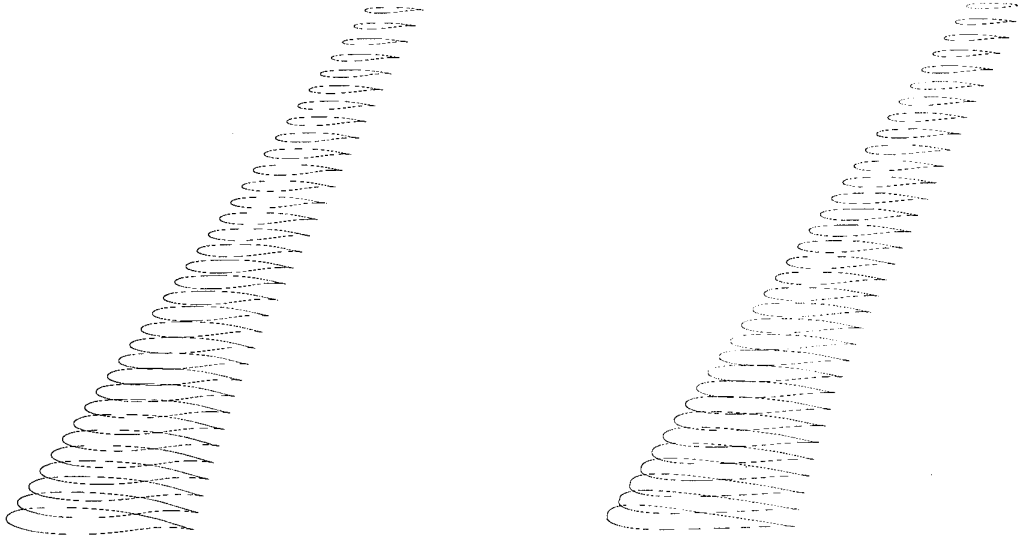


18c: span station  $z = 0.50$



18d: span station  $z = 0.75$

Figure 18: FLO67 check on redesigned wing.  
 $M = 0.82, C_L = 0.4975, C_D = 0.0107, \alpha = 0.200^\circ$



19a: Initial Wing  
 $C_l = 0.5033, C_d = 0.0261, \alpha = -1.236^\circ$

19b: 10 Design Iterations  
 $C_l = 0.4956, C_d = 0.0132, \alpha = -0.028^\circ$

Figure 19: Lifting Design Case,  $M = 0.85$ , Fixed Lift Mode.  
Drag Reduction

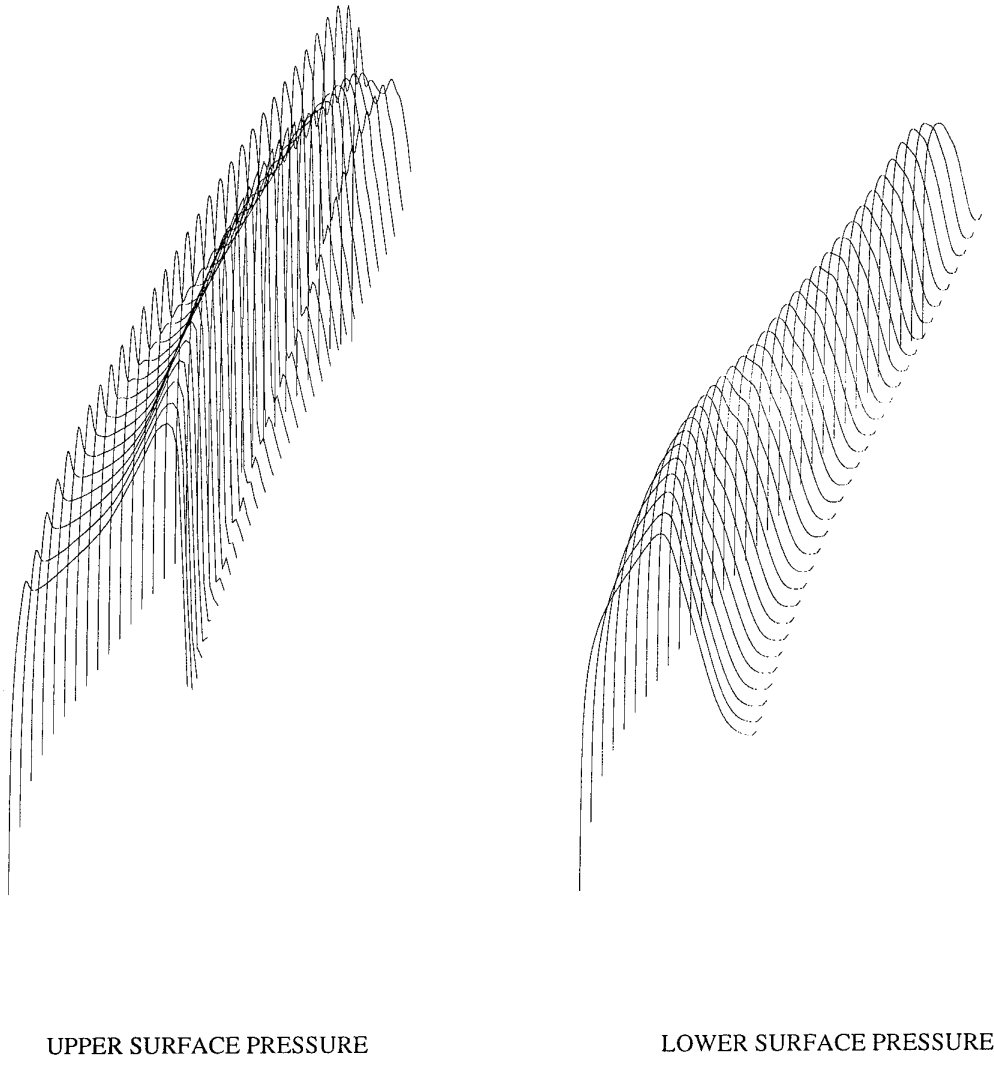
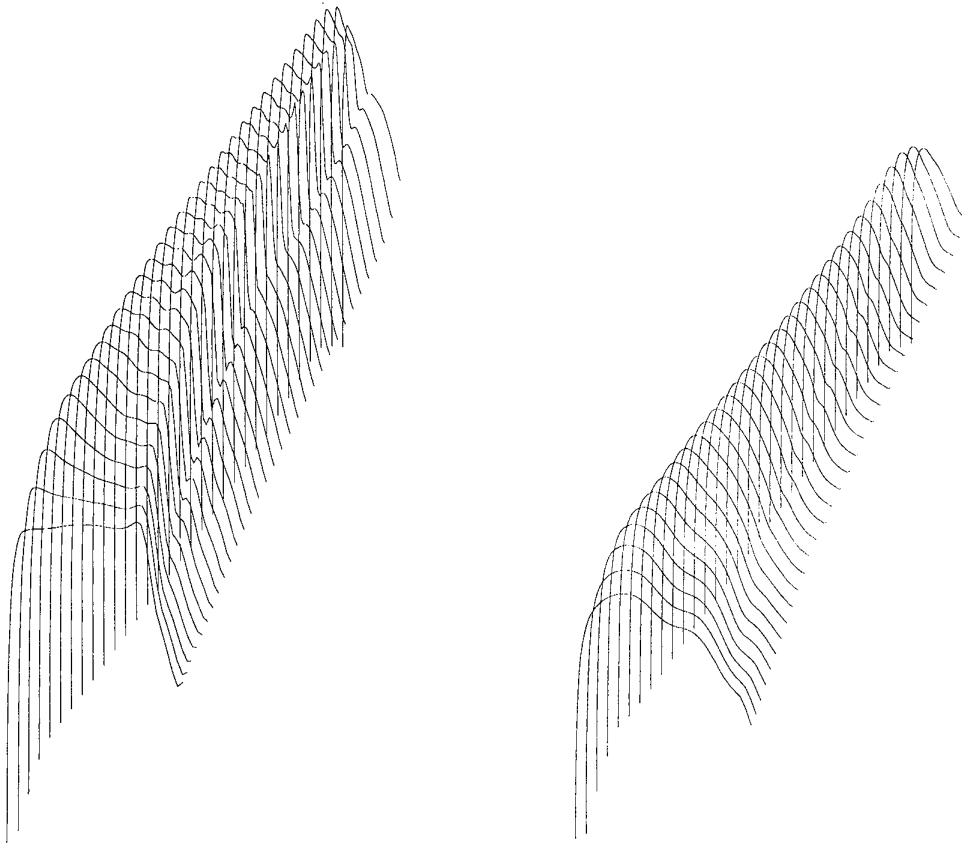


Figure 20: Lifting Design Case,  $M = 0.85$ , Fixed Lift Mode.  
Initial Airfoil: Modified Korn.  
 $C_L = 0.5033$ ,  $C_D = 0.0261$ ,  $\alpha = -1.236^\circ$   
Drag Reduction



UPPER SURFACE PRESSURE

LOWER SURFACE PRESSURE

Figure 21: Lifting Design Case,  $M = 0.85$ , Fixed Lift Mode.  
Design after 10 cycles  
 $C_L = 0.4956$ ,  $C_D = 0.0132$ ,  $\alpha = -0.028^\circ$   
Drag Reduction

RESIDUAL-CORRECTION TYPE AND RELATED COMPUTATIONAL METHODS FOR  
AERODYNAMIC DESIGN PART I AIRFOIL AND WING DESIGN

Th.E.Labrujère  
Theoretical Aerodynamics Department  
National Aerospace Laboratory  
A.Fokkerweg 2  
1059 CM AMSTERDAM  
The Netherlands

**SUMMARY**

The present paper discusses the problem of inverse shape design, where the geometry of a wing should be determined such that it will have a prescribed surface pressure distribution at the design condition considered. A survey is given of so-called decoupled-solution methods for this problem. With this type of methods the flow field around a current estimate of the wing and a subsequent new estimate of the wing are determined by two separate computational steps in an iterative process. A global description is given of the main features of the underlying theories and some examples of application are given. A detailed description is given of the NLR method for inverse shape design based on the residual-correction approach.

**LIST OF SYMBOLS**

$\alpha$  angle of attack

$\beta = \sqrt{1 - M_\infty^2}$

$\gamma$  ratio of specific heats

$\Gamma$  boundary of flow domain

$\delta$  velocity or pressure defect

$\delta z$  geometry correction

$\epsilon$  relaxation factor (see Eq.(12))

$\lambda$  co-state variable

$\xi$  independent coordinate parameter

$\rho$  density

$\phi$  velocity potential

$\Omega$  flow domain

$C_p = \frac{p - p_\infty}{0.5 \rho_\infty q_\infty^2}$ , pressure coefficient

$C_p^*$  pressure coefficient at sonic speed

$C_{p_{tar}}$  target value of pressure coefficient

$F$  functional associated with

design problem (see Eq.(1))

$M_\infty$  free stream Mach number

$\vec{n}$  unit normal vector

$p$  pressure

$q$  total velocity

$\vec{t}$  unit tangent vector

$u$  disturbance velocity component in x-direction

$u^*, u^{tar}$  disturbance velocities associated with  $C_p^*$  and  $C_{p_{tar}}$  respectively

$V_n$  normal velocity

$V_t$  tangential velocity

$w$  weight factor

$x, z$  Cartesian coordinates of airfoil contour

subscripts

$c$  refers to camber

$l$  refers to airfoil lower side

$le$  refers to airfoil leading edge

$sub$  refers to subsonic part

$sup$  refers to supersonic part

$t$  refers to thickness

$te$  refers to airfoil trailing edge

$u$  refers to airfoil upper side

$\infty$  refers to free stream conditions

superscripts

$t$  refers to target velocity or pressure

**1. INTRODUCTION**

The present paper considers methods to solve the problem of inverse wing design, i.e. to determine the shape of a wing such that on its surface an a priori prescribed (target) pressure distribution exists at the flow condition considered. The formulation of a well-posed inverse problem is not at all trivial, as has already been demonstrated by Betz (Ref.1) and by Mangler (Ref.2) for incompressible

flow. Incorporation of inverse methods in the practical design process has led to additional user requirements with respect to control over the geometry. As a consequence, the problem is often complicated by the introduction of constraints with respect to the geometry. Furthermore, in attempts to extend the range of applicability of inverse methods, increasingly complicated flow equations (full potential, Euler, Navier-Stokes) are being used. Both factors have led to a considerable increase in effort for the development of inverse design methods.

The paper will focus on iterative methods in which the flow variables and geometric variables are decoupled in the solution process. There are three major types of such methods: Dirichlet type methods, Neumann or residual-correction type methods, and variational type methods. All methods start with an initial guess of the geometry to be determined. Firstly, in each subsequent iteration step, a boundary value problem is solved for a given estimate of the geometry. With the Dirichlet type method this boundary value problem is of Dirichlet type. With the Neumann or residual-correction type methods, and with the variational type methods, this boundary value problem is of Neumann type. Secondly, a correction to the geometry is derived from the solution of this boundary value problem. With most methods it is tried to reduce the computational effort for the geometry correction as much as possible.

The idea to decouple the flow and geometry solution in inverse design is in most cases inspired by the desire to take maximum advantage of the fact that analysis methods have been developed for many applications, in different flow regimes, and in some cases with complex geometry. Another advantage of the decoupled-solution methods is the fact that, in general, geometric constraints can be implemented much easier in a separate geometry update procedure than in a

complete system of equations for flow as well as geometric variables.

In the last decade a large variety of the type of methods considered here has been developed. Nearly all 3-D design methods are of the Dirichlet or Neumann type. The least developed approach to the inverse design problem is that of optimal control (calculus of variations). Pironneau (Ref.3) gave an extensive survey of possible applications to optimum shape design for systems described by elliptic flow equations. Jameson (Ref.4) has also drawn attention to possible advantages of applying this approach. But up to now there seem to be few practical applications. However, because it seems to offer some perspective with respect to robustness and flexibility, attention may be paid to this type of approach.

The formulation of the aerodynamic wing design problem will be discussed, paying attention to the specification of design requirements, aspects of well-posedness, and the need for geometric constraints. A global description will be given of all three types of solution methods mentioned above, emphasizing the essential features. Some details will be given of methods which may be considered as representative of different approaches and of methods illustrating the latest developments. The paper addresses in particular the residual-correction approach. Developments at NLR are described in detail and computational results are shown for 2D as well as 3D applications.

## 2. THE AERODYNAMIC WING DESIGN PROBLEM

### 2.1 Design requirements

The aerodynamic wing design problem pertains to the determination of the shape of a wing such that it will fulfill requirements, which comprise both design goals and constraints in terms of aerodynamic characteristics and geometry.

The formulation of the aerodynamic design goals is in most cases done by defining an objective function or cost function, the minimum of which represents the solution to the design requirements. However, the actual form of the objective function, or rather the type of aerodynamic characteristics to be specified, is not at all obvious. Both specification of design goals in terms of force coefficients and specification in terms of target pressure distributions have their supporters.

According to Hicks (Ref.5): "The objective function can be any quantity which can be calculated by an aerodynamics code, e.g. drag, lift/drag ratio, etc. However, experience has shown that the choice of force coefficients as the objective function can lead to unacceptable pressure distributions".

With respect to target pressure distributions, Loes and Hinson (Ref. 6) remark: "Even with experienced designers, there is no assurance that the specified pressures will minimize drag, or weight, or whatever the aircraft design objective may be. Moreover, the need to specify design pressures implies a point design, and optimum aircraft efficiency might not be produced by an optimum point design". But, they also state: "Because of the inaccuracies in drag calculations, most successful three-dimensional transonic designs done by numerical optimization involve the use of a design objective based on pressure distributions".

And, finally, Volpe (Refs.7, 8) may be cited: "An obvious advantage of inverse methods is the control the designer has over the force characteristics of the airfoil profile and over the boundary layer development on its surface, a control gained through the pressure (speed) distribution that is specified".

Of course, the main advantage of defining the design requirements in

terms of force coefficients is its directness. But as mentioned above, it may lead to unacceptable pressure distributions associated with undesirable flow phenomena. On the other hand, the specification of pressure distributions to satisfy the design requirements provides more direct control over the flow quality, e.g. over the boundary layer development. At NLR, those considerations have led to the conviction that design requirements should be formulated in terms of prescribed pressure distributions, notwithstanding the fact that the specification of pressure distributions relies to a large extent on the experience of the designer.

Typically, the residual-correction type and related approaches consider the design problem formulated in terms of target pressure distributions. This implies the minimization of a cost function of the form

$$F = \int_S [C_p - C_{p_w}]^2 dS, \quad (3)$$

where the integration is over that part of the surface where the pressure has a prescribed value. This type of design problem is usually indicated as inverse shape design.

## 2.2 Well-posedness

The first method, applicable to the inverse design of 2D airfoils in incompressible flow, devised by Betz (Ref.1) and reconsidered by Mangler (Ref.2), was based on conformal mapping of the airfoil onto a circle. It was shown that three conditions had to be satisfied by the prescribed pressure distribution in order to ensure the existence of a closed airfoil generating that pressure distribution at a prescribed free stream condition. These constraints are given by the integral relations:

$$\int_0^{2\pi} \log \left| \frac{q_0(\omega)}{q_\infty} \right| \begin{Bmatrix} 1 \\ \cos\omega \\ \sin\omega \end{Bmatrix} d\omega = 0, \quad (4)$$

where  $q_0(\omega)$  is the tangential velocity on the airfoil surface derived from the prescribed pressure distribution,  $q_\infty$  is the freestream speed and  $\omega$  is the angular coordinate in the circle plane.

The first constraint expresses the regularity condition establishing a unique relation between the prescribed velocity and the freestream speed. The other two constraints are derived from the requirement of a closed airfoil contour.

Later, attention was again drawn to these constraints, amongst others by Lighthill (Ref.9, 9). Since then, the necessity to take these "Betz-Mangler constraints" into account in order to formulate a well-posed problem for inverse airfoil design has been the subject of discussion. The possible existence of similar consistency constraints for other types of flow has also been studied. Woods (Ref.10) was able to formulate such constraints for compressible 2D subcritical flow as described by the Von Karman-Tsien gas model. But, so far, no explicit formulation of similar constraints for more general types of flow has appeared. Nevertheless, it is commonly assumed that similar constraints exist for all inverse 2D (and probably 3D) airfoil design problems.

### 2.3 Geometric constraints

The early 2D conformal mapping methods demonstrated yet another consequence of arbitrarily prescribing the pressure distribution, viz. the appearance of self-intersecting geometries ("cross-over", "fish tail" airfoils) as a solution to the problem. So, even if all consistency constraints are satisfied by the target pressure distribution so that the inverse design problem is well-posed in the sense

indicated in the previous section, the result might still not have practical value.

Some authors have drawn the conclusion that in this case the design problem has to be reformulated by modifying the target pressure distribution. This, however, leads to a trial and error process of which the success strongly depends on the expertise of the designer.

Other authors have devised methods that allow the incorporation of geometric constraints in an attempt to reduce the class of admissible solutions to "realistic" airfoils. In this way uncertainty with respect to correct pressure distribution behaviour near the leading edge stagnation point can be removed by prescribing part of the leading edge geometry. In this way the inverse problem may be recast in a mixed direct-inverse problem, where one part of the geometry is prescribed whereas the other part is designed. Alternatively, the inverse problem may be formulated as a least squares minimization problem such that the prescribed pressure distribution as well as the geometric constraints are satisfied approximately in a least squares sense. Then, also such constraints as trailing edge thickness can be handled. Unfortunately, the existence of a (unique) solution of the minimization problem has never been proven.

Apart from the above described need for constraints related to the well-posedness of the inverse problem and constraints to prevent non-physical solutions, geometric constraints may be required for a more practical reason, e.g. from the point of view of the structural engineer. This may lead to constraints on airfoil thickness, leading edge radius, trailing edge angle, wing twist, wing-body junction etc. The development of computational design methods reflects the search for methods offering well-posedness (i.e. to take into account the Betz-Mangler type constraints) as well as options

for additional geometric and also aerodynamic constraints, such as a prescribed lift coefficient.

#### 2.4 Free parameters

The problem of formulating a well-posed inverse design problem can be partly solved by introducing auxiliary functions containing free parameters in the prescribed pressure distribution  $C_{p, \text{tar}}$ . The values of the parameters are determined as part of the solution so that by means of the auxiliary functions the prescribed pressure distribution is modified such that the (unknown) consistency requirements will be (automatically) satisfied to the best possible extent. Of course, the specific choice for the type of adjustable free parameters and auxiliary functions determines implicitly the class of admissible solutions.

Some guidance with respect to the choice of the free parameters has been presented by Volpe & Melnik (Ref.7) They have shown that for 2D airfoil flow the regularity condition associated with the relation between the free stream speed and the prescribed pressure distribution may be satisfied by introducing the free stream speed as a free parameter while maintaining a specified location of the leading edge stagnation point. Drela (Ref.11) chose to fix the free stream speed, but left the location of the leading edge stagnation point in physical space unspecified.

The consistency constraints associated with trailing edge closure are sometimes neglected and it is hoped that these will be implicitly fulfilled.

The introduction of auxiliary functions with free parameters has been extensively investigated by Soemarwoto (Ref. 12) for inverse 2D airfoil design in incompressible flow. He introduced functions allowing displacement of the leading edge stagnation point and adjustment of the pressure distribution behaviour near the trailing edge for avoiding the

occurrence of "fish tails" and allowing trailing edge closure. Three free parameters were introduced for control of the modifications.

### 3. DIRICHLET TYPE METHODS

#### 3.1 Global description

The idea underlying the Dirichlet type methods is similar to the idea of simulating boundary layer displacement effects by means of a normal velocity prescribed at the boundary. Firstly, it is assumed that a sufficiently close estimate of the geometry to be determined is given so that only small modifications are required for computation of the new geometry. Considering the flow fields about both geometries, it may be assumed that the streamlines around the new geometry can be generated from the streamlines around the given geometry by superimposing a flow normal to the given streamlines. This implies, of course, the assumption of a transpiration (outflow as well as inflow) at the boundary of the initial geometry as illustrated in Fig.1.

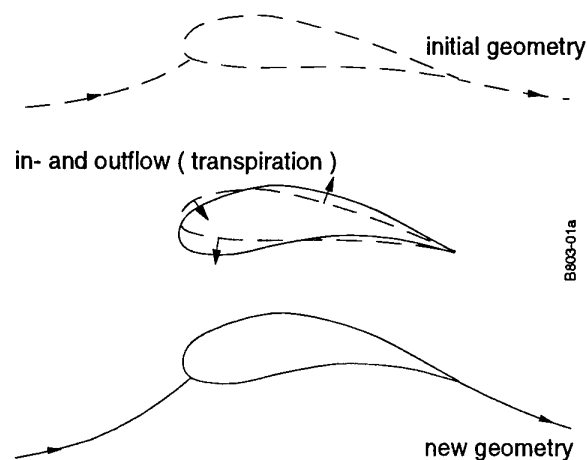


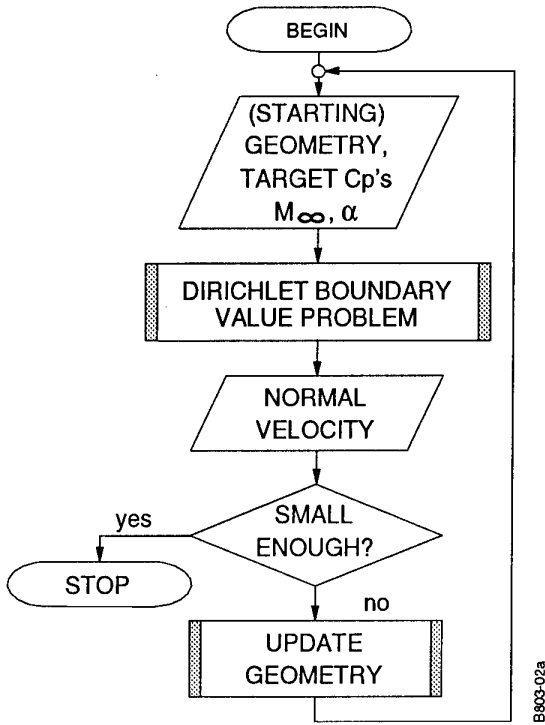
Fig.1 Surface displacement simulation by transpiration.

The iterative process of the Dirichlet type methods (see Fig.2) is based on this concept. The first computational step comprises the solution of a Dirichlet boundary value problem in which the boundary condition is

derived from the target pressure distribution.

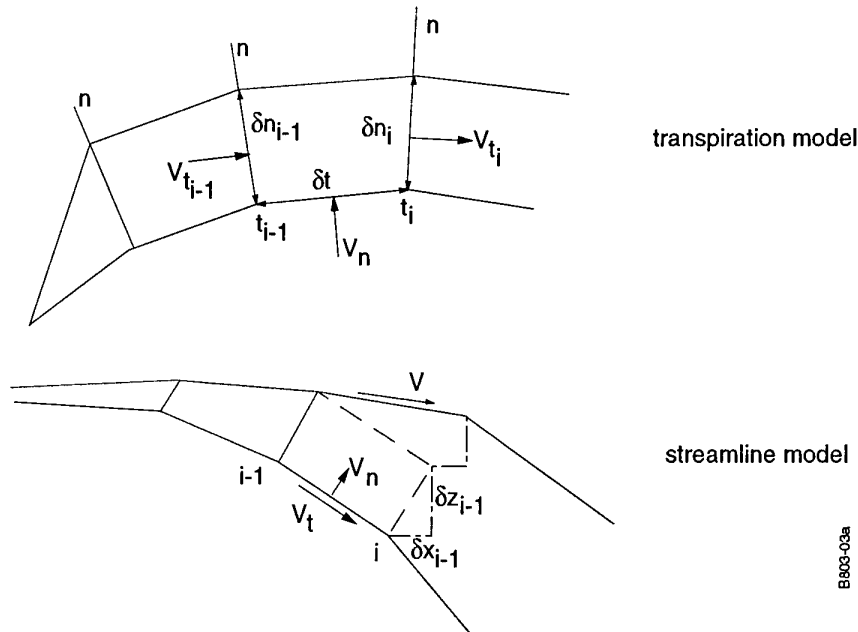
In the case of 2D airfoil design for potential flow the derivation of such a boundary condition is straightforward. In potential flow there is a unique relation between the value of the pressure coefficient at a point on an airfoil contour and the magnitude of the tangential velocity at that point. Based on the assumption of small modifications for the determination of the new airfoil contour, and the consequently small values of the transpiration velocity, the tangential velocity distribution along the given airfoil contour in the new flow field may be approximated by the specified velocity distribution along the new (unknown) airfoil contour. Then, by integrating along the given airfoil contour, the value of the potential along the airfoil contour may be determined apart from an arbitrary constant. This determines the Dirichlet boundary condition.

In more complex cases, such as 3D wing design, the derivation of the Dirichlet boundary condition is no longer obvious.



B803-02a

Fig.2 Flow chart of Dirichlet type method



B803-03a

Fig.3 Geometry correction based on transpiration model and on streamline model

For instance, assuming again potential flow and the availability of an approximation of the tangential velocity components in chordwise and spanwise direction, the conversion, by integration, into values of the potential at the wing surface leads to an additional unknown function of the spanwise coordinate.

Detailed discussion of this problem is considered to be out of the scope of the present paper and the reader is referred to the relevant literature.

The second computational step in the iterative process comprises the determination of geometry modifications. Solving the Dirichlet boundary value problem leads to a flow field around the given geometry with a non-zero normal velocity ("transpiration") distribution at the surface. The geometry modifications, determined according to either the transpiration model or the streamline model, aim to remove this transpiration. Fig.3 illustrates these concepts for 2D airfoil design.

The transpiration model is based on mass flux conservation. Considering the cell formed by the points  $i-1$  and  $i$  on the old and on the new airfoil contour, application of the mass balance results in

$$\Delta(\rho V_t \delta n) = \rho V_n \delta t, \quad (5)$$

which may be discretized as

$$\rho_i V_{t_i} \delta n_i - \rho_{i-1} V_{t_{i-1}} \delta n_{i-1} = \frac{\rho_{i-1} V_{n_{i-1}} + \rho_i V_{n_i}}{2} \delta t. \quad (6)$$

From Eq. (6) the successive  $\delta n_i$  values can be solved.

The streamline model is based on alignment of the airfoil contour with the streamlines. This implies that the tangent to the contour is directed along the local velocity  $\vec{V} = \vec{V}_t + \vec{V}_n$ . In discretized form this results in

$$x_{i_{\text{new}}} = x_{i_{\text{old}}} + \delta x_{i-1} + \left[ \left( \frac{V_n}{V_t} \right)_{i-1} + \left( \frac{V_n}{V_t} \right)_i \right] \frac{\delta t}{2} n_x, \quad (7a)$$

$$z_{i_{\text{new}}} = z_{i_{\text{old}}} + \delta z_{i-1} + \left[ \left( \frac{V_n}{V_t} \right)_{i-1} + \left( \frac{V_n}{V_t} \right)_i \right] \frac{\delta t}{2} n_z. \quad (7b)$$

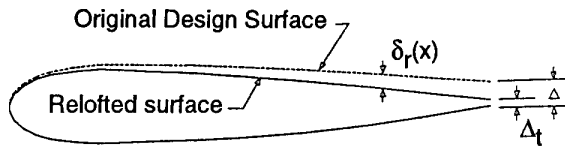
In the majority of Dirichlet type methods, existing flow solvers have been modified in order to accept Dirichlet type boundary conditions (derived from the prescribed pressure distribution), usually in addition to the common Neumann type boundary condition (zero normal velocity). In this way, methods have been developed for solving purely inverse as well as mixed direct-inverse problems.

### 3.2 Survey of developments

A typical example of a Dirichlet type method is that of Henne (Ref.13) for transonic wing design, where the transpiration model is used for determination of the geometry update. The computational process utilizes the transonic full potential code FLO22 of Jameson and Caughey (Ref.14) with a specified velocity potential as Dirichlet boundary condition. In Ref. 1 some examples are presented showing the capability of the method for redesign of existing wings. Application of constraints is not discussed.

Another typical example is the conformal mapping method of Volpe (Refs.7, 8) for inverse design of airfoils in transonic flow. Here, the geometry corrections are calculated utilizing the streamline model. Being a purely inverse method, the Betz-Mangler constraints are taken into account, but there is no possibility for applying additional constraints.

In 1987 Gally and Carlson (Ref.15) presented an extension of an earlier Dirichlet type method developed for orthogonal grids (Ref.16) to a body-fitted non-orthogonal curvilinear grid for the mixed direct-inverse transonic wing design problem. The method utilizes the finite volume full potential code FLO30 of Jameson and Caughey (Ref.17) in which the boundary condition of zero normal velocity, applied in analysis, is replaced by specification of the perturbation potential in the inverse design regions. During the iteration procedure the actually used geometry is periodically updated by aligning it with the streamlines. By excluding the wing leading edge region from the inverse design regions, the problem of how to apply the regularity condition at the leading edge is circumvented. But this implies, of course, that the possibility for modification of the leading edge region is limited. Prescription of the trailing edge thickness is made possible by means of a relofting process in which a deviation of the calculated trailing edge thickness from the desired trailing edge thickness is removed by distributing it along the entire wing section contour. See Fig.4. As a direct consequence of this procedure, deviations from the target pressure distribution have to be accepted as a result; there is no further means of control.



$$\delta_r(x) = (\Delta_t - \Delta) \frac{x}{c}$$

Fig.4 Relofting to force trailing edge closure (Ref.16)

Dirichlet type methods based on panel methodology have been developed by Fornasier (Ref.18) and Kubrynski (Ref.19). Despite the limitation with respect to the description of real flow, panel methods are still widely applied because of their capability to treat complex configurations.

Fornasier (Ref.18) has developed a panel method for direct/inverse shape design of general 3D configurations in subsonic and supersonic flow. Surface distributions of sources as well as of doublets are utilized. This offers the opportunity to relate the local source strength to the normal component of the free stream velocity and to relate the tangential derivative of the doublet strength to the tangential velocity. As such, the source distribution provides direct information on the geometry, and the doublet distribution provides direct information on the flow field. Direct and inverse problems lead to the same type of equations, and as a consequence mixed direct-inverse problems can be treated equally well. In the regions with given geometry the source strength is pre-determined, whereas in regions with prescribed velocity the doublet strength is pre-determined using the current guess of the geometry. Application of the boundary condition of zero internal perturbation potential leads to a linear system of equations from which the remaining unknown singularity strengths are determined. The new source distribution is then used to update the geometry.

The panel method of Kubrynski (Ref.19) has features similar to that of Fornasier. Here, also, source as well as doublet distributions are used, although the definition of the singularity strengths is different. The source strengths are related to the mass flow through the body surface (zero in the analysis case) and the doublet strengths are related to the velocity potential at the body surface. The boundary condition of zero internal potential is applied to

derive an integral equation for the doublet strengths. An inverse or mixed direct-inverse problem is solved by the following iteration process. For a given guess of the geometry, the doublet distribution is determined for a source distribution of zero strength. Then a geometry correction is determined aiming at minimizing the difference between the approximated actual pressure and the target pressure. The geometry is not actually updated, but using the transpiration concept the required geometry correction is related to a mass flow

through the body surface and thus determines a new value of the local source strength. The source distribution thus determined gives rise to an incremental doublet distribution associated with a change in the approximated actual pressure distribution. After minimizing the differences between the approximated actual pressure and the target pressure, the shape of the configuration is updated and the whole process is repeated until satisfactory convergence has been obtained.

An interesting feature of this method is the fact that the pressure distribution may be prescribed on one part of the configuration and that a different part of the configuration may be reshaped in an attempt to realize that pressure distribution. This is of particular interest for e.g. fuselage-wing, pylon-wing, pylon-nacelle interference problems. Fig. 5 shows an example of wing-body design, where the shape of the fuselage has been redesigned such that a straight isobar pattern on the wing is obtained.

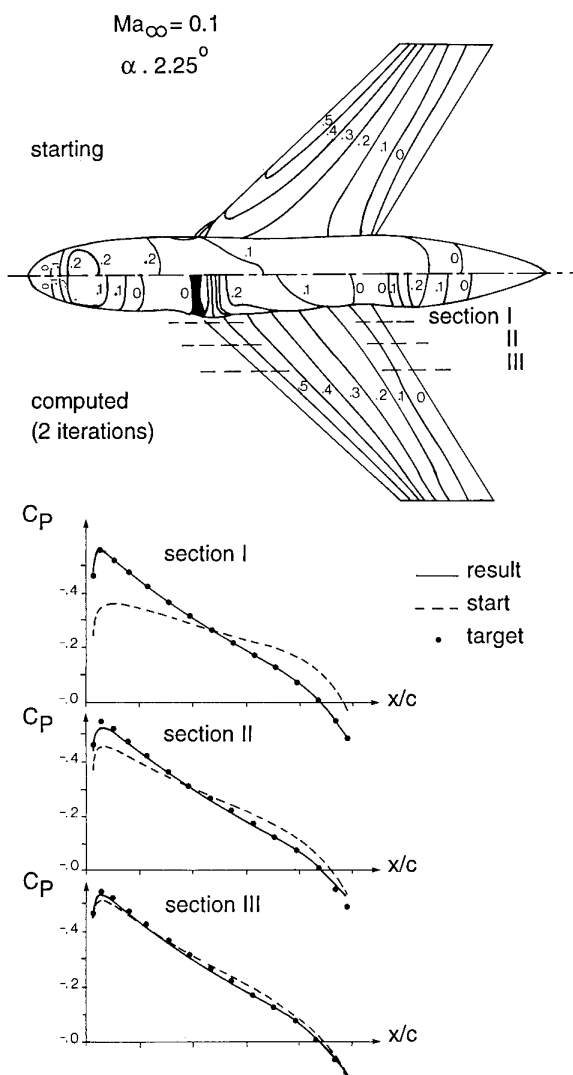


Fig.5 Wing and fuselage, before (top) and after (bottom) design process (Ref.19)

#### 4. NEUMANN OR RESIDUAL-CORRECTION TYPE METHODS

##### 4.1 Global description

Solving the Neumann problem for a given estimate of the geometry to be determined leads to a pressure distribution along the contour, which deviates from the target pressure distribution. In the methods based on the residual-correction approach, the key problem is to relate the calculated differences between the actual pressure distribution on the current estimate of the geometry and the target pressure distribution (the "residuals") to proper corrections of the geometry. The iterative process obtained when following this approach is illustrated in Fig.6.

Obviously, the art in developing a residual-correction method is to find an optimum between the computational effort for determining the proper geometry corrections and the number of

iterations needed to obtain a converged solution. In order to solve this problem two different approaches may be followed. In one approach the geometry corrections are estimated by means of simple correction rules, based on relations between local geometry corrections and pressure differences known from linearized flow theory. In the other approach the geometry correction is determined by solving an approximate inverse problem, which is derived from the actual inverse problem e.g. by applying similarity rules or by linearizing the flow equations. In the latter case, the gain in computational effort is due to the reduced complexity of the

approximate inverse problem as compared with the actual inverse problem. The Neumann type methods try to utilize the analysis methods for the solution of the Neumann problem as a "black-box".

4.2 Survey of developments

Since Barger and Brooks (Ref.20) presented their streamline curvature method for inverse design of supercritical and subcritical airfoils in which they utilized the possibility to relate a local change in surface curvature to a change in local velocity, quite a number of methods has been developed following that concept. Subsequent refinements and

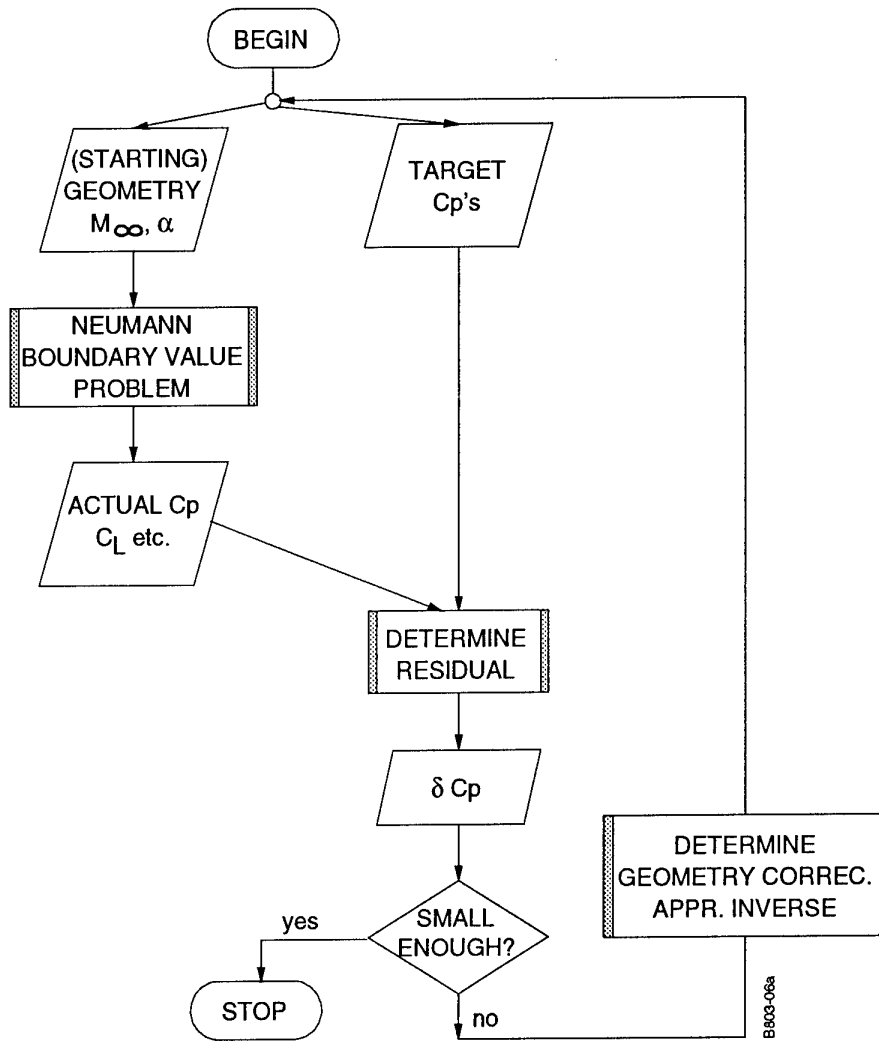


Fig.6 Flow chart of the Neumann type methods

modifications made the concept applicable to design problems based on the full potential equation (e.g. Campbell and Smith (Ref.21)), the Euler equations (e.g. Bell and Cedar (Ref.22)) and the Navier-Stokes equations (e.g. Malone et al (Ref.23)). Greff et al (Ref.24) described a 2-D airfoil design code for viscous-transonic flow. They followed the approach of formulating an approximate inverse problem for subsonic flow. This problem is defined using a modified Von Karman-Tsien rule for the derivation of an equivalent subsonic target from the equivalent differences between the transonic pressure distribution on the current estimate of the geometry and the transonic target pressure distribution. The approximate inverse problem is solved by means of an inverse panel method.

Takanashi (Ref.25) presented a method for transonic wing design using for the geometry correction an integral equation method that solves an approximate inverse problem on the basis of transonic small disturbance theory.

So far, the method of Takanashi (Ref.25) seems to be the most widely applied residual-correction method. It has been coupled with analysis methods on the basis of Euler equations as well as Navier-Stokes equations. It has been applied to 2D as well as 3D transonic and supersonic design problems (Fujii & Takanashi (Ref.26)). Hua & Zhang (Ref.27) have modified this method by replacing the numerical integrations applied in the integral equation method by analytical integrations, thus reducing computing time.

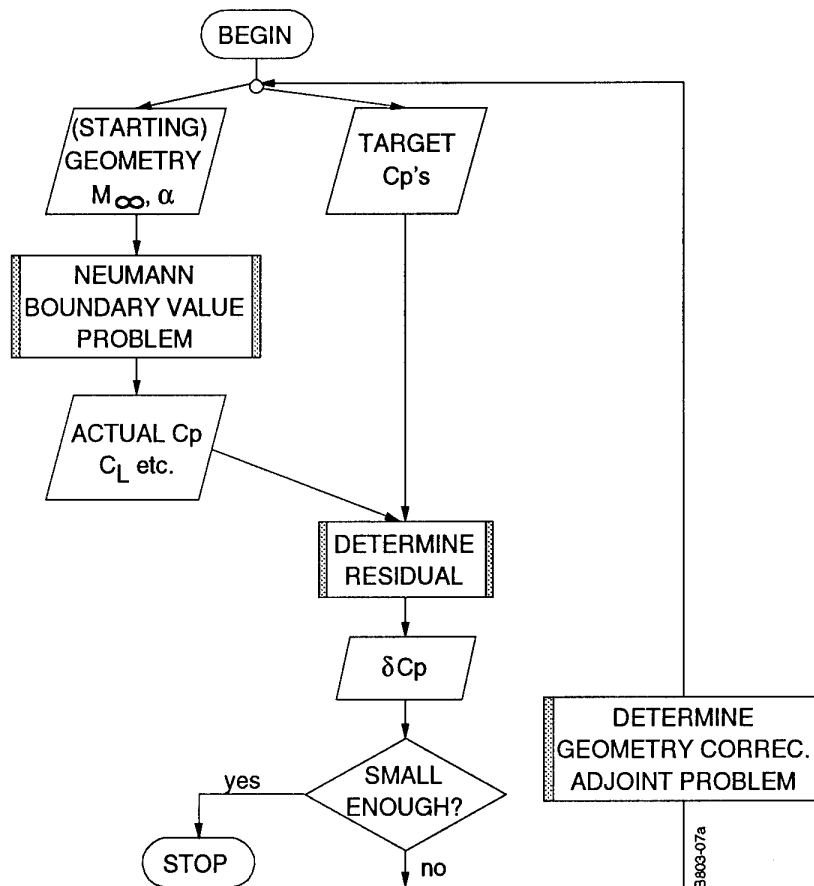


Fig.7 Flow chart of the variational type methods

They also added a smoothing technique in order to smooth the curvature of the designed geometry. The approach of Takanashi (Ref.25) has also been followed by Zhu et al (Ref.28) for transonic airfoil design; they introduced a modification for taking into account the regularity condition at the leading edge stagnation point. Also the method developed at NLR for transonic wing design (Ref.31) follows the approach of defining an approximate inverse problem, utilizing linearized compressible flow theory. Constraints on the geometry are introduced, leading to a least squares minimization problem which is solved with the aid of linearized panel methodology. The method will be described in some detail in section 6.

## 5. VARIATIONAL TYPE METHODS

### 5.1 Global description

Application of the calculus of variations ("optimal control theory") to the solution of the inverse design problem leads an iterative process as depicted in Fig.7. In each subsequent iteration step two strongly related flow problems have to be solved. One is the Neumann problem of flow analysis for a given geometry, the other is the so-called adjoint problem in which the residual differences between current and target pressure distribution determine the boundary condition. Usually this adjoint problem is of the same type as the corresponding analysis problem, which implies that a solution method may be readily derived from an available analysis method. It is attempted to determine the geometry correction as accurately as possible using the solution to the adjoint problem for the determination of a search direction for the geometry update. Application of this type of geometry correction method leads to an increase of computational effort as compared with simpler types of geometry correction methods. It might, however, be more robust and the speed of convergence of the whole process might be increased.

The concept of the variational approach may be best explained with the aid of a simple inverse airfoil design problem. To this end, consider the non-lifting incompressible potential flow around a symmetric airfoil so that the leading and trailing edge stagnation points are fixed. Assume the tangential velocity on the airfoil contour to be prescribed as a function of the chordwise coordinate  $x$  and the airfoil contour to be represented by  $z(x)$ . Then the inverse design problem may be formulated as the minimization of the functional :

$$F(z) = \int_{\Gamma} [\phi_t(z) - V_t]^2 dt. \quad (8)$$

Here  $t$  is the arclength of the contour,  $\phi_t$  is the actual tangential velocity and  $V_t$  is the target velocity.

Considering incompressible potential flow around a given airfoil the equations

$$\Delta \phi = 0 \quad \text{in } \Omega, \quad (9)$$

$$\frac{\partial \phi}{\partial n} = 0 \quad \text{on } \Gamma, \quad (10)$$

$$\frac{\partial \phi}{\partial n} = \vec{q}_\infty \cdot \vec{n}_\infty \quad \text{on } \Gamma_\infty, \quad (11)$$

determine the velocity potential  $\phi$  in the flow domain  $\Omega$  apart from a constant which may be determined by prescribing the potential at some point. The flow domain  $\Omega$  is bounded on the inner side by the airfoil contour  $\Gamma$  and on the outer side at infinity by  $\Gamma_\infty$ . For a given airfoil contour and given velocity potential  $\phi$  in the flow domain, the adjoint problem amounts to the determination of the co-state variable  $\lambda$ , apart from a constant, from the following equations:

$$\Delta\lambda = 0 \quad \text{in } \Omega, \quad (12a)$$

$$\frac{\partial\lambda}{\partial n} = -2 \frac{\partial}{\partial t} (\phi_t - V_t) \quad \text{on } \Gamma, \quad (12b)$$

$$\frac{\partial\lambda}{\partial n} = 0 \quad \text{on } \Gamma_0. \quad (12c)$$

With the aid of the solution to this problem, the variation of the functional F can be determined from:

$$\delta F = \oint_{\Gamma} h(x) \delta z(x) dx, \quad (13)$$

with

$$h(x) = -\nabla\lambda\nabla\phi + \frac{d}{dx} [\phi_t - V_t]^2 \frac{dz}{dt}. \quad (14)$$

For two successive estimates of the airfoil contour  $z^i$  and  $z^{i+1}$  the difference between the associated values of the functional F is to first order approximated by

$$F^{i+1} - F^i \approx \delta F. \quad (15)$$

Thus, applying a geometry correction by choosing  $z^{i+1} = z^i + \delta z$  with  $\delta z(x) = -\epsilon h(x)$  and  $\epsilon > 0$ , such that  $\delta F < 0$ , a reduction of F is ensured.

### 5.2 Survey of developments

Pironneau (Ref.3) gave an extensive survey of the possibilities for application to optimum shape design for systems described by elliptic flow equations.

An application of the variational approach to the inverse design of airfoils in subsonic potential flow is the pioneering work of Angrand (Ref.32). Beux and Dervieux (Refs.33, 34) treated the case of inverse design for internal subsonic flow governed by the Euler equations. Cabuk et al (Ref.35) applied the variational approach to the problem of optimizing a diffuser such that a maximum pressure rise is provided.

## 6. THE NLR RESIDUAL CORRECTION METHOD

### 6.1 Basic principle

The NLR residual correction method is based on the assumption that it is possible to split the design process into two major steps, which can be iterated until satisfactory results have been obtained. In the first step, the flow about the current estimate of the geometry is calculated by means of an analysis code for the flow regime under consideration, thus giving the deviation from the specified target (the residual).

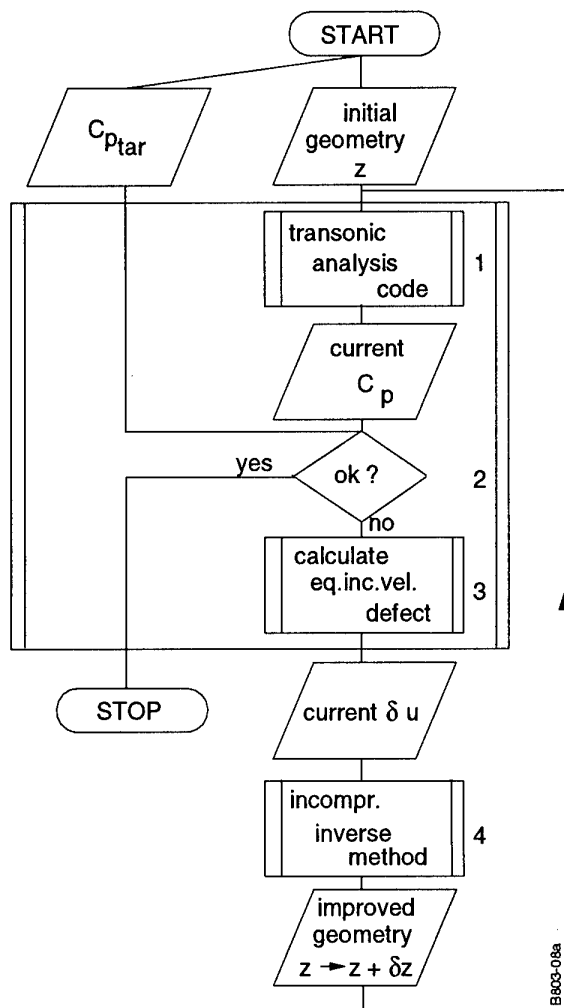


Fig.8 NLR Residual correction method, outer loop

In the second step, a geometry correction is calculated from the current residual by means of an approximative procedure involving the specification of an equivalent incompressible inverse flow problem which is more amenable to fast computational methods. For simplicity the method will be described in more detail for two-dimensional airfoil design. The computational process is initiated by specifying :

- the design condition in terms of angle of attack, Mach number and Reynolds number,
- a target pressure distribution,
- a starting airfoil at a starting angle of attack,
- geometric constraints,
- weight factors for the design conditions, for the geometric constraints and for the upper and lower surface target pressure distributions.

The computation proceeds by utilizing the following loop in an iterative fashion (see Fig.8):

1. Calculate the flow about the current estimate of the airfoil geometry  $z=z[x]$  for the operating condition (or design point) considered and obtain the current pressure distribution  $C_p[x]$  on the airfoil surface.

2. Decide whether or not the current airfoil geometry  $z=z[x]$  needs further improvement, by comparing the current pressure distribution  $C_p[x]$  with the target pressure distribution  $C_{p_{tar}}[x]$  and by considering the convergence history.

3. If further improvement of the current airfoil geometry  $z=z[x]$  is considered necessary, calculate the equivalent incompressible perturbation velocity defect  $\delta u$  on the airfoil contour from the target pressure distributions  $C_{p_{tar}}[x]$  and the current pressure distributions  $C_p[x]$ .

4. Calculate the airfoil geometry correction  $\delta z=\delta z[x]$  as will be described

below, obtain a new estimate for the airfoil geometry from

$$z[x] \Rightarrow z[x] + \delta z[x]. \quad (16)$$

5. Iterate the whole process until satisfactory results in terms of approximations of the pressure distributions and geometric requirements are obtained.

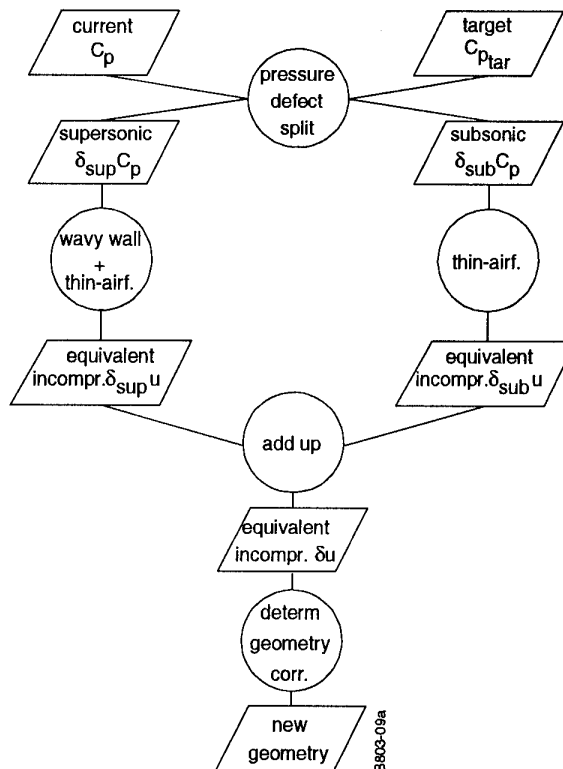


Fig.9 Calculation of incompressible perturbation velocity defect (NLR method)

During the process, the weight factors mentioned above may be used to balance the different design requirements. The inverse calculation consists of two major steps as indicated in Fig.9. In the first step the transonic pressure-defect distribution is replaced by an equivalent subsonic perturbation velocity defect distribution by applying a so-called pressure defect splitting technique. In the second step this equivalent velocity distribution is used for the

determination of the geometry corrections.

### 6.2 Equivalent subsonic velocity

The pressure defect splitting technique, which is used to distinguish between a subsonic and supersonic part of the pressure defect, is illustrated in Fig.10. The split made is based primarily on the assumption that subsonic thin-airfoil theory is applicable if the local actual pressure and the local target pressure are both subsonic, and that supersonic wavy-wall theory is applicable if both pressure coefficients are supersonic. In case one pressure coefficient is subsonic and the other supersonic the critical pressure coefficient is used as upper or lower limit. In Ref.30 a detailed description of the derivations is given.

The subsonic and supersonic parts of the pressure defect  $\delta C_p$  are defined as

$$\delta_{\text{sup}} C_p = \min(C_{p_{\text{ar}}}, C_p^*) - \min(C_p, C_p^*) , \quad (17a)$$

$$\delta_{\text{sub}} C_p = \max(C_{p_{\text{ar}}}, C_p^*) - \max(C_p, C_p^*) , \quad (17b)$$

where  $C_p$  is the actual pressure coefficient,  $C_{p_{\text{tar}}}$  is the target pressure coefficient, and  $C_p^*$  is the critical pressure coefficient. The subsonic and supersonic parts of the pressure-defect distribution are each converted into incompressible perturbation velocity defects  $\delta_{\text{sub}} u$  and  $\delta_{\text{sup}} u$ , from which the equivalent incompressible perturbation velocity defect is obtained as

$$\delta u = \epsilon (\delta_{\text{sub}} u + \delta_{\text{sup}} u) , \quad (18)$$

where  $\epsilon$  is a relaxation parameter.

### 6.3 Geometry corrections

Utilizing thin-airfoil theory and consequently splitting the velocity defect in a symmetrical and an anti-symmetrical part, the determination of the geometric corrections is formulated as a least squares problem.

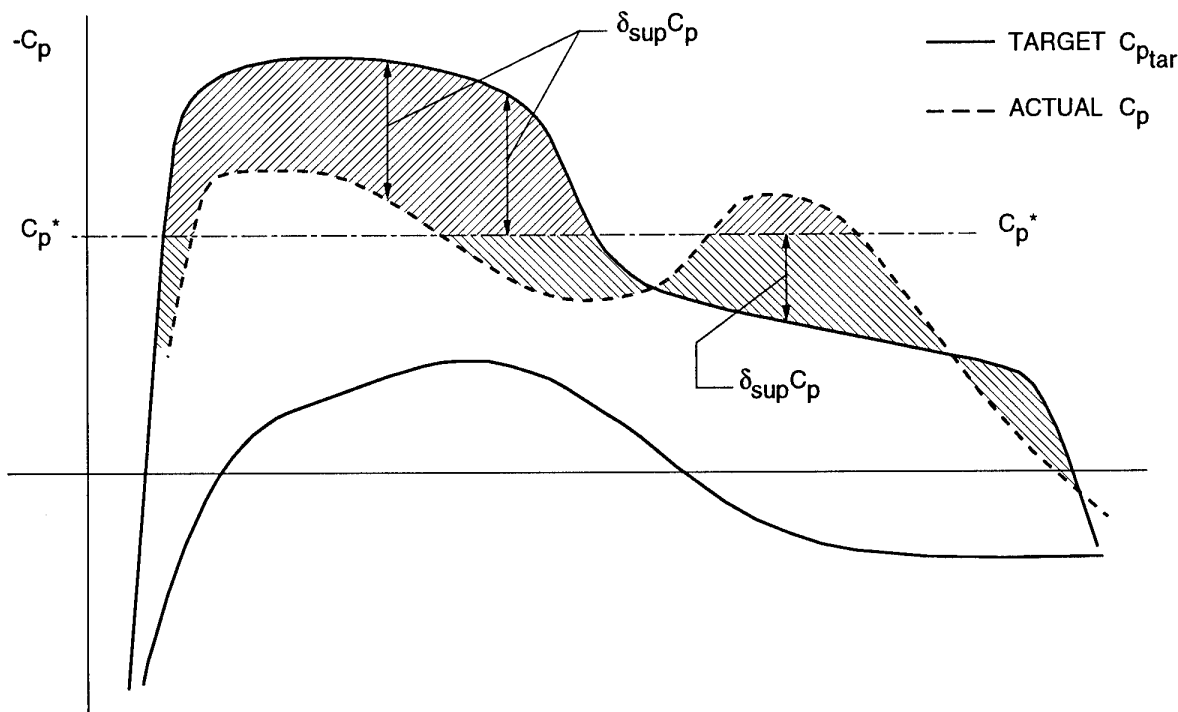


Fig.10 Pressure defect splitting (NLR method)

The solution to this problem is obtained by solving a system of linear algebraic equations for camber and thickness corrections, which are derived from the minimization of a functional of the form

$$\begin{aligned}
 Q(z_c, z_t) = & \\
 & w_u \sum (\text{equiv. vel. def. res.})_u^2 + \\
 & + w_l \sum (\text{equiv. vel. def. res.})_l^2 + \\
 & + \sum w_t (\text{thickness constr. res.})^2 + \\
 & + \sum w_c (\text{camber constr. res.})^2 \quad (19)
 \end{aligned}$$

Constraints on the geometry have been limited to the requirement that the airfoil thickness and/or the camber will approximately satisfy prescribed values. Weight factors are given by  $w$ ; the subscripts  $u, l, t, c$  refer to upper and lower side, to thickness and camber respectively.

### 6.4 Computational results

#### Test case 1.

The translation of the transonic design problem into an equivalent incompressible design problem raises the question of feasibility. The results obtained by running a reconstruction test case may demonstrate the feasibility. The NACA64A410 airfoil has been specified as initial geometry.

Both the inviscid and the viscous transonic pressure distributions were calculated for the Korn airfoil at zero angle of attack and Mach number 0.75. Hence, in fact two test cases were defined by prescribing each of these pressure distributions as a target for the design process with the NACA airfoil as a start.

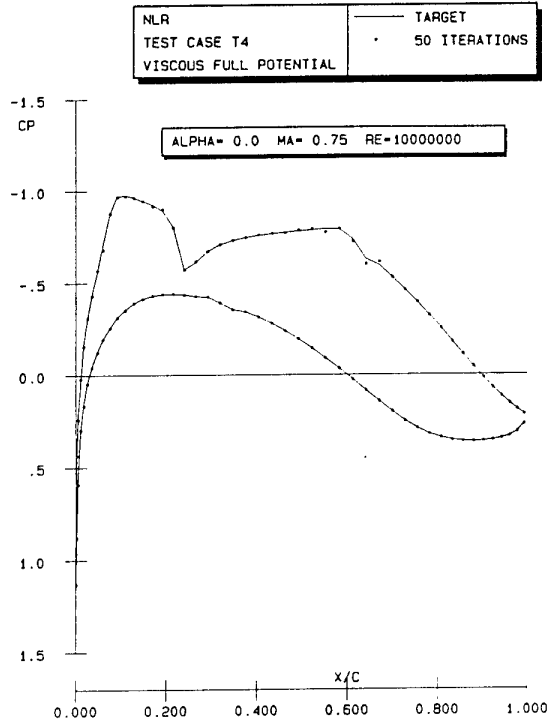
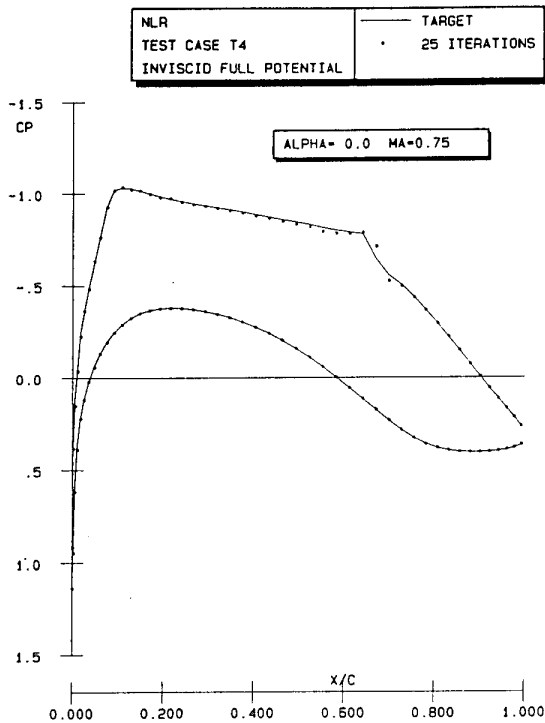


Fig.11 Reconstruction of Korn airfoil ; pressure distributions

In the inviscid case, application of the design method led to recovery of the Korn airfoil in about 25 iterations, each iteration involving one flow analysis calculation and one geometry update. For the viscous case about 50 iterations were needed for recovery of the Korn airfoil.

In Fig. 11 the pressure distributions on the reconstructed airfoils (inviscid and viscous) are compared with the target pressure distributions. The pressure distributions on the reconstructed airfoils deviate only slightly from the target, which reflects the almost complete recovery of the original airfoil. The convergence history of the process is presented in Fig. 12, where the value of the cost function defined by:

$$F = \oint (C_{pa} - C_{pt})^2 ds \quad (20)$$

and the value of the  $L_2$  norm defined by:

$$L_2(z) = \int_{\text{upper side}} (z_a - z_t)^2 dx + \int_{\text{lower side}} (z_a - z_t)^2 dx \quad (21)$$

are given as a function of the number of iterations. The integration is along the airfoil contour, subscript "a" refers to the actual and subscript "t" to the target pressure distribution or airfoil contour.

#### Test case 2.

This test case is a 3D wing design problem, which is used to demonstrate the applicability of the residual-correction approach.

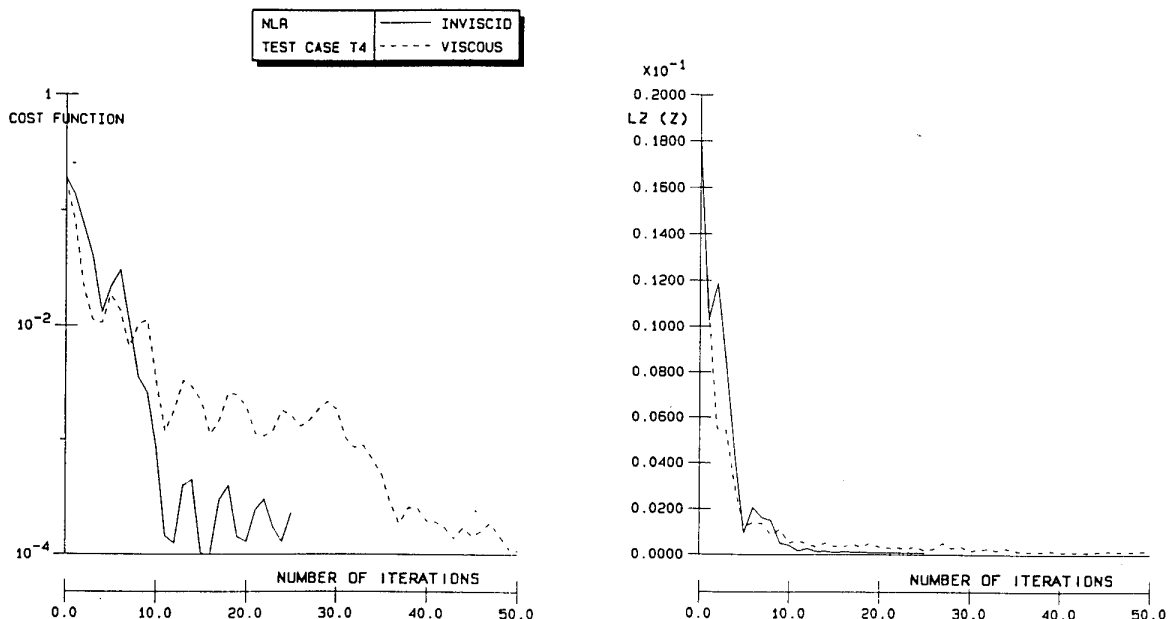


Fig. 12 Reconstruction of Korn airfoil ; convergence history

This design aims to improve the inviscid low speed high lift pressure distribution for a known wing-body configuration.

Starting point is the DLR-F4 wing-body configuration for which a target pressure distribution is specified in a number of chordwise wing sections. The target has been obtained by modifying a calculated pressure distribution, such that, at a certain lift coefficient, the supersonic pressure peaks were reduced to subsonic values, retaining approximately the original spanwise lift distribution.

This design problem requires modifications at the wing nose region mainly. It is known to represent a difficult case for the NLR approach, which relies on a linearized approximation of the inverse problem. The resulting wing geometry is shown for five computational sections in Fig.13 in comparison with the initial geometry. Comparison of the pressure distribution on the designed wing with the target pressure distribution at the same sections (see Fig.14) shows that it appears to be possible to design a wing geometry with the desired characteristics along almost the full span. Fig.15 shows the resulting isobars. The leading edge region shows acceptable reasonably smooth contours.

Fig.16 gives the values of the  $L_1$  and  $L_2$  norms for the differences between actual and target pressure distribution defined by:

$$L_1(C_p) = \frac{1}{N} \sum_{i=1}^N |C_{p_i}^i - C_{p_i}^i|$$

$$L_2(C_p) = \frac{1}{N} \sqrt{\sum_{i=1}^N (C_{p_i}^i - C_{p_i}^i)^2}$$
(22)

as a function of the number of iterations (analysis computations). These figures, showing a sizeable reduction of the norms in iteration 0 to 13, are

typical for straightforward application of the residual-correction approach starting with a given mate of the wing geometry. However, at that point of computation, the design process was continued with refined adjustments of the geometry and geometry constraints in order to improve geometry regularity (both chordwise and spanwise). This "fine tuning" requires a relatively large effort, but is quite effective in terms of geometry, and results in an improved approximation of the target pressure distribution. The obtained reduction of the norms is about 1 to 2 orders of magnitude.

## 7. CONCLUDING REMARKS

A survey has been given of strongly related inverse aerodynamic wing design methods. The main feature that the methods considered have in common is the fact that the flow field around a current estimate of the wing and the subsequent new estimate of the wing shape are determined in two separate computational steps. The basic principles of these methods have been discussed and some examples of application have been given. Some attention has been paid to the question of well-posedness of the design problem. In the case of 2D airfoil design plausible strategies to address this aspect have been indicated in the literature. Though successful applications for 3D wing design have been reported, an answer to the question of well-posedness of the 3D inverse wing design problem has yet not been found.

The majority of methods for inverse design of 3D wings seems to be of the residual-correction type. The main reasons for this include: the possibility to take full advantage of the existence and improvement of analysis methods, which are implemented as "black boxes", and the possibility to combine different analysis methods with the same correction procedure in order to solve the inverse problem for flows of different complexity.

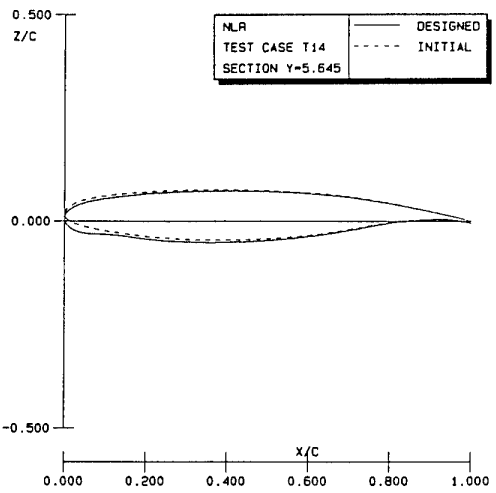
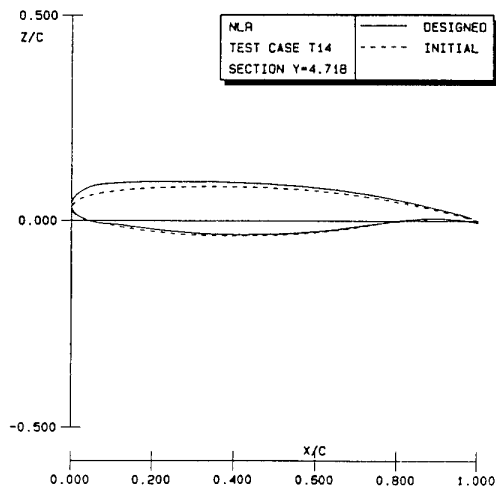
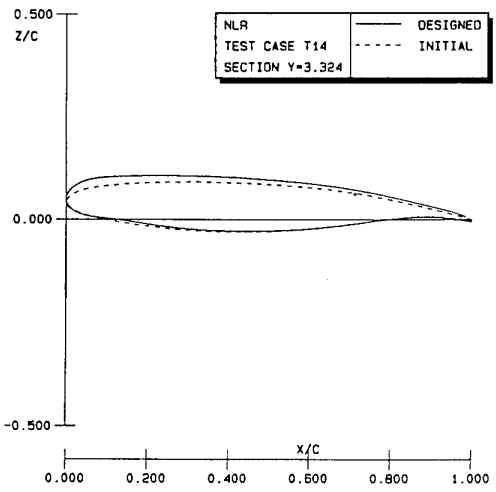
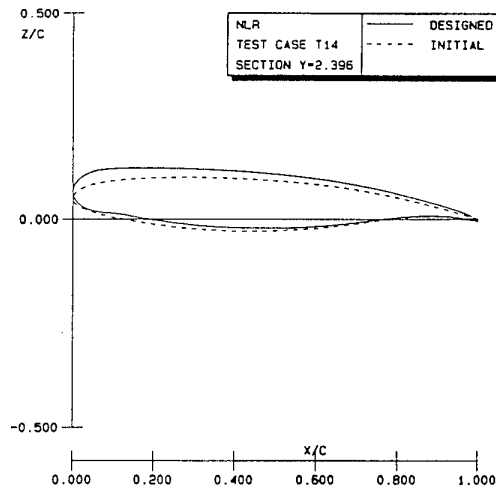
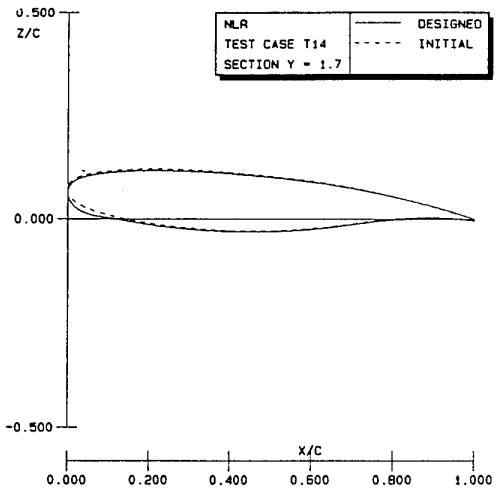


Fig.13 Wing design : initial and resulting geometry

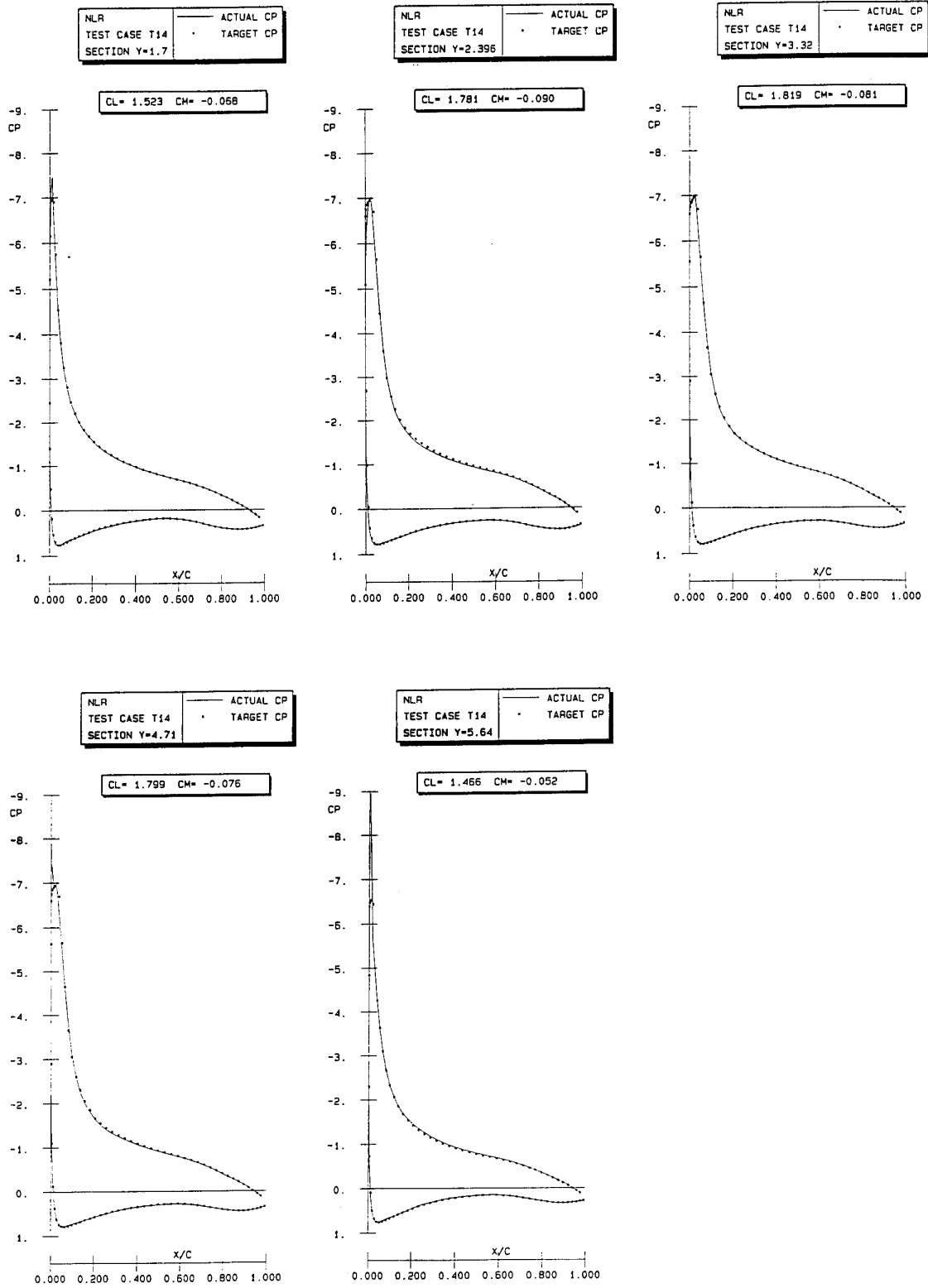


Fig.14 Wing design : chordwise pressure distributions

Also at NLR, these considerations have led to the development of residual-correction methods for 2D airfoil as well as 3D wing design.

For real practical applications there is a need for further development of the inverse methods, even in 2D, due to the lack of methods that take geometric constraints (apart from trailing edge thickness) into account.

In this respect the application of the variational approach seems to offer a perspective, especially for problems where the design requirements are formulated in terms of prescribed pressure distributions. The approach does not particularly lead to limitations in geometry representation and allows for the implementation of geometric and other constraints.

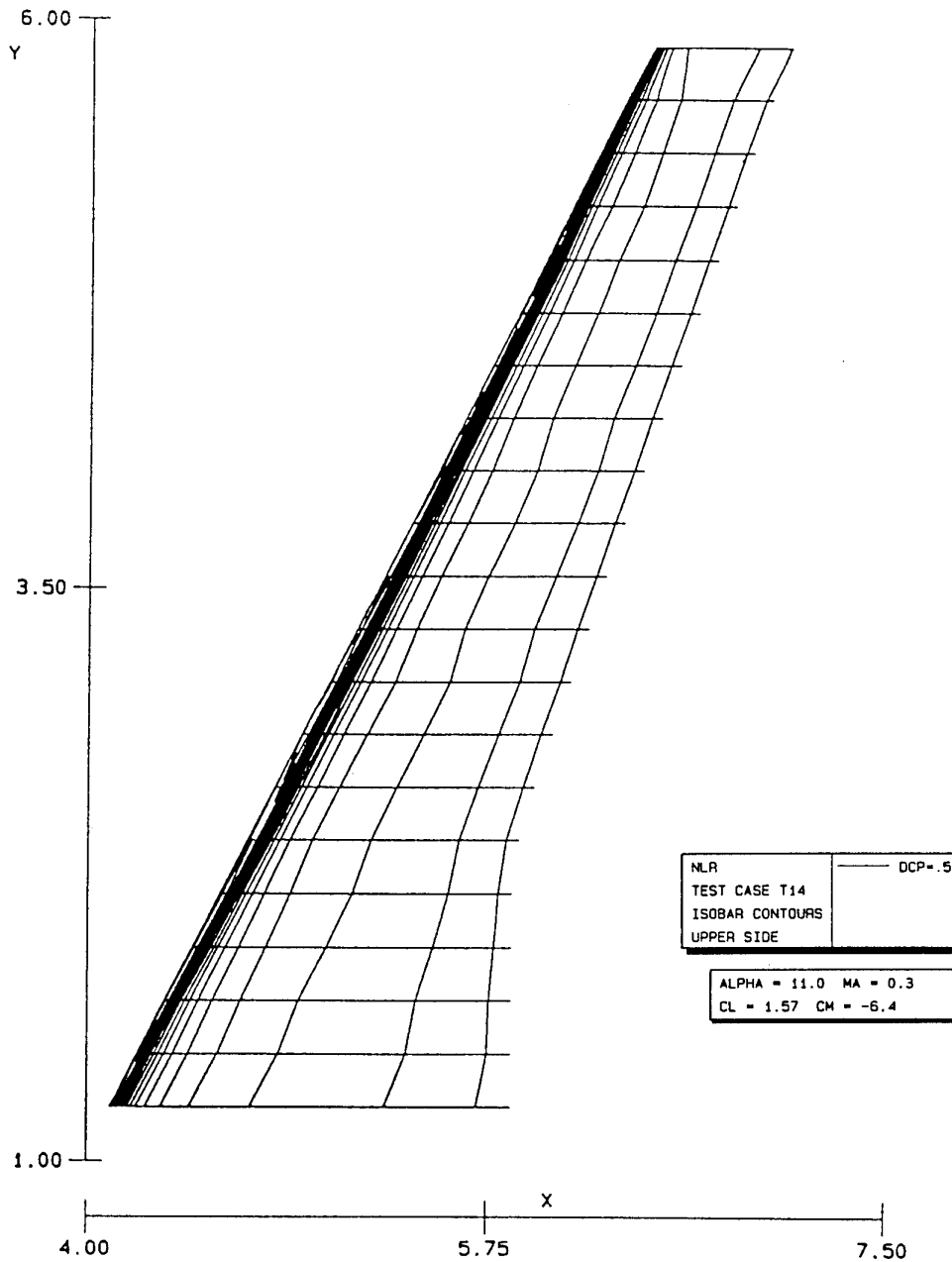


Fig.15 Wing design : isobar pattern

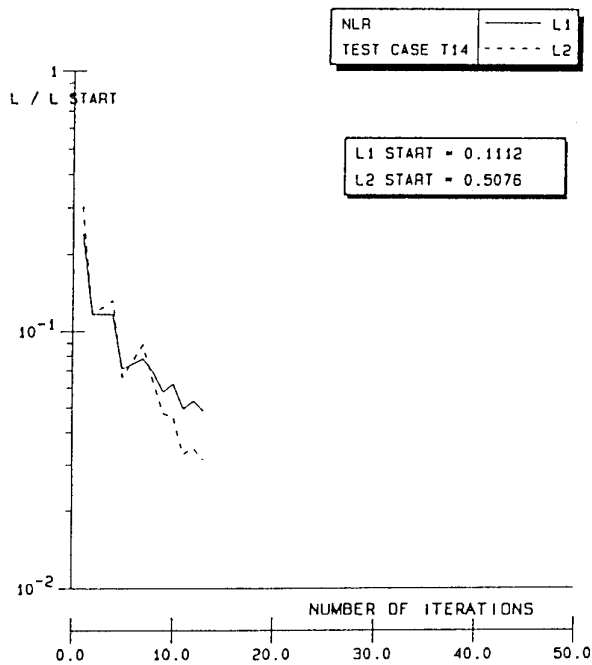


Fig.16 Wing design : convergence history of wing pressure distribution

## 8. REFERENCES

1. Betz, A. "Änderung eines Profils zur Erzielung einer vorgegebenen Änderung der Druckverteilung." Luftfahrtforschung, Vol.11, p.158-164 (1934)
2. Mangler, W. "Die Berechnung eines Tragflügelprofils mit vorgeschriebener Druckverteilung". Jahrbuch Deutsche Luftfahrtforsch., S I 46-I 53 (1938)
3. Pironneau, O. "Optimal shape design for elliptic systems". In Springer Series in Computational Physics Springer-Verlag (1983)
4. Jameson, A. "Aerodynamic design via control theory" NASA CR -181749 ICASE Report No.88-64 (1988)
5. Hicks, R.M. "Transonic wing design using potential-flow codes. Successes and failures". SAE TP 810565 (1981)
6. Lores, M.E. and Hinson, B.L. "Transonic design using computational aerodynamics". AIAA TP A82-35553 17-02 (1982)
7. Volpe, G. and Melnik, R.E. "The role of constraints in the inverse design problem for transonic airfoils". AIAA-81-1233 (1981)
8. Volpe, G. "Inverse design of airfoil contours: Constraints Numerical method and Applications". AGARD-CP No.463, Loen, Norway (1989)
9. Lighthill, M.J. "A new method of two-dimensional aerodynamic design". R & M 2112 (1945)
10. Woods, L.C. "Aerofoil design in two-dimensional subsonic compressible flow". R & M 2845 (1952)
11. Drela, M. "Two-dimensional transonic aerodynamic design and analysis using the Euler equations" GTL report no 187 (1986)
12. Soemarwoto, B.I. "Robust inverse shape design in aerodynamics". NLR TP 93432 L (1993)
13. Henne, P.A. "An inverse transonic wing design method". AIAA-80-0330 (1980)
14. Jameson, A. and Caughey, D. A. "Numerical calculation of the transonic flow past a swept wing". New York Univ. ERDA Rep. COO 3077-140 (1977)
15. Gally, T.A. and Carlson, L.A. "Inviscid transonic wing design using inverse methods in curvilinear coordinates". AIAA-87-2551 (1987)
16. Carlson, L.A. "Transonic airfoil design using cartesian coordinates". NASA CR-2578, (1976)
17. Jameson, A. and Caughey, D. A. "A finite volume method for transonic potential flow calculations".

- Proc.AIAA 3rd Comput. Fluid Dyn. Conf. Albuquerque, pp.35-54 (1977)  
(1993)
18. Fornasier, L. "An iterative procedure for the design of pressure-specified three-dimensional configurations at subsonic and supersonic speeds by means of a higher-order panel method" AGARD-CP No.463, Loen, Norway (1989)
19. Kubrynski, K. "Design of 3-dimensional complex airplane configurations with specified pressure distribution via optimization". Proc. 3rd Int. Conf. Inverse Des. Concepts and Optim. in Eng. Sci. ICIDES III (1991)
20. Barger, R.L. and Brooks, C.W. "A streamline curvature method for design of supercritical and subcritical airfoils" NASA TN D-7770 (1974)
21. Campbell, R.L. and Smith, L.A. "A hybrid algorithm for transonic airfoil and wing design" AIAA-87-2552 (1987)
22. Bell, R.A. and Cedar, R.D. "An inverse method for the aerodynamic design of three-dimensional aircraft engine nacelles" Proc. 3rd Int. Conf. Inverse Des. Concepts and Optim. in Eng. Sci. ICIDES III (1991)
23. Malone, J.B., Narramore, J.C. and Sankar, L.N. "An efficient airfoil design method using the Navier-Stokes equations". AGARD-CP No.463, Loen, Norway (1989)
24. Greff, E., Forbrich, D. and Schwarten, H. "Application of direct inverse analogy method (DIVA) and viscous design optimization techniques". Proc. 3rd Int. Conf. Inverse Des. Concepts and Optim. in Eng. Sci. ICIDES III (1991)
25. Takanashi, S. "An iterative procedure for three-dimensional transonic wing design by the integral equation method". AIAA-84-2155 (1984)
26. Fujii, K. and Takanashi, S. "Aerodynamic aircraft design methods and their notable applications - Survey of the activity in Japan -". Proc. 3rd Int. Conf. Inverse Des. Concepts and Optim. in Eng. Sci. ICIDES III (1991)
27. Hua, J. and Zhang, Z.Y. "Transonic wing design for transport aircraft". ICAS-90-3.7.4 (1990)
28. Zhu Ziqiang, Xia Zhixun and Wu Liyi "An inverse method with regularity condition for transonic airfoil design". Proc. 3rd Int. Conf. Inverse Des. Concepts and Optim. in Eng. Sci. ICIDES III (1991)
29. Fray, J.M.J and Slooff, J.W. "A constrained inverse method for the aerodynamic design of thick wings with given pressure distribution in subsonic flow" NLR MP 80017 U (1980)
30. Fray, J.M.J, Slooff, J.W., Boerstoeel, J.W. and Kassies, A. "Design of transonic airfoils with given pressure, subject to geometric constraints". NLR TR 84064 U (1984)
31. Brandsma, F.J. and Fray, J.M.J. "A system for transonic wing design with geometric constraints based on an inverse method" NLR TP 89179 L (1989)
32. Angrand, F. "Méthodes numériques pour des problèmes de conception optimale en aérodynamique" Thèse de 3ème cycle, Univ.Paris VI (1980)
33. Beux, F. and Dervieux, A. "Exact-gradient shape optimization of a 2D Euler flow. INRIA contribution to Brite/Euram project 1082. 12-month report part 1. (1991)
34. Beux, F. and Dervieux, A. "A hierarchical approach for shape optimization." INRIA contribution to Brite/Euram project 1082. 12-month report part 2. (1991)

35. Cabuk, H., Sung, C.-H. and Modi, V. "Adjoint operator approach to shape design for internal incompressible flows". Proc. 3rd Int. Conf. Inverse Des. Concepts and Optim. in Eng. Sci. ICIDES III (1991)

RESIDUAL-CORRECTION TYPE AND RELATED COMPUTATIONAL METHODS FOR AERODYNAMIC  
DESIGN

Part II : MULTI-POINT AIRFOIL DESIGN

Th.E.Labrujère

National Aerospace Laboratory Theoretical Aerodynamics Department  
A.Fokkerweg 2 1059 CM Amsterdam The Netherlands

**SUMMARY**

The present paper considers the problem of multi-point airfoil design, where the geometry of an airfoil is to be determined such that it will approximate simultaneously, at different design points, a priori specified aerodynamic requirements. Some attention is paid to approaches published in the open literature. The main part of the paper concerns work in progress at NLR. Some preliminary results are shown.

**LIST OF SYMBOLS**

$\alpha$	angle of attack	MAW	influence coefficient for a unit value of the co-state variable
$\Gamma$	inner boundary of flow domain	$M_\infty$	free stream Mach number
$\Gamma_T$	discontinuity line	$\vec{n}$	unit normal vector
$\Gamma_\infty$	outer boundary of flow domain	p	pressure
$\delta$	velocity or pressure defect	p1 } p2 } p3 }	parameters used for modification of target velocity distribution
$\delta z$	geometry or pressure	q	total velocity
$\lambda$	co-state variable	Q	least squares functional (see Eq.(26))
$\mu$	doublet strength	R	residual
$\mu_T$	doublet strength on slit $\Gamma_T$	s, t	arclength
$\xi$	independent coordinate	$\vec{t}$	unit tangent vector
$\sigma$	source strength	T	total arclength of airfoil contour
$\tau$	parameter used as independent variable for airfoil contour specification	u	disturbance velocity component in x direction
$\rho$	density	$V_n$	normal velocity
$\phi$	velocity potential	$V_t$	tangential velocity
$\Omega$	flow domain	w, W	weight factors
$c_d$	drag coefficient	W1, W2	weight on first and second target respectively
$c_l$	lift coefficient	x, z	Cartesian coordinates of airfoil contour
$C_p$	$= \frac{P - P_\infty}{0.5 \rho_\infty q_\infty^2}$ , pressure coefficient	$\vec{X}$	vector of design variables
F	functional associated with design problem (see Eq.(1))	subscripts	
L	augmented functional associated with variational approach (see Eq.(28))	c	refers to camber
MAD	aerodynamic influence coefficient for a doublet of unit strength	d	refers to doublet
MAS	aerodynamic influence coefficient for a source of unit strength	l	refers to airfoil lower side
		le	refers to airfoil leading edge
		s	refers to source
		t	refers to thickness
		tar	refers to target
		te	refers to airfoil trailing edge
		u	refers to airfoil upper side
		$\infty$	refers to free stream conditions
		superscripts	
		i	refers to operating condition
		-	refers to the inner side of the airfoil
		+	refers to the outer side of the airfoil

## 1. INTRODUCTION

Aircraft have to operate under a number of quite different conditions, which in general implies that for the aerodynamic design process different requirements will be formulated for different flow conditions.

Ideally, aerodynamic design aims at the fulfilment of all requirements. Mostly, this is attempted by initially optimizing the aerodynamic shape for the cruise condition, for instance with respect to lift, drag and pitching moment. Possible optimization with respect to requirements for other (off-design) operating conditions is then a matter of painful trial and error.

Nowadays, computational design algorithms are available from the literature which can help the designer to determine the shape of a wing such that it meets a priori specified requirements for one single flow condition. Surveys of these methods can be found in Refs.1-7.

The present paper discusses the problem of designing an airfoil such that it will meet, to the best possible extent, a priori specified requirements for a number of flow conditions. Solving this problem should lead to one single airfoil shape, optimized with respect to all specified requirements and satisfying a number of constraints on aerodynamic and geometric characteristics. Methods for solving this problem are only in the early stages of development. It is emphasized, that the present paper does not present a ready to hand method for the solution of the multi-point design problem, but rather tries to indicate key problems yet to be solved.

Most methods based on the direct numerical optimization approach, and originally developed for single-point design, are equally well applicable to the multi-point design problem. So, not surprisingly, up to now, most

applications to multi-point design use direct optimization (Refs.8-12). Some other applications show the use of inverse shape design methods (Refs.13-15). At NLR work is in progress to explore the possibilities to solve the multi-point design problem for subsonic/transonic flow, by applying the residual correction approach (Refs.16-18).

The paper discusses the formulation of the multi-point design problem. A global survey of the above mentioned approaches is given by reviewing some examples of application. A more detailed description of the NLR residual-correction approach is given and preliminary results are shown.

The approach applied at NLR is based on the assumption that it is possible to split the design process into two major steps, which can be iterated until satisfactory results have been obtained. In the first step, the flow about the current estimate of the geometry to be determined is calculated by means of an analysis code for the flow regime under consideration, thus giving the deviation from the specified target (the residual). In the second step, a geometry correction is calculated from the current residual by means of an approximative procedure involving the specification of an equivalent incompressible inverse flow problem which is more amenable to fast computational methods. When this approach is applied to multi-point design, the second step leads to the specification of an equivalent incompressible multi-point design problem.

The feasibility of the residual-correction approach for multi-point design, in particular the replacement of the actual problem by an equivalent incompressible multi-point design problem, is addressed by presenting results of a two-point reconstruction test case and results of a two-point viscous subsonic/transonic airfoil design problem. The latter example concerns the design of an airfoil

which combines favourable high speed and low speed performance. The design requirements are formulated by specifying a target pressure distribution for each of the two operating conditions, defined by angle of attack and free stream Mach number.

Preliminary results are shown of developments for obtaining a robust and fast geometry correction method, involving the solution of the equivalent incompressible multi-point design problem.

## 2. THE MULTI-POINT AIRFOIL DESIGN PROBLEM

### 2.1 Design requirements

The multi-point airfoil design problem involves the optimization of a single airfoil shape such that a priori specified requirements with respect to a number of operating (design) conditions will be met to the best possible extent. Thus, the design problem considered here can be defined as the minimization of an objective function of the form

$$F = \sum_{i=1}^n W^i F^i(\vec{X}), \quad (1)$$

where the summation is over the  $n$  operating conditions and the vector  $\vec{X}$  is the set of design variables. The function  $F^i$  will attain its minimum when the design requirements for the corresponding operating condition  $i$  are fulfilled. The  $W^i$  are weight factors that balance the requirements for the different operating conditions.

With respect to the specific form of the objective function, i.e. the formulation of the design requirements in terms of aerodynamic characteristics, the same type of discussion may take place as with single-point design. When considering direct numerical optimization for solving the present problem, an objective function is easily formulated in terms of global

aerodynamic characteristics. For instance, improvement of overall airfoil performance may be attempted by considering the minimization of

$$F = \sum_{i=1}^n W^i c_d[\alpha^i, M_\infty^i, \vec{X}], \quad (2)$$

possibly subject to constraints on e.g. lift- and moment coefficients and constraints due to geometric requirements.

Just like in single-point design, led by the wish to have more direct control over the load distribution and over e.g. boundary layer development, the designer may prefer specification of the design requirements in terms of target pressure distributions. In airfoil design for e.g. full potential flow this implies specification of target tangential velocity distributions, and thus the objective function may assume the form

$$F = \sum_{i=1}^n W^i \int_{\Gamma} [V_t^i(s) - V_{t_{tar}}^i(s)]^2 ds. \quad (3)$$

Here, the aerodynamic designer has the difficult task to specify each target pressure distribution as the balanced result of desired (sometimes conflicting) aerodynamic characteristics and of aerodynamic constraints that are better not violated.

The form (3) of the objective function is a necessity when considering the application of inverse shape design methods or residual-correction type methods.

### 2.2 Well-posedness

In contrast with the single-point inverse design problem, the multi-point design problem as stated above has never been investigated with respect to well-posedness, at least not to the present author's knowledge.

Moreover, assuming the existence of solutions to the multi-point design problem formulated in terms of global aerodynamic characteristics, as in

Eq.(2), it seems questionable whether the solution would be unique. For instance, given the fact that there may be designed many airfoils with the same value of the drag coefficient, it seems obvious that multi-point drag minimization might easily lead to more than one solution even if the same minimum value of the objective function is attained.

These doubts about the existence of unique solutions seem to be enforced by the investigations reported in Ref.10. Here, a procedure is described for transonic airfoil design based on wave drag minimization. This procedure is directed such that certain aerodynamic constraints are deliberately violated, at least initially, in order to speed up convergence. This is motivated by the observation that violated constraints have a large influence on the definition of the search direction for the optimization. Also, it is observed that the value of either term in the objective function does not necessarily decrease during minimization. It is concluded that constraints have to be formulated in addition to the objective function in order to obtain a more completely defined design problem.

The above considerations suggest that the multi-point design problem will be "more completely" defined, if the problem is formulated in terms of target velocity distributions for all operating conditions, like in Eq.(3). Moreover, when considering single-point design for any specified operating condition, the existence of a unique solution seems plausible (Ref.7) for target velocity distributions satisfying the consistency constraints, formulated by Betz (Ref.19) and Mangler (Ref.20). So, when the multi-point design problem is formulated with the aid of this type of targets, the problem seems, at least, to be better posed than when considering problems that have the form of Eq.(2).

In the case of single-point inverse shape design, the question of well-posedness has led to the introduction of auxiliary functions with free parameters, enabling modification of the target velocity distribution. During the solution of the design problem, these functions are determined such that the modified velocity distribution satisfies the Betz-Mangler constraints. In fact, the parameter values are obtained as part of the solution, and an airfoil shape is obtained that produces the modified target. The introduction of a set of such auxiliary functions with free parameters for each of the specified velocity distributions in the case of multi-point design is an obvious consequence of that approach.

### 2.3 Geometric constraints

In general, the role of geometric constraints in the multi-point design process is not different from the role in single-point design. Typically, they control the shape of the airfoil and must be satisfied irrespective of the operating conditions.

However, in some approaches to the multi-point design problem, especially those where purely inverse single-point design methods are extended, different parts of the geometry are used to satisfy different design requirements (Refs. 13-15). In such cases, particular geometric constraints are associated with particular operating conditions.

### 2.4 Design variables

With respect to direct numerical optimization, it is commonly acknowledged that this approach is feasible only if the number of design variables is small enough to keep the computing cost within limits. This is attained via a careful selection of shape functions and associated parameters for modification of the geometry. Of course, this will be even more true for multi-point optimization, because of the fact that each objective function evaluation

then involves the computation of a number of analysis problems instead of only one.

Most inverse shape design methods and residual-correction methods, based on completely different geometry correction procedures when compared with direct numerical optimization, do not lead to such a strong demand for limitation of the design variables. In most cases, airfoil contour coordinates or coefficients of some parametric representation of the contour are introduced as design variables. Extension to the multi-point design problem does not substantially change this situation.

### 3. SURVEY OF DEVELOPMENTS

Though little has been published so far on the development of multi-point design methods, a few examples of application, found in the literature, may be used to illustrate the usefulness of computational multi-point design. The methods presented in Refs.8-12 are based on direct numerical optimization involving minimization of objective functions formulated in terms of global aerodynamic characteristics. Refs.13-15 present inverse shape design methods adapted to multi-point design.

Renaux and Thibert (Ref.8) have shown that two-point design can be used effectively to improve the design of helicopter blade airfoils. They considered as objective function the sum of the drag coefficients for two design points corresponding to the advancing (low drag, high Mach number) and the retreating (high lift, low Mach number) blade conditions in forward flight. As initial geometry a single-point optimized airfoil OA213 was chosen and a new blade airfoil OA312 was designed. Fig.1 and 2 demonstrate the improvement obtained in comparison with the starting airfoil. Fig.1 shows that the new airfoil has lower drag under advancing-blade conditions. This will be due to the reduction of the average

velocity level, which has a favourable effect on the boundary layer development leading to a reduction of the viscous drag, and also the strengths of the shocks are reduced. As a consequence, there is also a decrease of the nose-down pitching moment coefficient.

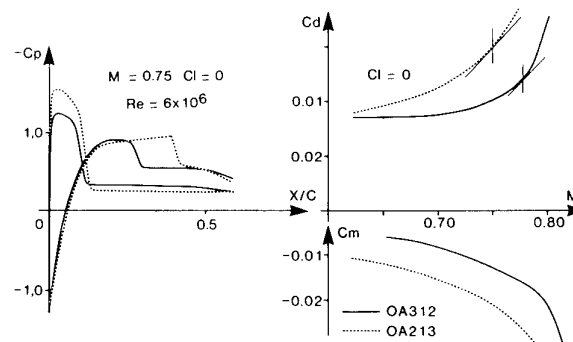


Fig.1 Measured aerodynamic characteristics of the OA213 and OA312 airfoils in advancing-blade conditions (Ref.8).

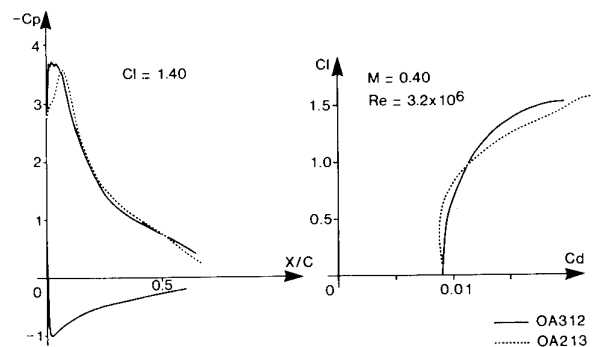


Fig.2 Measured aerodynamic characteristics of the OA213 and OA312 airfoils in retreating-blade conditions (Ref.8).

Fig. 2 shows that the new airfoil also has a lower drag under retreating-blade conditions at the high lift level. Furthermore, Fig.3 gives a comparison of airfoil shapes and total performance, showing that improvement of the performance at high speed has been obtained without loss of  $c_{lmax}$  at low Mach numbers.

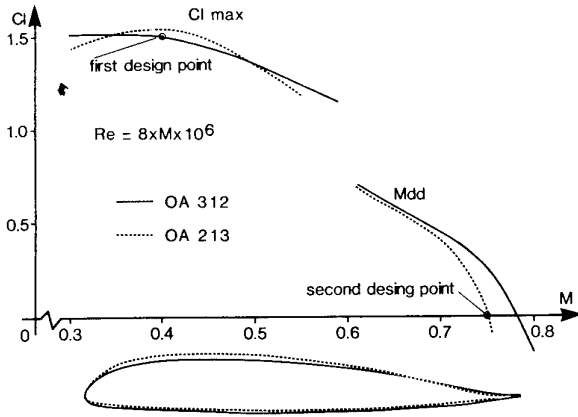


Fig. 3 Performances of OA213 and OA312 airfoils. Experimental data. (Ref. 8).

Another two-point design application aiming at drag reduction, is presented by Drela in Ref. 11. Here, the objective function is a weighted sum of the drag coefficients at two operating conditions with different lift coefficients but at the same Mach number ( $M_\infty=0.1$ ) and relatively low Reynolds number ( $Re=250,000$ ). The purpose of the computations was to improve an existing airfoil LA203A. The effectiveness of the two-point design is demonstrated by comparing the result with that of the single-point designs at each of the two operating conditions. Fig. 4 shows the calculated polars for the three airfoils thus obtained in comparison with that of the original airfoil. It appears that the single-point designed airfoils (at  $c_l=1.08$  and  $c_l=1.5$ ) have a considerably reduced drag coefficient at the design points. However, with the  $c_l=1.5$  optimized airfoil such a drag reduction is realized only at the design point, whereas with the  $c_l=1.08$  optimized airfoil the reduction in drag is paid for by a large negative effect on the high lift behaviour. The latter observation was the motive to place a larger weight on the drag coefficient at  $c_l=1.5$  than on the other drag coefficient in the objective function. The two-point optimization polar shows a far more attractive overall behaviour of the airfoil with a considerable overall reduction of the drag at the cost of a significant, but perhaps acceptable deterioration

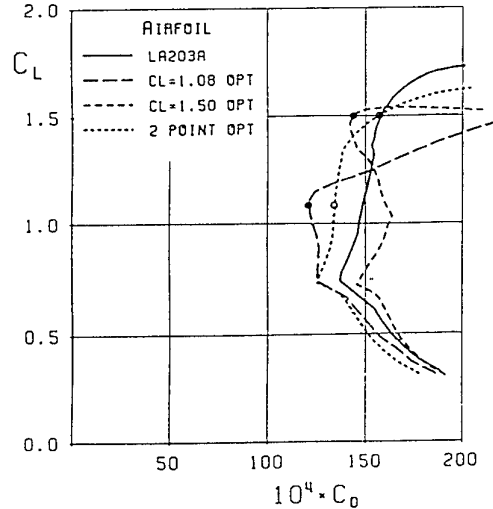


Fig. 4 Calculated polars for original LA203A, single-point, and two-point optimized airfoils. (Ref. 11)

of the high lift performance. Fig. 5 shows the new airfoil shapes in comparison with the original airfoil.

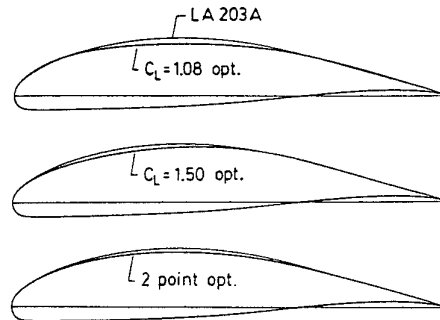


Fig. 5 Geometry comparison between optimized airfoils and original LA203A airfoil. (Ref. 11).

Close examination of the shapes learns that rather small changes in the geometry are responsible for the rather large differences in overall behaviour. It should be remarked, however, that this is typical for the low Reynolds number flows considered here. It could be expected that a similar design exercise for high Reynolds number flow should show far smaller discrepancies between the respective polars, especially in the lower drag region, implying a less explicit optimum than in the present example.

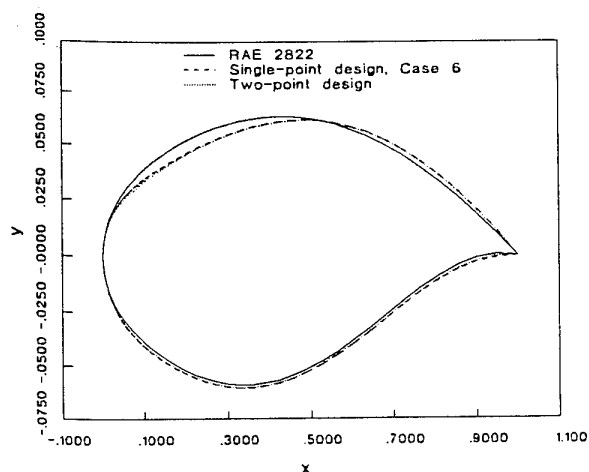
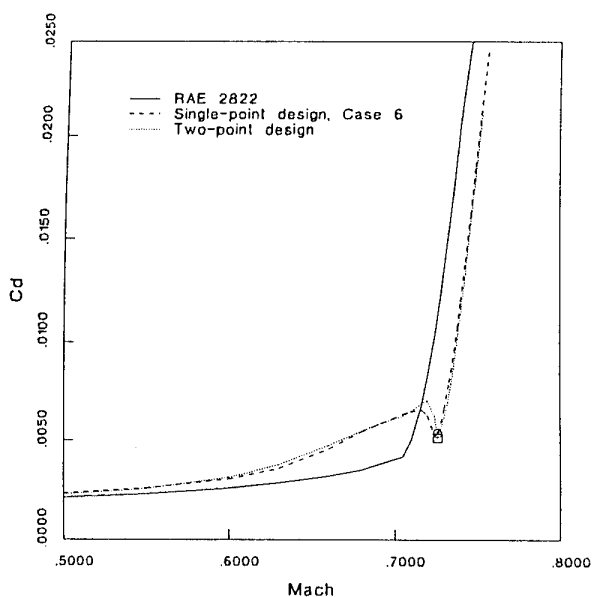


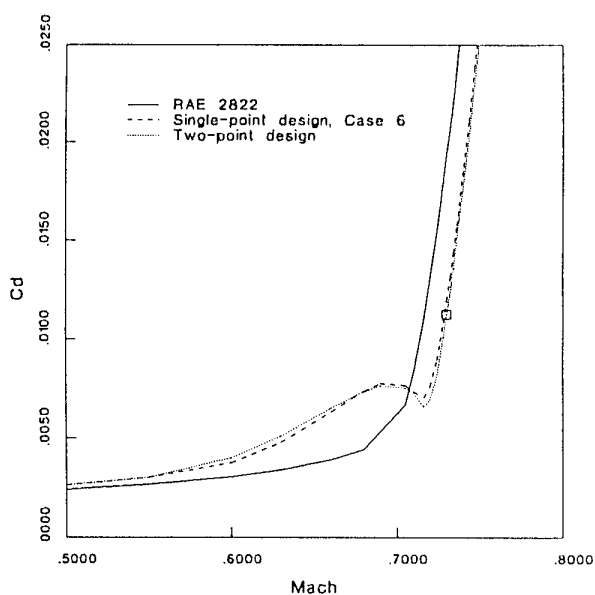
Fig.6 RAE 2822  $\alpha$ /Mach design, airfoil geometry comparisons. (Ref.12).

As a last example of numerical optimization, results presented in Ref.12 by Hager et al may be mentioned. These results have been obtained by two-point optimization for inviscid transonic flow, considering also a weighted sum of drag coefficients. In contrast with the previous examples the design points considered were rather close, viz.  $M_\infty=0.726$  at angle of attack  $\alpha=2.44^\circ$  and  $M_\infty=0.730$  at angle of attack  $\alpha=2.78^\circ$ . So, not surprisingly, the two-point optimization result closely resembles the result obtained with single-point optimization for the first operating condition. See Fig.6. As a consequence, also the  $c_d$ -Mach curves presented in Fig.7 show a close agreement between the single-point and the two-point optimized airfoils. The design goal of drag reduction in the operating region considered has been attained, apparently. This is paid for, however, by an increase of the drag in the lower Mach region up to about Mach=.7 and an unattractive behaviour of the drag rise curve from a flight dynamics point of view.

In the above described examples, the multi-point design problem has been formulated such that the resulting solution represents a compromise between, in general, conflicting requirements associated with different



a) Mach number evaluation,  $\alpha = 2.44^\circ$



b) Mach number evaluation,  $\alpha = 2.78^\circ$

Fig.7 RAE 2822  $\alpha$ /Mach design, drag rise curves for the angles of attack of the operating conditions considered. (Ref.12)

operating conditions. In some cases, however, in particular when designing airfoils for the low Reynolds number regime (e.g. for sailplane wings), the requirements for different operating conditions can be associated with

different parts of the geometry. In such cases it is possible, in principle, to satisfy the requirements to the same level of accuracy as in single point design for that particular part of the airfoil. Selig and Maughmer (Refs.13,14) have presented a method for multi-point inverse shape design based on conformal mapping. The method is based on the assumption that the airfoil contour can be divided into a number of segments, each of which should be designed such that a prescribed velocity distribution is generated on that particular segment at a certain angle of attack. If the thus specified targets satisfy the Betz-Mangler constraints it is possible to fulfil the different requirements exactly. In order to demonstrate the capabilities of the method an example of such a two-point airfoil design is presented in Ref.13. The resulting airfoil shape together with the velocity distributions for both design angles of attack is shown in Fig.8.

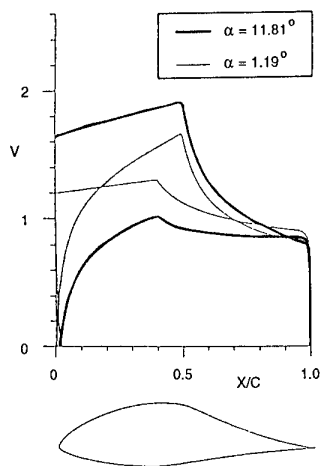


Fig.8 Airfoil and velocity distributions at  $\alpha=1.19^\circ$  and  $\alpha=11.81^\circ$ . (Ref.13).

The linear velocity distribution for  $\alpha=11.81^\circ$  on the upper surface has been prescribed along the upper surface forward part of the contour and the linear velocity distribution for  $\alpha=1.19^\circ$  on the lower surface has been prescribed along the lower surface forward part of the contour.

#### 4. NLR RESIDUAL-CORRECTION APPROACH

##### 4.1 Introduction

At NLR, the applicability of the residual-correction approach to multi-point subsonic/transonic design is investigated. In algorithms based on this approach, analysis calculations with a current estimate of the geometry are used to determine the subsonic/transonic residuals for each of the specified design conditions. According to the technique described in Part I (Ref.7), each of these residuals is subsequently used for the specification of an equivalent target velocity distribution for a corresponding incompressible design condition. In this way, an equivalent incompressible multi-point design problem is obtained, the solution of which leads to a correction of the geometry.

The success of the residual-correction approach highly depends on the flexibility of the correction procedure with respect to application of geometric constraints, its robustness with respect to large geometry modifications and the computing time needed for the solution of the equivalent incompressible design problem. Therefore, at NLR a few alternatives for the geometry correction procedure have been considered.

In the current NLR methods for single-point airfoil and wing design linearized thin airfoil theory is utilized to reduce the equivalent incompressible design problem, defined in the inner iteration loop as described in part I (Ref.7), to a linearized inverse flow problem. In that approach the flow disturbance, caused by the airfoil, is split into an anti-symmetric disturbance attributed to the camber of the airfoil and a symmetric disturbance attributed to the thickness of the airfoil. Reversely, by splitting a required disturbance velocity into an anti-symmetric and a symmetric part, corrections to camber and thickness

can be determined. This linearized inverse problem can be solved by means of a least squares approach utilizing a planar panel method with singularity distributions along the airfoil chord (Refs.21,22). The extension of this approach for the solution of a multi-point design problem has been considered. An apparent disadvantage of the thin airfoil linearization is that it deteriorates near the leading edge of the airfoil. Therefore, the least squares approach without this linearization is considered as an alternative. Furthermore, the application of the calculus of variations, involving the formulation of the design problem as a minimization problem, has been considered in particular with respect to its flexibility to handle geometric constraints. All three algorithms developed in this way are based on panel methodology for simulation of the incompressible flow around an airfoil.

With regard to the geometric shape of the airfoil it is assumed that the contour is a closed curve of which the coordinates are given by  $x$  and  $z$  (see Fig.9) as functions of a parameter  $\tau$ .

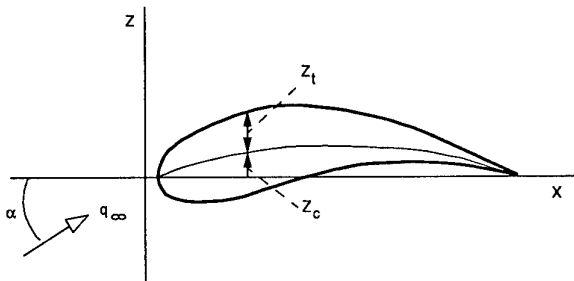


Fig.9 Airfoil axis system

The parameter  $\tau$  is chosen such that  $\tau=0$  denotes the trailing edge lower side and  $\tau=1$  denotes the trailing edge upper side, so that

$$x = x(\tau) \text{ with } x(0)=x(1)=1, \quad (4)$$

$$z = z(\tau) \text{ with } z(0)=z(1)=0.$$

Furthermore, the arclength, measured along the airfoil contour is given by  $t=t(\tau)$ , with

$$t(0) = 0,$$

$$t(\tau) = \int_0^\tau \frac{dt}{d\tau'} d\tau', \quad (5)$$

$$t(1) = T,$$

where

$$\frac{dt}{d\tau} = \sqrt{\left(\frac{dx}{d\tau}\right)^2 + \left(\frac{dz}{d\tau}\right)^2}. \quad (6)$$

By considering two points with the same  $x$ -coordinate on the upper and the lower side of the airfoil, camber and thickness can be defined as

$$z_c = \frac{1}{2}(z_u + z_l), \quad (7)$$

$$z_t = \frac{1}{2}(z_u - z_l).$$

#### 4.2 Geometry correction by means of a linearized panel method

As indicated in the previous section, the correction procedure in the current NLR residual-correction method for single-point airfoil design is based on (linearized) thin-airfoil theory. And consequently, the velocity defect is split in a symmetrical and an anti-symmetrical part. The determination of the geometric corrections is formulated as a least squares problem in terms of camber and thickness corrections.

Using the equivalent incompressible velocity distribution, symmetrical and anti-symmetrical perturbation velocities  $\delta u_t$  and  $\delta u_c$  are defined for each design condition.

According to thin airfoil theory there exists an integral relation between changes in thickness and symmetric perturbation velocities. This leads to the definition of the following residual

$$R_t^i(x) = \delta u_t^i(x) + \frac{1}{\pi} \int_{x_{1e}}^{x_{te}} \delta z_t(\xi) \frac{d\xi}{(x-\xi)^2} \quad (8)$$

A similar relation exists between changes in camber and anti-symmetric perturbation velocities. This leads to the definition of the residual

$$R_c^i(x) = \delta u_c(x) + \frac{1}{\pi} \int_{x_{1e}}^{x_{te}} \frac{d\delta z_c}{d\xi} \sqrt{\frac{x_{te}-x}{x-x_{1e}}} \sqrt{\frac{\xi-\xi_{1e}}{\xi_{te}-\xi}} \frac{d\xi}{(x-\xi)} \quad (9)$$

By setting  $R_t^i(x)=0$  the symmetric velocity defect  $\delta u_t$  is related to the required correction of the thickness distribution, and by setting  $R_c^i(x)=0$  the anti-symmetrical velocity defect  $\delta u_c$  is related to the required correction of the camber distribution.

Constraints on the geometry are limited to the requirement that the airfoil thickness and/or camber will approximately satisfy prescribed values. Accordingly, the camber and thickness corrections are determined such that the following functional is minimized,

$$\begin{aligned} F(z_t, z_c) = & \sum_i \left( \int_{x_{1e}}^{x_{te}} w_u^i(x) [R_t^i(x) + R_c^i(x)]^2 dx + \right. \\ & \left. + \int_{x_{1e}}^{x_{te}} w_l^i(x) [R_t^i(x) - R_c^i(x)]^2 dx \right) + \\ & + \sum_j w_{tj} [\delta z_t(x_j) - \delta z_t^t(x_j)]^2 + \\ & + \sum_k w_{ck} [\{\delta z_c(x_k) - \delta z_c(x_{i_k})\} + \\ & \quad - \{\delta z_c^t(x_k) - \delta z_c^t(x_{i_k})\}]^2 \end{aligned} \quad (10)$$

The first summation is over the different operating conditions, indicated by the superscript  $i$ . The second summation is over the points  $j$  where the value of the thickness is prescribed. The third summation over  $k$  concerns the pairs of points  $(k, i_k)$  where the camber is prescribed by means of the difference between the values in these points. The weight factors are given by  $w^i$ ; the subscripts  $u, l, t, c$  refer to upper and lower side, and to thickness and camber respectively.

Utilizing a planar panel method with constant singularity strengths on the panels, the above functional is discretized. By setting the derivatives with respect to the unknown parameters of the discretized functional thus obtained equal to zero, a linear system of algebraic equations is obtained. Its solution leads to corrections for the design variables thickness and camber. No attempt has been made to take the Betz/Mangler constraints into account. Undesirable geometric shapes are avoided by making use of the options for geometric constraints as described above.

#### 4.3 Computational results

##### Two-point reconstruction

The translation of the transonic multi-point design problem into a sequence of equivalent incompressible multi-point design problems raises the question of feasibility. In order to demonstrate the feasibility, a two-point reconstruction test case has been run. To this end, inviscid pressure distributions were calculated on the Korn airfoil for an angle of attack  $\alpha=0^\circ$  and Mach number  $M_\infty=0.75$ , and for an angle of attack  $\alpha=5^\circ$  and Mach number  $M_\infty=0.3$ . These pressure distributions were prescribed as targets for a two-point design problem with the NACA64A410 airfoil as starting geometry.

Application of the design method led to an almost complete recovery of the original Korn airfoil in 10 iterations

(see Fig.10), each iteration involving two flow analysis calculations and one geometry update.

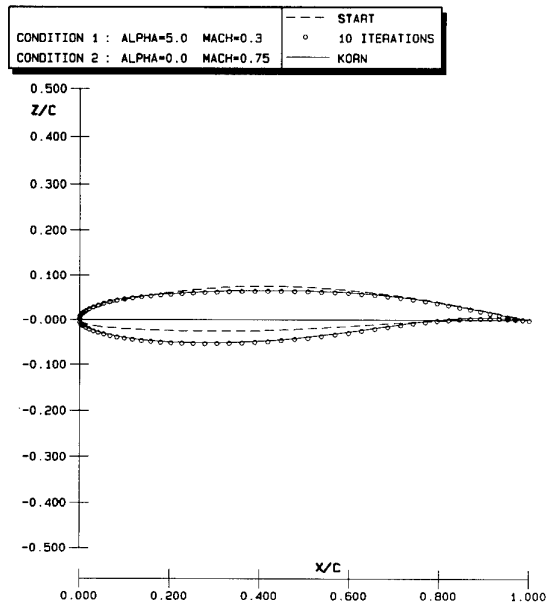


Fig.10 Two-point reconstruction of Korn airfoil ; geometry

In Figs.11a and 11b the pressure distributions on the reconstructed airfoil are compared with the target pressure distributions. The pressure distributions on the reconstructed airfoils deviate only slightly from the targets.

#### Two-point design

An example two-point design case has been run to investigate the possibility to determine the geometry of an airfoil such that it combines favourable characteristics at two different operating conditions. Similar design problems may be encountered e.g. at the design of a transport aircraft outer wing section (no flap, no slat) or at the design of a helicopter rotor blade section such as described in chapter 3 when discussing the results presented in Ref.8.

The present design problem was defined by prescribing two viscous target pressure distributions, one for Mach number  $M_\infty=0.2$  ( $Re=0.5 \cdot 10^7$ ) associated

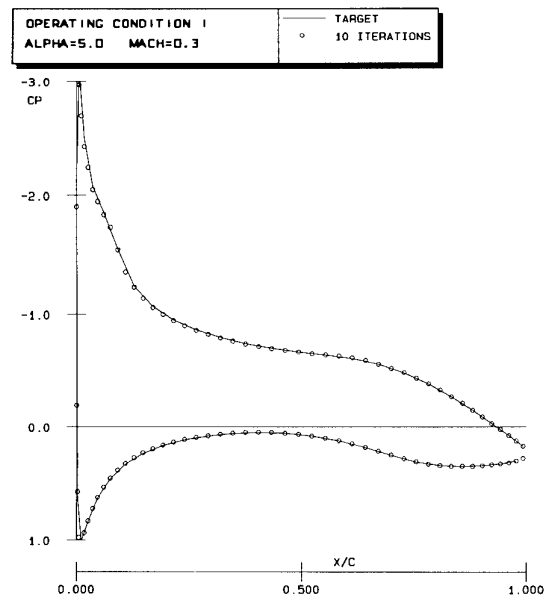


Fig.11a Two-point reconstruction of Korn airfoil; pressure distribution for operating condition 1.

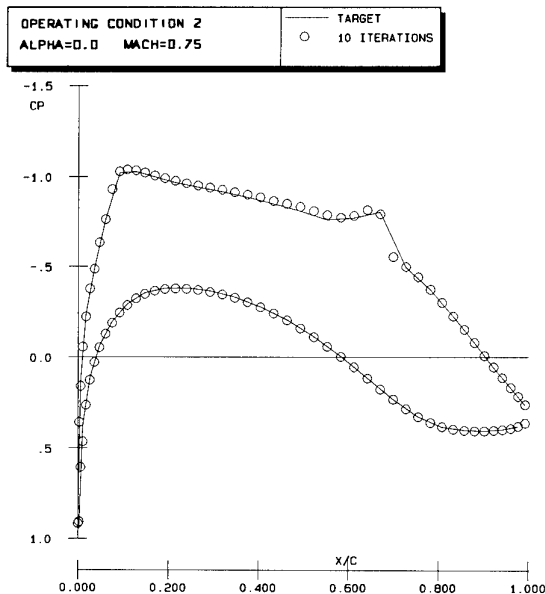


Fig.11b Two-point reconstruction of Korn airfoil; pressure distribution for operating condition 2.

with a high lift capacity, and another for Mach number  $M_\infty=0.77$  ( $Re=10^7$ ) chosen for its favourable high speed performance. Two weight factors were introduced to balance the requirements. Dealing with viscous target

pressure distributions presents no special problem if a viscous full-potential interaction code is used in the computational outer loop of the residual correction method.

The target pressure distributions have been obtained by means of a separate computational process (Ref.23) in which the pressure distributions themselves were optimized with respect to desirable aerodynamic characteristics (one for high lift, and one for low drag) without making an

a priori connection with the airfoil that should produce these pressure distributions. Such an a priori connection could be, for instance, that the two-point design problem was in fact a redesign problem, where the targets were expertly changed in some small detail with respect to the velocity distribution of the original airfoil. Therefore, it may be expected that the present two-point design will in general involve substantial discrepancies between targets and realized pressure distributions.

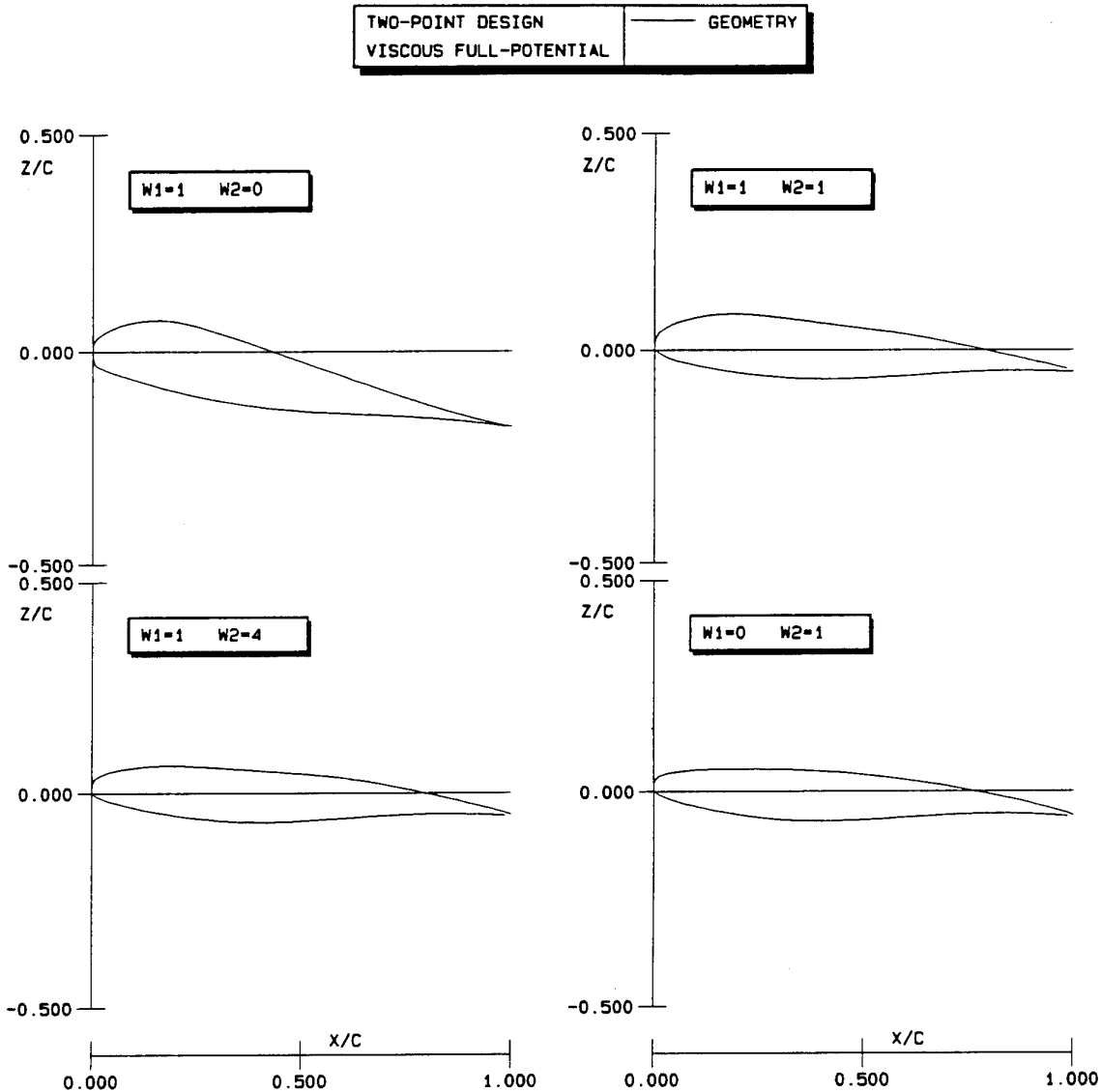


Fig.12 Two-point airfoil design with different weight factor combinations ; geometry

Calculations have been performed for four choices of the weight factors showing the transition of a high lift airfoil (weight factor  $W^2$  set equal to zero) into a high speed airfoil (weight factor  $W^1$  set equal to zero).

The NACA4412 airfoil has been used as starting geometry. Fig.12 shows the different airfoil shapes obtained in this way and Fig.13 shows the corresponding pressure distributions.

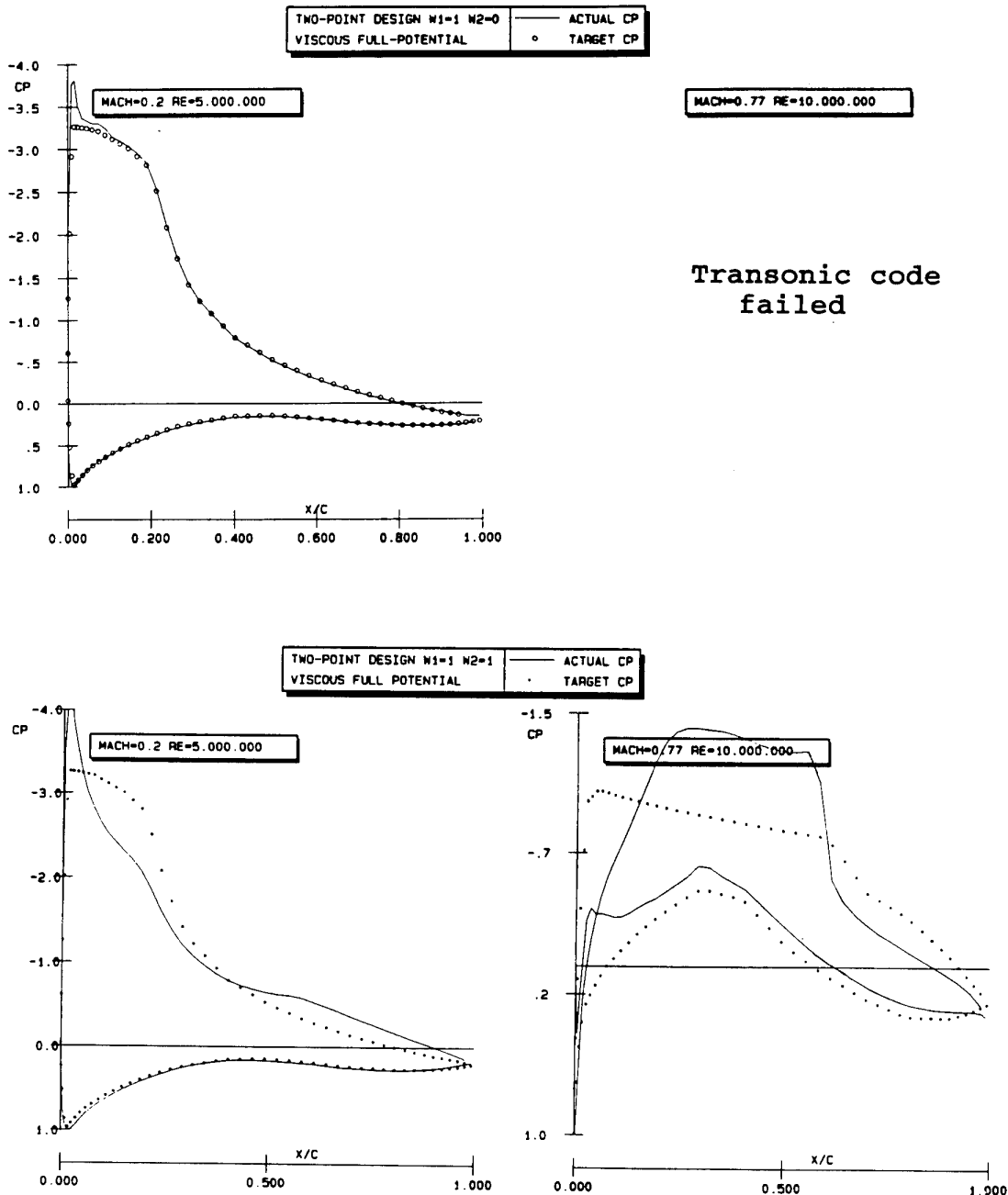


Fig.13 Two-point airfoil design with different weight factor combinations ; pressure distributions.

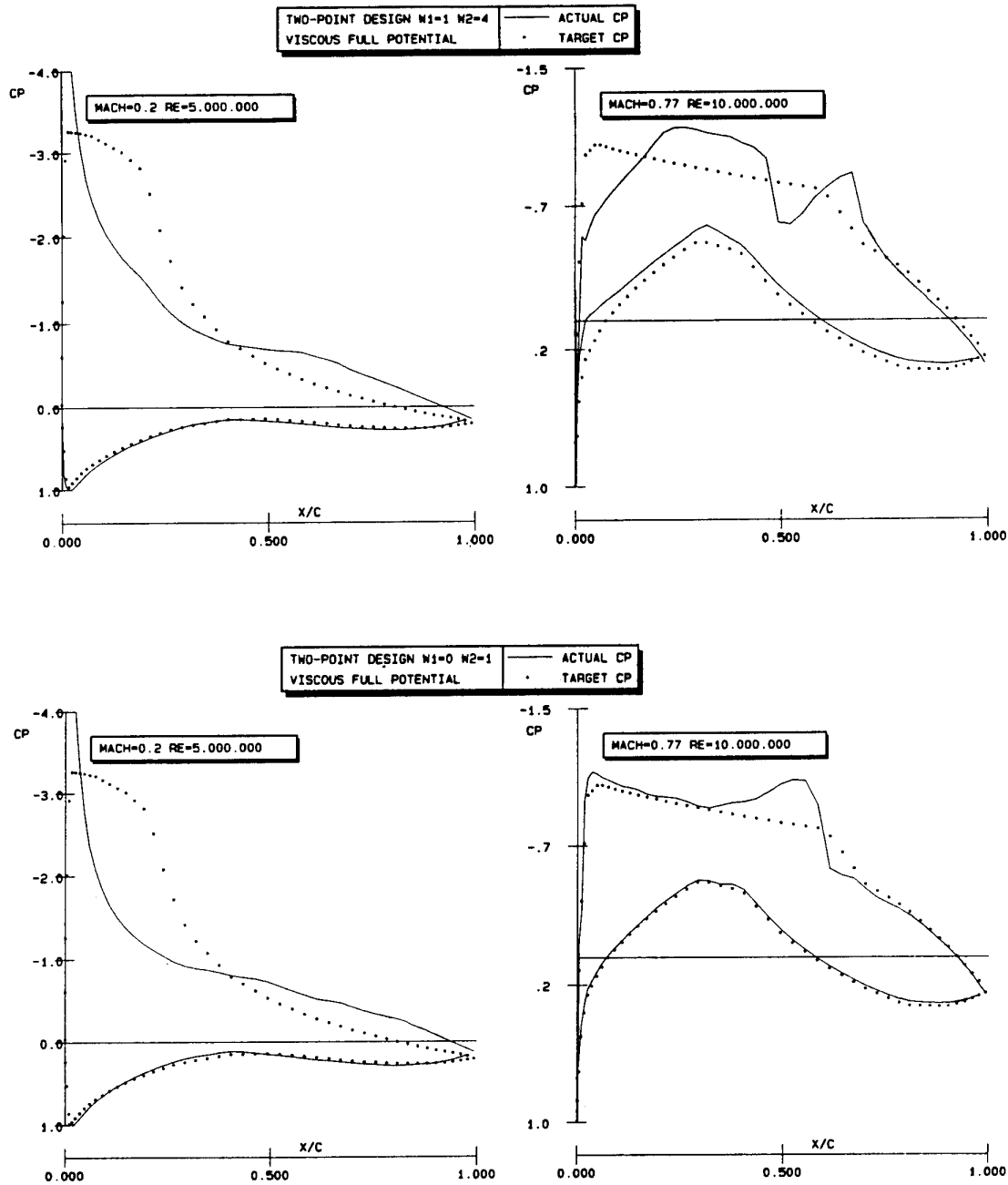


Fig.13 (contd) Two-point airfoil design with different weight factor combinations ; pressure distributions.

As such, the results demonstrate that the design process in itself works. However, it does indeed not directly lead to the determination of a new airfoil fulfilling the design requirements, as was already expected

above. The reason is that the present two-point design involves two completely incompatible targets, in the sense that there does not exist one single airfoil which will produce both specified pressure distributions at the specified operating conditions.

The question of how to deal with such incompatibility is one of the subjects of current investigations at NLR with respect to multi-point design.

But even for the single-point designs, there are discrepancies from the targets. There are two obvious reasons for this. Firstly, the geometry correction procedure, based on a linearized panel method, frequently gives rise to distortion of the leading edge airfoil shape, as illustrated in Fig.14. Usually, this leads eventually to a breakdown of the iteration process. The consequent discrepancies from the target are evident in the upper left result in Fig.13.

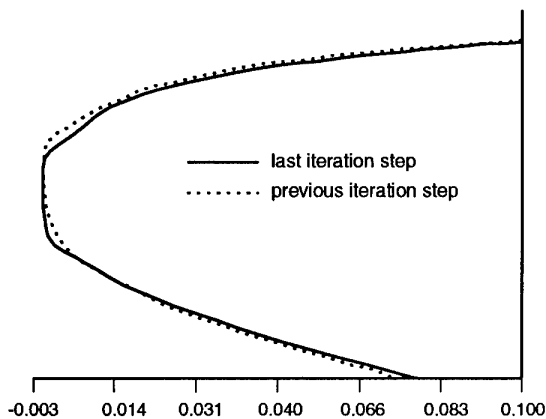


Fig. 14 Distorted airfoil shape leading to breakdown of iteration process.

Secondly, it will in general not be possible to specify a pressure distribution with a (weak) shock such that it is fully consistent with the shock-capturing properties implied by the analysis code. This is probably one of the causes of the discrepancies between target and realized pressure distribution appearing in the lower right result in Fig.13 (contd). But these discrepancies will also be due to the premature end of the iteration process caused by the limitations of the geometry correction procedure, as illustrated in Fig.14.

For the present example no attempts have been made to overcome the problems discussed above. The results presented, were considered satisfactory for the present demonstration.

#### 4.4 Conclusion

With the computational results presented above it has been shown that the NLR residual-correction method with its replacement of the actual design problem by an equivalent incompressible design problem, is a feasible approach to the multi-point design problem. Application to the reconstruction test case indeed led to an almost complete recovery of the target geometry, and application to the design problem resulted in an apparent compromise between two incompatible requirements. The shortcomings of the present method are to be found in the correction procedure, especially at the airfoil leading edge.

A major difficulty with the present formulation of the multi-point design problem has been indicated, viz. the question of how to deal with incompatibility in the design goals. The two-point design example presented here illustrates this problem very clearly. On the other hand it may be expected that in practice, multi-point design will indeed appear in the form of a redesign problem, where the targets will be specified by expertly modifying existing velocity distributions for a number of operating conditions. The incompatibility will then possibly be not so extreme.

As is remarked above, the feasibility of translating the actual design problem into an equivalent incompressible flow problem has been demonstrated. Therefore, the remainder of the present paper will focus on attempts to improve the solution of the equivalent multi-point design problem.

## 5. NON-LINEARIZED APPROACHES TO THE EQUIVALENT INCOMPRESSIBLE MULTI-POINT DESIGN PROBLEM

### 5.1 Redefinition of the problem

The equivalent incompressible multi-point design problem is defined such that for each design condition  $i$  a desired velocity distribution is specified as a function of the fractional arclength

$$\bar{t} = \frac{t}{T}. \quad (11)$$

The requirements according to the Betz-Mangler constraints, associated with trailing edge closure and compatibility of target velocity and free stream velocity, are addressed by introducing a certain amount of freedom in the target velocity distributions. To this end, the specified target velocity distribution is augmented with auxiliary functions, containing three parameters which may be utilized to modify the target, simultaneously with solving the design problem such that the Betz-Mangler constraints will be fulfilled. Such a set of three parameters is associated with each operating condition and their values will be determined as part of the solution.

Thus, following Ref.24, the target velocity is considered to have the form

$$V_{tar}^i = g^i[\bar{t}, p_1^i, p_2^i, p_3^i]. \quad (12)$$

Here,  $p_1^i$  scales the tangential velocity level such that compatibility of the target velocity and the free stream velocity is established. As has been remarked in part I of the present paper (Ref.7), the forward stagnation point location can be used as a second degree of freedom in the target. One of the auxiliary functions chosen in Ref.24 achieves a coordinate transformation correlating the stagnation point location with the parameter  $p_3^i$ . A third degree of freedom (with a parameter  $p_2^i$ ) is used to adjust the velocity level near the

trailing edge for compliance with trailing edge closure (or a prescribed trailing edge thickness). If the target is specified such that all consistency constraints are implicitly fulfilled, the parameters assume the values  $p_1^i=1$ ,  $p_2^i=0$ , and  $p_3^i=0$ ; and the original target is not modified.

Both alternative algorithms considered here for solving the present equivalent incompressible multi-point design problem are based on application of a first order panel method for the determination of the flow around an airfoil, utilizing piecewise constant doublet and source distributions on the airfoil contour. A description of this method is given in appendix A.

According to this flow simulation, the total velocity potential is determined by

$$\phi^i = \phi_\infty^i + \phi_d^i + \phi_s^i \quad (13)$$

where the velocity potential of the undisturbed flow  $\phi_\infty^i$  is given by

$$\phi_\infty^i = \vec{q}_\infty^i \cdot \vec{x}, \quad (14)$$

with

$$\vec{q}_\infty^i = \begin{bmatrix} \cos(\alpha^i) \\ \sin(\alpha^i) \end{bmatrix}, \quad (15)$$

and where the magnitude of the onset flow velocity has been set equal to one.

The velocity potential due to the doublet distribution  $\phi_d^i$  is determined by

$$\phi_d^i = \frac{-1}{2\pi} \int_0^T \mu^i(s) \frac{\partial}{\partial s} \left[ \tan^{-1} \frac{z(t)-z(s)}{x(t)-x(s)} \right] ds + \mu_T^i \tan^{-1} \frac{z-z_{te}}{x-x_{te}}, \quad (16)$$

and the velocity potential due to the source distribution is determined by

$$\phi_s^i = \frac{1}{2\pi} \int_0^T \sigma^i(s) \ln[(x(t)-x(s))^2 + (z(t)-z(s))^2]^{1/2} ds. \quad (17)$$

Applying the panel method, the design problem may be defined as the minimization of the functional

$$F = \sum_i W^i F^i, \quad (18)$$

with

$$F^i = \int_0^1 (V_t^i - V_{tar}^i)^2 d\tau \quad (19)$$

$$= \int_0^1 \left( \frac{\partial \phi^i}{\partial t} - V_{tar}^i \right)^2 d\tau,$$

under the condition

$$\phi_d^i + \phi_s^i = 0, \quad (20)$$

which is equivalent to the Neumann condition of zero normal velocity on the airfoil contour, and the condition

$$\mu_T^i = \mu^i(1) - \mu^i(0), \quad (21)$$

which takes account of the Kutta condition at the trailing edge.

A discretized form of Eq.(13) is obtained by evaluating the integrand at the midpoints of the panels and taking it constant along the panels. Solution of the design problem then involves the minimization of the discretized functional

$$F = \sum_i W^i F^i = \sum_i \left[ W^i \sum_{k=2}^{k=N} \left( \frac{\partial \phi^i}{\partial t} - V_{tar}^i \right)_k^2 \Delta \tau_k \right], \quad (22)$$

under the conditions

$$[\phi_d^i + \phi_s^i]_k = 0, \quad (23)$$

for  $k=2(1)N$ , and

$$\mu_T^i = \mu_N^i - \mu_2^i. \quad (24)$$

Here, the indices  $k$  refer to the panel midpoints;  $k=2$  denotes the first midpoint near the trailing edge on the airfoil lower side,  $k=N$  denotes the last midpoint near the trailing edge on the airfoil upper side.

Considering the minimization of the functional, obvious design variables are the angles of attack  $\alpha^i$  and the velocity parameters  $p_k^i$ . With respect to the representation of the airfoil contour,  $x$  as well as  $z$  may be considered as unknown functions, that are to be determined during the design process. Above, it has been assumed that the velocity distribution is specified as a function of the fractional arclength. The prescribed velocity will be attained on the airfoil contour at given values of the arclength. So, because of the fact that the contour coordinates  $x$  and  $z$  are connected through the arclength, only one of these functions is actually required as design variable. However, it has appeared that a greater flexibility for modification of the airfoil contour is obtained when both  $x$  and  $z$  are considered as design variables while prescribing the arclength. Thus, the functional will be minimized with respect to the design variables  $\alpha^i$ ,  $x$ ,  $z$  and the parameters  $p_k^i$ .

## 5.2 Least squares approach

The design problem as formulated in the previous section may be solved in the least squares sense by considering the minimization of the augmented functional

$$Q = F + H = \sum_i [W^i F^i + H^i] = \sum_i \left[ W^i \int_0^1 \left( \frac{\partial \phi^i}{\partial t} - V_{tar}^i \right)^2 d\tau + \int_0^1 \left( (\phi_d^i + \phi_s^i)^2 \right) d\tau \right]. \quad (25)$$

This functional will attain its minimum (zero) when the design requirements for all operating conditions are fulfilled (the first term then vanishes) and when for all operating conditions the Neumann condition of zero normal velocity on the airfoil contour is satisfied (the second term then vanishes).

During the investigations based on this approach to the solution of the design problem it appeared to be necessary to have some control over the values of the parameters  $p_k^i$ . Furthermore, the designer obviously wishes to keep the deviations from his specified targets as small as possible. Therefore, the functional (25) is augmented further (in discretized form) to

$$Q = \sum_i [W^i \sum_{k=2}^{k=N} (\frac{\partial \phi^i}{\partial \tau} - V_{tar}^i)_k^2 \Delta \tau_k + \sum_{k=2}^{k=N} ((\phi_d^i + \phi_s^i)_k^-)^2 \Delta \tau_k + W_p^i [(p_1^i - 1)^2 + p_2^i{}^2 + p_3^i{}^2]]. \quad (26)$$

The weight factor in the last term enables the designer to control the deviation of the free parameters from their ideal values (1,0,0) if no modification is needed to satisfy the Betz-Mangler constraints.

The functional  $Q$  has essentially the form

$$Q = \sum_{n=1}^N [f_n(\vec{z})]^2, \quad (27)$$

where  $\vec{z}$  is the vector of design variables  $\alpha^i, x_j, z_j, \mu_m^i$  and  $p_k^i$ , and where the  $f_n$  form together a vector  $\vec{f}$ . This type of minimization problem can efficiently be solved by means of the method described in Ref.25. The computational algorithm proceeds as follows :

1. Given  $\vec{z} = \vec{z}^{(i)}$ , compute the vector of residuals  $\vec{f}^{(i)}$  and the Jacobian  $J^{(i)}$ ; the Jacobian is derived by

differentiating the residuals  $f_n$  with respect to the design variables.

2. Determine the search direction by computing  $\vec{s}^{(i)} = -J^{(i)+} \vec{f}^{(i)}$ , where  $J^{(i)+}$  is the generalized inverse of  $J^{(i)}$ .
3. Set  $\vec{z}^{(i+1)} = \vec{z}^{(i)} + \lambda \vec{s}^{(i)}$ , and determine  $\lambda > 0$  such that  $Q[\vec{z}^{(i+1)}] < Q[\vec{z}^{(i)}]$ .
4. If preset conditions with respect to the variation of  $\vec{z}$ , or with respect to the residuals  $f_n$ , are fulfilled, convergence is considered to be attained; then terminate the iteration process, otherwise repeat from 1.

### 5.3 Variational approach

As an alternative to the least squares approach for solving the equivalent incompressible multi-point design problem as defined in section 5.1 the variational approach may be considered. To that end consider the augmented functional

$$\begin{aligned} L &= F + G = \\ &= \sum_i [W^i F^i + G^i] = \\ &= \sum_i [W^i \int_0^1 \{ \frac{\partial \phi^i}{\partial \tau} - V_{tar}^i \}^2 d\tau + \\ &\quad + \int_0^1 \lambda^i(\tau) (\phi_d^i + \phi_s^i)^- d\tau], \end{aligned} \quad (28)$$

where  $\lambda^i(\tau)$  is a differentiable function. By minimizing the functional  $L$  with respect to the functions  $x(\tau), z(\tau), \lambda^i(\tau)$  and  $\mu^i(\tau)$ , and the parameters  $p_1^i, p_2^i, p_3^i$  and  $\alpha^i$ , the solution of the multi-point design problem will be obtained. To that end, the variation of  $L$  is considered.

Variation of the functional with respect to  $\lambda^i$  leads to the observation that

$$\begin{aligned} \delta L_\lambda &= \sum_i \delta G_\lambda^i = \\ &= \sum_i \int_0^1 \delta \lambda^i(\tau) (\phi_d^i + \phi_s^i)^- d\tau \end{aligned} \quad (29)$$

will be identically zero if  $\mu^i$  is varied within the class of functions

satisfying Eqs.(20) and (21), i.e. potential flow with zero normal velocity at the airfoil contour and satisfying the Kutta condition.

Similarly, it may be observed that the variation of L with respect to  $\mu^i$  will vanish identically if the co-state variable  $\lambda^i$  is varied within the class of solutions of the adjoint state equations

$$\begin{aligned} & \frac{1}{2}\lambda^i(\tau) + \\ & - \frac{1}{2\pi} \int_0^1 \lambda^i(\tau') \frac{\partial}{\partial \tau} \left\{ \tan^{-1} \frac{z(\tau) - z(\tau')}{x(\tau) - x(\tau')} \right\} d\tau' + \\ & + 2W^i \frac{d}{d\tau} \left[ \frac{\frac{\partial \phi^i}{\partial \tau} - V_{tar}^i}{\frac{dt}{d\tau}} \right] = 0, \end{aligned} \quad (30)$$

Just like in the previous section a discretized form of the functional is obtained,

$$\begin{aligned} L &= \sum_i [W^i F^i + G^i] = \\ &= \sum_i [W^i \sum_{k=2}^{k=N} (\frac{\partial \phi^i}{\partial \tau} - V_{tar}^i)^2 \Delta \tau_k + \\ & \quad \sum_{k=2}^{k=N} \lambda_k^i (\phi_d^i + \phi_s^i)_k \Delta \tau_k]. \end{aligned} \quad (32)$$

Here, the adjoint state variable  $\lambda$  is assumed to be piecewise constant on each panel. Then, the computational procedure for calculating the design variables  $\alpha^i$ ,  $\mu_j^i$ ,  $\lambda_k^i$ ,  $x_j$ ,  $z_j$  and  $p_k^i$  proceeds as follows :

1. Solve the analysis problem for each design condition for an estimate of the airfoil shape. Application of the panel method, described in appendix A, involves the solution of a system of algebraic equations of the form

$$\begin{aligned} & [\phi_d^i + \phi_s^i]_k^- = \\ & = \sum_{j=1}^{j=N} MAD_{k,j} \mu_j^i + \sum_{j=1}^{j=N-1} MAS_{k,j+1} \sigma_{j+1}^i = 0, \end{aligned} \quad (33)$$

for  $k=2(1)N$ , and

$$\mu_1^i = \mu_N^i - \mu_2^i. \quad (34)$$

By solving this system of linear equations, the doublet strength is determined. Then the velocity distribution along the airfoil contour is calculated by means of a finite difference approximation of

$$V_t^i = \frac{\partial \phi^i}{\partial t} = - \frac{d\mu^i}{dt} + \frac{\partial \phi_\infty^i}{\partial t}. \quad (35)$$

2. For each operating condition, solve the adjoint problem which in its continuous formulation is defined by Eqs.(26) and (27). Its discrete form, associated with Eqs(29) and (30) is given by

$$\begin{aligned} & \sum_{k=2}^{k=N} MAW_{m,k} \lambda_k^i \Delta \tau_k + \\ & + 2W^i \sum_{k=2}^{k=N} (V_{tk}^i - V_{tar,k}^i) \frac{\partial V_{tk}^i}{\partial \mu_m^i} \Delta \tau_k = 0, \end{aligned} \quad (36)$$

for  $m=2(1)N$ , where

$$MAW_{2,k} = MAD_{k,2} - MAD_{k,1},$$

$$MAW_{m,k} = MAD_{k,m}, \quad \text{for } m=3(1)N-1, \quad (37)$$

$$MAW_{N,k} = MAD_{k,N} + MAD_{k,1}.$$

Here, the right hand side is calculated from the current velocity distribution determined in step 1. From this system of equations the discrete values of the adjoint state variable  $\lambda_k^i$  are calculated for a given airfoil contour at the operating condition considered.

3. Determine the gradient of the discretized functional as defined by

Eq.(28). The gradient is calculated using the derivatives of the functional  $L$  with respect to the design variables. Determine a new estimate of the design variables by applying a suitable optimization procedure, using the above gradient information. Thus, obtain a modified airfoil shape, defined by  $x(\tau)$  and  $z(\tau)$ , new angles of attack  $\alpha^i$  and new values for the velocity parameters  $p_j^i$

4. Iterate 1 through 3 until convergence has been achieved.

In the third step of the latter minimization procedure any appropriate optimization method can be applied, in principle. However, because of its flexibility with respect to applying geometric constraints, at NLR the optimization method available as subroutine EO4UCF in the NAG Fortran Library (See Ref.26) has been chosen. This subroutine is based on a sequential quadratic programming (SQP) algorithm in which the search direction is the solution of a quadratic programming problem. The algorithm treats bounds, linear constraints and nonlinear constraints separately.

#### 5.4 Computational results

##### Auxiliary velocity functions

Prior to presenting results obtained using the algorithms described in sections 5.2 and 5.3, some remarks may be made on the role of the auxiliary functions and free parameters introduced in the target velocity distribution as indicated in section 5.1. For the time being, the auxiliary functions and their parameters have been chosen according to Ref.24, where an inverse airfoil design method is described following essentially the same algorithm as described in section 5.3.

Results for a design exercise presented in Ref.24 are reproduced in Figs. 15 and 16. The target velocity distribution specified in this exercise violates the Betz-Mangler

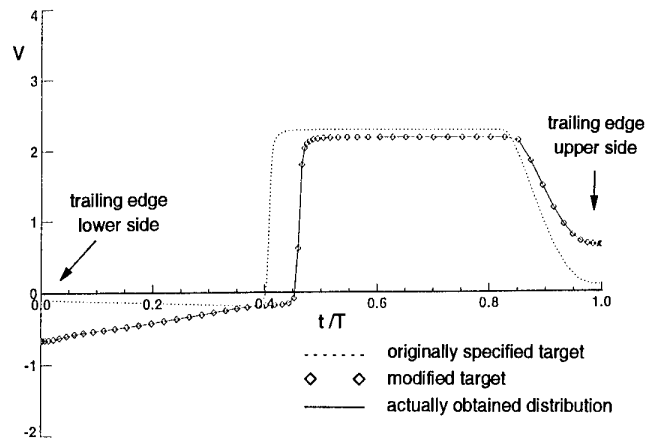


Fig.15 Velocity distributions of a design exercise presented in Ref.24

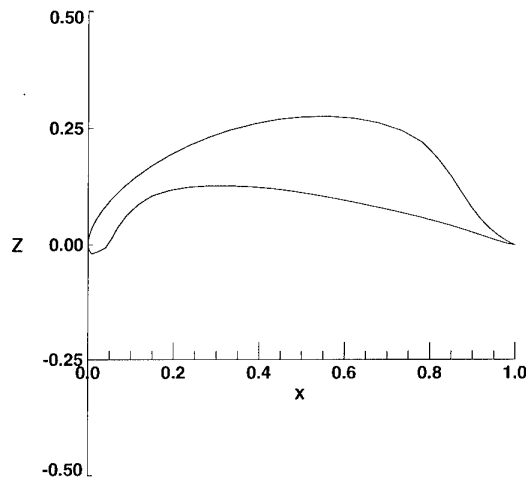


Fig.16 Airfoil producing the velocity distribution depicted in Fig.15

constraints in a rather extreme way, such that large modifications were needed in order to obtain a consistent velocity distribution. This is illustrated in Fig.15 where the originally specified target is compared with the modified target and the eventually obtained velocity distribution on the designed airfoil. The degrees of freedom introduced in the target velocity distribution, as described in section 5.1 are turned to

full account, as appears from the large displacement of the forward stagnation point and the modification of the behaviour near the trailing edge on the lower as well as on the upper side of the airfoil. The NACA0012 airfoil was chosen as starting geometry for the design process. Attempts to apply the design procedure without modifying the original target led to divergence of the minimization process, indicating that the problem was ill-posed. Application of the design procedure with simultaneous modification of the target showed convergence to an optimal solution represented by the airfoil of Fig.16 and the actual velocity distribution depicted in Fig.15. The airfoil that resulted from this design exercise is not attractive from the aerodynamic wing designer's point of view. It illustrates, however, the flexibility and robustness obtained for single-point design by introducing the auxiliary functions to obtain some degree of freedom in the prescribed target velocity distribution.

#### Feasibility

The feasibility of the algorithms is examined by considering a single-point test case, which involves the reconstruction of the NACA4418 airfoil starting with the NACA0012 airfoil. Fig.17a shows the recovery of the airfoil contour and Fig.17b shows the recovery of the velocity distribution. The same result is obtained with either of the alternative algorithms. However, there is a large difference between both algorithms with respect to the computing time involved. This is illustrated in Fig.18 where the value of both objective functions divided by their starting value is plotted against the number of function evaluations. During the larger part of the computational process, the rate of convergence of the variational approach, involving the actual minimization of the objective function defined by Eq.(20), is much smaller

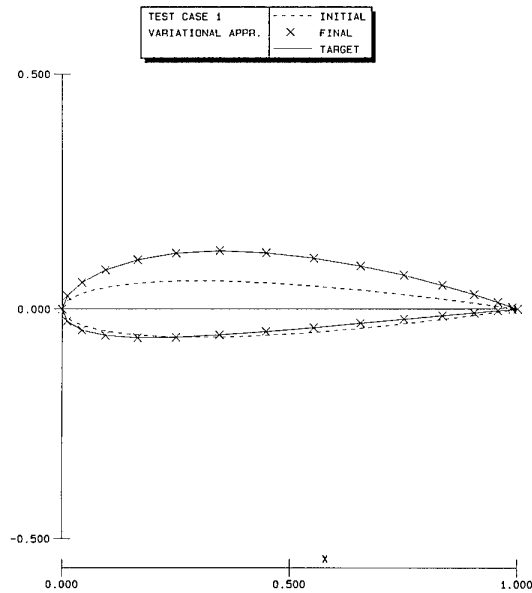


Fig.17a Reconstruction of NACA4418 starting with NACA0012

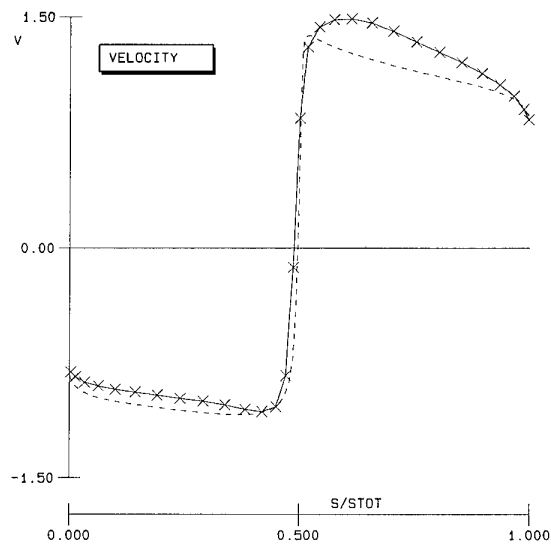


Fig.17b Recovery of velocity distribution, for the reconstructed NACA4418 airfoil

than the rate of convergence of the least squares approach, involving the solution of the set of non-linear equations following from the optimality conditions for the objective function of Eq.(18).

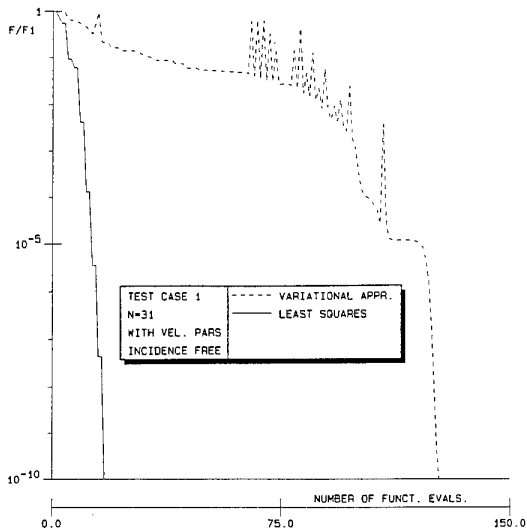


Fig.18 Convergence history at reconstruction of NACA4418

#### Design variables

In section 5.1 it has been remarked that it would be beneficial to obtain more flexibility in the contour representation by introducing the x-coordinates as additional design variables. This may be demonstrated by means of a second single-point design test case. This test case involves the determination of an airfoil shape which, in the incompressible inviscid flow considered here, will produce the pressure distribution specified as target for subsonic viscous flow (Mach number  $M_\infty=0.2$  and Reynolds number  $Re=5.10^6$ ) in the two-point design problem defined in section 4.3. Approximation of a viscous velocity distribution near the trailing edge of an airfoil in inviscid flow will inevitably lead to a cusped contour. Moreover, it is likely that a cross-over of upper and lower side of the contour will be encountered. Hence, it may be expected that the target cannot be fully realized in incompressible inviscid flow, so that the auxiliary functions should take care of an appropriate modification of the target.

Both algorithms described in section 5.2 and in section 5.3, were applied to this test case. And either

algorithm was applied with two different sets of design variables; one set composed of the z-coordinates of the airfoil contour and the free parameters of the auxiliary velocity functions, and a second set obtained by adding the x-coordinates. The NACA0012 airfoil was used as starting geometry.

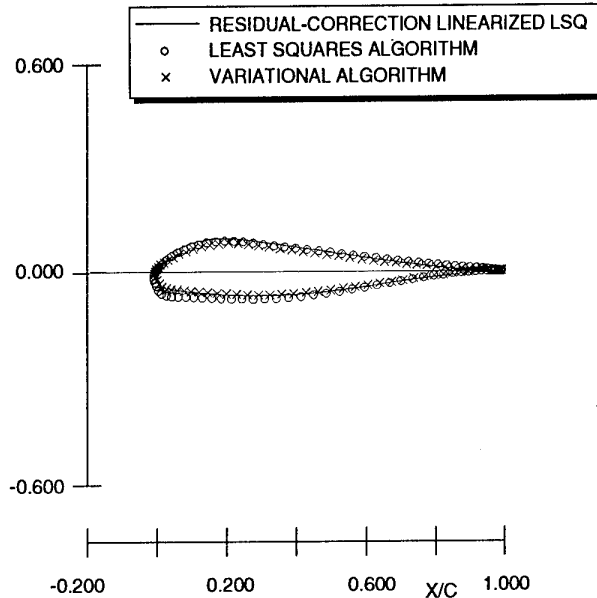


Fig.19 Single-point design (fixed x) for the subsonic target defined in section 4.3 (resulting airfoil shapes).

The results obtained with the first set of design variables (fixed x) are shown in Figs.19 and 20. There is a rather large discrepancy between the results of the two alternative algorithms. This will be due to the fact that a converged result could not be obtained by means of the variational algorithm because of cross-over near the trailing edge; the larger part of the discrepancy between both results is caused by violating the Kutta condition. This could have been avoided by applying a constraint on the trailing edge angle. But with respect to the present investigation the result in the leading edge region is of more importance. Both algorithms produced a solution with a qualitatively wrong behaviour in that region (see also Fig.21).

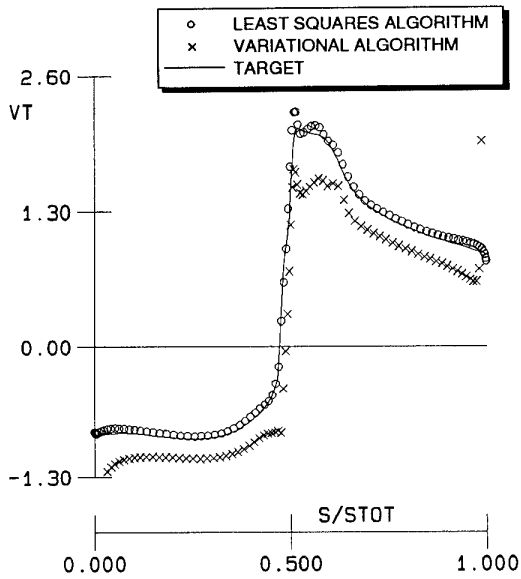


Fig.20 Single-point design (fixed  $x$ ) for the subsonic target defined in section 4.3 (resulting velocity distributions).

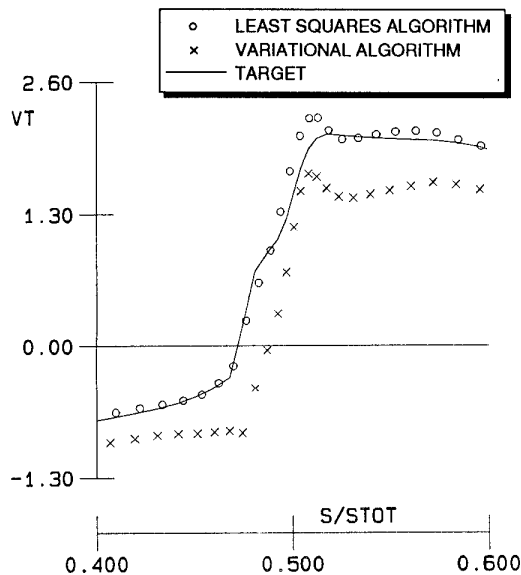


Fig.21 Single-point design (fixed  $x$ ) for the subsonic target defined in section 4.3 (resulting velocity distribution in the leading edge region).

A far more satisfactory result has been obtained by applying the two algorithms with the second set of design variables (variable  $x$ ).

Discrepancies between the results of the two alternative algorithms are hardly noticeable as illustrated by Figs.22 through 24.

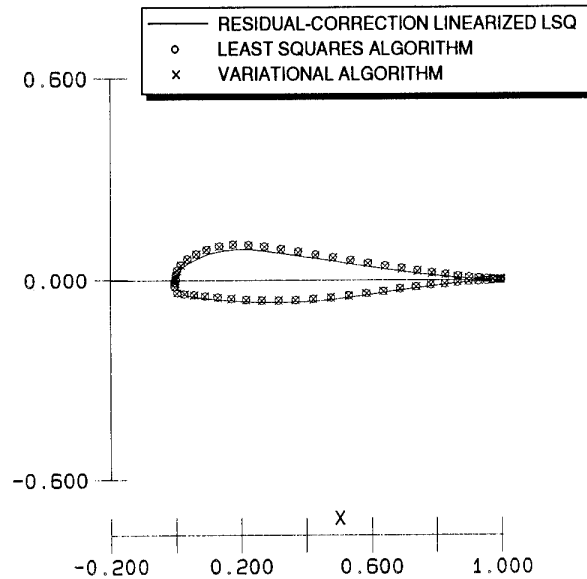


Fig.22 Single-point design (variable  $x$ ) for the subsonic target defined in section 4.3 (resulting airfoil shapes).

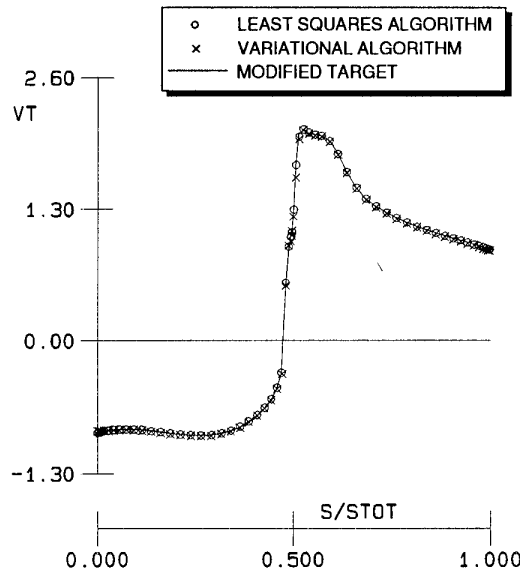


Fig.23 Single-point design (variable  $x$ ) for the subsonic target defined in section 4.3 (resulting velocity distributions).

In Figs. 23 and 24 the high degree of convergence of the computations is reflected in the close agreement between the realized velocity distribution and the modified target. From these results the conclusion can be drawn that the introduction of the x-coordinates as extra design variables leads indeed to a greater flexibility, and as a consequence to a better result.

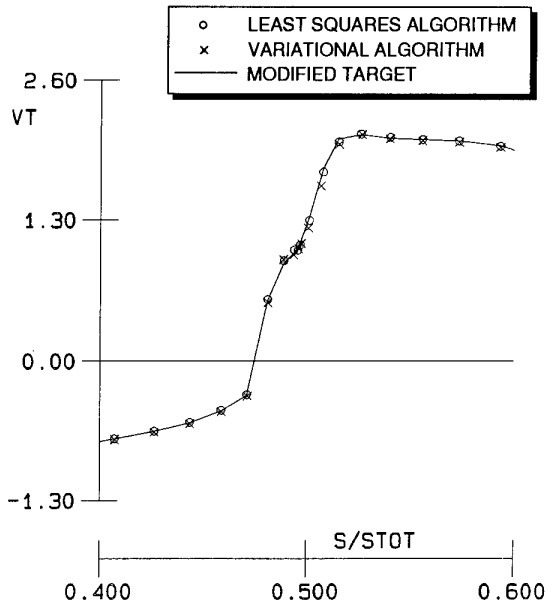


Fig.24 Single-point design (variable  $x$ ) for the subsonic target defined in section 4.3 (resulting velocity distribution in the leading edge region).

#### Two-point design test case

As a final example of application, preliminary results for a two-point design test case are presented. The test case closely resembles the test case discussed in section 4.3, but it has been defined in a different way:

- First of all two airfoils were defined. One airfoil is very similar to that discussed in the previous single-point example, i.e. an airfoil with a favourable high lift capacity in subsonic operating conditions. The other airfoil has low drag under transonic operating conditions (see Fig.25).

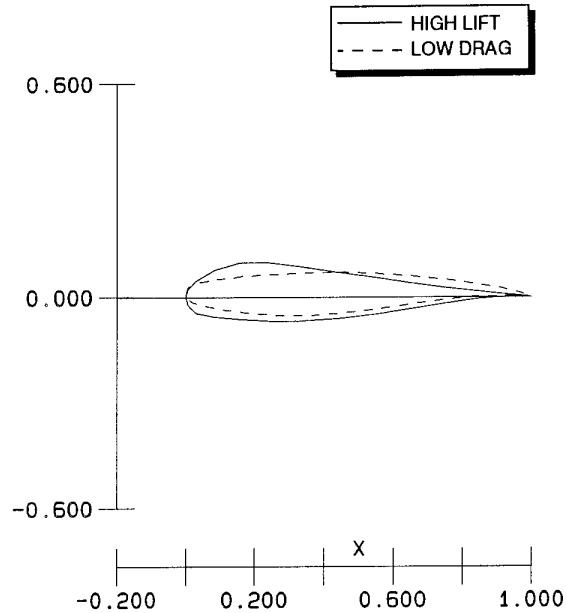


Fig.25 Two-point design test case, basic airfoils.

- For these airfoils the velocity distributions in incompressible potential flow were subsequently calculated for an angle of attack  $\alpha=10.8^\circ$  with the first airfoil (high lift) and for an angle of attack  $\alpha=1.0^\circ$  on the second airfoil (low drag). These calculated velocity distributions define the target velocity distributions for the two-point design test case.

- As a starting geometry for the design process the NACA0012 airfoil was chosen again.

The computations have been performed by means of the least squares algorithm, using as design variables  $x$ ,  $z$ ,  $p_1, p_2, p_3$  and the angle of attack associated with the second operating condition. The values of the weight factors in the functional defined by Eq.(26) were chosen to be  $W^1=W^2=0.5$  and  $W_p^1=W_p^2=0.3$ . It may be noted that for  $W^1=0$  and for  $W^2=0$  the design problem is reduced to a single-point problem, and, because of the way in which the targets have been defined, in fact into a reconstruction problem.

The results are presented in Figs.26 through 28. It appears from Fig.26 that, just like with the result of chapter 4.3, the designed airfoil has characteristics of both basic airfoils.

Due to the incompatibility of the targets, neither of the targets has been realized completely. The velocity distributions at the lower side of the airfoil are closely approximated (see Fig.27), but in the region near the leading edge at the upper side of the airfoil rather large discrepancies remain. Apparently, this region in particular, determines the specific characteristics of the basic airfoils used for the definition of the present test case.

The auxiliary functions in the target velocity that enable modification of the specified target, such that the Betz-Mangler constraints will be satisfied do not play a significant role in the computational process.

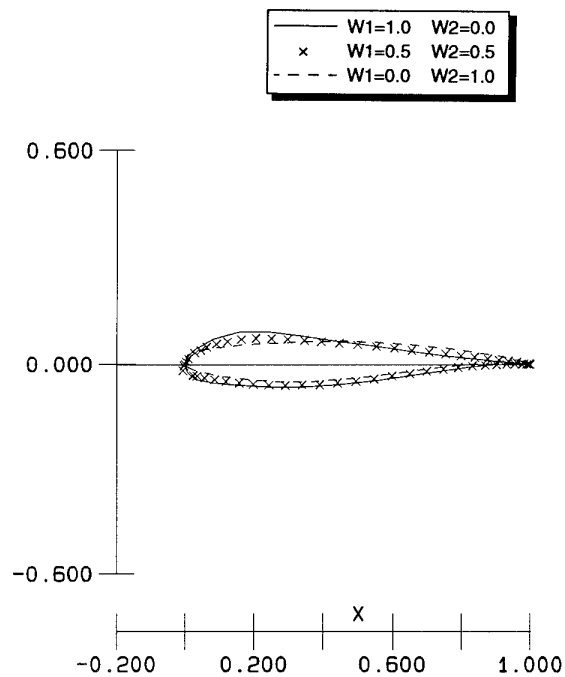
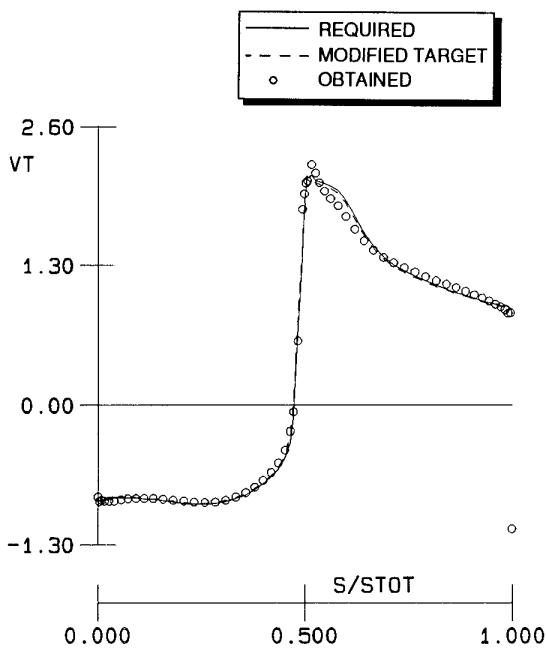
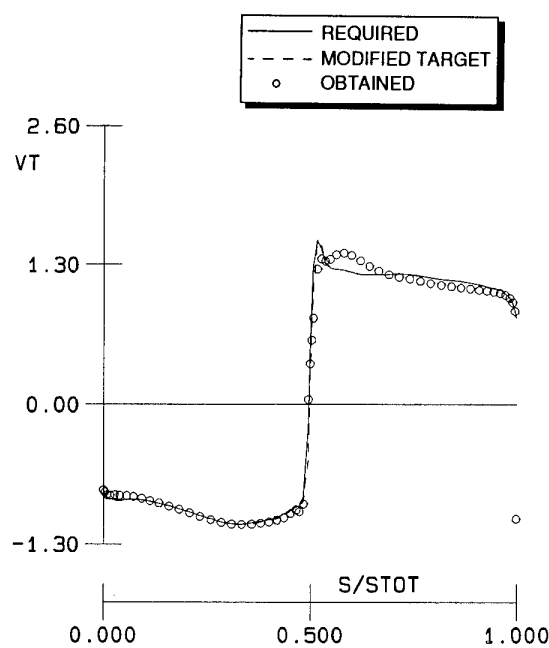


Fig.26 Two-point design test case; airfoil shape compared with both basic airfoils.



a) Operating condition 1



b) Operating condition 2

Fig.27 Two-point design test case; velocity distributions.

Because of the fact that velocity distributions computed for the basic airfoils have been assigned as targets, the auxiliary functions are not needed to fulfil the Betz-Mangler constraints. On the other hand, modification of the specified targets could possibly have removed their mutual incompatibility. Although the targets are slightly modified (see Fig.27), the freedom introduced by the auxiliary functions is apparently not adequate for that purpose. As a consequence of the incompatibility the minimum of the functional will not be zero. This is shown in Fig.28, where the convergence history of the iteration process is illustrated by presenting the subsequent values of the functional versus the number of its evaluations. Though a significant reduction of the value of the functional is obtained, the minimum is still rather large when compared with the minimum obtained in the case of a reconstruction problem (compare Fig.18).

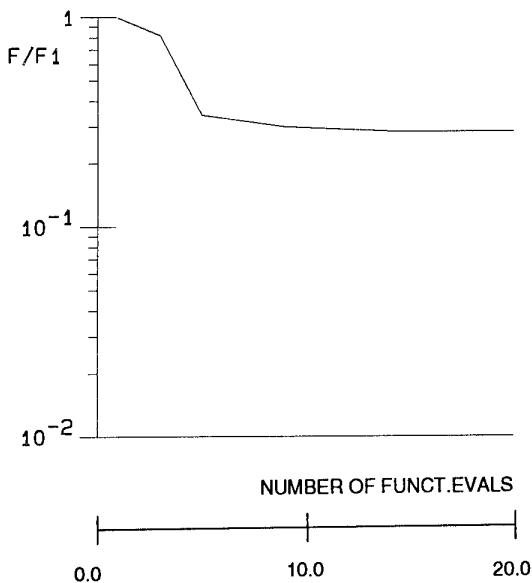


Fig.28 Two-point design test case; convergence history.

## 6. CONCLUSIONS

The feasibility of multi-point airfoil design has been demonstrated with the

aid of some examples. Its benefit is most obvious in situations where requirements for completely different operating conditions, such as with helicopter blades under advancing and retreating conditions, must be fulfilled. But it appears also possible to improve e.g. the drag polar of an airfoil by applying multi-point instead of single-point design. The existence of a unique solution to the multi-point design problem seems questionable, in particular if the design requirements are formulated in terms of global aerodynamic characteristics. From this point of view, it seems likely that formulation of design requirements in terms of prescribed pressure distributions is to be preferred. On the other hand, when operating conditions are considered that lead to the specification of conflicting requirements, the prescribed pressure distributions will in general be incompatible, in the sense that there does not exist one single airfoil that will produce the specified pressure distributions at each specified operational condition.

Most applications found in the literature concern redesign of airfoils aiming at drag reduction. Direct numerical optimization techniques are applied to a cost function that is the weighted sum of drag coefficients. Alternatively, the cost function may be a weighted sum of the squared differences between the prescribed target pressure distributions and the actually realized pressure distributions for a number of operating conditions. Such a cost function is considered when applying a residual-correction method for inverse shape design. By taking one of the weights equal to one, and the other weights equal to zero, the thus formulated design problem reduces to a single-point design problem. If each of these single-point problems can be formulated such that it is well-posed, in the sense that there exists of a unique solution, the corresponding multi-point design

problem can be expected to be at least "better-posed" than without such premise.

At NLR research is in progress on a residual-correction method. This method assumes the availability of a computer program for the calculation of the pressure distribution on an airfoil in full-potential flow, possibly taking boundary layer effects into account. Deviations from the specified target pressure distributions (the residuals) are translated into airfoil geometry corrections, using an approximate inverse method. This approximate inverse method is formulated as an equivalent incompressible multi-point airfoil design problem. The feasibility of this approach has been demonstrated for a two-point reconstruction test case. An example two-point design case has also illustrated the applicability of the approach to reach a solution, even if there are conflicting requirements.

The requirements for the above introduced equivalent incompressible multi-point design problem are specified in terms of prescribed target velocity distributions. Auxiliary functions with free parameters are introduced for each design point in order to allow the adjustment of each target to fulfil the Betz-Mangler constraints. The efficiency of this procedure to ensure the existence of a solution for single-point design is illustrated. Indeed, the introduction of such functions allows the prescription of highly arbitrary velocity distributions. In the case of multi-point design the auxiliary functions with free parameters have, of course, exactly the same role. However, it was found that the freedom introduced by the functions considered here is not adequate for solving the incompatibility problem.

The equivalent incompressible multi-point design problem is formulated as a minimization problem. Two

alternative approaches for the solution of this problem have been considered. One approach is based on a least squares approximation and involves the solution of a set of non-linear equations. The other approach is based on a gradient search technique, derived using the calculus of variations, and involves the solution of an adjoint problem. The algorithm based on the least squares approach uses much less computer time than the algorithm based on the gradient search approach. Otherwise, results obtained by the two algorithms are in perfect agreement with each other. A converged result has been shown for a two-point design test case, demonstrating the still existing incompatibility problem.

The equivalent incompressible multi-point design problem is solved, utilizing the method of singularity distributions for simulation of the flow around the airfoil. Numerical calculations are performed by means of panel methods. A fast computational method is obtained by using a planar panel method to calculate corrections to camber and thickness separately. However, the geometry corrections thus obtained frequently give rise to distortions of the leading edge geometry. Completely satisfactory results are obtained only when a non-planar panel method is applied for the calculation of corrections to x- as well as z-coordinates of the points representing the airfoil geometry.

Further investigations at NLR will concern the incompatibility problem and, with a view to practical application, the implementation of geometric constraints in the least squares algorithm. Possibilities to accelerate the algorithm based on the variational approach will be examined. Moreover, although the present NLR residual-correction method is formally based on transonic full-potential flow, its applicability is not strictly limited to such flow. Because the residual-correction approach only requires geometry corrections in the

right direction, extension to inviscid flow governed by the Euler equations, or even to viscous flow, is straightforward, as long as a computer program for the analysis of such flow is available and the flow conditions considered are such that transonic full potential flow is a reasonable approximation of the inviscid outer flow.

## 7. REFERENCES

1. Hicks, R.M. "Transonic wing design using potential-flow codes. Successes and failures". SAE TP 810565 (1981)
2. Lores, M.E. and Hinson, B.L. "Transonic design using computational aerodynamics". AIAA TP A82-35553 17-02 (1982)
3. Jameson, A. "Aerodynamic design via control theory" NASA CR -181749 ICASE Report No.88-64 (1988)
4. Bocci, A.J. "Aerofoil design techniques" ARA Memo 318 AGARD-CP No.463, Loen, Norway (1989)
5. Sobieczky, H. "Progress in inverse design and optimization in aerodynamics" AGARD-CP No.463, Loen, Norway (1989)
6. Labrujère, Th.E. and Slooff, J.W. "Computational methods for the aerodynamic design of aircraft components" Ann. Rev. Fluid Mech. 1993 Vol.25 pp183-214
7. Labrujère, Th.E. "Residual-correction type and related computational methods for aerodynamic wing design" VKI Special Course on "optimum Design Methods in Aerodynamics" (1994)
8. Renaux, J. and Thibert, J.J. "The use of numerical optimization for airfoil design" AIAA-85-5026 (1985)
9. Renaux, J. and Allongue, M. "The use of numerical optimization for helicopter airfoil and blade design" AGARD-CP No.463, Loen, Norway (1989)
10. Ghielmi, L., Marazzi, R. and Baron, A. "A tool for automatic design of airfoils in different operating conditions" AGARD-CP No.463, Loen, Norway (1989)
11. Drela, M. "Viscous and inviscid inverse schemes using Newton's method" AGARD Report No.780 (1990)
12. Hager, J.O., Eyi, S. and Lee, K.D. "A multi-point optimization for transonic airfoil design" AIAA-92-4681-C (1992)
13. Selig, M.S. and Maughmer, M.D. "A multi-point inverse airfoil design method based on conformal mapping" AIAA-91-0069 (1991)
14. Selig, M.S. and Maughmer, M.D. "Generalized multi-point inverse airfoil design" AIAA-91-3333-CP (1991)
15. Kubrynski, K. "Design of 3-dimensional complex airplane configurations with specified pressure distribution via optimization". Proc. 3rd Int. Conf. Inverse Des. Concepts and Optim. in Eng. Sci. ICIDES III (1991)
16. Labrujère, Th.E. and v.d.Vooren, J. "Calculus of variations applied to 2D multi-point airfoil design" NLR TP 92361 L (1992)
17. Labrujère, Th.E. and v.d.Vooren, J. "A residual-correction method applied to 2D multi-point airfoil design and 3D single-point wing design" NLR TP 92524 U (1992)
18. Labrujère, Th.E. and v.d.Vooren, J. "Development of an algorithm for computational multi-point wing design. Algorithm definition" NLR CR 93111 L (1992)
19. Betz, A. "Änderung eines Profils zur Erzielung einer vorgegebenen Änderung der Druckverteilung."

Luftfahrtforschung, Vol.11,p.158-164 (1934)

20. Mangler,W. "Die Berechnung eines Tragflügelprofils mit vorgeschriebener Druckverteilung". Jahrbuch Deutsche Luftfahrtforsch., S I 46-I 53 (1938)

21. Fray, J.M.J., Slooff, J.W., Boerstoeel, J.W., Kassies, A. "Design of transonic airfoils with given pressure subject to geometric constraints" NLR TR 84064 U, 1984.

22. Brandsma, F.J., Fray, J.M.J.: "A system for transonic wing design with geometric constraints based on an inverse method." NLR TP 89179 L, 1989.

23. Egmond, J.A. van, "Numerical optimization of target pressure distributions for subsonic and transonic airfoil design" NLR TP 89155 L (1989)

24. Soemarwoto, B.I. "Robust inverse shape design in aerodynamics". NLR TP 93432 L (1993)

25. Fletcher, R. "Generalized inverse methods for the best least squares solution of systems of non-linear equations" Comp. J. 10 pp 392-399 (1968)

26. Numerical Algorithms Group Ltd. "NAG Fortran Library Mark 14" (1990)

#### Appendix A : FIRST ORDER PANEL METHOD

Consider the incompressible potential flow in a domain  $\Omega$ , bounded on the inner side by the airfoil contour  $\Gamma$  and on the outer side at infinity by a contour  $\Gamma_\infty$  (see Fig.A.1), where the undisturbed velocity is given by

$$\vec{q}_\infty^i = \begin{pmatrix} U_\infty^i \\ V_\infty^i \end{pmatrix} \quad (\text{A.1})$$

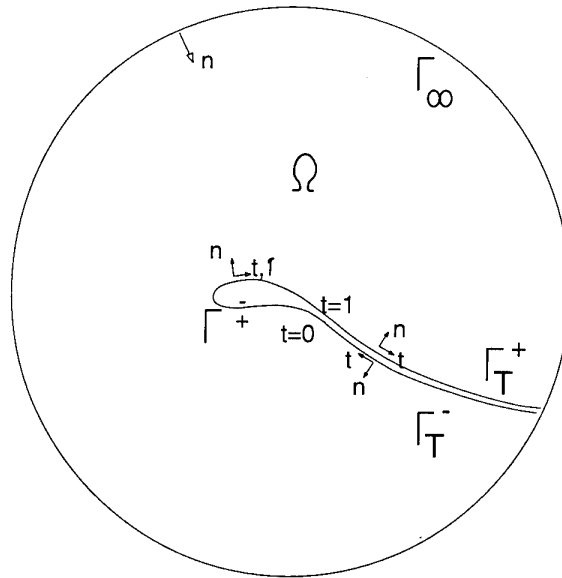


Fig.A.1 Two-dimensional flow domain

In order to allow the existence of a discontinuous velocity potential, as in the case of a lifting airfoil, assume a discontinuity line  $\Gamma_T$  (upper side of the slit in Fig.A.1) which extends from the trailing edge to infinity downstream, but of which the precise location is otherwise irrelevant.

In  $\Omega$  the flow is governed by the Laplace equation

$$\Delta \phi^i = 0, \quad (\text{A.2})$$

while the flow around a given airfoil satisfies the following conditions:

$$\begin{aligned} \frac{\partial \phi^i}{\partial n} &= \vec{q}_\infty^i \cdot \vec{n} && \text{on } \Gamma_\infty, \\ \frac{\partial \phi^i}{\partial n} &= 0 && \text{on } \Gamma, \end{aligned} \quad (\text{A.3})$$

$$\frac{\partial \phi^i}{\partial t} \Big|_{t=0} + \frac{\partial \phi^i}{\partial t} \Big|_{t=1} = 0 \quad \text{on } \Gamma,$$

(Kutta condition).

$$\left(\frac{\partial \phi^i}{\partial t}\right)^+ + \left(\frac{\partial \phi^i}{\partial t}\right)^- = 0 \quad \text{on } \Gamma_T, \quad (\text{A.4})$$

$$\left(\frac{\partial \phi^i}{\partial n}\right)^+ + \left(\frac{\partial \phi^i}{\partial n}\right)^- = 0 \quad \text{on } \Gamma_T,$$

(Continuity).

This system of equations determines the velocity potential apart from a constant which may be chosen arbitrarily.

The flow may be simulated by means of a distribution of sources and doublets on the airfoil contour  $\Gamma$  and a doublet distribution of constant strength  $\mu_T$  on the slit  $\Gamma_T$ . The Kutta condition is fulfilled by taking the doublet strength on the slit equal to the jump in doublet strength at the trailing edge:

$$\mu_T = \mu(1) - \mu(0). \quad (\text{A.5})$$

The doublet distribution gives rise to a velocity potential

$$\phi_d^i = -\frac{1}{2\pi} \int_0^T \mu^i(s) \frac{\partial}{\partial s} \left[ \tan^{-1} \frac{z(t) - z(s)}{x(t) - x(s)} \right] ds + \mu_T^i \tan^{-1} \frac{z - z_T}{x - x_T}. \quad (\text{A.6})$$

The source distribution gives rise to a velocity potential

$$\phi_s^i = \frac{1}{2\pi} \int_0^T \sigma^i(s) \ln[(x(t) - x(s))^2 + (z(t) - z(s))^2]^{1/2} ds. \quad (\text{A.7})$$

The undisturbed flow has a velocity potential

$$\phi_\infty^i = \vec{q}_\infty^i \cdot \vec{x}, \quad (\text{A.8})$$

where

$$\vec{q}_\infty^i = \begin{bmatrix} \cos(\alpha^i) \\ \sin(\alpha^i) \end{bmatrix}, \quad (\text{A.9})$$

and the magnitude of the onset flow velocity has been set equal to one.

The total velocity potential is given by

$$\phi^i = \phi_\infty^i + \phi_d^i + \phi_s^i \quad (\text{A.10})$$

The doublet distribution gives rise to a jump in potential across the airfoil contour

$$(\phi^i)^+ - (\phi^i)^- = -\mu^i. \quad (\text{A.11})$$

The source distribution gives rise to a jump in normal velocity across the airfoil contour

$$\left(\frac{\partial \phi^i}{\partial n}\right)^+ - \left(\frac{\partial \phi^i}{\partial n}\right)^- = \sigma^i. \quad (\text{A.12})$$

Zero normal velocity at the outer side of the airfoil surface will be ensured by choosing the strength of the source distribution equal to

$$\sigma^i = -\frac{\partial \phi_\infty^i}{\partial n} \quad (\text{A.13})$$

and determining the strength of the doublet distribution such that

$$(\phi_s^i + \phi_d^i)^- = 0, \quad (\text{A.14})$$

which implies that

$$\left[\frac{\partial}{\partial n} (\phi_s^i + \phi_d^i)\right]^- = 0, \quad (\text{A.15})$$

and thus

$$\left[\frac{\partial \phi^i}{\partial n}\right]^+ = \frac{\partial \phi_\infty^i}{\partial n} + \left[\frac{\partial}{\partial n} (\phi_s^i + \phi_d^i)\right]^- + \sigma^i = 0. \quad (\text{A.16})$$

On the inner side of the airfoil contour there holds

$$\begin{aligned}
 [\phi_a^i + \phi_s^i]^- &= \\
 &= \frac{1}{2} \mu^i - \frac{1}{2\pi} \int_0^T \mu^i \frac{\partial}{\partial s} \tan^{-1} \frac{z(t) - z(s)}{x(t) - x(s)} ds + \\
 &+ \frac{1}{2\pi} \mu_T^i \tan^{-1} \frac{z(t) - z_T}{x(t) - x_T} \\
 &+ \frac{1}{2\pi} \int_0^T \sigma^i \ln [(x(t) - x(s))^2 + \\
 &+ (z(t) - z(s))^2]^{1/2} ds'. \quad (A.17)
 \end{aligned}$$

Upon application of condition (A.14), this expression produces an integral equation for the doublet strength  $\mu^i$ . And, by virtue of Eq. (A.10) and Eq. (A.14), the tangential velocity at the outer side of the airfoil contour is determined from

$$V_t^i = \left[ \frac{\partial \phi^i}{\partial t} \right]^+ = - \frac{d\mu^i}{dt} + \frac{\partial \phi_\infty^i}{\partial t}. \quad (A.18)$$

A straightforward solution of the integral equation can be obtained by applying a panel method. A simple and cheap panel method can be derived if it is assumed that the airfoil contour will be given by  $N$  discrete points (upper and lower trailing edge point included) and that an approximation of the contour may be obtained by connecting these points by straight line segments (the panels), and furthermore taking the source and doublet strengths constant on each line segment.

Taking as collocation points the midpoints of the panels, the integral equation is reduced to a system of linear equations for the unknown doublet strengths  $\mu_j^i$ ,  $j=1(1)N$

$$\begin{aligned}
 [\phi_a^i + \phi_s^i]_k^- &= \\
 &= \sum_{j=1}^{j=N} MAD_{k,j} \mu_j^i + \sum_{j=1}^{j=N-1} MAS_{k,j+1} \sigma_{j+1}^i = 0 \quad (A.19)
 \end{aligned}$$

for  $k=2(1)N$ ,

where  $\mu_1^i$  denotes the constant doublet strength on the slit  $\Gamma_T$ , which is related to the doublet strength on the airfoil contour by means of the approximated Kutta condition

$$\mu_1^i = \mu_N^i - \mu_2^i. \quad (A.20)$$

Solving this system of linear equations, the doublet strength is determined and subsequently, the velocity distribution along the airfoil contour is calculated by means of a finite difference approximation of Eq. (A.18).

## OPTIMAL SHAPE DESIGN FOR AERODYNAMICS

O. PIRONNEAU  
Université Paris VI  
Labo Analyse Numérique  
Tour 55-65 — 5<sup>ème</sup> étage  
4 Place Jussieu  
75252 Paris Cedex 05  
FRANCE

### Abstract

*After a brief recall on the history of the field of optimal shape design, we shall present a few applications to aerodynamics, then recall the variational approach, the numerical methods and the recent developments both in applied mathematics and in computer sciences*

### Plan :

1. Introduction
2. Industrial examples.
3. Existence results.
4. Principle of resolution
5. Numerical implementation
6. New approaches.

## 1. INTRODUCTION

Among applied mathematicians, optimal shape design is an old problem. However very few cases could be solved analytically until recently, especially when the physical system involves a Partial Differential Equation (PDE). Hadamard (1910) is credited with the first formula for the sensitivity of a PDE with respect to the shape of the domain. However the field as we know it now,

really began with Cea et al (1973) as an off spring of optimal control theory (Lions (1968)) and the calcul of variation developed by the Chicago school in the nineties.

In France the author (1973), Murat-Simon (1976), Cea (in Haug et al (1978)) gave methods to derive optimality conditions for the continuous problem and Begis et al (1976) Morice (1976) and Marrocco et al (1978) for the discretized problem with their numerical solutions.

There are now at least four books on the field:

- Two which are proceedings of summer schools (Haug et al (1981) and Delfour (1992))
- One by the author (Pironneau (1984))
- One with analytical solutions (Banichuck (1980))
- A recent one by Haslager et al (1989)

Theoretical results on the existence of solutions were obtained by Chenais (1975) and counter examples produced by Tartar (1975) in a key paper which linked optimal shape design with homogenization theory, though this concerns structures more than fluids.

For fluids, numerical results were few. Several reasons but mostly because these computations are quite costly and very delicate, particularly in 3D. The situation is changing. The design of wave riders and optimal supersonic transporters are sufficiently important to invest in the field. In Europe there is a Brite program on optimal shape design.

These lectures will begin with a few applications of Optimal Shape Design to aerospace engineering. Then we will spend a good deal of time on the numerical procedure by gradient methods.

Most design engineers do their optimization by hand. But it is generally believed that intuitive optimization is not possible beyond 8 degrees of freedom. Thus if it is ever shown that 3D wings can be optimized with respect to shape, it will be done by computer.

A numerical fluid solver can be viewed as a black box with an input, the wing shape, and an output, the drag. There are commercial packages which find the minimum of a functional with respect to parameters and require only a subroutine to evaluate the functional for a given design. These packages are usually based on local variation methods (Powell(1970)), involving polynomial fits of the functional from point evaluations. They are expensive here because they require  $O(P^2)$  solutions of the flow solver when  $P$  is the number of design variables.

Whenever possible, i.e. when the problem is *differentiable* it is much cheaper to use a gradient or a Newton method. The drawback is that one must do a sensitivity analysis to find the gradient of the functional with respect to the design variables.

There are interesting developments in computer sciences around what is known as "differentiation by program". It has been shown on a problem of meteorology that these derivatives could be found automatically. We will end the lectures with an introduction to this new field.

## 2. INDUSTRIAL EXAMPLES.

### 2.1 Wing design

The example is the optimization of a wing with respect to drag or lift. To reduce the drag by a few percents means a great cost saving on commercial planes.

For viscous drag the Navier-Stokes equations must be used. For wave drag the Euler system is sufficient.

For a wing  $S$  moving at constant speed  $u_\infty$  the drag is

$$F = \int_S [\mu(\nabla u + \nabla u^T) - \frac{2\mu}{3}\nabla \cdot u]n - \int_S pn \quad (1)$$

As usual  $u$  is the fluid velocity,  $\mu$  the viscosity and  $p$  the pressure. The Navier-Stokes equations should be used ( $\theta$  is the temperature):

$$\partial_t \rho + \nabla \cdot (\rho u) = 0 \quad (2)$$

$$\partial_t(\rho u) + \nabla \cdot (\rho u \otimes u) + \nabla p - \mu \Delta u - \frac{1}{3}\mu \nabla(\nabla \cdot u) = 0, \quad (3)$$

$$\partial_t[\rho E] + \nabla \cdot [u \rho E] + \nabla \cdot (p u) = \nabla \cdot \{ \kappa \nabla \theta + [\mu(\nabla u + \nabla u^T) - \frac{2}{3}\mu] \nabla \cdot u \} \quad (4)$$

The definition of energy

$$E = \frac{u^2}{2} + \theta \quad (5)$$

and the law of perfect gas  $p = (\gamma - 1)\rho\theta$  closes the system.

The problem is to minimize  $F \cdot u_\infty$  with respect to the shape of  $S$ .

There are several *constraints*:

- A geometrical constraint: the volume of  $S$  greater than a given value or the solution will be a point.

- An aerodynamic constraint: the lift must be greater than a given value or the wing will not fly.

The problem is difficult because it involves the compressible Navier-Stokes equations at high Reynolds number. It can be simplified by conserving only the wave drag ie the pressure term only in the definition of  $F$  (Jameson (1987)). Then the viscous terms can be dropped in the Navier-Stokes equations ( $\mu = \kappa = 0$ ).

Assuming irrotational flow an even greater simplification replaces the Euler equations by the compressible potential equation or even the incompressible potential flow:

$$u = \nabla\phi, \quad \rho = (1 - |\nabla\phi|^2)^{1/(\gamma-1)}, \quad p = \rho^\gamma, \quad \nabla \cdot \rho u = 0. \quad (6)$$

Or even, if at low Mach number, by the incompressible potential flow equation:

$$u = \nabla\phi, \quad -\Delta\phi = 0. \quad (7)$$

But then the full expression for  $F$  must be kept.

Constraints on admissible shapes are numerous:

- Minimal thickness, given length.
- Minimum admissible curvature
- Minimal angle at the trailing edge...

Another problem arises due to instability of optimal shapes with respect to data. It will be seen that the leading edge of the solution is a wedge. Thus if the incidence angle for  $u_\infty$  is changed the solution becomes very bad. A multi-point functional must be used in the optimization,  $\sum u_\infty^i F^i$  at given lift  $F_3^i$  where  $F^i$  is computed from a Navier-Stokes equations with boundary conditions  $u = u_\infty^i$ .

## 2.2 Ribblets

Consider a flat plate with groves dug on the surface parallel to the mean flow. It has been shown that such configurations have less drag than the flat plate per unit surface area.

The phenomenon may actually be turbulent in its principle (Moin (1993)) because these groves or ribblets trap the large vortices and prevent horse shoe formations. It is beyond the limit of present computers to hope to solve such problems by optimal design methods. However even the laminar case leads to

an optimization and it is not true that the flat plate is the best surface for drag per unit surface area for a Poiseuille flow.

Ribbllets are well within the logarithmic layer and near the viscous sublayer. Thus Poiseuille flow is a rough but sensible approximation. Then the problem is:

$$\min_{\Sigma} u_{\infty} \cdot \int_{\Sigma} [\nu(\nabla u + \nabla u^T) - pn] \quad (8)$$

with  $(u, p)$  solution of

$$\vec{u} = \begin{pmatrix} 0 \\ 0 \\ u(x, y) \end{pmatrix} \text{ and } p = p(z) \quad (9)$$

$$\nabla p - \nu \Delta u = \begin{pmatrix} 0 \\ 0 \\ \frac{\partial p}{\partial z} - \nu \Delta_{x,y} u \end{pmatrix} = 0 \quad (10)$$

Let, with  $p = kz$ ,

$$-\nu \Delta u + k = 0 \quad (11)$$

With a periodic distribution of grooves  $\Sigma$  and a Neumann condition on the upper artificial boundary which simulates the matching with the boundary layer  $S$  the problem becomes:

$$\min_{\Sigma} \left( - \int_{\Sigma} \frac{\partial u}{\partial n} \right) \quad (12)$$

with  $(u, k)$  solution of:

$$\begin{aligned} -\nu \Delta u + k &= 0 \quad \text{in } \Omega \\ u &= 0 \quad \text{on } \Sigma \\ \frac{\partial u}{\partial n} &= 0 \quad \text{on } S \\ u &= x - \text{periodic} \end{aligned} \quad (13)$$

A constraint on the flux needs to be added to fix  $k$ :

$$\int_{\Omega} u = d, \quad (14)$$

## 2.4 Shock wave sound reduction

Some supersonic carrier are considered too noisy. An optimization of the shock wave jump and / or the jets can be performed with respect to the far field noise. Again the full problem involves the Navier-Stokes equations but simpler approximations like Lighthill's can be used and in the far field it is the wave equation which is solved.

### 2.5 Stealth airplanes.

In this line of problems a simpler one is the optimization of the far-field energy of a radar wave reflected by an airplane in flight.

The equations are Maxwell's but the constraints may be aerodynamical ( lift above a given lower limit) and thus requires the solution of the fluid part. The design variables are:

- The shape of the wing
- The thickness of the paint
- The material characteristics ( $\epsilon, \mu$ ) of the absorbing paint.

A simple representative in this class is the case of T.M. polarization for the incoming radar wave and a 2D design:

$$\min_{S \in \mathcal{O}} \left\{ \int_{\Gamma_\infty} |\nabla \varphi|^2 : \omega^2 \varphi + \Delta \varphi = 0, \varphi|_S = g, i\omega \varphi + \frac{\partial \varphi}{\partial n} |_{\Gamma_\infty} = 0 \right\} \quad (15)$$

The class of admissible forms  $\mathcal{O}$  may include a constraint on the lift given by (6).

Here again, the theoretical complexity of the problem can be appreciated from the following question:

Would ribblets of the size of the radar wave improve the design?

Actually homogenization can answer the question as in Achdou (1991) (see also Artola (1991) and Achdou et al (1991)) It shows that indeed ribblets improve the design.

But then boundary condition on  $S$  in (15) can be replaced by an averaged condition on a surface without ribblets:

$a\varphi + b\partial\varphi/\partial n$  given with  $a$  and  $b$  depending on the ribblet shape.

### 2.6 Academic test cases

To illustrate the technics the best is to consider a simple problem such an optimization for potential flow

$$\min_{\Omega} \left\{ \int_D |\nabla \varphi - u_d|^2 : -\Delta \varphi = 0 \text{ in } \Omega, \frac{\partial \varphi}{\partial n} |_{\partial \Omega} = g \right\} \quad (16)$$

or with a stream function in 2D

$$\min_{\Omega} \left\{ \int_D |\nabla \psi - v_d|^2 : -\Delta \psi = 0 \text{ in } \Omega, \psi|_{\partial\Omega} = f \right\} \quad (17)$$

This is in fact an "inverse problem" because one seeks a shape which produces a velocity as near to  $u_d$  as possible in the region  $D$  of  $\Omega$ .

### 3. EXISTENCE OF SOLUTIONS

Let  $v_d \in L^2(\Omega)$ ,  $f \in H^{-1}(\Omega)$  and  $\psi(\Omega)$  be the solution of

$$-\Delta \psi = f \text{ in } \Omega, \quad \psi|_{\partial\Omega} = 0 \quad (18)$$

Given  $O, D$  non empty and bounded with  $O \supset D$  we seek

$$\min_{\Omega \in \mathcal{O}} J(\Omega) = \int_D |\nabla \psi(\Omega) - v_d|^2 \quad (19)$$

with  $\mathcal{O}$  a subset in the the class of open sets  $\Omega$  of  $R^n$  such that  $O \supset \Omega \supset D$ ,  $mes(\Omega) = 1$ .

Chenais (1975) showed that there exists a solution provided that the class  $\mathcal{O}$  is restricted to  $\Omega$  locally on one side of their boundaries and verifying the *Cone Property*:

*For every  $x \in \partial\Omega$  it is possible to place the vertex of a cone  $C_\epsilon(x)$  with angle  $\epsilon$  such that  $\Omega \supset C_\epsilon(x) \cap B_\epsilon(x)$  where  $B_\epsilon(x)$  is the sphere of radius  $\epsilon$  and centre  $x$ .*

This condition rules out oscillating boundaries. We also know (Pironneau (1984), see also Crouzeix (1991)) that if  $J(\psi)$  is the energy of the PDE

$$J(\Omega, \psi) = \int_{\Omega} [|\nabla \psi|^2 - 2f\psi]$$

then there exists a solution with the single hypothesis that  $\Omega$  be an open set included in  $O$  because (1)(2) is equivalent to

$$\min_{\psi \in H_0^1(O), mes(supp\psi) \geq 1} J(O, \psi) \quad (20)$$

In 2D an interesting result has been obtained by Sverak (1992):

**Theorem .**

If  $O = \bigcup_N$  is the set of open sets containing  $D$  (possibly with a constraint on the area such as  $\text{area} \geq 1$ ) and whose connected components are bounded by  $N$  then (1)(2) has a solution.

In other words, if a numerical algorithm generates a sequence of shapes which have each a small criteria, then two things can happen:

- Either the accumulation points will be solutions
- Or there will be more and more holes.

This result is false in 3D as it is possible to make shapes with spikes such that the 2D approximation will look like a surface with holes and yet the 3D surface remains singly connected.

*Proof.* The proof will not be given in the lecture. It is sketched here for the reader to see the kind of tools which are used in such studies.

The proof relies on a compactness result for the Hausdorff topology and on a result of potential theory which is valid only in 2D.

The Hausdorff distance between 2 closed sets  $A, B$  is  $\delta(A, B) = \max\{d(B, A), d(A, B)\}$  where  $d(A, B) = \sup_{x \in A} d(x, B)$ . For this distance we have the following :

if  $F_n$  is a uniformly bounded sequence , then there is a closed bounded set  $F$  and a subsequence converging in the sense of Hausdorff to  $F$ .

Equivalently let  $\Omega_n$  be a sequence of open sets in  $R^d$  with  $\Omega_n \subset O$ . Then one can extract a subsequence, also denoted by  $\Omega_n$  converging in the sense of Hausdorff to a  $\Omega$ , that is, verifying:

$$\forall C \subset \Omega, \exists m : C \subset \Omega_n \forall n \geq m \text{ and } \forall x \in O - \Omega, \exists x_n \in O - \Omega_n : x_n \rightarrow x. \quad (21)$$

So a minimizing subsequence for (2) will have the following properties

$$J(\Omega_n) \rightarrow \inf J(\Omega) \quad (22)$$

$$-\Delta \psi_n = f \text{ in } \Omega_n, \quad \psi \in H^1(\Omega_n) \text{ and } \psi_n \rightarrow \psi \text{ in } H^1(O) \text{ weak with ,}$$

$$-\Delta \psi = f \text{ in } \Omega, \quad \inf J(\Omega) = \int_D |\nabla \psi - v_d|^2. \quad (23)$$

But we do not know how to show that

$$\psi = 0 \text{ in } O - \Omega \quad (24)$$

For this an information on the characteristic function  $\chi_n$  of  $O - \Omega_n$  is needed because

$$0 = \chi_n \psi_n \rightarrow \chi \psi, \Rightarrow \psi(x) = 0 \text{ pp si } \chi(x) \neq 0. \quad (25)$$

Sverak uses another argument to replace(25). First he shows that it is sufficient to study the case  $f=1$ . If  $\Omega^n$  denotes the solution in  $H_0^1(\Omega_n)$  of  $-\Delta \Omega^n = 1$  then the convergence of  $\Omega^n$  towards its weak limit is almost uniform (this is the difficult point) when the number of connected components is finite. This results from the theory of sub-harmonic functions is not true in 3D.

### Corollary

*With the Navier-Stokes equations for incompressible flows there exists an optimal wing profile with given area in 2D*

### Proof

Let  $\Omega^n$  be a minimizing sequence. Let  $u^n$  be the corresponding solution of the Navier-Stokes equations :

$$-\nu \Delta u^n + \nabla \cdot (u^n \otimes u^n) + \nabla p^n = 0, \quad \nabla \cdot u^n = 0 \text{ in } \Omega^n \quad (26)$$

Let  $\Omega^n$  be bounded with two connected components, the wing profile  $S^n$  where  $u^n = 0$  and the boundary which approximates infinity  $\partial \Omega^n - S$  on which  $u^n = u_\infty$ .

As  $u^n$  is bounded in  $H_0^1(O)^2$  there exists a subsequence which converges weakly; let  $u$  be the limit. As  $\nabla \cdot (u^n \otimes u^n) \rightarrow \nabla \cdot (u \otimes u)$  in  $W^{-1,p}(O)$  for all  $p$  we must show that  $\{\Omega^n, u^n\}$  is a solution of the Stokes problem

$$-\Delta u^n + \nabla p^n = f^n \quad \nabla \cdot u^n = 0 \quad u^n|_{S^n} = 0,$$

Then  $f^n \rightarrow f$  in  $W^{-1,p}(O)$ ,  $O - \Omega^n \rightarrow O - \Omega$  Hausdorff, ,  $u^n \rightarrow u$  in  $H^1$  weak implies that

$$-\Delta u + \nabla p = f \quad \nabla \cdot u = 0 \quad u^n|_S = 0.$$

A similar result is also shown in Sverak(1992).

## 4 SOLUTION BY GRADIENT METHODS

### 4.1 Optimal shape design problem in Stokes flow

Energy conservation allows to reframe the minimum drag problem as:  
Find

$$\min_{\Omega \in \mathcal{O}} E(\Omega) = \min_{\Omega \in \mathcal{O}} \nu \int_{\Omega} |\nabla \vec{u}|^2$$

subject to :

$$\begin{cases} -\nu \Delta \vec{u} + \nabla p = 0 & \text{in } \Omega \\ \nabla \cdot \vec{u} = 0 & \text{in } \Omega \\ \vec{u}|_S = 0 \\ \vec{u}|_{\Gamma_{\infty}} = \vec{u}_{\infty} \end{cases} \quad (27)$$

An example of  $\mathcal{O}$  is :

$$\mathcal{O} = \{\Omega : \text{volume } \tilde{S} = 1, \partial\Omega = S \cup \Gamma_{\infty}\},$$

where  $\tilde{S}$  = the domain defined by the closed boundary  $S$ .

For deriving the optimality conditions, we need to do some calculus of variation on  $E(\Omega)$ . So, we consider that  $\Omega$  is the optimum solution and  $\Omega' \in \mathcal{O}$  is a domain "near"  $\Omega$  (see figure 3) defined by its boundary  $\Gamma' = \partial\Omega'$ , with

$$\Gamma' = \{x + \alpha(x)\vec{n}(x), \text{ s.t. } \alpha = \text{regular, small, } \forall x \in \Gamma\}$$

$$\Gamma = \partial\Omega.$$

For every  $\alpha$  admissible, we have :

$$E(\Omega') \geq E(\Omega) \quad (28)$$

Define

$$\delta\Omega = \Omega \cup \Omega' - \Omega \cap \Omega', \quad (29)$$

and associate a convention to it, that

$$\int_{\delta\Omega} f \equiv \int_{\Omega' - \Omega \cap \Omega'} f - \int_{\Omega - \Omega \cap \Omega'} f$$

Define also

$$\delta\vec{u} = \vec{u}(\Omega') - \vec{u}(\Omega) \quad (30)$$

extending  $\vec{u}$  smoothly in  $\tilde{S}$ . Then

$$\begin{aligned} \delta E &= E(\Omega') - E(\Omega) = v\delta\left(\int_{\Omega} |\nabla \vec{u}|^2\right) = \\ &v \int_{\delta\Omega} |\nabla \vec{u}|^2 + 2v \int_{\Omega} \nabla \delta \vec{u} \cdot \nabla \vec{u} + o(\delta\Omega, \delta \vec{u}). \end{aligned} \quad (31)$$

When  $\delta\Omega$  is smooth and  $\nabla \vec{u}$  is continuous, then

$$v \int_{\delta\Omega} |\nabla u|^2 = v \int_{\Gamma} \alpha |\nabla u|^2 d\gamma + o(\|\alpha\|_{c^2}) = v \int_{\Gamma} \alpha \left| \frac{\partial u}{\partial n} \right|^2 d\gamma + o(\|\alpha\|_{c^2}) \quad (32)$$

(cf.[9]).

In order to complete the computation of  $\delta E$ , we need the following lemma :

**Lemma 1.** *Equations(7) imply*

$$-v\Delta \delta u + \nabla \delta p = 0 \text{ in } \Omega \quad (33)$$

$$\nabla \cdot \delta u = 0 \text{ in } \Omega \quad (34)$$

$$\delta u|_{\Gamma_{\infty}} = 0 \quad (35)$$

$$\delta u|_S = -\alpha \frac{\partial u}{\partial n} \quad (36)$$

**Proof :** We have the relations :

$$\delta(-v\Delta u + \nabla p) = 0 \Rightarrow -v\Delta \delta u + \nabla \delta p = 0 \quad (37)$$

$$\delta(\nabla \cdot u) = 0 \Rightarrow \nabla \cdot \delta u = 0 \text{ in } \Omega \cap \Omega' \quad (38)$$

$$\delta u|_{\Gamma_{\infty}} = 0 \quad (39)$$

if  $u_{\infty}$  is constant and  $\Gamma_{\infty}$  the same in  $\Omega$  and  $\Omega'$ . Finally

$$\delta u|_S \simeq \delta u|_{\partial(\Omega \cap \Omega')} = \begin{cases} +u(\Omega')|_S, & \text{if } \alpha > 0 \\ -u(\Omega)|_S, & \text{if } \alpha < 0 \end{cases} \quad (40)$$

Using Taylor's expansion, we obtain :

$$\begin{aligned}
u(\Omega')|_S &= u(\Omega')(x' - \alpha n) = u(\Omega')(x') - \alpha \frac{\partial u}{\partial n}(\Omega')|_{S'} + o(|\alpha|) \quad (41) \\
&= -\alpha \frac{\partial u}{\partial n}(\Omega')|_{S'} + o(|\alpha|), \text{ since } u(\Omega')(x') = 0
\end{aligned}$$

and

$$u(\Omega)|_S = 0. \quad (42)$$

So,

$$\delta u|_S = -\alpha \frac{\partial u}{\partial n}|_S. \quad (43)$$

Finally, if all equalities are up to higher order terms, we have :

$$\nu \int_{\delta\Omega} |\nabla u|^2 = \nu \int_S \alpha \left| \frac{\partial u}{\partial n} \right|^2 d\gamma \quad (44)$$

□

**Remark :** A lot of regularity is needed to perform the previous calculation, but it can be justified by other methods also such a in Murat-Simon (1976). and

$$\begin{aligned}
\nu \int_{\Omega} \nabla \delta u \nabla u &= \nu \int_{\Omega} (-\Delta u) \delta u + \nu \int_{\Gamma} \frac{\partial u}{\partial n} \delta u d\gamma = \quad (45) \\
\int_{\Omega} p \nabla \cdot \delta u - \int_{\Gamma} p \delta u \cdot n d\gamma &+ \nu \int_{\Gamma} \frac{\partial u}{\partial n} \delta u d\gamma = \\
&= \int_{\Gamma} \left( \nu \frac{\partial u}{\partial n} - pn \right) \cdot \delta u d\gamma = - \int_S \nu \alpha \left| \frac{\partial u}{\partial n} \right|^2 d\gamma,
\end{aligned}$$

because, if  $\vec{s}$  denotes the tangent component,

$$\delta u|_{\Gamma_{\infty}} = 0, \quad \delta u|_S = -\alpha \frac{\partial u}{\partial n} \text{ and } n \cdot \frac{\partial u}{\partial n} = -\vec{s} \cdot \frac{\partial u}{\partial \vec{s}} = 0 \text{ on } \Gamma. \quad (46)$$

Hence,

$$\nu \int_{\Omega} \nabla \delta \vec{u} \cdot \nabla \vec{u} = -\nu \int_S \alpha \left| \frac{\partial \vec{u}}{\partial \vec{n}} \right|^2 d\gamma$$

and

$$\delta E \simeq -\nu \int_S \alpha \left| \frac{\partial u}{\partial n} \right|^2 d\gamma. \quad (47)$$

We have proved the

**Proposition 3 :** *The variation of  $E$  with respect to  $\Omega$  is :*

$$\delta E = -\nu \int_S \alpha \left| \frac{\partial u}{\partial n} \right|^2 d\gamma + o(\alpha) \quad (48)$$

□

### Consequences

1) Supposing that  $\mathcal{O} = \{S : S \supset C\}$ , since  $|\frac{\partial u}{\partial n}|^2 > 0$ ,  $C$  is the solution. Indeed any  $\alpha < 0$  will give  $\delta E > 0$ . In other words, any fairing around  $C$  will increase the drag in Stokes flow.

2) If  $\mathcal{O} = \{S : Vol \tilde{S} = 1\}$ , then  $\delta E \geq 0$  for every  $\alpha$  with

$$\int_{\Gamma} \alpha d\gamma = o(|\alpha|). \quad (49)$$

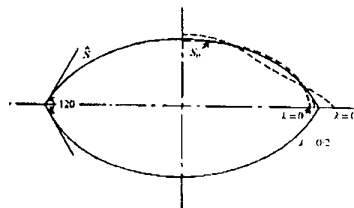
Hence, if  $u$  is smooth, (47) and (49) imply

$$\left| \frac{\partial u}{\partial n} \right|_{|\Gamma} = \text{constant}. \quad (50)$$

Lighthill (cf. Pironneau (1986)) showed that near the leading and the trailing edge the only possible axisymmetric flow which can give  $|\frac{\partial u}{\partial n}| = \text{constant}$  on  $S$  is an  $S$  conical of half angle equal to  $60^\circ$ .

To compute an axisymmetric surface  $S$  which satisfies (7) and (50) we could try one iteration of gradient method starting from the ellipsoid with minimum drag to which is added a conical front and rear end near the leading and trailing stagnation point.

The result is shown on figure 1. A decrease of drag of 5% was found with respect to the optimum ellipsoid.



## 4.2 Optimal shape design in laminar flow

We consider the minimum drag energy problem where the state equation is the Navier-Stokes equations.

The mathematical formulation of such a problem is :

Find

$$\min_{S \in \mathcal{O}} E(\Omega) = \nu \int_{\Omega} |\nabla u|^2$$

with  $u$  subject to

$$-\nu \Delta u + \nabla p + u \nabla u = 0, \quad \text{in } \Omega \quad (51)$$

$$\nabla \cdot u = 0, \quad \text{in } \Omega \quad (52)$$

$$u|_S = 0 \quad (53)$$

$$u|_{\Gamma_{\infty}} = u_{\infty} = \text{constant} \quad (54)$$

and  $\mathcal{O} = \{S : \text{vol} \tilde{S} = 1\}$ ,  $\Gamma = \partial\Omega = S_{\infty} \cup \Gamma$  smooth.

We shall derive the optimality condition for this problem. In order to do this we must express the variation of  $E(\Omega)$  in terms of the variation of  $\Omega$ .

We consider that  $\Omega$  is the optimal solution and that  $\Omega'$  is a domain obtained by a small perturbation of  $\Omega$  defined as before :  $\Omega'$  has the boundary

$$\partial\Omega' = S' \cup \Gamma_{\infty} \text{ where } S' = \{x + \alpha n : x \in S\}.$$

We call  $u'$  the solution of (51)-(54) on  $\Omega'$  and we define :

$$\delta E = E(\Omega') - E(\Omega) = \nu \int_{\delta\Omega} |\nabla u|^2 + 2\nu \int_{\Omega} \nabla u \nabla \delta u + o(\delta u, \alpha). \quad (55)$$

We can prove the following in the same way we proved Lemma 1 :

**Lemma 2 :** Equations (31)-(34) imply that

$$-\nu \Delta \delta u + \nabla \delta p + u \nabla \delta u + \delta u \nabla u = 0 \quad (56)$$

$$\nabla \cdot \delta u = 0 \quad (57)$$

$$\delta u|_{\Gamma_\infty} = 0 \quad (58)$$

$$\delta u|_S = -\alpha \frac{\partial u}{\partial n} \quad (59)$$

□

Lemma 2 is not sufficient to get rid of the second term in the right side of (55).

So, we introduce the adjoint equation :

Let  $(\vec{P}, q)$  be the solution of :

$$-v\Delta\vec{P} + \nabla q - u\nabla\vec{P} - (\nabla\vec{P})u = -2v\Delta u \quad \text{in } \Omega \quad (60)$$

$$\nabla \cdot \vec{P} = 0 \quad \text{in } \Omega \quad (61)$$

$$\vec{P}|_\Gamma = 0 \quad (62)$$

In order to compute  $\delta E$  we use Lemma 2 and equations (60)-(62).

Multiplying (60) by  $\delta u$  and integrating on  $\Omega$ , we obtain :

$$\begin{aligned} -2v \int_{\Omega} \Delta u \cdot \delta u &= -v \int_{\Omega} \Delta \vec{P} \cdot \delta u - \\ &\int_{\Omega} \nabla \vec{P} u \cdot \delta u - \int_{\Omega} u \nabla \vec{P} \cdot \delta u dx + \int_{\Omega} \nabla q \cdot \delta u \end{aligned} \quad (63)$$

We use Green's formula and integrations by parts in (63) :

$$- \int_{\Omega} \nabla \vec{P} u \cdot \delta u = \int_{\Omega} u \nabla \delta u \cdot \vec{P} - \int_{\Gamma} (\vec{P} \cdot \delta u)(u \cdot n) d\gamma = \int_{\Omega} u \nabla \delta u \cdot \vec{P} dx \quad (64)$$

because  $\nabla \cdot u = 0$  in  $\Omega$  and  $\vec{P}|_\Gamma = 0$ . Now

$$\begin{aligned} - \int_{\Omega} u \nabla \vec{P} \cdot \delta u &= \int_{\Omega} \delta u \nabla u \cdot \vec{P} + \int_{\Omega} \vec{P} \cdot u \nabla \cdot \delta u \\ - \int_{\Gamma} (\vec{P} \cdot u)(\delta u \cdot n) d\gamma &= \int_{\Omega} \delta u \nabla u \cdot \vec{P}. \end{aligned} \quad (65)$$

as  $\nabla \cdot \delta u = 0$  in  $\Omega$  and  $\vec{P}|_\Gamma = 0$ .

The last integral in (63) is zero, because :

$$\int_{\Omega} \nabla q \cdot \delta u = - \int_{\Omega} q \nabla \cdot \delta u + \int_{\Gamma} q \delta u \cdot n d\gamma = 0$$

as  $\nabla \cdot \delta u = 0$  in  $\Omega$  and

$$\delta u \cdot n = \begin{cases} 0 & \text{on } \Gamma_\infty \\ -\alpha \frac{\partial u}{\partial n} \cdot n = 0 & \text{on } S. \end{cases}$$

Using these results in (63), we obtain :

$$\begin{aligned} -2\nu \int_{\Omega} \Delta u \cdot \delta u &= \nu \int_{\Omega} \nabla \vec{P} \cdot \nabla \delta u - \nu \int_{\Gamma} \frac{\partial \vec{P}}{\partial n} \cdot \delta u d\gamma & (66) \\ &+ \int_{\Omega} u \nabla \delta u \cdot \vec{P} + \int_{\Omega} \delta u \nabla u \cdot \vec{P} \\ &= -\nu \int_{\Omega} \Delta \delta u \cdot \vec{P} + \nu \int_{\Gamma} \vec{P} \cdot \frac{\partial(\delta u)}{\partial n} d\gamma \\ &- \nu \int_{\Gamma} \frac{\partial \vec{P}}{\partial n} \cdot \delta u d\gamma + \int_{\Omega} u \nabla \delta u \cdot \vec{P} \\ &+ \int_{\Omega} \delta u \cdot \nabla u \cdot \vec{P}. \end{aligned}$$

If we multiply (36) by  $\vec{P}$ , integrate on  $\Omega$  and use Green's formula, we obtain :

$$\begin{aligned} -\nu \int_{\Omega} \Delta \delta u \cdot \vec{P} + \int_{\Omega} u \nabla \delta u \cdot \vec{P} + \int_{\Omega} \delta u \nabla u \cdot \vec{P} & (67) \\ \int_{\Omega} \nabla \delta p \cdot \vec{P} = - \int_{\Gamma} \delta p \vec{P} \cdot n d\gamma = 0, \end{aligned}$$

since  $\nabla \cdot \vec{P} = 0$  in  $\Omega$  and  $\vec{P}|_{\Gamma} = 0$ . In addition,  $\nu \int_{\Gamma} \vec{P} \cdot \frac{\partial(\delta u)}{\partial n} d\gamma = 0$ , so (66) gives

$$-2\nu \int_{\Omega} \Delta u \cdot \delta u = -\nu \int_{\Gamma} \frac{\partial \vec{P}}{\partial n} \cdot \delta u d\gamma = \nu \int_S \alpha \frac{\partial \vec{P}}{\partial n} \cdot \frac{\partial u}{\partial n} d\gamma \quad (68)$$

because of (58) and (59).

Using Green's formula in the left side of (68), we find :

$$-2\nu \int_{\Omega} \Delta u \cdot \delta u = 2\nu \int_{\Omega} \nabla u \cdot \nabla \delta u - 2\nu \int_{\Gamma} \frac{\partial u}{\partial n} \delta u d\gamma. \quad (69)$$

The equality of (68) and (69) gives :

$$2\nu \int_{\Omega} \nabla u \cdot \nabla \delta u = \nu \int_S \alpha \left( \frac{\partial \vec{P}}{\partial n} \cdot \frac{\partial u}{\partial n} - 2 \left| \frac{\partial u}{\partial n} \right|^2 \right) d\gamma. \quad (70)$$

From equation (44) we know that :

$$\nu \int_{\delta\Omega} |\nabla u|^2 = \nu \int_S \alpha \left| \frac{\partial u}{\partial n} \right|^2 d\gamma.$$

Using (44) and (70) in (55), we find that :

$$\delta E = \nu \int_S \alpha \left( \frac{\partial \vec{P}}{\partial n} - \frac{\partial u}{\partial n} \right) \cdot \frac{\partial u}{\partial n} d\gamma. \quad (71)$$

We have proved the

**Proposition 4** : The variation of  $E$  with respect to  $\Omega$  is :

$$\delta E = \nu \int_S \alpha \left( \frac{\partial \vec{P}}{\partial n} - \frac{\partial u}{\partial n} \right) \cdot \frac{\partial u}{\partial n} d\gamma + o(\alpha)$$

□

For the chosen admissible set  $\mathcal{O}$  we have that  $\delta E \geq 0$  for every  $\alpha$  with  $\int_{\Gamma} \alpha d\gamma = 0$ .

So, the optimality condition for this problem is :  $\frac{\partial u}{\partial n} \cdot \left( \frac{\partial \vec{P}}{\partial n} - \frac{\partial u}{\partial n} \right) = \text{constant}$  on  $S$ .

We remark at the equations (60)-(62) and (51)-(54) that when  $\nu \rightarrow \infty$ , the solution  $\vec{P} \rightarrow 2u$ , so the previous result on the optimality condition for the Stokes problem is recovered. This is how far we can go without using a computer.

If we wish to use a computer in order to solve this problem, we must use a *gradient method*.

A gradient method is based on the following observation :

Suppose we have to find  $\min_{z \in \mathbb{R}^N} J(z)$ . Taylor's expansion of this function gives :

$$J(z + \delta z) = J(z) + \text{grad}_z J \cdot \delta z + o(|\delta z|), \quad (72)$$

so taking  $\delta z = -\lambda \text{grad} J(z)$ ,  $\lambda > 0$  we find :

$$J(z + \delta z) - J(z) = -\lambda |\text{grad} J(z)|^2 + o(|\delta z|), \quad (73)$$

that is if  $|\text{grad} J(z)| \neq 0$  and  $\lambda \ll 1$  we have

$$\lambda |\text{grad}J(z)|^2 \gg o(\lambda |\text{grad}J(z)|)$$

and we obtain :

$$J(z - \lambda \text{grad}J(z)) < J(z). \quad (74)$$

In other words, the sequence defined by :

$z^0$  given

$$z^{n+1} = z^n - \lambda \text{grad}J(z^n), n = 0, 1, 2, \dots$$

is such that  $J(z^n)$  converges to a local minimum of  $J(z)$ .

An improvement of the method is, with every computation of  $z^n$ , to compute

$$\lambda^n = \text{solution of } \min_{\lambda \in \mathbb{R}} J(z^n - \lambda \text{grad}J(z^n)) \quad (75)$$

and to use  $\lambda^n$  instead of  $\lambda$  to compute  $z^{n+1}$  according to (74).

We have to remark, however, that minimizing a one parameter function is not simple and is usually done by trial-and-error methods.

An *application* of a gradient method to the optimum design problem in laminar flow would be :

Start with  $S^0$ ,  $n = 0$

loop

- |                                    |  |
|------------------------------------|--|
| [                                  | 1. Solve (51)-(54) for $(u, p)$ around $S^n$   |
|                                    | 2. Solve (60)-(62) for $(\vec{P}, q)$ around $S^n$   |
|                                    | 3. Choose $\alpha = -\frac{\partial u}{\partial n} \cdot \left( \frac{\partial \vec{P}}{\partial n} - \frac{\partial u}{\partial n} \right)  _{S^n}$ |
|                                    | and take   |
|                                    | $\alpha' = \alpha - \frac{1}{ S^n } \int_{S^n} \alpha d\gamma$   |
| 4. Set $S^{n+1} = S^n + \alpha' n$ |  |
|                                    | if $\alpha$ is too small, stop   |

Notice that this algorithm achieves

$$\int_{S^n} \alpha' \frac{\partial u}{\partial n} \cdot \left( \frac{\partial \vec{P}}{\partial n} - \frac{\partial u}{\partial n} \right) d\gamma < 0. \quad (76)$$

This method also has certain difficulties.

First of all, we have to solve the Navier-Stokes equations and this is not simple because of the presence of the boundary layer where  $|u|$  has a large gradient

A boundary layer  $\Sigma$  develops around  $C$  when the Reynolds number is large. In order to solve (51)-(54) we observe that :

$$-\Delta u = \nabla \times \nabla \times u - \nabla(\nabla \cdot u) \quad (77)$$

$$u \nabla u = -u \times \nabla \times u + \nabla\left(\frac{u^2}{2}\right) \quad (78)$$

so taking :

$$p = p_\infty - \frac{|u|^2}{2}$$

$$\nabla \times u = 0$$

$$\nabla \cdot u = 0$$

will satisfy (51)-(52) but not the boundary conditions (33)-(34).

We can use however this observation to derive the following *numerical method*:

a) In  $C = \Omega - \Sigma$  find  $\phi$  such that :

$$\Delta \phi = 0 \quad (79)$$

$$\frac{\partial \phi}{\partial n} \Big|_{\Gamma_\infty} = u_\infty \cdot n \quad (80)$$

$$\frac{\partial \phi}{\partial n} \Big|_{\partial \Sigma} = 0 \quad (81)$$

b) Solve Navier-Stokes equations in  $\Sigma$  only with  $\Gamma_\infty$  replaced by  $\partial \Sigma$  and  $u|_{\partial \Sigma} = \nabla \phi|_{\partial \Sigma}$ . It can be shown that this step can be carried out by one relaxation sweep in the direction of the flow only (Prandtl's boundary layer approximation). The same method can be used for the adjoint system

Another disadvantage is that the convergence of the method has the form of figure 2 :

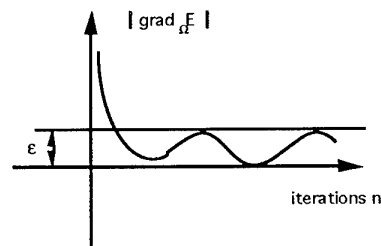


Figure 2

The functional  $E(\Omega^n)$  oscillates near the minimum. This is due to numerical noise,  $\varepsilon$ , that is the error on the computation of  $\frac{\partial u}{\partial n}|_S$  and  $\frac{\partial \bar{P}}{\partial n}|_S$ . These errors depend merely on the discretization errors of the numerical methods we used to solve Navier-Stokes and the adjoint state equations.

These errors can prevent the computation of the optimal solution below a certain precision, sometimes not so low (Figure 6).

Since we use a discretization to solve equations (51)-(54) and (60)-(62), we should change the problem and try to compute the optimality condition for the discrete problem.

More precisely, if we discretize  $\Omega$  by the points  $\{q^i\}$ ,  $i = 1, \dots, N$ , we have that  $E(\Omega)$  is approximated by  $E_h(\Omega) = E_h(q^i)$  and we have to compute the derivatives

$$\frac{\partial E_h}{\partial q_j^i}, i = 1, \dots, N, j = 1, 2 \quad (82)$$

in order to compute the variation of  $E_h$  with respect to  $\Omega$ .

An *alternative* to this computation is to use Newton's method in order to find  $S$  such that

$(u, p)$  is solution of Navier-Stokes equations

$(\bar{P}, q)$  is solution of adjoint state equations

$\frac{\partial u}{\partial n} \cdot (\frac{\partial \bar{P}}{\partial n} - \frac{\partial u}{\partial n})$  is constant

and  $\frac{\partial^2 E}{\partial \alpha^2} \geq 0$ , (because this algorithm could find a maximum instead of a minimum).

In order to introduce the discretized optimization methods, we consider a simpler problem.

### 4.3. Nozzle optimization problem

Find  $S$  such that

$$\min_{S \in \mathcal{O}} \int_D |\nabla \phi - u|^2$$

subject to :

$$-\Delta \phi = 0 \quad \text{in } \Omega \quad (85)$$

$$\frac{\partial \phi}{\partial n}|_\Gamma = g \quad (86)$$

where  $g$  is a function with  $\int_{\Gamma} g d\gamma = 0$ ,  $g|_S = 0$  and  $\Gamma = \partial\Omega$ .  
The geometry and the function  $g$  are shown in the figure 3 :

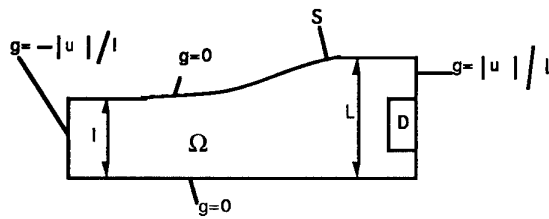


Figure 3

Figure 3 shows half of the nozzle, where the horizontal boundary is a symmetry line.

We shall derive the optimality condition using the adjoint state equation for the continuous problem first and we will give an idea of what happens in the discrete case.

Consider the variational formulation of (85) :

Find  $\phi \in H^1(\Omega)/\mathbb{R}$  such that

$$\int_{\Omega} \nabla \phi \cdot \nabla w = \int_{\Gamma} g w d\gamma, \forall w \in H^1(\Omega). \quad (87)$$

We have also :

$$\delta E = 2 \int_D (\nabla \phi - u) \cdot \nabla \delta \phi dx. \quad (88)$$

We differentiate (77) and we obtain :

$$\int_{\Omega} \nabla \delta \phi \cdot \nabla w + \int_{\delta\Omega} \nabla \phi \cdot \nabla w = 0, \quad (89)$$

because  $g|_S = 0$  and the rest of the boundary is supposed fixed.

When the perturbation of  $S$  to  $S'$  is "small", so we can write :

$$S' = \{x + \alpha n : x \in S\}$$

and we obtain :

$$\int_{\delta\Omega} \nabla \phi \cdot \nabla w = \int_S \alpha \nabla \phi \cdot \nabla w d\gamma. \quad (90)$$

We introduce the adjoint state equation :

Find  $p \in H^1(\Omega)$  such that :

$$\int_{\Omega} \nabla p \cdot \nabla w = 2 \int_D (\nabla \phi - u) \cdot \nabla w dx, \forall w \in H^1(\Omega). \quad (91)$$

Taking  $w = \delta \phi$  in (91) we find (see (88)) :

$$\delta E = \int_{\Omega} \nabla p \cdot \nabla \delta \phi \quad (92)$$

Taking  $w = p$  in (89) we find (using (90) too) :

$$\int_{\Omega} \nabla p \cdot \nabla \delta \phi = - \int_S \alpha \nabla \phi \cdot \nabla p d\gamma \quad (93)$$

and therefore :

$$\delta E = - \int_S \alpha \nabla \phi \cdot \nabla p d\gamma + o(\alpha). \quad (94)$$

We have to find an expression similar to (94) for the discrete case.

For discretization we use the *Finite Element Method* of degree 1 on triangles. More precisely, we divide  $\Omega$  in triangles and approximate  $\Omega$  by  $\Omega_h = \cup_k T_k$ , where the  $T_k$  are triangles.

The division of  $\Omega$  is such that the vertices of  $\partial \Omega_h$  belong to  $\partial \Omega$  and for the intersection of 2 triangles we allow only one of the three possibilities :

$$T_i \cap T_j = \begin{cases} \emptyset \\ \text{or 1 edge, } i \neq j \\ \text{or 1 vertex} \end{cases}$$

An admissible triangulation would be one like in figure 4.

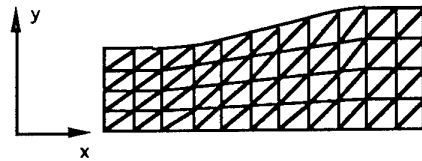


Figure 4

We consider the function space :

$$H_h = \{w_h \in C^0(\bar{\Omega}_h) : w_h|_{T_k} \in P^1\}$$

The dimension of  $H_h$  equals the number of vertices  $q^i$  of the discretization and every function  $\phi_h$  belonging to  $H_h$  is completely determined by  $\phi_h(q^i)$ .  $\square$   
 We define the hat functions :

$$w^i \in H_h$$

$$w^i(q^j) = \delta_{ij}$$

In one dimension these functions are as shown in figure 5 :

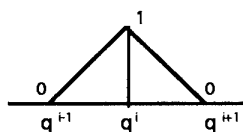


Figure 5

We have:  $H_h = \text{span}\{w^i\}$ .  $\square$

We define the discrete form of the variational formulation (87) :  
 Find  $\phi_h \in H_h$  such that :

$$\int_{\Omega} \nabla \phi_h \cdot \nabla w^j = \int_{\Gamma} g w^j d\gamma, \forall j \quad (95)$$

So, the discretized optimization problem is :  
 Find

$$\min_{S_h} \int_D |\nabla \phi_h - u|^2 = \min_{S_h} E(\Omega_h)$$

with  $\phi_h$  subject to (95),  $S_h$  discrete approximation of  $S$ .

Since we want to find  $S_h$ , the optimization parameters are the vertices  $q^j \in S_h$ .

But, if we change an internal vertex  $q^i \notin S_h$ , then  $E(\Omega_h)$  changes.

Thus, in fact,  $E(\Omega_h)$  is a function of all vertices  $q^1, \dots, q^N$ .

If we note  $E(\Omega_h) = E(q^1, \dots, q^N)$ , we have to find the derivatives

$$\frac{\partial E}{\partial q_j^i}, i = 1, \dots, N, j = 1, 2. \quad (96)$$

Let us show how the calculus of variation of  $E(\Omega_h)$  works in the discrete case.

*Calculus of variations of  $E(\Omega_h)$*

We suppose that  $q^k$  is an internal or boundary node of the triangulation and that  $q^k \notin D$  (the case  $q^k \in D$  is uselessly complicated but contains no major additional difficulties).

We move  $q^k$  to the position  $q^k + \delta q^k$ .

We write formally :

$$\delta E = 2 \int_D (\nabla \phi_h - u) \cdot \nabla \delta \phi_h dx \quad (97)$$

and from (95), we obtain by differentiation :

$$\int_{\Omega_h} \nabla \delta \phi_h \cdot \nabla w^j + \int_{\delta \Omega_h} \nabla \phi_h \cdot \nabla w^j + \int_{\Omega_h} \nabla \phi_h \cdot \nabla \delta w^j = 0 \quad (98)$$

because  $g|_S = 0$  and  $w^j$  varies if we change the triangulation (this variation gives the last integral in (78)).

We observe also that  $\delta \phi_h \notin H_h$ , because the two solutions which give the variation  $\delta \phi_h$  are not obtained in the same triangulation.

Since by definition  $\phi_h \in H_h$ , we have :

$$\phi_h(x) = \sum_{i=1}^N \phi_i w^i(x) \quad (99)$$

so

$$\delta \phi_h(x) = \sum_{i=1}^N \delta \phi_i w^i(x) + \sum_{i=1}^N \phi_i \delta w^i(x). \quad (100)$$

We call

$$\delta \tilde{\phi}_h = \sum_{i=1}^N \delta \phi_i w^i(x) \in H_h.$$

But the second sum in (100) doesn't belong to  $H_h$ .

In order to use the equation (98), we have to state the following lemmas :

**Lemma 3 :** When  $q^k$  moves to  $q^k + \delta q^k$ , then the function  $w^i(x)$  changes to  $w^i(x) + \delta w^i(x)$  with

$$\delta w^i(x) = -w^k(x) \nabla w^i \cdot \delta q^k + o(\delta q^k) \quad (101)$$

□

We can explain better Lemma 3 by referring to figure 6 :

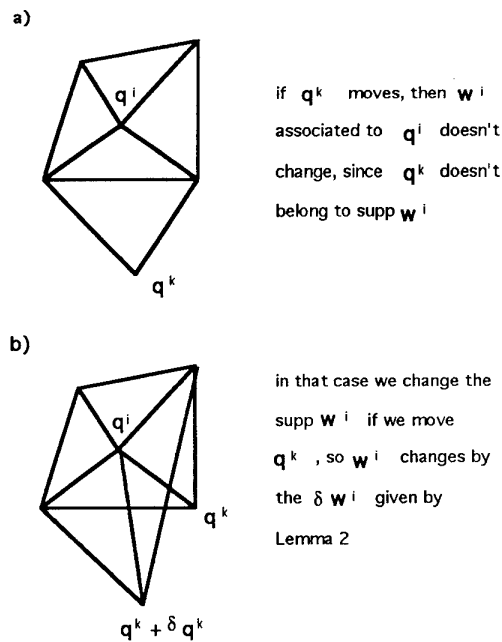


Figure 6

**Lemma 4 :** If  $f|_{T_k} \in C^1$ , then

$$\int_{\delta\Omega_h} f = \int_{\Omega_h} \delta q^k \cdot \nabla(f w^k) + o(\delta q^k), \quad (102)$$

where  $\int_{\Omega_h} f = \sum_k \int_{T_k} f$  by definition.  $\square$

For the proof of these two lemmas, see O. Pironneau (1984)

The previous lemmas allow to compute all the integrals in (98) and to obtain an expression for  $\delta E(\Omega_h)$ , if we define the (discrete) adjoint state equation : Find  $p_h \in H_h$  such that

$$\int_{\Omega} \nabla p_h \cdot \nabla w^j = 2 \int_D (\nabla \phi_h - u) \cdot \nabla w^j, \quad \forall j. \quad (103)$$

We can prove that the discrete variation of  $E(\Omega_h)$  is given by the following

**Theorem** When  $q^k$  moves to  $q^k + \delta q^k$ , the  $E(\Omega_h)$  varies by

$$\begin{aligned}
\delta E(\Omega_h) &= \int_{\Omega} (\nabla \phi_h \cdot \nabla w^k)(\nabla p_h \cdot \delta q^k) & (84) \\
&+ \int_{\Omega_h} (\nabla w^k \cdot \nabla p_h)(\nabla \phi_h \cdot \delta q^k) dx - \\
&\int_{\Omega_h} (\nabla \phi_h \cdot \nabla p_h)(\nabla w^k \cdot \delta q^k) dx + o(\delta q^k).
\end{aligned}$$

□

According to the theorem, we can write

$$\delta E = \chi^k \cdot \delta q^k \quad (105)$$

and therefore a *gradient method* is :

Change  $q^k$  to  $q^k - \lambda \chi^k$ , with  $\lambda \simeq$  optimum step size. Stop when  $\chi^k \simeq 0, \forall k$ .

## 5. PROBLEMS CONNECTED WITH THE NUMERICAL IMPLEMENTATION.

### 5.1 Independence from E

Note that the adjoint state  $p$  depends on the criterion  $t$ . On the other hand if the software is to be provided as a black box to the industry it must be such that it is easy to :

- change the design criterion
- add geometrical constraints.

Suppose that we minimize a functional of the general form :

$$E(\phi, \Omega) = \int_D f(\phi) dx, \quad \phi = \{\phi^j\}, j = 1, \dots, r. \quad (106)$$

Since the second member of the adjoint state equation(103) is  $\delta E$ , we must be able to compute  $\frac{\partial E}{\partial \phi_j}$  independently of  $E(\phi, \Omega)$ .

This computation can be done by finite differences because :

$$\frac{\partial E}{\partial \phi_j} \simeq \frac{E(\phi_h + \delta \phi_h u^j, \Omega_h) - E(\phi_h, \Omega_h)}{\delta \phi_j} \quad (107)$$

This computation is not expensive. The number of elementary computations is of order  $N$ . Indeed, if  $N$  is the number of the mesh nodes, the calculation

cost is of the order  $N$ , which is the same cost as the solution of a laplacian (cf. Arumugam(1989)).

### 5.2 Add geometrical constraints

To add geometrical constraints is easy if we give a parametrized description of the domain and its triangulation.

If the boundary to optimize is described by  $r$  parameters  $\alpha_j$ , we can define it by a curve (ex. spline) defined by  $\alpha_j$  and then generate the triangulation with vertices  $\{q^i\}$ ,  $i = 1, \dots, N$  on the curve.

Since in this case only the parameters  $\alpha_j$  move independently, we must compute the variation of  $E$  with respect to  $\alpha_j$ . But

$$\frac{\partial E}{\partial \alpha_j} = \sum_{k,i} \frac{\partial E}{\partial q_i^k} \cdot \frac{\partial q_i^k}{\partial \alpha_j}, i = 1, \dots, N, k = 1, 2. \quad (108)$$

Therefore, we must be able to compute  $\frac{\partial q_i^k}{\partial \alpha_j}$  and this is done also by finite differences :

$$\frac{\partial q_i^k}{\partial \alpha_j} \simeq \frac{q_i^k(\alpha_j + \delta \alpha_j) - q_i^k(\alpha_j)}{\delta \alpha_j} \quad (109)$$

which is not computationally expensive.

**Remark :** One could think that we can compute everything by finite differences, even

$$\frac{\partial E}{\partial q_i^k} \simeq \frac{E(q_i^k + \delta q_i^k) - E(q_i^k)}{\delta q_i^k} \quad (110)$$

but this is far too expensive, since we have to solve the state equation every time we compute  $E(q_i^k)$ . So, the computational cost of (100) is  $2N * O(N) \simeq O(N^2)$  which is the cost of solution of  $N$  partial differential equations.

### 5.3 Other discretization methods

We have shown above that the finite element method is well suited to Optimal Shape Design because the same principles can be used on the discrete system. In Brackman (1987) and Makinen (1990) an extension to Iso-parametric elements can be found. Chenais (1993) shows also that with Cea's artificial domain velocity it is possible to have the discrete derivatives equal to the continuous derivatives discretized. Finally Finite Volume methods computations of derivatives can be found in Dervieux (1993).

### 5.4 Automation of the computations.

Computation of derivatives of functional is, as we have seen a lengthy and crafty work. Further very often it is found in practice that the criteria must be changed and adapted to the problem because the solution found do not satisfy a forgotten constraint or because of instabilities with respect to data. Each time the computation must be done again!

One way out, as we have said is to work with Quasi-Newton methods on the optimality conditions rather than on gradient algorithm for the minimization problem. Then it is no longer important that the derivative of the discrete problem be exact. It suffices to discretize the derivative of the continuous problem.

With the GMRES algorithm ( Saad (1986), our experience is that this second method works well when the problem is not too stiff like inverse problem (Vossinis (1992)). For the minimum drag problem on the Navier-Stokes equations it failed .

We have also explained above that it is possible to use a finite difference formula for the terms which change often, i.e; the cost function and some part of the constraints. It is not possible to use it to find the adjoint equation. There the only hope is automatic differentiation as shown below.

### 5.5 Remeshing.

Working in the physical domain with changing shapes requires remeshing. The possible approaches.

1. A Delaunay-Voronoi automatic mesh generator is used at each step. Though the motion of inner vertices affects the derivatives (it can be computed by finite differences) these effects are small usually.
2. The inner vertices are linked to the outer vertices. From the programming point of view this is usually hard. It means that the mesh generator is fully parametrized.
3. The motion of the inner vertices is linked to the motion of the outer ones (Marrocco et al (1978) ):

$$\delta q^i = \frac{\sum_k \frac{\delta q^k}{\|q^i - q^k\|}}{\sum_k \|q^i - q^k\|^{-1}}. \quad (111)$$

where  $q^k$  is a boundary vertex and  $q^i$  is an inner vertex.

It is wise also to test that no triangle area becomes negative in the motion. This is the easiest and also best method in most cases (even in 3D).

### 5.6 Computation of the adjoint equation by differentiation by program.

Usually the computer program for the flow solver is written before hand and the optimal shape design analysis comes after.

The idea is to say that the PDE is known from a long sequence of equalities each of which is easy to differentiate. If each program line is thus differentiated a linearized flow solver is found. Then an adjoint equation is easier to found.

A review article on these methods can be found in (Gilbert et al (1991) for example).

Consider the equation

$$-\frac{d^2u}{dx^2} + \sin u = 1, \quad \forall x \in ]0, 1[, \quad u(0) = u(1) = 0, \quad (112)$$

discretized by the finite difference method :

$$\begin{aligned} u_0 &= 0 \\ u_N &= 0 \\ \text{do } i &= 1..N - 1 \\ &v_i = \sin u_i \\ &N^2(2u_i - u_{i+1} - u_{i-1}) + \sin u_i = 1 \\ \text{end\_do.} \end{aligned} \quad (113)$$

As is often the case, while programming, the intermediate variable  $v_i$  is introduced.

A DO loop being in fact identical to a long sequence of program statement let us introduced a lagrange multiplier for each line and construct the Lagrangian:

$$L = p_0 u_0 + p_2 u_N + \sum_1^{N-1} p_{i+1} (v_i - \sin u_i) + N^2 p_{N+i} (2u_i - u_{i+1} - u_{i-1} + v_i - 1) \quad (114)$$

This Lagrangian contains only simple function so it can be differentiated with respect to  $u$  and  $v$  by any formal computation program (Maple, Mathematica...)

Thus the adjoint program is obtained:

$$\begin{aligned} \frac{\partial L}{\partial u_0} &= p_0 - p_{N+1} \\ \frac{\partial L}{\partial u_i} &= -p_{i+1} \cos u_i + N^2(2p_{N+i} - p_{N+i-1} - p_{N+i+1}) \\ \frac{\partial L}{\partial u_N} &= p_2 - p_{N+i-1} \\ \frac{\partial L}{\partial v_i} &= p_{i+1} + p_{N+i} \end{aligned} \quad (115)$$

This way the left hand side of the adjoint equation can be computed and all can be automatized. The limit of the method is the memory of the computer. Branching instructions are no problem. Consider the case where  $\sin u$  is replaced by  $\sin |u|$  and programmed as

$$\begin{aligned} \text{if } u_i > 0 \text{ then } v_i &= \sin u_i \\ \text{else } v_i &= \sin(-u_i) \end{aligned} \quad (116)$$

Then there will be two Lagrangian and after differentiation one will obtain

$$\begin{aligned} \text{if } u_i > 0 \text{ then } \frac{\partial L}{\partial u_i} &= -p_{i+1} \cos u_i + N^2(2p_{N+i} - p_{N+i-1} - p_{N+i+1}) \\ \text{else } \frac{\partial L}{\partial u_i} &= -p_{i+1} \cos(-u_i) + N^2(2p_{N+i} - p_{N+i-1} - p_{N+i+1}) \end{aligned} \quad (117)$$

#### REFERENCES.

Y. Achdou, O. Pironneau: Optimization of a photocell. *J. Optimal Control and Appl.* (a paraitre)

Y. Achdou: Numerical optimization of a photocell. *Comp. Meth. in Applied Mech. and Eng.* (to appear)(a paraitre).

Y. Achdou: Effect of a metallized coating on the reflection of an electromagnetic wave. *Note CRAS* (1992).

G. Anagnostou, E. Ronquist, A. Patera: A computational procedure for part design. *Comp. Methods Applied Mech and Eng.* July (1992).

F. Angrand: Numerical methods for optimal shape design in aerodynamics, Thesis in French, Univ. Paris 6, (1980).

M. Artola, M. Cessenat: Propagation des ondes electromagnetiques dans un milieu composite. *note CRAS* 311(1):77-82, (1990).

G. Arumugam: Optimum design et applications a la mecanique des fluides. *Universite Paris 6 These.* 1989.

G. Arumugam, O. Pironneau : On the problems of riblets as a drag reduction device, *Optimal Control Applications & Methods*, Vol. 10, (1989).

- N.V. Banichuk: *Introduction to optimization of structures*. Springer (1990).
- D. Begis, R. Glowinski: Application of FEM to approximation of an optimum design problem. *Appl. Math. Optim* 2(2) (1975).
- F. Beux, A. Dervieux: Exact-gradient shape optimization of a 2D Euler flow. INRIA report 1540 (1991).
- M. Crouzeix: Variational approach of a magnetic shaping problem. *Eur. J. Mech B/fluids* 10, 5:527-536 (1991).
- J. Cea: Conception optimale ou identification de forme: calcul rapide de la dérivée directionnelle de la fonction cout. *Modélisation Math Anal, AFCET*, Dunod (1986).
- J. Cea, A.Gioan, J. Michel: Some results on domain identification. *Calcolo* 3/4 (1973).
- D. Chenais: Shape optimization in shell theory. *Eng. Opt.* 11:289-303 (1987).
- J.C. Gilbert, G. Le Vey, J. Masse: La différentiation automatique des fonctions représentées par des programmes. INRIA report 1557 (1991).
- J. Haslinger, P. Neittaanmäki: *Finite element approximations for optimal shape design*. Wiley 1989.
- E.J. Haug, J. Cea: *Optimization of distributed parameter structures* vol I and II, Sijthoff and Noordhoff (1981).
- A. Jameson: Automatic design of transonic airfoils to reduce the shock induced pressure drag. Proc. 31st Israel Annual conf on aviation and aeronautics. Feb 1990.
- W.G. Litvinov: The problem of the optimal shape of an hydrofoil. *J Optimization, theory and appl.* (to appear)
- J. Hadamard: *Lecon sur le calcul des variation*. Gauthier-Villards (1910)
- R. Mäkinen: Finite Element design sensitivity analysis for non linear potential problems. *Comm Applied Numer Methods*. 6:343-350 (1990).
- A. Marrocco, O. Pironneau: Optimum design with Lagrangian Finite Element. *Comp. Meth. Appl. Mech. Eng.* 15-3 (1978).

- M. Masmoudi: Conception de circuit passif de très haute fidélité. Matapli no 31 (1990).
- F. Moens: Réalisation d'une méthode d'optimisation numérique pour la définition de profils hypersustentés. Rapport ONERA 43/1736, 1991.
- F. Murat, J. Simon: Etude de problèmes d'optimum design. Proc. 7th IFIP conf. Lecture notes in Computer sciences, 41, 54-62, 1976.
- P. Neittaanmäki, A. Stachurski: Solving some optimal control problems using the Barrier Penalty function method. Appl Math Optim 25:127-149 (1992)
- P. Neittaanmäki: Computer aided optimal structural design Surv. Math. Ind. 1:173-215, 1991.
- O. Pironneau: On optimal shapes for Stokes flow. J. Fluid Mech, (1973).
- O. Pironneau: "*Optimal shape design for elliptic systems*", Springer-Verlag, (1984).
- B. Rousselet: Shape design sensitivity of a membrane. J Optimization Theory and appl. 40, 4:595-623 (1983).
- S. Ta'asan, G. Kuruvila: Aerodynamic Design and optimization in one shot. AIAA paper 92-0025
- L. Tartar: Control problems in the coefficients of PDE. In Lecture notes in Economics and Math systems. A. Bensoussan ed. Springer, (1974).
- A. Vossinis : Optimization Algorithms for Optimum Shape design problems (to appear).
- G. Volpe: Geometric and surface pressure restrictions in airfoil design. AGARD report 780 (1990).
- D. Young, R. Melvin, F. Johnson, J. Bussioletti, L. Wigton, S. Samant: Application of sparse matrix solvers as effective preconditionners. SIAM J. Sci. Stat. Comput. 10-6:1118-1199, (1989).
- J.P. Zolesio: Les dérivées par rapport au noeuds des triangulations et leurs utilisations en identification de domaines. Ann, Sc. Math, Quebec 8, 97-120, (1984).

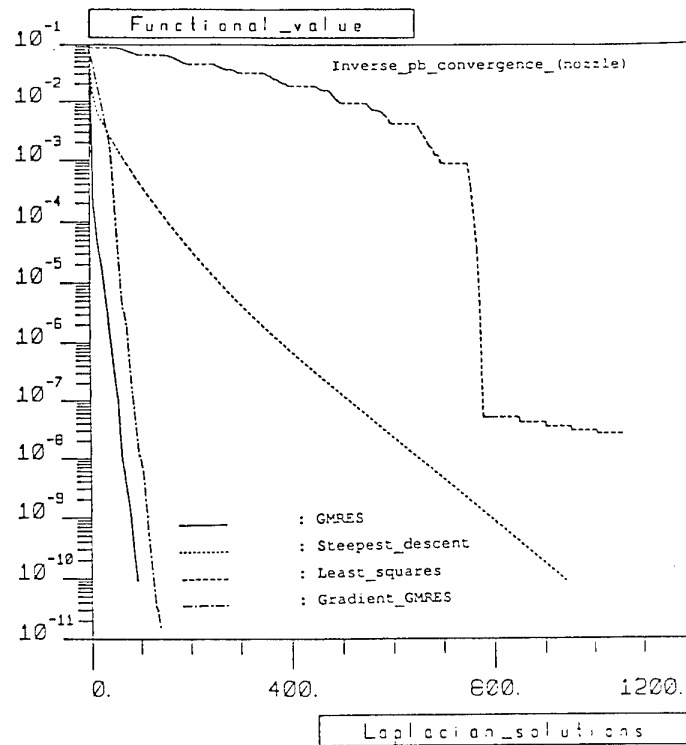
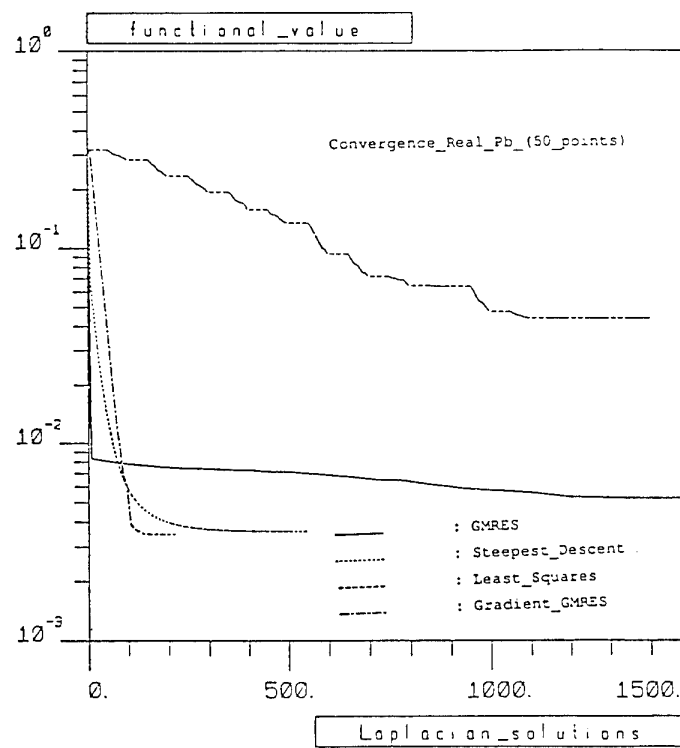


Figure 7 Nozzle optimization with 50 optimization parameters. Convergence comparison for an inverse problem



from A. Vossinis

Figure 8 Nozzle optimization with 50 optimization parameters. Convergence comparison for a real problem

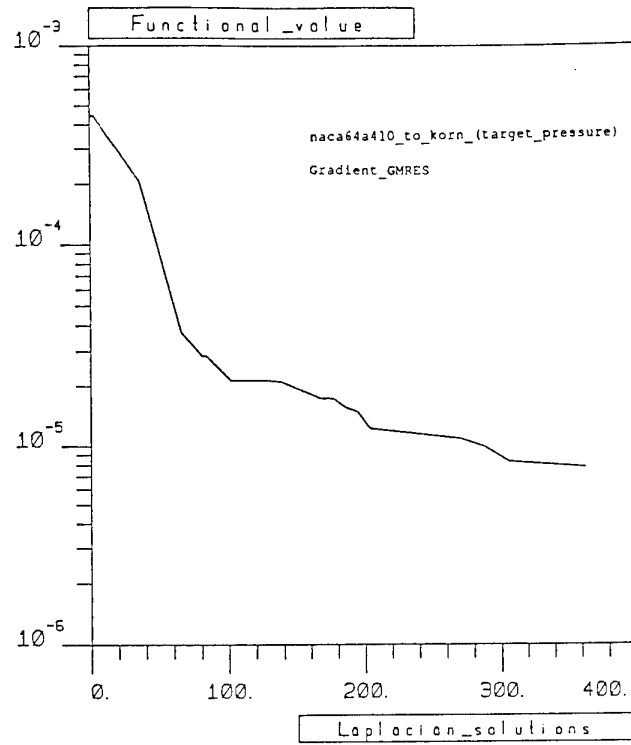
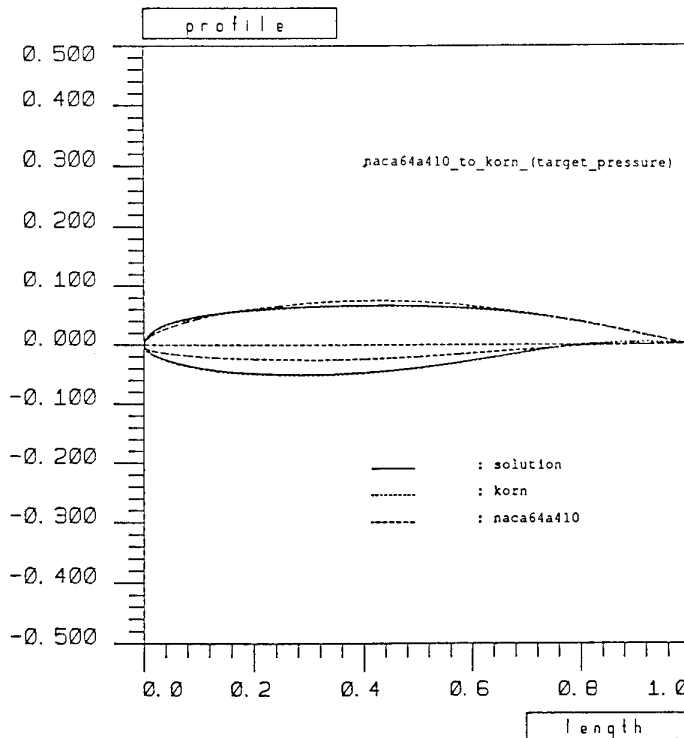


Figure 9 Pressure recovery inverse problem in incompressible flow, initial airfoil NACA64A410, final Korn's airfoil. Airfoil optimization with 20 optimization parameters. Convergence of Gradient-GMRES



from A. Vossinis

Figure 9 Pressure recovery inverse problem in incompressible flow, initial airfoil NACA64A410, final Korn's airfoil. Airfoil optimization with 20 optimization parameters. Airfoil convergence

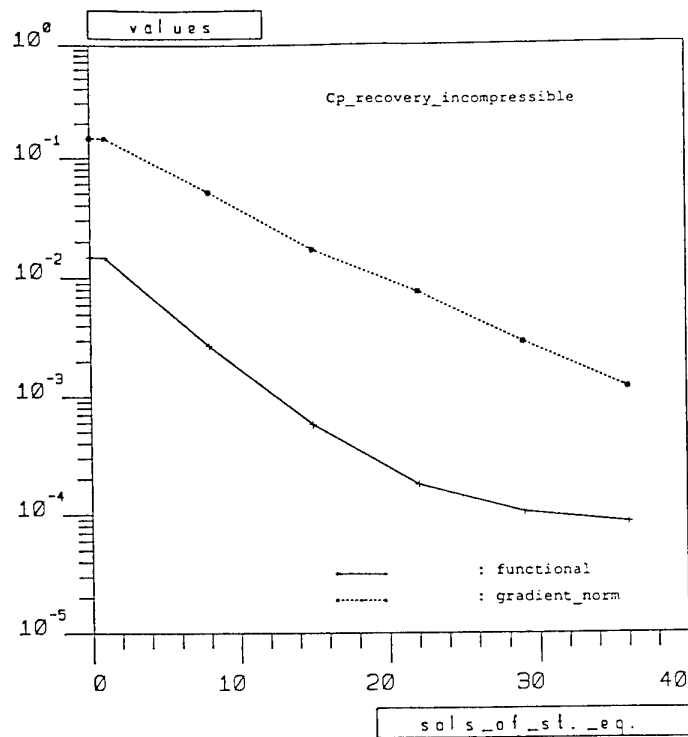
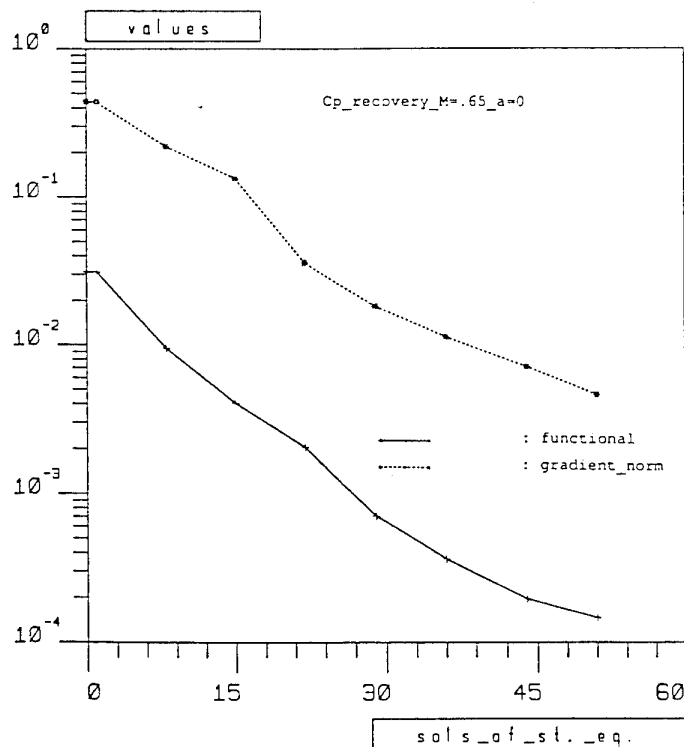


Figure 10. Cp recovery inverse problem, incompressible flow, angle of attack=0, initial airfoil NACA64A410, final Korn's airfoil. Functional and gradient norm convergence vs nb of functional calls



from A. Vossinis

Figure 11. Cp recovery inverse problem,  $M_\infty = .65$ , angle of attack=0, initial airfoil NACA64A410, final Korn's airfoil. Functional and gradient norm convergence vs nb of functional calls

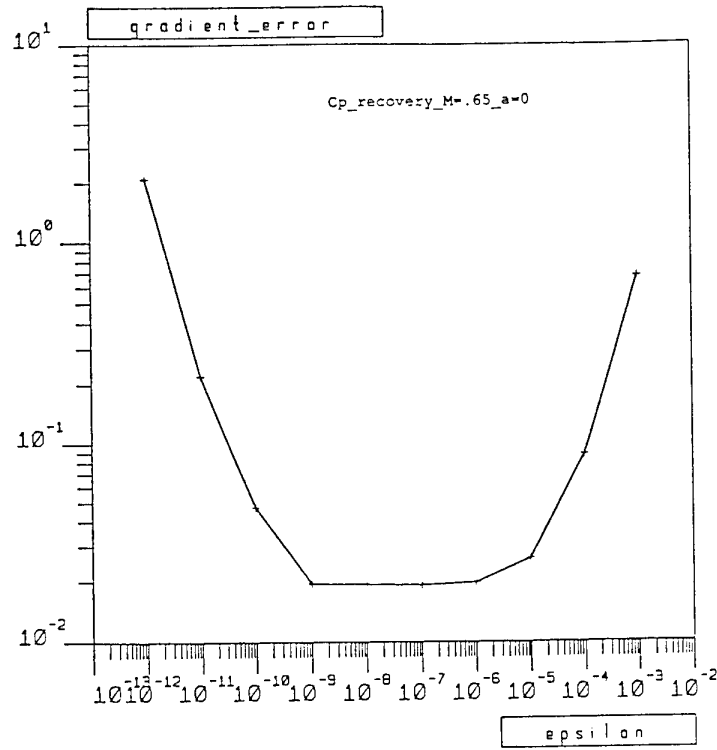
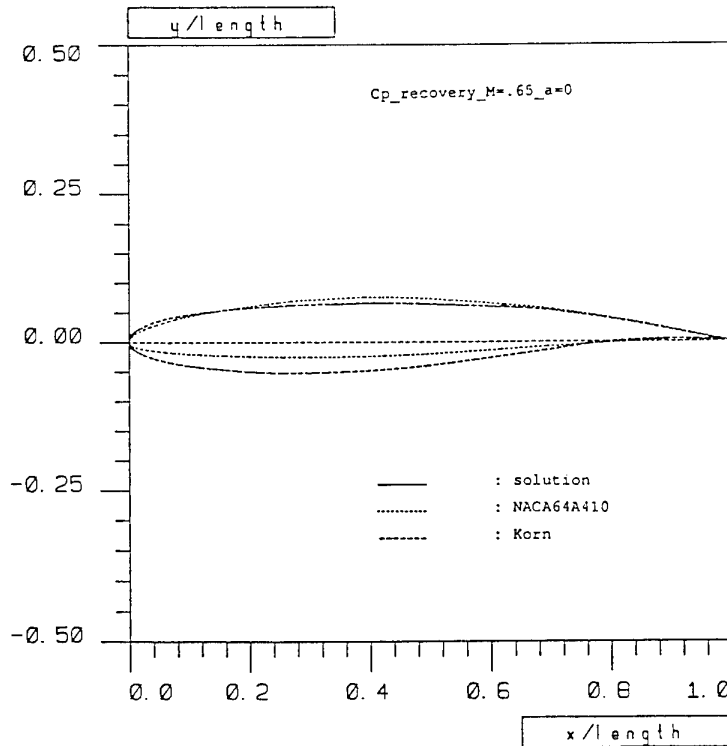


Figure 12.: Cp recovery inverse problem,  $M_\infty = .65$ , angle of attack=0, initial airfoil NACA64A410, final Korn's airfoil. Exact and Finite Differences gradient error



from A. Vossinis

Figure 13. Airfoil convergence for incompressible and compressible flow

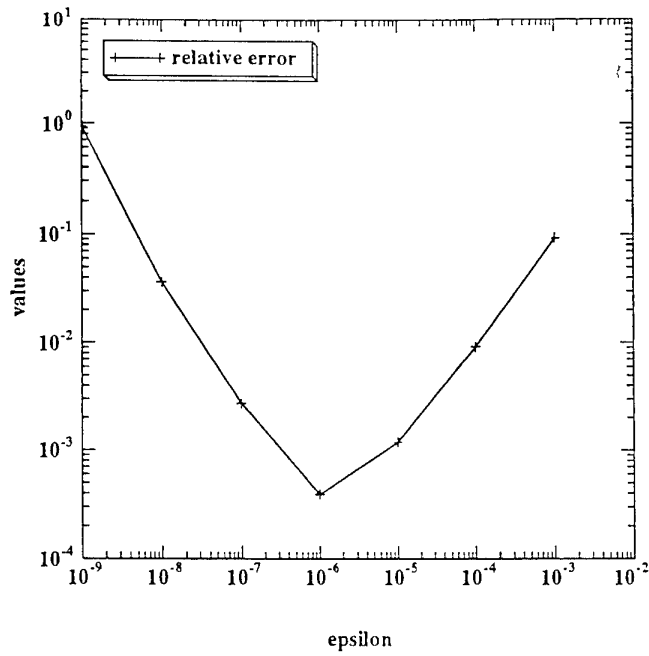
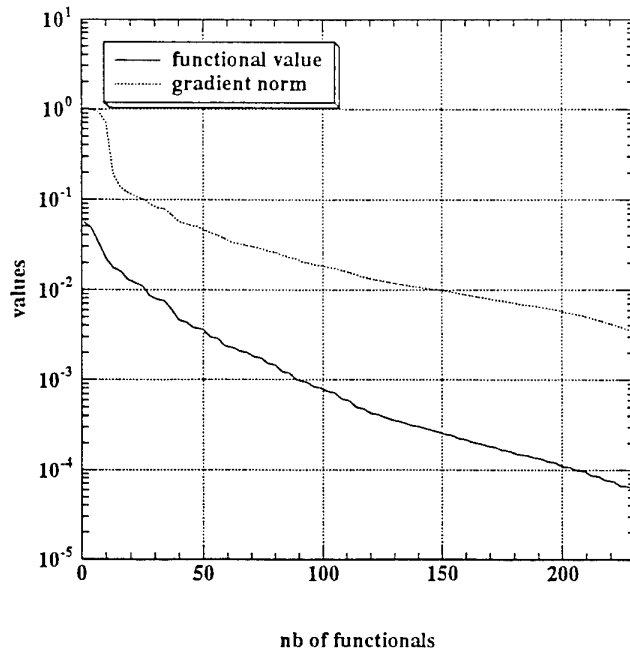


Figure 14 Cp recovery inverse problem,  $M_\infty = .75$ , angle of attack=0, initial airfoil NACA64A410, final Korn's airfoil. Relative error of functional gradient



from A. Vossinis

Figure 15 Cp recovery inverse problem,  $M_\infty = .75$ , angle of attack=0, initial airfoil NACA64A410, final Korn's airfoil. Functional and gradient convergence

from A. Vossinis

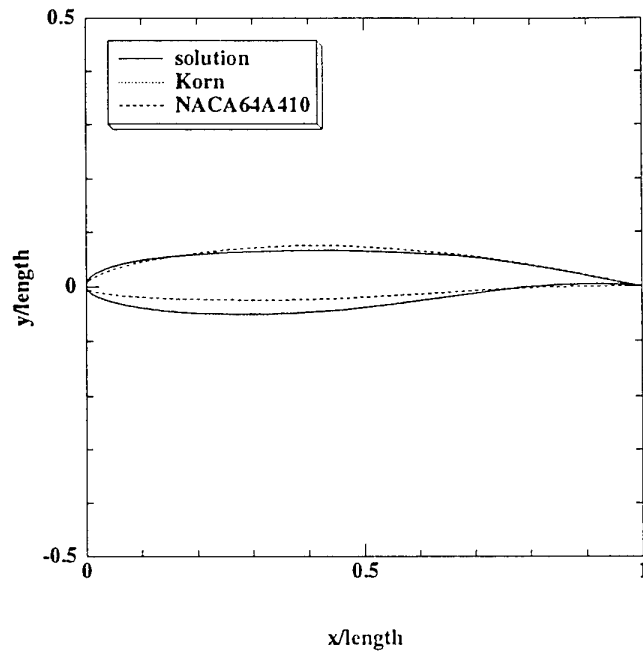


Figure 16 Cp recovery inverse problem,  $M_\infty = .75$ , angle of attack=0, initial airfoil NACA64A410, final Korn's airfoil. Airfoil convergence

## Stealth Airplane

optimisation

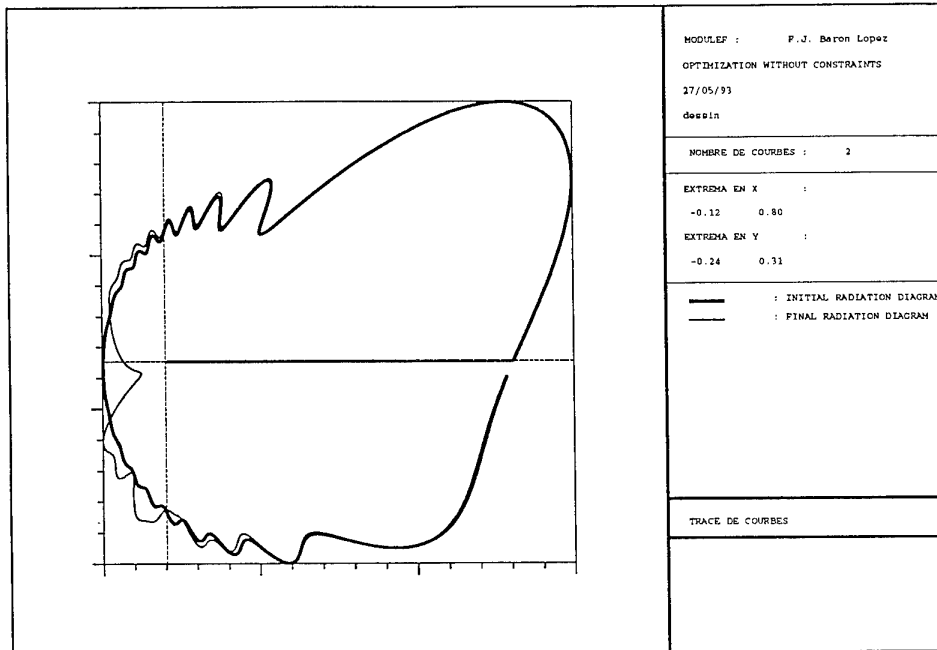


Figure 17.7: Initial and final SER. Weakly constrained

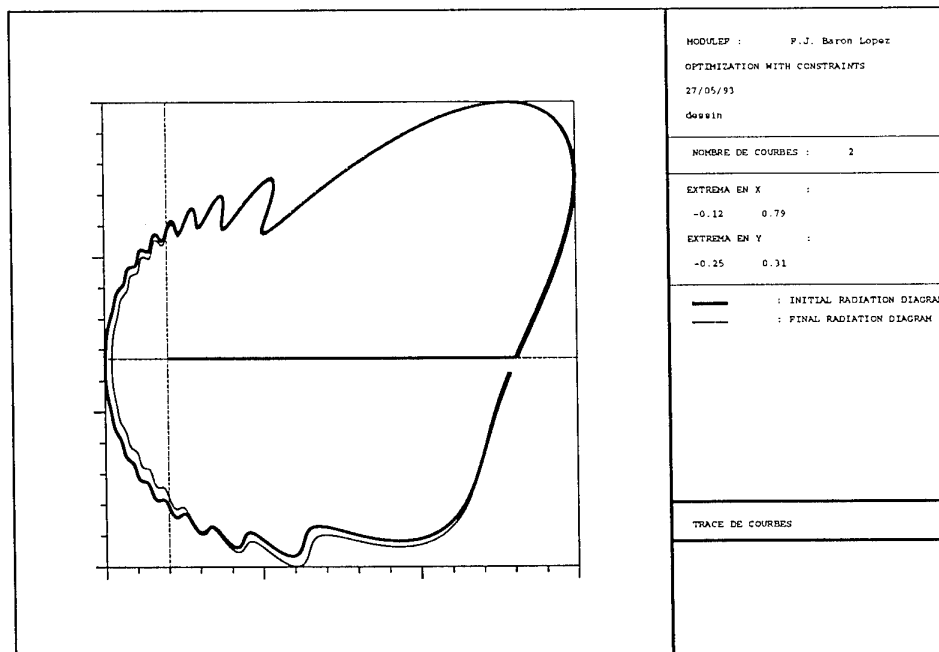


Figure 17.8: Initial and final SER. Strongly constrained

from A. Baron

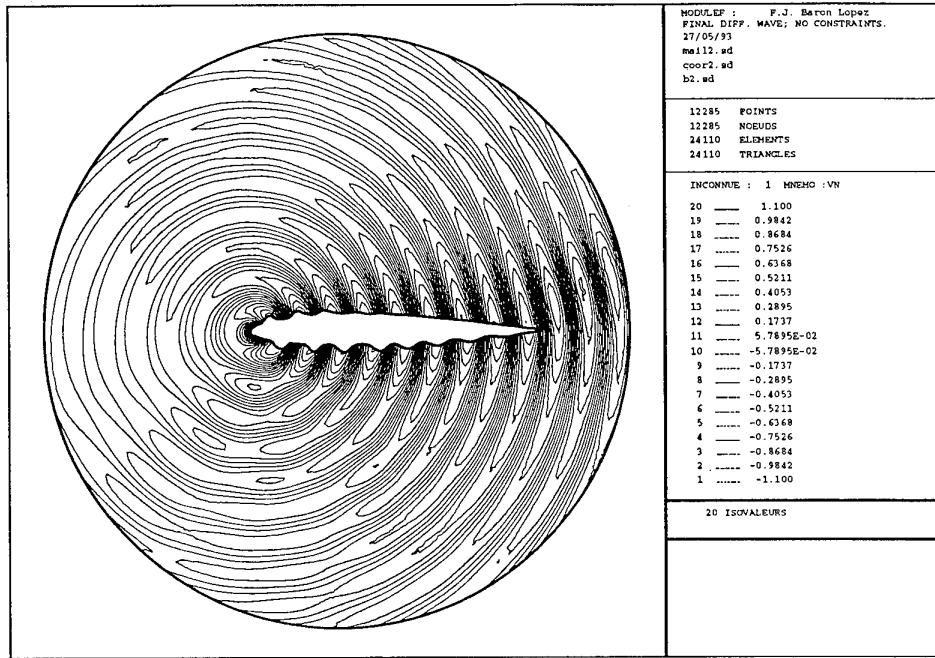


Figure 19: Final diffracted wave. Weakly constrained

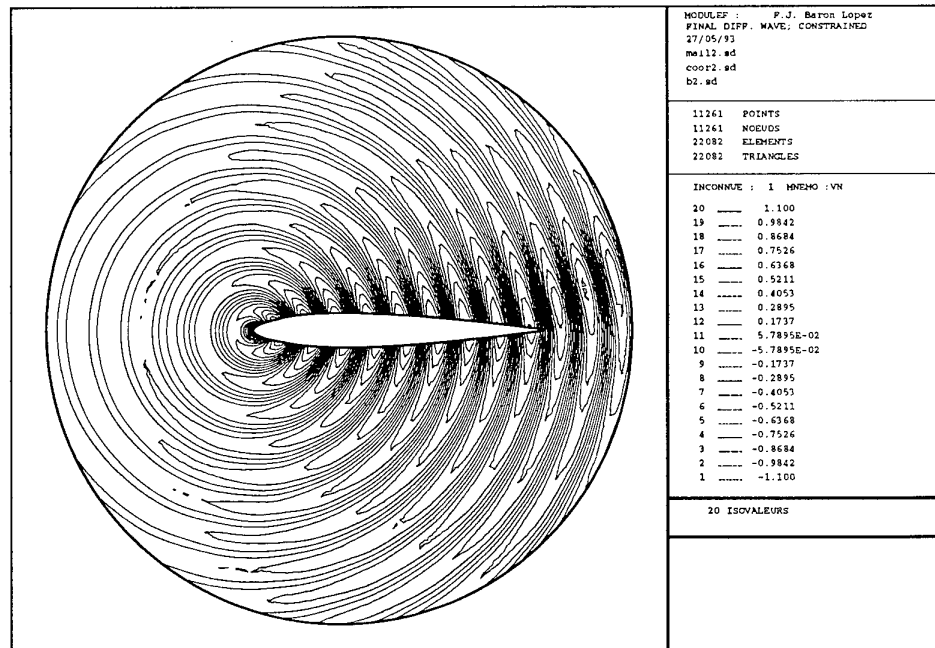


Figure 20: Final diffracted wave. Strongly constrained

from A. Baron

## Airfoil Optimization by the *One-Shot* Method

G. Kuruvila\*  
ViGYAN, Inc.  
Hampton, VA 23666-1325  
USA

Shlomo Ta'asan†  
Institute for Computer Applications in Science and Engineering  
Hampton, VA 23681-0001  
USA

M. D. Salas‡  
NASA Langley Research Center  
Hampton, VA 23681-0001  
USA

### SUMMARY

An efficient numerical approach for the design of optimal aerodynamic shapes is presented in this paper. The objective of any optimization problem is to find the optimum of a cost function subject to a certain state equation (Governing equation of the flow field) and certain side constraints. As in classical optimal control methods, the present approach introduces a costate variable (Lagrange multiplier) to evaluate the gradient of the cost function. High efficiency in reaching the optimum solution is achieved by using a multigrid technique and updating the shape in a hierarchical manner such that smooth (low-frequency) changes are done separately from high-frequency changes. Thus, the design variables are changed on a grid where their changes produce nonsmooth (high-frequency) perturbations that can be damped efficiently by the multigrid. The cost of solving the optimization problem is approximately two to three times the cost of the equivalent analysis problem.

### LIST OF SYMBOLS

$C_p$	pressure coefficient
$F$	cost function
$f_k$	$k$ th shape function
$i$	unit vector in $x$ -direction
$j$	unit vector in $y$ -direction
$M_\infty$	free stream Mach number
$n$	unit normal
$t$	unit tangent
$U_\infty$	free stream velocity
$y^{U,L}$	$y$ -coordinate of the upper and lower surface of the airfoil
$\alpha$	amplitude of shape functions (design variables)
$\bar{\alpha}$	direction of change of $\alpha$
$\alpha_k^{U,L}$	components of $\alpha$ (upper and lower surface amplitudes of the $k$ th shape function)
$\Gamma$	circulation
$\gamma$	ratio of specific heats
$\epsilon$	magnitude of change of $\alpha$
$\zeta$	angle of attack

$\Theta$	$\theta$ corrected for Mach number
$\theta$	angular position of a far-field location
$\lambda$	Lagrange multiplier
$\mu_k$	$k$ th component of the gradient of $F$
$\rho$	density
$\phi$	full velocity potential
$\phi_0$	target potential
$\Upsilon$	coefficient of the delta function

### 1. INTRODUCTION

Analysis of flow fields using computational fluid dynamics (CFD) has come a long way. Today, accurate computation of the flow field around realistic aircraft configurations using the Navier Stokes equations with turbulence modeling can be done at affordable cost and reasonable turnaround time. Design and optimization of aircraft configurations, on the other hand, is far from this level of maturity. In the last two decades, many different techniques have been developed to design aerodynamically better aircraft. These techniques can be classified into three broad categories, namely inverse design methods, loosely coupled optimization (LCO), and tightly coupled optimization (TCO).

The inverse design method,<sup>1-6</sup> pioneered by Lighthill, requires a priori knowledge of a desirable pressure or velocity distribution and some strategy for obtaining a shape that produces this distribution. The quality of the shape obtained from the inverse design method is strictly a function of the distribution it is required to match. Therefore, a weakness of this approach is its dependence on the experience and knowledge of the designer to establish desirable velocity or pressure distributions. In addition, the method does not lend itself to the imposition of constraints.

In the LCO approach, an analysis code interacts with a numerical optimization code to find a shape that meets some design objective (i.e., minimizes some cost function). To achieve this goal, the analysis problem is solved many times to find the best combination of perturbations to the design variables that both minimizes the cost function and satisfies the constraints. This process is repeated until the cost function cannot be further reduced. Examples of this approach are found in Refs. 7-10. The approach can be viewed as a two part process: an inner loop that finds both a direction and a step size to update the design variables and an outer loop that repeats the inner loop until the cost function reaches a minimum. If each inner-loop pass requires  $N$  solutions of

\* Research Engineer

† Senior Scientist

‡ Chief Scientist, Fluid Mechanics and Acoustics Division

the analysis problem (where  $N$  is proportional to the number of design variables) and the outer loop requires  $C$  iterations (where  $C$  depends on how far the initial conditions are from a minimum), then the cost of this approach is approximately  $N \times C$  times the cost of the analysis problem. The LCO method can be improved by analytically evaluating the sensitivity derivatives needed to update the design variables.<sup>11</sup> Usually this requires the inversion of a very large matrix. For three-dimensional problems, the size of this matrix can render the method impractical with current computer technology.

Even greater efficiency can be achieved through a TCO method. With this method, the optimization and analysis problems are attacked simultaneously. The TCO problem requires the solution of an adjoint problem equivalent in complexity to the analysis problem. This results in an overall cost that is proportional to  $2C$ . The factor of 2 results from doubling the number of equations that govern the problem. This approach has been discussed in Ref. 12. Even this procedure can become prohibitively expensive for practical aerodynamic design and optimization problems.

The *One-Shot* method<sup>13,14</sup> overcomes the unacceptable cost of the existing design and optimization procedures. It brings the cost of design and optimization to the same order as that of a single analysis. High performance is achieved by exploiting the property of the partial differential equations (associated with the scales (frequency) of the errors) which govern the physics of the flow and by the efficient damping out of high-frequency error components with multigrid. Consider the subsonic flow over an airfoil profile. The change in the shape of the profile of a given wavelength produces changes of the same wavelength in the solution. These changes penetrate into the flow field only up to a distance that is proportional to the wavelength of the perturbation. Thus, while the high-frequency changes in the shape of the airfoil produce changes in the solution that are of high frequency and remain local to the neighborhood of the airfoil, the smooth (low-frequency) changes in the shape produce smooth changes to the solution and are global in nature. Typically, any relaxation scheme quickly damps the high-frequency components of the error on a grid. Multigrid efficiently damps the whole spectrum of error components by relaxing the governing equations on a sequence of grids of varying resolution.

Therefore, the basic idea of the *One-Shot* method is to change the shape of the airfoil profile in a hierarchical manner such that smooth changes are made separately from high-frequency changes. Because each of these changes involves a different scale, the governing equation of the flow field can be solved efficiently on grids of appropriate resolution. Thus, the flow field due to smooth changes in the shape of the airfoil is solved on coarse grids, and the flow field due to increasingly high-frequency shape changes is solved on increasingly fine grids. This breaks the optimization procedure into a sequence of suboptimization problems, each of a given scale; therefore, the problem is well conditioned. The resulting optimization procedure is very efficient because the work on a particular scale is done on the appropriate grid. (All conditioning results from working on many scales simultaneously.) The *One-Shot* method is implemented within a full approximation scheme (FAS) full multigrid (FMG) algorithm. The solution process starts on the coarsest grid, where only the smooth component of the shape function is updated. This solution is interpolated to the next finest grid, where it serves as an initial approximation of the solution on that grid. This process is continued until the finest grid is reached. Thus, smooth (low-frequency) shapes are updated on coarse grids; high-frequency shapes

are updated on finer grids. The fine- to coarse-grid transfers are designed such that the optimization problem at each grid level is driven by the fine-grid residual. The resulting algorithm has an estimated overall cost that ranges from two to three times the cost of the analysis problem.

The successful application of the *One-Shot* method to the aerodynamic shape design problem was first reported in Ref. 14. The capability of the method was demonstrated by using the small-disturbance potential equation as the governing equation of the flow field. However, in that study, the issue of updating the grid was avoided. In the present study, the full potential equation is used as the governing equation; hence, the grid must be updated as the shape changes. In this work, the adjoint equation and the corresponding gradient of the cost function are derived. The solution procedure and some typical results are also presented.

## 2. CONSTRAINED MINIMIZATION PROBLEM

A general constrained minimization problem can be stated as

$$\min_{b, Q} F[b, Q(b)] \quad (2.1)$$

subject to

$$R[b, Q(b)] = 0 \quad (2.2)$$

and

$$C_n[b, Q(b)] \leq 0 \quad (n = 1, 2, \dots, N) \quad (2.3)$$

where  $F$  is the cost function;  $b$  the design variables; and  $Q$ , the state variables. The set of state equations is denoted by  $R$  and the side constraints are denoted by  $C_n$ ;  $C_n$  is referred to as a side constraint because the state equation is considered to be the primary constraint of the problem.

In aerodynamic minimization problems, the cost function is, for example, the drag coefficient  $C_d$  or the ratio of drag to lift  $C_d/C_l$ . The design variables are, typically, the shape parameters that define the shape of the body in the flow field. The state equations are the governing equations of the flow field and their boundary conditions. Depending on the level of fidelity of the mathematical model, the governing equations are the Navier-Stokes equations, the Euler equations, or the potential equations. The side constraints are either geometric constraints like the maximum thickness of the airfoil section, the volume of the wing, or aerodynamic constraints like maximum lift ( $\max C_l$ ).

### 2.1 The Necessary Conditions

The objective of the minimization problem is to find  $b^*$  and the corresponding  $Q^*$  such that  $F(b^*, Q^*)$  is a minimum and the state equations and the side constraints are satisfied. A necessary condition for  $b^*$  to be at a minimum is

$$\nabla_b F(b^*, Q^*) = 0 \quad (2.4)$$

where

$$\nabla_b F \equiv \frac{\partial F}{\partial b} + \left( \frac{dQ}{db} \right)^T \frac{\partial F}{\partial Q} \quad (2.5)$$

( $\nabla_b F$  will be referred to as the gradient of  $F$ ). This necessary condition can be proved by contradiction as follows. The

Taylor-series expansion of  $F$  in the neighborhood of  $b^*$  and  $Q^*$  can be written as

$$F(b^* + \varepsilon \bar{b}, Q^* + \varepsilon \bar{Q}) = F(b^*, Q^*) + \varepsilon \bar{b}^T \nabla_b F(b^*, Q^*) + O(\varepsilon^2) \quad (2.6)$$

where  $\varepsilon$  is a positive scalar and  $\bar{b}$  is a vector;  $\varepsilon \bar{b}$  is the change in  $b^*$ , and  $\varepsilon \bar{Q}$  is the corresponding change in  $Q^*$  that satisfies the state equations and the side constraints. If  $\nabla_b F(b^*, Q^*)$  is nonzero, then a vector  $\bar{b}$  must exist for which

$$\bar{b}^T \nabla_b F(b^*, Q^*) < 0 \quad (2.7)$$

(e.g.,  $\bar{b} = -\nabla_b F(b^*, Q^*)$ ). A vector  $\bar{b}$  that satisfies (2.7) is called a descent direction at  $b^*$ . Given any descent direction  $\bar{b}$ , a positive scalar  $\bar{\varepsilon}$  exists such that for all positive  $\varepsilon$  that satisfy  $\varepsilon \leq \bar{\varepsilon}$ ,

$$\varepsilon \bar{b}^T \nabla_b F(b^*, Q^*) + O(\varepsilon^2) < 0 \quad (2.8)$$

If we substitute (2.8) into (2.6), then

$$F(b^* + \varepsilon \bar{b}, Q^* + \varepsilon \bar{Q}) \leq F(b^*, Q^*) \quad (2.9)$$

for all such  $\varepsilon$ . Hence, unless  $\nabla_b F(b^*, Q^*) = 0$ , the neighborhood of  $b^*$  contains points with a lower function value than  $F(b^*, Q^*)$ . The other necessary conditions that must be satisfied at the minimum are the state equations and the side constraints.

## 2.2 The Minimization Process

At some initial  $b$ , any minimization process seeks to find a descent direction  $\bar{b}$  and a step size  $\varepsilon$  in which to change  $b$  such that

$$F(b + \varepsilon \bar{b}, Q + \varepsilon \bar{Q}) \leq F(b, Q) \quad (2.10)$$

where  $\varepsilon \bar{Q}$  is the corresponding change in  $Q$  that satisfies the state equations and the side constraints. This process is repeated several times until a minimum is reached.

### The Descent Direction

A descent direction  $\bar{b}$  can be determined as follows. The Taylor series expansion of  $F$  about  $b$  and  $Q$  can be written as

$$F(b + \varepsilon \bar{b}, Q + \varepsilon \bar{Q}) = F(b, Q) + \varepsilon \bar{b}^T \nabla_b F(b, Q) + O(\varepsilon^2) \quad (2.11)$$

where  $\nabla_b F$  is given by (2.5). Equation (2.11) clearly shows that if

$$\bar{b} = -\frac{\nabla_b F(b, Q)}{|\nabla_b F(b, Q)|} \quad (2.12)$$

then (2.10) is satisfied. Equality occurs in (2.10) at the minimum when  $\nabla_b F(b^*, Q^*) = 0$ , where  $b^*$  is the optimum value of the design variables and  $Q^*$  is the corresponding value of the state variables that satisfies the state equations. Therefore, to obtain the descent direction, the gradient of  $F$  must be evaluated. The efficient and accurate evaluation of this gradient is one of the important but difficult steps in any minimization scheme. The formula for the gradient of  $F$ , given by (2.5), is not a very useful one because, in general,  $dQ/db$  is difficult to determine. However, by using the adjoint method, this difficulty can be easily overcome. This method is outlined in section 2.3.

### The Step size

Once the descent direction has been determined, the next step is to evaluate the step size  $\varepsilon$ . One approach is to do a line search. The objective of the line search is to find  $\varepsilon$  such that  $\|\nabla_b F(b + \varepsilon \bar{b}, Q + \varepsilon \bar{Q})\|^2$  is a minimum. That is,

$$\frac{\partial \|\nabla_b F(b + \varepsilon \bar{b}, Q + \varepsilon \bar{Q})\|^2}{\partial \varepsilon} = 0 \quad (2.13)$$

If we use a Taylor series expansion, then we can write

$$\begin{aligned} & \|\nabla_b F(b + \varepsilon \bar{b}, Q + \varepsilon \bar{Q})\|^2 \\ &= \|\nabla_b F(b, Q) + \varepsilon \nabla_b^2 F(b, Q) \bar{b} + \varepsilon^2 C + O(\varepsilon^3)\|^2 \\ &= [\nabla_b F(b, Q)]^T \nabla_b F(b, Q) + 2\varepsilon [\nabla_b F(b, Q)]^T \nabla_b^2 F(b, Q) \bar{b} \\ &+ \varepsilon^2 \left\{ \bar{b}^T [\nabla_b^2 F(b, Q)]^T \nabla_b^2 F(b, Q) \bar{b} + 2[\nabla_b F(b, Q)]^T C \right\} \\ &+ O(\varepsilon^3) \end{aligned} \quad (2.14)$$

where  $C$  denotes the  $O(\varepsilon^2)$  term of the expansion. Note that  $\nabla_b^2 F$  includes the variation with respect to  $Q$ . If we set the derivative with respect to  $\varepsilon$  on the right-hand side of (2.14) equal to 0 and solve for  $\varepsilon$ , then

$$\varepsilon = -\frac{[\nabla_b F(b, Q)]^T \nabla_b^2 F(b, Q) \bar{b}}{\bar{b}^T [\nabla_b^2 F(b, Q)]^T \nabla_b^2 F(b, Q) \bar{b} + 2[\nabla_b F(b, Q)]^T C + O(\varepsilon^2)} \quad (2.15)$$

Near the minimum, because  $\nabla_b F$  is small, the second term in the denominator is negligible in comparison with the first term; hence, it is dropped. Therefore, if we also neglect the  $O(\varepsilon^2)$  terms in (2.15), then the step size becomes

$$\varepsilon = -\frac{[\nabla_b F(b, Q)]^T \nabla_b^2 F(b, Q) \bar{b}}{\bar{b}^T [\nabla_b^2 F(b, Q)]^T \nabla_b^2 F(b, Q) \bar{b}} \quad (2.16)$$

where  $\nabla_b^2 F$  is a symmetric matrix and is often referred to as the Hessian. Computation of the Hessian is expensive; the cost is proportional to the number of design variables. However,  $\nabla_b^2 F \bar{b}$  can be evaluated relatively easily with finite differences as follows:

$$\nabla_b^2 F(b, Q) \bar{b} = \frac{\nabla_b F(b + \varepsilon \bar{b}, Q + \varepsilon \bar{Q}) - \nabla_b F(b, Q)}{\varepsilon} \quad (2.17)$$

where  $\varepsilon$  is a trial perturbation. To find the step size, the design variables are perturbed with an arbitrarily small  $\varepsilon$ , and the new values of the state variables that satisfy the state equations and the side constraints are determined. Next, the new gradient  $\nabla_b F(b + \varepsilon \bar{b}, Q + \varepsilon \bar{Q})$  is evaluated, followed by  $\nabla_b^2 F(b, Q) \bar{b}$ . Then, the step size is determined with (2.16).

### 2.3 The Adjoint Method

As stated earlier, the efficient and accurate evaluation of the gradient of  $F$  is one of the important but difficult steps in any minimization scheme. The most elegant way of determining this gradient is to use the adjoint method. The adjoint equations, also referred to as the costate equations, can be derived as follows. In the following derivation and in the rest of the paper, we assume that no side constraints exist. For a small change  $\varepsilon \delta b$  in  $b$  and a corresponding change  $\varepsilon \delta Q$  in  $Q$  that satisfies the state equations (2.2), we can show that

$$\varepsilon \delta b^T \left( \frac{\partial R}{\partial b} \right)^T + \varepsilon \delta Q^T \left( \frac{\partial R}{\partial Q} \right)^T + O(\varepsilon^2) = 0 \quad (2.18)$$

With (2.5), we can write

$$\varepsilon \delta b^T \nabla_b F = \varepsilon \delta b^T \frac{\partial F}{\partial b} + \varepsilon \delta Q^T \frac{\partial F}{\partial Q} \quad (2.19)$$

where

$$\delta Q = \frac{dQ}{db} \delta b \quad (2.20)$$

If we add a term, which is the product of (2.18) and an arbitrary multiplier  $\lambda$ , to (2.19), then we get

$$\begin{aligned} \varepsilon \delta b^T \nabla_b F &= \varepsilon \delta b^T \frac{\partial F}{\partial b} + \varepsilon \delta Q^T \frac{\partial F}{\partial Q} \\ &+ \varepsilon \left[ \delta b^T \left( \frac{\partial R}{\partial b} \right)^T + \delta Q^T \left( \frac{\partial R}{\partial Q} \right)^T \right] \lambda + O(\varepsilon^2) \end{aligned} \quad (2.21)$$

The arbitrary multiplier  $\lambda$  is often referred to as either the Lagrange multiplier, the costate variable, or the adjoint variable. If we rearrange (2.21), then we get

$$\begin{aligned} \varepsilon \delta b^T \nabla_b F &= \varepsilon \delta b^T \left[ \left( \frac{\partial R}{\partial b} \right)^T \lambda + \frac{\partial F}{\partial b} \right] \\ &+ \varepsilon \delta Q^T \left[ \left( \frac{\partial R}{\partial Q} \right)^T \lambda + \frac{\partial F}{\partial Q} \right] + O(\varepsilon^2) \end{aligned} \quad (2.22)$$

If we choose  $\lambda$  such that

$$\left( \frac{\partial R}{\partial Q} \right)^T \lambda + \frac{\partial F}{\partial Q} = 0 \quad (2.23)$$

then (2.22) becomes

$$\varepsilon \delta b^T \nabla_b F = \varepsilon \delta b^T \left[ \left( \frac{\partial R}{\partial b} \right)^T \lambda + \frac{\partial F}{\partial b} \right] + O(\varepsilon^2) \quad (2.24)$$

Equation (2.23) is the set adjoint equations or the costate equations. The adjoint equations are similar to the linearized form of the state equations. They include the adjoint boundary conditions that correspond to the boundary conditions of the state equations. If we neglect the  $O(\varepsilon^2)$  terms of (2.24), then the gradient of  $F$  can be written as

$$\nabla_b F = \left( \frac{\partial R}{\partial b} \right)^T \lambda + \frac{\partial F}{\partial b} \quad (2.25)$$

The gradient of  $F$  given by (2.25) is much easier to evaluate than the one given by (2.5). By introducing the Lagrange multiplier, the need to evaluate  $\delta Q$  has been eliminated. The

adjoint equations form an additional set of necessary conditions that must be satisfied at the minimum. In summary, the necessary conditions that must be satisfied at the minimum are

$$\begin{aligned} R[b, Q(b)] &= 0 \\ \left( \frac{\partial R}{\partial Q} \right)^T \lambda + \frac{\partial F}{\partial Q} &= 0 \\ \nabla_b F = \left( \frac{\partial R}{\partial b} \right)^T \lambda + \frac{\partial F}{\partial b} &= 0 \end{aligned} \quad (2.26)$$

The derivation presented above is for a general constrained minimization problem. In the following section, the adjoint equations and the gradient of the cost function are derived for a specific set of state equations and a cost function.

## 3. DESIGN OF OPTIMAL AIRFOIL SHAPES

The design of optimal airfoil shapes is a constrained minimization problem. The objective is to find the optimal shape of the airfoil that will minimize a cost function  $F$  subject to the state equation of the flow field and side constraints.

### 3.1 The State Equations

The analysis problem, defined by the state equation, consists of finding the flow over a specified shape for a given free-stream Mach number and angle of attack. In order to focus on the optimization procedure, the flow model considered is the subsonic potential flow over an airfoil profile.

Consider the steady irrotational flow past a two-dimensional airfoil.<sup>15,16</sup> The governing equation of the flow field, known as the full potential equation, is

$$\text{div}(\rho \nabla \phi) = 0 \quad (3.1)$$

The boundary condition on the airfoil is

$$\nabla \phi \cdot \mathbf{n} = 0 \quad (3.2)$$

At infinity the boundary condition is

$$\nabla \phi = U_\infty \quad (3.3)$$

For the Kutta condition, the circulation  $\Gamma$  around the airfoil is such that

the velocity at the trailing edge is finite and continuous (3.4)

In these equations,  $\phi = \phi(x, y)$  is the full velocity potential,  $\rho = \rho(\phi)$  is the density,  $\mathbf{n}$  is the unit normal, and  $U_\infty$  is the free-stream velocity. The density  $\rho$  is given by

$$\rho = \left[ 1 - \frac{\gamma - 1}{2} M_\infty^2 (|\nabla \phi|^2 - 1) \right]^{\frac{1}{\gamma - 1}} \quad (3.5)$$

where  $M_\infty$  is the free-stream Mach number and  $\gamma$  is the ratio of specific heats. If  $\zeta$  is the angle of attack of the airfoil, then the free-stream velocity is given by

$$U_\infty = U_\infty [\cos(\zeta) \mathbf{i} + \sin(\zeta) \mathbf{j}] \quad (3.6)$$

where  $\mathbf{i}$  and  $\mathbf{j}$  are the unit vectors in the  $x$  and  $y$  directions, respectively.

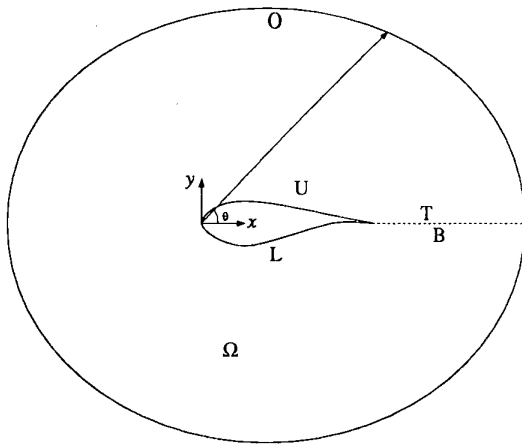


Figure 1. Computational domain.

### 3.2 The Computational Domain

The computational domain is shown in Figure 1. The interior of the flow field is denoted by  $\Omega$ ; the upper and lower surfaces of the airfoil are denoted by  $U$  and  $L$ , respectively. The far-field boundary, located at a finite distance from the airfoil (30 to 50 airfoil chord lengths) is denoted by  $O$ . To impose the Kutta condition around the airfoil, an artificial boundary or cut that begins at the airfoil and extends to the far field is introduced. A jump in potential that is equal to  $\Gamma$  is allowed across the cut. For convenience, this cut is chosen to emanate from the trailing edge of the airfoil. The top and bottom sides of the cut can be denoted by  $T$  and  $B$ , respectively. The jump across the cut can be written as

$$\phi^T - \phi^B = \Gamma \quad (3.7)$$

The value of the  $\Gamma$  is determined by requiring that the velocity perpendicular to the trailing edge bisector be equal to 0 at the trailing edge. A good approximation for  $\Gamma$  is given by

$$\Gamma = \phi_{t.e.}^T - \phi_{t.e.}^B \quad (3.8)$$

where *t.e.* refers to the trailing edge of the airfoil (refer to Appendix C for details). To satisfy mass conservation across the cut, derivatives of the potential normal to the cut are required to be continuous.

At the far-field boundary, the circulation modifies the velocity as follows:

$$\nabla\phi \cdot \mathbf{n} = U_\infty \cdot \mathbf{n} + \frac{\Gamma}{2\pi} \nabla\Theta \cdot \mathbf{n} \quad (3.9)$$

where

$$\Theta = 2\pi - \tan^{-1} \left( \sqrt{1 - M_\infty^2} \tan \theta \right) \quad (3.10)$$

and  $\theta$  is the angular position of a far-field point. For convenience,  $\mathbf{n}$  is the unit normal on the boundary. The far-field boundary condition given by (3.9) is consistent with the infinity condition stated by (3.3).

### 3.3 The Design Variables

The airfoil is represented as follows:

$$y^U = \sum_{k=1}^K \alpha_k^U f_k(x) \quad (0 \leq x \leq 1) \quad (3.11)$$

$$y^L = \sum_{k=1}^K \alpha_k^L f_k(x)$$

where  $\alpha_k^U$  and  $\alpha_k^L$  are the amplitudes of the shape functions  $f_k$  on the upper and lower surfaces of the airfoil, respectively. The design variables  $\alpha_k$  must be determined to obtain the optimal shape of the airfoil. Let  $\alpha$  denote a vector whose elements are the design variables. That is,

$$\alpha = [\alpha_1^U, \alpha_2^U, \dots, \alpha_K^U, \alpha_1^L, \alpha_2^L, \dots, \alpha_K^L]^T \quad (3.12)$$

The functionality of the shape functions will be presented later.

### 3.4 The Optimization Problem

The model problem chosen is the design of an airfoil shape that can match a given target potential. Given a target potential distribution  $\phi_0$  around an airfoil, the objective is to find  $\alpha$  that will minimize

$$F[\alpha, \phi(\alpha)] \equiv \int_{U+L} (\phi - \phi_0)^2 d\sigma \quad (3.13)$$

subject to the state equations, where  $d\sigma$ , which is an element of the airfoil, can be written as

$$d\sigma^2 = dx^2 + dy^2 \quad (3.14)$$

Note that the choice of this particular cost function does not make it an inverse-design problem. Unlike inverse-design problems, the minimization is done over a finite number of design variables. This approach also can be used, for example, to find the optimal shape of an airfoil that has the minimum  $D/L$  (Drag/Lift) subject to geometric and aerodynamic constraints.

To make the presentation of the derivation of the adjoint equations simple and easy to understand, the flow is assumed to be incompressible (i.e.,  $M_\infty = 0$ ); therefore,  $\rho = 1$ . In this case, the full potential equation reduces to the Laplace equation. Also, no side constraints are considered in this derivation. Therefore, the specific optimization problem considered here is

$$\min_{\alpha, \phi} \int_{U+L} (\phi - \phi_0)^2 d\sigma \quad (3.15)$$

subject to

$$\text{div}(\nabla\phi) = 0 \quad \text{in } \Omega \quad (3.16a)$$

$$\nabla\phi \cdot \mathbf{n} = 0 \quad \text{on the airfoil} \quad (3.16b)$$

$$\nabla\phi \cdot \mathbf{n} = U_\infty \cdot \mathbf{n} + \frac{\Gamma}{2\pi} \nabla\Theta \cdot \mathbf{n} \quad \text{in the far field} \quad (3.16c)$$

$$\phi^T - \phi^B = \Gamma \quad \text{along the cut} \quad (3.16d)$$

where  $\Gamma$  is given by (3.8).

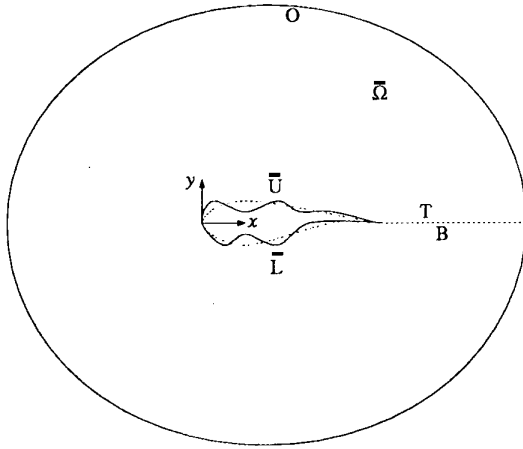


Figure 2. Domain after perturbation.

### 3.5 The Adjoint Equations

As stated earlier, the objective of the optimization procedure is to seek a descent direction and a step size in which the design variables can be changed so that the cost function is decreased. To determine the descent direction and the step size, the gradient of the cost function with respect to the design variables  $\nabla_{\alpha} F$  must be evaluated (refer to section 2.2). As shown in section 2.3 the adjoint method offers an elegant means of evaluating the gradient. The derivation of the adjoint equations is presented below.

Let the design variables be perturbed such that

$$\alpha \rightarrow \alpha + \varepsilon \bar{\alpha} \quad (3.17)$$

where  $\varepsilon \bar{\alpha}$  is the change in  $\alpha$ ;  $\varepsilon$  and  $\bar{\alpha}$  are the step size (magnitude) and direction, respectively, of the change in  $\alpha$ . Figure 2 shows the domain after the perturbation, where  $\bar{U}$  and  $\bar{L}$  denote the upper and lower surfaces, respectively, of the new airfoil and  $\bar{\Omega}$  denotes the new domain. The shape of the resulting airfoil  $\bar{y}^{\bar{U}, \bar{L}}$  and the corresponding potential  $\bar{\phi}$  that satisfies the governing equation and its boundary conditions in the new domain can be written as

$$\bar{y}^{\bar{U}, \bar{L}} = y^{U, L} + \varepsilon \bar{y}^{U, L} \quad (3.18)$$

$$\bar{\phi} = \phi + \varepsilon \bar{\phi} \quad (3.19)$$

where  $\varepsilon \bar{y}$  represents the change in the airfoil shape and  $\varepsilon \bar{\phi}$  represents the corresponding change in the potential. We can show from (3.13) that

$$\begin{aligned} \bar{\alpha}^T \nabla_{\alpha} F &= \int_{\bar{U}} 2(\phi - \phi_0) \frac{y_x \bar{y}}{\sqrt{1 + y_x^2}} \nabla \phi \cdot \mathbf{t} d\sigma \\ &\quad - \int_{\bar{L}} 2(\phi - \phi_0) \frac{y_x \bar{y}}{\sqrt{1 + y_x^2}} \nabla \phi \cdot \mathbf{t} d\sigma \\ &\quad + \int_{\bar{U} + \bar{L}} (\phi - \phi_0)^2 \frac{y_x \bar{y}_x}{1 + y_x^2} d\sigma \\ &\quad + \int_{\bar{U} + \bar{L}} 2(\phi - \phi_0) \bar{\phi} d\sigma \end{aligned} \quad (3.20)$$

where  $y_x = dy/dx$  and  $\mathbf{t}$  is the unit tangent (refer to Appendix A for details). The objective of this derivation is to eliminate  $\bar{\phi}$ , where

$$\bar{\phi} = \frac{d\phi}{d\alpha} \bar{\alpha} \quad (3.21)$$

From the governing equation and its boundary conditions (3.16), we can show that

$$\text{div}(\nabla \bar{\phi}) = 0 \quad \text{in } \Omega \quad (3.22a)$$

$$\nabla \bar{\phi} \cdot \mathbf{n} = \nabla(\bar{y} \nabla \phi \cdot \mathbf{t}) \cdot \mathbf{i} \quad \text{on the airfoil} \quad (3.22b)$$

$$\nabla \bar{\phi} \cdot \mathbf{n} = \frac{\bar{\Gamma}}{2\pi} \nabla \Theta \cdot \mathbf{n} \quad \text{at the far field} \quad (3.22c)$$

$$\bar{\phi}^T - \bar{\phi}^B = \bar{\Gamma} \quad \text{along the cut} \quad (3.22d)$$

where

$$\bar{\Gamma} = \bar{\phi}_{t.e.}^T - \bar{\phi}_{t.e.}^B \quad (3.23)$$

If we introduce a Lagrange multiplier  $\lambda$  and use (3.22a), then (3.20) can be written as

$$\begin{aligned} \bar{\alpha}^T \nabla_{\alpha} F &= \int_{\bar{U}} 2(\phi - \phi_0) \frac{y_x \bar{y}}{\sqrt{1 + y_x^2}} \nabla \phi \cdot \mathbf{t} d\sigma \\ &\quad - \int_{\bar{L}} 2(\phi - \phi_0) \frac{y_x \bar{y}}{\sqrt{1 + y_x^2}} \nabla \phi \cdot \mathbf{t} d\sigma \\ &\quad + \int_{\bar{U} + \bar{L}} (\phi - \phi_0)^2 \frac{y_x \bar{y}_x}{1 + y_x^2} d\sigma \\ &\quad + \int_{\bar{U} + \bar{L}} 2(\phi - \phi_0) \bar{\phi} d\sigma \\ &\quad + \iint_{\Omega} \text{div}(\nabla \bar{\phi}) \lambda d\Omega \end{aligned} \quad (3.24)$$

If we integrate by parts, the last integral can be written as

$$\begin{aligned} \iint_{\Omega} \text{div}(\nabla \bar{\phi}) \lambda d\Omega &= \iint_{\Omega} \text{div}(\nabla \lambda) \bar{\phi} d\Omega \\ &\quad - \int_{\tau} \lambda (\nabla \bar{\phi} \cdot \mathbf{n}) d\tau + \int_{\tau} (\nabla \lambda \cdot \mathbf{n}) \bar{\phi} d\tau \end{aligned} \quad (3.25)$$

where the unit normal  $\mathbf{n}$  points into the flow field  $\Omega$ ;  $d\tau$  is an element on  $\tau$ , which is the path of integration around the domain  $\Omega$  and can be expressed as

$$\tau = \bar{L} + \bar{U} + \bar{T} + \bar{O} + \bar{B} \quad (3.26)$$

If the integrals are split along  $\tau$  into different components and substituted into (3.24), then we can write

$$\begin{aligned} \bar{\alpha}^T \nabla_{\alpha} F &= \int_{\bar{U}} 2(\phi - \phi_0) \frac{y_x \bar{y}}{\sqrt{1 + y_x^2}} \nabla \phi \cdot \mathbf{t} d\sigma \\ &\quad - \int_{\bar{L}} 2(\phi - \phi_0) \frac{y_x \bar{y}}{\sqrt{1 + y_x^2}} \nabla \phi \cdot \mathbf{t} d\sigma \\ &\quad + \int_{\bar{U} + \bar{L}} (\phi - \phi_0)^2 \frac{y_x \bar{y}_x}{1 + y_x^2} d\sigma + \int_{\bar{U} + \bar{L}} 2(\phi - \phi_0) \bar{\phi} d\sigma \\ &\quad + \iint_{\Omega} \text{div}(\nabla \lambda) \bar{\phi} d\Omega \\ &\quad - \int_{\bar{U} + \bar{L}} \lambda (\nabla \bar{\phi} \cdot \mathbf{n}) d\sigma + \int_{\bar{U} + \bar{L}} (\nabla \lambda \cdot \mathbf{n}) \bar{\phi} d\sigma \\ &\quad - \int_{\bar{T} + \bar{B}} \lambda (\nabla \bar{\phi} \cdot \mathbf{n}) d\tau + \int_{\bar{T} + \bar{B}} (\nabla \lambda \cdot \mathbf{n}) \bar{\phi} d\tau \\ &\quad - \int_{\bar{O}} \lambda (\nabla \bar{\phi} \cdot \mathbf{n}) d\tau + \int_{\bar{O}} (\nabla \lambda \cdot \mathbf{n}) \bar{\phi} d\tau \end{aligned} \quad (3.27)$$

Because  $\nabla\bar{\phi}$  is continuous across the cut and  $\mathbf{n}$  points in opposite directions along the top and bottom boundaries of the cut, we can write

$$\int_{T+B} \lambda(\nabla\bar{\phi} \cdot \mathbf{n})d\tau = \int_{\text{Cut}} (\lambda^T - \lambda^B)(\nabla\bar{\phi} \cdot \mathbf{n})d\tau \quad (3.28)$$

If we assume that  $\nabla\lambda$  is continuous across the cut, then we can write

$$\int_{T+B} (\nabla\lambda \cdot \mathbf{n})\bar{\phi}d\tau = \bar{\Gamma} \int_{\text{Cut}} \nabla\lambda \cdot \mathbf{n}d\tau \quad (3.29)$$

If we use (3.28), (3.29), and (3.22b-d), then equation (3.27) can be written as

$$\begin{aligned} \bar{\alpha}^T \nabla_{\alpha} F &= \int_U 2(\phi - \phi_0) \frac{y_x \bar{y}}{\sqrt{1+y_x^2}} \nabla\phi \cdot \mathbf{t}d\sigma \\ &- \int_L 2(\phi - \phi_0) \frac{y_x \bar{y}}{\sqrt{1+y_x^2}} \nabla\phi \cdot \mathbf{t}d\sigma \\ &+ \int_{U+L} (\phi - \phi_0)^2 \frac{y_x \bar{y}_x}{1+y_x^2} d\sigma + \int_{U+L} 2(\phi - \phi_0) \bar{\phi}d\sigma \\ &+ \iint_{\Omega} \text{div}(\nabla\lambda) \bar{\phi}d\Omega \\ &- \int_{U+L} \lambda \nabla(\bar{y} \nabla\phi \cdot \mathbf{t}) \cdot \mathbf{i}d\sigma + \int_{U+L} (\nabla\lambda \cdot \mathbf{n}) \bar{\phi}d\sigma \\ &- \int_{\text{Cut}} (\lambda^T - \lambda^B)(\nabla\bar{\phi} \cdot \mathbf{n})d\tau + \bar{\Gamma} \int_{\text{Cut}} \nabla\lambda \cdot \mathbf{n}d\tau \\ &- \frac{\bar{\Gamma}}{2\pi} \int_{\text{O}} \lambda(\nabla\Theta \cdot \mathbf{n})d\tau + \int_{\text{O}} (\nabla\lambda \cdot \mathbf{n}) \bar{\phi}d\tau \end{aligned} \quad (3.30)$$

If we substitute for  $\bar{\Gamma}$  from (3.23) and rearrange, then (3.30) becomes

$$\begin{aligned} \bar{\alpha}^T \nabla_{\alpha} F &= \int_U 2(\phi - \phi_0) \frac{y_x \bar{y}}{\sqrt{1+y_x^2}} \nabla\phi \cdot \mathbf{t}d\sigma \\ &- \int_L 2(\phi - \phi_0) \frac{y_x \bar{y}}{\sqrt{1+y_x^2}} \nabla\phi \cdot \mathbf{t}d\sigma \\ &+ \int_{U+L} (\phi - \phi_0)^2 \frac{y_x \bar{y}_x}{1+y_x^2} d\sigma - \int_{U+L} \lambda \nabla(\bar{y} \nabla\phi \cdot \mathbf{t}) \cdot \mathbf{i}d\sigma \\ &+ \iint_{\Omega} \text{div}(\nabla\lambda) \bar{\phi}d\Omega \\ &+ \int_{U+L} [\nabla\lambda \cdot \mathbf{n} + 2(\phi - \phi_0)] \bar{\phi}d\sigma \\ &+ (\bar{\phi}_{i.e.}^U - \bar{\phi}_{i.e.}^L) \left( \int_{\text{Cut}} \nabla\lambda \cdot \mathbf{n}d\tau - \frac{1}{2\pi} \int_{\text{O}} \lambda \nabla\Theta \cdot \mathbf{n}d\tau \right) \\ &+ \int_{\text{O}} (\nabla\lambda \cdot \mathbf{n}) \bar{\phi}d\tau - \int_{\text{Cut}} (\lambda^T - \lambda^B)(\nabla\bar{\phi} \cdot \mathbf{n})d\tau \end{aligned} \quad (3.31)$$

We choose  $\lambda$  such that

$$\begin{aligned} \text{div}(\nabla\lambda) &= 0 && \text{in } \Omega \\ \nabla\lambda \cdot \mathbf{n} + 2(\phi - \phi_0) - \Upsilon\delta(x - x_{i.e.}) &= 0 && \text{on } L \\ \nabla\lambda \cdot \mathbf{n} + 2(\phi - \phi_0) + \Upsilon\delta(x - x_{i.e.}) &= 0 && \text{on } U \\ \nabla\lambda \cdot \mathbf{n} &= 0 && \text{in the far field} \\ \lambda^T - \lambda^B &= 0 && \text{along the cut} \end{aligned} \quad (3.32)$$

where

$$\Upsilon = \int_{\text{Cut}} \nabla\lambda \cdot \mathbf{n}d\tau - \frac{1}{2\pi} \int_{\text{O}} \lambda \nabla\Theta \cdot \mathbf{n}d\tau \quad (3.33)$$

and  $\delta$  denotes the Dirac delta function (*i.e.* stands for trailing edge of the airfoil). Equations (3.32) are the adjoint equation and its boundary conditions (also called the costate equations). These equations are similar to the linearized state equations. The size of the system is the same as the size of the state equations and can be solved with the same technique used to solve the state equations.

Because  $\text{div}(\nabla\lambda) = 0$  in  $\Omega$ , we obtain the following from the divergence theorem:

$$\int_{\Gamma} \nabla\lambda \cdot \mathbf{n}d\tau = 0 \quad (3.34)$$

Therefore, for (3.32) to have a solution, we can show that

$$\int_{U+L} (\phi - \phi_0)d\sigma \equiv 0 \quad (3.35)$$

Equation (3.16) clearly shows that a constant can be added to  $\phi$ . We can choose this constant  $\phi_c$  such that

$$\int_{U+L} (\phi + \phi_c - \phi_0)d\sigma = 0 \quad (3.36)$$

Therefore,

$$\phi_c = - \frac{\int_{U+L} (\phi - \phi_0)d\sigma}{\int_{U+L} d\sigma} \quad (3.37)$$

### 3.6 The Gradient of $F$

If (3.32) is substituted into (3.31), then it reduces to

$$\begin{aligned} \bar{\alpha}^T \nabla_{\alpha} F &= \int_U 2(\phi - \phi_0) \frac{y_x \bar{y}}{\sqrt{1+y_x^2}} \nabla\phi \cdot \mathbf{t}d\sigma \\ &- \int_L 2(\phi - \phi_0) \frac{y_x \bar{y}}{\sqrt{1+y_x^2}} \nabla\phi \cdot \mathbf{t}d\sigma \\ &+ \int_{U+L} (\phi - \phi_0)^2 \frac{y_x \bar{y}_x}{1+y_x^2} d\sigma \\ &- \int_{U+L} \lambda \nabla(\bar{y} \nabla\phi \cdot \mathbf{t}) \cdot \mathbf{i}d\sigma \end{aligned} \quad (3.38)$$

If we integrate the last integral by parts, then we get

$$\begin{aligned} &- \int_{U+L} \lambda \nabla(\bar{y} \nabla\phi \cdot \mathbf{t}) \cdot \mathbf{i}d\sigma \\ &= \int_{U+L} (\bar{y} \nabla\phi \cdot \mathbf{t}) \nabla\lambda \cdot \mathbf{i}d\sigma + \int_{U+L} \frac{y_x y_{xx} \bar{y}}{1+y_x^2} \lambda \nabla\phi \cdot \mathbf{t}d\sigma \\ &= \int_U \frac{\bar{y}}{\sqrt{1+y_x^2}} (-y_x \nabla\lambda \cdot \mathbf{n} + \nabla\lambda \cdot \mathbf{t}) \nabla\phi \cdot \mathbf{t}d\sigma \\ &+ \int_L \frac{\bar{y}}{\sqrt{1+y_x^2}} (y_x \nabla\lambda \cdot \mathbf{n} - \nabla\lambda \cdot \mathbf{t}) \nabla\phi \cdot \mathbf{t}d\sigma \\ &+ \int_{U+L} \frac{y_x y_{xx} \bar{y}}{1+y_x^2} \lambda \nabla\phi \cdot \mathbf{t}d\sigma \end{aligned} \quad (3.39)$$

If (3.39) is substituted into (3.38) and rearranged, then we can write

$$\begin{aligned} & \tilde{\alpha}^T \nabla_{\alpha} F \\ &= \int_{\bar{U}} [(\phi - \phi_0)^2 \tilde{y}_x + \lambda \nabla \phi \cdot \mathbf{t} y_{xx} \tilde{y}] \frac{y_x}{1 + y_x^2} d\sigma \\ &+ \int_{\bar{U}} [2(\phi - \phi_0) y_x - \nabla \lambda \cdot \mathbf{n} y_x + \nabla \lambda \cdot \mathbf{t}] \frac{\nabla \phi \cdot \mathbf{t} \tilde{y}}{\sqrt{1 + y_x^2}} d\sigma \\ &+ \int_{\bar{L}} [(\phi - \phi_0)^2 \tilde{y}_x + \lambda \nabla \phi \cdot \mathbf{t} y_{xx} \tilde{y}] \frac{y_x}{1 + y_x^2} d\sigma \\ &- \int_{\bar{L}} [2(\phi - \phi_0) y_x - \nabla \lambda \cdot \mathbf{n} y_x + \nabla \lambda \cdot \mathbf{t}] \frac{\nabla \phi \cdot \mathbf{t} \tilde{y}}{\sqrt{1 + y_x^2}} d\sigma \end{aligned} \quad (3.40)$$

If we substitute for  $\tilde{y}$  from (3.11), then (3.40) can be written as

$$\tilde{\alpha}^T \nabla_{\alpha} F = \sum_{k=1}^K \tilde{\alpha}_k^U \mu_k^U + \sum_{k=1}^K \tilde{\alpha}_k^L \mu_k^L \quad (3.41)$$

where

$$\begin{aligned} \mu_k^U &= \int_{\bar{U}} [(\phi - \phi_0)^2 (f_k)_x + \lambda \nabla \phi \cdot \mathbf{t} y_{xx} f_k] \frac{y_x}{1 + y_x^2} d\sigma \\ &+ \int_{\bar{U}} [2(\phi - \phi_0) y_x - \nabla \lambda \cdot \mathbf{n} y_x + \nabla \lambda \cdot \mathbf{t}] \frac{\nabla \phi \cdot \mathbf{t} f_k}{\sqrt{1 + y_x^2}} d\sigma \end{aligned} \quad (3.42)$$

and

$$\begin{aligned} \mu_k^L &= \int_{\bar{L}} [(\phi - \phi_0)^2 (f_k)_x + \lambda \nabla \phi \cdot \mathbf{t} y_{xx} f_k] \frac{y_x}{1 + y_x^2} d\sigma \\ &- \int_{\bar{L}} [2(\phi - \phi_0) y_x - \nabla \lambda \cdot \mathbf{n} y_x + \nabla \lambda \cdot \mathbf{t}] \frac{\nabla \phi \cdot \mathbf{t} f_k}{\sqrt{1 + y_x^2}} d\sigma \end{aligned} \quad (3.43)$$

Equations (3.42) and (3.43) are the components of the gradient of  $F$ . When  $\phi$  satisfies the state equations (3.16) and  $\lambda$  satisfies the costate equations (3.32), then the components of the gradient of  $F$  can be evaluated with (3.42) and (3.43). Because  $\nabla_{\alpha} F = 0$  at the minimum, we can clearly see that

$$\left. \begin{aligned} \mu_k^U &= 0 \\ \mu_k^L &= 0 \end{aligned} \right\} \quad \text{for } k = 1, 2, \dots, K \quad (3.44)$$

### 3.7 A Design Strategy

Figure 3 shows a typical design strategy. In this process, at some initial conditions the state and adjoint equations are solved, and the gradient of  $F$  is computed. If the gradient is equal to 0, then a minimum has been reached and the iteration is terminated; otherwise, the new descent direction  $\tilde{\alpha}$  and the step size  $\epsilon$  are computed, and the design variables are updated. The iteration is repeated until the gradient vanishes. The cost of this strategy can be estimated as follows. Let the cost of solving the state equations be equal to  $K$ . The cost of solving the adjoint equation is at most equal to  $K$ . Let the number of design iterations required be  $N$ . Therefore, the total cost of doing the optimal design is approximately  $2KN$  with  $N$ , at best, equal to the number of design variables. In practice, especially for nonlinear problems,  $N$  is many times the number of design variables. A factor of 100 is not unrealistic. One way to bring the total design cost down is to reduce the magnitude of  $K$ . One of the most practical and proven ways of achieving this is by using multigrid. Here, a multigrid scheme

is used to relax the state and adjoint equations. At the end of one or several multigrid cycles, the optimizer is called and the design variables are updated. In this process, the design variables are updated only on the finest grid. A schematic of this strategy is shown in Figure 4.

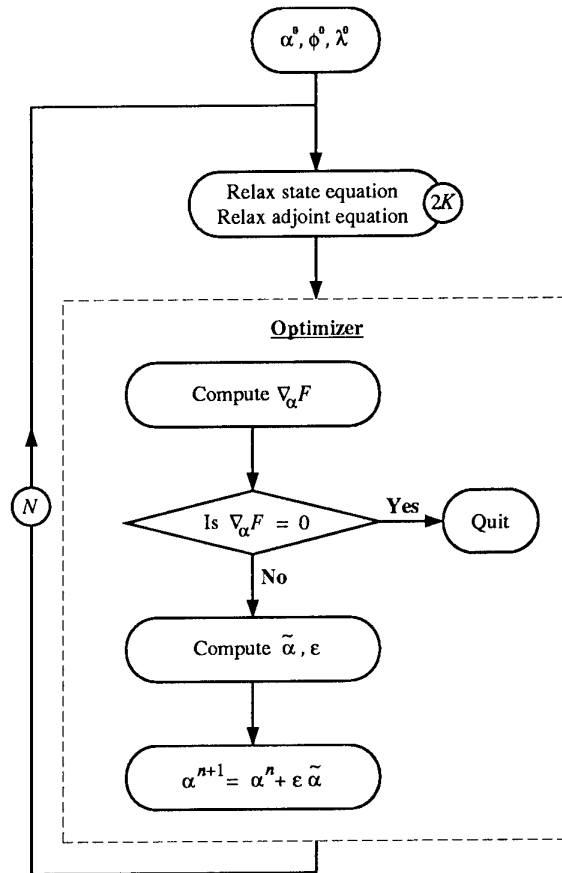


Figure 3. A design strategy flowchart.

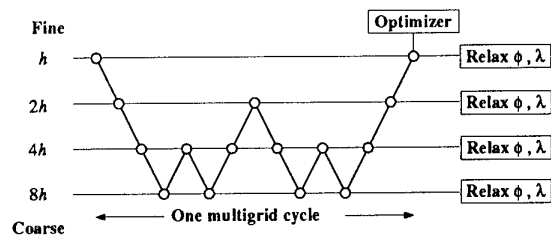


Figure 4. A multigrid strategy.

## 4. THE ONE-SHOT METHOD

The *One-Shot* method goes one step further by embedding the design process within the multigrid cycles. This method essentially makes  $N = 1$ . Thus, the cost of optimal design is approximately equal to  $2K$ . In this method, high efficiency is obtained by exploiting two key phenomena. The first one is the ability of multigrid to efficiently reduce high-frequency components of the error due to a perturbation, and the second one is the nature of propagation of perturbations in a flow field. These phenomena are explained below.

#### 4.1 Multigrid Efficiency

In any relaxation (smoothing) process, the high-frequency error components of the space discretization operator of the differential equation under consideration are generally damped in a few iterations. The low-frequency components are the slowest to be damped. Consider a one-dimensional domain of length  $L$  discretized into  $N$  cells of uniform grid spacing  $h = L/N$ , where the grid index ranges from 0 to  $N$ . This grid will be referred to as the  $h$  grid. If we assume periodic boundary conditions, then the error at the  $n$ th grid point can be written in Fourier series as

$$\epsilon_n = \sum_{j=-N}^N A_j e^{i\theta_j n} \quad (4.1)$$

where  $A_j$  is the amplitude of the  $j$ th harmonic and  $i = \sqrt{-1}$ . The phase angle  $\theta$  can be written as

$$\theta_j = \frac{j\pi}{N} \quad (4.2)$$

The phase angle covers the domain  $(-\pi, \pi)$  in increments of  $\pi/N$ . The value  $|\theta| = \pi$  corresponds to the highest frequency that is visible on this grid, namely the frequency of wavelength  $2h$ . If a coarse grid ( $H$  grid) is constructed by removing every other grid point of the  $h$  grid, then the highest frequency that is visible on this grid corresponds to  $|\theta| = \pi/2$  (i.e., the frequency of wavelength  $4h \equiv 2H$ ). Therefore, the frequencies that correspond to  $\pi/2 < |\theta| \leq \pi$  and are visible on the  $h$  grid cannot be represented on the  $H$  grid. These frequencies are considered to be high frequencies on the  $h$  grid and the relaxation scheme can damp these frequencies in a few iterations. The remaining frequencies in the spectrum, which correspond to  $0 \leq |\theta| \leq \pi/2$  and are well represented on the  $H$  grid, are referred to as low frequencies on the  $h$  grid. The frequencies that are visible on the  $H$  grid can also be separated into high and low frequencies, based on how well they are represented by the next coarsest grid. The high frequencies that correspond to the  $H$  grid can be damped quickly by a few iterations of the relaxation scheme on this grid.

In the multigrid method,<sup>17,16</sup> high efficiency is obtained by relaxing the discretized equation on successively coarser grids, where the high-frequency error components that correspond to each grid are damped efficiently. In the design process, high efficiency is obtained by changing only those design variables that produce high-frequency perturbations in the flow field on any grid. Therefore, the basic premise of the *One Shot* method, on any grid, is to make changes in the design variables that produce high-frequency perturbations in the flow field.

#### 4.2 The Effect of Airfoil Perturbation on the Flow Field

The other phenomenon that is exploited by the *One-Shot* method has to do with the way in which a disturbance is propagated in a flow field. In a subsonic flow, for example, a smooth perturbation is propagated through the entire flow field and a high-frequency perturbation is felt only in a small neighborhood around the source of the perturbation. That is, high-frequency components of the perturbation decay rapidly away from the source. This phenomenon is illustrated in the following analysis.

Consider the small-disturbance potential equation in the half-space  $0 \leq y < \infty$ ,  $-\infty < x < \infty$ . If the flow is incompressible, the governing equation is

$$\nabla^2 \phi = 0 \quad (4.3)$$

and the boundary condition applied at  $y = 0$  is

$$\frac{\partial \phi}{\partial y} = \frac{\partial f}{\partial x} \quad (4.4)$$

where  $f(x)$  is the shape of the boundary over which the flow must be determined. If  $\phi + \tilde{\phi}$  is the potential due to a change in shape to  $f + \tilde{f}$ , the governing equation for change in potential  $\tilde{\phi}$  is

$$\nabla^2 \tilde{\phi} = 0 \quad (4.5)$$

and the boundary condition at  $y = 0$  is

$$\frac{\partial \tilde{\phi}}{\partial y} = \frac{\partial \tilde{f}}{\partial x} \quad (4.6)$$

Let

$$\frac{\partial \tilde{f}}{\partial x} = e^{i\omega x} \quad (4.7)$$

where  $\omega$  is the frequency of the perturbation. A solution to the governing equation (4.5) that satisfies the boundary condition is

$$\tilde{\phi} = e^{-|\omega|y} e^{i\omega x} \quad (4.8)$$

The magnitude of  $\tilde{\phi}$  is

$$|\tilde{\phi}| = e^{-|\omega|y} \quad (4.9)$$

Figure 5, which is the plot of (4.9) for a few select frequencies,

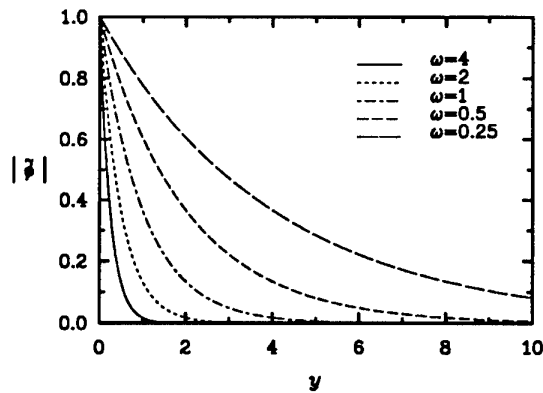


Figure 5.  $|\tilde{\phi}|$  versus  $y$ .

shows that the region where  $\tilde{\phi}$  is large becomes thinner as the frequency increases. Let  $y^*$  be a location where  $\tilde{\phi}$  is less than some small  $\epsilon$ . That is,

$$|\tilde{\phi}(\omega, y^*)| < \epsilon = e^{-\beta} \quad (4.10)$$

If we substitute for  $\tilde{\phi}$ , then

$$e^{-|\omega|y^*} = e^{-\beta} \quad (4.11)$$

Therefore,

$$y^* = \frac{-\ln(\varepsilon)}{|\omega|} \quad (4.12)$$

Equation (4.12) clearly shows that as the frequency of the perturbation  $\omega$  increases  $y^*$  decreases. Table 1 shows  $y^*$  for a few select frequencies when  $\varepsilon = 10^{-4}$ . For the discrete

Table 1.  $y^*$  versus  $\omega$

$\omega$	1/4	1/2	1	2	4
$y^*$	27.6	13.8	6.9	3.5	1.7

problem, (4.9) can be written as

$$|\tilde{\phi}| = e^{-(|\omega|h)(y/h)} = e^{-|\theta|(j-1)} \quad (j = 1, 2, \dots, J+1) \quad (4.13)$$

where  $\pi/J \leq \theta \leq \pi$  is the frequency scaled to the grid spacing  $h$ . Figure 6 shows the response to different frequencies for the discrete problem. Table 2 shows the grid location  $j^*$  beyond which  $|\tilde{\phi}| \leq 10^{-4}$ . It shows that the high frequency perturbations are significantly damped by about the fifth grid point ( $j = 0$  is the first grid point).

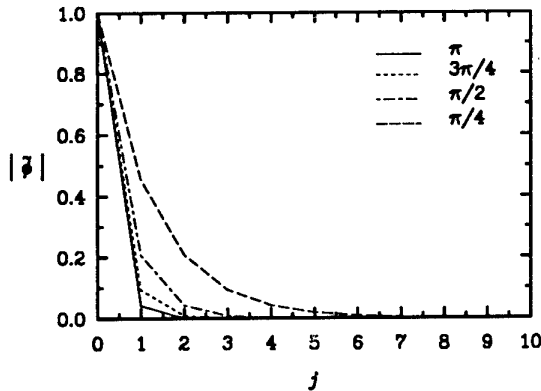


Figure 6.  $|\tilde{\phi}|$  versus  $j$ .

Table 2.  $j^*$  versus  $\theta$

$\theta$	$\pi/4$	$\pi/2$	$3\pi/4$	$\pi$
$j^*$	8.8	4.4	2.9	2.2

In the *One-Shot* method, a shape function is perturbed on a grid where it produces high-frequency error components. As described above, these errors penetrate only a small distance into the flow field. Hence, they can be quickly damped by a few relaxations of the discrete equations in a small neighborhood around the airfoil.

### 4.3 The Shape Functions

As presented earlier (section 3.3), the airfoil is represented as follows:

$$y^{U,L} = \sum_{k=1}^K \alpha_k^{U,L} f_k(x) \quad (4.14)$$

where  $\alpha_k^U$  and  $\alpha_k^L$  are the design variables and  $f_k$  are the shape functions. As explained in the previous two sections, to obtain high design efficiency, the changes in the design variables on a grid should produce nonsmooth (high-frequency) perturbations in the flow field. This is achieved by using a set of orthonormal functions as shape functions. Orthonormal functions are increasingly oscillatory. Each of them is assigned to a grid where a change in the amplitudes causes nonsmooth perturbations in the flow field. Often, basis functions that correspond to some known airfoil shape must be used. If these functions are not orthonormal, the corresponding orthonormal functions can then be determined by a Gram-Schmidt process.<sup>18</sup> A Gram-Schmidt procedure for orthonormalization can be developed with the property of orthonormal functions, namely,

$$\int_0^1 f_m(x) f_n(x) dx = 0 \quad (m \neq n) \quad (4.15)$$

$$\int_0^1 f_m^2(x) dx = 1$$

Let  $g_k(x)$  be the functions that are not orthonormal. First, the orthogonal set  $\bar{f}_k(x)$  is found from the following relations:

$$\begin{aligned} \bar{f}_1(x) &= g_1(x) \\ \bar{f}_2(x) &= g_2(x) + a_{21} \bar{f}_1(x) \\ &\vdots \\ \bar{f}_k(x) &= g_k(x) + \sum_{m=1}^{k-1} a_{km} \bar{f}_m(x) \end{aligned} \quad (4.16)$$

where

$$a_{km} = - \frac{\int_0^1 g_k(x) \bar{f}_m(x) dx}{\int_0^1 \bar{f}_m^2(x) dx} \quad (4.17)$$

Finally, the orthonormal functions are found by normalizing  $\bar{f}_k(x)$  as follows:

$$f_k = \frac{\bar{f}_k(x)}{\sqrt{\int_0^1 \bar{f}_k^2(x) dx}} \quad (4.18)$$

The Gram-Schmidt process described above can be programmed in symbolic language to find the expressions for  $f_k$ , or it can be implemented by numerical integration, in which case the shape functions are defined as an array of numbers.

As an example, consider the NACA 0012 airfoil, defined by

$$y^U = \sum_{k=1}^4 \beta_k g_k(x) \quad (0 \leq x \leq 1) \quad (4.19)$$

$$y^L = -y^U$$

where  $\beta_k$  and  $g_k$  are given in Table 3. The NACA 0012 shape has been slightly modified to ensure that it closes at the trailing edge. The same shape can be expressed in terms of the orthonormal functions as

$$y^U = \sum_{k=1}^4 \alpha_k f_k(x) \quad (0 \leq x \leq 1) \quad (4.20)$$

$$y^L = -y^U$$

where the orthonormal functions  $f_k$  of the basis functions and their corresponding amplitudes  $\alpha_k$  are given in Table 4. The orthonormal shape functions are shown in Fig. 7. Note that the number of zeros of  $f_k$  is equal to  $k + 1$ .

Table 3. Shape Functions and Amplitudes of NACA 0012

$k$	$\beta_k$	$g_k$
1	0.17814	$\sqrt{x-x}$
2	0.10128	$x(1-x)$
3	-0.10968	$x^2(1-x)$
4	0.06090	$x^3(1-x)$

Table 4. Orthonormal shape functions and amplitudes of NACA 0012

$k$	$\alpha_k \times 10^4$	$f_k$
1	439.474	$5.17723g_1$
2	28.2339	$14.7573(g_2 - .928571g_1)$
3	-5.85699	$54.7884(g_3 - .901236g_2 + .432099g_1)$
4	2.85283	$213.472(g_4 - 1.27406g_3 + .504011g_2 - .164439g_1)$

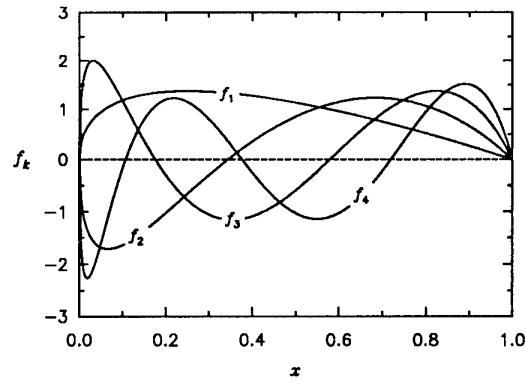


Figure 7. Orthonormal shape functions of NACA 0012 airfoil.

#### 4.4 The One-Shot Design Strategy

In the *One-Shot* method, the optimizer is embedded within the multigrid cycle as shown in Figure 8. The design variables are updated on a level where the corresponding shape functions produce high-frequency error components. In general, the low-frequency shape functions are updated on coarse levels, and higher frequency functions are updated on finer grids. For example, the design variables  $\alpha_1^U$  and  $\alpha_1^L$  are updated on the coarsest grid  $8h$ ;  $\alpha_1^U, \alpha_2^U, \alpha_3^U, \alpha_4^U, \alpha_1^L, \alpha_2^L, \alpha_3^L, \alpha_4^L$  are updated on the next finest grid  $4h$ . Some overlap of the design variables is permitted. Thus,  $\alpha_1^U$  and  $\alpha_1^L$  are updated on grid  $4h$  also. None of the design variables are updated on the finest grid  $h$ . The cost of solving the state or the adjoint equations on a coarse grid is only one-fourth of the cost of solving them on the next finest grid. Because the shape functions are perturbed only on levels where they generate high-frequency errors, a local relaxation around the airfoil is sufficient to damp out the errors, which reduces computing costs. Therefore, the overall cost of the design is dominated by the cost required to solve the state and adjoint equations on the finest grid. The total cost of the design process is approximately two to three times that of one analysis.

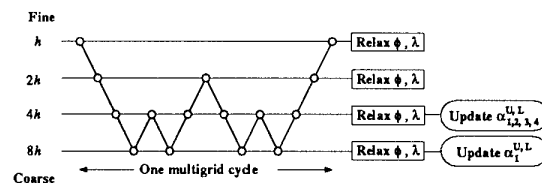


Figure 8. The *One-Shot* strategy.

#### 4.5 The Discretization and Solution Procedure

##### The State Equations

The computational domain is discretized with an O type of grid. The governing equation and its boundary conditions cast in curvilinear coordinates are discretized with the finite-volume approach. The Gauss-Seidel line-relaxation scheme is used to form the tridiagonal systems of equations in both curvilinear coordinate directions. These systems are solved with the Thomas algorithm. Note that the tridiagonal system is periodic in the direction that is around the airfoil. A FAS multigrid scheme is used to accelerate the convergence rate of the solution. The FMG process is used to obtain a good initial solution on the finest grid. The details of the discretization, the relaxation, and the multigrid acceleration are given in Appendix B.

##### The Adjoint Equations

The adjoint equations are discretized and solved in the same manner as the state equations. As in the case of the state equations, a FAS multigrid scheme and the FMG process are used to accelerate the convergence rate of the solution.

##### The Gradient of $F$

The gradient of the cost function involves only quantities on the airfoil. These quantities are discretized in a manner that is consistent with the discretization of the state and adjoint equations. The gradient is transferred to the coarse grid in a FAS manner.

##### Updating the Grid

During the design process, the grid is updated by moving only the grid points close to the airfoil and linearly decaying the change at the airfoil in this neighborhood. The outer boundary of this region is determined as follows. Let

$$y_{\max} = \eta \max(\varepsilon \dot{y}) \quad (4.23)$$

where  $\eta$  is an arbitrary constant;  $\eta = 10$  in this study. Among the grid lines that go around the airfoil, the one that is nearest to the  $y_{\max}$  location is taken to be the outer boundary of the region within which the grids are changed. The entire grid is regenerated at the beginning of each FMG stage also. With this approach, by the time the FMG process reaches the finest grid, only a few lines around the airfoil must be moved.

## 5. THE RESULTS

### Test Case 1

As our first test problem, we recover the NACA 0012 airfoil shape using the potential distribution obtained from the analysis of NACA 0012 at an angle of attack of  $0^\circ$  and  $M_\infty = 0$  as the target potential  $\phi_0$ . Figure 9 shows the computed  $C_p$  distribution obtained from the analysis run. A five-level W-cycle multigrid with  $128 \times 64$  cells on the finest grid was used. The FMG process was used to obtain a good initial approximation for the finest grid. The analysis converged to machine zero ( $< 10^{-10}$ ) in 10 multigrid cycles.

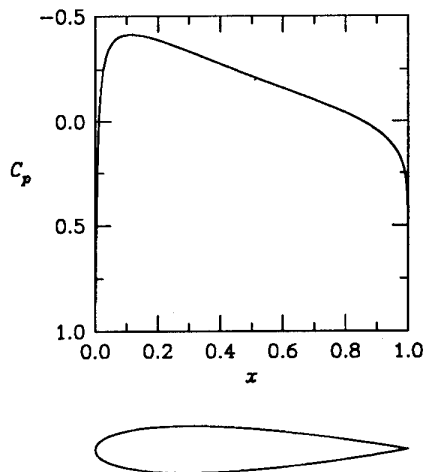


Figure 9. Computed  $C_p$  distribution for NACA 0012.

The design run was similar to the analysis run. During the design process, both the state and costate equations were relaxed at any multigrid level. The shape functions used were the orthonormal functions based on the NACA 0012 shape functions. The design variables were distributed such that on the coarsest level ( $8 \times 4$ ) only  $\alpha_1^U$  and  $\alpha_1^L$  were updated. On the next finest level ( $16 \times 8$ ), all the design variables ( $\alpha_{1,2,3,4}^{U,L}$ ) were updated. None of the design variables were updated on the next three levels, including the finest level. Thus, most of the design overhead was limited to the two coarsest grids. The FMG process was used to obtain a good initial approximation of the shape for the finest grid. Figure 10 shows the results of this run. The residuals of the state and costate equations and the gradient of the cost function reached machine zero in 12 multigrid cycles. The cost function at convergence was equal to  $3 \times 10^{-13}$ , which indicates that NACA 0012 was indeed recovered.

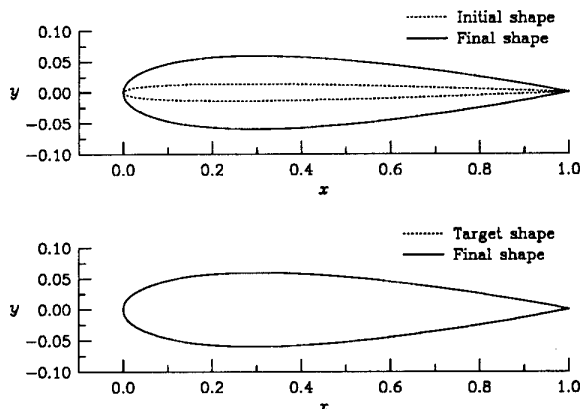


Figure 10. Test case 1.

### Test Case 2

For test case 2, we selected the airfoil FX 60-126/1, a cambered airfoil whose coordinates are tabulated in Ref. 19. Figure 11 shows the  $C_p$  distribution for this airfoil at an angle of attack of  $0^\circ$  and  $M_\infty = 0$ . This airfoil is not smooth, which is reflected in the computed  $C_p$  distribution. Using this solution as the target, we tried to recover the shape with the NACA 0012 shape functions. Figure 12 shows the resulting shape. Although the designed shape did not fall

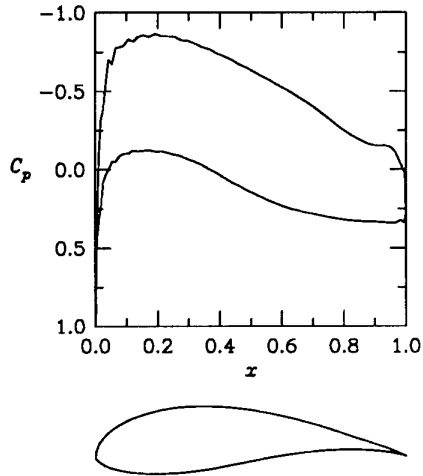


Figure 11. Computed  $C_p$  distribution for FX 60-126/1.

right on top of the target shape, the residuals of the state and costate equations and the gradient of the cost function reached machine zero, which indicates that a minimum was reached. The cost function reached a value of  $6 \times 10^{-9}$ .

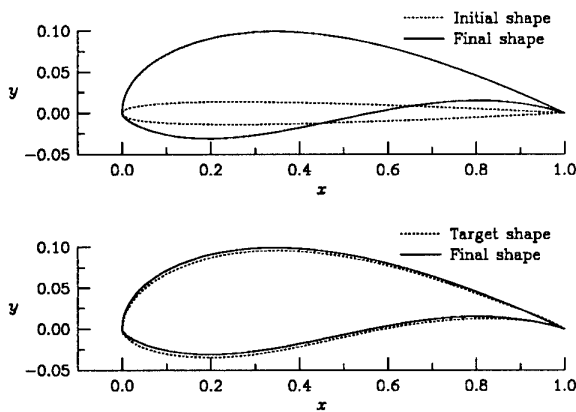


Figure 12. Test case 2.

Next, an experiment was done to see how well the FX 60-126/1 airfoil can be represented with the NACA 0012 shape function. Figure 13 shows the result. The NACA 0012 shape functions clearly do a good job everywhere except near the trailing edge. The reason why the optimum shape in the previous experiment does not correspond to the shape

obtained from the shape fitting is not clear; one reason may be the poor quality of the grid because the airfoil is not smooth.

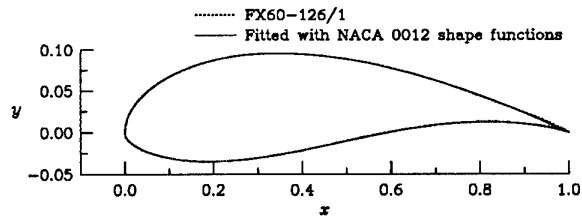


Figure 13. Shape fitting with NACA 0012 shape functions.

### Test Case 3

A third test was done; this time the fitted airfoil was used to generate the target potential. This shape is very close to the FX 60-126/1 airfoil and is smooth because it is based on smooth shape functions. The result of the design is shown in figure 14. As expected, the final shape fell on top of the target shape. The residuals of the state and costate equations and the gradient of the cost function are shown in figure 15.

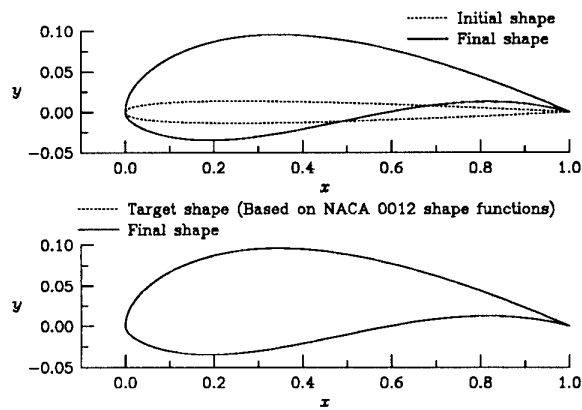


Figure 14. Test case 3.

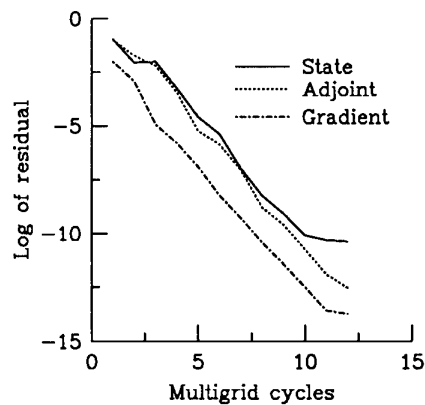


Figure 15. Convergence history.

### The Efficiency of One-Shot Method

Finally, the performance of the *One-Shot* method with respect to pure analysis is presented. The efficiency of a design method is defined as the ratio of the central processing unit (CPU) time that is required for the complete design process  $t_D$  to the CPU time that is required to do one analysis  $t_A$ . Figure 16 shows this ratio  $t_D/t_A$  plotted against the number of grid cells for the last test case. The figure shows that as the grid becomes finer the cost of design drops in comparison with the cost of one analysis. For the finest grid considered here, this ratio dropped below 4. The efficiencies for the other cases were similar.

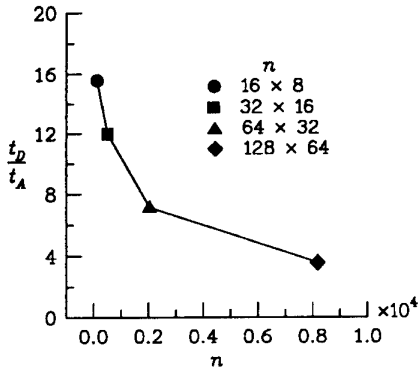


Figure 16. Efficiency of the *One-Shot* Method.

### 6. CONCLUDING REMARKS

An efficient method for the design of optimal airfoil shapes has been presented in this paper. This method brings the cost of the design process to the same order as that of the analysis problem. It offers great potential in designing optimal aircraft configurations efficiently at a reasonable computer cost. However, much work is still required before practical use can be made of this method.

### ACKNOWLEDGMENTS

The authors would like to thank Jonay Campbell, MHSI, for her help in editing the manuscript. The first and second authors were supported by the National Aeronautics and Space Administration (NASA) under contract nos. NAS1-19672 and NAS1-19480, respectively.

### REFERENCES

- 1 M. J. Lighthill. A New Method of Two Dimensional Aerodynamic Design. *ARC Rand M 2112*, 1945.
- 2 F. Bauer, P. Garabedian, and D. Korn. *A Theory of Supercritical Wing Sections with Computer Programs and Examples*. Springer-Verlag, 1972.
- 3 J. L. Steger and J. M. Klineberg. A Finite Difference Method for Transonic Airfoil Design. *AIAA J.*, Vol. 11, No. 5, May 1973, pp. 628-635.
- 4 L. A. Carlson, R. R. Ratcliff, T. A. Gally, and R. L. Campbell. Inverse Wing Design in Transonic Flow Including Viscous Interaction. In *Transonic Symposium: Theory, Application, and Experiment.*, NASA CP 3020, Vol. I, Part 2, 1989, pp. 497-520.
- 5 G. Volpe and R. E. Melnik. The Design of Transonic Aerofoils by a Well Posed Inverse Method. *Int. J.*

*Numerical Methods in Engineering*, Vol. 22, 1986, pp. 341-361.

- 6 M. Giles, M. Drela, and W. T. Thompkins. Newton Solution of Direct and Inverse Transonic Euler Equations. In *AIAA 7th Computational Fluid Dynamics Conference.*, 1985, pp. 394-402.
- 7 M. R. Hicks, M. E. Murman, and G. N. Vanderplaats. An Assessment of Airfoil Design by Numerical Optimization. *NASA TM X 3092*, July 1974.
- 8 G. A. Wrenn. An Indirect Method for Numerical Optimization Using the Kreisselmeier-Steinhauser Function. *NASA CR 4220*, March 1989.
- 9 G. B. Cosentino and T. L. Holst. Numerical Optimization Design of Advanced Transonic Wing Configurations. *NASA TM 85959*, May 1984.
- 10 K. D. Lee and S. Eyi. Transonic Airfoil Design by Constrained Optimization. *AIAA 9th Applied Aerodynamics Conference*, September, 1991, Baltimore, MD. AIAA Paper 91-3287.
- 11 A. C. Taylor, G. W. Hou, and V. M. Korivi. Sensitivity Analysis, Approximate Analysis, and Design Optimization for Internal and External Viscous Flows. *AIAA Aircraft Design Systems and Operations Meeting*, September, 1991, Baltimore, MD. AIAA Paper 91-3083.
- 12 A. Jameson. Automatic Design of Transonic Airfoils to Reduce the Shock Induced Pressure Drag. In *31st Israel Annual Conference on Aviation and Aeronautics*, February 21-22, 1990.
- 13 S. Ta'asan. *One Shot Methods for Optimal Control of Distributed Parameters Systems I: Finite Dimensional Control*. *ICASE Report No. 91-2*, January 1991.
- 14 Shlomo Ta'asan, G. Kuruwila, and M. D. Salas. Aerodynamic Design and Optimization in *One Shot*. *AIAA 30th Aerospace Sciences Meeting & Exhibit*, January, 1992, Reno, NV. AIAA Paper 92-0025.
- 15 K. Karamcheti. *Principles of Ideal-Fluid Aerodynamics*. Robert E. Krieger Publishing Company, 1980.
- 16 C. Hirsch. *Numerical Computation of Internal and External Flows. Vol. 1*. John Wiley & Sons, 1990.
- 17 A. Brandt. Multilevel Adaptive Solutions to Boundary-Value Problems. *Mathematics of Computation*, Vol. 31, April 1977, pp. 333-390.
- 18 R. Courant and D. Hilbert. *Methods of Mathematical Physics, Vol. I.*, Interscience Publisher, Inc., N.Y., 7th Printing, 1966, pp. 48-54.
- 19 D. Althaus and F. X. Wortmann. *Stuttgarter Profilkatalog I*. Friedr. Vieweg & Sohn, Braunschweig, West Germany, 1981, pp. 96-97.

### Appendix A

#### The Normal and the Tangent

Let the upper surface of the airfoil be

$$y - f(x) = 0 \quad (\text{A.1})$$

If the unit normal  $\mathbf{n}$  and the unit tangent  $\mathbf{t}$  are chosen such that the normal points into the flow field and  $\mathbf{t} \times \mathbf{n}$  points out of the paper, then

$$\mathbf{n} = \frac{-f_x \mathbf{i} + \mathbf{j}}{\sqrt{1 + f_x^2}} \quad (\text{A.2})$$

$$\mathbf{t} = \frac{\mathbf{i} + f_x \mathbf{j}}{\sqrt{1 + f_x^2}}$$

where  $\mathbf{i}$  and  $\mathbf{j}$  are the unit vectors in the  $x$ - and  $y$ -directions, respectively, and  $f_x = df/dx$ . From (A.2) the following inverse relations can be written

$$\begin{aligned}\mathbf{i} &= (-f_x \mathbf{n} + \mathbf{t}) / \sqrt{1 + f_x^2} \\ \mathbf{j} &= (\mathbf{n} + f_x \mathbf{t}) / \sqrt{1 + f_x^2}\end{aligned}\quad (\text{A.3})$$

Let the upper surface be perturbed in the  $y$ -direction such that the new shape is

$$\bar{y} = f(x) + \varepsilon \bar{f}(x) \quad (\text{A.4})$$

The new normal  $\bar{\mathbf{n}}$  and the new tangent  $\bar{\mathbf{t}}$  can be expressed as

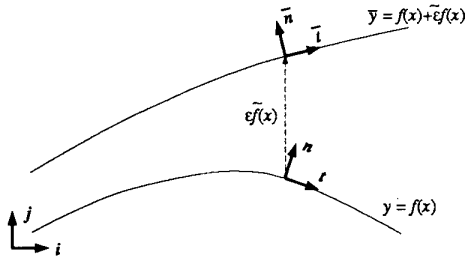


Figure 17. Perturbation of upper surface.

$$\begin{aligned}\bar{\mathbf{n}} &= \frac{-(f_x + \varepsilon \bar{f}_x) \mathbf{i} + \mathbf{j}}{\sqrt{1 + (f_x + \varepsilon \bar{f}_x)^2}} \\ \bar{\mathbf{t}} &= \frac{\mathbf{i} + (f_x + \varepsilon \bar{f}_x) \mathbf{j}}{\sqrt{1 + (f_x + \varepsilon \bar{f}_x)^2}}\end{aligned}\quad (\text{A.5})$$

With some algebraic manipulation we can show that

$$\begin{aligned}\bar{\mathbf{n}} &= \mathbf{n} - \varepsilon \frac{\bar{f}_x}{\sqrt{1 + f_x^2}} \mathbf{t} + O(\varepsilon^2) \\ \bar{\mathbf{t}} &= \mathbf{t} + \varepsilon \frac{\bar{f}_x}{\sqrt{1 + f_x^2}} \mathbf{n} + O(\varepsilon^2)\end{aligned}\quad (\text{A.6})$$

If the lower surface of the airfoil is given by

$$y - f(x) = 0 \quad (\text{A.7})$$

and the normal and the tangent are such that  $\mathbf{n}$  points into the flow and  $\mathbf{t} \times \mathbf{n}$  points out of the paper, then

$$\begin{aligned}\mathbf{n} &= \frac{f_x \mathbf{i} - \mathbf{j}}{\sqrt{1 + f_x^2}} \\ \mathbf{t} &= \frac{-\mathbf{i} - f_x \mathbf{j}}{\sqrt{1 + f_x^2}}\end{aligned}\quad (\text{A.8})$$

From (A.8), the inverse relation can be written as



Figure 18. Normal and tangent on lower surface.

$$\begin{aligned}\mathbf{i} &= (f_x \mathbf{n} - \mathbf{t}) / \sqrt{1 + f_x^2} \\ \mathbf{j} &= (-\mathbf{n} - f_x \mathbf{t}) / \sqrt{1 + f_x^2}\end{aligned}\quad (\text{A.9})$$

The new normal and the tangent on the lower surface (perturbed in the  $y$ -direction) are also given by (A.6).

### The Infinitesimal Segment $d\sigma$

The infinitesimal segment  $d\sigma$  on the original airfoil can be written as

$$\begin{aligned}d\sigma^2 &= dx^2 + dy^2 \\ &= dx^2 + \left(\frac{df}{dx}\right)^2 dx^2 + h.o.t. \\ &= dx^2 (1 + f_x^2) + h.o.t.\end{aligned}\quad (\text{A.10})$$

The corresponding infinitesimal segment  $d\bar{\sigma}$  on the new airfoil can be expressed as

$$\begin{aligned}d\bar{\sigma}^2 &= dx^2 + d\bar{y}^2 \\ &= dx^2 \left[1 + (f_x + \varepsilon \bar{f}_x)^2\right] + h.o.t.\end{aligned}\quad (\text{A.11})$$

From (A.11) we can show that

$$d\bar{\sigma} = d\sigma \left(1 + \varepsilon \frac{f_x \bar{f}_x}{1 + f_x^2}\right) + O(\varepsilon^2) \quad (\text{A.12})$$

### A.1 The Gradient of the Cost Function

Let the change in the design variable be such that

$$\alpha \rightarrow \alpha + \varepsilon \bar{\alpha} \quad (\text{A.13})$$

The resulting airfoil shape  $\bar{y}^{\bar{U},\bar{L}}$  (Fig. 19) and the corresponding potential  $\bar{\phi}$  that satisfies the governing equation and its boundary conditions in the new domain  $\bar{\Omega}$  can be written as

$$\bar{y}^{\bar{U},\bar{L}}(x) = y^{U,L}(x) + \varepsilon \bar{y}^{U,L}(x) \quad (\text{A.14})$$

$$\bar{\phi} = \phi + \varepsilon \bar{\phi} \quad (\text{A.15})$$

The cost function on the original airfoil is

$$F[\alpha, \phi(\alpha)] \equiv \int_{U+L} (\phi - \phi_0)^2 d\sigma \quad (\text{A.16})$$

On the new airfoil, the cost function can be written as

$$F(\alpha + \varepsilon \bar{\alpha}, \bar{\phi}) = \int_{\bar{U}+\bar{L}} (\bar{\phi} - \phi_0)^2 d\bar{\sigma} \quad (\text{A.17})$$

If we use a Taylor series expansion, the potential on the new airfoil can be shifted to the original airfoil as follows:

$$\begin{aligned}\bar{\phi}^{\bar{U},\bar{L}} &= \bar{\phi}^{U,L} + \varepsilon \bar{y} \left(\frac{\partial \bar{\phi}}{\partial y}\right)^{U,L} + O(\varepsilon^2) \\ &= \phi^{U,L} + \varepsilon \bar{\phi}^{U,L} + \varepsilon \bar{y} (\nabla \phi \cdot \mathbf{j})^{U,L} + O(\varepsilon^2)\end{aligned}\quad (\text{A.18})$$

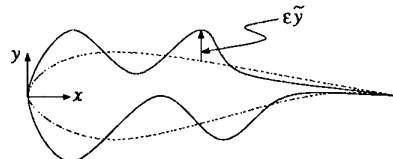


Figure 19. Perturbed airfoil shape.

If we substitute for  $d\bar{\sigma}$  from (A.12) and for  $\bar{\phi}$  from (A.18) and use (A.3) and (A.9), (A.17) can be written as

$$\begin{aligned}
F(\alpha + \varepsilon\bar{\alpha}, \bar{\phi}) &= F(\alpha, \phi) \\
&+ \varepsilon \int_U 2(\phi - \phi_0) \frac{y_x \bar{y}}{\sqrt{1 + y_x^2}} \nabla \phi \cdot t d\sigma \\
&- \varepsilon \int_L 2(\phi - \phi_0) \frac{y_x \bar{y}}{\sqrt{1 + y_x^2}} \nabla \phi \cdot t d\sigma \\
&+ \varepsilon \int_{U+L} (\phi - \phi_0)^2 \frac{y_x \bar{y}_x}{1 + y_x^2} d\sigma \\
&+ \varepsilon \int_{U+L} 2(\phi - \phi_0) \bar{\phi} d\sigma + O(\varepsilon^2)
\end{aligned} \tag{A.19}$$

The left-hand side of (A.19) can be expressed as

$$F(\alpha + \varepsilon\bar{\alpha}, \bar{\phi}) = F(\alpha, \phi) + \varepsilon \bar{\alpha}^T \nabla_\alpha F + O(\varepsilon^2) \tag{A.20}$$

where

$$\nabla_\alpha F \equiv \frac{\partial F}{\partial \alpha} + \left( \frac{d\phi}{d\alpha} \right)^T \frac{\partial F}{\partial \phi} \tag{A.21}$$

and  $\nabla_\alpha F$  are the components of the gradient of the cost function. If we compare (A.19) and (A.20), we obtain

$$\begin{aligned}
\bar{\alpha}^T \nabla_\alpha F &= \int_U 2(\phi - \phi_0) \frac{y_x \bar{y}}{\sqrt{1 + y_x^2}} \nabla \phi \cdot t d\sigma \\
&- \int_L 2(\phi - \phi_0) \frac{y_x \bar{y}}{\sqrt{1 + y_x^2}} \nabla \phi \cdot t d\sigma \\
&+ \int_{U+L} (\phi - \phi_0)^2 \frac{y_x \bar{y}_x}{1 + y_x^2} d\sigma \\
&+ \int_{U+L} 2(\phi - \phi_0) \bar{\phi} d\sigma
\end{aligned} \tag{A.22}$$

## A.2 The State Equations

### The Governing Equation

For incompressible flow, the governing equation in the domain  $\Omega$  is

$$\text{div}(\nabla \phi) = 0 \tag{A.23}$$

After the airfoil is perturbed, the governing equation in the new domain  $\bar{\Omega}$  is

$$\text{div}(\nabla \bar{\phi}) = 0 \tag{A.24}$$

where

$$\bar{\phi} = \phi + \varepsilon \bar{\phi} \tag{A.25}$$

In the region that is the intersection of both domains, we can write

$$\text{div}(\nabla \bar{\phi}) - \text{div}(\nabla \phi) = 0 \tag{A.26}$$

From (A.26) we can show that

$$\text{div}(\nabla \bar{\phi}) = 0 \quad \text{in } \Omega \cap \bar{\Omega} \tag{A.27}$$

Therefore, in the limit as  $\varepsilon \rightarrow 0$ , we can write

$$\text{div}(\nabla \bar{\phi}) = 0 \quad \text{in } \Omega \tag{A.28}$$

### The Airfoil Boundary Condition

The boundary condition on the airfoil is

$$\nabla \phi \cdot \mathbf{n} = 0 \tag{A.29}$$

where  $\mathbf{n}$  is the unit normal on the airfoil. If  $\bar{\mathbf{n}}$  is the unit normal on the new airfoil, then the boundary condition on the new airfoil can be written as

$$\nabla(\phi + \varepsilon \bar{\phi}) \cdot \bar{\mathbf{n}} = 0 \tag{A.30}$$

With (A.6) and (A.18), the boundary condition on the new airfoil, shifted to the original airfoil, can be written as

$$\nabla(\phi + \varepsilon \bar{\phi} + \varepsilon \bar{y} \nabla \phi \cdot \mathbf{j}) \cdot \left( \mathbf{n} - \varepsilon \frac{\bar{y}_x}{\sqrt{1 + y_x^2}} \mathbf{t} \right) + O(\varepsilon^2) = 0 \tag{A.31}$$

If we expand (A.31), substitute (A.29), and neglect the high-order terms, we can write

$$\nabla \bar{\phi} \cdot \mathbf{n} = -\nabla(\bar{y} \nabla \phi \cdot \mathbf{j}) \cdot \mathbf{n} + \frac{\bar{y}_x}{\sqrt{1 + y_x^2}} \nabla \phi \cdot \mathbf{t} \tag{A.32}$$

Note that (A.32) is true on the original airfoil.

With (A.2), (A.3), (A.8), (A.9) and the boundary condition (A.29) we can show that

$$\begin{aligned}
\nabla \bar{\phi} \cdot \mathbf{n} &= \nabla(\bar{y} \nabla \phi \cdot \mathbf{t}) \cdot \mathbf{i} - \frac{\bar{y}}{\sqrt{1 + y_x^2}} \nabla^2 \phi \quad \text{on } U \\
\nabla \bar{\phi} \cdot \mathbf{n} &= \nabla(\bar{y} \nabla \phi \cdot \mathbf{t}) \cdot \mathbf{i} + \frac{\bar{y}}{\sqrt{1 + y_x^2}} \nabla^2 \phi \quad \text{on } L
\end{aligned} \tag{A.33}$$

Because  $\nabla^2 \phi = 0$  (the governing equation), we can write

$$\nabla \bar{\phi} \cdot \mathbf{n} = \nabla(\bar{y} \nabla \phi \cdot \mathbf{t}) \cdot \mathbf{i} \quad \text{on the airfoil} \tag{A.34}$$

### The Far-Field Boundary Condition

At the far field,

$$\nabla \phi \cdot \mathbf{n} = U_\infty \cdot \mathbf{n} + \frac{\Gamma}{2\pi} \nabla \Theta \cdot \mathbf{n} \tag{A.35}$$

where  $\mathbf{n}$  is the unit normal on the far-field boundary. After the perturbation, we can write

$$\nabla(\phi + \varepsilon \bar{\phi}) \cdot \mathbf{n} = U_\infty \cdot \mathbf{n} + \frac{\Gamma + \varepsilon \bar{\Gamma}}{2\pi} \nabla \Theta \cdot \mathbf{n} \tag{A.36}$$

If we subtract (A.35) from (A.36), we obtain

$$\nabla \bar{\phi} \cdot \mathbf{n} = \frac{\bar{\Gamma}}{2\pi} \nabla \Theta \cdot \mathbf{n} \tag{A.37}$$

### The Cut

Along the cut

$$\phi^T - \phi^B = \Gamma \tag{A.38}$$

where

$$\Gamma = \phi_{t.e.}^T - \phi_{t.e.}^B \tag{A.39}$$

After the perturbation,

$$(\phi + \varepsilon \bar{\phi})^T - (\phi + \varepsilon \bar{\phi})^B = \Gamma + \varepsilon \bar{\Gamma} \tag{A.40}$$

From (A.38) through (A.40), we obtain

$$\bar{\phi}^T - \bar{\phi}^B = \bar{\Gamma} \tag{A.41}$$

where

$$\bar{\Gamma} = \bar{\phi}_{t.e.}^T - \bar{\phi}_{t.e.}^B \tag{A.42}$$

### A.3 Summary

From the cost function, we get

$$\begin{aligned} \bar{\alpha}^T \nabla_{\alpha} F &= \int_U 2(\phi - \phi_0) \frac{y_x \bar{y}}{\sqrt{1 + y_x^2}} \nabla \phi \cdot \mathbf{t} d\sigma \\ &- \int_L 2(\phi - \phi_0) \frac{y_x \bar{y}}{\sqrt{1 + y_x^2}} \nabla \phi \cdot \mathbf{t} d\sigma \\ &+ \int_{U+L} (\phi - \phi_0)^2 \frac{y_x \bar{y}_x}{1 + y_x^2} d\sigma \\ &+ \int_{U+L} 2(\phi - \phi_0) \bar{\phi} d\sigma \end{aligned} \quad (\text{A.43})$$

where  $\epsilon \bar{\alpha}$  are the changes in the design variables and  $\nabla_{\alpha} F$  are the components of the gradient of the cost function.

From the state equations, we obtain

$$\begin{aligned} \text{div}(\nabla \bar{\phi}) &= 0 && \text{in } \Omega \\ \nabla \bar{\phi} \cdot \mathbf{n} &= \nabla(\bar{y} \nabla \phi \cdot \mathbf{t}) \cdot \mathbf{i} && \text{on the airfoil} \\ \nabla \bar{\phi} \cdot \mathbf{n} &= \frac{\bar{\Gamma}}{2\pi} \nabla \Theta \cdot \mathbf{n} && \text{at the far field} \\ \bar{\phi}^T - \bar{\phi}^B &= \bar{\Gamma} && \text{along the cut} \end{aligned} \quad (\text{A.44})$$

where

$$\bar{\Gamma} = \bar{\phi}_{i.e.}^T - \bar{\phi}_{i.e.}^B \quad (\text{A.45})$$

Because

$$\text{div}(\nabla \bar{\phi}) = 0 \quad \text{in } \Omega \quad (\text{A.46})$$

then

$$\iint_{\Omega} \text{div}(\nabla \bar{\phi}) d\Omega = 0 \quad (\text{A.47})$$

If we use the divergence theorem, then we can write

$$\iint_{\Omega} \text{div}(\nabla \bar{\phi}) d\Omega = \int_{\tau} \nabla \bar{\phi} \cdot \mathbf{n} d\tau = 0 \quad (\text{A.48})$$

where  $\tau$  denotes the boundary of  $\Omega$ . Equation (A.48) implies that in order for (A.44) to have a solution

$$\frac{\bar{\Gamma}}{2\pi} \int_{\Omega} \nabla \Theta \cdot \mathbf{n} d\tau + \int_{U+L} \nabla(\bar{y} \nabla \phi \cdot \mathbf{t}) \cdot \mathbf{i} d\sigma = 0 \quad (\text{A.49})$$

These integrals can be easily shown to be equal to 0.

### Appendix B

Presented here is the discretization and the solution procedure for the governing equations and the boundary conditions. Note that the compressible full potential equations are considered here.

### B.1 The Grid

An O type of grid is used to discretize the computational domain. The grid lines form a set of curvilinear coordinates  $(\xi, \eta)$ , where

$$\begin{aligned} \xi &= \xi(x, y) \\ \eta &= \eta(x, y) \end{aligned} \quad (\text{B.1})$$

The  $\xi$ -direction is clockwise around the airfoil, and the  $\eta$ -direction is radial away from the airfoil. Figure 20 shows a coarse schematic of an O type of grid. The cells in the  $\xi$ -direction run from 1 to  $I$ , and cells in the  $\eta$ -direction run from 1 to  $J$ . The grid-line  $j = 1/2$  from  $i = 1/2$  to  $i = I + 1/2$  represents the airfoil. Not shown are the ghost cells around the boundaries of the domain, where the boundary conditions are applied.

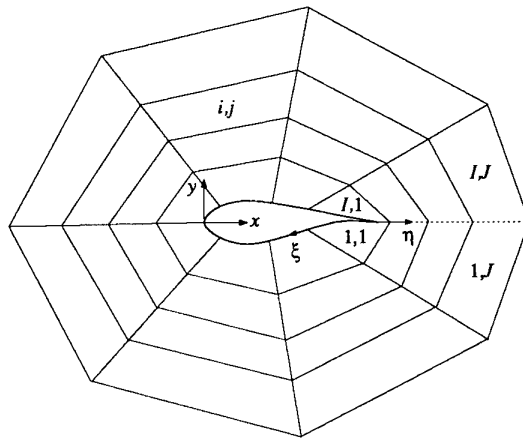


Figure 20. The grid.

### B.2 The Governing Equation

The governing equation is discretized with the finite-volume approach. The velocity potential  $\phi$  is a cell-average value and is located at the cell center  $(i, j)$ . The fluxes at the cell faces are evaluated with central differences. Hence, this discretization is effective only for subsonic flows. In the generalized curvilinear coordinate system  $(\xi, \eta)$ , the compressible full potential equation (3.1) can be written as

$$\frac{\partial}{\partial \xi} \left( \rho \frac{U}{J} \right) + \frac{\partial}{\partial \eta} \left( \rho \frac{V}{J} \right) = 0 \quad (\text{B.2})$$

where

$$\rho = \left[ 1 - \frac{\gamma - 1}{2} M_{\infty}^2 (\phi_x^2 + \phi_y^2 - 1) \right]^{\frac{1}{\gamma - 1}} \quad (\text{B.3})$$

is the density and

$$\begin{aligned} U &= \xi_x \phi_x + \xi_y \phi_y \\ V &= \eta_x \phi_x + \eta_y \phi_y \end{aligned} \quad (\text{B.4})$$

are the contravariant velocity components;  $\xi_x$ ,  $\xi_y$ ,  $\eta_x$ , and  $\eta_y$  are the metric coefficients; and  $J$  is the Jacobian of the transformation. Note that  $J$  is also used to denote the

outermost cell in the  $\eta$ -direction. The velocity components  $\phi_x$  and  $\phi_y$  can be expressed as

$$\begin{aligned}\phi_x &= \phi_\xi \xi_x + \phi_\eta \eta_x \\ \phi_y &= \phi_\xi \xi_y + \phi_\eta \eta_y\end{aligned}\quad (\text{B.5})$$

If the inverse of the transformation  $x = x(\xi, \eta)$  and  $y = y(\xi, \eta)$  is known, the metric coefficients and the Jacobian can be expressed as

$$\begin{aligned}\xi_x &= J y_\eta \\ \xi_y &= -J x_\eta \\ \eta_x &= -J y_\xi \\ \eta_y &= J x_\xi\end{aligned}\quad (\text{B.6})$$

$$J = 1/(x_\xi y_\eta - x_\eta y_\xi) \quad (\text{B.7})$$

Figure 21 shows a typical cell in the flow field. The coordinates of the vertices of the cell are known from the grid generation. That is,

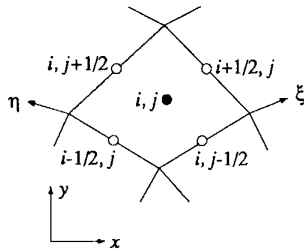


Figure 21. A cell in flow field.

coordinates of the vertices of the cell are known from the grid generation. That is,

$$\begin{aligned}x &= x\left(i \pm \frac{1}{2}, j \pm \frac{1}{2}\right) \\ y &= y\left(i \pm \frac{1}{2}, j \pm \frac{1}{2}\right)\end{aligned}\quad (\text{B.8})$$

By choosing  $\delta\xi = \delta\eta = 1$ , a finite-volume discretization of the governing equation (B.2) for the cell  $(i, j)$  can be written as

$$\left(\frac{\rho U}{J}\right)_{i+\frac{1}{2},j} - \left(\frac{\rho U}{J}\right)_{i-\frac{1}{2},j} + \left(\frac{\rho V}{J}\right)_{i,j+\frac{1}{2}} - \left(\frac{\rho V}{J}\right)_{i,j-\frac{1}{2}} = 0 \quad (\text{B.9})$$

Equation (B.9) is a consistent approximation to the integral form of the full potential equation.

Consider the first term in (B.9). If we substitute from (B.4) and (B.6), then we can write

$$\left(\frac{\rho U}{J}\right)_{i+\frac{1}{2},j} = \rho_{i+\frac{1}{2},j} (y_\eta \phi_x - x_\eta \phi_y)_{i+\frac{1}{2},j} \quad (\text{B.10})$$

where

$$(x_\eta)_{i+\frac{1}{2},j} = x_{i+\frac{1}{2},j+\frac{1}{2}} - x_{i+\frac{1}{2},j-\frac{1}{2}} \quad (\text{B.11})$$

The evaluation of  $y_\eta$  is similar. If we use (B.6), then the velocity components given by (B.5) can be written as

$$\begin{aligned}\phi_x &= \bar{J} \bar{y}_\eta \phi_\xi - \bar{J} \bar{y}_\xi \phi_\eta \\ \phi_y &= -\bar{J} \bar{x}_\eta \phi_\xi + \bar{J} \bar{x}_\xi \phi_\eta\end{aligned}\quad (\text{B.12})$$

The bars over the metric coefficients and the Jacobian indicate that they are evaluated with some mean values of  $x$  and  $y$ .

To ensure that the numerical discretization satisfies a uniform flow field identically, (B.12) is discretized as

$$\begin{aligned}(\phi_\xi)_{i+\frac{1}{2},j} &= \phi_{i+1,j} - \phi_{i,j} \\ (\phi_\eta)_{i+\frac{1}{2},j} &= \frac{1}{4}(\phi_{i+1,j+1} - \phi_{i+1,j-1} + \phi_{i,j+1} - \phi_{i,j-1})\end{aligned}\quad (\text{B.13})$$

and

$$\begin{aligned}(\bar{x}_\xi)_{i+\frac{1}{2},j} &= x_{i+1,j} - x_{i,j} \\ (\bar{x}_\eta)_{i+\frac{1}{2},j} &= \frac{1}{4}(x_{i+1,j+1} - x_{i+1,j-1} + x_{i,j+1} - x_{i,j-1})\end{aligned}\quad (\text{B.14})$$

where

$$x_{i,j} = \frac{1}{4}(x_{i-\frac{1}{2},j-\frac{1}{2}} + x_{i+\frac{1}{2},j-\frac{1}{2}} + x_{i+\frac{1}{2},j+\frac{1}{2}} + x_{i-\frac{1}{2},j+\frac{1}{2}}) \quad (\text{B.15})$$

Evaluation of  $\bar{y}_\xi$  and  $\bar{y}_\eta$  are similar.  $\bar{J}$  is evaluated as

$$\bar{J} = 1/(\bar{x}_\xi \bar{y}_\eta - \bar{x}_\eta \bar{y}_\xi) \quad (\text{B.16})$$

Similarly, we can write

$$\left(\frac{\rho V}{J}\right)_{i,j+\frac{1}{2}} = \rho_{i,j+\frac{1}{2}} (-y_\xi \phi_x + x_\xi \phi_y)_{i,j+\frac{1}{2}} \quad (\text{B.17})$$

where

$$(x_\xi)_{i,j+\frac{1}{2}} = x_{i+\frac{1}{2},j+\frac{1}{2}} - x_{i-\frac{1}{2},j+\frac{1}{2}} \quad (\text{B.18})$$

and  $y_\xi$  is evaluated similarly. The various pieces of the velocity components given by (B.12) are discretized as

$$\begin{aligned}(\phi_\xi)_{i,j+\frac{1}{2}} &= \frac{1}{4}(\phi_{i+1,j+1} - \phi_{i-1,j+1} + \phi_{i+1,j} - \phi_{i-1,j}) \\ (\phi_\eta)_{i,j+\frac{1}{2}} &= \phi_{i,j+1} - \phi_{i,j}\end{aligned}\quad (\text{B.19})$$

and

$$\begin{aligned}(\bar{x}_\xi)_{i,j+\frac{1}{2}} &= \frac{1}{4}(x_{i+1,j+1} - x_{i-1,j+1} + x_{i+1,j} - x_{i-1,j}) \\ (\bar{x}_\eta)_{i,j+\frac{1}{2}} &= x_{i,j+1} - x_{i,j}\end{aligned}\quad (\text{B.20})$$

where  $x_{i,j}$  is given by (B.15). Similarly,  $\bar{y}_\xi$  and  $\bar{y}_\eta$  are evaluated.

### B.3 The Boundary Conditions

The boundary conditions are imposed with one set of ghost cells around the computational domain. For the cells adjacent to the airfoil  $(i, 1)$ , the metric coefficients except  $(\bar{x}_\xi)_{i+1/2,1}$  are computed as

$$\begin{aligned}(\bar{x}_\eta)_{i+\frac{1}{2},1} &= x_{i+\frac{1}{2},\frac{3}{2}} - x_{i+\frac{1}{2},\frac{1}{2}} \\ (\bar{x}_\xi)_{i,\frac{1}{2}} &= x_{i+\frac{1}{2},\frac{1}{2}} - x_{i-\frac{1}{2},\frac{1}{2}} \\ (\bar{x}_\eta)_{i,\frac{1}{2}} &= \frac{1}{2}(x_{i+\frac{1}{2},\frac{3}{2}} - x_{i+\frac{1}{2},\frac{1}{2}} + x_{i-\frac{1}{2},\frac{3}{2}} - x_{i-\frac{1}{2},\frac{1}{2}})\end{aligned}\quad (\text{B.21})$$

Similarly, the corresponding metric coefficients that are functions of  $y$  are also evaluated.

### The Airfoil

If we use (3.2), (B.4), and (B.6), then we can write that (on the airfoil)

$$(\nabla\phi \cdot \mathbf{n})\sqrt{(x_\xi^2 + y_\xi^2)} = \frac{V}{J} = 0 \quad (\text{B.22})$$

Figure 22 shows a ghost cell adjacent to the airfoil. The

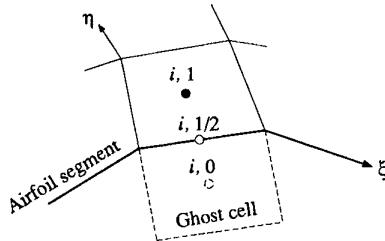


Figure 22. Ghost cell adjacent to airfoil.

value of  $\phi_{i,0}$  is set such that

$$\left(\frac{V}{J}\right)_{i, \frac{1}{2}} = 0 \quad (\text{B.23})$$

### The Far Field

Figure 23 shows a ghost cell adjacent to the far-field boundary. Similar to (B.22), we can show from (3.9) that at the far-field boundary

$$\frac{V}{J} = \left(\mathbf{U}_\infty \cdot \mathbf{n} + \frac{\Gamma}{2\pi} \nabla\Theta \cdot \mathbf{n}\right)\sqrt{(x_\xi^2 + y_\xi^2)} \quad (\text{B.24})$$

The value of  $\phi_{i,J+1}$  is set such that

$$\begin{aligned} &\left(\frac{V}{J}\right)_{i, J+\frac{1}{2}} \\ &= \left(\mathbf{U}_\infty \cdot \mathbf{n} + \frac{\Gamma}{2\pi} \nabla\Theta \cdot \mathbf{n}\right)_{i, J+\frac{1}{2}} \sqrt{(x_\xi^2 + y_\xi^2)}_{i, J+\frac{1}{2}} \end{aligned} \quad (\text{B.25})$$

The value of the circulation  $\Gamma$  is given by (refer to Appendix C for details)

$$\Gamma = \phi_{I,1} - \phi_{1,1} \quad (\text{B.26})$$

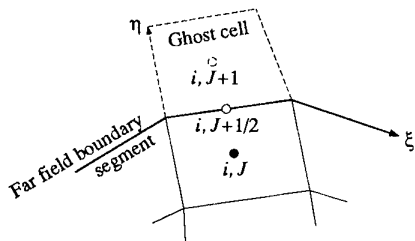


Figure 23. Ghost cell adjacent to far-field boundary.

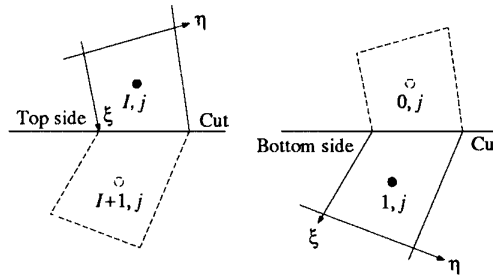
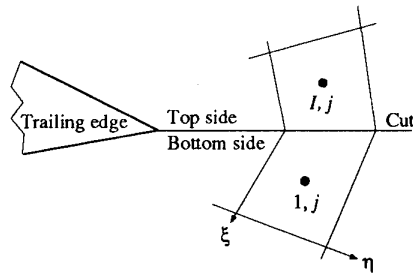


Figure 24. Ghost cells along cut.

### The Cut

Figure 24 shows the ghost cells along the top and bottom sides of the cut. The potential along the cut has a jump prescribed by (B.26). However, because the gradient of the potential normal to the cut must be continuous, the potential in these ghost cells is set as follows:

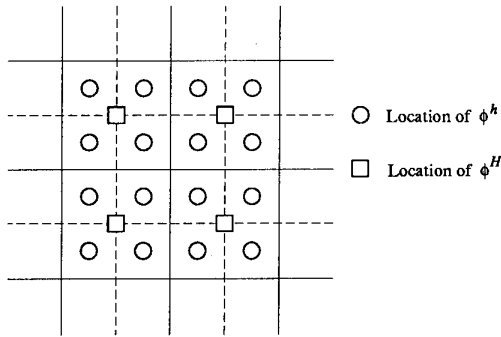
$$\begin{aligned} \phi_{0,j} &= \phi_{I,j} - \Gamma \\ \phi_{I+1,j} &= \phi_{1,j} + \Gamma \end{aligned} \quad (\text{B.27})$$

### B.4 The Solution Procedure

The discrete equations are solved with a Gauss-Seidel line-relaxation scheme. The nonlinearity introduced by the density  $\rho$  is handled by lagging its value by one iteration. Two systems of tridiagonal equations, one implicit in the  $\xi$ -direction and the other implicit in the  $\eta$ -direction, are solved sequentially with the Thomas algorithm. Note that the tridiagonal system implicit in the  $\xi$ -direction is periodic. A full approximation scheme (FAS) multigrid is used to accelerate the rate of convergence. Line relaxation is used to avoid the degradation in the performance of the multigrid scheme because of the presence of grid cells with large aspect ratios.

### B.5 The Multigrid Acceleration

A multigrid scheme is used to accelerate the convergence rate of the governing equations. In the multigrid process, starting with the fine grid, the problem is solved on a succession of increasingly coarser grids, and the corrections  $\delta\phi$  from the coarser grids are successively transferred back to the fine grid to obtain a new approximation to the solution. In this process, the component of the error that appears as a high frequency on a grid is damped very quickly by the iteration on that grid. Thus, low-frequency components of the error are damped on coarser grids, and the high-frequency components are damped on finer grids. This property of the multigrid is exploited by the *One-Shot* method during the design

Figure 25. Location of  $\phi$  in fine and coarse grids.

process. Because the full potential equations are nonlinear, a FAS multigrid is used.

A two grid FAS multigrid algorithm is presented below. Let the fine grid on which solution is sought be represented by  $h$  and the coarse grid be represented by  $H$ . Also, let  $h$  and  $H$  represent grid sizes, where  $H > h$ . A coarse grid can be built by removing every second grid point from a fine grid. This makes  $H = 2h$ . For the cell-centered scheme, this method of coarsening combines four fine grid cells to form a coarse grid cell. Figure 25 shows the location of  $\phi^h$  and  $\phi^H$  on a fine and a coarse grid, respectively. Now, consider the following problem on grid  $h$ :

$$\mathcal{L}^h(\phi^h) = \mathcal{R}^h \quad (\text{B.28})$$

where  $\mathcal{L}^h(\phi^h)$  is a nonlinear equation and  $\mathcal{R}^h$  is its right-hand side. Equation (B.28) represents the discretized full potential equation or any of the boundary conditions. After a few relaxations of (B.28) on grid  $h$ , if we assume that the remaining error is smooth enough to be approximated on a coarse grid, then  $\phi$  and its residuals are transferred to the coarse grid  $H$  and an equivalent coarse grid problem is solved on this grid. The equivalent coarse grid problem can be written as

$$\mathcal{L}^H(\phi^H) = \mathcal{R}^H \quad (\text{B.29})$$

where

$$\mathcal{R}^H = \bar{I}_h^H [\mathcal{R}^h - \mathcal{L}^h(\phi^h)] + \mathcal{L}^H(\bar{I}_h^H \phi^h) \quad (\text{B.30})$$

and  $\bar{I}_h^H$  and  $I_h^H$  are the restriction operators that transfer  $\phi^h$  and its residuals to the coarse grid. Equation (B.29) is solved on the coarse grid, and the corrections  $\delta\phi^H$  are transferred back to the fine grid  $h$  to update  $\phi^h$  as follows:

$$\phi_{New}^h = \phi_{Old}^h + I_h^h \delta\phi^H \quad (\text{B.31})$$

where

$$\delta\phi^H = \phi^H - I_h^H \phi^h \quad (\text{B.32})$$

and  $I_h^H$  is the interpolation operator that transfers the corrections to the fine grid. This process is repeated until the residual of (B.28) reaches machine zero.

In the two-grid algorithm described above, we assume that the solution to (B.29) is accurate. In the multigrid algorithm, the solution on grid  $H$  is obtained by another two-grid iteration, where  $H$  is the fine grid and  $2H = 4h$  is the coarse grid. If this process is repeated this process on grid  $2H$  and so on, the "exact" solution is obtained on a very coarse grid. The sequence in which the transfer and relaxation are

performed between successive grids is done in various ways. Two of the more popular methods, V cycle and W cycle, are shown in Fig. 26. The V cycle consists of a sequence of relaxation and transfer to coarser grids with the "exact" resolution on the coarsest grid, followed by a sequence of relaxation and transfer back to the finest grid. In the Coarser levels are visited more often in the W cycle than in the V cycle. The W cycle, although 50 percent more expensive than V cycle, is more robust.

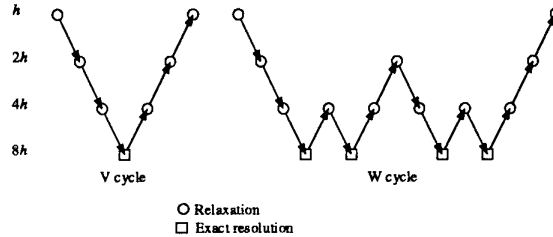


Figure 26. Multigrid cycling strategies.

### Appendix C

The Kutta condition states that the circulation  $\Gamma$  around the airfoil should be such that  
the velocity is finite and continuous at the trailing edge.

The value of  $\Gamma$  is determined by requiring that the velocity that is perpendicular to the trailing edge bisector be equal to 0 at the trailing edge. In Fig. 27, let  $u_t$  and  $u_n$  be the

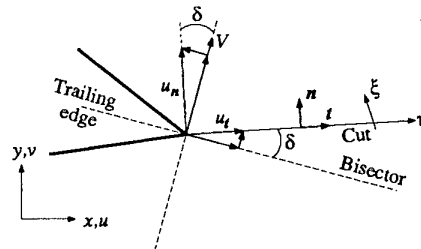


Figure 27. Velocity at trailing edge.

velocity components along the cut and perpendicular to the cut, respectively. Let the unit vectors in the corresponding directions be  $\mathbf{t}$  and  $\mathbf{n}$ , respectively. Let  $\delta$  be the angle between the trailing edge bisector and the cut. The velocity  $V$  perpendicular to the trailing-edge bisector, can be written as

$$V = u_n \cos \delta + u_t \sin \delta \quad (\text{C.1})$$

where

$$\begin{aligned} u_n &= (u, v) \cdot \mathbf{n} \\ u_t &= (u, v) \cdot \mathbf{t} \end{aligned} \quad (\text{C.2})$$

As shown in Appendix B, the Cartesian velocity components  $u$  and  $v$  can be expressed as

$$\begin{aligned} u &= \phi_x = +J(y_\eta \phi_\xi - y_\xi \phi_\eta) \\ v &= \phi_y = -J(x_\eta \phi_\xi - x_\xi \phi_\eta) \end{aligned} \quad (\text{C.3})$$

and the unit vectors can be expressed as

$$\begin{aligned} \mathbf{n} &= (y_\eta/r, -x_\eta/r) \\ \mathbf{t} &= (x_\eta/r, y_\eta/r) \end{aligned} \quad (\text{C.4})$$

where

$$r = \sqrt{x_\eta^2 + y_\eta^2} \quad (\text{C.5})$$

If we substitute (C.2) through (C.5) into (C.1), it can be written as

$$V = [J(x_\eta^2 + y_\eta^2)\phi_\xi - J(x_\xi x_\eta + y_\xi y_\eta)\phi_\eta] \frac{\cos \delta}{r} + \phi_\eta \frac{\sin \delta}{r} \quad (\text{C.6})$$

To satisfy the Kutta condition, we require that  $V = 0$ . That is,

$$\phi_\xi + \left[ \frac{-J(x_\xi x_\eta + y_\xi y_\eta) + \tan \delta}{J(x_\eta^2 + y_\eta^2)} \right] \phi_\eta = 0 \quad (\text{C.7})$$

If the cut is aligned with the trailing edge bisector, then  $\delta = 0$ . If the grid is orthogonal, then  $x_\xi x_\eta + y_\xi y_\eta = 0$ . Therefore, if

the grid is orthogonal and the trailing-edge bisector is aligned with the cut, then (C.7) reduces to

$$\phi_\xi = 0 \quad (\text{C.8})$$

or

$$\phi_{t.e.}^T - (\phi_{t.e.}^B + \Gamma) = 0 \quad (\text{C.9})$$

where T and B refer to the top and bottom sides of the cut, respectively (see Fig. 1) and *t.e.* stands for the trailing edge. The value of  $\Gamma$  is easily obtained from (C.9).

In practice, particularly while designing an airfoil, the grid is not orthogonal nor is the trailing edge bisector aligned with the cut. However, numerical experiments have shown that the effect of the second term in (C.7) is of high order. Hence, a good approximation for the value of  $\Gamma$  can be obtained from (C.9).

# Tools for Applied Engineering Optimization

A. Van der Velden\*  
 EF 14 Aerodynamic Design Section  
 Deutsche Aerospace Airbus  
 Hünefeldstrasse 1-5  
 2183 Bremen  
 GERMANY

## 1 Abstract

This paper is an introduction to applied optimization of engineering problems, with an emphasis on aircraft design. First, the optimization problem is described—namely, the objective function and the problems often involved in its optimization, the variables or parameters over which the objective function is optimized, and the constraints upon the objective function. Formulation of the optimization problem to ensure rapid and accurate convergence is discussed and illustrated with specific examples. Three classes of optimization methods: evolution, downhill simplex and gradient optimization, are discussed. The robustness and speed of these optimization methods are evaluated and compared. Finally, a number of practical implementation issues related to optimization are highlighted.

## 2 Introduction

Over the last twenty years, many methods have been developed for optimizing aircraft solutions for various objectives (*e.g.* minimum cost or weight). Industry has traditionally optimized aircraft by varying parameters with respect to each other, and then comparing the respective cost or objective functions. Even though the variation of parameters is useful for optimization over a few parameters, it is impractical for the hyperdimensional ( $N > 20$ ) problems encountered in the design of aircraft.

If we consider, for example, a simple problem with ten possible discrete values for five parameters, we will have to calculate and compare  $10^5$  discrete solutions. For a typical objective function evaluation time of five minutes, a *year* of CPU time would be required to merely calculate the various configura-

tions. Because of this immense cost, industry has been limited to investigating a tiny fraction of the design space. A possible solution to this problem is to reduce the design problem to an objective function topography that has as many dimensions as design parameters and then to find the global minimum using optimization algorithms. Constraints are enforced by locally increasing the objective function to values higher than the global minimum. The development of robust nonlinear optimization algorithms which can rapidly solve hyperdimensional optimization problems with current computer technology is therefore essential if we wish to evaluate the entire design space and thereby restore flexibility to the aircraft design process.

## 3 The Objective Function

The objective function is the function which will be minimized—*i.e.* its value will determine whether the parameter or variable values are “optimal.”

### 3.1 The objective function topography

The objective function will often have a complex topography. All optimization methods have at least some difficulty with topographical features such as: narrow valleys where the function is low for a narrow range of one or more parameters; large relatively flat plains where the function does not vary significantly, and multiple valleys, or local minima. An objective function  $f$  which illustrates these complex topographical features can be described by the following system of nonlinear transcendent equations (Fig. 1):

$$f = 1 + \sum_{i=1}^n (A_i - B_i)^2, \quad (1)$$

\*Aerospace Specialist, Deutsche Aerospace Airbus GmbH, Hünefeldstrasse 1-5, D-28183 Bremen, Germany. ©1994 by A. Van der Velden.

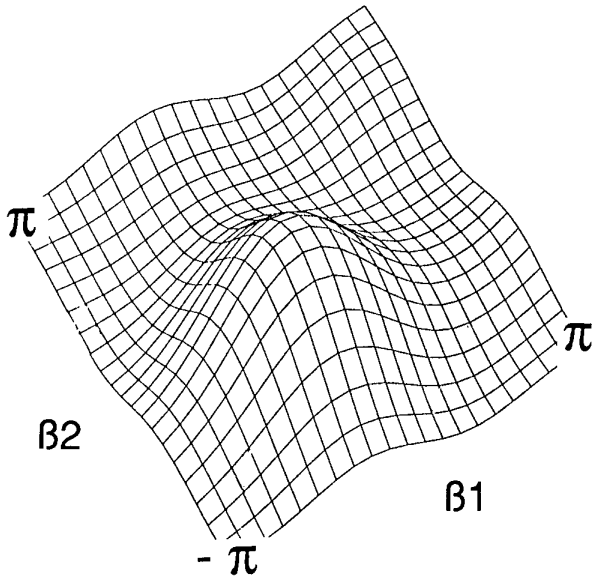


Figure 1: Objective function topography.

where

$$\begin{aligned} A_i &= \sum_{j=1}^n (a_{i,j} \sin \alpha_j + b_{i,j} \cos \alpha_j), \\ B_i &= \sum_{j=1}^n (a_{i,j} \sin \beta_j + b_{i,j} \cos \beta_j), \end{aligned} \quad (2)$$

and

$$\begin{aligned} \alpha &= \begin{bmatrix} 1.0 & 2.0 \end{bmatrix}, \\ a &= \begin{bmatrix} 0.5 & 1.0 \\ 1.5 & 2.0 \end{bmatrix}, \\ b &= \begin{bmatrix} -2.0 & -1.5 \\ -1.0 & -0.5 \end{bmatrix}. \end{aligned} \quad (3)$$

The vector  $\beta$  represents the free parameters. The minimum value of  $f$  is reached when  $\beta = \alpha$ . The topography of this function is relatively smooth, but all the parameters are strongly coupled, and this objective function is difficult to optimize because of its numerous local minima and saddle points. This function will be used later in this paper to illustrate and evaluate various optimization methods. In the rest of this section we will describe the types of topographical features which complicate optimization problems.

### 3.2 Minima and saddle points

A minimum is a point where varying each parameter results in a higher objective function value. If a function has more than one minimum, the smallest is described as a global minimum and the others as local minima. Although the optimum we want to find is the global minimum, *every* optimization strategy can mistake a local for a global minimum.

A saddle point is a point where all the partial derivatives with respect to the parameters of the objective function are zero (*i.e.* a critical point), but a variation in at least one parameter will result in a better (more optimal) objective function value.

### 3.3 Narrow valleys or gorges and large plains

Narrow valleys or gorges occur when there exist parameter(s) with a very narrow range over which the objective function value is small. Since the existence of gorges implies that the objective function parameters are strongly coupled, improvements in the objective function value are possible only when several parameters are varied simultaneously. In this case, the optimization can converge only slowly, especially for curved gorges.

Only strategies with a good selection of step sizes and direction have a chance of finding the minimum of such a narrow valley. This type of topography is typically encountered in the optimization of a highly constrained system; we have in practice observed up to fifteen coupled constraints in such cases. Even if we develop an optimization strategy which is successful in narrow valleys, the design corresponding to the minimum may be difficult if not impossible to implement.

Large flat plains, although the inverse topography of gorges, also pose problems. Over large parameter variations, little changes. In this topography, it is difficult to decide in what direction to search for the minimum.

### 3.4 Holes or singularities and poles

Holes or singularities are the extreme case of narrow valleys—minima which occupy a vanishingly small volume in space, which often occur in the middle of large plains. Again, we have strong coupling between the parameters. Holes are often due to numerical error in the optimization, and should therefore be

considered inherent features of the objective function only when they are greater in extent than the error associated with the numerical method. Although a hole may correspond to an interesting design, usually the design parameter range is so limited that it is impossible to manufacture.

A pole is a point where the optimization program generates an infinite objective function magnitude. This can be, for example, due to a divide by zero inside the analysis or to the choice of an unsuitable objective function, *e.g.* choosing to maximize  $C_L/C_D$  by minimizing  $C_D/C_L$  while allowing - 0 values of  $C_L$ .

### 3.5 Steps

Steps (steep cliffs) occur in both analytically and numerically defined objective functions. If we then consider such a "steplike" objective function at the edge of the step, we find that the derivative of the parameter is infinite. Similarly, in the middle of a step, the derivative will be zero.

### 3.6 Roughness and noise

Roughness in the objective function is defined as stochastic (over the parameter being varied) variation in the objective function value around a mean value when the parameters are varied slightly. It is distinguished from noise, which is defined to be the *nonreproducible* random variation in the objective function value, in that roughness remains constant over successive evaluations of the objective function for identical parameter values. Practically, however, these two fine-scale features cause similar optimization difficulties and are usually not considered parts of the solution.

### 3.7 Topographical improvement

A great deal of time and effort can usually be saved by preconditioning the objective function and its parameter space before we even begin to optimize the objective function. Since the convergence criteria or optimization tolerances are fixed during the optimization, the objective function should be normalized by an estimate of its global minimum, to ensure that the objective function does not vary too slowly with respect to the convergence criteria. The objective code should also be searched *extensively* for singularities and poles [8]. If possible, poles and singularities should be removed, or the parameter range(s) should

be conditioned to exclude them. The roughness of the objective function can usually be improved by increasing the numerical accuracy of the iterations. Note however that this conditioning may corrupt the optimization, and in certain cases it may be simpler and cheaper to use an appropriate method to optimize the unconditioned objective function.

## 4 The Choice of Variables and Constraints

### 4.1 Variables

We should select the set of design variables (parameters) which result in an objective function topography which best avoids the topographical difficulties described in the previous section. The number of parameters should be minimized, to speed up convergence and to simplify the objective function topography.

The variables should also be decoupled as much as possible, to minimize the number of gorges. For example, if we are interested in optimizing the length  $l$  and the diameter  $D$  of a fuselage with respect to supersonic (wave+friction) drag for a given minimum volume, and define  $l$  and  $D$  as the two variables, the drag topography will show a diagonal valley in the  $l - D$  plane, and therefore for every improvement in drag, both  $l$  and  $D$  will have to be varied. If we select  $l$  and  $l/D$  as the variables, however, the drag topography will be much simpler: the optimizer will find the optimum value for  $l/D$ , and keep it relatively constant as it reduces  $l$  until the volume hits its minimum constraint. Decoupling design variables is, unfortunately, more an art than a science, since it is very difficult to predict or visualize hyperdimensional interactions.

Finally, we should select a set of variables which minimizes the number of local minima in the objective function topography. A common mistake which is made in airfoil optimization is the choice of Fourier series as shape functions for airfoils. Although Fourier series are a convenient decomposition from both a mathematical and computational point of view, the resulting objective function will be inherently periodic, with many local minima, making it difficult to find a global minimum with any optimization method.

## 4.2 Constraints

Constraints here are constraints on either individual parameters or upon functions of the design parameters. They can be applied by imposing a penalty upon the objective function that is quadratic in the extent of constraint violation. In our case a fixed penalty to the normalized objective is added for a predefined constraint violation (tolerance). In general, there is still a sizable negative objective function gradient in the direction of an active constraint (Fig. 2). An improvement in the objective will then result in a constraint violation. This problem can be solved by making the constraint more severe. However it is not very smart to make the constraints too severe, since severe penalties create gorges in the topography. The author only classifies constraints as violated when they exceed their limits by an allowed tolerance. If the constraint lies in between his constraint boundary and its tolerance a constraint is active but not violated.

The selection of constraints is always tricky. For every active constraint imposed, a variable has to exist that can be varied to improve the constraint violation. Although this may result in a larger number of variables, it is generally better to optimize over a large flexible set than a small rigid set of parameters. An "optimal" selection of variables and constraints will depend greatly upon the intuition of the designer.

## 5 A Comparison of Optimization Tools

### 5.1 Criteria

Although optimizers promise a faster and more extensive investigation of design space, to be useful in aircraft design, they must meet these criteria:

- The optimizer should be robust. Robustness here means that the optimizer finds the global minimum for a given objective function.
- The optimizer should be able to cope with hyperdimensional parameter spaces.
- The optimizer should be practical in terms of computational time and cost. In our evaluations, the computation time did not exceed 16 hours (overnight) on workstations.

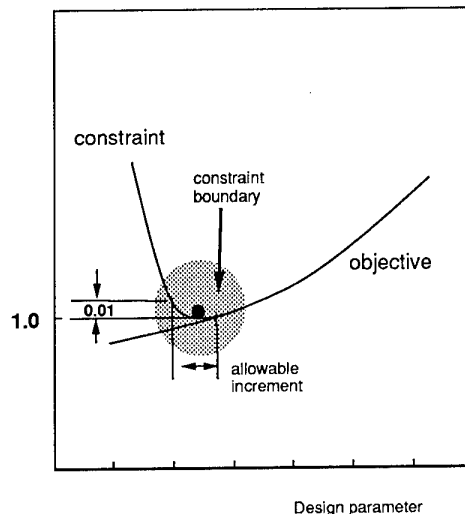


Figure 2: An active constraint.

In our study [4], a number of optimization methods were investigated with respect to these criteria. In general these methods can be divided into three groups: evolution, downhill simplex, and gradient methods. These methods will be described in the rest of this section.

### 5.2 Evolution methods

The most advanced evolution methods use mutation or recombination and selection to minimize the objective function. We start out with a large number of points randomly distributed over the design space, if possible with at least one point for every dimension of the problem. In mutation, each of the points produces a number of new points that are normally distributed around the original point. The best point out of this next generation of points is selected. In recombination, a random number of points exchange parameter values. Again, the best points are selected for the next iteration. This recombination mechanism allows points to move towards a point with a low objective function value. A standard deviation represents the average step size. This standard deviation adds one dimension to every parameter in each point in our algorithm [4]. In this way those points

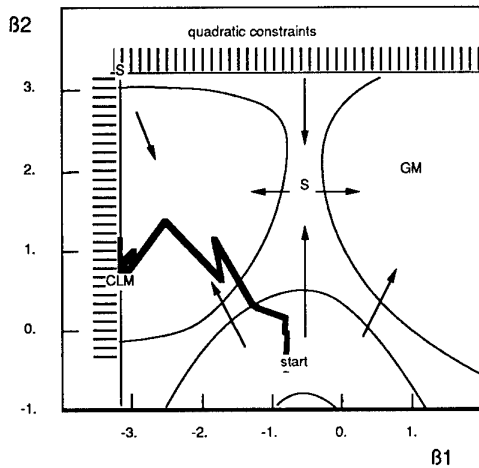


Figure 3: Evolution method.

with the best standard deviation have the highest chance of finding the global minimum.

Initially, the evolution method converges very rapidly, but it has trouble converging to the exact solution. It does however deal well with complex topographies. Fig 3 illustrates this method on the example of Figure 1. Only the best point for every new iteration (generation) is shown. Initially, the strategy goes down the slope in the direction of the left central plain. After this plain is reached, it “escapes” to the local minimum in the corner with the second lowest objective function value of the topography. More than 1200 function calls were required to reach this local minimum.

### 5.3 Downhill simplex methods.

A simplex, a geometrical body with  $n + 1$  vertices [3], is in two-dimensions a triangle, and in three dimensions, a tetrahedron. The downhill simplex method calculates and compares the objective function for the vertices of a simplex in the variable space, selects the worst one, and moves this point through the opposite face of the simplex to a lower point. If this new vertex is better, the old one is deleted. If there is no improvement after a number of steps, the

method “shrinks” the simplex by reducing the length of each side. Figure 4 shows this method applied to the Figure 1 example. Initially, the method cannot decide whether to go right or left. It then jumps to the right, bounces against the constraints and finds the global minimum, after only 48 function calls.

Contrary to popular belief, this method has the highest probability of finding the global minimum when it is started with very big initial steps (up to 10% of expected range). The initial simplex will then span a greater fraction of the design space and the chances of getting trapped in a local minimum are lessened. However, for complex hyperdimensional topographies, the method can easily break down inside the simplex. This can be avoided at some cost by often restarting the optimization.

This kick-start method [6] is based on the premise that since it is impossible to know whether one has reached a global or a local minimum, large step sizes should always be allowed unless one is certain that the global minimum has been found. This modified simplex method is a systematic repetition of the regular simplex method with a minimum number of large steps. The number of steps in the inside loop should be sufficient to allow the simplex to converge if the start vector is optimal ( $\sim 6N$ ). This way the step sizes remain large until the optimum is reached. Convergence is achieved when convergence is achieved both in the inside as well as in the outside loop.

### 5.4 Gradient methods

Gradient methods follow the path of the steepest gradient to the local minimum. The partial derivatives of the objective function with respect to the design parameters are calculated, the search direction is determined from these derivatives, and pursued until a local minimum is found. The whole procedure is repeated until the objective function shows no further improvement.

Fig 5 shows a gradient method applied to the example of Figure 1. At the starting point, the gradients are calculated, and encouraged by the initial downward slope, the algorithm immediately jumps to the opposite side of the design space, hitting the domain constraints. The algorithm then travels along the domain constraint in the direction of the negative gradient. This leads it to a saddle point where it gets stuck. More than 120 function calls were required to find an objective function value that was more than

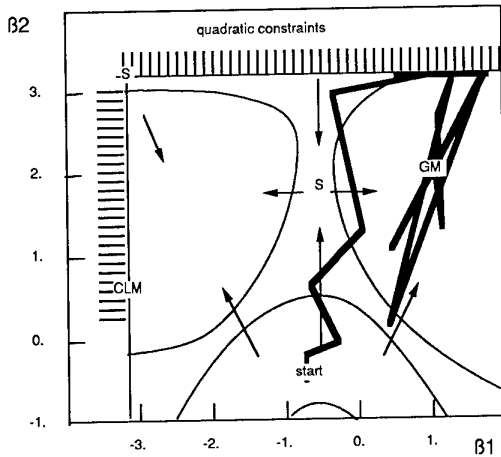


Figure 4: Downhill simplex method.

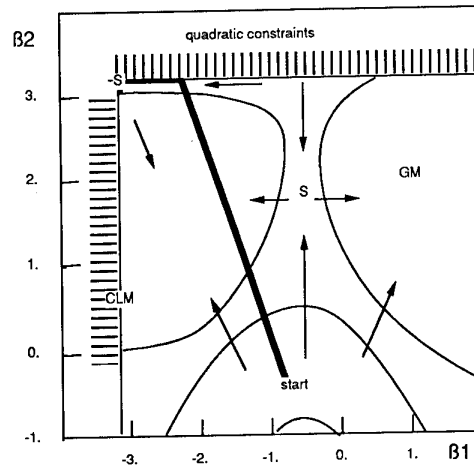


Figure 5: Gradient method.

nine times the one found by the simplex strategy.

The various gradient methods are distinguished by how the derivatives are determined. Some require explicit mathematical derivatives, while others use a finite difference approach like the variable metric method [7] used here. They are further distinguished by differences in the step sizes and the number of steps per iteration. The selection of the algorithm is often of lesser importance than the choice of minimum and maximum allowed step sizes. The minimum step size must be greater than the objective function roughness, or else the method will break down immediately. The maximum step size, on the other hand, should be small enough to properly investigate the objective function topography, and to avoid optimizer failure when an erroneous search direction is chosen.

Gradient methods converge very rapidly for simple objective function topographies. They are usually not appropriate for complex topographies, since their speed is greatly reduced and they seldom find the global minimum—usually, the strategy will become stuck in the first local minimum found.

### 5.5 Optimizer performance

These methods were investigated and calibrated in terms of speed and robustness. Speed was defined here as the number of function calls required to find the global minimum plus the time spent and lost by the designer restarting the algorithm when it becomes trapped in a local minimum. Typically half a day is spent simply interpreting the result of an optimization over several hours. This interpretation cost usually exceeds the function call cost.

Robustness  $R$  was defined as the mean harmonic error of the best optimized objective  $g_{best}$  normalized by the local optimum  $g_{i,opt}$  for a set of 24 randomly chosen start vectors:

$$R = \frac{1}{m} \sum_{i=1}^m \frac{g_{best}}{g_{i,opt}}. \quad (4)$$

The start vectors were identical for every optimizer test.

This criterion was chosen based upon the experience of the author, who was interested in the optimization of aircraft configurations. It is very sensitive when the local minimum that was found during run  $i$ ,  $g_{i,opt}$ , is near the global minimum  $g_{best}$ , and quite insensitive when the optimization completely fails. If

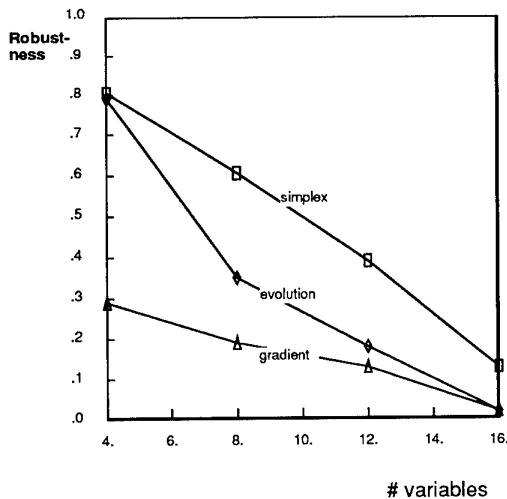


Figure 6: Robustness of optimizers for the trigonometric problem.

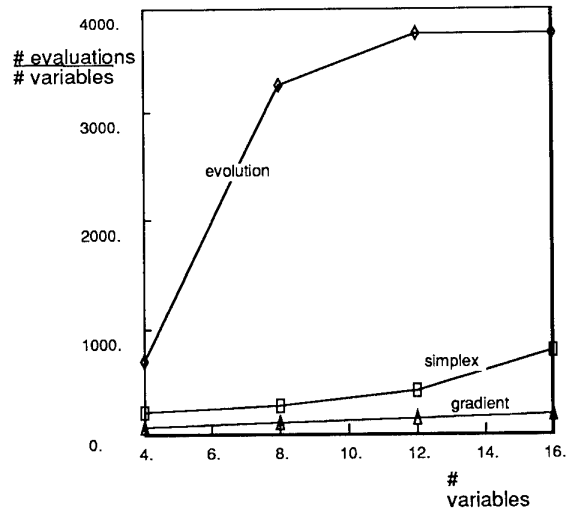


Figure 7: Computational cost for the trigonometric problem.

a design is terrible, it is thrown away immediately. If a design is close to the value expected for the optimum, it could easily be confused with the optimum. Since in aircraft designs we are usually interested in improvements of even a few percent, such mistakes should be heavily penalized. Other advantages of this criterion are its simplicity and its general applicability. Finally, this criterion has the advantage that all the optimization results are considered.

Figure 6 shows the robustness of the optimizers for the example problem of Figure 1. For this problem every optimizer started at the same random point; the problem was evaluated for identical randomly generated arrays  $a$  and  $b$ , as well as vector  $\alpha$ . Figure 7 shows the corresponding relative computational cost.

In Figure 8, the robustness  $R$  of the problem of minimizing the weight of a multi-bar truss system with a varying number of trusses of standard dimensions is shown. The standardization of the trusses further complicates this highly non-linear problem; it introduces steps in the objective function. Figure 9 shows the corresponding relative computational cost.

Although one could argue that for this problem the gradient method is more robust for a given com-

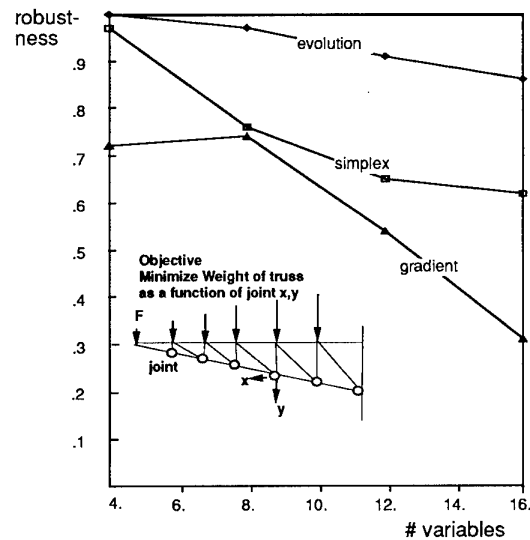


Figure 8: Robustness of optimizers for multi-bar truss system.

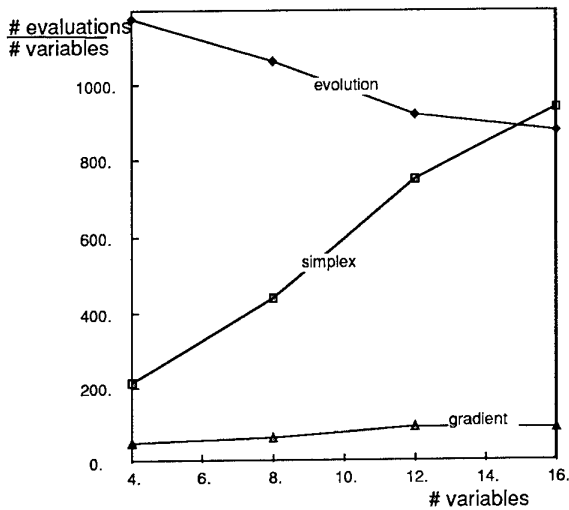


Figure 9: Computational cost for the multi-bar truss problem.

computational cost, note that computational cost is *not* organization (corporate) cost. For example, if the workstation is used overnight, it is irrelevant whether the machine takes one or sixteen hours. However, it does matter whether the machine comes up with the right answer in the morning, since one more workday could be lost. We also found that the only reason the gradient optimizer found any right answers at all was related to the fact that the optimizer started near the optimum by chance. For the higher dimensional problems with a complicated topographies this chance diminishes rapidly.

In view of the very different behavior of the optimization methods it is not possible to select a single "optimum optimizer." Only the genetic algorithm and kick-simplex methods were reliable enough to even be considered for application to the multidisciplinary aircraft design problem described in reference [6]. The kick-simplex method has better performance for the rough objective functions created by the calculation of drag in our CFD codes. For the relatively smooth drag objective function calculated with panel codes, gradient methods had performance comparable to the kick-simplex method. Cocktails—combinations of optimizers—are even more robust

than simple restarts of one scheme. Given the huge number of possible combinations, we were unable to include this possibility in our evaluations. An estimate of the optimal sequence of optimizers, and number of steps per optimizer, can be obtained by running the problem for each individual optimizer and determining the sequence by finding the optimizer with the most rapid convergence for a given optimization phase. One robust rapidly converging cocktail would then be to start with the evolution strategy, then switch near the end to the kick-simplex method. Similarly, a good cocktail for smooth topographies would be the combination of a Monte Carlo (random) method with a gradient method. The gradient method is started from numerous randomly generated points in space, and the best resultant point is retained.

## 6 Implementation Aspects

In this section we will discuss some aspects pertinent to the practical implementation of optimization methods in the industry.

### 6.1 Objective

If at all possible, one should use the same objective functions (codes) that will later be used to determine the final performance of the design. Keeping the I/O format of an existing industrial code is also highly recommended, to take advantage of the experience of other engineers with these analyses. In addition, optimization, at least in aerodynamic design, improves the design by only a few percent; therefore, the difference (error) between the objective optimum and the objective used to determine the final performance must be significantly less than the incremental improvement due to the optimization. The industrial organization will then be less skeptical about the improvement claimed. In industry, where a large group of engineers must agree upon the validity of the claimed improvement, this acceptance issue is critical.

Figure 10 maps out the organizational implementation of these recommendations. The optimization program is independent of the objective function analysis code, which keeps its I/O format. An interface program between the optimizer and the analysis code creates a new input file based upon the recommendations of the optimizer. The interface program

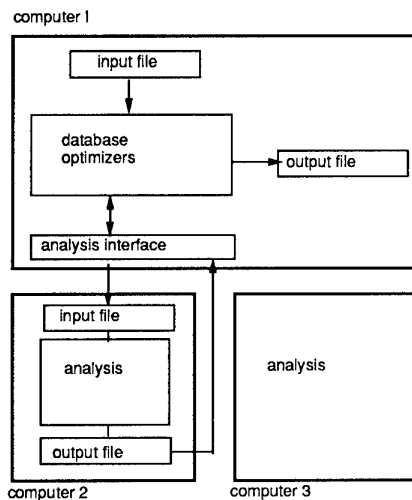


Figure 10: Optimizer analysis code organization.

then calls the analysis code, reads its output, and converts the output into a value for the objective. On a workstation network, the analysis code does not need to run on the same machine as the optimizer and interface. If the analysis code or the workstation executing the analysis routine crashes, the interface will interpret this as a bad design result and pass a large (nonoptimal) objective function value to the optimization algorithm. This approach allows easy parallelization of the problem.

## 6.2 Sensible objective functions, variables and constraints

Apart from the obvious requirements for a sensible objective function, we need at least as many *active degrees of freedom* to improve the design as there are *active constraints*. In industry, many engineers have a tendency to put too many constraints into the design, effectively freezing the design in its previous form. In academia, many researchers use too few constraints, and therefore work with oversimplified topographies. These topographies are of course easy to optimize, but seldom yield useful results.

## 6.3 Time

The fewer problematic topographical features the objective function has the more rapidly convergence is achieved with an appropriate optimizer. For very smooth objective functions without many local minima it is even possible to use gradient methods. In practical cases, we rarely have a smooth design space; such rapidly converging algorithms are therefore seldom useful. We are therefore practically limited to evolution and simplex methods, which despite recent developments are still much more computationally intensive than classic gradient methods. Since for most complicated topographies the optimizer almost never finds the global minimum, and instead wastes a lot of computational time meeting convergence criteria, it is usually better to roughly determine the location of local minima and restart the optimizer as often as possible.

## 6.4 Post-optimality processing

It is probably a wise policy to be sceptical towards any optimization results. Try to understand what the optimizer has found. A good approach is to make a 1-D parameter scan of the design space for every design variable while monitoring the constraint violations. Such a parameter scan is shown in Figure 11. The bypass ratio of a supersonic transport is constrained by noise regulations at values below 1.2. Above 1.6 the aircraft is no longer able to meet its range. The unconstrained objective function has an optimum below 1.0. With this approach one can easily illustrate the active constraints. These active constraints together with the objective function can also suggest design improvements by applying technologies that change the constraints. If the result is identical to that before optimization, the solution was probably not allowed enough flexibility. If the solution is too good to be true, most likely the analysis is no longer valid, and the design variables should then be limited to the range of analysis validity.

## 7 Acknowledgements

I would like to thank our mathematical assistant Silke Logemann for her programming, Mathias Hadenfeld for his work on the evolution algorithm and Dr. Minami Yoda for her editing of this paper. We used a modified version of the optimization shell Genie, from Ilan Kroo of Desktop Aeronautics.

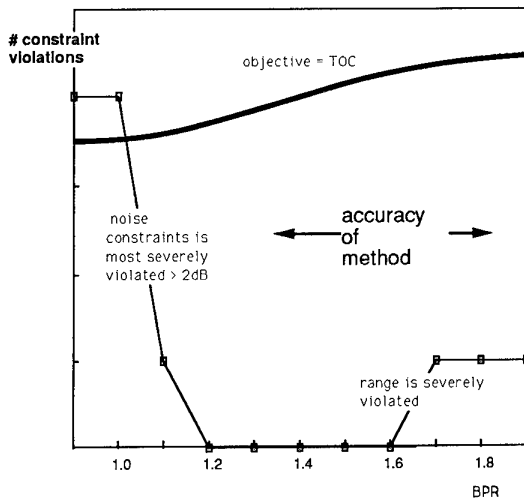


Figure 11: Post-optimality parameter scan.

## 8 Conclusion

In this paper we have discussed strategies for minimizing various complex engineering objective function topographies. The concept of robustness is defined, and used to compare various optimizer types. In general it is not possible to recommend a single optimizer as the best. However the use of many restarts, large step sizes and combinations of different optimizers significantly improves the chance for success. Using a single optimizer and tight convergence criteria does not help to find the global minimum. In addition we discussed a number of practical issues related to optimization.

## References

- [1] Schwefel, H.P. "Evolutionsstrategie und numerische Optimierung," Ph. D. thesis, Verfahrenstechnik TU Berlin 1975.
- [2] Rechenberg, I. "Evolutionsstrategie — Optimierung technischer Systeme nach Prinzipien der biologischen Evolution", Fromman-Holzboog 1973.

- [3] Nelder J.A. & Mead R. "Downhill Simplex Method in Multidimensions", *Computer Journal*, 7, pp. 308-313 1965.
- [4] Hadenfeld M. "Anwendung und Bewertung von Evolutions Strategien für die Optimierungsaufgaben beim Vorentwurf von Flugzeugen," Master's thesis, TU Braunschweig, July 1993.
- [5] Kroo I. "An Interactive System for Aircraft Design and Optimization," Aerospace Design Conference, AIAA 92-1190, Jan. 1992.
- [6] Van der Velden A., "Multi-Disciplinary SCT Design Optimization" AIAA 93-3931, aug. 1993
- [7] Jacoby, Kowalik, and Pizzo, "Iterative Methods for Nonlinear Optimization Problems", by Jacoby, Kowalik, and Pizzo, Prentice-Hall, 1972.
- [8] Braunschädel A., "Erprobung numerischer aerodynamischer Verfahren für Überschallverkehrsflugzeuge an verschiedenen Konfigurationen" diplom-arbeit Fach hochschule Aachen, 1994

# The Global Aircraft Shape

A. Van der Velden\*  
 EF 14 Aerodynamic Design Section  
 Deutsche Aerospace Airbus  
 Huenefeldstrasse 1-5  
 2183 Bremen  
 GERMANY

## 1 Abstract

This work describes the methodology used to compare supersonic design concepts and its use in industry. The design concepts are analyzed with a modular synthesis model and compared on the basis of operating economy with specified performance and environmental impact. The analysis routines of the synthesis model are mainly configuration independent and represent fixed levels of structural, aerodynamic and propulsion technology. The specialist departments are responsible for the content of the routines, and later verify the design with more refined methods. At present more than two hundred variables describe the aircraft geometry, engine characteristics and mission. More than twenty of those variables representing the aircraft and its flight-profile are optimized simultaneously as a function of Mach number, payload and range. Because the various designs are analyzed with the same routines and optimization procedures they can be easily compared. This aircraft pre-optimization results in a significant reduction of the number of follow-on detail-design cycles, especially for non-conventional designs.

## 2 List of Principal Symbols

l	length
L / D	lift-to-drag ratio
h	altitude
BPR	engine bypass ratio
DEM	design empty mass
DA	Deutsche Airbus
DASA	Deutsche Aerospace
M	Mach number
MTO	maximum takeoff weight
OFW	oblique flying wing
S	reference wing area
SMC	seat mile cost per passenger
SCT	Supersonic Civil Transport

s.f.c.	specific fuel consumption (N/hr/N)
SLS	sea level static
SWB	symmetric wing body
$\frac{t}{c}$	thickness to chord ratio
$T_{t,4,max}$	maximum turbine entry temperature
w	width

### Greek Letters

$\epsilon_{c,max}$	maximum engine pressure ratio
$\Lambda$	sweep angle
$\Delta O_3$	ozone depletion
$\Delta P$	sonic boom sea-level overpressure

## 3 Introduction

In the early days of aviation, the technology to design aircraft was less complex and the requirements on product safety minimal. As a consequence, aircraft could be designed by small groups of people. Such small groups can communicate directly and therefore work very efficiently. For instance: In 1936 it took Kurt Tank exactly one year to conceive and produce the Focke Wulf Condor, the first transatlantic airliner. However as the technology became more complex, aircraft designers had to specialize to cope with the increased flow of information. In addition, the growing market required improved safety and accurate performance guarantees. Such performance and safety guarantees could only be made by extensive analysis and testing of the aircraft design. Due to this increased work-load an aircraft is no longer designed by a single group, but by hundreds of specialists in many departments. This subdivision of work further increased productivity and enabled the development of the complicated but safe transport aircraft we have today.

Although the specialists can fit the aircraft with the best technology available in their field, it is unclear whether this will always lead to the best aircraft. The best aircraft can only be designed with a truly interdisciplinary effort. The number of people

\*Aerospace Specialist Deutsche Aerospace Airbus GmbH, Hünefeld strasse 1-5 P.O. Box 107845 D-28183 Bremen 1 Germany Copyright: 1994 by A. Van der Velden.

and independent locations increases the design cycle time and decreases the amount of interaction between the disciplinary groups. Progress is thereby limited to incremental improvements making it difficult if not virtually impossible to achieve the breakthroughs in aircraft design still common thirty years ago. This paper will present a possible solution to this problem that was developed at Stanford University and Deutsche Airbus. This paper is similar to a previous paper presented at the AIAA Aircraft Design Conference in Monterey [12].

### 4 Overview

We will first discuss a design strategy which given a mission finds the optimum aircraft design in the analysis parameter space. This parameter space is determined by the various disciplinary groups. Based upon this input robust physically correct analysis modules are developed. Finally improved non-linear optimization techniques are used to find the best design using these modules in this parameter space. This strategy reduces the number of design cycles and allows us to evaluate more configurations.

As an example we will describe how this strategy is applied to the design of an SCT configuration. The main assumptions of the analysis routines will be described as well as the objective function. Finally we will compare several near-term technology supersonic configurations as a function of mission specifications.

### 5 MIDAS: A Design Process

How do we best achieve flexibility and efficiency in our design process while effectively using the talent available to the organization? Figure 1 shows our solution called Multi-Disciplinary Intergration of Deutsche Airbus Specialists.

On the highest level there exists a global model of aircraft performance and economy as a function of its specification and a set of design variables. The analysis routines in the global model are supplied by the departments who have final responsibility. In about an hour numerical optimization of these design variables will provide an estimate of the aircraft's main characteristics and geometric dimensions. Figure 2 shows the convergence history of a global optimization.

After the optimized design is finished it is critically evaluated by the specialists. Once the decision is made to develop a design further, the departments verify the pertinent results of the global optimization in greater detail. This verification includes the design of a more detailed geometry on the basis of the global optimization output, much like putting

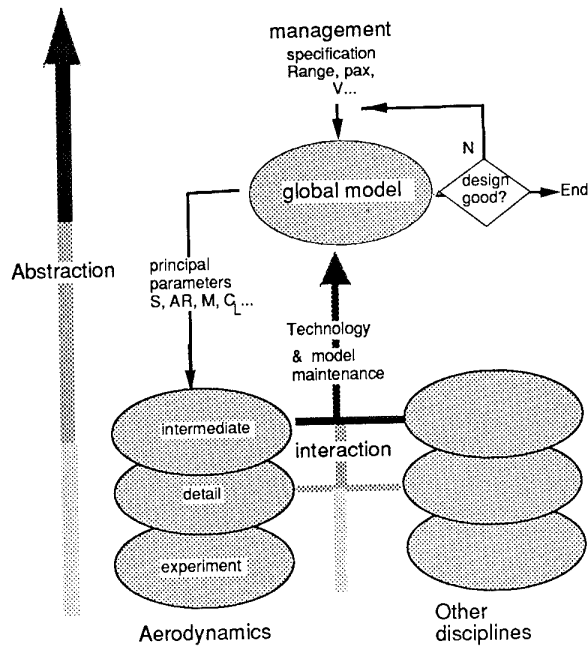


Figure 1: Overview of the MIDAS Design Process

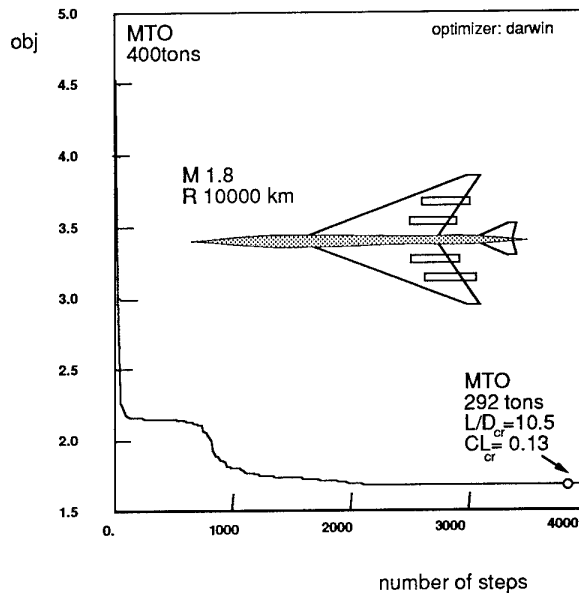


Figure 2: Global Optimization

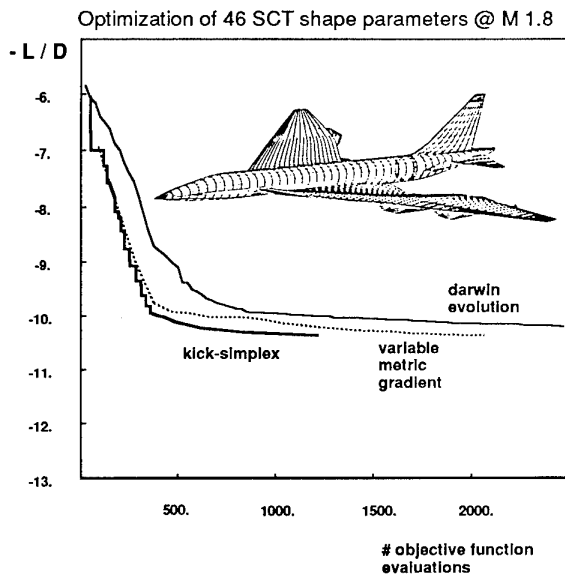


Figure 3: Intermediate Aerodynamic Optimization

the flesh on a skeleton. The values predicted by this intermediate model are compared to those for the global model and if necessary the global model is corrected and the process is repeated. Typically, no more than three iterations are required. In some cases the intermediate design level is also automated resulting in a closed global-intermediate loop. In this case only computational limitations prevent further integration. Note that at the intermediate design level, within each department a new group of parameters must be optimized which justify the simplifying assumptions made at the global level. For instance in the global aerodynamic model, the assumption is made that there exists a wing camber distribution that has near minimum potential drag for a given planform. The wing planform is optimized during the global optimization cycle. At the intermediate level, the camber (represented by shape functions) is then optimized to achieve minimum lift dependent wave drag for this planform and lift. Finally the resultant ratios of the achieved minimum lift dependent wave drag to the global theoretical minimum is used as a correction factor in the next global optimization. Figure 3 shows the convergence history of the intermediate aerodynamic optimization for several optimizers.

If this ratio exceeds an allowed percentage, the model itself should be corrected. The intermediate model should not introduce parameters that conflict

with the global model variables. Given the extent of this subject we will not present the intermediate models in this paper. To date we have used this method to obtain two SCT configurations. The configurations presented here have many of the features of these proprietary designs.

## 5.1 Analysis Method Requirements

For successful optimization of a parameter space we also have to make the analysis routines suitable for this purpose. A number of points have to be considered in addition to the ones mentioned in part I [11]:

- **Coordination of input and output.** This requirement forces the development to be coordinated by only a few people and therefore presents the most significant "bottleneck" for industrial application.
- **Modelling: What to model?** In principle we are always modelling cost and benefit. Clear paths should be established between the major design parameters and the cost equations. The benefits of a noise suppressor are easily defined, the number of dB suppressed at a reference condition can simply be used as an input parameter. But at what cost? Here is where the specialist is invaluable. He will calculate how much benefit to the aircraft he can guarantee as a function of various physical quantities (jet exhaust velocity...) for what cost (thrust-loss and suppresser complexity...). An accurate prediction of these relations is of course to his professional advantage since that will indirectly determine his task in the intermediate detailed design.
- **Modelling: Generality versus accuracy.** In many cases design optimization has consisted out of coding up hand book methods and running an optimizer on top of this. Unfortunately handbook methods require common sense which computers don't have. Computers are bad with rules of thumb since they do not know what is behind them. But computers are fast and can solve the general equations upon which the rules of thumb are based. In general good programming practices are:

Handbook methods have been developed for humans, not machines. The handbook methods tend to categorize each problem into a narrow group and provide the solution for the narrower problem. It can be easily understood that this will lead to physical inconsistencies in the formulation of the problem which prohibit the use

of an optimizer. After coding up ten thousand lines of code with inconsistent physics the chances that any useful information would be generated are very small indeed. Good programming practices are:

- Use only one equation to describe one variable (e.g. one equation for wing weight). If this is not possible make sure that each equation representing the same variable contains the identical set of parameters and that the derivatives at the cross-over points are continuous if possible. Boundary condition discontinuities between the equations representing the same parameter are definitely unwanted.
- Base the equations on physical realities, do not fudge the model beyond reasonable levels to fit one existing data set. In my thesis [2] the structural model for the wing was (almost) the same as for the fuselage. Wing and fuselage were both analyzed with shell theory. In general such generalizations are less accurate for individual cases, but globally more correct. Accuracy is not a problem since the errors caused by these generalizations can be ironed out at the more detailed levels and fed back to the global optimization in the form of a correction factor.
- Keep the number of variables to an absolute minimum. Ask yourself whether a variable is really necessary.
- Be careful with iterations inside the objective function and evaluate their effect on objective function smoothness.

## 6 Present Method Advantages

The present method has a number of advantages over more traditional design methods. This method:

- **clarifies the goals** of a design project and provide a means of communication between the disciplines. Most of the time it is not very clear what the objective of an aircraft design is. By agreeing on an objective function (for instance SMC) and a number of constraints it is possible to settle interdisciplinary differences.
- **automatically debugs** the analysis routines. Small model inconsistencies are usually not noticed by the expert user because he only trusts his model in a limited range. The optimizer will exploit any weakness in the model and therefore make it clear.

- **cleanly compares** between competing configurations. To compare aircraft they have to be analyzed with the same technologies and missions. In addition they have to be preferably analyzed with the same set of equations.
- **reduces the number of detail-design cycles.** As the experiences at DA have shown, a good baseline design will cut the number of follow-on detail cycles, thus significantly reducing the time required to design an aircraft.
- **shortens the design cycles.** Project management will get a fast first estimate of influence of the specification or technology on the aircraft performance and economy.
- **allows post optimality analysis.** Assuming that the objective function can be linearized with respect to the design variables at the (local) minimum we can verify whether we found a (local) minimum by determining the partial derivative of the objective function with respect to the design variables. They all should be zero. A good impression whether a minimum is local or global can be found by plotting each design variable with respect to the objective function over a range including the (local) minimum.
- **reduces the amount of data** produced. No more complicated biased thumbprint plots are necessary to understand a single design point. Simple graphs can be used to scan the entire design space of best configurations. Active and nearly active constraints can be monitored to indicate important performance criteria or important technologies.
- allows the **progress** that is made in the **analysis** routines to be directly translated into an **improved design**.

## 7 Application of the Method to Supersonic Civil Transports

### 7.1 Introduction and Basic Assumptions of the Comparison

In this study the synthesis model is used to make a comparison between conventional<sup>1</sup> supersonic and subsonic transport configurations and the oblique flying wing transport based on operating economy and other figures of merit for a range of missions with specified performance and acceptable environmental impact.

<sup>1</sup>Delta wing or swept wing type

We will consider two types of aircraft: the OFW's or oblique flying wings and the SWB's or symmetric wing bodies. The symmetric wing bodies include aircraft geometries as varied as those of the A340 and Concorde. The OFW was described in detail in previous references by the author [2] [7] [8] [9] and by Waters, Ardema and Kroo [6]. The passenger comfort level was held as constant as possible to allow objective comparison between the configurations. The seat layout is 10 % first class (40" pitch), 30 % business (36" pitch) and the rest economy (32" pitch).

All aircraft are evaluated with the same analysis routines. All aircraft are designed with the same level of structural, aerodynamic and propulsion technology. This level is based on that achieved by the next generation of transports. Features are:

- Aerodynamics: Skin friction is based on fully turbulent flow with characteristic sand grain roughness. The 'potential' flow drag is based on the theoretical minimum drag for a given distribution of lift and volume. This drag is then corrected based on the actual achieved drag levels in the detailed design. This correction factor therefore reflects the potential drag improvement that is still achievable. Factors of 1.1 for the volume dependent wave drag and 1.2 for the lift dependent wave drag are typical. Ref. [2] describes the 1992 status of the aerodynamic global model.
- Structure: Structural calculations are based on a mix of composite materials and metallic alloys. DA experience shows that intermediate carbon fibers with BMI resins achieve strain levels in excess of 0.5 % resulting in weight savings over conventional primary structures in excess of 25 %. The airframe life was specified to be over 75,000 hours with 50,000 supersonic flying hours and 25,000 pressure cycles. A minimum skin thickness of 2 mm was specified to minimize foreign object damage. Weight is calculated with shell-theory. An overview of recent developments in structural technology in Germany can be found in prof. Arendts publication [5].
- Propulsion: A turbofan engine with mixing and a variable throat area was used. Polytropic component efficiencies are typical of the current generation: between 88 and 93% for the compressor, fan and turbine. Noise suppression of up to 9 dB is allowed. A more detailed discussion of powerplant optimization at DASA (intermediate level) can be found in reference [1].

In addition the supersonic aircraft will have some

technology that is not yet available for subsonic aircraft:

- An active gear to reduce the taxi and landing loads by 16 % on supersonic aircraft.
- Flutter mode control load alleviation, which would allow increased sweep with thin wings.
- Active stability and control for the unstable oblique flying wing. A commercially safe active stability and control system for the oblique flying wing has not yet been demonstrated. Without such a system the oblique flying wing is not possible.
- Powerplant variable geometry inlet and nozzle design.
- Improved navigational and environmental control systems.
- Noise suppression up to 9 dB versus 6 dB for subsonic aircraft.

The costs of these additional technologies are included in the cost model. This level of technology is based on the current DA-SCT development program. The objective function that is used throughout this study is operating cost relative to a subsonic reference. The influence of the cost of development on sales price is included. The objective is calculated by the algorithm shown in Figure 4. This study compares the relative operating cost of various aircraft for the same mission, permitting comparisons of one concept with respect to the other.

## 7.2 Variables and Constraints

Input requires more than 200 variables for a full definition of the aircraft. Roughly one third of these variables are technology constants and are assumed to remain constant.

All designs were optimized with respect to 19 of the following 24 engine cycle, mission and geometry variables. The variables marked with a star (\*) were used on all designs. The other variables were used only when their best value could not be determined in advance (For instance, in the case of the flying wing the length of the fuselage is set to zero.). For these variables the default best value is given.

1. \* Maximum takeoff mass  $M_{to}$
2. \* Bypass ratio BPR.
3. \* Maximum turbine entry temperature sea-level static  $T_{t,4,ref}$
4. \* The corresponding total pressure ratio  $\epsilon_c$

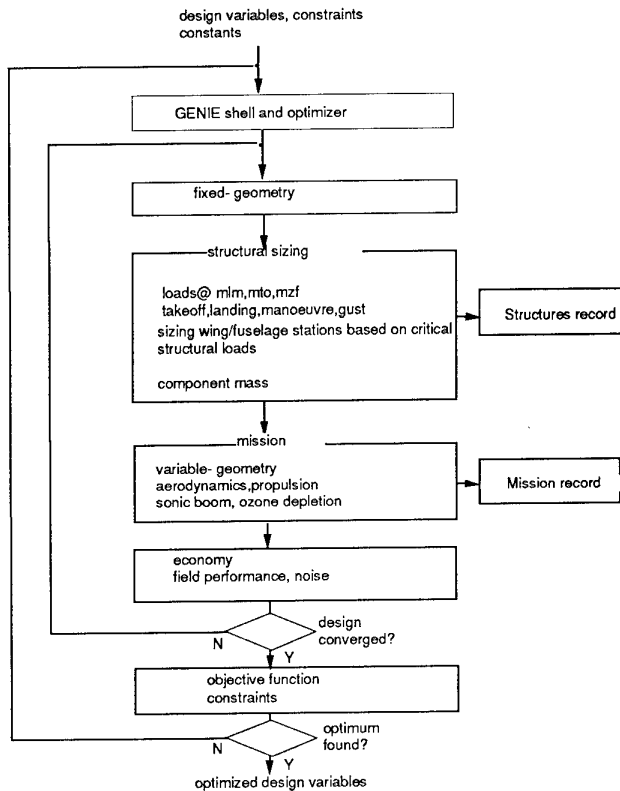


Figure 4: Objective Function Algorithm

5. ★ Combustor temperature cutback during takeoff  $\Delta T_{4,to}$ .
6. ★ Combustor temperature cutback at take-off noise control point and start climb  $\Delta T_{4,cutback}$ .
7. ★ Initial cruise altitude  $h_{cruise}$ .
8. ★ End of first climb segment Mach number  $M_{climb}$ , or the altitude at the end of the first climb segment  $h_{climb}$  for fixed  $M_{climb}$ .
9. ★ Holding Mach number  $M_{hold}$  for given altitude;  $M_{hold}$  is also the Mach number at the start of climb.
10. ★ Diversion Mach number  $M_{div}$  or altitude.
11. Ratio of stalling speed to lift-off speed  $V_{LOF}/V_S$ . Only used as a design variable for wing-body configurations. In particular, the delta-wing configurations tend to take off at lift-off speeds greater than this value because of high take-off drag. For flying wings the value of  $V_{LOF}/V_S$  is set to 1.2, the lower bound.
12. ★ Wing Area  $S$ .
13. Wing Aspect ratio  $AR$ . It is only a design variable for wing-body configurations. For flying wings, the aspect ratio is determined by the wing area  $S$  and the wing thickness-to-chord ratio and the heuristic

design rule that the payload should fit inside the structure without excess (vertical) space.

14. Fuselage length  $l_f$ . This is only a design variable for wing-body configurations.
15. ★ Cabin diameter. Determines the fuselage diameter of SWB's wings and the maximum absolute thickness of OFW's.
16. ★ Spanwise location of two powerplants on half wing:  $y_{prop1}$  and  $y_{prop2}$
17. Spanwise location of two fuel tanks on half wing:  $y_{tank1}$  and  $y_{tank2}$  and the spanwise width of the tanks. For most long range wing-body configurations a large fraction of the available wing volume for fuel was actually used, so rearranging fuel tanks does not affect the wing bending weight greatly. For flying wings this did turn out to be an important design variable since only about half of the available wing volume for fuel was used by the fuel tanks.
18. ★ Spanwise location of the main gear legs  $y_{gear}$
19. Wing Root thickness-to-chord ratio  $[\frac{t}{c}]_{root}$ . This is an important variable for wing-body configurations, but flying wing configurations all converged to the maximum allowed thickness of 16.3 %, so it was fixed at this value.
20. Climb sweep  $\Lambda_{climb}$ . This is only of significance for variable sweep configurations.
21. Take-off sweep  $\Lambda_{to}$ . This is only of significance for variable sweep configurations.
22. ★ Cruise sweep  $\Lambda_{cr}$ . This is the same as the sweep for fixed sweep configurations.

The variables are constrained by the following considerations:

- Geometry (22 Constraints); location of up to 4 powerplants, 3 gear legs and 4 fuel tanks, as well as the structural box. The x-location of the centroids of these items is determined by balance considerations. The y-location of the powerplant, fuel tanks and gear legs are determined by the optimization of these variables with respect to the objective function. These variables are constrained to not interfere with each other's location. The powerplant is placed outside the direct vicinity of the passenger cabin to protect passengers from engine explosion debris. The relative location of these items is especially important for the oblique flying wing in order to achieve the benefits of span loading.

The gear track was limited to 35 m to enable operation from runways that are at least 150 feet wide. The maximum thickness-to-chord ratio could not exceed 16.3%. The volume of the fuel tanks was sufficient to accommodate all the required fuel as well as a fuel volume equivalent to half the payload. The mean trailing edge sweepback angle was limited to  $30^\circ$  for arrow wings due to the expected aero-elastic and control problems of more highly swept thin wings [10]. The maximum aircraft width is limited to 65 m. (B747-400) and the length to 102 m. This leads to a maximum structural span of 120 m for OFW's.

- **Engine Cycle (3 Constraints).** The engine is constrained by the required top of climb thrust margin of 10 % and the required climb gradients. There was no upper limit to the engine size. The turbine entry temperature was not allowed to exceed 1800K. The bypass ratio was between 0 and 6.
- **Flight Profile Settings (7 Constraints).** The flight profile is shown in fig. 5. Thrust, sweep, altitude and Mach number can be set at takeoff, takeoff thrust-cutback, midpoint climb, start cruise and end cruise. For a specific mission segment definition point either the Mach number or the altitude was fixed during the optimization. The turbine entry temperatures and pressure ratios were always kept smaller than the maximum reference numbers selected for the cycle. The variable mission thrust settings make it possible to meet the noise regulations with thrust-cutback. Since the design loads are calculated based on the prescribed mission it is possible to minimize the aircraft loads in conjunction with the geometry. The lift-off speed is not less than 1.2 times the trimmed stall speed.
- **Performance constraints (4 Constraints).** The range was constrained to a value not smaller than the design range and not more than 200km greater than the design range. The takeoff field length was constrained to 3300 m (11000ft) to allow operations from most international runways. The one-engine out screen height climb requirement was set in accordance with the FAR25<sup>25</sup> regulations. A minimum all engine climb gradient of 4% must be maintained at the takeoff FAR-36 cutback thrust level.
- **Environmental constraints (4 Constraints).** All the designs in the study meet the FAR 36 stage 3 levels. In addition the total ozone depletion is not to exceed 5.0% for a fleet replacing the current B747 (capacity:  $1.25 \times 10^{12}$  skm/year) as

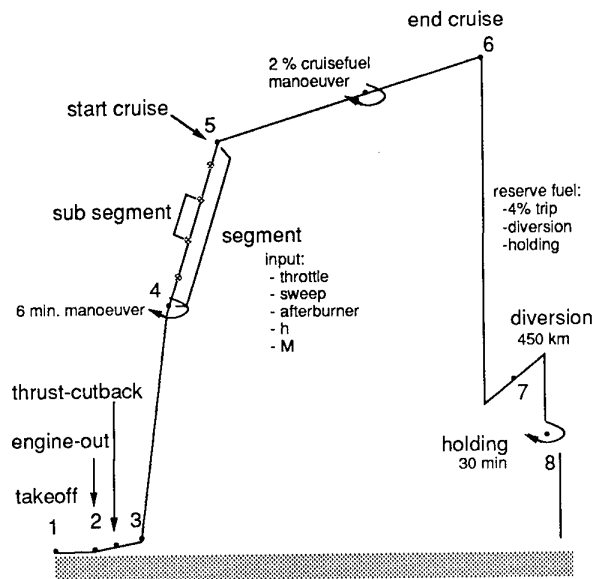


Figure 5: Flight Profile

suming conventional combustors. This level of predicted depletion is consistent with the current HSCT program goal described in reference [3] assuming that low emission combustors are used. The mean sonic boom overpressures are not allowed to exceed  $144 \frac{N}{m^2}$ .

### 7.3 Comparison of Optimized Configurations

In this section we will compare optimized configurations. The comparisons are made for designs with fixed mission parameters, such as constant range, payload, and Mach number.

#### Reference Aircraft

The baseline mission is 250 passengers over a 9000 km range. Figure 6 shows the top views of the optimized conventional configuration and the optimized OFW.

For a cruise Mach number of 0.8 table 1 shows a typical cruise lift-to drag ratio of 20.4 for the OFW as compared to 19.8 for the conventional configuration. The SMC of the oblique flying wing is also 5 % lower than that of the conventional configuration. Another salient difference between the two is the cruising altitude. The start cruising altitude of the OFW about a kilometer higher than for the SWB. This is due to the lower wing loading of the OFW.

<sup>2</sup>The results are very similar for symmetric flying wings.

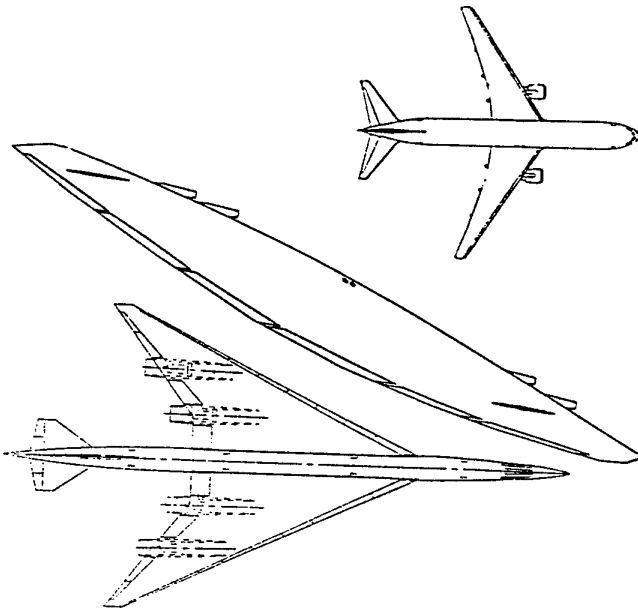


Figure 6: Optimized Configurations that Transport 250 Passengers Over a 9000 km Range

The required thrust is about the same for both configurations. For payloads of 250 passengers and higher the flying wing seems to be economically competitive with subsonic aircraft. Both configurations will be able to meet more strict noise regulations without excessive weight penalties. The 5 % advantage in SMC probably does not outweigh the development risk and the lower cabin volume per passenger in an OFW as compared to a wide body subsonic airliner.

Table 2 compares a 250 passenger OFW and an SWB for a cruise Mach number of 1.6 and a range of 9000 km. The Mach number of 1.6 is chosen for easy comparison with the OFW as well as to easily meet the proposed ozone layer depletion constraint. At this Mach number the OFW is clearly superior to the SWB. Interestingly enough, the cruise lift-to-drag ratio of the OFW is only 10 % better than that of the SWB. The optimizer chose to improve the lift-to-drag of the SWB up to the level of the OFW at the expense of the structure. The structure of the SWB is almost 40 % heavier than for the OFW. In the case of the OFW lift-to-drag ratios of around 11 during cruise were achieved without a large structural penalty because of span loading and the fact that the OFW wing is much thicker. Even though the OFW is much better than the SWB its SMC is still not close to those of the subsonic transports. Though both configurations are not constrained by sonic boom or

Item	OFW	SWB
Cruise Speed	M 0.8	M 0.8
passengers	250	250
Range	9200 km	9200 km
Geometry:		
Wing Area ( $m^2$ )	965	357
Root, Tip t/c	0.163, 0.12	0.145, 0.104
cabin l x w (m)	32.5 x 5.9	42 x 4.8
total l x w (m)	92 x 13.5	60 x 60
Weights:		
DEM (kg)	62544	70101
MTO (kg)	134623	146554
Powerplant:		
SLS Thrust (kN)	4 x 78	4 x 72.5
BPR	5.0	5.0
$\epsilon_{c,max}$	50	50
$TT4_{max}$ (K)	1795	1737
Operation:	Initial Cruise	
L / D	20.4	19.9
s.f.c.	0.59	0.59
h	13300 m	12173
Rel. SMC	0.95	1.
Environment:		
Mean $\Delta P$ ( $\frac{M}{m^2}$ )	0	0
Side. Noise (dB)	86	90
T.O Noise (dB)	101	102
$\Delta O_3$	0	0

Table 1: Comparison of Subsonic Aircraft

ozone layer depletion, they are both constrained by takeoff noise. Because of its better takeoff lift-to-drag ratio and lower wing loading the OFW cuts back the engine at takeoff to meet the noise requirement. Since the SWB is more constrained by performance requirements it has to be designed with an increased bypass ratio. The bypass ratio for the SWB is more than twice the BPR of the OFW. The OFW is close to violating the ozone depletion requirement because it is flying higher. Its maximum sonic boom overpressure is only half of that of the SWB.

**Effect of range**

Figure 7 shows that this OFW is able to achieve ranges of up to 6500 nm (12000 km) without excessive cost. Span-loading enables the OFW to improve both range and SMC. From a range of 7000 km on the OFW is constrained by the maximum span of 120 m. The SWB seems to be most attractive for the transatlantic range. Beyond 11000 km its maximum takeoff weight snowballs, even with our aggressive technology assumptions.

**Effect of cruise Mach number**

At Mach 2.0 the SWB's performance stays about the same while the OFW's performance worsens. Even though the cruise lift-to-drag of the OFW is less than that of the SWB at Mach 2.0, their difference in SMC is about the same as the Mach 1.6 case. Beyond Mach 1.8 the OFW

Item	OFW	SWB
Cruise Speed	M 1.6	M 1.6
passengers	250	250
Range	9125 km	9010 km
Geometry:		
Wing Area ( $m^2$ )	1193	720
Root, Tip t/c	0.163, 0.12	0.042, 0.030
cabin l x w (m)	32.5 x 5.9	62 x 3.7
total l x w (m)	120 x 13.5	93 x 45
Weights:		
DEM (kg)	96675	133784
MTO (kg)	222805	297542
Powerplant:		
SLS Thrust (kN)	4 x 214	4 x 261
BPR	1.0	2.41
$c_{c,max}$	31.4	29.3
$TTA_{max}$ (K)	1780	1780
Operation:		
L / D	11.5	10.4
s.f.c.	0.95	0.93
h	15790	13650
Rel. SMC	1.36	1.81
Environment:		
Mean $\Delta P$ ( $\frac{N}{m^2}$ )	40	92
Side. Noise (dB)	102	102
T.O Noise (dB)	104	105
$\Delta O_3$	-4.11 %	-1.5

Table 2: Comparison of Supersonic Aircraft

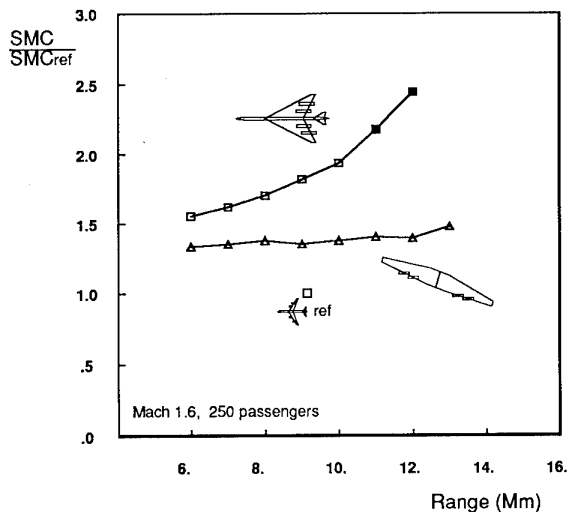


Figure 7: Relative SMC as a Function of Range

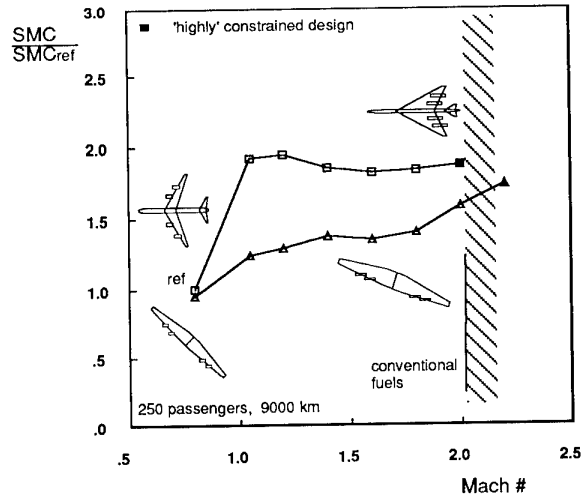


Figure 8: Relative SMC as a function of Mach number

has to be swept too reduce volume dependent drag. The constraint on its maximum size prohibits the increase in the span to offset the corresponding higher lift dependent drag. Figure 8 shows the influence of the increase in speed from Mach 0.8 to 2.0 on SMC for the SWB's and the OFW's. The dominant influence is the price of wave drag added to supersonic configurations. At supersonic speeds there is still an increase in SMC with increasing Mach number due to the increased specific airframe complexity. Mach numbers in excess of 2.0 where not considered due to thermal stability problems with conventional fuels for trips in excess of 3 hours. In addition we found that the SWB designs were constrained by as many as a dozen constraints at the same time. This is caused by incompatibility of low-speed and high-speed flight that does not exist by the OFW aircraft.

#### Effect of payload size:

Because of the poor volume efficiency of the OFW configurations, the optimum SWB payload of 250 passengers may not be large enough. For the OFW a payload of 400 passengers is better. It is not possible at this time to design a 400 passenger SWB SCT configuration since such an aircraft would have an excessive mtow. But in the case of the OFW the increment in performance is such that it outweighs the reduced market size. Figure 9 shows the effect of increased payload on the SMC of the OFW. If we compare the 250 and 400 passenger OFW's we find that the maximum takeoff weight has increased 35% while the

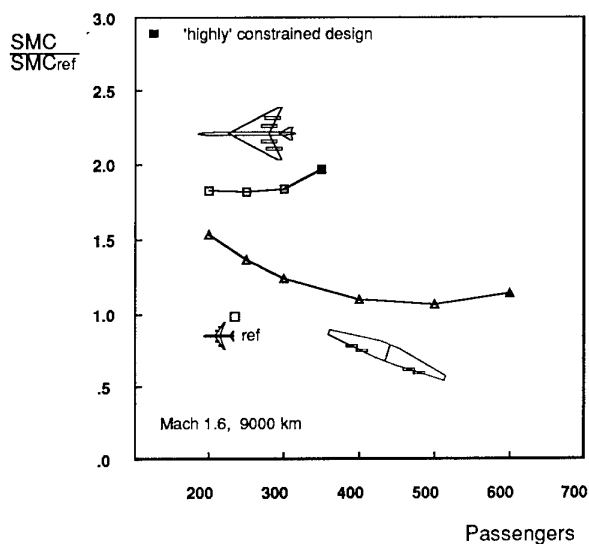


Figure 9: Relative SMC as a function of Payload Size

payload has increased 60%. Increasing the payload further decreases the SMC to values close to those of competitive subsonic transports. A more detailed explanation of the improved economy of the oblique flying wing transport over the symmetric wing body can be found in ref [2].

## 8 Acknowledgements

I would like to thank two people who were not referenced in this paper. First of all our mathematical assistant Silke Logemann for all the excellent programming she did in support of this project. And finally Minami Yoda for her constructive editing.

## 9 Conclusion

In this paper we discussed a design strategy which given a mission finds the optimum aircraft design in the analysis parameter space. This parameter space is determined by the various disciplinary groups. Based upon this input robust physically correct analysis modules were developed. Improved non-linear optimization techniques were used to find the best design using these modules in this parameter space. This strategy reduced the number of design cycles and allowed us to evaluate more configurations.

This method was used to study the relative performance of symmetric wing body (SWB) and oblique flying wing (OFW) supersonic transports over a wide range

of missions. The best OFW in terms of SMC, are large (400 passengers) and long range (12000 km) with cruising speeds around Mach 1.7. The best SWB's have around 250 passengers and fly transatlantic with a cruising speeds around Mach 1.8. In terms of operating cost per passenger, the best OFW is 73 % better than the best SWB. Even though the symmetric wing body design presents a lower risk solution due to the extensive database that is available for such a design, this configuration is only viable with high ticket surcharges. The oblique flying wing does promise this economic viability but the unavailability of an extensive database prohibit near-term launch.

## References

- [1] Hertel J., and Albers M., "The impact of Engine and Aircraft Design Interrelations on DOC and its Application to Engine Design Optimization", Aircraft Design, Systems and Operations Meeting AIAA 93-3930, Monterey California August 1993
- [2] Van der Velden A., "Aerodynamic Design and Synthesis of the Oblique Flying Wing Supersonic Transport", PhD-thesis Stanford University, Dept. Aero Astro SUDAAR 621, June 1992
- [3] Johnston H. S., "Topical Review of Stratospheric Aircraft and Global Ozone," Dept. Chemistry UCB, unpublished feb. 1989
- [4] Kroo I., "An Interactive System for Aircraft Design and Optimization," Aerospace Design Conference, AIAA 92-1190, jan. 1992
- [5] Arendts F.J., "Aktuelle Entwicklungen in der Strukturtechnik", *Z. Flugwiss. Weltraumforsch.* 16, page 231-246 1992.
- [6] Waters, Ardema, Kroo, "Structural and Aerodynamic Considerations for an Oblique All-Wing Aircraft", Aircraft Design, Systems and Operations Conference AIAA 92-4420, Hilton Head August 1992.
- [7] Van der Velden A.J.M., "The Conceptual Design of a Mach 2.0 Oblique Flying Wing Supersonic Transport," NASA CR 1777529, May 1989
- [8] Van der Velden A.J.M., Ilan Kroo, "A Numerical Method for Relating Two- and Three-Dimensional Pressure Distributions on Transonic Wings," AIAA/AHS/ASSEE Aircraft Design and Operations Meeting, AIAA 90-3211,1990
- [9] Van der Velden A.J.M., Kroo I., "The Sonic Boom of an Oblique Flying Wing," *Journal of Aircraft* jan-feb 1994.
- [10] Bobbitt P.J., "Theoretical and Experimental Pressure Distributions for a 71.2 Degree Swept Arrow-Wing Configuration at Subsonic, Transonic, and Supersonic Speeds," NASA Langley Res. Center NASA CP-001, 1976

- [11] Van der Velden A.J.M., "Tools for Applied Engineering Optimization", AGARD R 803, april 1994.
- [12] Van der Velden A., "Multi-Disciplinary SCT Design Optimization" AIAA 93-3931, aug. 1993

# Aerodynamic Shape Optimization

A. Van der Velden\*  
 EF 14 Aerodynamic Design Section  
 Deutsche Aerospace Airbus  
 Hünefeldstrasse 1-5  
 2183 Bremen  
 GERMANY

## 1 Abstract

This paper will discuss examples of aerodynamic shape optimization at Deutsche Airbus in Bremen. First, we will introduce a general approach to aerodynamic shape design based on minimization of aircraft life energy cost. Realistic constraints are introduced on lift, pitching moments and thickness. This method is applied to the quasi-3D design of multipoint transonic wings which are analyzed by a full potential code with a coupled boundary layer calculation. Finally, this method is applied to the wing-body design of a Supersonic Civil Transport that is analyzed with a linear potential code with real flow corrections and a decoupled boundary layer calculation.

## 2 Introduction

Since the early days of aviation history, engineers have sought to improve wing design methods. The first successful attempts at designing an airfoil were made around 1900 by Kutta and Joukowski. The next major development was the use of simple geometric shape functions to characterize airfoil shapes; the NACA airfoil classification system using this method is described in reference [1]. Unfortunately these NACA airfoils had high drag at transonic speeds, and therefore more refined shapes with reduced (or no) transonic shocks were required. More recently, successful transonic airfoils have been designed by defining a (nearly) shock-free transonic pressure distribution and using an inverse solver to find the corresponding airfoil geometry. At DA the SUPDES method developed by Greff and Mantel [8] [7]—a decoupled solution solver which uses residual correction—has been used for several years. This method starts with an initial guess for the geometry

and calculates the pressure distribution for this geometry. Then the geometry is revised based on the difference in pressure between the calculated and desired pressure distributions. Although this full potential code has a viscous analysis option, the analysis is inviscid in the initial design phase.

Although this method is presently used, it suffers from a number of weaknesses:

- The method can cope with only one pressure distribution per design, and it is therefore difficult to develop a design for more than one design point. Multipoint designs are possible only through the intuition and experience of the aerodynamic designer. This experience is not always pertinent for designs with significantly different missions.
- It is sometimes physically impossible to derive a geometry for a given pressure distribution. One is therefore limited to small modifications to existing pressure distributions in the leading and trailing edge regions. Unfortunately, the leading and trailing edge geometries greatly influence the lift and drag of the airfoil. Furthermore, even small pressure distribution modifications often result in a wavy geometry that must be smoothed.
- This method is able to design airfoils for a given pressure distribution, but it is not always clear whether these airfoils have the lowest drag. Figure 1 [2] shows an example of a "shock-free" transonic airfoil with a wave drag of more than 200 counts ( $C_D = 0.02$ ). This result clearly demonstrates that the wave drag of an airfoil depends on the entire flow field and is not directly related to a smooth pressure distribution.
- It is difficult to analyze the effects of complex airfoil geometry constraints such as spar depths and pitching moments.

\*Aerospace Specialist, Deutsche Aerospace Airbus GmbH, Hünefeldstrasse 1-5 P.O. Box 107845, D-28183 Bremen Germany. ©1994 by A. Van der Velden.

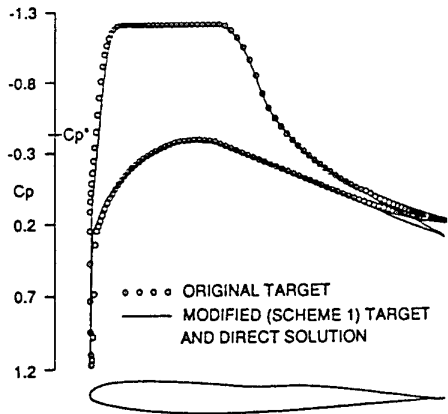


Figure 1: Design of a shock-free high wave drag airfoil by Volpe (1989) using an inverse method.

- The inverse airfoil design method can be computationally quite expensive. This is especially true if the airfoils are evaluated based on overall performance, instead of at a single design point. In a recent case, it took skilled engineers more than half a year to design a single high-performance wing for the next generation of transports.

A solution to these problems was proposed by VanderPlaats and Hicks [4]. They used the numerical optimization techniques to modify a geometrical shape such that an arbitrary objective function representing the design goals could be minimized. Even though this breakthrough took place almost twenty years ago, computer speeds have not increased sufficiently to make this method practical with the shape functions they proposed. Even now, recent literature reviews such as Labrujere and Slooff [6] note that practical direct numerical optimization of wings is not possible due to the great computational expense.

Despite its drawbacks, some authors, for example Lee [5], have applied direct numerical optimization, minimizing the drag of a single point airfoils (Fig. 2). Unfortunately, the designs produced with these methods are inferior to designs from experienced engineers using inverse methods.

In this report we will show that it is possible to produce true viscous multipoint designs that compare favorably with designs made by experienced engineers.

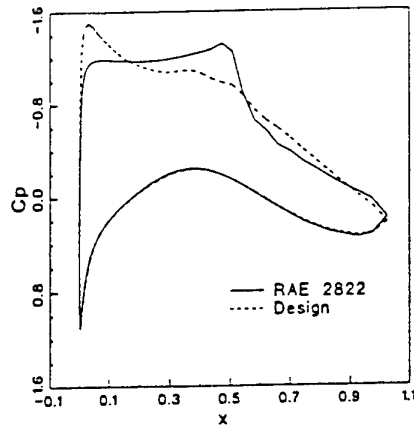


Figure 2: Design of a single point airfoil using direct optimization by Lee [5].

### 3 General Methodology

Multipoint aerodynamic optimization can in general be described using the form of the general engineering optimization described in [15]:

- Select objective function.
- Select variables and constraints.
- Select optimizer(s).
- Optimize and analyze the results.

#### 3.1 Drag as an objective function

Consider the objective function  $O$  described by the total energy loss due to aircraft drag during the operation of the aircraft over  $n$  missions:

$$O = \sum_{i=1}^n p_i \int_{x=0,i}^{r_i} c_d q S dx. \quad (1)$$

In this expression,  $p_i$  is the probability of mission  $i$ , and  $r_i$  is the block range for that mission. This expression can be simplified by weighing the drag over a number of representative design points:

$$O = \sum_{i=1}^m w_i c_d. \quad (2)$$

In our experience, five design points are enough to adequately describe a good multipoint design.

### 3.2 Variables

The variables of our problem describe the aerodynamic shape of the aircraft. Over the last two decades, many engineers have tried to accurately describe the shape of a wing with only a few parameters while still keeping flexibility. There are three general classes of aerodynamic shape functions:

- *Linear combination* of existing airfoils. This geometric approach to the airfoil design problem is a derivative of the original NACA method [1]. Although this method is computationally efficient, at DA this method has often given only trivial solutions (e.g. the old airfoil) due to the low flexibility inherent to this geometrical representation. In addition, there is little physical foundation for the implicit assumption that the drag (objective) of a linear combination of airfoils is linearly or at all related to the drag of the individual airfoils.
- *Analytical* shape functions are linearly superimposed to define a wing geometry. Examples of these include Hicks-Henne functions, Wagner functions and the patched polynomials discussed in reference [5], as well as the Legendre polynomials used by Reneaux [18] and the splines used by Cosentino [19]. Unfortunately, the number of parameters required for these shape functions is usually too great to allow multipoint three-dimensional design. In every case a minimum of 30–40 points are required to accurately define each airfoil. Even if only five airfoils are sufficient for defining a wing, about 200 parameters will be necessary. This number of variables is simply too great for practical optimization at present. Cosentino optimizes a 3D wing, by allowing variations over only a small portion of the wing. Lee has proposed patched polynomials as a way of flexibly modeling an airfoil section with only sixteen parameters. Although this approach does produce a flexible geometry, the performance of the sections designed with this method cannot compete with those produced by experienced engineers using inverse methods.
- *Special aero-functions* were proposed by Reneaux [18] as a means of designing airfoils with a minimum number of parameters. This approach automates the steps which an experienced designer follows when using an inverse

method. 'Good' pressure distribution types are defined, along with the shape or special aero-functions which produce these pressure distributions. Unfortunately, for a given pressure distribution type, these aero-functions vary with Mach number, and this method is then impractical for multipoint designs. This method therefore has all the disadvantages of inverse methods discussed in the Introduction.

At DA [14] the author has introduced another type of function, a highly nonlinear special aero-function, which could optimize the shape of a 3D transonic wing with adequate flexibility using current computer technology. It is currently in the validation phase at DA. Its application will be demonstrated in the next section.

### 3.3 Constraints

The type and number of constraints are highly problem-dependent. Typical constraints for commercial wing designs are:

- *Lift and angle of attack*. Either the lift  $C_L$  or angle of attack  $\alpha$  are constrained or defined as input values. For the horizontal tail plane, both can be simultaneously constrained.
- *Minimum and maximum lift*. Maximum lift at low speed ( $\approx 50\text{m/s}$ )  $C_{L,max}$  for a given Reynolds number influences takeoff and landing performance and is therefore an important issue. For horizontal tails, the minimum lift at low speed  $C_{L,min}$  is an important constraint.
- *Buffet onset* at 1.3g relative to 1g cruise. Even though buffet onset is difficult to predict exactly, a conservative estimate can be made using the trailing edge separation criterion [17] based on trailing edge pressure coefficients.
- *Pitching moment*  $C_m$ . This is usually not particularly important for subsonic transports but is a major issue for supersonic transports. The hinge moment  $C_{m,h}$  is an important constraint in the design of control surfaces.
- The aircraft thrust must be at least equal to the drag also at off-design points, of which the most critical are usually at the high lift and high Mach number corner of the envelope. The allowed drag

creep as a function of Mach number or lift is also often constrained.

- *Geometry.* The airfoil thickness and thickness distribution are usually subject to structural and geometric constraints.
- *Engine installation.* The airfoil pressure distribution should take into account the disturbances due to engine installation. This can result in limitations to the lower leading edge suction.

### 3.4 Optimization and testing

The objective function space for our shape function was wavy (*i.e.* had several local minima) and had surface roughness, which was due to the iterations in the CFD analysis. The existence of local minima is clearly illustrated in Figure 3. Each solution here is at least a local minimum drag solution for the transonic airfoil problem.

In case 1, transition strips were simulated at 0.05c at the upper surface and 0.07c at the lower surface. The design converges to a drag of 115.0 counts with a weak shock at 0.3c. The design parameters were then randomized and the transition on the upper surface was changed to 0.15c. The optimizer now takes advantage of the laminar flow on the upper surface, resulting in a negative pressure gradient up to the 0.15c point. This, however, results in a much stronger shock at 0.4c. The optimizer now finds a local minimum drag value of 115.2 counts, 0.2 counts higher than the first case. After repeated restarts, the design finally reconverges to the first solution, implying that the possibility of laminar flow on the upper surface does not help to lower the overall drag. To avoid getting stuck in such local minima, the kick-simplex method was used in every case.

When the objective function is evaluated with the code used to do the performance prediction—as in the previous example—little additional testing is required. After the optimization has converged, the complete set of polars is calculated to search for anomalies between the points where the objective function was evaluated. At the design point, additional calculations are done with 3D Navier-Stokes/Euler codes to verify the simplifying assumptions made in the objective function analysis.

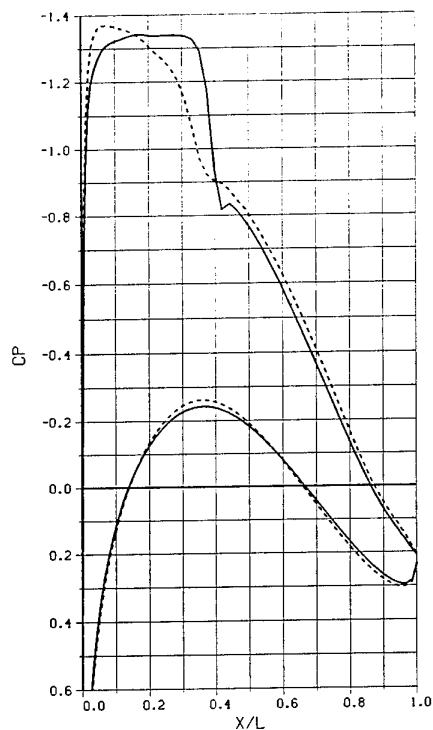


Figure 3: Two (locally) optimal pressure distributions.

## 4 Quasi 3D Transonic Multi-point Design

### 4.1 Optimization and analysis methods

At DA the production codes VICWA, XLS and Eppler are used. To calculate the drag polar of the entire wing, the quasi-3D polars created with these methods are used in combination with a Truckenbrodt vortex lattice method that calculates induced drag. Quasi-3D assumes the absence of spanwise pressure gradients along the iso-chord points. A Navier-Stokes calculation verifies the absence of these gradients. The Navier-Stokes method is not yet accurate enough to be used for performance calculations, and is therefore at this time not used for objective function analysis.

The **Eppler** code [12] couples a conformal mapping incompressible flow calculation with a semi-empirical boundary layer method. It is used to calculate the incompressible maximum and minimum lift and corresponding angles of attack.

**XLS** is a nonconservative full potential code with a momentum integral boundary layer and a nonisentropic shock-point operator which includes the effect of sweep and taper [11]. Comparisons of an early

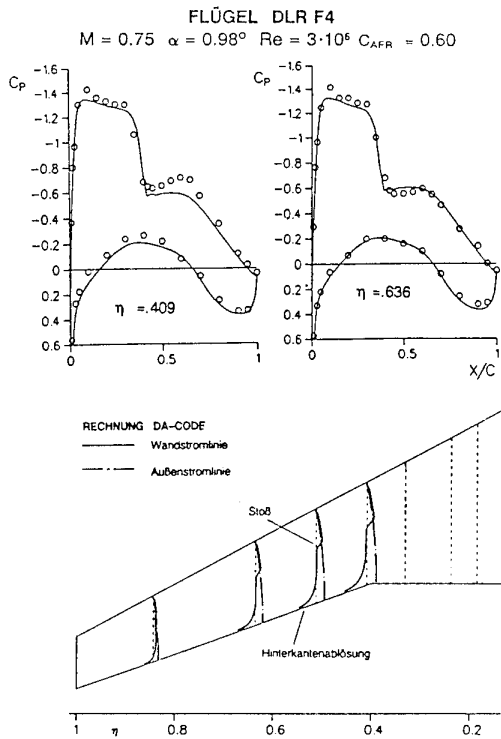


Figure 4: VICWA conical transonic analysis.

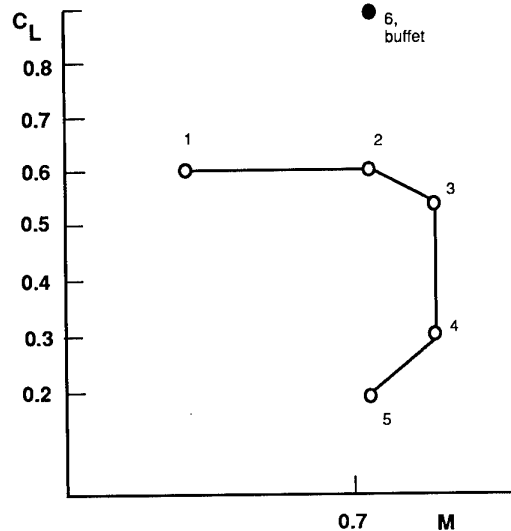


Figure 5: Transonic wing design points.

version of this code with other codes can be found in reference [10].

**VICWA**, the successor of XLS described in reference [13], analyzes a viscous conical transonic flow. The boundary layer is calculated using a finite difference numerical method. For an isobaric transonic wing, this method predicts the drag and the pressure distribution quite well, even with fairly strong shock-boundary layer interactions. Figure 4 shows measured and calculated pressure distributions as well as the 3D boundary layer development for the DLR F4 configuration. One flow analysis takes about 3 min on an 80 Mflops HP workstation.

In our optimization code, the user is free to select any of these methods for any of the points where the analysis is performed. The methods all have flexible constraints on thickness, pitching moment, lift, drag, buffet and maximum and minimum lifts. From a "good" starting solution the code requires about 50 flow field calculations per design point to find the global minimum. If started from other points, the code will still find the global minimum, but at least one restart is typically required.

#### 4.2 A multipoint wave drag-bucket wing section

The objective of this study was to design a wing with a large envelope of low wave drag to achieve superior operational flexibility. The wing, which had moderate sweep and was operated between Mach numbers 0.7 and 0.8, had been previously been designed using inverse methods. Figure 5 shows the design points of this wing section. Since the quasi-3D method treats the wing as a number of sections we will limit ourselves to the description of the 38% semi-span section. Figure 6 shows the optimization convergence history for the most important parameters describing this airfoil. The highly nonlinear interaction of the design parameters can be observed. To illustrate the flexibility of the method the engineer responsible for the inverse design was allowed to select the design starting point shown in Figure 6

This starting point was a 16% thick reflexed airfoil that was totally unsuitable for transonic speeds. The code was only barely able to analyze the design points for the starting airfoil. The thickness was constrained to be at least 12.5%. The drag rise between points 1 and 2 and points 1 and 3 was limited to 10 and 25 counts respectively. Nevertheless, the

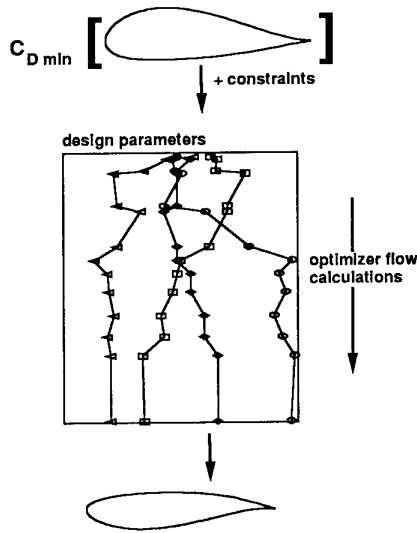


Figure 6: Design convergence history.

direct numerical optimization algorithm was able to find a good solution to the problem. Figure 7 compares the performance of the multipoint inverse design, which incorporates departmental transonic design experience, with the optimizer design.

At the primary cruise Mach number both designs perform equally well, but outside the normal operational lift range the inverse design is slightly better. However, the higher drag values during buffet onset for the direct numerical design are not necessarily bad, since we do not want to operate the aircraft here. At the extreme end of the envelope the direct numerical design is clearly superior to the inverse design. At point 3 in the cruise envelope, a difference of 20 counts in drag exists between the inverse and direct numerical designs. To operate the aircraft at this point a larger engine would be required for the inverse design.

To investigate the influence of tradeoffs we modified the objective function to include thickness. Every 0.01 increment in aircraft thickness-to-chord-ratio was weighted as 10 counts in drag. The design converged to a thickness of 15.3%. Figure 8 shows its drag polars.

The maximum thrust required is the same for both wings, even though one wing is much thicker. The di-

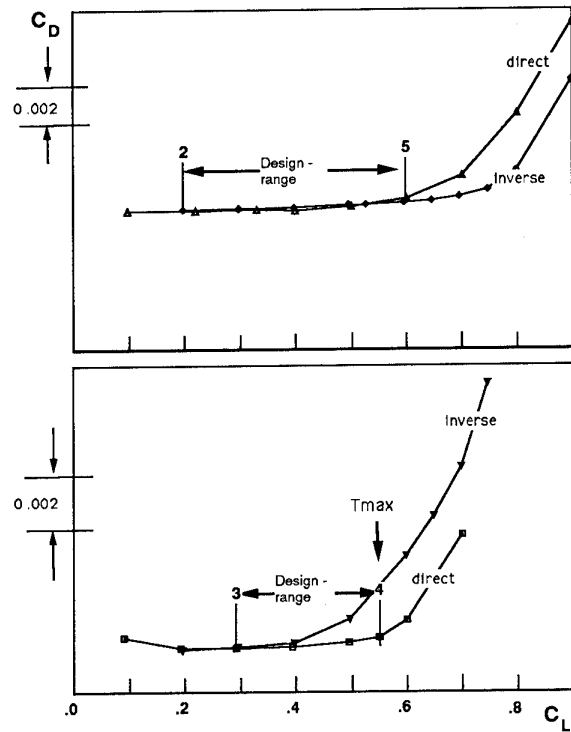


Figure 7: Comparison of the 12.5% inverse and direct designs.

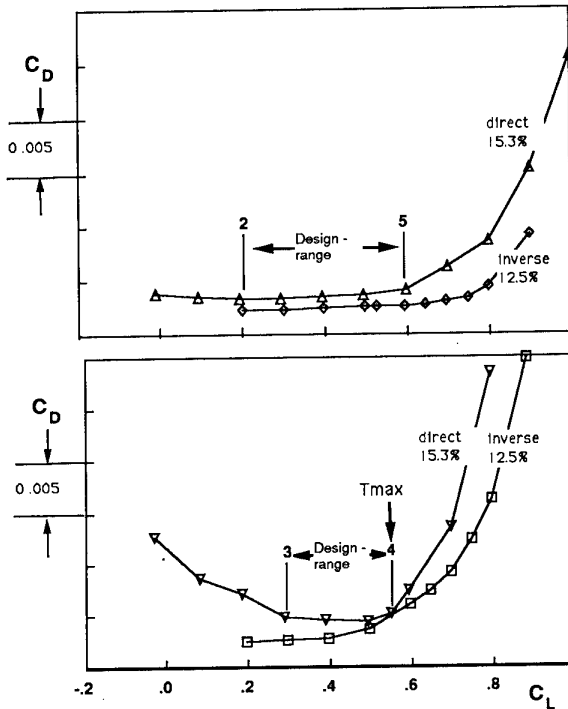


Figure 8: Comparison of 12.5% inverse design and 15.3% direct designs.

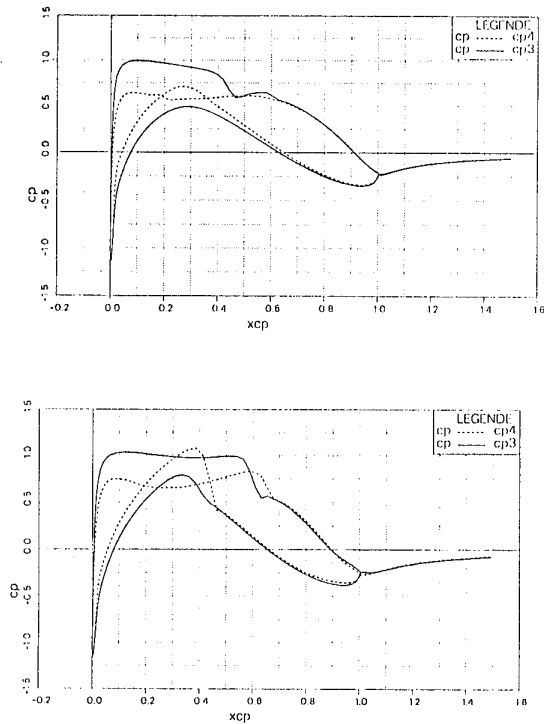


Figure 9: Pressure distributions at point 3 for 12.5% (top) 15.3% (bottom) thick direct designs.

rect design seems to have a completely flat wave drag topography over the design range. The drag is equal at both the low and the high lift coefficients. The drag creep constraint of 15 counts between points 2 and 3 was active. The author has never before observed such a wave drag behavior for a wing section. The physical explanation of this phenomenon is shown in Figure 9, which shows the pressure distribution at point 3 for the 12.5% and 15.3% direct designs. For the 15.3% thick airfoil, we see a flat rooftop pressure distribution with a normal shock recompression and a Stratford-type recovery at  $C_{L,3}$ . At  $C_{L,4}$ , we see an even stronger shock on the lower surface. The optimization procedure has balanced both shock systems to produce an quasi-constant total wave drag. This design was later rejected because of its high wing-nacelle interference.

### 4.3 A multipoint horizontal tail design

Figure 10 shows the horizontal tail plane design points of a current large transonic passenger transport. Our objective function is the weighted sum of the drag at four design points. The design operational range of the horizontal tail is between M 0.8

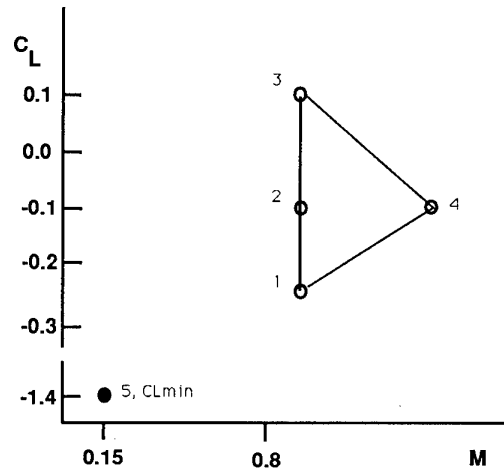


Figure 10: Horizontal tail plane design points.

and 0.9+. The wing was rather highly swept.

The design had the following constraints:

- Thickness:  $8.8\% < t/c < 9.2\%$ .
- Minimum lift:  $C_{L,min} < -1.4$ .
- Minimum angle of attack:  $\alpha < -12^\circ$ .
- Hinge moment:  $-0.0015 < C_{m,h} < 0.0015$ .

Surprisingly enough, the optimized design was very similar to the inverse design. It showed only slight improvement in terms of drag and displayed the same solution type. Figure 11 shows the inverse and the direct design pressure distributions at point 4. Even though there are some obvious differences, it is surprising to see that the pressure distributions are so similar. One can even observe the slight reflex in the trailing edge pressure distribution which relieves the hinge moment.

The optimization of this horizontal tail was much harder than that of the transonic wing design due to problems in the calculation of the minimum lift and angle of attack. During the optimization there is a continuous struggle between the constraints on minimum lift and the demands on low high-speed drag, which was why a double sided thickness constraint

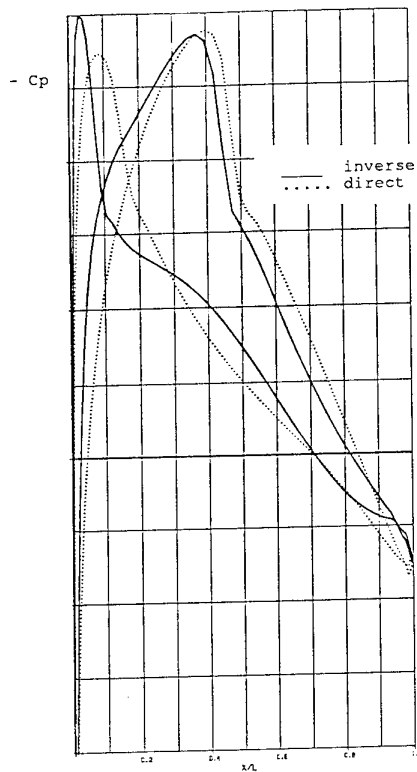


Figure 11: Comparison of the inverse and the direct design horizontal tail pressure distributions at point 4.

was used. Thicker airfoils allowed good minimum lift performance but had bad high speed performance.

## 5 Supersonic Civil Transport Design

### 5.1 Optimization and analysis methods

A linear panel code with real flow corrections was used to analyze drag for 3D supersonic wing body configurations. This analysis code was developed by the author from Woodward's wing-body code [21], and solves the linear Prandtl-Glauert equation for a thin panel geometry. The power plants are modeled as stream tubes which displace ambient fluid and hence cause wave drag. Friction is calculated stripwise over the curved geometry assuming a fully turbulent boundary layer. No effort was made to couple the boundary layer equation to the potential flow pressure distribution. Potential drag is calculated with surface integration and a calculated value of the leading edge thrust. The correct leading edge thrust is found by combining the far-field drag as calculated by the Lomax supersonic area rule [24] and

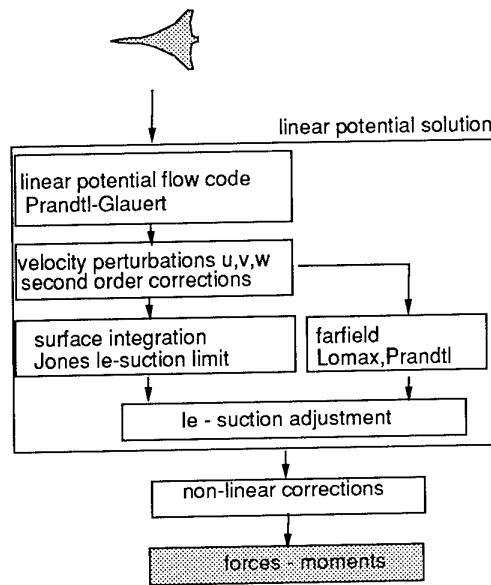


Figure 12: A coarse panel method with empirical flow corrections to evaluate forces and moments.

Treffz-plane integration. The leading edge suction is then corrected for real flow effects using the method of Carlson [23]. The Torenbeek quasi-empiric method [28] is used to model the effect of flap deflection. An overview of this method is given in Figure 12. A more detailed description can be found in the author's thesis [3].

The forces and moments calculated with this method compare well with values measured from the NASA Ames Oblique Wing development program, a generic SCT, a generic fighter and the Munroe NASA arrow wing tests. Figure 13 shows the calculated and measured forces and moments for a generic SCT with 12 degrees leading and 3 degrees trailing edge flap deflection at Mach 1.05—a difficult case for panel calculations. Our method, which was applied to a panel half-model with a resolution of no more than 120 panels, took one second per flow point on our workstations. The Euler method EUFLEX [27] with a decoupled boundary layer calculation took about an hour on a Cray.

### 5.2 3D supersonic thickness, area and camber distribution

The design presented here is part of a MIDAS design cycle described previously in ref. [16]. The global design was optimized for a Mach number of 1.8 and therefore had a fixed wing area, leading edge sweep, taper ratio and thickness distribution. The fuselage was defined by its mean diameter and its length.

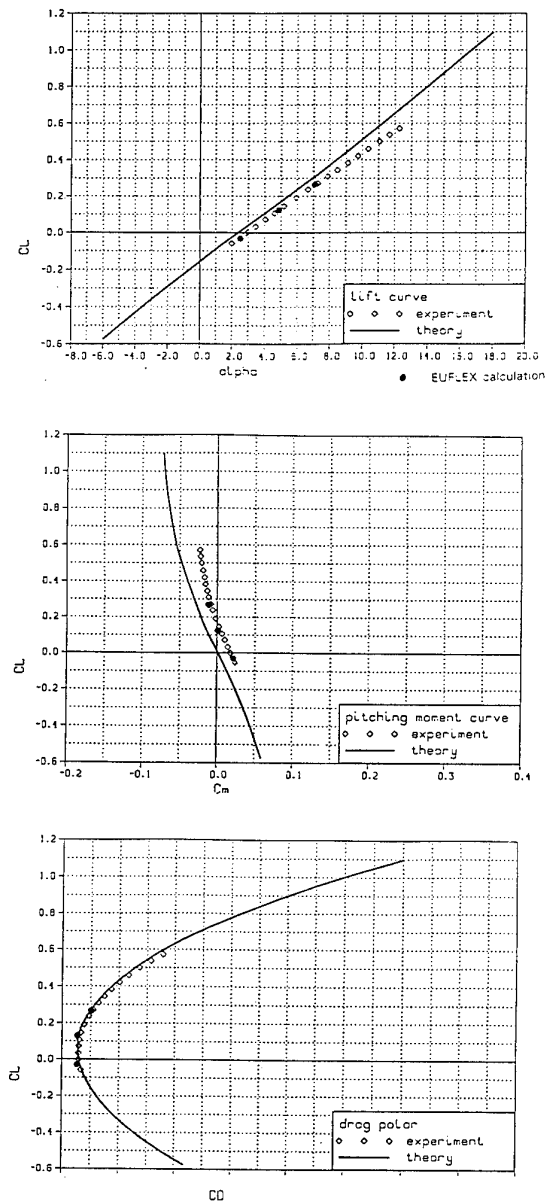
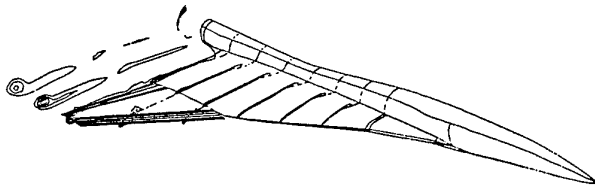


Figure 13: Forces and moments of a generic SCT.

In the global model a preliminary area distribution was determined, and the assumption was made that there existed a thickness, area and camber distribution which would produce a lift-to-drag ratio of 10.4 at Mach 1.8 with a lift coefficient of 0.135. The objective of the aerodynamic shape optimization is to find the best aerodynamic shape for this condition and compare it with the value that was projected by the global model. In this detailed geometric shape optimization we must therefore derive a shape that *does not interfere* with and *enables the assumptions* of the multidisciplinary global optimum.

The design is defined with analytical functions that are similar to the NACA four series definition. Because pressures at supersonic speeds are related to the local gradients of the geometry  $dz/dx$ , it is not necessary to have shape functions which model the second derivative well. The camber is represented by a linear combination of a NACA four digit mean line [1] to model parabolic camber  $p$  and a transformed sine function to model reflex  $r$ .

Forward of the maximum ordinate  $p_p$  the camber  $y_p$  is described by:

$$y_p = \frac{m_p}{p_p^2} (2p_p x - x^2). \quad (3)$$

Behind of the maximum ordinate  $p_p$  the camber  $y_p$  is described by:

$$y_p = m_p \left( \frac{(1 - 2p_p) + 2p_p x - x^2}{(1 - p_p)^2} \right). \quad (4)$$

To this parabolic camber a transformed reflexed camber distribution is added. Forward of the maximum ordinate  $p_r$  the camber  $y_r$  is described by:

$$y_r = m_r \sin \left( \frac{\pi x}{p_r} \right). \quad (5)$$

Behind of the maximum ordinate  $p_r$  the camber  $y_r$  is described by:

$$y_r = m_r \sin \left( \frac{\pi (x - p_r)}{1 - p_r} + \pi \right). \quad (6)$$

The reflexed camber has a discontinuity in the derivative around  $p_r$ , which is smoothed by the coarse panel resolution. The shape functions mentioned in this section are superseded by the proprietary shape functions mentioned in the previous section and only serve to illustrate the method. The wing thickness is modeled on the basis of the transformed parabolic

camber equations. Equation 3 is transformed so that it touches a circle with radius  $r$  at the leading edge. The nose radius  $r$  is used explicitly by the analysis method to calculate the leading edge suction. Since for a single supersonic design point a sharp leading edge parallel to the local flow direction is always better than a rounded nose, a value for the leading edge radius of  $0.005c$  was selected to improve off-design performance. The wing thickness  $t$ , area  $S$  and the leading and trailing edge sweeps were previously determined in the global optimization; modifying their values would invalidate the global aircraft weight calculations. The wing shape is defined by four airfoil sections. Six design variables are used for each section:

- Angle of attack  $\alpha$  and twist angles  $\alpha_t$ ,
- Parabolic camber amplitude  $m_p$ , location  $p_p$ ,
- Reflex camber amplitude  $y_r$  and location  $p_r$ ,
- Parabolic thickness location  $p_t$ .

The fuselage is defined by 22 fuselage crosssections, which bring the total number of variables to 46. The analysis method assumes that a geometry of minimum drag exists between these discrete crosssections. The time required to reach a fully converged design was about an hour.

The following constraints were used:

- $C_L < 0.135$ ,
- $C_m = 0$ ,
- Cruise floor angle  $< 3^\circ$ ,
- Minimum dimensions for cockpit, landing gear and fuselage diameter (3.5 m),
- Bank, pitch wing and nacelle clearance,
- Acceptable wing-body fairing,
- Twist angles limited to  $\pm 5^\circ$ .

Figure 14 shows the initial and final wing shape. The coarse panels do not resolve the  $0.005c$  leading edge radius. Figure 15 shows the convergence of the lift-to-drag objective function versus the number of function calls for various optimization methods. All methods converged to the same solution. The optimized panel geometry is shown in Figure 16. The Catic 3D model based on this coarse panel geometry is

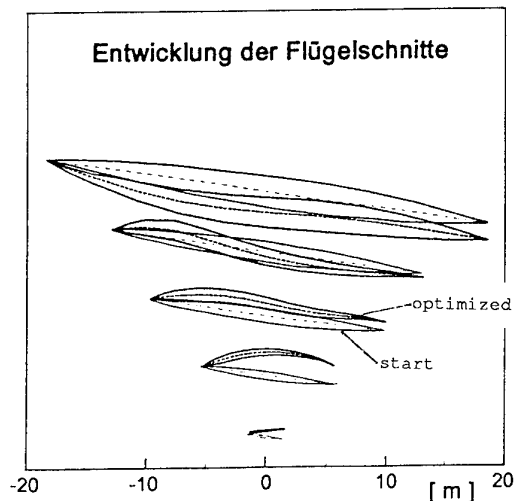


Figure 14: Optimization of the wing shape.

shown in Figure 17. This geometry was in turn used by other departments to make more accurate structural calculations and systems integrations studies, and is also suitable for Euler or Navier-Stokes flow calculations.

## 6 Conclusion

In this paper we present a general method for aerodynamic shape design, based on direct numerical optimization of aero-shape functions. The method was applied to the multipoint design of a transonic wing and a horizontal tail, and also with simpler shape functions to the design of a 3D supersonic wing body configuration. This method is computationally efficient and competitive with designs obtained using current industrial methods, resulting in overall organizational time savings of approximately a factor of three and producing designs of comparable to better quality than those produced by inverse methods. It is therefore practical for industrial application.

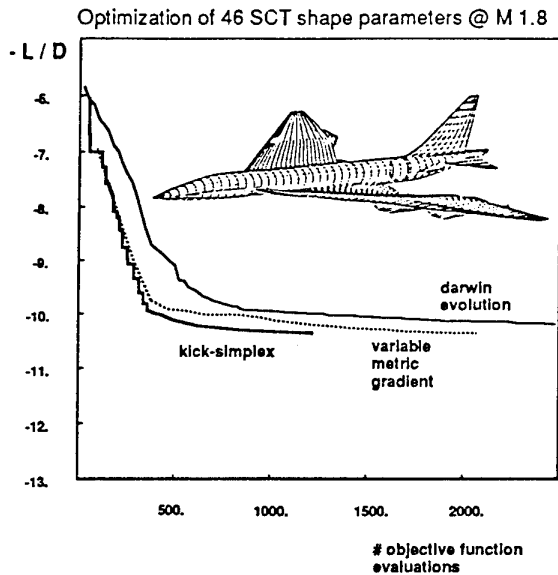


Figure 15: Optimization of the wing shape.

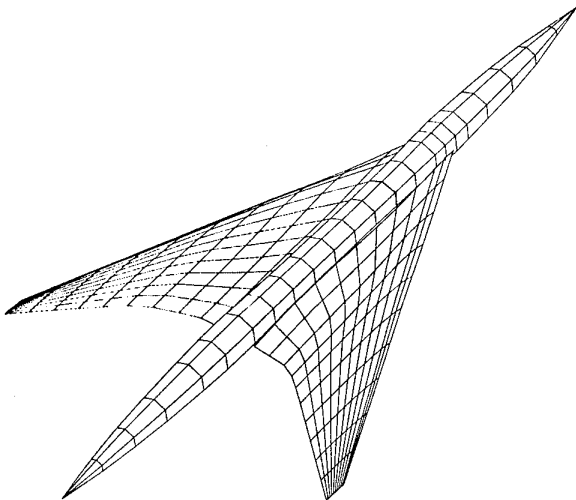


Figure 16: SCT optimized panel geometry.

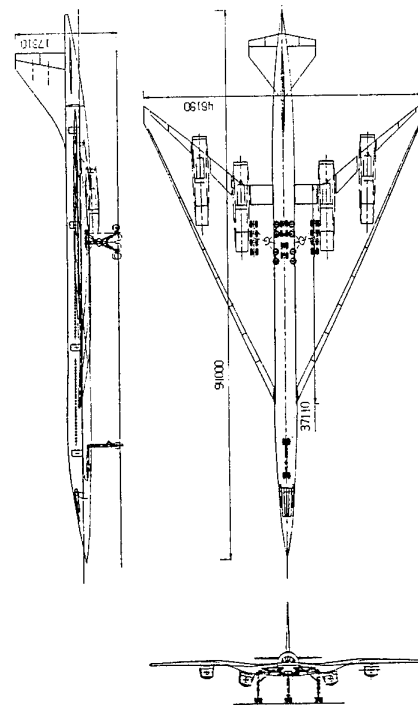


Figure 17: Catia 3D View.

## 7 Acknowledgements

I would like to thank Ralph Carmichael of NASA Ames for his earlier help with the wingbody code, and my colleagues at Stanford University: Prof. Ilan Kroo, Peter Gage and Sean Wakayama, who helped me with my initial attempts to use optimization. Herbert Stuke, Volker Cleemann, and Dr. Dargel of DA Bremen provided critical support converting the Eppler, XLS and VICWA codes to run on our HP workstations; because of their expertise, it took only three weeks from conception to testing of the quasi 3D multipoint airfoil optimization method.

I am grateful to Volker Cleemann for providing the horizontal tail example and Detlev Forbrich for local minimum drag example. Much of this work would not have been possible without the programming assistance of Silke Logemann. I would also like to thank Dr. M. Yoda for her editing of this paper. Finally, I would like to thank Dr. Mertens for his organizational and personal support.

## References

- [1] Abbot, I. & von Doenhoff, A. "Theory of Wing Sections," Dover Publications, New York 1949.

- [2] Sobieczky, H. "Progress in inverse design and optimization in aerodynamics," AGARD 1989, Paper 1.
- [3] Van der Velden, A. "Aerodynamic design and synthesis of the oblique flying wing supersonic transport," Ph.D. thesis, Stanford University, Dept. Aero./Astro. SUDAAR 621, UMI Microfilm #DA9234183, June 1992.
- [4] Hicks, R., van der Plaats, G., Murman, King, R. "Airfoil Section drag reduction at transonic speeds by numerical optimization," SAE Paper 760477, 1976.
- [5] Lee, K.D. "Application of computational fluid dynamics in transonic aerodynamic design," AIAA paper 93-3481-CP, 1993.
- [6] Labrujere, E. & Slooff, J.W. "Computational methods for the aerodynamic design of aircraft components," *Ann. Rev. Fluid Mech.*, 1993.
- [7] Greff, E. & Mantel, J. "An engineering approach to the inverse transonic wing design problem," *Communications in Applied Numerical Methods* 2, pp. 47-56, 1986.
- [8] Greff, E., Forbrich, D., Schwarten, H. "Application of direct inverse analogy method and viscous design optimization techniques," III. International Conference on Inverse Design Concepts in Engineering Science (ICIDES III), 1991.
- [9] Van der Velden, A.J.M. "Multi-disciplinary SCT design optimization," AIAA paper 93-3931, 1993.
- [10] Holst, T. "Viscous transonic airfoil workshop compendium of results," AIAA paper 87-1460, 1987.
- [11] Dargel, G. & Thiede, P. "Viscous transonic airfoil flow simulation by an efficient viscous-inviscid interaction method," AIAA paper 87-0412, Jan. 1987.
- [12] Eppler, R. & Somers, D. "A computer program for the design and analysis of low-speed airfoils," NASA TM 80210, 1980.
- [13] Dargel, G. "Ein Programmsystem für die Berechnung Transsonischer Profil- und Konischer Flügelströmungen auf der Basis Gekoppelter Potential- und Grenzschichtlösungen," DGLR Bericht 92-07, Köln 1992.
- [14] Van der Velden, A. "Multi-point optimization of airfoils," Deutsche Aerospace Airbus Bericht EF-1979, Nov. 1993 (not published).
- [15] Van der Velden, A. "Tools for applied engineering optimization," AGARD R 803, Apr. 1994.
- [16] van der Velden, A. "The global aircraft shape," AGARD R 803, Apr. 1994.
- [17] Greff, E. "In-flight measurement of static pressures and boundary layer state with integrated sensors," *J. Aircraft* 28 (5), May 1991.
- [18] Reneaux, J. "Numerical optimization methods for airfoil design," Recherche Aerospaciale no. 1984-5, 1984.
- [19] Burgreen G.W., Baysal O., "Three-Dimensional Aerodynamic Shape Optimization of Wings Using Sensitivity Analysis" AIAA paper 94-0094, 1994
- [20] Cosentino, G.M. & Holst T.L. "Numerical optimization design of advanced transonic wing configurations," *J. Aircraft* 23 (3), 1986.
- [21] Woodward, F.A., "Analysis and design of supersonic wing-body combinations, including flow properties in the near-field," NASA CR-73106, 1967.
- [22] Bore, C.L. "Propulsion streamtubes in supersonic flow and supercritical intake cowl," *Aeronautical J.*, September 1993.
- [23] Carlson, H.W., Mack, R.J. & Barger, R.L. "Estimation of attainable leading-edge thrust for wings at subsonic and supersonic speeds," NASA TP-1500, 1979.
- [24] Lomax, H. "The wave drag of arbitrary configurations in linearized flow as determined by areas and forces in oblique planes," Ames Aeronautical Laboratory, NACA RM A55A18, 1955.
- [25] Emlinton, E. & Lord, W.T. "Note on the numerical evaluation of the wave drag of smooth slender bodies using optimum area distributions for minimum wave drag," *J. Roy. Aero. Soc.*, Jan. 1956.

- [26] Braunschädel, A., "Erprobung numerischer aerodynamischer Verfahren für Überschallverkehrsflugzeuge an verschiedenen Konfigurationen," Diplomarbeit Technische Hochschule Aachen, 1994.
- [27] Krämer, E. & Gottman, T. "Berechnung des Strömungsfeldes eines Überschallflugzeugs mit Vorder- und Hinterkantenklappen im Transschall mit Hilfe des EUFLEX - Verfahrens," DASA-LME211-S-PUB-531, München 1993.
- [28] Torenbeek, E. *Synthesis of Subsonic Airplane Design*, Delft University Press, 1982.

## REVIEW OF THE EUROPT PROJECT AERO-0026

**B. Mantel, J. Periaux, B. Stoufflet**

Dassault Aviation  
Avions Marcel Dassault-Bleuguet  
78 Quai Marcel Dassault  
92214 Saint-Cloud Cedex  
FRANCE

### 1. Introduction

Despite progress toward automated shape design in Industry has been penalized until now by excessive computing costs, useful innovative design methodologies have been recently proposed (cf. Dervieux /9/ and Jameson /10/, Young /15/, Salas /16/) for computing different academic and industrial designs of nozzles, airfoils and wing-body combinations operating in inviscid flows modelled by the potential and Euler equations.

Since the designer has a precise idea of the pressure distribution that will produce the desired performance, not only optimization problems but also inverse problems have to be considered in current design.

The goal of this lecture is to describe the major ingredients of new algorithms developed by european partners of the AERO 89-0026 project which allow accurate and cost effective numerical solutions of optimizations problems and also to illustrate the capabilities of design softwares on test cases proposed in a Workshop for validation purpose. Industrial applications illustrating these methodologies are also presented.

Finally a new emergent search method for non linear optimization problems provided by simple Genetic Algorithms (GAs) is briefly described and illustrated by a few examples related to inverse problems and applied to reduction of viscous drag.

### 2. Choice of criteria and constraints

Shape design problems in Aeronautics require that aircrafts operate under a number of quite different conditions. Different criteria or objective functions are defined such as the linear combination of aerodynamic coefficients ( $C_d$ ,  $C_m$ ,  $C_l$ ,  $C_p$ ) or the distance between the pressure on a current airfoil and a targeted pressure distribution at one (single-point) or several (multi-point) operating conditions of the shape in order to compute one solution of the constrained minimization problems.

Another important part of the design problem is the specification of constraints that should be applied during the optimization process: feasibility of industrial shapes including physical acceptability (wing thickness, trailing edge thickness and pressure gradient, base drag), redesign (translation, rotation and contour of wing section), structural limitation (local thickness, trailing edge thickness, angle and radius) require the satisfaction of equality and/or inequality constraints attached to a design problem.

It has been shown in the project that a careful numerical implementation of constraints is essential in order not to deteriorate the efficiency of an optimizer. Moreover satisfaction of constraints drive severe limits on the class of admissible solutions.

### 3. Development of methodologies for solving inverse and optimization problems.

Most of partners have proposed from existing softwares the extension or development of novel optimizers based on exact or estimated gradient for solving reconstruction, inverse and optimization problems.

Some of them which have been used intensively to compute proposed test cases of a Workshop and also applications are described thereafter:

i) *a 3-D panel method using a potential flow analysis solver ( Deutsche Airbus).*

A panel code capable of treating complete configurations has been extended by an inverse option. Two types of patches are considered: "*design patches*", whose surface is derived from given pressures and "*analysis patches*", whose pressures are given from given surface. To solve such mixed problems the panel code is embedded in an iterative loop, which minimizes the sum of squared pressure deviation by a cost effective variant of the Levenberg-Marquardt strategy.

ii) *a 2-D finite difference BFGS Newton method using a full potential flow analysis solver (Alenia ).*

The integrated optimization procedure is composed of three modules: an optimization module, an aerodynamic module and an interface module that handles the geometric modifications of the airfoil. The optimization routines are coming from the ADS package /1/: for unconstrained problems a quasi-Newton method like the BFGS variable metric method is used while for constrained problems a method based on the feasible direction algorithm /2/ has been selected.

iii) *a 2-D finite element (resp. finite volume) GMRES ( resp. GRAD-GMRES) method without adjoint operator evaluation (resp. on optimality conditions) using a full potential (resp. Euler ) flow analysis solver (Dassault Aviation).*

For the potential flow solver reconstruction and inverse problems are solved by gradient methods and by the GMRES algorithm /3/ with an estimated gradient computation using a Krylov parameter equal to five. These methods are used and compared for airfoil reconstruction problems. In the case of optimization problems, a penalization method is applied to take into account the constraints and the associated unconstrained minimization algorithm is a descent method based on an estimated gradient.

For the Euler flow solver, the optimization is based on gradient algorithm combined with hierarchical techniques developed by INRIA Sophia Antipolis.

iv) *a 2-D finite element GMRES method via an adjoint equation using a transonic potential flow analysis solver ( INRIA Rocquencourt ).*

The nonlinear version of the GMRES algorithm is used in order to solve the optimality conditions in unconstrained optimization problems; the exact computation of the gradient of the cost function is done by the use of an adjoint state using the theory of control. /4/,/5/

v) *a 2-D finite element hierarchical parametrization method using an Euler flow analysis solver (INRIA Sophia Antipolis).*

A hierarchy of levels is introduced in a gradient-based optimization process and applied to a shape optimization problem with subsonic and transonic Euler flow analysis solver in which a smooth parametrization of the iterated shapes is a severe prerequisite. A large number of parameters is handled progressively and the convergence is not deteriorated by increasing the nodes number. In the case of approximate gradients computed by divided differences, the hierarchical approach is still more favourable. /6/

vi) *a linearized panel residual correction method applied to multi point airfoil design and single point wing design for subsonic and transonic conditions (NLR).*

The method is based on full potential theory and minimizes a cost function weighting the deviations from specified target pressure distribution for each design condition in a least square sense. Deviations from specified target pressure distributions (residuals) are translated into airfoil geometry corrections, by means of an approximate inverse calculation using a linearized panel method./7/

vii) *a single pass finite difference method for the solution of the inverse potential problem (NTUA).*

Potential and streamfunction variables originating from a Clebsch formulation are introduced in order to map the physical space onto a computational one via a body-fitted coordinate transformation. A fast novel procedure based on differential geometry and generalized tensor analysis arguments is employed to formulate the method. The assumption of orthogonal streamsurfaces reduces the number of dependent variables by one, simplifying the governing equations to an elliptic partial differential

equation for the velocity magnitude and a second order ordinary differential equation for the streamtube aspect ratio.

#### 4. Geometry representation and mesh regeneration.

In most cases the airfoil or wing geometry is done with spline approximation. The general basis function which have been investigated are the so called Bezier-splines curve segment approximation or the B-spline functions. In many optimization procedures developed by partners the use of Bezier splines has been favoured (Dassault Aviation, Deutsche Airbus, Alenia, INRIA, UPC) because changes in the position of a control vertex often maintain a smooth curve. This approach has been also intensively used by Deutsche Airbus with local parameters in section definition of 3-D inverse designs.

In the context of shape optimization problems analyzed by finite element methods the sensitivities of the different ingredients (B-spline, finite element mesh, flow behaviour and error estimator) have been studied in details by UPC. They provide informations to build up a finite element mesh from one design to the next with a specified and controlled level of error. The robustness and reliability of the methodology has been checked out via several 2-D applications.

The extension to 3-D problems remains the most critical step which requires the control of the mesh deformation during the iterative design procedure.

#### 5. Workshop.

A workshop has been organized within the AERO-0026C contract to validate optimum design methodologies developed within a two year period. During the kick off meeting partners agreed to define a set of test cases to compare in terms of accuracy and efficiency optimum shape design computations issued from their respective methodologies. The selected cases included *three types* of problems:

Type 1: *Reconstruction test cases* where pressure distribution for a given configuration serves as target criterion to rebuild this configuration from an initial guess;

Type 2: *Inverse test cases* where a pressure distribution serves as design criterion to calculate an optimal configuration corresponding to the target;

Type 3: *Optimization problems* with possible constraints to design shapes (not unique !) that correspond to a minimum of the criteria.

The flow analysis solvers used in this Workshop are solutions of the full/potential (resp. Euler) equations for a given shape. These solvers

correspond to the simulation of compressible/incompressible irrotational flows (resp. compressible rotational flows). Among the test cases described in the sequel two of them involve the coupling of the full potential equation with a boundary layer model in order to simulate the viscous effects of the flows.

### 5.1 Definition of nine test cases.

The following *nine mandatory* test cases including various parameters of the design - criteria, possible constraints, type of equation of the flow analysis solver, values of Mach numbers, angles of attack and possible Reynolds numbers- and output formats have been defined by partners:

*Test case 1 :*

2-D half nozzle reconstruction problem : subsonic case; Mach=.2;

*Test case 2 :*

2-D half nozzle optimization problem: subsonic case; Mach=.2 ;

*Test case 3 :*

2-D half nozzle optimization problem: subsonic case; Mach=.5 ;

*Test case 4 :*

Korn airfoil reconstruction problem: shockless transonic case; Mach=.75,  $\alpha = 0^\circ$ ;

*Test case 6 :*

Single point RAE2822 airfoil drag minimization problem: shocked transonic case; Mach=.73,  $\alpha = 2^\circ$ ;

*Test case 8 :*

two point NACA4412 airfoil inverse design with viscous corrections : subsonic target (Mach= .2;  $\alpha = 7.8^\circ$ ,  $Re = .5 \cdot 10^{**7}$ ) and transonic target (Mach=.77;  $\alpha = 0^\circ$ ,  $Re = 10^{**7}$ ); constraints: chord=1; trailing edge angle  $> 10^\circ$ , thickness  $t/c = 11\%$ ; weight factors: (.5 ;.5);

*Test case 10 :*

Williams two element configuration reconstruction problem: subsonic case (Mach=0; chord angles of the design profiles:  $\theta_1 = 1.67$ ,  $\theta_2 = 10.13$ );

*Test case 14 :* single point DLR -F4 wing : subsonic case; Mach=.3,  $\alpha = 6^\circ$ ;

*Test case 17 :* 3-D double turning nozzle reconstruction problem: incompressible case (Mach= 0 )and subsonic compressible case (Mach=.2).

Other *optional* test cases can be found in the available report entitled "Workshop on selected inverse and optimum design problems".

The nine test problems were defined with the following features:

- i) they should be on simple 2-D or 3-D analytical or well referenced geometries well suited for a wide range of solution and optimization methods (finite differences, finite volumes, finite elements;
- ii) accurate flow analysis solvers and efficient optimizers should be used simultaneously to compute efficiently feasible shapes;
- iii) they should not include at this stage laminar Navier Stokes flow solvers too much costly for shape optimization problems.

Test cases T4 and T10 and T14 were chosen because of existing well documented results.

The main challenge was the search of shapes - reconstruction or optimization- with subsonic and/or transonic inviscid flows including possible viscous corrections.

### 5.2 Contributors

Participation to the workshop was based on a final assessment task for partners having developed optimization softwares during the contract. After two years most of partners or teams contributed to this event and their involvement is described on Table 1. Very few people run multi point or 3-D test cases with viscous corrections which still require large and costly computer facilities. Different approaches for the flow analysis solvers and optimizers have been used by authors as shown on Tables 2, 3.

### 5.3 Results and comments.

Some of the most significant results obtained by contributors are shown on the following list of figures:

Fig. 1: Use of adaptive mesh refinement techniques and sensitivity analysis : initial shape and initial mesh- final shape and final mesh (T1-UPC);

Fig. 2: Distribution in the final nozzle shape and convergence history (T3-INRIA);

solver: mesh of the initial profile, initial and final Cp distribution, shape and cost function convergences (T4-Dassault Aviation);

Fig. 4: Optimized RAE 2822 airfoil with BFGS variable metric optimizer using an augmented objective function : Cp distribution and convergence history; drag and total cost function convergence (T6-Alenia and Dassault Aviation);

Fig. 5: Optimized RAE 2822 airfoil with drag minimization using the non linear GMRES solver for the optimality conditions : initial and final Cp - initial and final airfoil (T6-INRIA);

Fig. 6: Two point airfoil design with different weight factor combination; geometry (T8-NLR);

Fig. 7: Comparison of final and target pressure distribution with the Marquardt method (T10-Deutsche Airbus);

Fig. 8: Wing design: initial and resulting geometry with the residual correction approach (T14-NLR);

Fig. 9: Comparison of initial, target and converged pressure distributions at inner four stations with the modified Levenberg Marquardt strategy (T14- Deutsche Airbus);

Fig. 10: Perspective view of the reproduced 3-D nozzle ; mach number from direct and inverse calculations with the one pass method along the center line and on three sections normal to the center line  $s=1/3, 1/2$  and  $2/3 s_{max}$  (T17-NTUA).

Among the various methodologies used by partners some associated algorithms have shown good potentiality for further industrial applications:

A1. The extended inverse option of the panel code capable of treating complete wing-pylon -nacelle- fuselage configurations (Deutsche Airbus /9/);

A2. Exact gradient optimizers with Euler and Navier Stokes solvers if further extension to second order approximation of the advection terms can be obtained via automatic symbolic differentiation requiring reasonable programming efforts (INRIA /10/ and Dassault);

A3. Hierarchical methods providing undoubtedly a significant increment in efficiency when combined with different methods of optimization and mathematical parametrization (INRIA);

A4. Optimality conditions and a hierarchy of parametrization allowing the use of fast "one shot" methods relying on simultaneous and hierarchical solution of the optimality system (INRIA);

A5. Extension of the inverse inviscid potential-streamfunctions method introduced by Stanitz to rotational flows, a very fast method needing only one equivalent "direct" problem solution (NTUA /11/);

A6. A residual correction method for single and multi-point transonic inverse design formulated as an equivalent incompressible design problem using a fast integral equation methodology (NLR /12/);

A7. Sensitivity analysis and automatic adapting meshes for complex flows (UPC);

From a first comparison of the results it appears that the discrepancy of computed solutions is much larger for optimization or inverse design problems than for usual direct problems solved by flow analysis solvers.

At the present time the difficulties encountered by several existing design methods can be explained by the following remarks:

R1. Existence and uniqueness of the discretized design solution is still an open problem;

R2. Concerning nozzle reconstruction problems without constraints the results look quite similar and significant CPU time differences occur only in the choice of the methodology (two examples : a 2-D reconstruction nozzle obtained in 18 mn of CPU on a Personal Iris 35TG workstation (UPC) and a 3-D reconstruction nozzle obtained in 100 sc for 20 GMRES iterations on a Alliant FX 80 (NTUA);

R3. Airfoil inverse problems solved with specified pressure distribution and constraints both on the geometry and the aerodynamics characteristics to prevent nonphysical solutions suffer from a lack of well posedness. In multi point design the optimization of the aerodynamic shape still remain highly dependent of the a priori weighted compromise between the required characteristics for different design conditions /13/;

R4. Direct optimization methods seems much more flexible and do not rely on the designer's knowledge by the minimization of any aerodynamic cost function; but a designed solution seems highly dependent of the initial guess and the choice of the optimizer which should operate

with non linear constraints. Moreover a major role is played by the number of control variables and the concept of hierarchical parametrization seems a very interesting concept to reduce the computational effort (two examples: a 2-D transonic potential optimization of an airfoil obtained after 40mn of CPU on a CDC 910/600 workstation(Alenia) and a 2-D transonic Euler optimization of a nozzle obtained after 4000 sc on a Convex C210(INRIA).

R5. Until now no accurate design with complex viscous flows on complicated industrial geometries has been achieved. The computation of 3-D accurate design with complex flows using adapted meshes remains a great challenge in a near future.

For some progress on these problems some lines of research are suggested thereafter:

L1. improvement of the accuracy of the design by 3-D automatic adaptive remeshing and appropriate choice of control variables;

L2. acceleration of the convergence by fast one shot methods and hierarchical parametrization with appropriate preconditionners;

L3. systematic use of new parallelizable algorithms on new MIMD parallel architectures;

It is noticeable that the best designs were provided by optimizers exhibiting a part of the above properties.

## 6. Applications to industrial design.

After two years research activities several industrial examples solved with a 3-D subsonic inverse panel method at Deutsche Airbus have demonstrated the power and usefulness of automated tools to actual aircraft design problems. One selected example described on Figure 11 deals with an airplane configuration with propfan engines at the tail. The rear part of the panel model with fuselage-tail, fin, pylone and nacelle is depicted. For such a configuration the flow on the pylon has to be controlled accurately since a too high velocity level should permit shock induced separation on the pylon, a situation which cannot be accepted aerodynamically. The problem which has been solved by the inverse method is to design a part of the fuselage tail geometry controlled by a pressure distribution on the pylon. Figure 12 shows the resulting fuselage surface, the solid lines corresponding to the initial geometry and the dotted lines to the designed one. The target pressure distribution is achieved three iterations.

A preliminary investigation of the behaviour of riblets under laminar viscous flows conditions for drag reduction has been proposed by Tritech. The numerical results obtained demonstrate that flows for Reynolds numbers up to  $10^8$  can be stabilized with a suitably designed riblet. A further development in design procedure using Navier Stokes or turbulent viscous flow analysis solvers /14/ is the next step to allow a better understanding of the mechanism of the riblets.

## 7. Genetic Algorithms (GAs) : a robust search procedure for optimization problems.

"The real world of search contains discontinuities and multimodal search spaces. Traditional optimization methods suffer from restrictive requirements of continuity and derivative existence and are insufficiently robust in unintended domains" (Goldberg, /17/).

This section introduces briefly the main ingredients for understanding genetic algorithms and present two applications in shape optimization.

### 7.1 Introduction.

Details of the introductory material described in this section can be found in Goldberg (ref /17/), Davis (ref /18/), Poloni (ref /19/), Galante (ref /20/).

Genetic Algorithms (GAs) are search procedures based on the mechanics of natural selection (Darwin); they have been introduced by J. Holland, Univ. of Michigan, the field's inventor in the early 70' who explained the adaptive process of natural systems and designed artificial systems softwares based on mechanisms of natural systems. He laid down the two main principles for GAs: the ability of simple representations (bit strings) to encode complicated structures and the power of simple transformations to improve such structures (schemata theory).

More recently D. Goldberg brought GAs in optimization theory for quantitative study of optima and introduced a major thrust in the 80' in research into the GAs

### 7.2 Why GAs are attractive ?

A major line of research for GAs has been robustness. GAs are computationally simple yet powerful in their search for improvement; they are not limited by restrictive assumptions about the search space (continuity, existence of derivatives, unimodality).

discontinuous environments : a classical example in structural optimisation described in Galante (ref /20/) is the minimisation of the weight of trusses where multiple peak functions are unsuitable for search by traditional methods.

GAs are search procedures which use semi-random choice; randomized search which does not imply directionless search allow a wider exploration of the search space compared to conventional methods which are not so robust but work well in a narrow problem domain;

### 7.3 How GAs are different from conventional numerical optimization tools ?

Genetic Algorithms are different from traditional methods of search and optimizations in the following way:

(a) GAs are *blind* or indifferent to problem specifics and treat them as a black box : an example in shape optimization is the value of the drag on an airfoil;

(b) GAs use *codings* of decision variables by adapting artificial chromosomes or individuals rather than adapting the parameters themselves. In practice the GA user codes the possible solutions as finite length strings;

(c) GAs process *successive populations* in successive generation compared to point by point conventional methods which use only local information and can be trapped on a false optimum;

(d) GAs use *randomized operators* instead of strictly deterministic rules.

Items (a) to (d) contribute to the robustness of GAs.

### 7.4. Mechanics of GAs

GAs as search procedure to optimize airfoil shape in Aerodynamics use the following tools with the correspondence terminology:

- (i) gene = design parameter
- (ii) individual= design configuration
- (iii) population= group of configurations
- (iv) generation= population evolution
- (v) fitness function = quality of the design
- (vi) social success= optimality of the design

As in the natural process of reproduction the genetic informations stored

individuals. An airfoil defined by cubic spline coefficients (i) is represented by a bit string. The optimization process will start from multiple points of the configuration space (iii) created randomly; the quality of individuals of the population are evaluated through a *fitness function* (v) and the search process is repeated with new generation of individuals until optimality of the design (vi).

The process of evaluating the fitness and the reproduction process are inherently parallel making the implementation of GAs on parallel computers very attractive.

The following transformation operators (*reproduction, cross over and mutation*) are applied to get a new population until the best individual is reached :

(R) *reproduction* : parents with highest fitness have the highest probability of selection (roulette wheel);

(C) *crossover*: a randomized yet structured recombination operator. Simple crossover proceeds in 3 steps: two strings are selected using *reproduction* ; then a cross site along the string is chosen uniformly at random; finally position values are swapped between the two strings following the cross site.

One example of crossover : if  $A=11111$  and  $B=00000$  and a random selection of a cross site turns up a 3, we obtain the two strings  $A'=11100$  and  $B'=00011$  and these strings will be placed in the new population.

(M) *mutation* : in a binary -coded GA, mutation is the occasional alteration of a bit position (the changing of a 1 to a 0 or vice versa); it is a protection against the loss of important genetic material at a particular position.

One example of mutation: if  $p_m=0.001$  is the probability of mutation and a random routine provides the successive random values (.760,.473,.894,.001) then the 4-bit old chromosome (0010) will be replaced by the new chromosome (0011)

The combined action of *reproduction* and *cross over* provide most of the innovation of genetic search; the low level of mutation in artificial genetic search is secondary importance of the operator when compared to reproduction and crossover.

### 7.5 Two examples in optimum shape design with GAs:

The GAs strategy is used two optimisation problems in current aerodynamics design: the first one (EX1) deals with the symmetric airfoil reconstruction which realizes a target pressure distribution on its surface for a given potential flow condition (ref. /21/). The second example (EX2)

presented is the optimization for minimum drag of a symmetric profile cascade (ref. /19/) for a given laminar Navier Stokes flow condition.

Innovative solutions of other critical non convex optimization problems such as *multi-point transonic design* can be investigated with GAs.

EX1: (from Periaux et al, ref /21/).

The control points representing the symmetric airfoil are coded in both binary or real value strings.(10 control points ). For the sake of comparison, we have constructed the target pressure from a NACA0012 airfoil by solving the full potential flow equation using a finite difference flow solver. As a reconstruction problem we expect to find an optimal shape to be the given shape.A L2-deviation from the target pressure for each individual is calculated for any shape via the solution of the non linear full potential equation which results in that the computing cost is directly proportional to CFD evaluations.

With the GA approach we have tested different flow cases.The parameters  $P_c=0.75$ ,  $P_m=0.01$  are not carefully selected but fixed for most test flow cases.The present method uses a population of 50 strings each of length 80 bits for the binary coding. Each string represents one possible configuration to the problem.

Figures GA 1-3 show the fitness function for all the examined configuration with three different Mach numbers 0.01, 0.3 and 0.6. It can be noted that the method presented can realize near optimal shapes after 20 generations which indicates that GAs seem to be slightly independent of the Mach number.Figure GA 4 shows the shape convergence for the Mach number=0.3. The minimum shapes for Generation#1 (dash line) and Generation#20 are presented in comparison with a standard NACA0012 (solid line).

Based on the above tested cases, the fitness function can quickly approach near optimal value, thus a hybrid technique ( Davis, ref. /18/) can be considered in practical applications, particularly in the case of costly CFD evaluations.

EX2 ( from G. Mosetti and C. Poloni ( Ref./19/).

The design problem is the minimisation of the viscous drag of symmetrical bodies with geometrical constraints. The shape of the body is parametrized by Bezier polynomial (3rd and 4th order) key points.*Five* parameters are used to define the position of the key points in the optimization procedure. Figure GA 5 shows the position and the constraints imposed to the key points.*Eight* possible values for each variable are considered and therefore the size of the search space to be explored is  $8^{**}5$ .

extensive use of a full Navier Stokes finite element solver (FIDAP 6.04) at  $Re=400$  with a chord =1 and a profile thickness of 10% and 21%. The initial population of 20 individuals has been created randomly and evolve for 10 generations. Figure GA 6 gives an idea of the configuration space explored and Figure GA 7 shows the computed drag coefficient for all the examined cases. Finally Figure GA 8 shows the typical mesh used in this computation and the shape of the optimum profile found for the two thicknesses considered and the evolution of the generation is depicted on Figure GA 9 where the drag of the best individual at each generation is plotted.

It has been found that the parameters that have the largest influence on the drag are the value of the first (curvature of the leading edge) and last gene (inflexion in the rear part of the airfoil). The total drag of the optimized profile is equal to the 80% of the mean drag found for the profiles computed in the first population.

#### 7.6. Conclusion on GAs and future directions

GAs are described as simple methods for solving complex problems with good parallelization properties.

The classical numerical optimization methods start from a *guessed point* and from it the search is performed until the nearest minimum is reached. On the contrary using GAs the search starts from a *set of points* which forms the initial *population* and explore the space using *semi random reproduction, crossover and mutation* operators.

The two examples presented have shown the method robust and efficient and a new tool in shape optimum design now works.

Its *discrete* formulation in *encoding* and ability in *searching* make the GA a powerful tool in Engineering.

The application of GAs to fluid optimization suggest the possibility to solve other great challenge problems (*transition* among others Challenges) in modern Aerodynamics requiring in a near future *active control* methodologies.

#### 8. Conclusion.

Subsonic and transonic airfoil and wing optimization procedures have been developed to treat optimization problems namely drag minimization, lift maximization or target pressure recovery with possible non linear constraints to satisfy geometrical requirements and control

aerodynamic characteristics in off-design conditions. The most significant outcomes of this project concerns progress accomplished in design with Euler solvers, fast one pass inverse methods for rotational flows, parametrization of non linear surfaces, hierarchical multi level method for control variables and automatic adaptive remeshing.

Results obtained from a workshop indicate quite large discrepancies both in design due to the quality of the flow analysis solver and the parametrization of the shape and in efficiency with the choice of the optimizer. These comparisons can provide useful guidelines for choosing optimization or inverse methods with inviscid potential or Euler flows.

It is clear that for practical 3-D applications including viscous effects much effort remains to be done. In particular achievement of cost effective and accurate designs with the above available novel methodologies and associated algorithms will have to be implemented in a near future on massively parallel computers.

#### 9. Acknowledgements.

The results and methods described in these notes have been obtained in cooperation with many colleagues in Europe through fruitful discussions. We would like to mention most particularly F. Beux, G. Bugada, K. Chaviaropoulos, A. Dervieux, D. Joannas, T. Labrujere, J. Miller, K. Papailiou, O. Pironneau, E. Onate, H. Schwarten and V. Selmin.

This work was supported by Brite Euram Grant # AERO-0026 . We wish to express our thanks to D. Knorzer from CEC, DGXII for continuous encouragements;

We are also grateful to S. Gosset for reading and preparing the manuscript.

The first author express his gratitude to M. Galante, M. Galan, J.J. Greffenstette, D. Goldberg, K. Kumar, C. Poloni, D. Quagliarella, M. Schoenauer and G. Winter for their stimulating introduction to Genetic Algorithms and helpful suggestions. He also would like to thank C.H. Chen for fruitful discussions and implementing the GA code during his visit at Dassault . His help in the preparation of the GA material in the present document is gratefully acknowledged.

10. References

- /1/ G.N. Vanderplaats: ADS- A Fortran Program for Automated Design Synthesis, User Manual, 1987.
- /2/ M. Zoutendik: Methods of Feasible Directions, Elsevier Publishing Co, Amsterdam, 1960.
- /3/ P.N. Brown, Y. Saad: Hybrid Krylov methods for non linear systems of equations. SIAM J. Sci. Stat. Comp., 27, 1990
- /4/ J.L. Lions, Optimal Control of Systems Governed by Partial Differential Equations, Springer Verlag, New York, 1971.
- /5/ O. Pironneau, Optimal Shape Design for Elliptic Systems, Springer-Verlag, New York, 1984.
- /6/ F. Beux, A. Dervieux, a hierarchical approach for shape optimization, INRIA Report, 1993.
- /7/ T.E. Labrujere, J. van der Voeren, Calculus of Variations applied to 2D Multi point Airfoil Design, 1st European ECCOMAS Conference on Fluid Dynamics, Elsevier, Brussels, September 1992.
- /8/ Proceedings of the Workshop on Optimum Design in Aerodynamics, J. Periaux et Al, Vieweg Verlag Publisher, 1993, to appear.
- /9/ A. Jameson, Computational Algorithms for Aerodynamic Analysis and Design, Contribution to the INRIA 25th Anniversary Conference on Computer Science and Control, December 1992
- /10/ F. Beux, A. Dervieux, Exact gradient shape optimization of a 2-D Euler flow, Finite Elements in Analysis and Design 12 (1992), p.p. 281-302
- /11/ H. Schwarten, H. Stuke, Pressure controlled surfaces - a 3D inverse panel as a design tool, Special Technological Sessions of the First European CFD Conference on Fluid Dynamics, Brussels, ECCOMAS, Elsevier, September 1992
- /12/ H. Choi, P. Moin, J. Kim, Direct numerical simulation of turbulent flow over riblets, CTR manuscript 137, NASA Ames Research Center and Stanford University, July 1992.
- /13/ Th. E. Labrujere, J.W. Sloff, Computational methods for the aerodynamic design of aircraft components, Annu. Rev. Fluid Mech. 1993. 25, p.p.183-214

/14/ P. Chaviaropoulos, V. Dedoussis, and K.D. Papailiou, A robust inverse method for airfoil design, 1st European ECCOMAS Conference on Fluid Dynamics, Elsevier, Brussels, September 1992., p.p. 581-588

/15/ W.P. Huffman, D.P. Young, Iterative Optimization for Aerodynamic Design, Boeing Computer Services, Technical Report MEA-TR-200, 1992

/16/ M. Salas, S. Ta'asan, G. Kuruvila, Aerodynamic Design and Optimization in One-Shot, AIAA 92-0025 (1992)

/17/ D.E. Goldberg, Genetic Algorithms in Search, Optimization and Machine Learning, Addison Wesley, 1989

/18/ L. Davis, Handbook of Genetic Algorithms, Van Nostrand Reinhold, New York, 1991

/19/ G. Mosetti, C. Poloni, Aerodynamic Shape Optimization by means of a Genetic Algorithm, Proc. of the 5th Int. Symp. on Computational Fluid Dynamics, Sendai, Vo.II, JSCFD, 1993

/20/ M. Galante, M. Cerrolaza, W. Annicchiarico, Optimization of Structural and Finite Element Models via Genetic Algorithms, Proc. of Structural Optimization 93, Vol. II, J. Herskovits Editor, Rio de Janeiro, Brazil, 1993

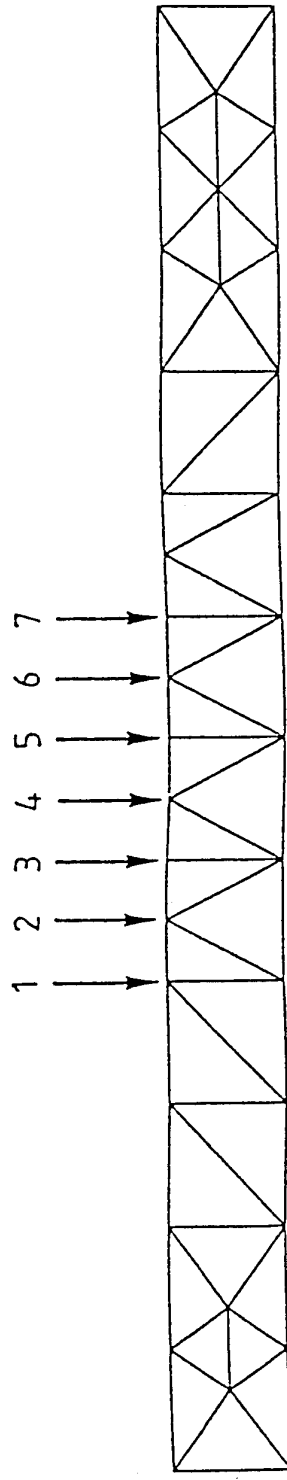
/21/ H.Q. Chen, J. Periaux, B. Stoufflet, B. Mantel, An Implementation of Genetic Algorithms for Aerodynamic Optimum Shape design, to appear

Partner	Dassault	Deutsche Airbus	Alenia	NLR	INRIA	NTUA	UPC
<b>Test Case</b>							
T1					X	X	X
T2					X		X
T3					X		
T4	X	X		X	X	X	X
T6	X		X		X		
T8				X			
T10		X					X
T14		X		X			
T17						X	
Table 1							
<b>Approximation</b>							
Panels		X		X			
Finite Difference			X			X	
Finite Volume		X		X	X		
Finite Elements	X				X		X
Table 2							
<b>Optimizer or Inverse Method.</b>							
One Pass Method.						X	
Hierarchical					X		
Steepest Descent					X		
Residual Correction				X			
Levenberg Marquardt		X					
Conjugate Gradient	X				X		
Feasible Direction			X				
BFGS			X				
Non Linear GMRES	X				X		X
Table 3							

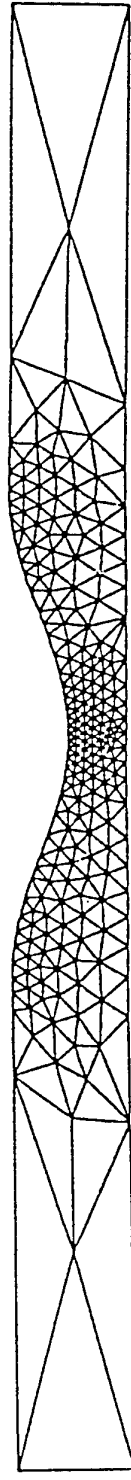
Table 1 : Involvement of the Partners in the Test Cases

Table 2 : Approximations of the Flow Analysis Solvers

Table 3 : Optimization or Inverse Methods



Initial shape, initial mesh and definition of the design variables.



Final shape and final mesh.

Fig.1.

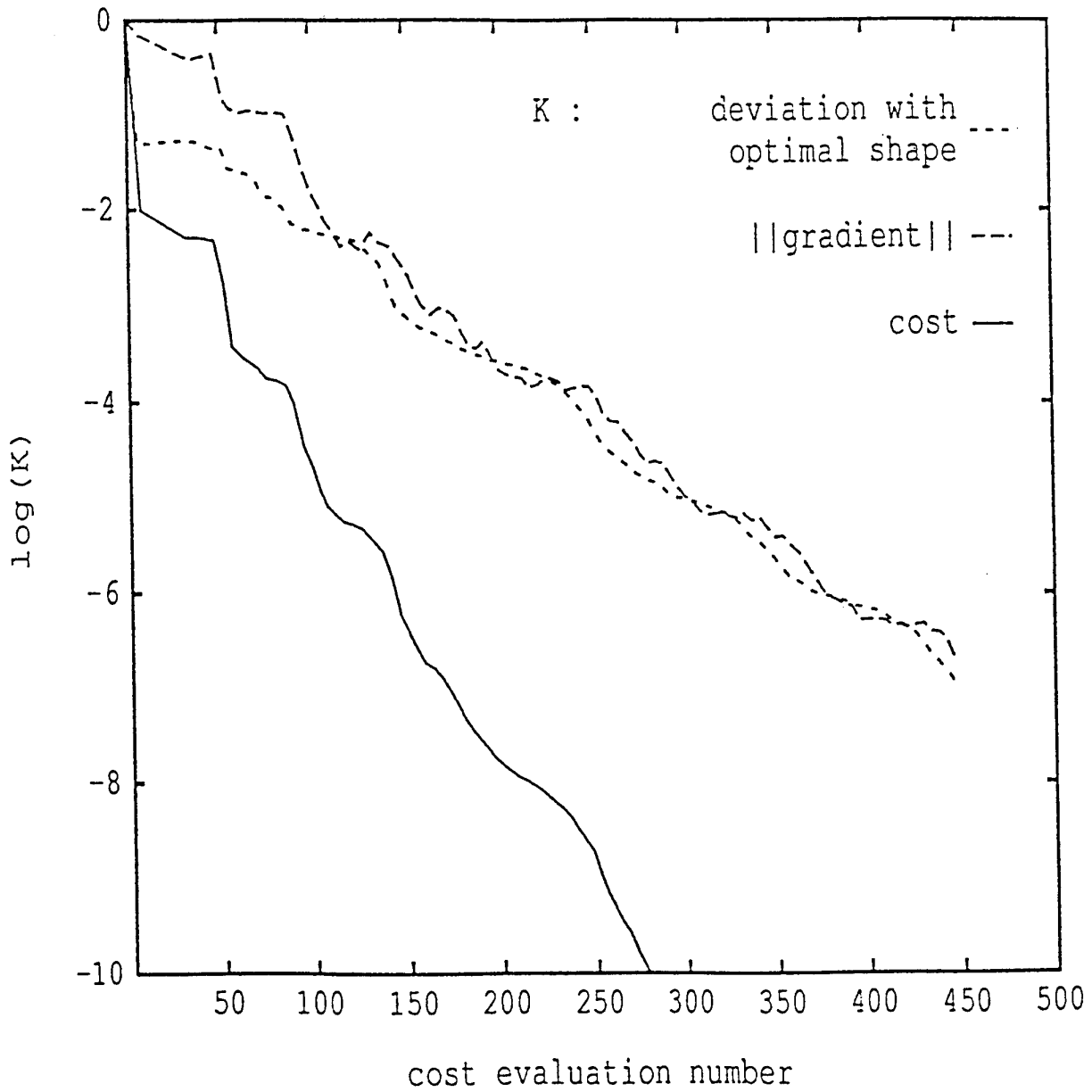


Fig.2. Transonic inverse problem : convergence history

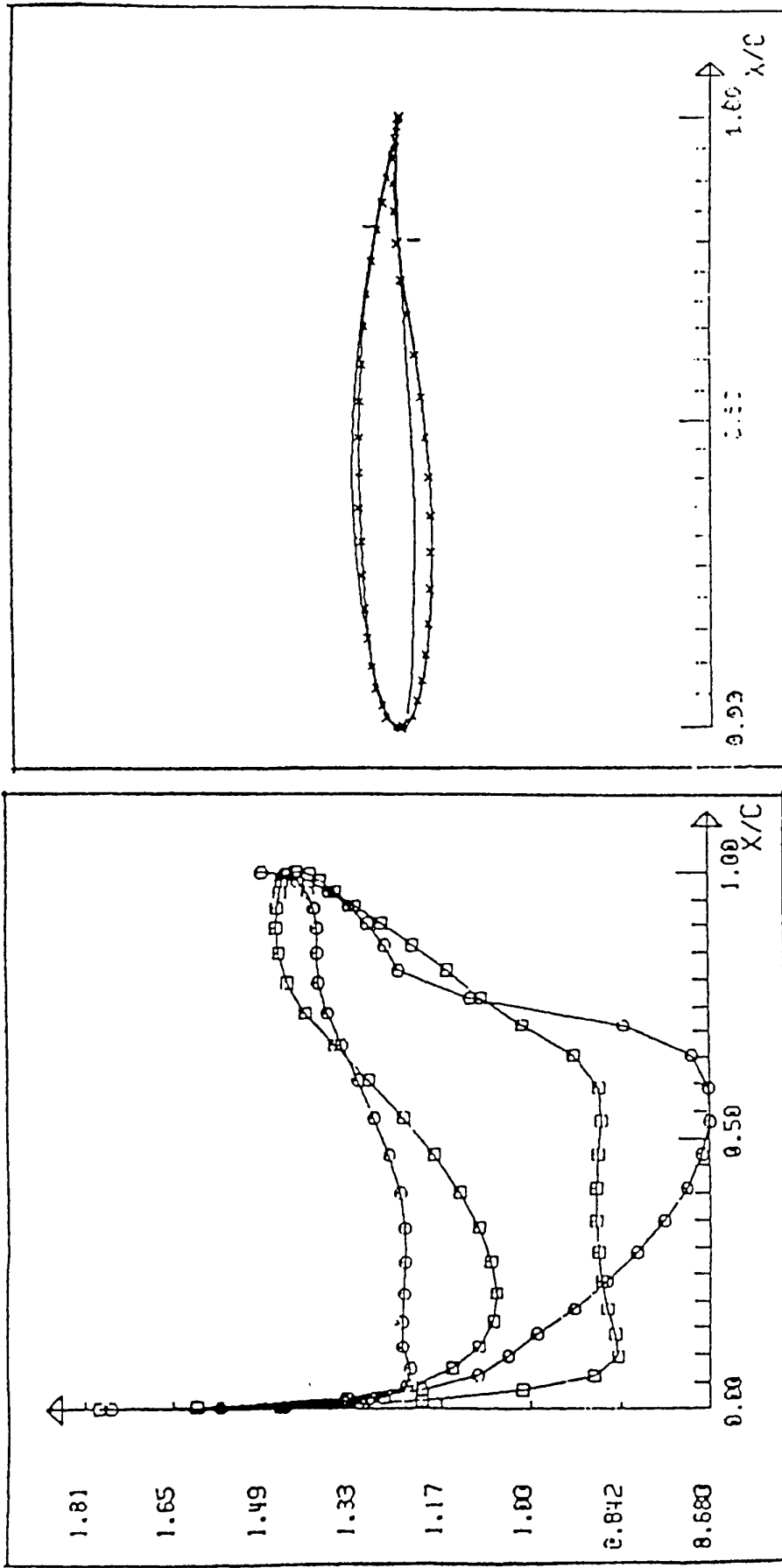


Fig.3. Inverse problem, pressure distribution,  $M=0.75$ ,  $\text{inc}=0$

(courtesy of Dassault Aviation)

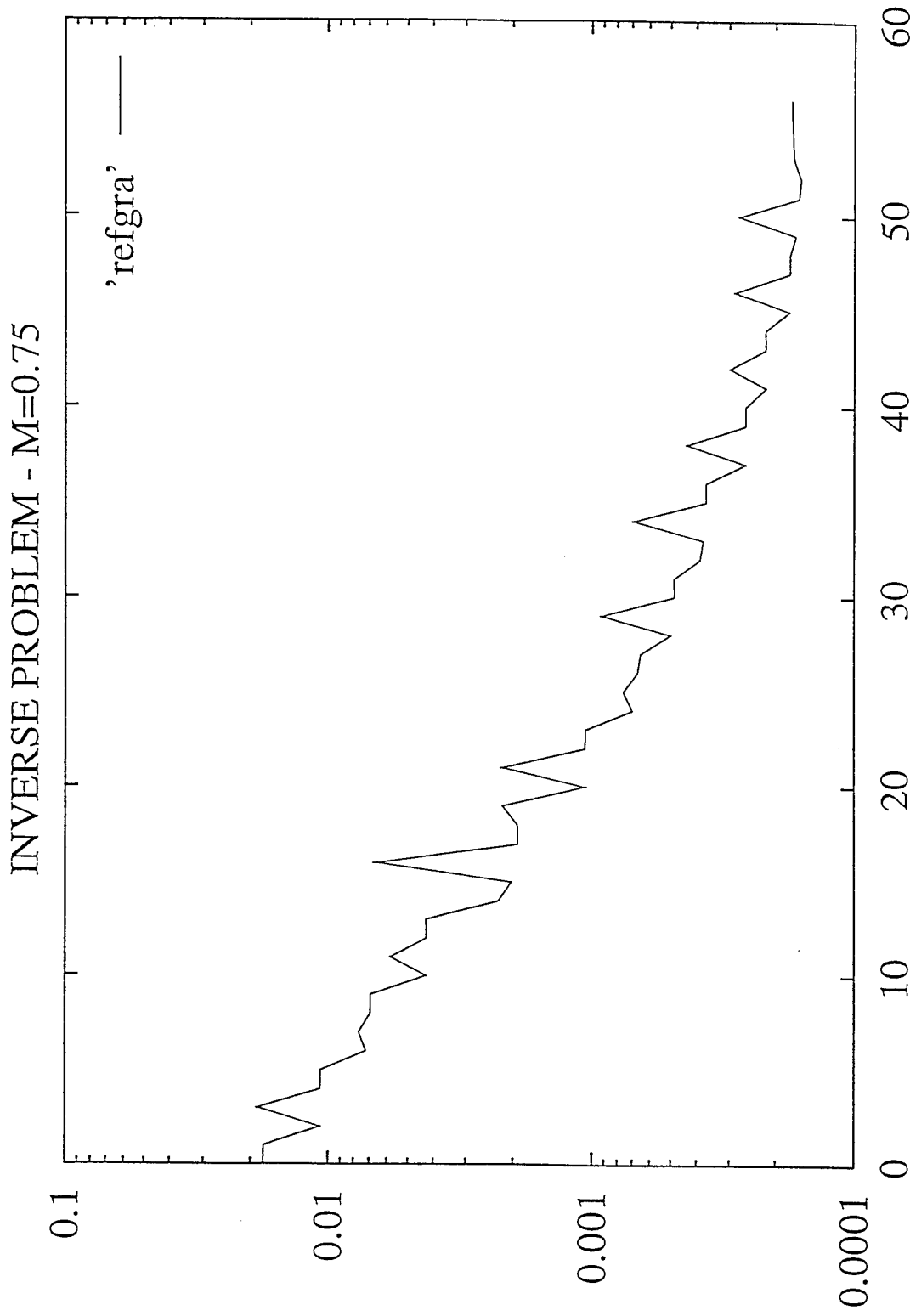


Figure 3A Convergence of the cost function for inverse problem at  $M=0.75$

(courtesy of Dassault Aviation)

# INVERSE PROBLEM

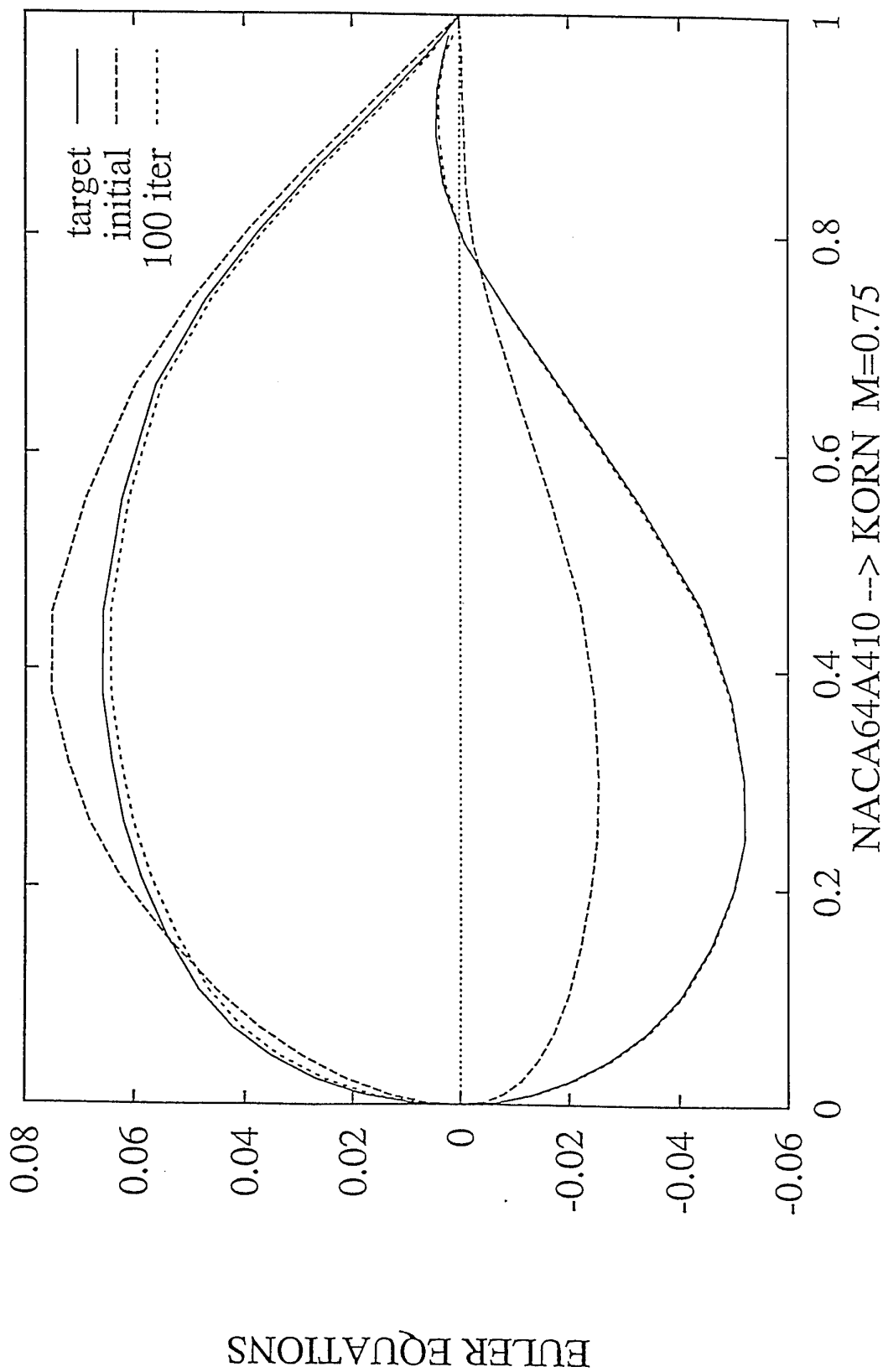


Figure 3B Comparison of profiles after 100 iterations (M=0.75)

(courtesy of Dassault Aviation)

(2557 Nodes ; 5039 Elements)

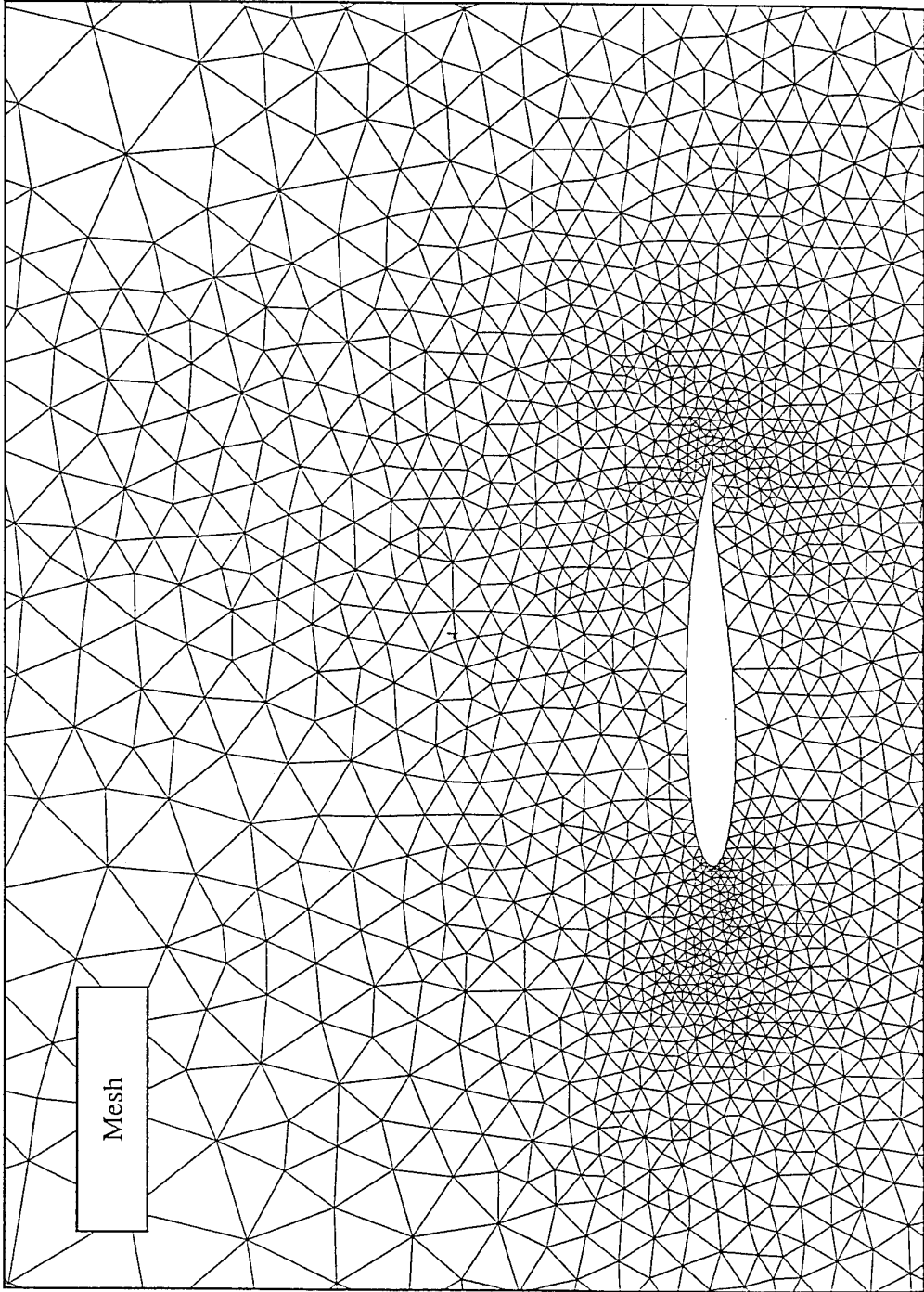


Figure 3c Maillage du profil initial

(courtesy of Dassault Aviation)

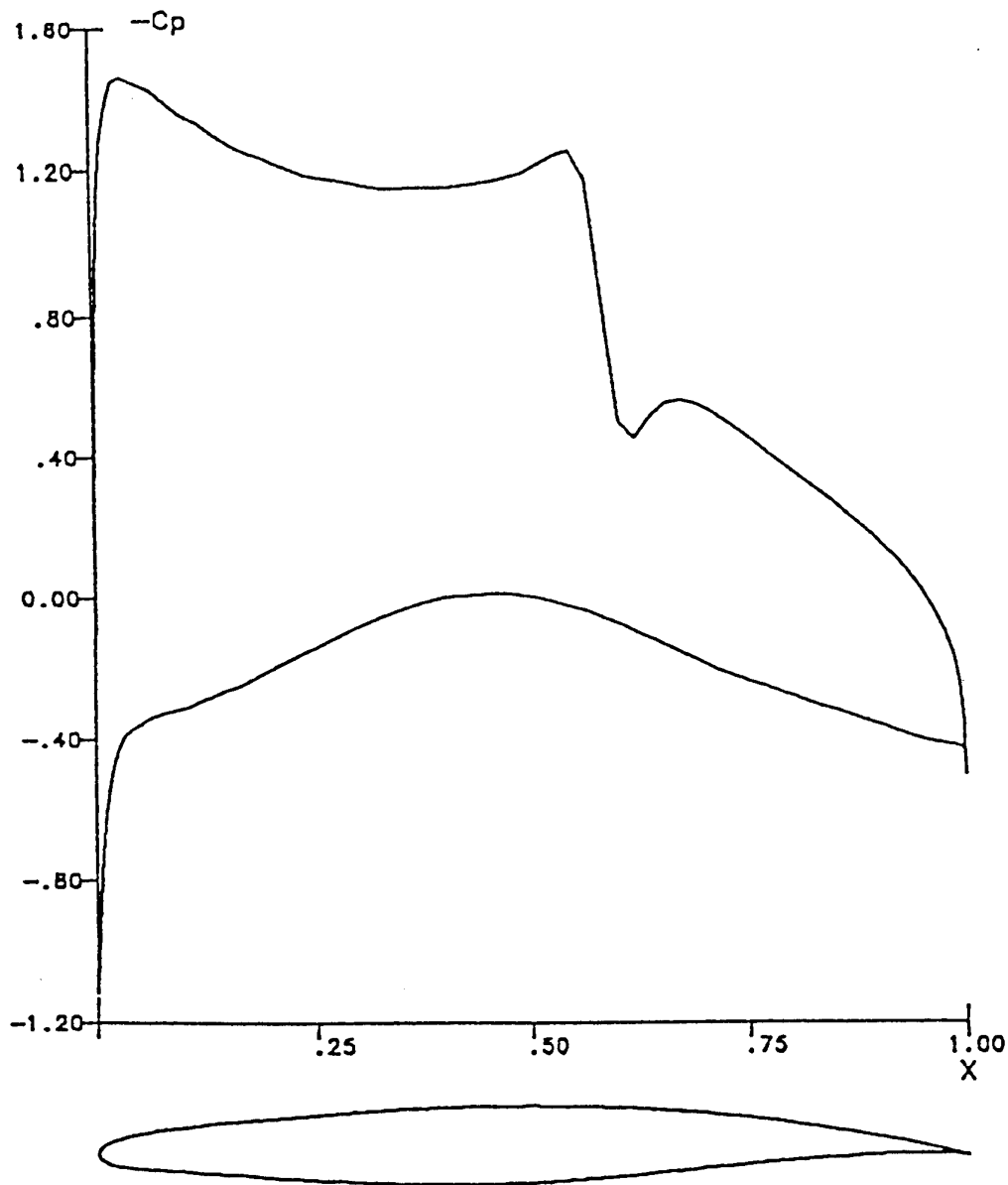


Fig.4.  $C_p$  distribution computed using an Euler solver

(courtesy of ALENIA)

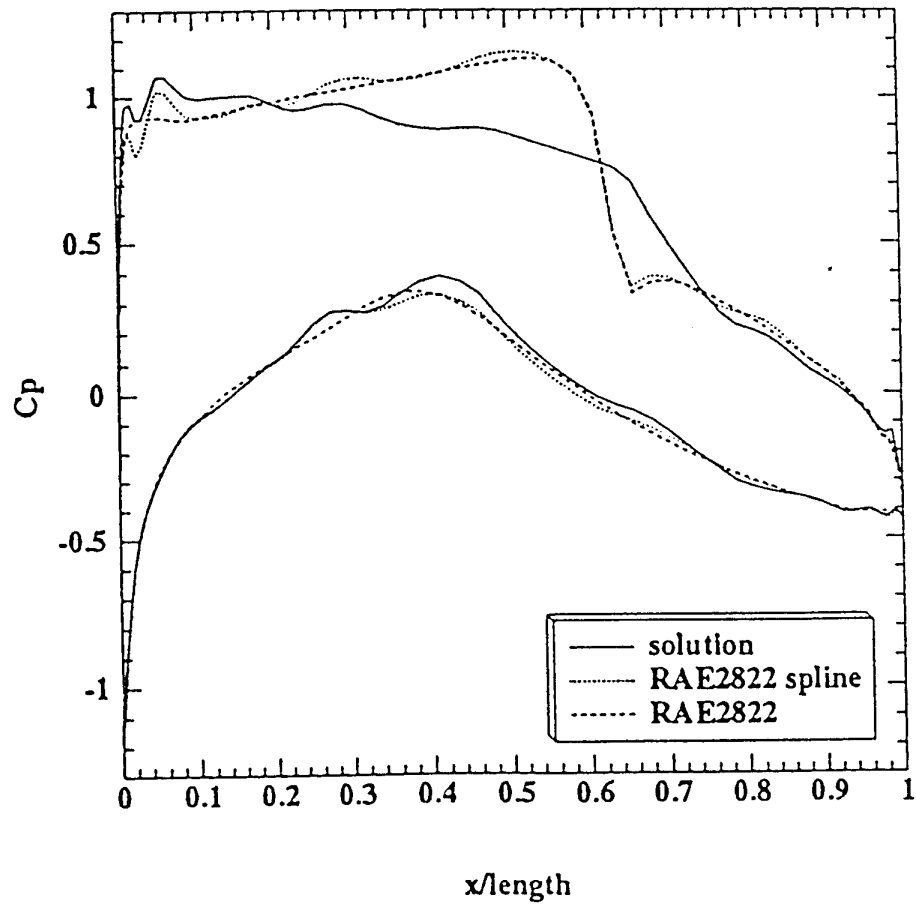


Fig.5. Drag minimization,  $M_\infty = 0.73$ , angle of attack =  $2^\circ$ , initial airfoil RAE2822.  
initial and final  $C_p$  for beta = 250

(courtesy of INRIA)

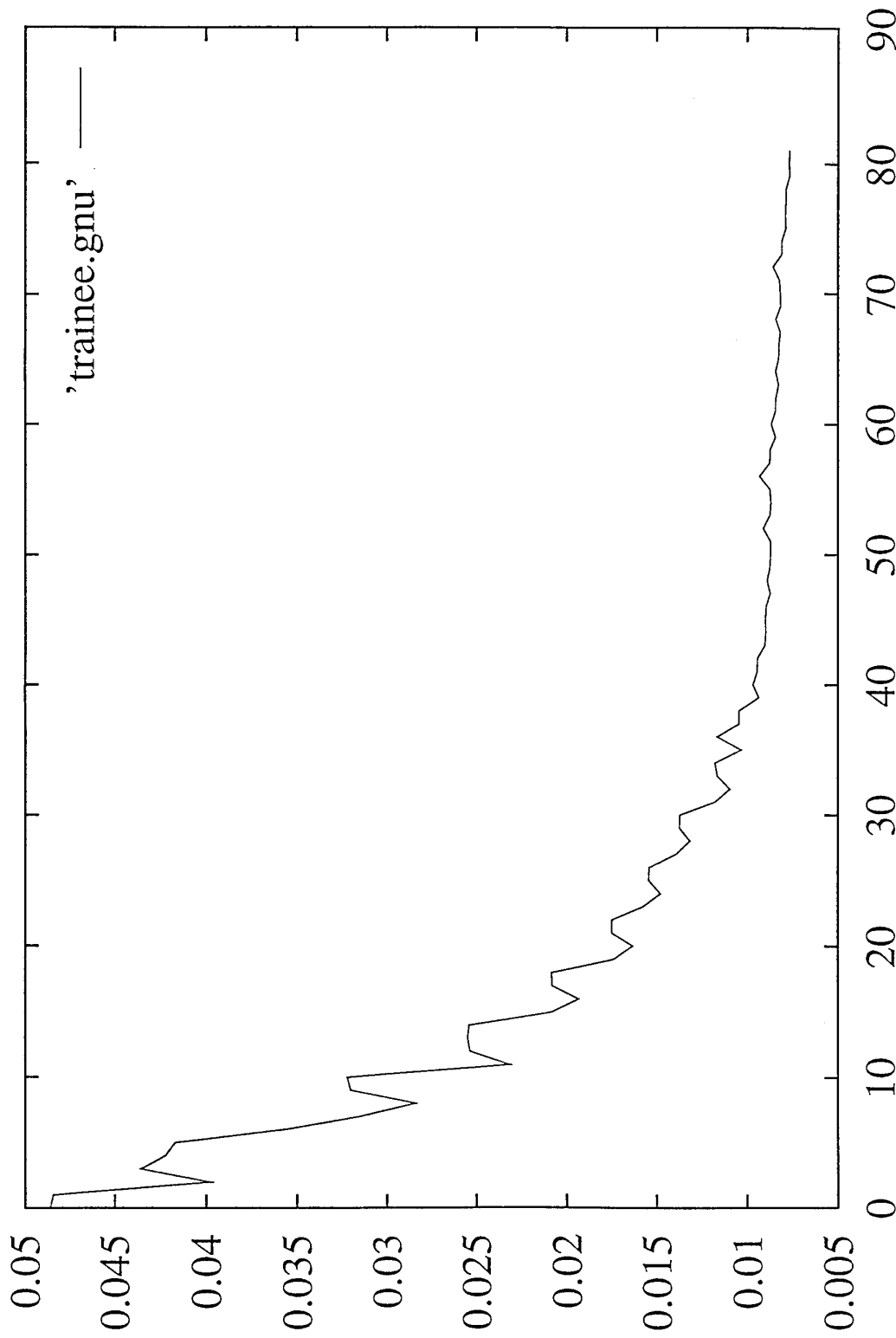


Figure 5A Minimization of drag from RAE2822 ( $M=0.73$ ,  $\alpha=2^\circ$ ) with first order Euler.  
History of total cost function

(courtesy of Dassault Aviation)

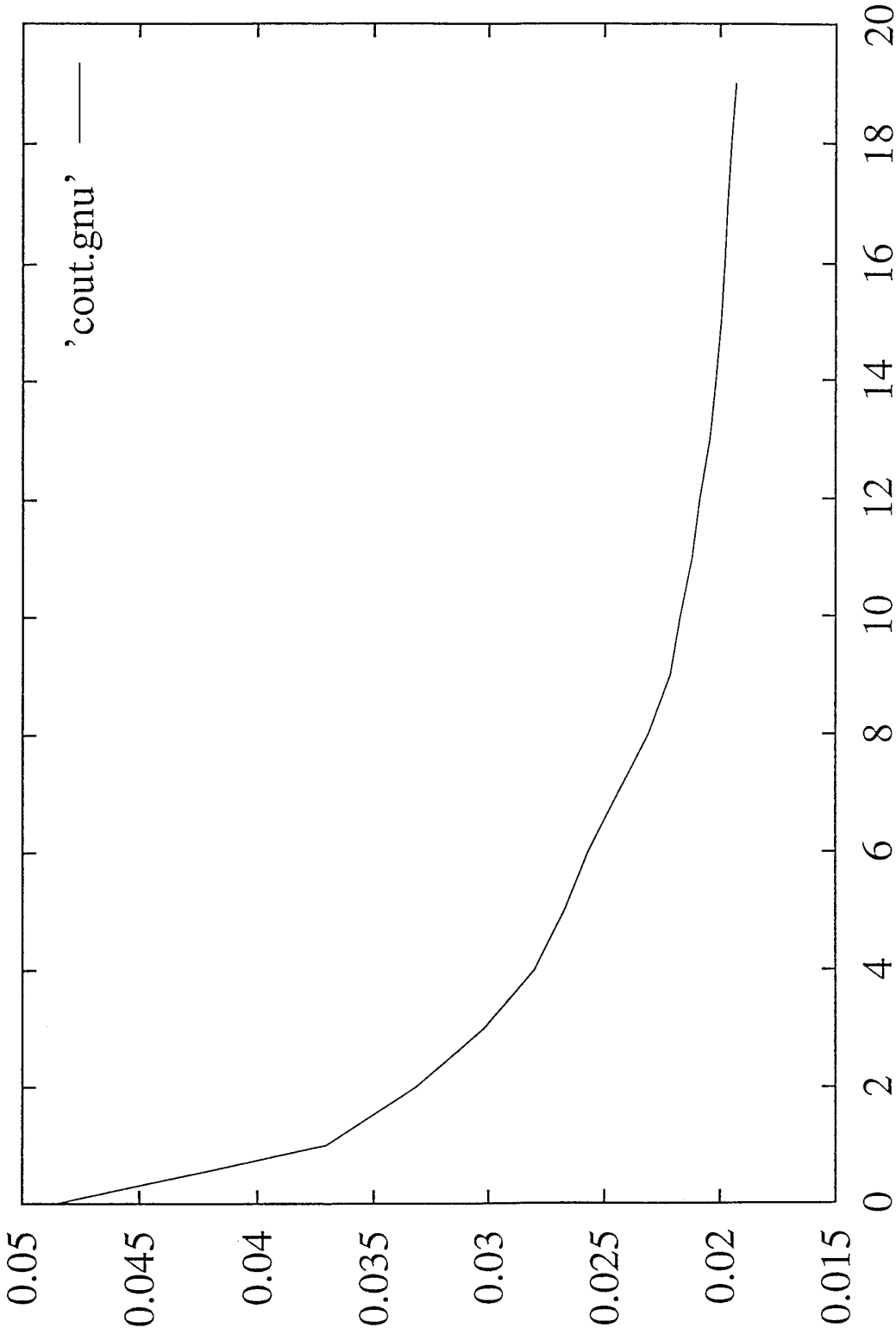


Figure 5B Minimization of drag from RAE2822 ( $M=0.73$ ,  $\alpha=2^\circ$ ) with first order Euler.  
History of drag value

(courtesy of Dassault Aviation)

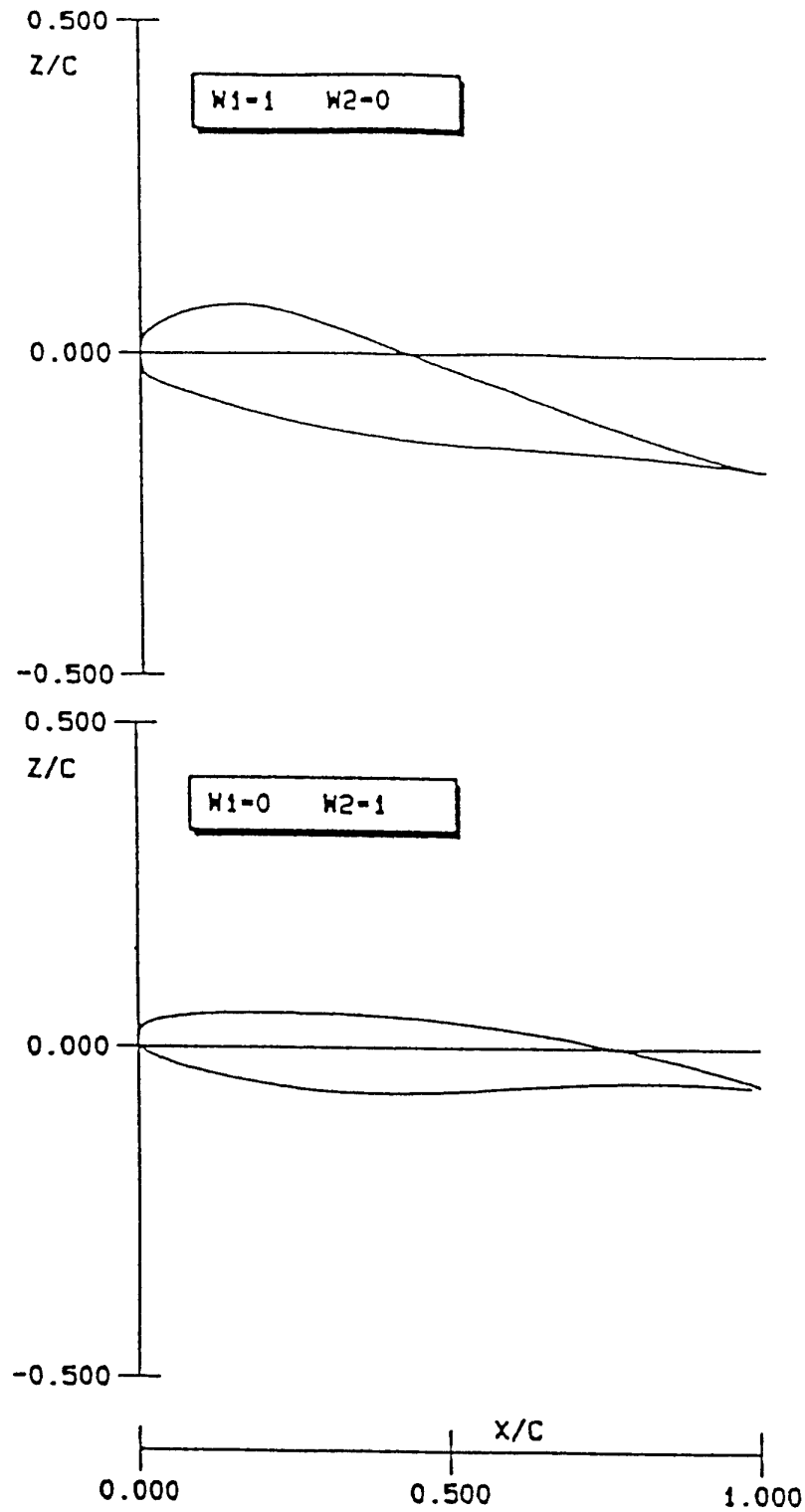


Fig.6. Two point airfoil design with 2 different weight factor combinations; geometry

(courtesy of NLR)

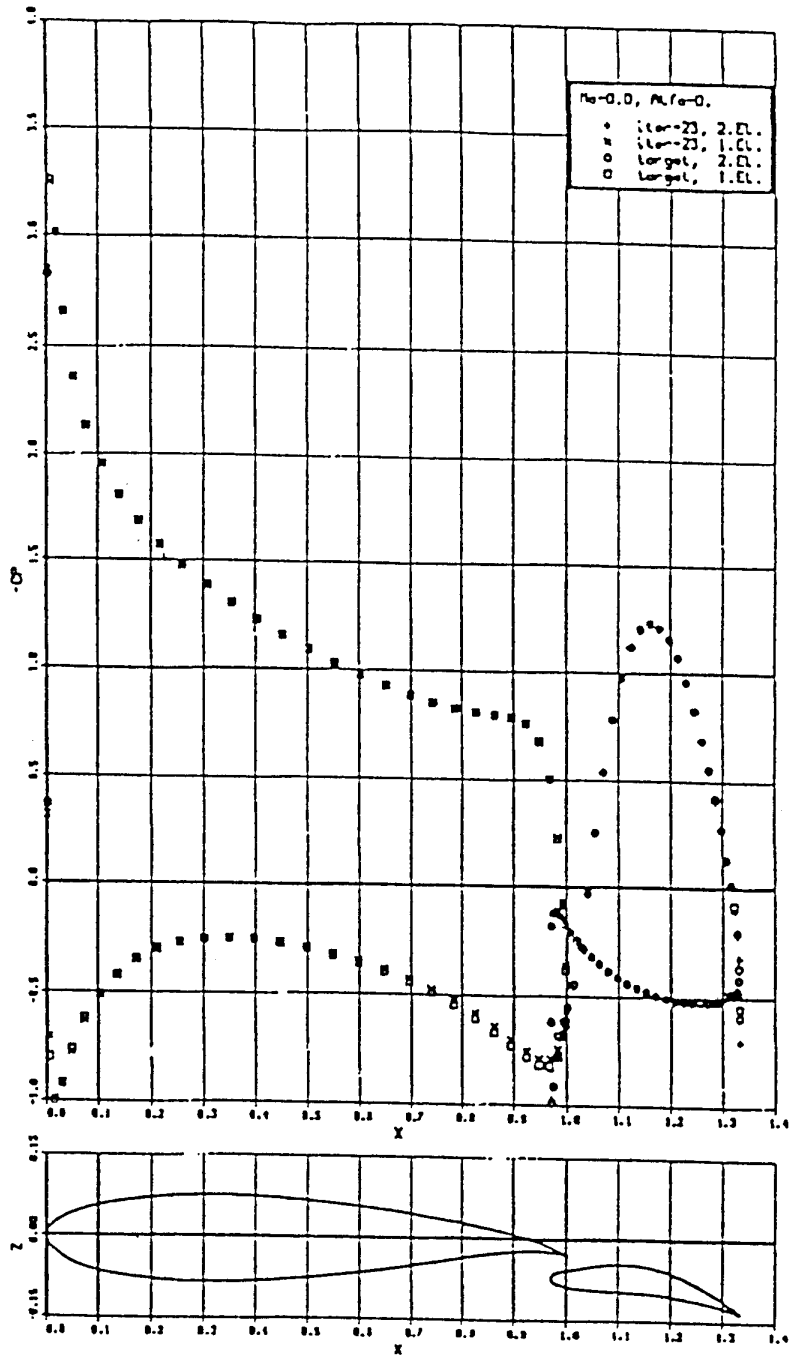


Fig.7. Converged state

(courtesy of Deutsche Airbus)

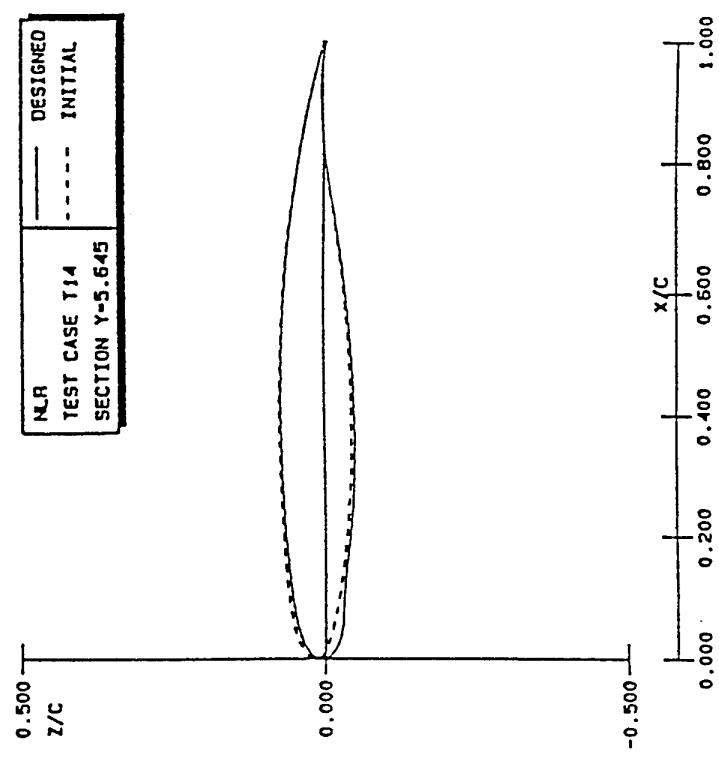
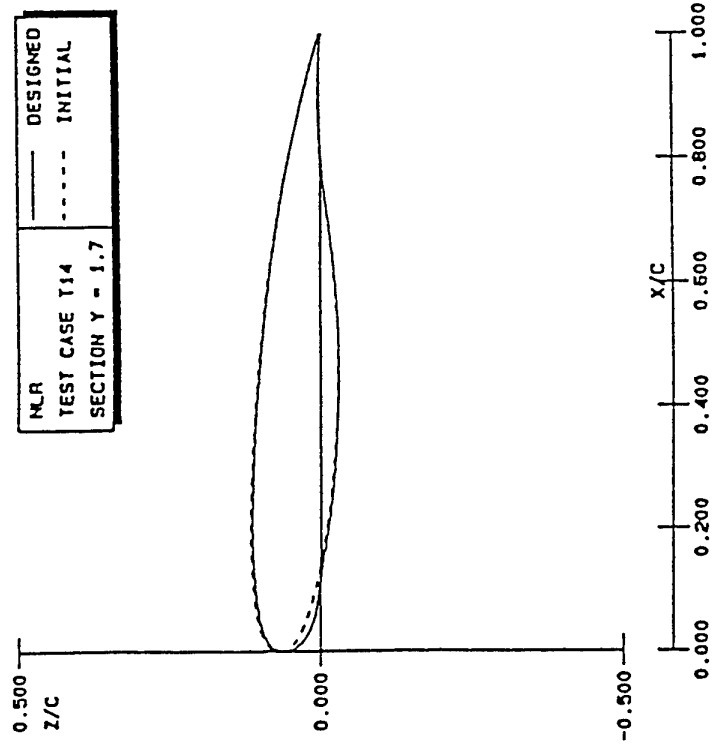


Fig.8. Wing design : initial and resulting geometry

(courtesy of NLR)

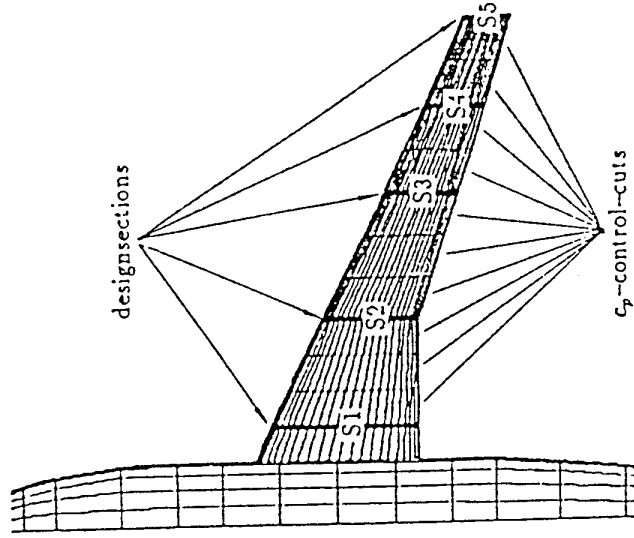
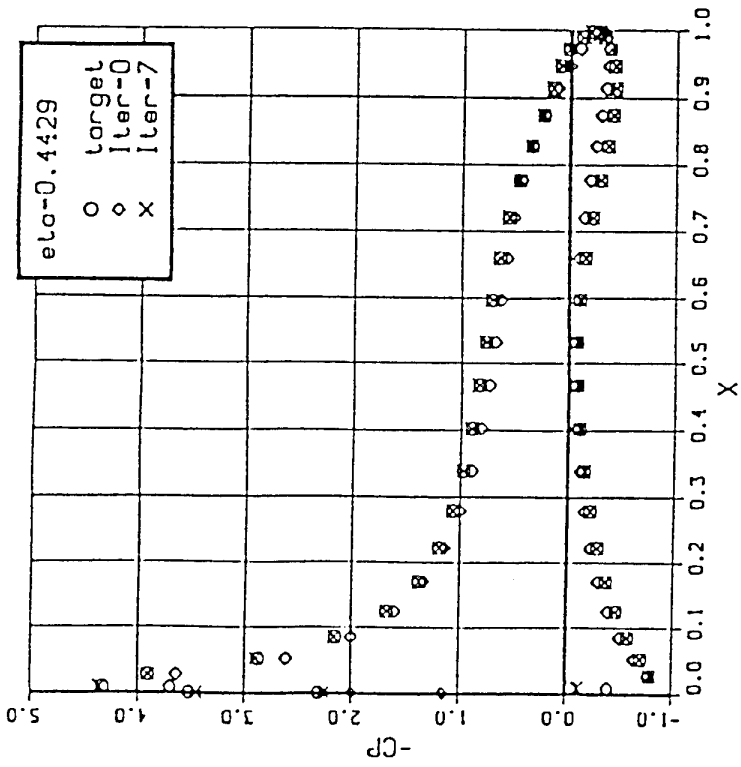
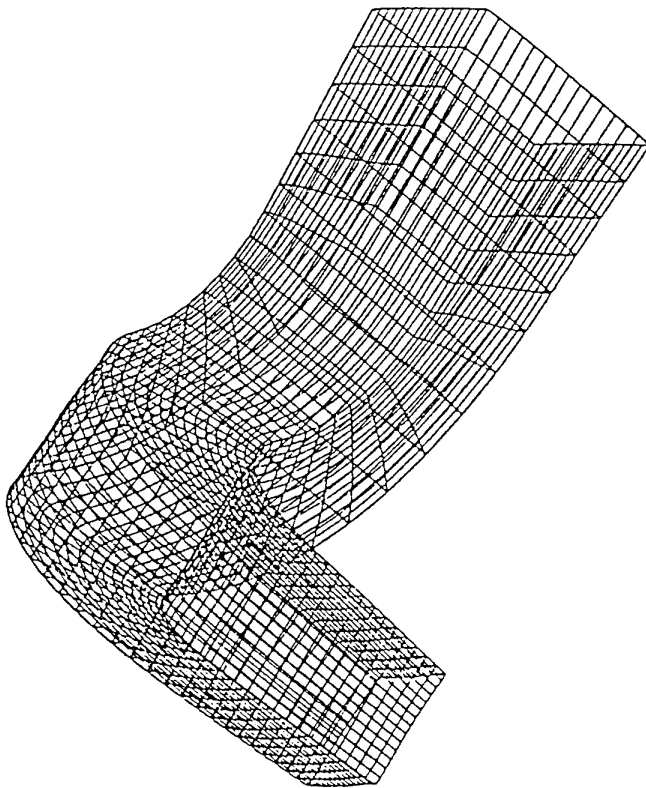
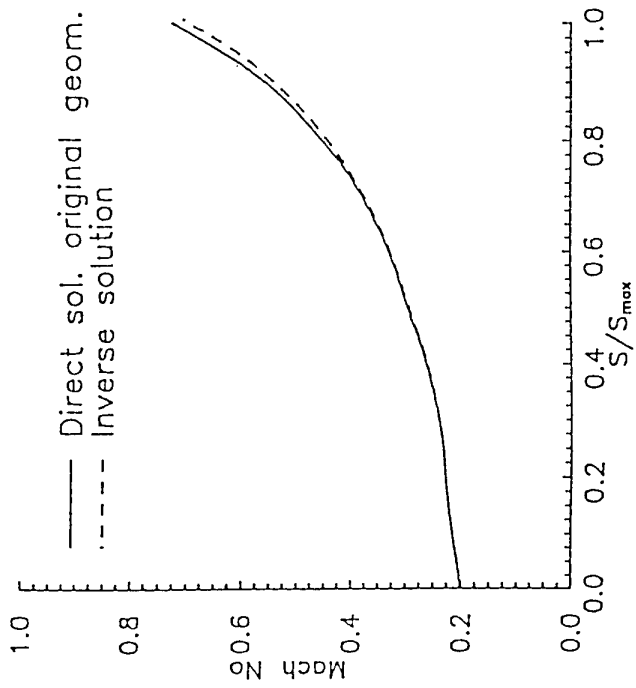


Fig.9. Comparison of initial, target and converged pressure distributions at inner station

(courtesy of Deutsche Airbus)



Views of the reproduced 3D nozzle : perspective view



Mach number distribution of inverse (---) and direct (—) calculations along the 3D nozzle center-line

Fig.10.

(courtesy of NTUA)

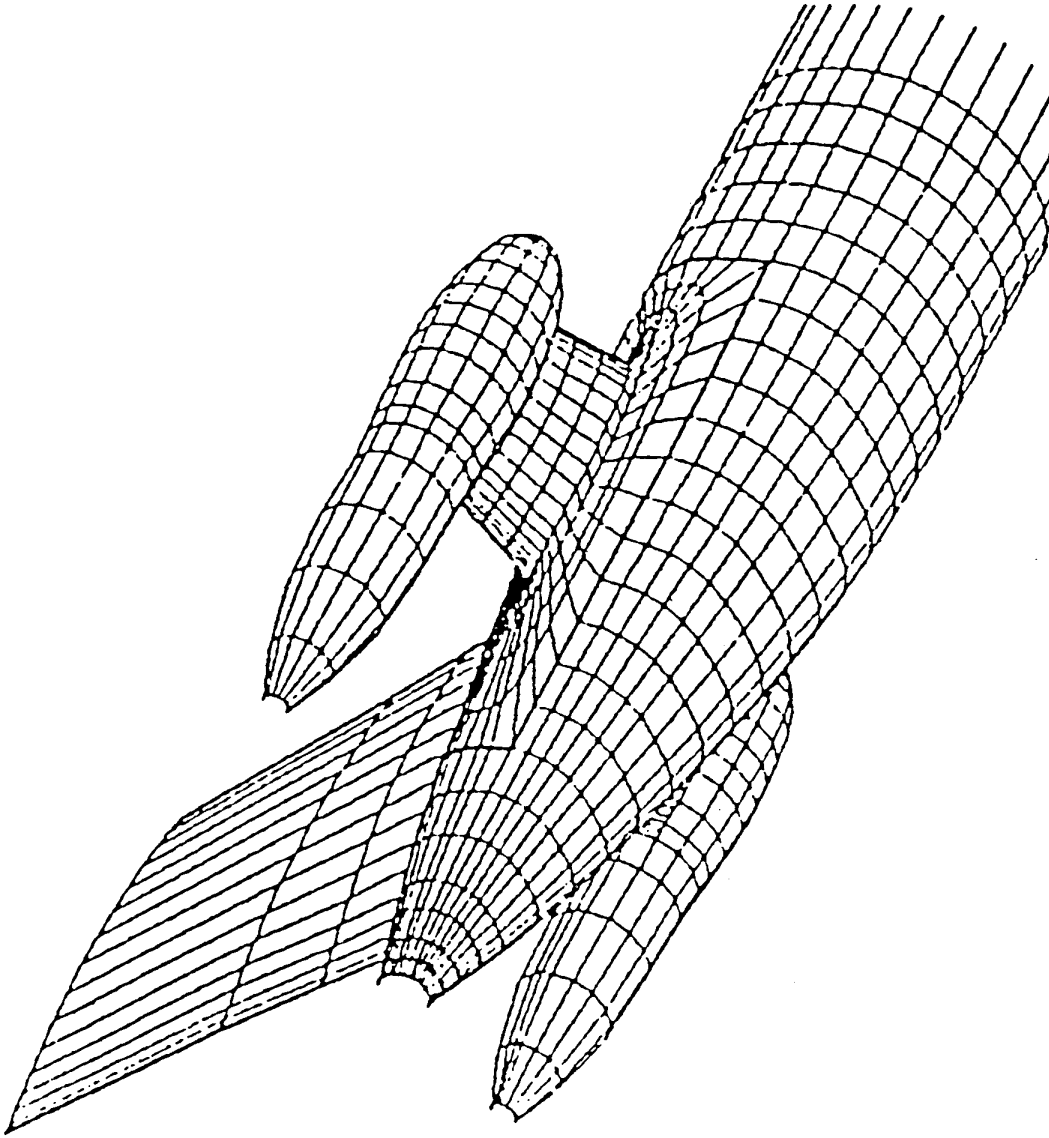


**Fig.11. Design of fuselage rear part**

(courtesy of Deutsche Airbus)

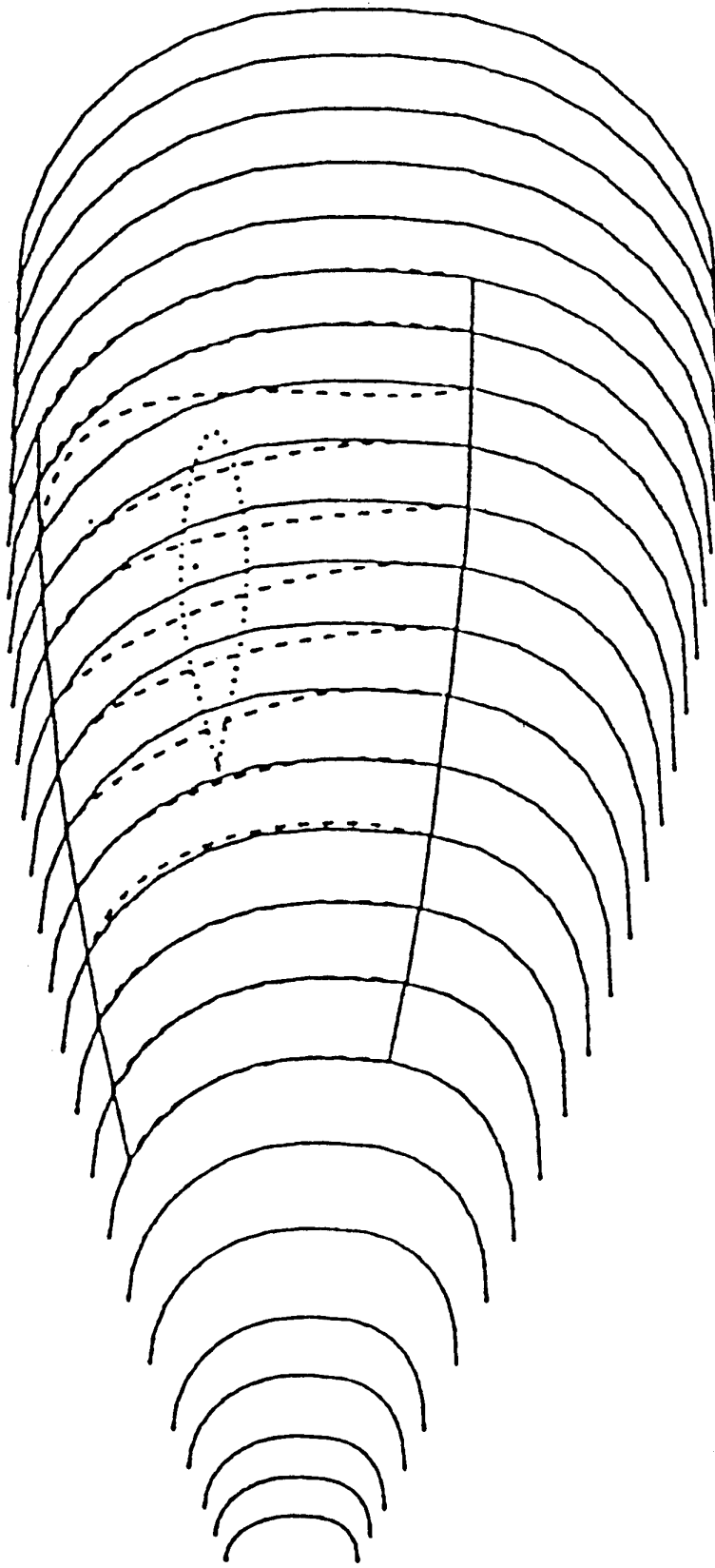


Fig.12. Comparison of initial and designed body patch

(courtesy of Deutsche Airbus)

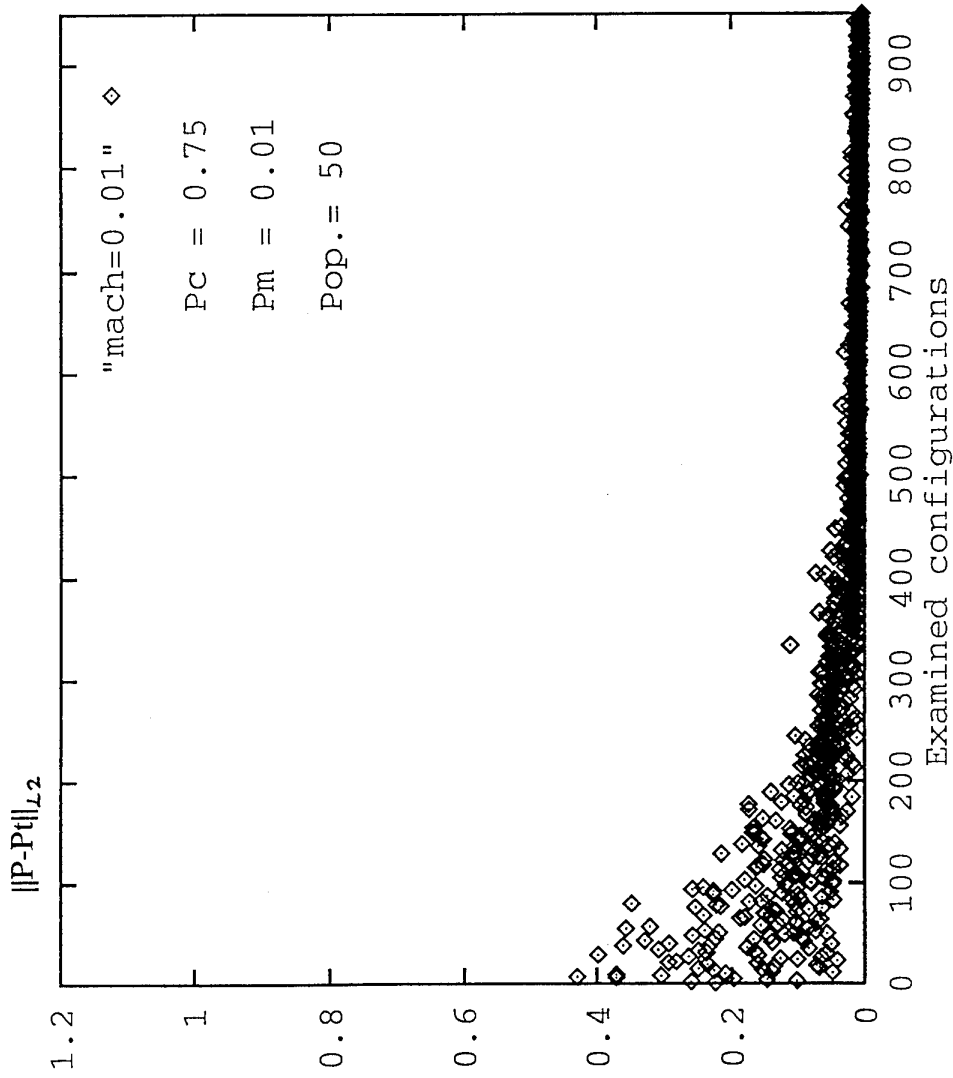


Figure GA-1 Fitness Function M = 0.01

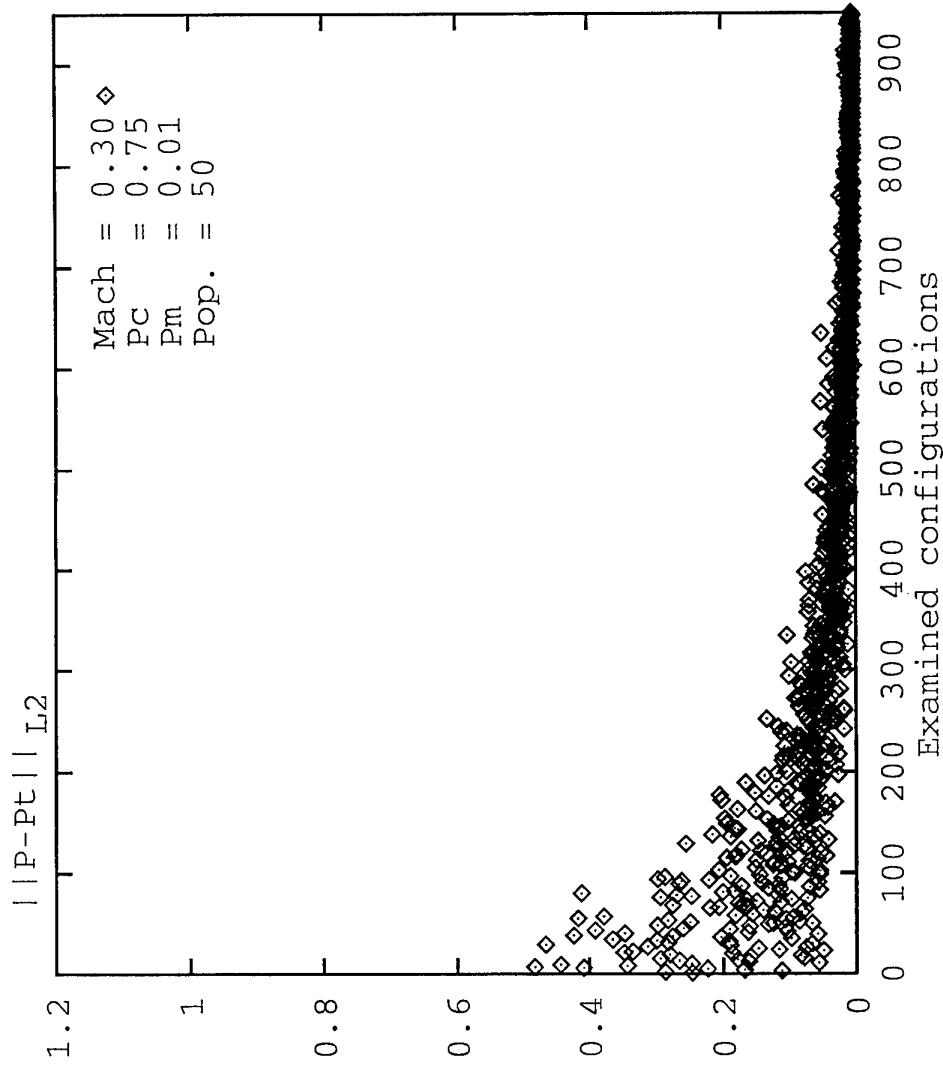


Figure GA-2 Fitness Function M = 0.3

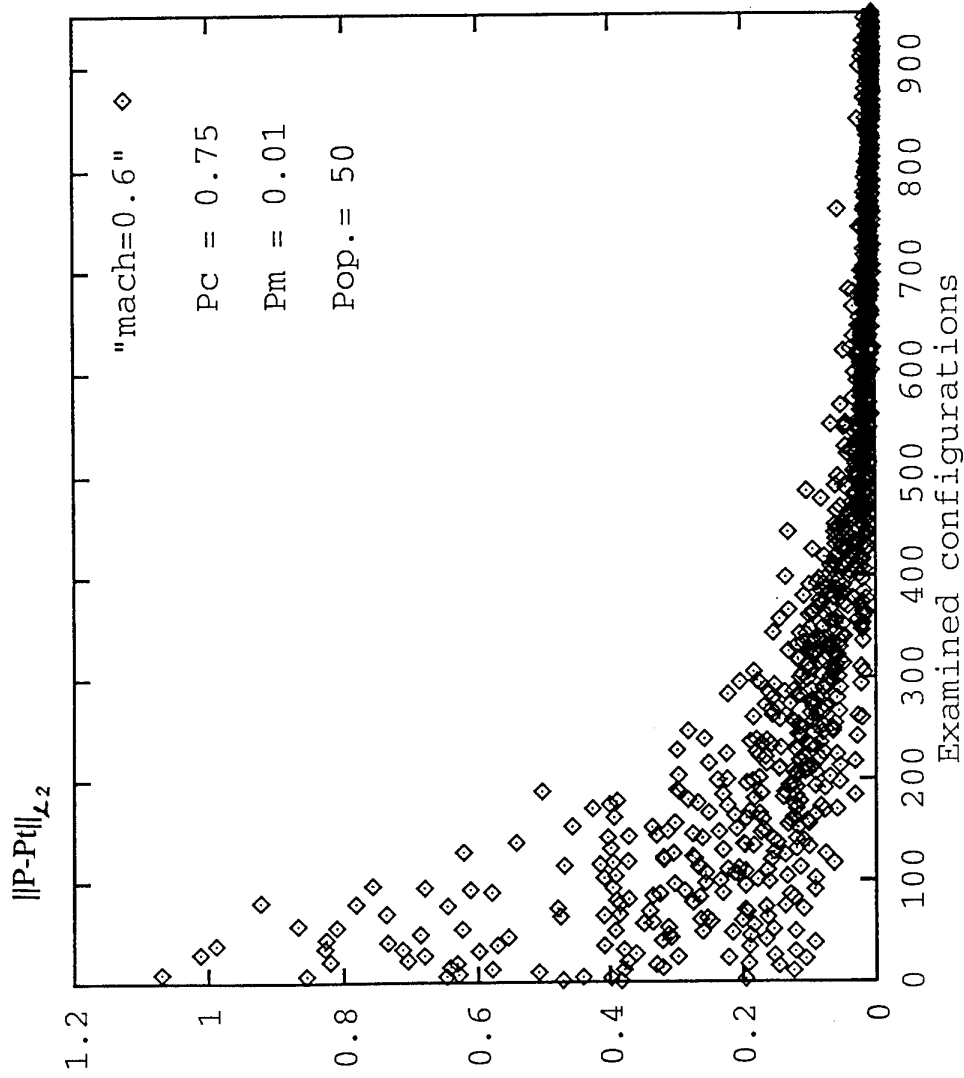


Figure GA-3 Fitness Function M = 0.6

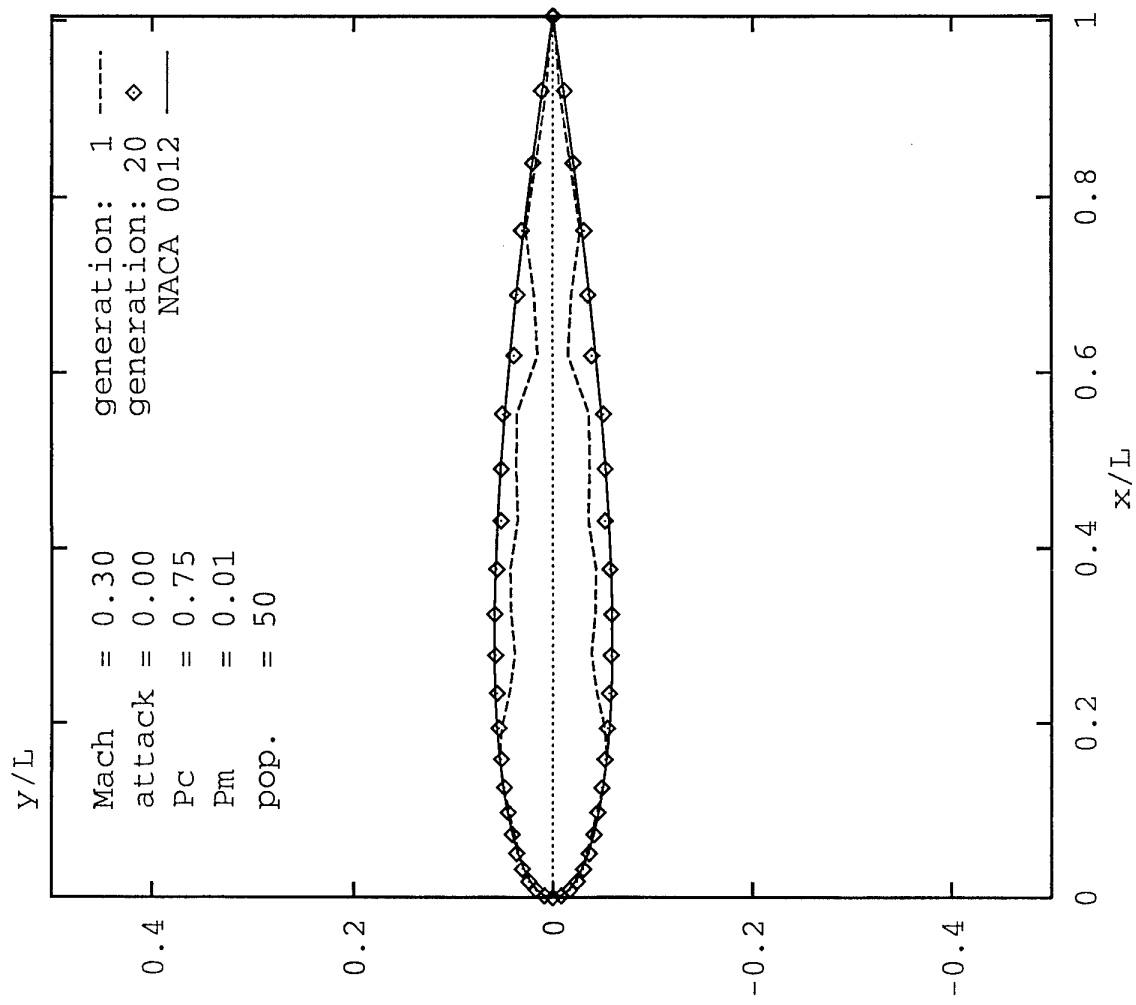


Figure GA-4 Shape Convergence for M = 0.3

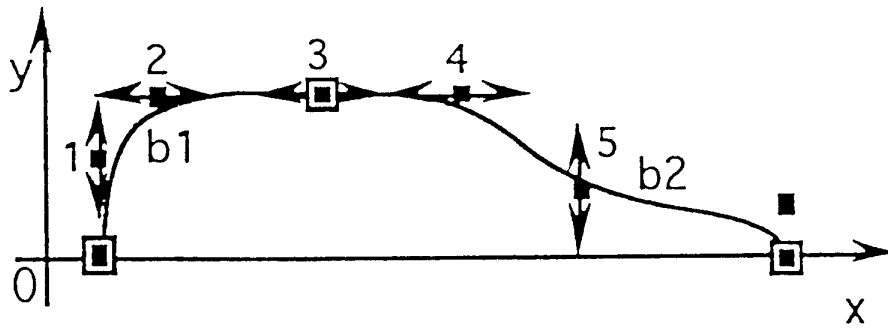


Figure GA-5 Parametric definition of the geometry in the case of the symmetric cascade

(Courtesy of Univ. of Trieste)

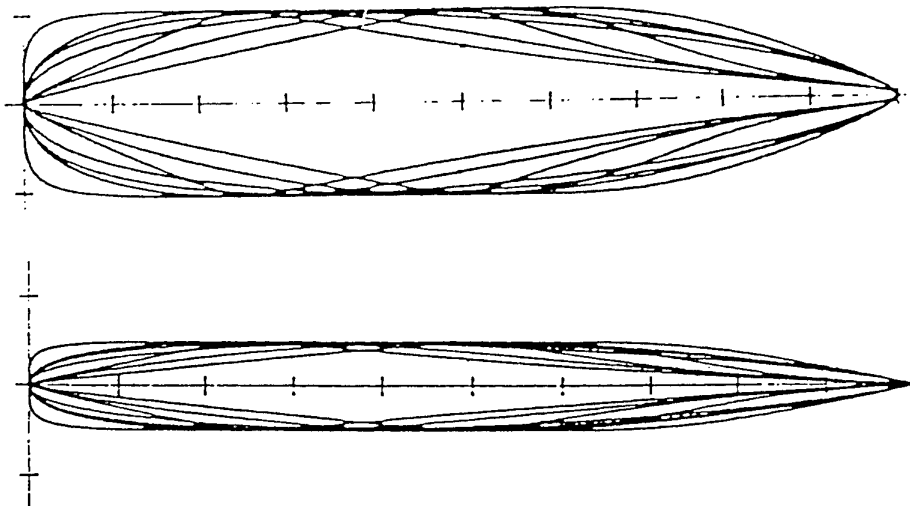
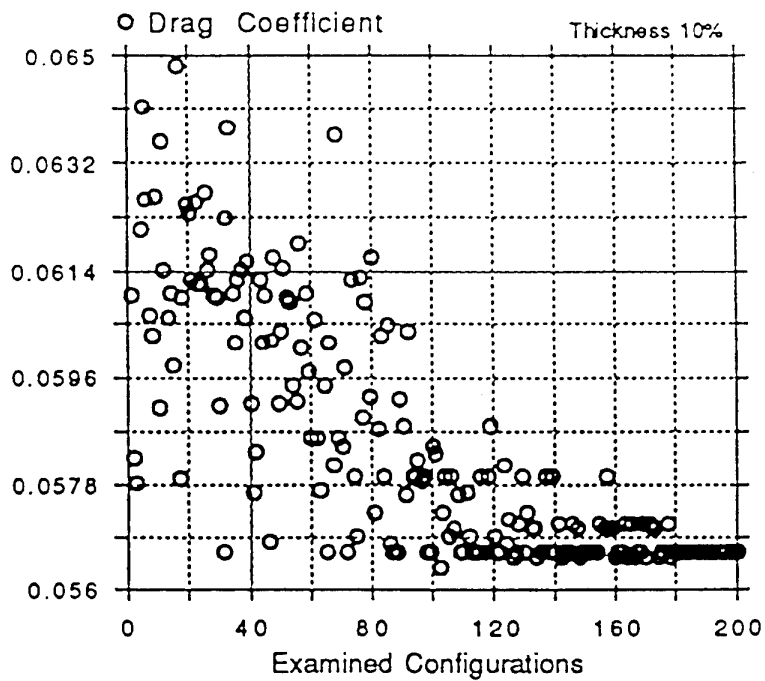
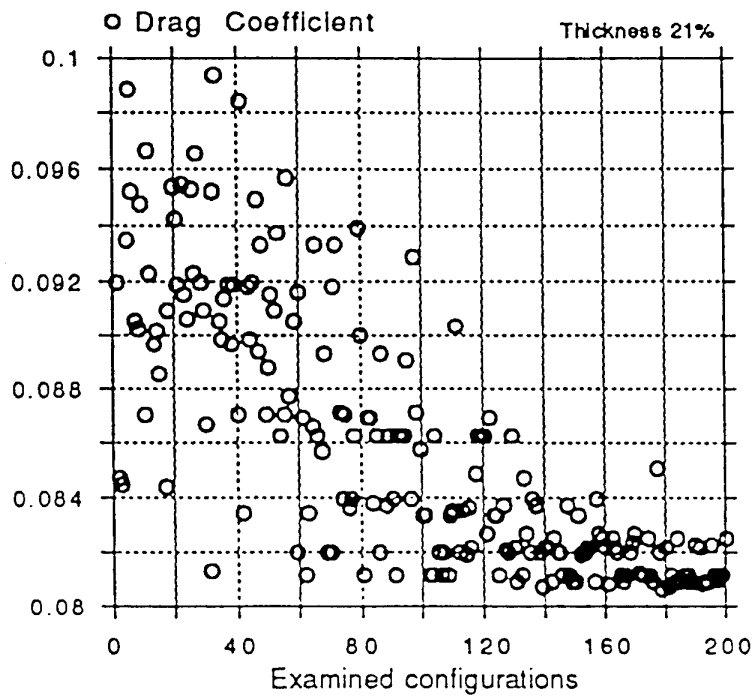


Figure GA-6 Profile shape for the maximum and minimum value of the optimization variables.



(Courtesy of Univ. of Trieste)

Figure GA-7 Computed drag coefficient for all the geometry tested.

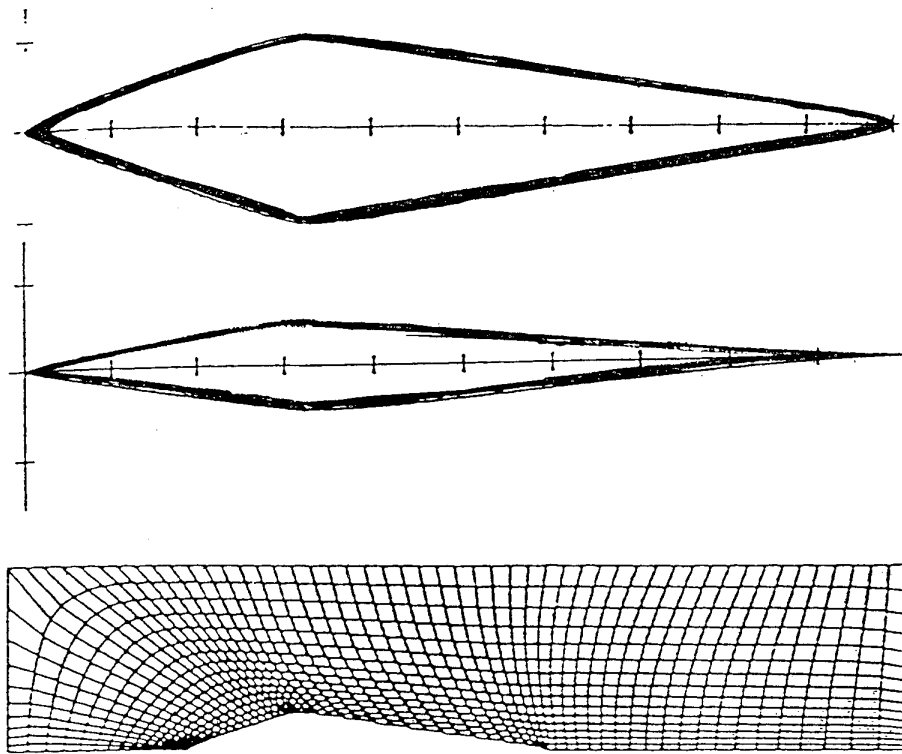


Figure GA-8 shows the typical mesh used in this computation and the shape of the optimum profile found for the two thickness considered.

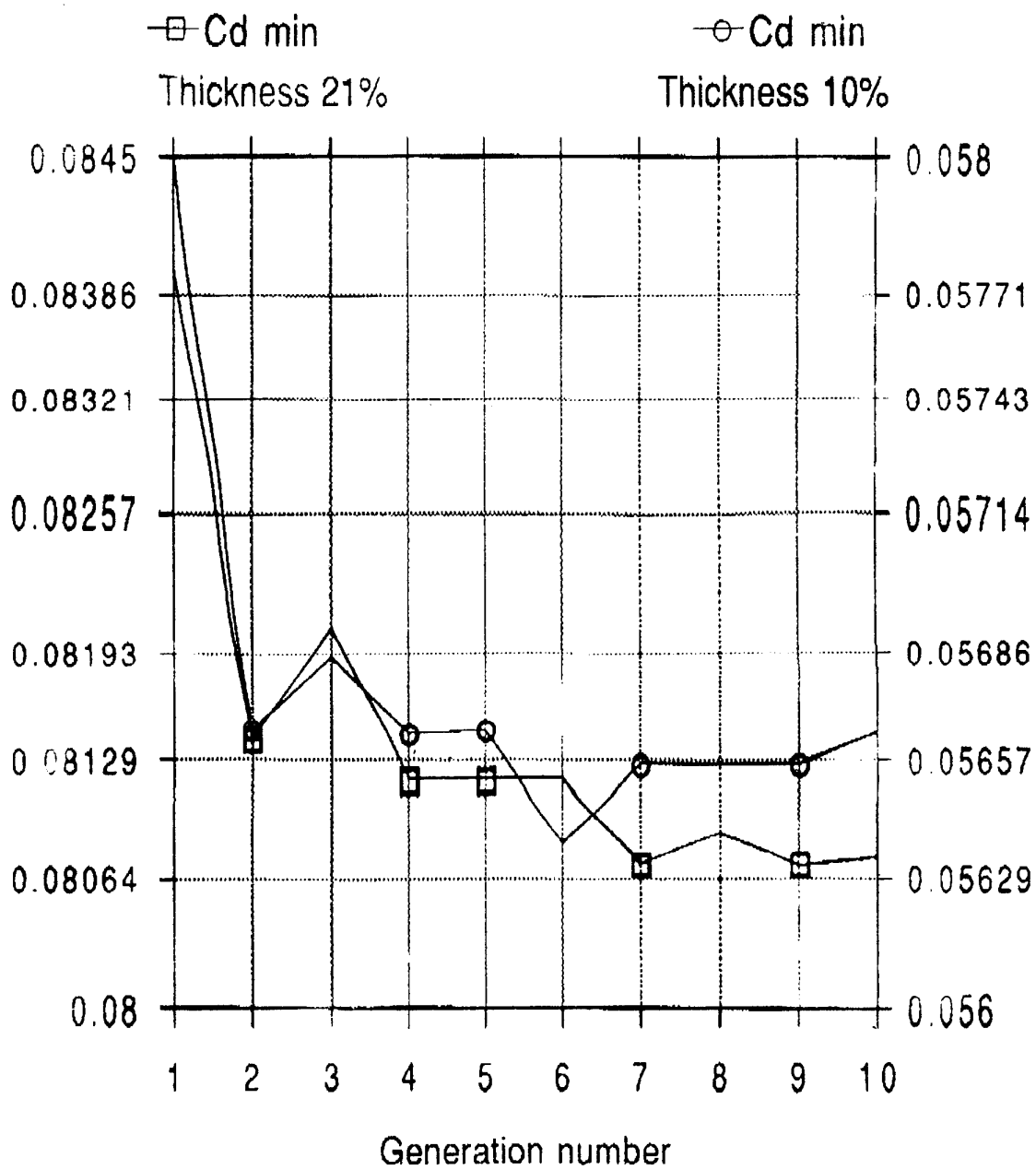


Figure GA-9 Drag of the Best Individual in the Generation  
(Courtesy of Univ. of Trieste)

**REPORT DOCUMENTATION PAGE**

<b>1. Recipient's Reference</b>	<b>2. Originator's Reference</b> AGARD-R-803	<b>3. Further Reference</b> ISBN 92-836-1007-5	<b>4. Security Classification of Document</b> UNCLASSIFIED						
<b>5. Originator</b>	Advisory Group for Aerospace Research and Development North Atlantic Treaty Organization 7 rue Ancelle, 92200 Neuilly-sur-Seine, France								
<b>6. Title</b>	Optimum Design Methods for Aerodynamics								
<b>7. Presented at</b>	An AGARD-FDP-VKI Special Course at the VKI, Rhode-Saint-Genèse, Belgium, 25-29 April 1994.								
<b>8. Author(s)/Editor(s)</b> Multiple			<b>9. Date</b> November 1994						
<b>10. Author's/Editor's Address</b> Multiple			<b>11. Pages</b> 280						
<b>12. Distribution Statement</b>	There are no restrictions on the distribution of this document. Information about the availability of this and other AGARD unclassified publications is given on the back cover.								
<b>13. Keywords/Descriptors</b>	<table> <tr> <td>Aerodynamics</td> <td>Optimization</td> </tr> <tr> <td>Wings</td> <td>Euler equations of motion</td> </tr> <tr> <td>Design</td> <td>Value engineering</td> </tr> </table>			Aerodynamics	Optimization	Wings	Euler equations of motion	Design	Value engineering
Aerodynamics	Optimization								
Wings	Euler equations of motion								
Design	Value engineering								
<b>14. Abstract</b>	<p>This volume is a compilation of the edited proceedings on the "Optimum Design Methods in Aerodynamics" course held at the von Karman Institute for Fluid Dynamics in Rhode-Saint-Genèse, Belgium, 25-29 April 1994.</p> <p>The course addresses the major ingredients of new algorithms for accurate and cost effective numerical solutions of design problems. A special emphasis is given to the following topics: fundamental mathematical properties of methodologies for solving optimization problems using control theory and variational formulations; numerical aspects of fast algorithms coupling constrained optimizers and flow analysis solvers and their implementation; geometric representations and choice of design variables; and real life 3-D applications encountered in Aerospace Engineering in order to demonstrate the usefulness of these design methodologies to practical design problems.</p>								

<p>AGARD-R-803 Advisory Group for Aerospace Research and Development North Atlantic Treaty Organization OPTIMUM DESIGN METHODS FOR AERODYNAMICS Published November 1994 280 pages</p> <p>This volume is a compilation of the edited proceedings on the "Optimum Design Methods in Aerodynamics" course held at the von Karman Institute for Fluid Dynamics in Rhode-Saint-Genèse, Belgium, 25-29 April 1994.</p> <p>The course addresses the major ingredients of new algorithms for accurate and cost effective numerical solutions of design problems. A special emphasis is given to the following topics: fundamental mathematical properties of methodologies for solving optimization problems using control theory and variational</p>	<p>AGARD-R-803 Advisory Group for Aerospace Research and Development North Atlantic Treaty Organization OPTIMUM DESIGN METHODS FOR AERODYNAMICS Published November 1994 280 pages</p> <p>This volume is a compilation of the edited proceedings on the "Optimum Design Methods in Aerodynamics" course held at the von Karman Institute for Fluid Dynamics in Rhode-Saint-Genèse, Belgium, 25-29 April 1994.</p> <p>The course addresses the major ingredients of new algorithms for accurate and cost effective numerical solutions of design problems. A special emphasis is given to the following topics: fundamental mathematical properties of methodologies for solving optimization problems using control theory and variational</p>	<p>AGARD-R-803 Advisory Group for Aerospace Research and Development North Atlantic Treaty Organization OPTIMUM DESIGN METHODS FOR AERODYNAMICS Published November 1994 280 pages</p> <p>This volume is a compilation of the edited proceedings on the "Optimum Design Methods in Aerodynamics" course held at the von Karman Institute for Fluid Dynamics in Rhode-Saint-Genèse, Belgium, 25-29 April 1994.</p> <p>The course addresses the major ingredients of new algorithms for accurate and cost effective numerical solutions of design problems. A special emphasis is given to the following topics: fundamental mathematical properties of methodologies for solving optimization problems using control theory and variational</p>	<p>AGARD-R-803 Advisory Group for Aerospace Research and Development North Atlantic Treaty Organization OPTIMUM DESIGN METHODS FOR AERODYNAMICS Published November 1994 280 pages</p> <p>This volume is a compilation of the edited proceedings on the "Optimum Design Methods in Aerodynamics" course held at the von Karman Institute for Fluid Dynamics in Rhode-Saint-Genèse, Belgium, 25-29 April 1994.</p> <p>The course addresses the major ingredients of new algorithms for accurate and cost effective numerical solutions of design problems. A special emphasis is given to the following topics: fundamental mathematical properties of methodologies for solving optimization problems using control theory and variational</p>
<p>AGARD-R-803 Advisory Group for Aerospace Research and Development North Atlantic Treaty Organization OPTIMUM DESIGN METHODS FOR AERODYNAMICS Published November 1994 280 pages</p> <p>This volume is a compilation of the edited proceedings on the "Optimum Design Methods in Aerodynamics" course held at the von Karman Institute for Fluid Dynamics in Rhode-Saint-Genèse, Belgium, 25-29 April 1994.</p> <p>The course addresses the major ingredients of new algorithms for accurate and cost effective numerical solutions of design problems. A special emphasis is given to the following topics: fundamental mathematical properties of methodologies for solving optimization problems using control theory and variational</p>	<p>AGARD-R-803 Advisory Group for Aerospace Research and Development North Atlantic Treaty Organization OPTIMUM DESIGN METHODS FOR AERODYNAMICS Published November 1994 280 pages</p> <p>This volume is a compilation of the edited proceedings on the "Optimum Design Methods in Aerodynamics" course held at the von Karman Institute for Fluid Dynamics in Rhode-Saint-Genèse, Belgium, 25-29 April 1994.</p> <p>The course addresses the major ingredients of new algorithms for accurate and cost effective numerical solutions of design problems. A special emphasis is given to the following topics: fundamental mathematical properties of methodologies for solving optimization problems using control theory and variational</p>	<p>AGARD-R-803 Advisory Group for Aerospace Research and Development North Atlantic Treaty Organization OPTIMUM DESIGN METHODS FOR AERODYNAMICS Published November 1994 280 pages</p> <p>This volume is a compilation of the edited proceedings on the "Optimum Design Methods in Aerodynamics" course held at the von Karman Institute for Fluid Dynamics in Rhode-Saint-Genèse, Belgium, 25-29 April 1994.</p> <p>The course addresses the major ingredients of new algorithms for accurate and cost effective numerical solutions of design problems. A special emphasis is given to the following topics: fundamental mathematical properties of methodologies for solving optimization problems using control theory and variational</p>	<p>AGARD-R-803 Advisory Group for Aerospace Research and Development North Atlantic Treaty Organization OPTIMUM DESIGN METHODS FOR AERODYNAMICS Published November 1994 280 pages</p> <p>This volume is a compilation of the edited proceedings on the "Optimum Design Methods in Aerodynamics" course held at the von Karman Institute for Fluid Dynamics in Rhode-Saint-Genèse, Belgium, 25-29 April 1994.</p> <p>The course addresses the major ingredients of new algorithms for accurate and cost effective numerical solutions of design problems. A special emphasis is given to the following topics: fundamental mathematical properties of methodologies for solving optimization problems using control theory and variational</p>

formulations; numerical aspects of fast algorithms coupling constrained optimizers and flow analysis solvers and their implementation; geometric representations and choice of design variables; and real life 3-D applications encountered in Aerospace Engineering in order to demonstrate the usefulness of these design methodologies to practical design problems.

ISBN 92-836-1007-5

formulations; numerical aspects of fast algorithms coupling constrained optimizers and flow analysis solvers and their implementation; geometric representations and choice of design variables; and real life 3-D applications encountered in Aerospace Engineering in order to demonstrate the usefulness of these design methodologies to practical design problems.

ISBN 92-836-1007-5

formulations; numerical aspects of fast algorithms coupling constrained optimizers and flow analysis solvers and their implementation; geometric representations and choice of design variables; and real life 3-D applications encountered in Aerospace Engineering in order to demonstrate the usefulness of these design methodologies to practical design problems.

ISBN 92-836-1007-5

formulations; numerical aspects of fast algorithms coupling constrained optimizers and flow analysis solvers and their implementation; geometric representations and choice of design variables; and real life 3-D applications encountered in Aerospace Engineering in order to demonstrate the usefulness of these design methodologies to practical design problems.

ISBN 92-836-1007-5

Aucun stock de publications n'a existé à AGARD. A partir de 1993, AGARD détiendra un stock limité des publications associées aux cycles de conférences et cours spéciaux ainsi que les AGARDographies et les rapports des groupes de travail, organisés et publiés à partir de 1993 inclus. Les demandes de renseignements doivent être adressées à AGARD par lettre ou par fax à l'adresse indiquée ci-dessus. *Veuillez ne pas téléphoner.* La diffusion initiale de toutes les publications de l'AGARD est effectuée auprès des pays membres de l'OTAN par l'intermédiaire des centres de distribution nationaux indiqués ci-dessous. Des exemplaires supplémentaires peuvent parfois être obtenus auprès de ces centres (à l'exception des Etats-Unis). Si vous souhaitez recevoir toutes les publications de l'AGARD, ou simplement celles qui concernent certains Panels, vous pouvez demander à être inclu sur la liste d'envoi de l'un de ces centres. Les publications de l'AGARD sont en vente auprès des agences indiquées ci-dessous, sous forme de photocopie ou de microfiche.

CENTRES DE DIFFUSION NATIONAUX

## ALLEMAGNE

Fachinformationszentrum,  
Karlsruhe  
D-76344 Eggenstein-Leopoldshafen 2

## BELGIQUE

Coordonnateur AGARD-VSL  
Etat-major de la Force aérienne  
Quartier Reine Elisabeth  
Rue d'Evere, 1140 Bruxelles

## CANADA

Directeur, Services d'information scientifique  
Ministère de la Défense nationale  
Ottawa, Ontario K1A 0K2

## DANEMARK

Danish Defence Research Establishment  
Ryvangs Allé 1  
P.O. Box 2715  
DK-2100 Copenhagen Ø

## ESPAGNE

INTA (AGARD Publications)  
Pintor Rosales 34  
28008 Madrid

## ETATS-UNIS

NASA Headquarters  
Code JOB-1  
Washington, D.C. 20546

## FRANCE

O.N.E.R.A. (Direction)  
29, Avenue de la Division Leclerc  
92322 Châtillon Cedex

## GRECE

Hellenic Air Force  
Air War College  
Scientific and Technical Library  
Dekelia Air Force Base  
Dekelia, Athens TGA 1010

## ISLANDE

Director of Aviation  
c/o Flugrad  
Reykjavik

## ITALIE

Aeronautica Militare  
Ufficio del Delegato Nazionale all'AGARD  
Aeroporto Pratica di Mare  
00040 Pomezia (Roma)

## LUXEMBOURG

Voir Belgique

## NORVEGE

Norwegian Defence Research Establishment  
Attn: Biblioteket  
P.O. Box 25  
N-2007 Kjeller

## PAYS-BAS

Netherlands Delegation to AGARD  
National Aerospace Laboratory NLR  
P.O. Box 90502  
1006 BM Amsterdam

## PORTUGAL

Força Aérea Portuguesa  
Centro de Documentação e Informação  
Alfragide  
2700 Amadora

## ROYAUME-UNI

Defence Research Information Centre  
Kentigern House  
65 Brown Street  
Glasgow G2 8EX

## TURQUIE

Millî Savunma Başkanlığı (MSB)  
ARGE Dairesi Başkanlığı (MSB)  
06650 Bakanliklar-Ankara

**Le centre de distribution national des Etats-Unis ne détient PAS de stocks des publications de l'AGARD.**

D'éventuelles demandes de photocopies doivent être formulées directement auprès du NASA Center for AeroSpace Information (CASI) à l'adresse ci-dessous. Toute notification de changement d'adresse doit être fait également auprès de CASI.

AGENCES DE VENTE

NASA Center for  
AeroSpace Information (CASI)  
800 Elkridge Landing Road  
Linthicum Heights, MD 21090-2934  
Etats-Unis

ESA/Information Retrieval Service  
European Space Agency  
10, rue Mario Nikis  
75015 Paris  
France

The British Library  
Document Supply Division  
Boston Spa, Wetherby  
West Yorkshire LS23 7BQ  
Royaume-Uni

Les demandes de microfiches ou de photocopies de documents AGARD (y compris les demandes faites auprès du CASI) doivent comporter la dénomination AGARD, ainsi que le numéro de série d'AGARD (par exemple AGARD-AG-315). Des informations analogues, telles que le titre et la date de publication sont souhaitables. Veuillez noter qu'il y a lieu de spécifier AGARD-R-nnn et AGARD-AR-nnn lors de la commande des rapports AGARD et des rapports consultatifs AGARD respectivement. Des références bibliographiques complètes ainsi que des résumés des publications AGARD figurent dans les journaux suivants:

Scientific and Technical Aerospace Reports (STAR)  
publié par la NASA Scientific and Technical  
Information Division  
NASA Headquarters (JTT)  
Washington D.C. 20546  
Etats-Unis

Government Reports Announcements and Index (GRA&I)  
publié par le National Technical Information Service  
Springfield  
Virginia 22161  
Etats-Unis  
(accessible également en mode interactif dans la base de  
données bibliographiques en ligne du NTIS, et sur CD-ROM)



AGARD holds limited quantities of the publications that accompanied Lecture Series and Special Courses held in 1993 or later, and of AGARDographs and Working Group reports published from 1993 onward. For details, write or send a telefax to the address given above. *Please do not telephone.*

AGARD does not hold stocks of publications that accompanied earlier Lecture Series or Courses or of any other publications. Initial distribution of all AGARD publications is made to NATO nations through the National Distribution Centres listed below. Further copies are sometimes available from these centres (except in the United States). If you have a need to receive all AGARD publications, or just those relating to one or more specific AGARD Panels, they may be willing to include you (or your organisation) on their distribution list. AGARD publications may be purchased from the Sales Agencies listed below, in photocopy or microfiche form.

NATIONAL DISTRIBUTION CENTRES

- |  |  |
|--|--|
| <b>BELGIUM</b><br>Coordonnateur AGARD — VSL<br>Etat-major de la Force aérienne<br>Quartier Reine Elisabeth<br>Rue d'Evere, 1140 Bruxelles        | <b>LUXEMBOURG</b><br><i>See Belgium</i>  |
| <b>CANADA</b><br>Director Scientific Information Services<br>Dept of National Defence<br>Ottawa, Ontario K1A 0K2                                 | <b>NETHERLANDS</b><br>Netherlands Delegation to AGARD<br>National Aerospace Laboratory, NLR<br>P.O. Box 90502<br>1006 BM Amsterdam |
| <b>DENMARK</b><br>Danish Defence Research Establishment<br>Ryvangs Allé 1<br>P.O. Box 2715<br>DK-2100 Copenhagen Ø                               | <b>NORWAY</b><br>Norwegian Defence Research Establishment<br>Attn: Biblioteket<br>P.O. Box 25<br>N-2007 Kjeller                    |
| <b>FRANCE</b><br>O.N.E.R.A. (Direction)<br>29 Avenue de la Division Leclerc<br>92322 Châtillon Cedex   | <b>PORTUGAL</b><br>Força Aérea Portuguesa<br>Centro de Documentação e Informação<br>Alfragide<br>2700 Amadora                      |
| <b>GERMANY</b><br>Fachinformationszentrum<br>Karlsruhe<br>D-76344 Eggenstein-Leopoldshafen 2   | <b>SPAIN</b><br>INTA (AGARD Publications)<br>Pintor Rosales 34<br>28008 Madrid   |
| <b>GREECE</b><br>Hellenic Air Force<br>Air War College<br>Scientific and Technical Library<br>Dekelia Air Force Base<br>Dekelia, Athens TGA 1010 | <b>TURKEY</b><br>Millî Savunma Başkanlığı (MSB)<br>ARGE Dairesi Başkanlığı (MSB)<br>06650 Bakanlıklar-Ankara                       |
| <b>ICELAND</b><br>Director of Aviation<br>c/o Flugrad<br>Reykjavik   | <b>UNITED KINGDOM</b><br>Defence Research Information Centre<br>Kentigern House<br>65 Brown Street<br>Glasgow G2 8EX               |
| <b>ITALY</b><br>Aeronautica Militare<br>Ufficio del Delegato Nazionale all'AGARD<br>Aeroporto Pratica di Mare<br>00040 Pomezia (Roma)            | <b>UNITED STATES</b><br>NASA Headquarters<br>Code JOB-1<br>Washington, D.C. 20546  |

**The United States National Distribution Centre does NOT hold stocks of AGARD publications.**

Applications for copies should be made direct to the NASA Center for AeroSpace Information (CASI) at the address below. Change of address requests should also go to CASI.

SALES AGENCIES

- |   |  |  |
|---|--|--|
| NASA Center for<br>AeroSpace Information (CASI)<br>800 Elkridge Landing Road<br>Linthicum Heights, MD 21090-2934<br>United States | ESA/Information Retrieval Service<br>European Space Agency<br>10, rue Mario Nikis<br>75015 Paris<br>France | The British Library<br>Document Supply Centre<br>Boston Spa, Wetherby<br>West Yorkshire LS23 7BQ<br>United Kingdom |
|---|--|--|

Requests for microfiches or photocopies of AGARD documents (including requests to CASI) should include the word 'AGARD' and the AGARD serial number (for example AGARD-AG-315). Collateral information such as title and publication date is desirable. Note that AGARD Reports and Advisory Reports should be specified as AGARD-R-nnn and AGARD-AR-nnn, respectively. Full bibliographical references and abstracts of AGARD publications are given in the following journals:

Scientific and Technical Aerospace Reports (STAR)  
published by NASA Scientific and Technical  
Information Division  
NASA Headquarters (JTT)  
Washington D.C. 20546  
United States

Government Reports Announcements and Index (GRA&I)  
published by the National Technical Information Service  
Springfield  
Virginia 22161  
United States  
(also available online in the NTIS Bibliographic  
Database or on CD-ROM)

